

ADVANCED CONCRETES AND THEIR STRUCTURAL APPLICATIONS

EDITED BY: Zhigang Zhang, Xijun Shi, Fangying Wang and Qian Zhang
PUBLISHED IN: Frontiers in Materials



frontiers

Frontiers eBook Copyright Statement

The copyright in the text of individual articles in this eBook is the property of their respective authors or their respective institutions or funders. The copyright in graphics and images within each article may be subject to copyright of other parties. In both cases this is subject to a license granted to Frontiers.

The compilation of articles constituting this eBook is the property of Frontiers.

Each article within this eBook, and the eBook itself, are published under the most recent version of the Creative Commons CC-BY licence.

The version current at the date of publication of this eBook is CC-BY 4.0. If the CC-BY licence is updated, the licence granted by Frontiers is automatically updated to the new version.

When exercising any right under the CC-BY licence, Frontiers must be attributed as the original publisher of the article or eBook, as applicable.

Authors have the responsibility of ensuring that any graphics or other materials which are the property of others may be included in the CC-BY licence, but this should be checked before relying on the CC-BY licence to reproduce those materials. Any copyright notices relating to those materials must be complied with.

Copyright and source acknowledgement notices may not be removed and must be displayed in any copy, derivative work or partial copy which includes the elements in question.

All copyright, and all rights therein, are protected by national and international copyright laws. The above represents a summary only. For further information please read Frontiers' Conditions for Website Use and Copyright Statement, and the applicable CC-BY licence.

ISSN 1664-8714

ISBN 978-2-83250-057-6

DOI 10.3389/978-2-83250-057-6

About Frontiers

Frontiers is more than just an open-access publisher of scholarly articles: it is a pioneering approach to the world of academia, radically improving the way scholarly research is managed. The grand vision of Frontiers is a world where all people have an equal opportunity to seek, share and generate knowledge. Frontiers provides immediate and permanent online open access to all its publications, but this alone is not enough to realize our grand goals.

Frontiers Journal Series

The Frontiers Journal Series is a multi-tier and interdisciplinary set of open-access, online journals, promising a paradigm shift from the current review, selection and dissemination processes in academic publishing. All Frontiers journals are driven by researchers for researchers; therefore, they constitute a service to the scholarly community. At the same time, the Frontiers Journal Series operates on a revolutionary invention, the tiered publishing system, initially addressing specific communities of scholars, and gradually climbing up to broader public understanding, thus serving the interests of the lay society, too.

Dedication to Quality

Each Frontiers article is a landmark of the highest quality, thanks to genuinely collaborative interactions between authors and review editors, who include some of the world's best academicians. Research must be certified by peers before entering a stream of knowledge that may eventually reach the public - and shape society; therefore, Frontiers only applies the most rigorous and unbiased reviews.

Frontiers revolutionizes research publishing by freely delivering the most outstanding research, evaluated with no bias from both the academic and social point of view. By applying the most advanced information technologies, Frontiers is catapulting scholarly publishing into a new generation.

What are Frontiers Research Topics?

Frontiers Research Topics are very popular trademarks of the Frontiers Journals Series: they are collections of at least ten articles, all centered on a particular subject. With their unique mix of varied contributions from Original Research to Review Articles, Frontiers Research Topics unify the most influential researchers, the latest key findings and historical advances in a hot research area! Find out more on how to host your own Frontiers Research Topic or contribute to one as an author by contacting the Frontiers Editorial Office: frontiersin.org/about/contact

ADVANCED CONCRETES AND THEIR STRUCTURAL APPLICATIONS

Topic Editors:

Zhigang Zhang, Chongqing University, China

Xijun Shi, Texas State University, United States

Fangying Wang, University of Nottingham, United Kingdom

Qian Zhang, Florida Agricultural and Mechanical University, United States

Citation: Zhang, Z., Shi, X., Wang, F., Zhang, Q., eds. (2022). Advanced Concretes and Their Structural Applications. Lausanne: Frontiers Media SA.
doi: 10.3389/978-2-83250-057-6

Table of Contents

- 05 *A Simplified Approach for Evaluating the Flexural Response of Concrete Beams Reinforced With FRP Bars***
Rui Sun, Ricardo Perera, Jintao Gu and Yi Wang
- 18 *Lightweight Neural Network for Real-Time Crack Detection on Concrete Surface in Fog***
Gang Yao, Yujia Sun, Yang Yang and Gang Liao
- 34 *Experimental Study on Preparation and Performance of Concrete With Large Content of Fly Ash***
Changyong Li, Haibin Geng, Siyi Zhou, Manman Dai, Baoshan Sun and Fenglan Li
- 44 *Corrosion Experimental Research on Local Damage of Epoxy-Coated Steel Bars in Concrete Under Marine Environment***
Hongfei Cao, Zhongda Lyu, Wei Dong, Zhuo Zhao, Weizhong Gan and Yonggang Wang
- 56 *Numerical Simulation on Cement Hydration and Microstructure Development in Repair-Substrate Interface***
Mingzhang Lan, Jian Zhou, Hui Li and Ying Wang
- 66 *Experimental Study on Bearing Capacity of Corroded Reinforced Concrete Arch Considering Material Degradation***
Jingzhou Xin, Jieyun Wang, Zengwu Liu, Xing You and Jianting Zhou
- 81 *Structural Design and Analysis for a Timber-Concrete Hybrid Building***
Xiaoyue Zhang, Lu Xuan, Wanru Huang, Lin Yuan and Pengcheng Li
- 95 *Effect of Extracted Titanium Tailing Slag on the Properties of Alkali-Activated Fly Ash-Ground Blast Furnace Slag Binder***
Shuping Wang, Jingjing Li, Xiaoxin Yun, Xuwei Lv, Yujie Zhao and Zhigang Zhang
- 105 *A Unified Model for Fibers With Divergent Pullout Behaviors in Strain Hardening Cementitious Composites (SHCC)***
Peiyun She, Jiajie Wang, Zhiming Pang and Cong Lu
- 119 *Chromatic Aberration Identification of Fair-Faced Concrete Research Based on Multi-Scale Lightweight Structured Data Algorithm***
Gang Yao, Wentong Sun, Yang Yang, Yujia Sun, Liangjin Xu and Jian Zhou
- 135 *Experimental Study of GFRP Reinforced Concrete Beams With U-Shaped CFRP Grid-Reinforced ECC Stay-in-Place Formwork***
Chang Wu, Yanli Su, Pu Zhang, Hong Zhu, Danying Gao and Shamim Ahmed Sheikh
- 150 *Numerical Investigation on the Dynamic Responses and Failure Criterion of RC Beam Under Impact***
Jinlong Guo, Guoping Jiang, Zhengyu Wu, An He and Jian Cai
- 160 *Experimental Study on Axial Compression Performance of Thin-Walled Steel Tube Lightweight Concrete Columns With Composite Section***
Yue Li, Yong Yan, Xue Meng, Kechao Zhang, Xiaorun Li and Chongming Gao

- 169 Numerical Analysis of Structural Performance of Concrete-GFRP Composite I-Beam**
Zhaohui Chen, Jiajie Xing, Qiwen Luo and Xiaoyue Zhang
- 182 Research on the Bonding Performance of UHPC–NC Interfaces With Different Sizes of Grooves**
Jun Yang, Junrun Xia, Chongsheng Cheng, Jieyun Wang, Jie Zhang and Gang Wang
- 196 Compressive Behavior of Corroded RC Columns Strengthened With Ultra-High Performance Jacket**
Jun Chen, Zongshan Wang, Anqi Xu and Jianting Zhou
- 210 Analytical Model of Crack Width in Hogging Moment Regions of Steel–Concrete Composite Beams Under Fatigue Loading**
Aiming Song, Hongtao Xu, Shui Wan and Qi Luo
- 222 Bending Performance of Epoxy Adhesive Joints of Prefabricated Concrete Elements**
Hongbo Peng, Zhongya Zhang, Yang Zou, Jincen Guo, Xiaoyan Zhang and Xingqi Zeng
- 234 Sectional Analysis of Reinforced Engineered Cementitious Composite Columns Subjected to Combined Lateral Load and Axial Compression**
Chang Wu, Yanli Su, Yu Sun, Chenhua Jin and Zuanfeng Pan
- 247 Study of the Hydration Temperature Field in the Hinge Seal Layer for a Large-Volume UHPC Arch Base**
Jun Yang, Jieyun Wang, Chao Luo, Yaxi Ding and Yonghui Fan
- 260 Interfacial Behavior of the Steel–UHPC Composite Deck With Toughened Epoxy Bonding**
Jinlong Jiang, Jingchen Leng, Jiangtao Zhang and Jincen Guo
- 276 Finite Element Analysis on Inelastic Mechanical Behavior of Composite Beams Strengthened With Carbon-Fiber-Reinforced Polymer Laminates Under Negative Moment**
Aiming Song, Hongtao Xu, Qi Luo and Shui Wan
- 289 Mechanical Performance and Failure Mode Research on the Braced Frame Joint of Tower Cranes in High-Rise Building Construction**
Yang Yang, Zhen Zhang, Liangjin Xu and Gang Yao



A Simplified Approach for Evaluating the Flexural Response of Concrete Beams Reinforced With FRP Bars

Rui Sun^{1*}, Ricardo Perera², Jintao Gu³ and Yi Wang^{4*}

¹Key Laboratory of New Technology for Construction of Cities in Mountain Area, Ministry of Education, School of Civil Engineering, Chongqing University, Chongqing, China, ²Department of Structural Mechanics, Technical University of Madrid, Madrid, Spain, ³AVIC, The First Aircraft Institute, Xi'an, China, ⁴School of Civil Engineering, Central South University, Changsha, China

OPEN ACCESS

Edited by:

Fangying Wang,
University of Nottingham,
United Kingdom

Reviewed by:

Liang Xia,
Huazhong University of Science and
Technology, China

Ju Chen,
Zhejiang University, China

*Correspondence:

Rui Sun
ruisun@cqu.edu.cn
Yi Wang
wangyi.ce@csu.edu.cn

Specialty section:

This article was submitted to
Structural Materials,
a section of the journal
Frontiers in Materials

Received: 26 August 2021

Accepted: 29 September 2021

Published: 28 October 2021

Citation:

Sun R, Perera R, Gu J and Wang Y
(2021) A Simplified Approach for
Evaluating the Flexural Response of
Concrete Beams Reinforced With
FRP Bars.
Front. Mater. 8:765058.
doi: 10.3389/fmats.2021.765058

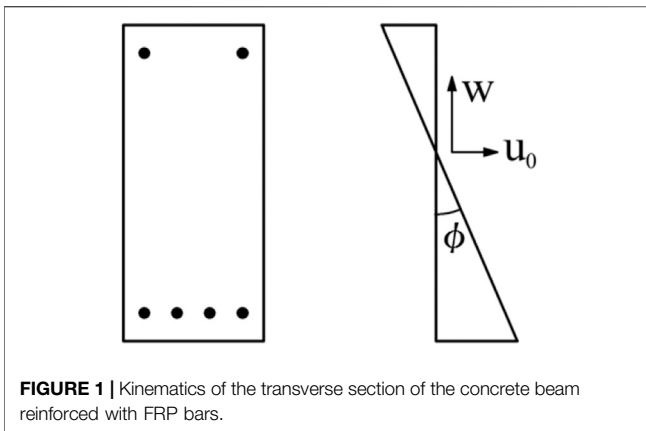
This paper is proposed for modelling concrete beams reinforced with fiber reinforced polymer (FRP) bars in a simplified way. In order to appropriately model the FRP-reinforced concrete beams the stiffness matrix is developed in the frequency domain using fast Fourier Transform. Numerical results with the proposed spectral model for the load-displacement response and the shear stress distribution between FRP reinforcement and surrounding concrete are obtained for beams statically tested. Tens of elements are deployed in this work due to the simplicity of the proposed model. Using the same spectral model the natural frequency and mode shapes are evaluated since the frequency-dependent stiffness matrix enables it to apply for dynamic study, e.g. modal analysis. The feasibility of the proposed numerical approach for performing dynamic analysis especially for high frequency excitations in an efficient way makes it a promising tool for use in the field of structural health monitoring according to the changes in dynamic characteristics.

Keywords: frp reinforcement, numerical simulation, simplified model, flexural behaviour, modal analysis

INTRODUCTION

The long-term durability of reinforced concrete structures has become a major concern over the past few decades, mainly due to the corrosion risk of steel reinforcements. Fibre-reinforced polymer (FRP) is being increasingly used in civil engineering as a reinforcement to replace steel bars because of its rather durable properties (Rizkalla and Nanni, 2003), especially in aggressive environments where steel reinforcements are easily corroded. Additionally, under some special circumstances, such as in the magnetic resonance imaging rooms of hospitals, there is a demand for electromagnetic permeability, and such needs can be met by FRP bars since they are non-metallic. Since FRP bars possess mechanical characteristics different from those of steel bars (e.g., lower elastic modulus, non-yielding properties), numerous experimental investigations have been carried out to study the behaviour of concrete members reinforced by FRP bars (Barris et al., 2009; Kassem et al., 2011; Al-Sunna et al., 2012; Barris et al., 2013; Miàs et al., 2013; Habeeb and Ashour, 2014; Acciai et al., 2016). Unlike concrete members with steel reinforcement, the experimental results showed that FRP reinforced concrete members behave elastically until failure due to the characteristics of the FRP reinforcement, and structural failure would occur at a relatively large displacement.

Some studies applied analytical models to determine the responses of FRP-RC members. Branson's equation, which was developed for the design of concrete beams reinforced with steel bars (Branson, 1977; ommittee 318 (2008)., 2008), was adjusted by introducing empirical coefficients



(Benmokrane et al., 1996) and a modified equivalent moment of inertia (Bischoff, 2005). In refs. Razaqpur et al. (2000); Rasheed et al. (2004), bilinear and tri-linear moment-curvature relationships have been used to derive closed-form equations for predicting the deflection of FRP-reinforced members. A local deformation model was developed in ref. Gravina and Smith (2008) to capture the flexural response and moment distribution of indeterminate concrete beams reinforced by FRP bars, in which the progressive cracking process with an increasing load was considered. An iterative analytical procedure was also proposed for the prediction of the flexural behaviour of FRP-reinforced concrete beams in ref. Almusallam (1997). During the iterative process, the neutral axis depth is changed until force equilibrium is reached. Furthermore, ref. Kara et al. (2013) presented an analytical model for evaluating the deflection of FRP-reinforced concrete structures, and the flexural and shear cracks in cracked regions were reduced by introducing an effective moment of inertia. Although several studies have been conducted to develop design formulas, many researchers have noted that deviations occur when using these equations to predict the deflection of FRP-reinforced concrete beams (Aiello and Ombres, 2000; Mota et al., 2006).

A two-dimensional finite element (FE) model was used to study the performance of concrete beams reinforced with steel and FRP bars (Bencardino et al., 2016), and it was shown that a 2D FE model can be used to simulate the load-deflection relationship of concrete beams reinforced with different ratios of steel and FRP. Furthermore, a spatial 3D FE model that is more realistic for simulation was used to calculate the flexural deflections of FRP-RC beams (Zhang et al., 2015), and the results show better agreement with the experimental data than the equations from the design code. To clarify the failure mechanism of FRP-RC members, a limit analysis strategy is integrated with an FE model (De Domenico et al., 2014) by using the linear matching method (LMM) and the elastic compensation method (ECM), which is adequate for obtaining the upper and lower bounds of the peak load value. Furthermore, to calculate both global deformation and local strain, several FE models were developed by considering the constitutive laws of materials and the interfacial bond-slip model of an

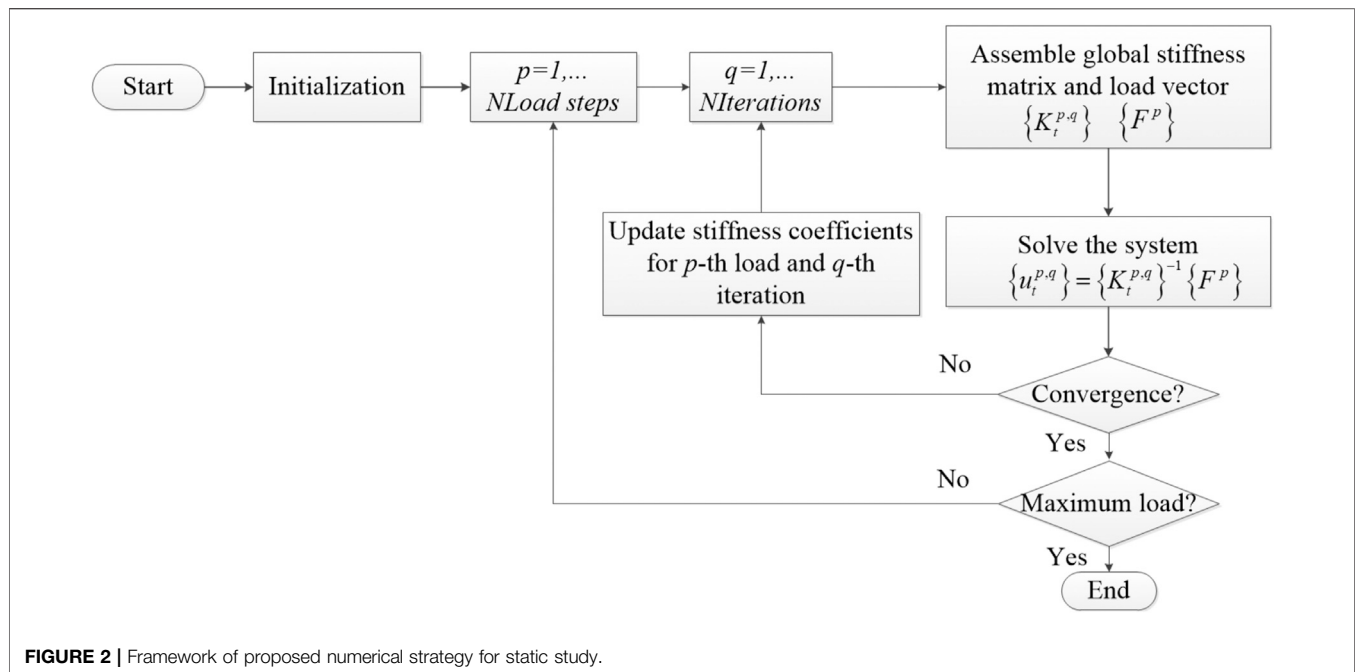
FRP bar and concrete (Nour et al., 2007; Rafi et al., 2008; Hawileh, 2012; Hawileh, 2015). A proportional integral derivative (PID) controller (Echeverria and Perera, 2013) was introduced into the 3D FE approach to capture the softening branch of the interfacial bond-slip performance between FRP rods and concrete.

Obviously, an analytical model can be used to evaluate the global behaviour of an FRP-RC beam, but it is very difficult to capture the local behaviours, e.g. concrete strain and shear stress distribution. Although this shortcoming can be overcome by using a refined FE model, a huge number of elements are needed, which results in a heavy computational cost and possibly a convergence problem due to the highly nonlinear properties of the materials and the interface. In refs. Perera and Bueso-Inchausti (2010); Sun et al. (2015), a 4-degree-of-freedom spectral element model was used to simulate the flexural behaviours of RC beams strengthened with externally bonded FRP strips by considering the interfacial bond slip between the FRP strip and the RC beam. This numerical approach has shown promise due to its simplicity since it is derived from the frequency domain. Thus, it is adopted in this study for determining the global and local performance of an FRP-RC beam by assuming a perfect bond between the FRP bars and the surrounding concrete for simplicity. Only 23 spectral elements are used to calculate the load-displacement response and concrete strain while tens of thousands elements are needed using FE model. The interfacial bond behaviour between FRP bars and concrete, which is a very local phenomenon, is also evaluated to study the development of shear stress distribution with the gradually increasing load. Obviously, the computational cost has been reduced dramatically due to the simplicity and efficiency of the proposed spectral element method, and the accuracy is verified comparing the numerical results with the experimental data.

Of particular interest is the ability of the present model to obtain the dynamic characteristics of FRP-RC beams, since to the best of the author's knowledge, few studies have focused on the dynamic analysis of FRP-RC beams (Capozucca and Bossoletti, 2014; Capozucca et al., 2015). By making a frequency sweep for the dynamic stiffness-matrix, the natural frequencies and mode shapes are efficiently calculated even in high frequency range as long as the uniformity of concrete beam remains unchanged (Trefethen, 2000; Gopalakrishnan et al., 2008). Structural damages can be identified according to the changes of dynamic characteristics under intact and damaged scenario, which makes the proposed model promising for damage detection due to its simplicity and efficiency.

SPECTRAL MODEL OF A CONCRETE BEAM REINFORCED WITH FRP BARS

Since one of the main advantages of the proposed spectral model is its simplicity for calculating the structural behaviour, in which the formulations are established in the frequency domain, it can be used to analyse the global and local responses of an FRP-RC



beam in this study. To this end, the governing equations are derived in this section. First, the axial and transverse displacement of the beam can be formulated as follows by using first-order shear deformation theory:

$$u_C(x, z, t) = u_0(x, t) - z\phi(x, t) \quad (1)$$

$$w(x, z, t) = w(x, t) \quad (2)$$

where u_C and w are the axial and transverse displacements in a concrete beam at a material point, respectively. As shown in **Figure 1**, $u_0(x, t)$ is the mid-plane axial displacement, ϕ represents the rotation of the cross section about the Y-axis, and z is the coordinate measured from the mid-plane. The strain of concrete can be derived as follows based on **Eq. 1** by introducing a linear strain-displacement relationship:

$$\varepsilon_x = u_{0,x} - z\phi_{,x} \quad (3)$$

where ε_x denotes the longitudinal strain in the RC beam and $(\cdot)_{,x}$ represents differentiation with respect to x .

The constitutive relation of the FRP bar is assumed to be linearly elastic, and the nonlinearity of the concrete material is considered since it has a great influence on the load-resisting mechanism. The nonlinear constitutive relationships of concrete in compression and tension are based on the CEB-FIP code in (fib, 2010). Furthermore, the bond behaviour between the bar and concrete is an essential aspect of the reinforced beam. Although the bond-slip relationship was discussed, it still highly depends on the surface condition, material strength and confinement provided by the surrounding concrete (Yan et al., 2016; Solyom and Balázs, 2020; Solyom and Balázs, 2021). Since one of the main purposes of this study is to numerically simulate FRP-RC beams in a simplified way to reduce computational costs, a perfect bond

relationship based on the equilibrium of FRP bars and the surrounding concrete is used in this work. Therefore, the stresses of the concrete and bar can be expressed as follows:

$$\sigma_C = E_C \varepsilon_C \quad \varepsilon_C = u_{0,x} - z_{cj}\phi, \quad (4)$$

$$\sigma_B = E_B \varepsilon_B \quad \varepsilon_B = u_{0,x} - z_{bj}\phi, \quad (5)$$

$$\tau_C = G_C \gamma_C \quad \gamma_C = w_{,x} - \phi \quad (6)$$

where σ and τ denote the axial and shear stresses, and the subscripts C and B represent the concrete and FRP bar, respectively. Additionally, the elastic and shear modulus of concrete E_C and G_C depend on the strain at every point throughout the concrete beam, which will be updated by the equivalent secant elastic moduli due to the material nonlinearity of the concrete. The longitudinal strain of the concrete and FRP bars, ε_C and ε_B , with coordinates of z_{jc} and z_{jb} , respectively, can be formulated based on **Eq. 3**.

Based on the expressions above, the strain energy of the reinforced beam composed of concrete and FRP bars is formulated as

$$U = \frac{1}{2} \int_L \int_{z_1}^{z_2} (\sigma_C \varepsilon_C + \tau_C \gamma_C) b_C dz dx + \frac{1}{2} \int_L \sum_{i=1}^{N_B} (\sigma_B \varepsilon_B) A_{Bj} dx \quad (7)$$

where z_1 and z_2 are the Z-coordinates of the bottom and top surfaces limiting the beam, respectively, and the variables b_C and L denote the width and length of the beam, respectively. N_B is the number of FRP bars, and the area of each bar is A_{Bj} . Since a perfect bond relationship between the FRP bars and the surrounding concrete is used in this work, the shear strain energy of FRP reinforcement is neglected for simplicity.

By introducing Hamilton's principle, the differential equations of motion can be derived by incorporating the kinematic energy

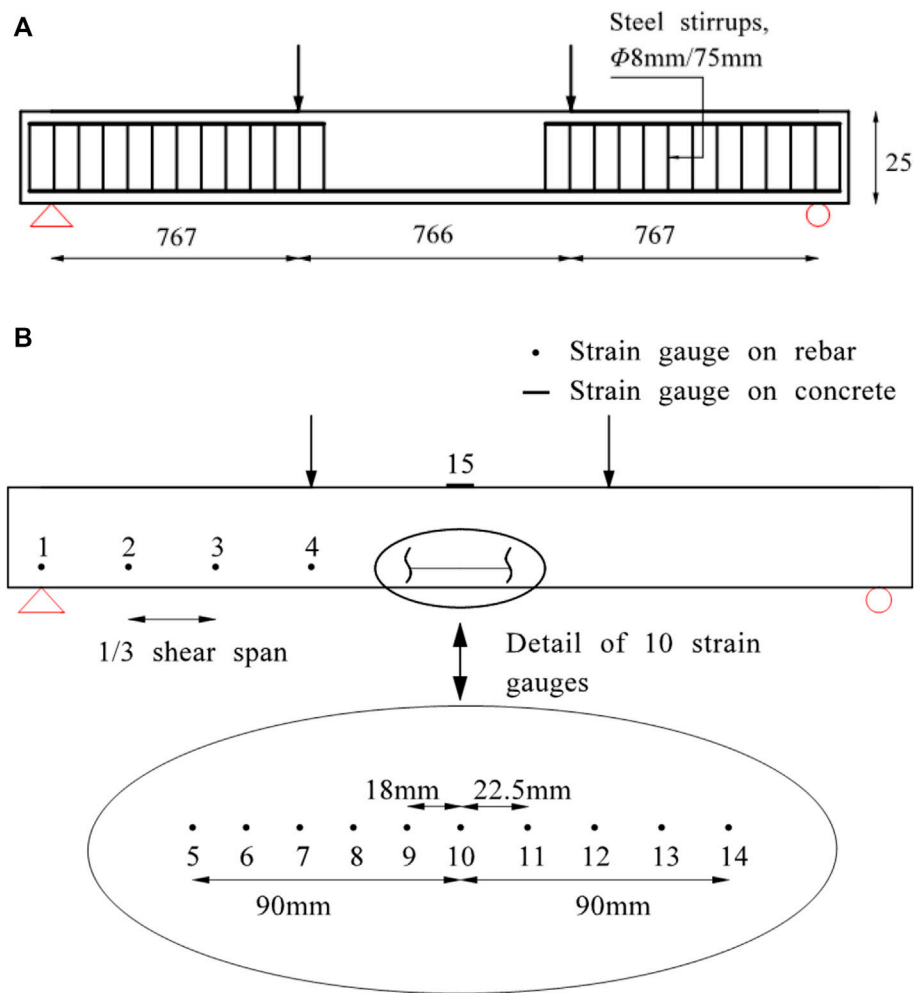


FIGURE 3 | (A) Experimental test setup, **(B)** arrangement of rebar and concrete strain gauges.

TABLE 1 | Material and geometrical properties of the tested specimens.

Specimens		BG1	BG2
Concrete	Elastic modulus (MPa)	29,300	
	Compressive strength (MPa)	37.7	
Main GFRP bar	Diameter (mm)	2φ9.5	2φ12.7
	Elastic modulus (MPa)	42,800	41,600
	Reinforcement ratio	0.0043	0.0077
RC beam	Span (mm)	2,300	
	Width (mm)	150	
	Height (mm)	250	

of the beam. The equations of motion for the displacement field are given by

$$\delta u_0 : I_0 \ddot{u}_0 - I_1 \ddot{\phi} - A_{11} u_{0,xx} + B_{11} \phi_{,xx} = 0 \quad (8)$$

$$\delta w : I_0 \ddot{w} - A_{22} w_{,xx} + A_{22} \phi_{,x} = 0 \quad (9)$$

$$\delta \phi : I_2 \ddot{\phi} - I_1 \ddot{u}_0 + B_{11} u_{0,xx} - D_{11} \phi_{,xx} - A_{22} w_{,x} + A_{22} \phi = 0 \quad (10)$$

and the boundary force equations are

$$N = A_{11} u_{0,x} - B_{11} \phi_{,x} \quad (11)$$

$$V = A_{22} w_{,x} - A_{22} \phi \quad (12)$$

$$M = -B_{11} u_{0,x} + D_{11} \phi_{,x} \quad (13)$$

where N , V and M are the boundary forces related to the variables u_0 , w and ϕ , respectively. $()_{,x}$ and $()_{,t}$ represent differentiation with respect to length and time.

The coefficients in Eqs 8–13, which are related to the material properties, are given by the following expressions:

$$[A_{11} \quad B_{11} \quad D_{11}] = \int_{z_1}^{z_2} E_C [1 \quad z \quad z^2] b_C dz + \sum_{j=1}^{N_B} E_{Bj} A_{sj} [1 \quad z_j \quad z_j^2] \quad (14)$$

$$[A_{22}] = \int_{z_1}^{z_2} G_C b_C dz \quad (15)$$

$$[I_0 \quad I_1 \quad I_2] = \int_{z_1}^{z_2} \rho_C [1 \quad z \quad z^2] b_C dz \quad (16)$$

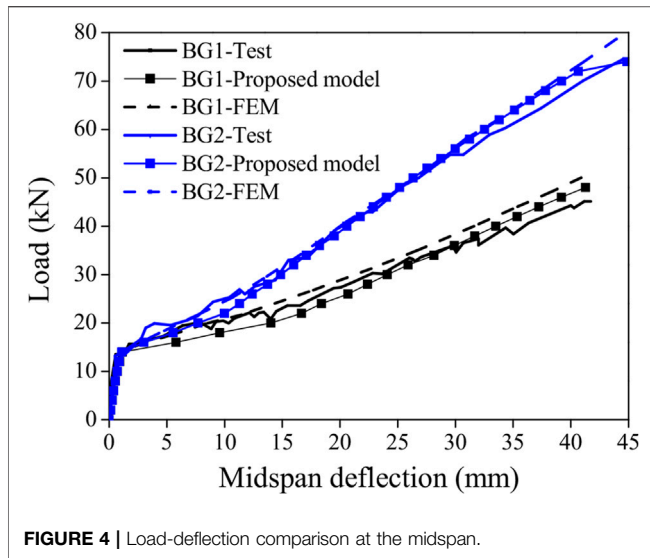


FIGURE 4 | Load-deflection comparison at the midspan.

where ρ_C denotes the density of concrete and E_{Bj} is the elastic modulus of each FRP bar. To model the progressive cracking process, the entire beam is divided into several layers through the height, and the material properties of the concrete in each layer will be updated by using the nonlinear stress-strain relationship of concrete. Furthermore, the elastic modulus of the FRP's E_B is treated as a constant due to its non-yielding properties.

By applying a fast Fourier transformation (FFT), the displacement field is transferred from time domain to frequency domain as follows:

$$\{u_0, w, \phi\} = \sum_{n=1}^N \sum_{m=1}^M \{\hat{u}_{mn}^*\} e^{-jk_{mn}x} e^{-j\omega_n t} \quad (17)$$

where N is the number of frequency sampling points, which depends on the Nyquist frequency. ω_n represents the circular frequency at the n th sampling point in the FFT, and k_{mn} denotes the m th wave number of ω_n . $\{\hat{u}_{mn}^*\} = (\hat{u}_0, \hat{w}, \hat{\phi})_{mn}$ is the vector of the wave coefficients related to the m th mode of the wave at frequency point ω_n . By introducing Eq. 17, Eqs 8–10 turn into the following formula:

$$[W]\{\hat{u}^*\} = 0 \quad (18)$$

where W is a 3×3 matrix with functions of frequency and wavenumber as follows:

$$[W] = \begin{pmatrix} A_{11}k^2 & 0 & -B_{11}k^2 + I_1\omega_n^2 \\ 0 & A_{22}k^2 - I_0\omega_n^2 & -jA_{22}k \\ -B_{11}k^2 + I_1\omega_n^2 & jA_{22}k & D_{11}k^2 - I_2\omega_n^2 + A_{22} \end{pmatrix} \quad (19)$$

For each frequency point, the wavenumber k_{mn} can be obtained by solving a 6-th order equation when W equals zero in Eq. 18, and the six related eigenvectors R_i ($i = 1, \dots, 6$) can be used to formulate the general solution of nodal displacement as

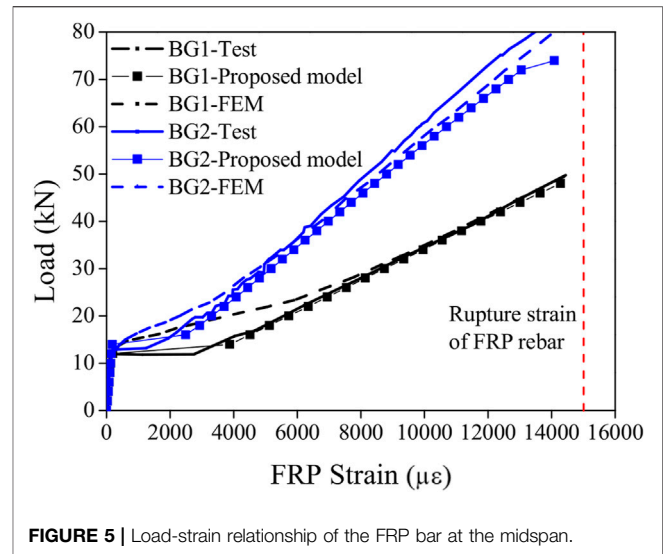


FIGURE 5 | Load-strain relationship of the FRP bar at the midspan.

$$\begin{aligned} \{u(x)\} &= \begin{pmatrix} \hat{u}_0(x) \\ \hat{w}(x) \\ \hat{\phi}(x) \end{pmatrix} = [\{R_1\} \quad \dots \quad \{R_6\}] \text{diag}(e^{-jk_i x})_{i=1,\dots,6} \{A\} \\ &= [R][D(x)]\{A\} \end{aligned} \quad (20)$$

Furthermore, the displacements of the two nodes in an element with a length of L can be expressed as

$$\begin{Bmatrix} u_1 \\ u_2 \end{Bmatrix} = \begin{bmatrix} R_1 \\ R_2 \end{bmatrix} \begin{bmatrix} D(0) \\ D(L) \end{bmatrix} \{A\} = [T_1]\{A\} \quad (21)$$

where $\{A\}$ is the vector of the constants, which depends on the associated boundary conditions. Substituting Eq. 21 into Eq. 20, the nodal displacements can be obtained as

$$\{u(x)\} = [R][D(x)][T_1]^{-1} \begin{Bmatrix} u_1 \\ u_2 \end{Bmatrix} = [N] \begin{Bmatrix} u_1 \\ u_2 \end{Bmatrix} \quad (22)$$

where $[N]$ is the matrix of the shape functions of the proposed spectral model. By combining the boundary forces given by Eqs 11–13, the dynamic stiffness matrix (DSM) $[K]$ is formed to compute the displacement in the frequency domain:

$$\begin{Bmatrix} \{f_1\} \\ \{f_2\} \end{Bmatrix} = \begin{bmatrix} F(0) \\ F(L) \end{bmatrix} \{A\} = [T_2][T_1]^{-1} \begin{Bmatrix} u_1 \\ u_2 \end{Bmatrix} = [K]_{6 \times 6} \begin{Bmatrix} u_1 \\ u_2 \end{Bmatrix} \quad (23)$$

Based on the derivation of the equations presented above, the 6×6 DSM $[K]$ is formulated, as shown in Eq. 23. Additional details regarding the FFT process and implementation of the spectral element model can be found in Trefethen (2000); Capozucca et al. (2015). The DSM, which is frequency-dependent, is established according to the governing equations and boundary conditions in Eqs 8–13, and it can be considered a combination of a mass matrix and a stiffness matrix that introduces exact dynamic shape functions. Since circular frequency ω_n is included in the DSM, dynamic factors of the FRP-RC beam such as natural frequencies and related mode shapes can be obtained. Furthermore, by making

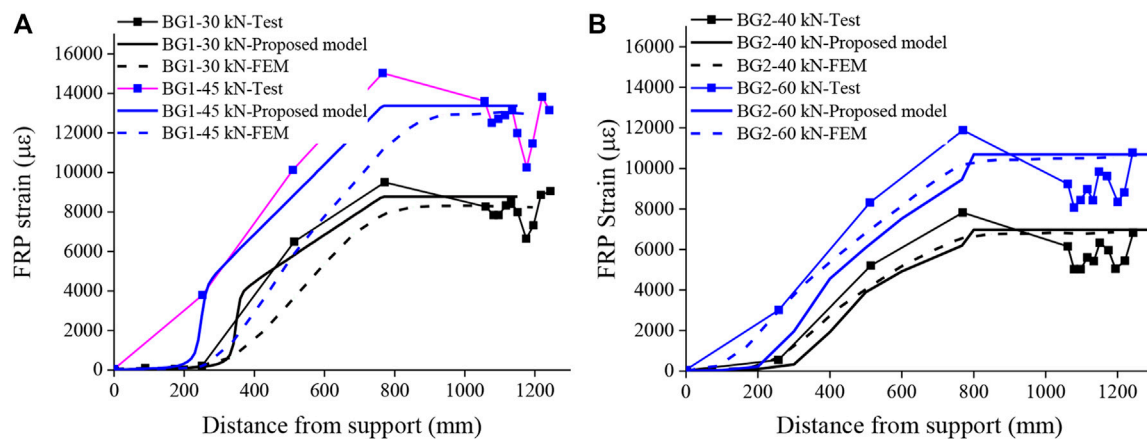


FIGURE 6 | FRP strain along the length of (A) BG1 and (B) BG2.

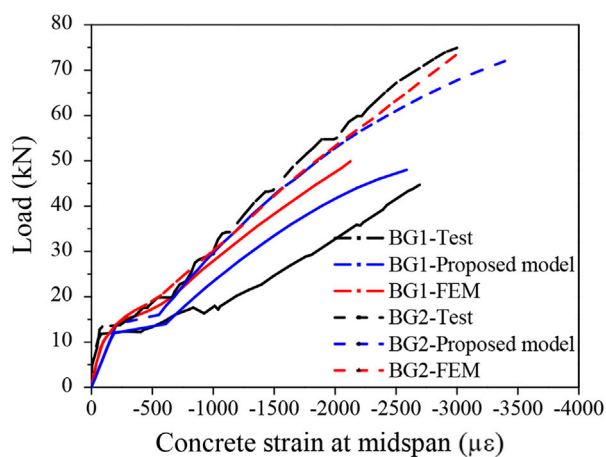


FIGURE 7 | Load-concrete strain comparison at the midspan.

ω_n in DSM tend to zero, it can be used to calculate the structural behaviour in static cases. The framework of proposed numerical strategy for static study is shown in **Figure 2**.

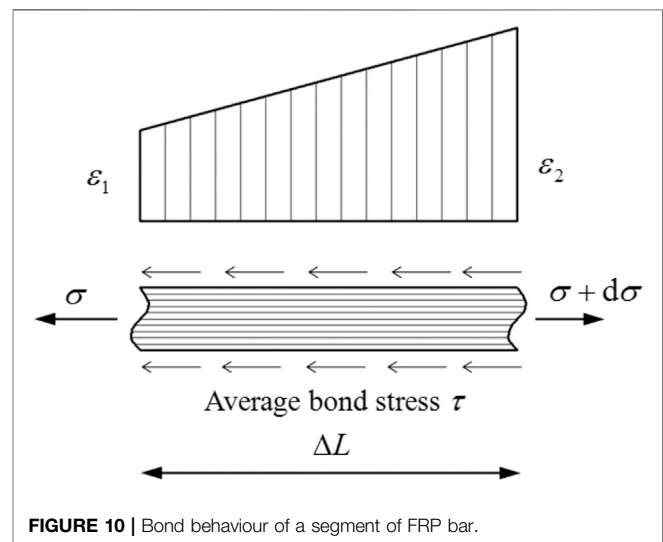
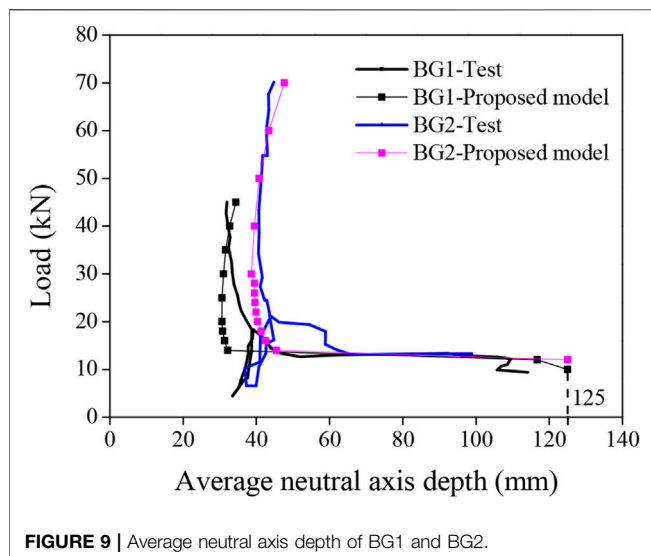
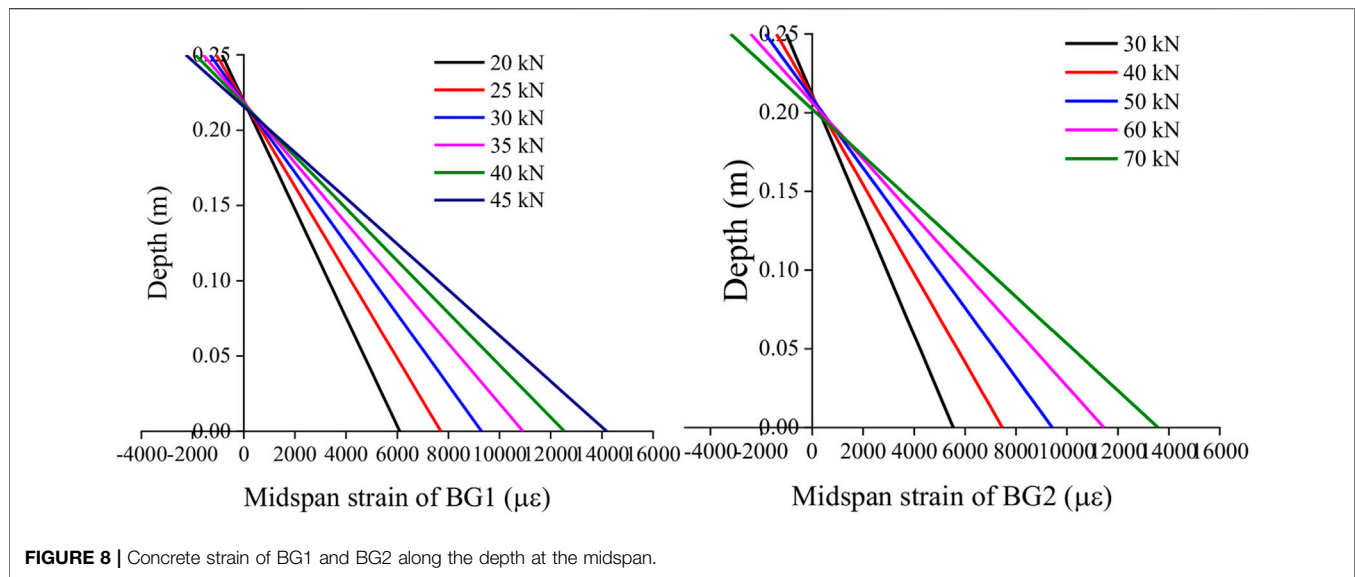
CASE STUDY OF THE PROPOSED MODEL

Concrete beams reinforced with FRP bars tested by Al-Sunna (2006) were selected to validate the capability of the proposed spectral model. In his tests, twenty-eight concrete beams and slabs reinforced with FRP or steel bars were fabricated, two FRP bars with nominal diameters of 6 mm were located in the compressive zone, and FRP bars with diameters of 9.5 and 12.7 mm were used as the main flexural reinforcement for concrete beams BG1 and BG2, respectively. The reinforced beams were 150 mm wide, 250 mm deep and 2,550 mm long, and the span between two supports was 2,300 mm. The experimental test setup is shown in **Figure 3**. The specimens were tested by progressive four-point loading with a shear span of 767 mm (one-third of the length), and two loading

platens were used to control the deflection of FRP-RC beams during testing. Fourteen strain sensors were installed to measure the local strain of the reinforced beam; four of them were adhered to the FRP bar to capture the strains of the bar, and the other ten gauges were located around the crack inducer at the midspan to measure the local behaviour at the crack locations. In this study, the experimental data of two concrete beams reinforced with GFRP (glass-fibre-reinforced polymer) are chosen to validate the accuracy of the proposed approach, and the material properties and geometrical parameters of the specimens are illustrated in **Table 1**.

As presented previously, the proposed approach can simulate the behaviours of a reinforced beam with only one spectral element if there is no discontinuity of the geometrical and material properties. Since the two specimens maintain their uniformity along the length of the beam, it is very convenient to evaluate global and local behaviours by using the proposed one-dimensional model due to its simplicity. The mechanical behaviours, particularly for local behaviours such as stress and strain, can be obtained with higher accuracy by using more elements, and the computational burden would simultaneously increase. Hence, the number of elements can be determined by balancing the computational costs and the desired degree of precision. To this end, the element size is chosen as 100 mm in this study, resulting in a total of 23 spectral elements for the RC beams. Obviously, the computational costs decrease remarkably by reducing the number of elements from tens of thousands in the FE model to tens of elements. Additionally, the static behaviour of the FRP-RC beams can be directly calculated by making the circular frequency ω_n of dynamic stiffness $[K]$ in **Eq. 23** go towards zero.

The longitudinal FRP bars are modelled as an elastic material by assigning the elastic modulus according to the tested data given in **Table 1**. The strain-stress relationship of concrete in the European Code (fib, 2010) is introduced in the present work. The nonlinear property of concrete is simulated by adopting a secant procedure, in which the elastic modulus of concrete is updated by the secant modulus associated with the concrete strain with the increasing load. The parameters of **Eqs 14–16** related to the material properties are represented by the equivalent secant modulus of concrete. The



cross section of each element is divided into twenty layers along the height of the beam to model the progressive cracking of concrete as the load increase. Furthermore, the applied load is divided into several sub-load steps, and the material properties of the RC beam would be updated implicitly in an iterative manner until force equilibrium is reached for each load step. By conducting this load-control strategy, the nonlinear behaviour throughout the FRP-RC beam can be evaluated in details.

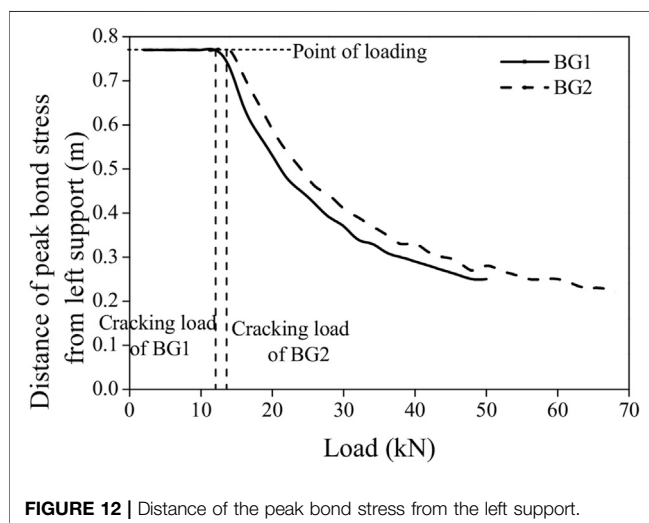
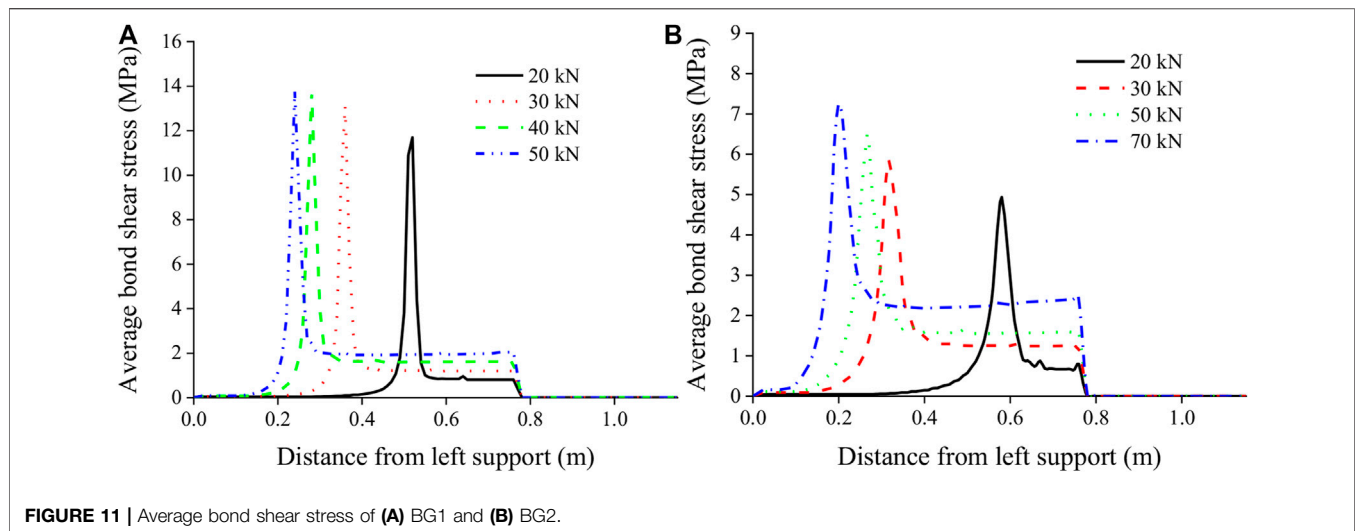
To model the mechanical behavior of FRP reinforced concrete beam using conventional finite element method, a refined mesh is usually required leading to a huge number of elements. However, a small number of elements are needed by using the proposed spectral approach, since only one spectral element is enough to calculate the structural response as the geometry and material remains uniform. In this study, an element size of 100 mm is selected in the proposed model resulting in only 23 spectral elements to numerically simulate

the flexural and local behaviors of the FRP-RC beam with a length of 2.3 m. Therefore, the computational burden is significantly released compared with the FE model due to the simplicity and efficiency of the proposed spectral approach.

VALIDATION OF THE PROPOSED MODEL

Flexural Behaviours

The FE model was implemented in Al-Sunna (2006) by using commercial software to numerically simulate the FRP-RC beams. The relationship between the load and the deflection at the midspan of specimens BG1 and BG2 obtained from the experimental test and numerical simulation are compared, as shown in **Figure 4**. In general, the load-deflection curves present an approximate bilinear response. Both of the beams exhibit a brittle elastic behaviour with no softening



prior to failure. In the first stage, before the first crack occurs at the load of 14 kN, the FRP-RC beams follow a linear elastic behaviour pattern with a steep slope. The reinforcement ratio of FRP bars has an insignificant effect on the stiffness of the load deflection curves with only a slight influence on the cracking loads for the two beams. In the second stage, a subsequent reduction in the slope is observed due to the progressive cracking of the beam occurs, which shows linear and non-ductile behaviour with increasing load because of the non-yielding properties of the FRP bars. The deflection of BG2 after the first crack has been reduced remarkably compared to that of BG1, and the geometrical and material properties are the same except for the amount of FRP reinforcement at the bottom of the RC beams. With the increase of reinforcement area, a greater increase in the stiffness and also the ultimate load of BG2 than BG1 is observed. Failure mode of BG1 might be governed by FRP rupture since the midspan deflection of BG1 is much higher than that of BG2 at the same load level. In general, a small deviation is noticed between the numerical and the test results, which indicates the ability of the

proposed approach to predict the pre- and post-cracking deflections of the FRP-RC beams and demonstrates the accuracy of the proposed spectral model.

Strain of the FRP bar

According to the material properties of the FRP bars, which are elastic until failure, the load-strain relationship of the FRP bar at the midspan is shown in **Figure 5**. The load-strain curves of the two RC beams show a linear relationship before concrete cracking at 14 kN. Afterwards, the rebar undergoes additional strain with the development of cracks at higher load levels. Finally, the FRP approaches the rupture strain, which is approximately 15,000 microstrains according to the test data. The non-yielding properties of the FRP bars cause the lack of ductility of FRP-RC beams, which would result in sudden brittle failure because of FRP rupture. This phenomenon is one of the main differences between concrete beams reinforced with steel and those with FRP. As reported in Al-Sunna (2006), the failure mode of BG1 is the rupture of FRP bars during the four-point loading test, while for BG2 it is concrete crushing immediately followed by the rupture of the FRP bars, which results in balanced failure. The prediction of the current numerical model is in good agreement with the experimental results and FE simulation.

By applying the proposed spectral model for both specimens, the strain distributions of the FRP bars under different load levels along the lengths of the beams are shown in **Figure 6**. The strains obtained by the experimental test and FE simulation are compared with the results predicted by the spectral approach and show good agreement. According to the results obtained from the proposed model, low strain of the bar is observed over the support of the beam, and increasing strain occurs from the shear span to the midspan, reaching a plateau between the two loading points. **Figure 6** reveals that the plateaus of the FRP stain at the midspan in the numerical simulation are different from those of the experimental results, in which strain concentration exists. This result is mainly due to the application of the smeared crack model in the proposed numerical approach to represent flexural cracks instead of a discrete crack model. The concrete and steel properties were updated using the secant modulus during the iterative nonlinear analysis until force equilibrium was reached as the load level increased. Therefore, the

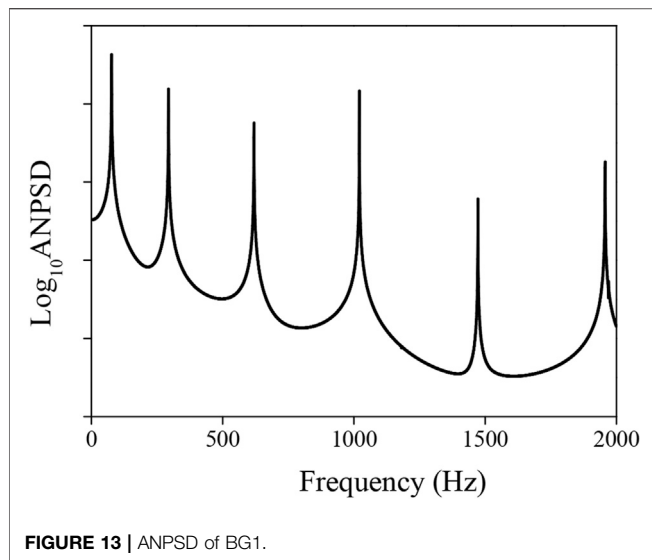


TABLE 2 | Comparison of the natural frequencies of BG1 and BG2.

Natural frequencies	BG1	BG2	Δf (%)
f_1 (Hz)	76.48	76.98	0.65
f_2 (Hz)	292.43	293.43	0.34
f_3 (Hz)	617.35	619.35	0.32
f_4 (Hz)	1017.75	1020.74	0.29
f_5 (Hz)	1468.63	1472.63	0.27
f_6 (Hz)	1952.51	1957.01	0.23

flexural cracks at the midspan are simulated uniformly by using the proposed spectral model. It can be observed that the measured FRP strains are more localized due to the penetration of cracks and their nearby openings; thus, the strain variation at the midspan exhibits conditions that are different than the average conditions assumed in the numerical simulation.

Concrete Strain

In the test, to measure the strain development of concrete, the strain gauges were located on top of the FRP-RC beams at the midspan. The typical load-strain relationships of both specimens are shown in **Figure 7**. As shown, the proposed numerical approach predicts the measured concrete strains for BG1 and BG2 reasonably well. Similar to

the development of the FRP strains in **Figure 6**, the concrete strain is negligible before cracking, and it increases remarkably with load until failure after concrete cracking at a load level of 14 kN. The experimental strain of the concrete on the top surface is compared with the predictions of the proposed model and FE simulation. The differences between the tested data and numerical results are shown in **Figure 7**. One of the reasons for this discrepancy may be the heterogeneity of the concrete material, as it is assumed to be homogeneous for the numerical calculation to simplify the nonlinear analysis. Nevertheless, considering the fact that only one-dimensional and two-dimensional elements are used for numerical simulation in the proposed spectral approach and FEM, respectively, the predicted global and local behaviours are reasonable, as presented previously, which demonstrates the reliability of the proposed spectral model.

As previously presented, the cross section of the reinforced beam was divided into several fibres to update the material properties during nonlinear analysis. Hence, the concrete strains of BG1 and BG2 at the midspan can be evaluated along the depth of the beam at different load levels. **Figure 8** shows the strain profiles on the cross section at different load levels for the two RC beams. The slopes of the strain profiles represent the curvature of the cross section. Obviously, the concrete strain across the depth of the section shows a linear relationship, and a larger strain in the compressive and tensile sections are observed at higher load levels.

By using the strain sensors located at the top of the reinforced concrete beam, the neutral axis depth can be deduced by using the curvature (φ) and concrete strain at the top fibre of the midspan (ε_c) as follows:

$$x = \frac{\varepsilon_c}{\varphi} \quad (24)$$

According to the distribution of the concrete strain along the depth of the cross section, as illustrated in **Figure 8**, the average neutral axis depth can be evaluated numerically by using linear interpolation. The numerical prediction and experimental neutral axis depth are compared in **Figure 9**. The neutral axis depth, which is located at the middle of the cross section, has a value of 125 mm before cracking and decreases significantly when a cracking load of 14 kN is reached. Thereafter, the neutral axis depth increases slightly until the maximum load level. The influence of the reinforcement ratio on the neutral axis depth is also shown in **Figure 9**; good agreement can be observed between the numerical simulation and the experimental results.

TABLE 3 | Comparison of frequency changes due to damage.

Natural frequencies	BG1			BG2		
	D0	D1	D2	D0	D1	D2
f_1 (Hz)	76.48	76.48	75.98	76.98	76.48	76.48
f_2 (Hz)	292.43	292.42	292.43	293.43	293.42	293.42
f_3 (Hz)	617.35	616.34	614.84	619.35	618.34	616.84
f_4 (Hz)	1017.75	1017.24	1016.74	1020.74	1020.24	1019.74
f_5 (Hz)	1468.63	1467.13	1465.63	1472.63	1471.13	1469.63
f_6 (Hz)	1952.51	1951.01	1951.01	1957.01	1954.51	1951.01

Note: D0-No damage; D1-10% damage; D2-20% damage.

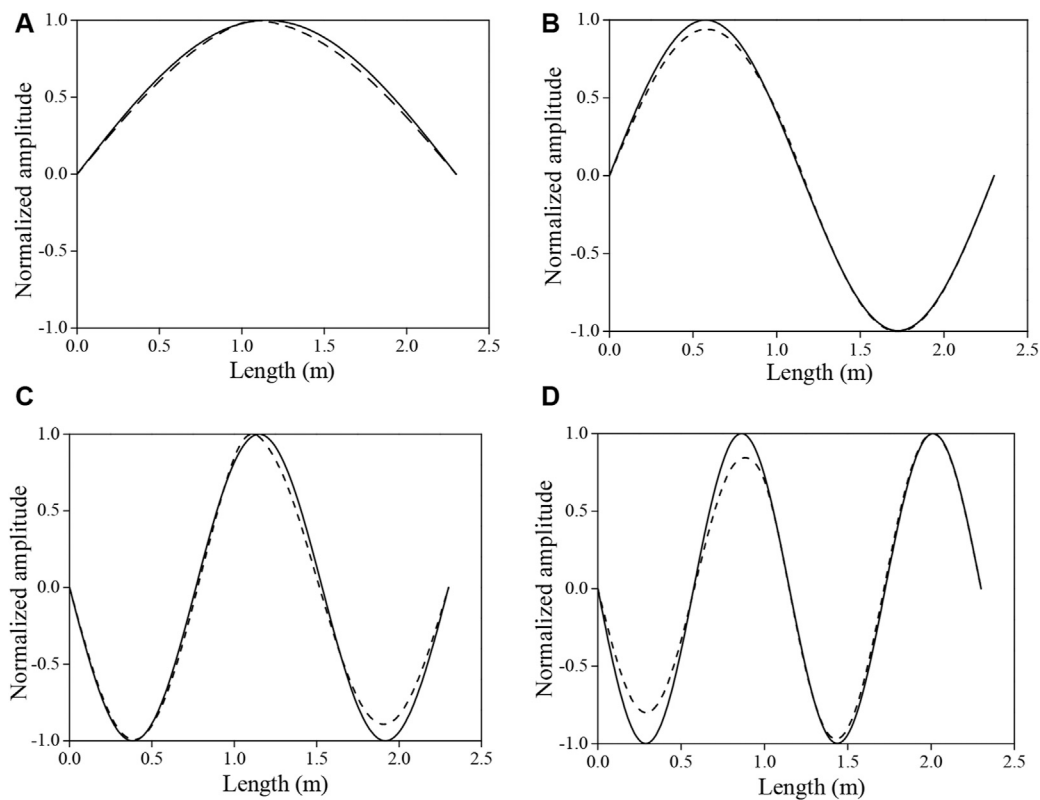


FIGURE 14 | First four mode shapes of BG1 of intact (solid line) and damaged (dash line) scenarios. **(A):** The first mode, **(B):** The second mode, **(C):** The third mode, **(D):** The fourth mode.

Bond Shear Stress

For a segment of the tensile bar surrounded by concrete with a length of ΔL , as shown in **Figure 10**, the bond shear stress can be considered to be uniformly distributed around the interface between the FRP bar and concrete. For a segment of the FRP bar, the force equilibrium can be formulated as

$$d\sigma A_{bar} = \tau C \Delta L \quad (25)$$

where σ is the axial stress of the bar, τ represents the average interfacial stress between the concrete and the bar, and C denotes the perimeter of a cross section of the FRP bar. Based on **Eq. 25**, the average bond stress can be obtained as

$$\tau = \frac{E_b d (\varepsilon_2 - \varepsilon_1)}{4 \Delta L} \quad (26)$$

where d is the diameter of the bar, and ε_1 and ε_2 denote the strains at both ends of the segment of the bar. From **Eq. 26**, it is clear that the average bond stress is proportional to the rate of change in the FRP strain along the length of bar, and the axial stress of the bar is balanced by the bond shear stress, which is provided by the confined concrete surrounding the reinforcement. Therefore, the bond stress can be calculated according to **Eq. 25** using the FRP strain obtained from the proposed model.

Different surface conditions of the FRP bars in the manufacturing process would affect the bond behaviour due to

the mechanical interlock between the deformed bar and the confined concrete. This effect is beyond the scope of this study, considering the simplicity of proposed one-dimensional model. Hence, to study the interfacial bond behaviour, the average bond shear stress along the length of bar is numerically evaluated using **Eq. 26**. A refined mesh is needed to study the interfacial bond stress, and the length of the proposed one-dimensional element is defined as 0.01 m, resulting in 230 spectral elements for the two specimens. Nevertheless, the computational cost has decreased dramatically compared with that of conventional FEM. Since few strain gauges were used in the test, the bond stresses along the lengths of the beams were not measured. To clarify, the numerical results are discussed in this section.

The average bond shear stress of BG1 and BG2 distributed along the length of the FRP bar are evaluated numerically, as shown in **Figures 11A,B**, respectively. As the smeared crack model is employed to model flexural cracks in this study, concrete cracking is represented by reducing the elastic modulus of each element. Hence, the bond stress concentrations near the flexural cracks are not represented in a distributed way. As shown, the predicted bond stress between the two loading points at the midspan of the RC beams tends to be zero, and it increases from the loading point to the shear span until reaching a peak stress. With increasing load, the value of peak bond stress increases. The location of the peak point would gradually move towards the supported end of the beam with increasing load, from 0.52 m at 20 kN to 0.24 m at 50 kN for

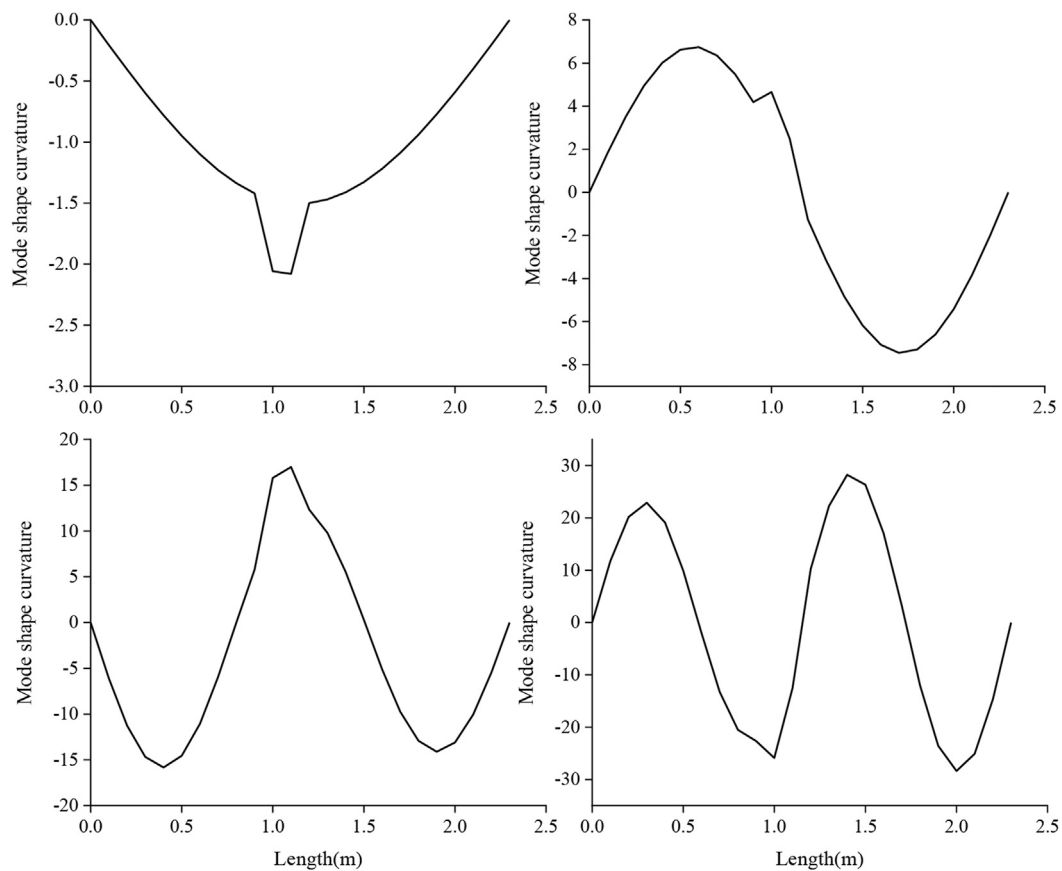


FIGURE 15 | First four mode shape curvatures of BG1 of damaged scenario.

BG1, and from 0.58 m at 20 kN to 0.2 m at 70 kN for BG2. This phenomenon demonstrates that the concrete surrounding the FRP bar might peel off near the beam's support at a high load level, as the maximum bond strength is exceeded. Furthermore, it is worth noting that the value of the peak bond stress of BG1 (from 11.69 to 13.79 MPa) is higher than that of BG2 (from 4.93 to 7.25 MPa) before the ultimate load is achieved, which means that debonding failure of the FRP bars at the support region might occur in an RC beam with a lower reinforcement ratio.

Figure 12 shows the distance of the peak bond stress from the left support of the reinforced beam under different load levels. The peak bond stresses are located at the point of loading initially and could migrate towards the supporting end of the beam as the load increased, until failure, as long as the cracking load is reached. The turning points of both curves are associated with the cracking load at load levels of 12 and 14 kN for BG1 and BG2, respectively. As seen in **Figure 12**, the location of the peak bond stress of BG1 is closer to the free end than BG2 at the same load level. Additionally, the peak stress of BG1 is higher than that of BG2, as shown in **Figure 11**. Therefore, it can be concluded that end-peeling, which usually occurs in a sudden and brittle way, is more likely to occur at the surface between the FRP bar and the surrounding concrete in BG1 than in BG2. Due to a higher axial stress resistance, a higher reinforcement ratio of

the FRP bars can enhance the shear bond performance of a reinforced beam.

DYNAMIC VALIDATION

As shown in **Eq. 23**, the DSM $[K]$, in which the circular frequency ωn is included, is established in the frequency domain. Since the DSM is frequency-dependent, only one element is sufficient to capture the natural frequencies as long as the material and geometrical properties remain unchanged throughout the entire element by making a frequency sweep over a wide frequency range. Therefore, the mesh refinement is no longer needed to capture the natural frequencies and related mode shapes especially in high frequency range, and a dramatic reduction of computational costs can be realized.

In this work, the signal of the excitation force is applied at the two loading points, and the dynamic responses are captured at four points equally spaced along the beam to simulate different output channels. Despite the fact that only one element can sufficiently represent entire reinforced beam (Sun et al., 2018) as long as the material and geometric properties remains unchanged, more elements are applied in this study so that the nodes of the spectral model correspond with the location of the applied load and output channels. After that, the frequency sampling points are

swept from 0 to 2,000 Hz to obtain the natural frequencies of the specimen, and the average normalized power spectral densities are obtained according to the spectra signatures from all channels.

A typical profile of the average normalized power spectral density (ANPSD) of BG1 is shown in **Figure 13**, and the natural frequencies can be obtained by the frequencies associated with the peak values in the curve. Using the same method, the modal frequencies of both specimens are shown in **Table 2**, and it is clear that the differences between BG1 and BG2 are quite small (from 0.23 to 0.65 percent), which shows that the increasing reinforcement ratio only slightly influences the modal frequencies.

Taking the computational efficiency and accuracy into account, the spectral method can also be used for damage identification by employing a vibration-based technique that can reflect changes in the stiffness, mass or damping ratio of a structure. To achieve this goal, the element size is set as 0.1 m, resulting in 23 elements for BG1 and BG2. Two damage scenarios (D1 and D2) are introduced by reducing the elastic modulus of the element at 1.0 m by 10–20 percent to numerically simulate the flexural crack at the midspan of the specimens. Using the same procedure, the frequency changes among the different levels of damage scenarios can be calculated, as shown in **Table 3**. The frequency changes can be clearly observed which demonstrate the influence of structural damage on natural frequencies.

The measurement of natural frequencies can exhibit the global structural changes, but it is insufficient when being used for the localization of structural damages. The mode shape curvature, which is extracted from the second-order differentiation of displacement mode shapes as shown in **Eq. 27**, is more sensitive for depicting structural damage than the frequency characteristics. Hence, it will be used herein to indicate the damage location of the reinforced beam.

$$\kappa_j = \frac{\phi_j(i+1) - 2\phi_j(i) + \phi_j(i-1)}{l_i^2} \quad (27)$$

In this study, mode shapes can be extracted directly from the nodal displacement related to each natural frequency since the proposed spectral model is formulated in the frequency domain. The damage scenario D2 (20% damage) of BG1 is chosen to study the alternation of mode shape curvature. The first four mode shape and mode shape curvature are shown in **Figures 14, 15**. According to the abrupt changes of mode shape curvature observed at the location of damaged element, the structural changes correlated to changes in material properties, which are usually caused by structural damage, can be clearly indicated.

Furthermore, an interesting application of the proposed model for damage identification is to be used as the baseline model of FRP-RC beams under a framework of model updating strategy, in which the static and dynamic measurements are usually used to update the baseline model in order to assess the structural conditions. Due to its simplicity and efficiency, the proposed one-dimensional spectral model enables the updating procedure to be conducted in a fast way, compared with that of FE model which requires high computational costs. From this preliminary study, it is found that the quantification of

structural damage at an early stage can be used to predict catastrophes and the proposed model has great potential to achieve this purpose.

CONCLUSION

This study numerically investigated the static and dynamic performances of a concrete beam reinforced with FRP bars by using a simplified spectral model. A one-dimensional spectral model is developed to study the flexural behaviour of FRP-RC beams, and the global deflection and local strain of concrete and FRP bars are calculated. Compared with experimental and FE results, the accuracy of the proposed model has been demonstrated, and satisfactory precision can be achieved by using a small number of elements. The interfacial bond behaviour between the FRP bar and the surrounding concrete is simulated. Despite the simplicity of the proposed one-dimensional model, the peak shear stress and its propagation towards the support end of the RC beam with increasing load have been appropriately captured. This phenomenon represents the tendency of end-peeling of FRP bars when the interfacial shear strength is exceeded.

Since the proposed spectral model is derived in the frequency domain, the dynamic characteristics of the FRP-RC beam, such as the natural frequencies and mode shapes, are obtained by using a small number of elements. Compared with the FE analysis, the computational costs are reduced dramatically due to the simplicity of the proposed model. Furthermore, damage location can be clearly observed based on the changes of the mode shape curvatures. Therefore, due to the simplicity and efficiency, the proposed model might be used as a baseline model for damage identification to prevent catastrophes at an early stage.

DATA AVAILABILITY STATEMENT

The original contributions presented in the study are included in the article/Supplementary Material, further inquiries can be directed to the corresponding authors.

AUTHOR CONTRIBUTIONS

RS conceived the work and wrote the manuscript. RP and JG developed the numerical model. YW analyzed the results and revised the manuscript.

FUNDING

The authors acknowledge the financial supports from the Fundamental Research Funds for the Central Universities (NO. 2020CDJ-LHZZ-017, 2021CDJQY-039), Chongqing Research Program of Basic Research and Frontier Technology (No. cstc2020jcyjmsxmX0946), and Spanish Ministry of Economy and Competitiveness (project BIA 2017-84975-C2-1-P).

REFERENCES

- Acciai, A., D'Ambrisi, A., De Stefano, M., Feo, L., Focacci, F., and Nudo, R. (2016). Experimental Response of FRP Reinforced Members without Transverse Reinforcement: Failure Modes and Design Issues. *Composites B: Eng.* 89, 397–407. doi:10.1016/j.compositesb.2016.01.002
- ACI Committee 318 (2008). *Building Code Requirements for Structural concrete (ACI318-08) and Commentary (ACI 318R-08)*. Farmington Hills (Mich, USA): American concrete institute.
- Aiello, M. A., and Ombres, L. (2000). Load-Deflection Analysis of FRP Reinforced Concrete Flexural Members. *J. Compos. Constr.* 4, 164–171. doi:10.1061/(asce)1090-0268(2000)4:4(164)
- Al-Sunna, R. (2006). *Deflection Behaviour of FRP Reinforced concrete Flexural Members, PhD Thesis*. Sheffield, UK: The University of Sheffield.
- Al-Sunna, R., Pilakoutas, K., Hajirasouliha, I., and Guadagnini, M. (2012). Deflection Behaviour of FRP Reinforced concrete Beams and Slabs: An Experimental Investigation. *Composites Part B: Eng.* 43, 2125–2134. doi:10.1016/j.compositesb.2012.03.007
- Almusallam, T. H. (1997). Analytical Prediction of Flexural Behavior of Concrete Beams Reinforced by FRP Bars. *J. Compos. Mater.* 31 (7), 640–657. doi:10.1177/002199839703100701
- Barris, C., Torres, L., Comas, J., and Miàs, C. (2013). Cracking and Deflections in GFRP RC Beams: an Experimental Study. *Composites Part B: Eng.* 55 (12), 580–590. doi:10.1016/j.compositesb.2013.07.019
- Barris, C., Torres, L., Turon, A., Baena, M., and Catalan, A. (2009). An Experimental Study of the Flexural Behaviour of GFRP RC Beams and Comparison with Prediction Models. *Compos. Structures* 91, 286–295. doi:10.1016/j.compstruct.2009.05.005
- Bencardino, F., Condello, A., and Ombres, L. (2016). Numerical and Analytical Modeling of concrete Beams with Steel, FRP and Hybrid FRP-Steel Reinforcements. *Compos. Structures* 140, 53–65. doi:10.1016/j.compstruct.2015.12.045
- Benmokrane, B., Chaallal, O., and Masmoudi, R. (1996). Flexural Response of concrete Beams Reinforced with FRP Reinforcing Bars. *ACI Struct. J.* 93 (1), 46–55. doi:10.14359/9839
- Bischoff, P. H. (2005). Reevaluation of Deflection Prediction for Concrete Beams Reinforced with Steel and Fiber Reinforced Polymer Bars. *J. Struct. Eng.* 131 (5), 752–767. doi:10.1061/(asce)0733-9445(2005)131:5(752)
- Branson, D. E. (1977). *Deformation of concrete Structures*. New York: McGraw-Hill.
- Capozucca, R., Blasi, M. G., and Corina, V. (2015). NSM Technique: Bond of CFRP Rods and Static/dynamic Response of Strengthened RC Beams. *Compos. Structures* 127, 466–479. doi:10.1016/j.compstruct.2015.03.013
- Capozucca, R., and Bossoletti, S. (2014). Static and Free Vibration Analysis of RC Beams with NSM CFRP Rectangular Rods. *Composites Part B: Eng.* 67, 95–110. doi:10.1016/j.compositesb.2014.06.005
- De Domenico, D., Pisano, A. A., and Fuschi, P. (2014). A FE-Based Limit Analysis Approach for concrete Elements Reinforced with FRP Bars. *Compos. Structures* 107, 594–603. doi:10.1016/j.compstruct.2013.08.039
- Echeverria, M., and Perera, R. (2013). Three Dimensional Nonlinear Model of Beam Tests for Bond of Near-Surface Mounted FRP Rods in concrete. *Composites Part B: Eng.* 54, 112–124. doi:10.1016/j.compositesb.2013.05.008
- fib (2010). *Model Code 2010*. Bull. 55 Vol. 1 (5) Lausanne, Switzerland: Federation Internationale du Beton; 2010.
- Gopalakrishnan, S., Ghakraborty, A., and Roy Mahapatra, D. (2008). *Spectral Finite Element Method*. 1st ed. London: Springer.
- Gravina, R. J., and Smith, S. T. (2008). Flexural Behaviour of Indeterminate concrete Beams Reinforced with FRP Bars. *Eng. Structures* 30, 2370–2380. doi:10.1016/j.engstruct.2007.12.019
- Habeeb, M. N., and Ashour, A. F. (2014). Flexural Behavior of Continuous GFRP Reinforced concrete Beams. *J. Compos. Constr.* 12 (2), 115–124. doi:10.1061/(asce)1090-0268(2008)12:2(115)
- Hawileh, R. A. (2015). Finite Element Modeling of Reinforced concrete Beams with a Hybrid Combination of Steel and Aramid Reinforcement. *Mater. Des.* (1980–2015) 65, 831–839. doi:10.1016/j.matdes.2014.10.004
- Hawileh, R. A. (2012). Nonlinear Finite Element Modeling of RC Beams Strengthened with NSM FRP Rods. *Construction Building Mater.* 27, 461–471. doi:10.1016/j.conbuildmat.2011.07.018
- Kara, I. F., Ashour, A. F., and Dundar, C. (2013). Deflection of concrete Structures Reinforced with FRP Bars. *Composites Part B: Eng.* 44, 375–384. doi:10.1016/j.compositesb.2012.04.061
- Kassem, C., Farghaly, A. S., and Benmokrane, B. (2011). Evaluation of Flexural Behavior and Serviceability Performance of concrete Beams Reinforced with FRP Bars. *J. Compos. Constr.* 15 (5), 682–695. doi:10.1061/(asce)cc.1943-5614.0000216
- Miàs, C., Torres, L., Turon, A., and Barris, C. (2013). Experimental Study of Immediate and Time-dependent Deflections of GFRP Reinforced concrete Beams. *Compos. Structures* 96, 279–285. doi:10.1016/j.compstruct.2012.08.052
- Mota, C., Alminar, S., and Svecova, D. (2006). Critical Review of Deflection Formulas for FRP-RC Members. *J. Compos. Constr.* 10 (3), 183–194. doi:10.1061/(asce)1090-0268(2006)10:3(183)
- Nour, A., Massicotte, B., Yildiz, E., and Koval, V. (2007). Finite Element Modeling of concrete Structures Reinforced with Internal and External Fibre-Reinforced Polymers. *Can. J. Civ. Eng.* 34 (3), 340–354. doi:10.1139/l06-140
- Perera, R., and Bueso-Inchausti, D. (2010). A Unified Approach for the Static and Dynamic Analyses of Intermediate Debonding in FRP-Strengthened Reinforced concrete Beams. *Compos. Structures* 92, 2728–2737. doi:10.1016/j.compstruct.2010.04.006
- Rafi, M. M., Nadjai, A., and Ali, F. (2008). Finite Element Modeling of Carbon Fiber-Reinforced Polymer Reinforced concrete Beams under Elevated Temperatures. *ACI Struct. J.* 105 (6), 701–710. doi:10.14359/20098
- Rasheed, H. A., Nayal, R., and Melhem, H. (2004). Response Prediction of concrete Beams Reinforced with FRP Bars. *Compos. Structures* 65, 193–204. doi:10.1016/j.compstruct.2003.10.016
- Razaqpur, A. G., Svecova, D., and Cheung, M. S. (2000). Rational Method for Calculating Deflection of Fiber Reinforced Polymer Reinforced Beams. *ACI Struct. J.* 97 (1), 175–184. doi:10.14359/847
- Rizkalla, S. H., and Nanni, A. (2003). *Field Applications of FRP Reinforcements: Case Studies*. Farmington Hills (Mich, USA): American Concrete Institute (ACI) Special Publication SP-215.
- Solyom, S., and Balázs, G. L. (2021). Analytical and Statistical Study of the Bond of FRP Bars with Different Surface Characteristics. *Compos. Structures* 270, 113953. doi:10.1016/j.compstruct.2021.113953
- Solyom, S., and Balázs, G. L. (2020). Bond of FRP Bars with Different Surface Characteristics. *Construction Building Mater.* 264, 119839. doi:10.1016/j.conbuildmat.2020.119839
- Sun, R., Perera, R., Sevillano, E., and Gu, J. (2018). Parameter Identification of Composite Materials Based on Spectral Model by Using Model Updating Method. *Int. J. Polym. Sci.*, 2018, 7310846–9. doi:10.1155/2018/7310846
- Sun, R., Sevillano, E., and Perera, R. (2015). A Discrete Spectral Model for Intermediate Crack Debonding in FRP-Strengthened RC Beams. *Composites Part B: Eng.* 69, 562–575. doi:10.1016/j.compositesb.2014.10.017
- Trefethen, L. N. (2000). *Spectral Methods in Matlab*. Philadelphia, USA, Siam.
- Yan, F., Lin, Z., and Yang, M. (2016). Bond Mechanism and Bond Strength of GFRP Bars to concrete: A Review. *Composites Part B: Eng.* 98, 56–69. doi:10.1016/j.compositesb.2016.04.068
- Zhang, L., Sun, Y., and Xiong, W. (2015). Experimental Study on the Flexural Deflections of concrete Beam Reinforced with Basalt FRP Bars. *Mater. Struct.* 48, 3279–3293. doi:10.1617/s11527-014-0398-0

Conflict of Interest: The authors declare that the research was conducted in the absence of any commercial or financial relationships that could be construed as a potential conflict of interest.

Publisher's Note: All claims expressed in this article are solely those of the authors and do not necessarily represent those of their affiliated organizations, or those of the publisher, the editors and the reviewers. Any product that may be evaluated in this article, or claim that may be made by its manufacturer, is not guaranteed or endorsed by the publisher.

Copyright © 2021 Sun, Perera, Gu and Wang. This is an open-access article distributed under the terms of the Creative Commons Attribution License (CC BY). The use, distribution or reproduction in other forums is permitted, provided the original author(s) and the copyright owner(s) are credited and that the original publication in this journal is cited, in accordance with accepted academic practice. No use, distribution or reproduction is permitted which does not comply with these terms.



Lightweight Neural Network for Real-Time Crack Detection on Concrete Surface in Fog

Gang Yao, Yujia Sun, Yang Yang* and Gang Liao

School of Civil Engineering, Chongqing University, Chongqing, China

OPEN ACCESS

Edited by:

Qian Zhang,
FAMU-FSU College of Engineering,
United States

Reviewed by:

Pengkun Liu,
Carnegie Mellon University,
United States
Yunchao Tang,
Zhongkai University of Agriculture and
Engineering, China

*Correspondence:

Yang Yang
20121601009@cqu.edu.cn

Specialty section:

This article was submitted to
Structural Materials,
a section of the journal
Frontiers in Materials

Received: 20 October 2021

Accepted: 08 November 2021

Published: 09 December 2021

Citation:

Yao G, Sun Y, Yang Y and Liao G
(2021) Lightweight Neural Network for
Real-Time Crack Detection on
Concrete Surface in Fog.
Front. Mater. 8:798726.
doi: 10.3389/fmats.2021.798726

Cracks are one of the most common factors that affect the quality of concrete surfaces, so it is necessary to detect concrete surface cracks. However, the current method of manual crack detection is labor-intensive and time-consuming. This study implements a novel lightweight neural network based on the YOLOv4 algorithm to detect cracks on a concrete surface in fog. Using the computer vision algorithm and the GhostNet Module concept for reference, the backbone network architecture of YOLOv4 is improved. The feature redundancy between networks is reduced and the entire network is compressed. The multi-scale fusion method is adopted to effectively detect cracks on concrete surfaces. In addition, the detection of concrete surface cracks is seriously affected by the frequent occurrence of fog. In view of a series of degradation phenomena in image acquisition in fog and the low accuracy of crack detection, the network model is integrated with the dark channel prior concept and the Inception module. The image crack features are extracted at multiple scales, and BReLU bilateral constraints are adopted to maintain local linearity. The improved model for crack detection in fog achieved an mAP of 96.50% with 132 M and 2.24 GMacs. The experimental results show that the detection performance of the proposed model has been improved in both subjective vision and objective evaluation metrics. This performs better in terms of detecting concrete surface cracks in fog.

Keywords: crack detection, deep learning, concrete surface, improved YOLOv4, ghostnet, dark channel prior

INTRODUCTION

Controlling concrete surface quality is one of the main challenges facing the concrete industry. High quality concrete surfaces leave an aesthetically pleasing impression, so architects and building owners are getting stricter about concrete surface quality (Chen et al., 2019; Wei et al., 2019). Crack, one of the most common affecting factors for concrete surface quality, has a significance impact on the safety and sustainability of concrete buildings. Therefore, crack detection plays an essential role in maintaining buildings.

Traditionally, human visual inspection was often used to assess defects on concrete surfaces (Peng et al., 2020). Nevertheless, the judgment conclusions drawn by different people are diverse under the identical concrete surface conditions (Laofor and Peansupap, 2012). Furthermore, the above method generally requires more labor force and time, and it does not produce consistent quantitative objective results. Hence, automatic defect inspection is extremely feasible to assess defects more efficiently and objectively.

In comparison with the deficiencies of the traditional human visual identification methods, there has been extensive research on the computer-based methods. Scholars have proposed a mass of

damage detection methods based on image processing techniques (IPT) have been proposed. Obviously, IPT is preponderant in identifying various surface defects. Yeum et al. once applied IPT to detect cracks (Yeum and Dyke, 2015), while integrating with sliding window technology. In the present study, the potentials of IPT are embodied distinctly. In recent years, many studies (Nishikawa et al., 2012; Choi et al., 2017) based on IPT have been carried out to replace human visual inspection. However, the detection performance is severely weakened in case the intensities of some noisy pixels are lower than those of crack pixels. Given edges and cracks are morphologically similar to a large extent, many researchers (Salman et al., 2013; Zalama et al., 2014) adopt filter-based methods special for edge detection to detect pavement cracks. The IPT-based method is effective and fast, but its robustness is still far from enough in the event of noises (mainly generated by lighting and distortion), which seriously affects the results (Koziarski and Cyganek, 2017). Denoising technology can overcome these problems desirably. Total variation image denoising is a prevailing method to reduce the noises of image data, thereby enhancing the edge detectability of images (Beck and Teboulle, 2009). Owing to the significant changes in the image data captured in real engineering, the application of transcendental knowledge in IPT is restricted. These traditional crack detection methods are obviously defective: each method is designed for a specific database or setting. The crack detectors often do not work, once the setting or database is changed. Moreover, it is difficult to extract semantic information (width and location of cracks, etc.) from images. In order to help inspectors detect defects, image processing algorithms are usually used. But the final results are still obtained relying on manual judgment (Oh et al., 2009).

At present, image acquisition equipment and computing capabilities are increasing improved, a host of machine learning algorithms (such as deep learning) have been used to recognize objects with acceptable results (Ciresan et al., 2012; He et al., 2015; Krizhevsky et al., 2017; Zhang et al., 2021). Deep learning techniques are data-driven approaches which do not require manually-designed rules. When building the model, it is just necessary to select a proper network structure for model output evaluation and a reasonable optimization algorithm. Wide attention has been attracted to the Convolutional Neural Network (CNN), as an effective recognition method (Lecun et al., 2015). In addition, it has been highlighted in image classification and object detection (Ren et al., 2017). A deep-learning-based method was developed to detect concrete bugholes (Wei et al., 2019; Yao et al., 2019; Wei et al., 2021), concrete cracks (Chen and Jahanshahi, 2018; Dung and Anh, 2019; Sun et al., 2021; Tang et al., 2021a; Yao et al., 2021), pavement cracks (Ji et al., 2020; Mei and Gül, 2020; Guan et al., 2021), and other defects (Lin et al., 2017; Cha et al., 2018; Li et al., 2019; Tang et al., 2021b; Jiang et al., 2021). The existing crack detection methods based on CNN generally have problems, such as complex network structures and excessive training parameters. One crucial technical problem is balancing the efficiency and accuracy of the detection.

At present, the mainstream framework of object detection based on deep learning is mainly divided into two categories: two-stage, based on the idea of target region proposal, and one-stage,

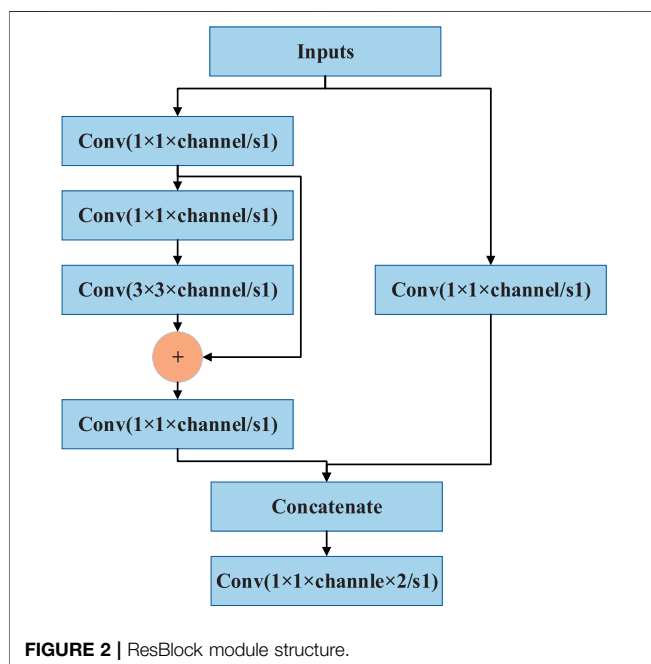
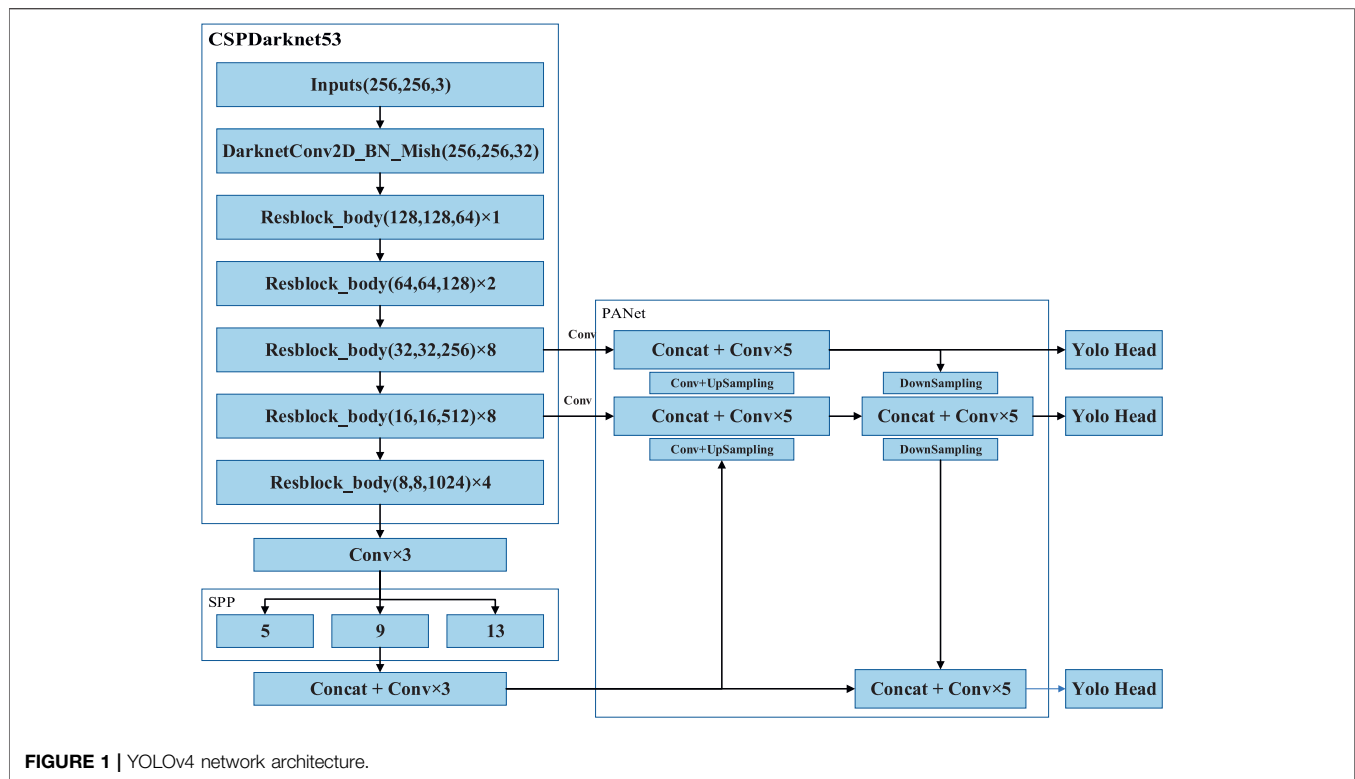
based on the idea of regression. Target region proposals in the two-stage category are extracted first, and the detection model is then trained based on them (such as RCNN (Girshick et al., 2013), Fast-RCNN (Girshick, 2015) and Faster-RCNN (Ren et al., 2017)). The one-stage category does not have the extraction operation of the target region proposal, and the target category and location information are directly generated by the detection network (such as SSD (Liu et al., 2016), YOLOv3 (Redmon and Ali, 2018) and YOLOv4 (Bochkovskiy et al., 2020)). Two-stage has higher task accuracy but slower speed, while one-stage can achieve real-time performance at the expense of accuracy. Therefore, in order to balance the detection efficiency and accuracy of the concrete surface cracks, the GhostNet Module concept (Han et al., 2020) is used for reference, and the backbone network architecture of YOLOv4 is improved so as to use fewer parameters to generate more features. The feature redundancy between networks is reduced, and the whole network is compressed. The multi-scale fusion method is adopted to effectively detect cracks on concrete surfaces, greatly overcoming the difficulty of manual detection.

At present, most relevant studies are carried out under conditions wherein the image information is clear and obvious. With the frequent occurrence of adverse weather (such as haze), the collected images will be degraded by the loss of detailed information, color distortion and image resolution. The recognition method of the network model in the clear image scene appears to be slightly lacking in practicality. When the target features of the collected images in fog are unclear and the resolution is problematic, the lightweight YOLOv4 network model is directly used for crack detection, and the detection performance will be reduced. Consequently, in this paper, the network model is integrated with the dark channel prior concept (Kaiming et al., 2011) and the Inception module (Szegedy et al., 2016). The image crack features are extracted at multiple scales, and BReLU bilateral constraints are adopted to maintain local linearity. Based on the atmospheric scattering model (Nayar and Narasimhan, 1999) and the improved YOLOv4 model, cracks on concrete surfaces can be detected effectively in fog. The proposed network model is compared with the YOLOv3 algorithm in subjective vision and objective evaluation metrics. The results show that the proposed method has better detection performance, and the model parameters and amount of calculations are greatly reduced.

THE LIGHTWEIGHT MODEL FOR CONCRETE CRACK DETECTION

The Principles of YOLOv4

The backbone network CSPDarknet53 of YOLOv4 is the core of the algorithm and is used to extract the target features. CSPNet can maintain accuracy and reduce computing bottlenecks and memory costs while being simplified. Drawing from the experience of CSPNet, YOLOv4 adds CSP to each large residual block of Darknet53. It divides the feature mapping of the base layer into two parts, then merges them through a cross-stage hierarchical structure to reduce the amount of calculations



while ensuring accuracy. The activation function of CSPDarknet53 uses the Mish activation function, and the subsequent network uses the Leaky ReLU function. The experiments demonstrated that this setting had higher accuracy in object detection. Unlike the YOLOv3 algorithm, which uses FPN for upsampling, YOLOv4 draws on the idea

of information circulation in the PANet network. Firstly, the semantic information of the layer features is propagated to the low-level network by upsampling, and is then fused with the high-resolution information of the underlying features to improve the small target detection effect. Next, the information transmission path from the bottom to the top is increased, and the feature pyramid is enhanced through downsampling. Finally, the feature maps of different layers are fused to make predictions. The specific network framework is shown in **Figure 1** (Bochkovskiy et al., 2020). The ResBlock_body is the residual block of CSPDarknet53, which can extract the target features of the image and reduce the computational bottleneck and the memory cost. The specific internal Module architecture is shown in **Figure 2** (Yao et al., 2021).

The Principles of the Ghost Module

The Ghost Module can use fewer parameters to generate more feature maps. Specifically, in view of the large amount of redundancy in the intermediate feature maps calculated by mainstream CNN, the deep neural network divides the ordinary convolutional layer into two parts. In the first part, the number of convolutions is strictly controlled, and the inherent feature maps are extracted by ordinary convolution operations. In the second part, a series of simple linear operations are used to generate more feature maps. Compared with the ordinary convolutional neural network, the total number of parameters and computational complexity required in the Ghost module are reduced without changing the size of the output feature map. The specific implementation is shown in **Figure 3** (Han et al., 2020).

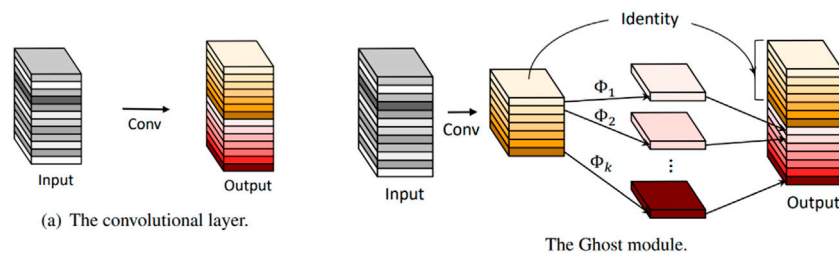


FIGURE 3 | Ordinary convolution operation and Ghost module operation.

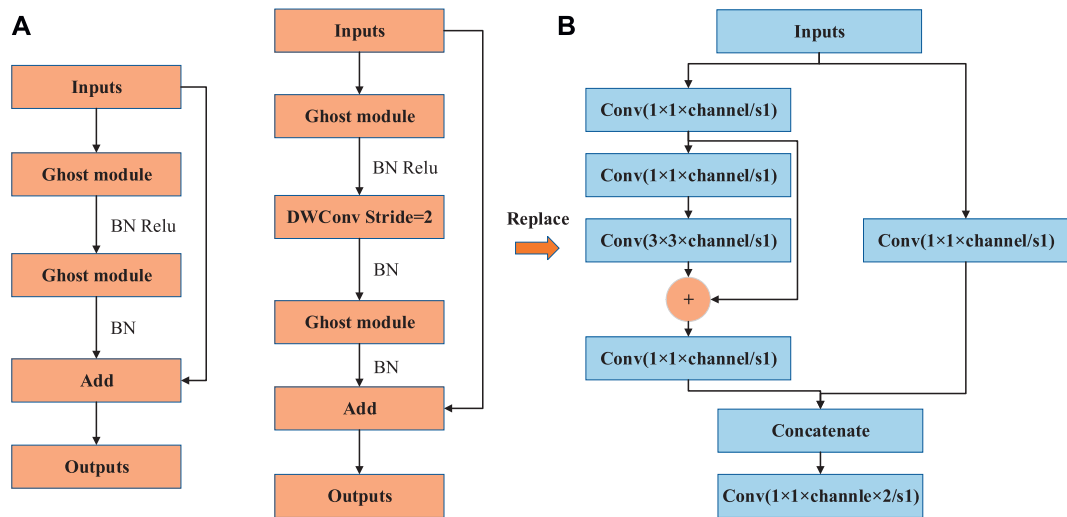


FIGURE 4 | Ghost bottleneck module and Resblock_body structure: (A) Ghost bottleneck structure with stride = 1, 2 (B) Resblock_body.

The memory and computation benefits achieved using the Ghost module are analyzed. The input data is $X \in R^{c \times h \times w}$, where c is the number of channels, w is the width and h is the height. $Y \in R^{n \times h \times w}$ is the output feature map with n channels, and $f \in R^{c \times k \times k \times n}$ is the convolutional kernel size. The FLOPs required by the ordinary convolution process are $n \times h \times w \times c \times k \times k$.

The Ghost module believes that the output feature maps are transformed by a few original feature maps through some cheap operations such as linear transformation. The size of the ordinary convolution kernel is $f' \in R^{c \times k \times k \times m}$, where $m \leq n$, and the output feature map is $Y' \in R^{h \times w \times m}$. In this way, in order to further obtain the required n feature maps, a series of cheap linear operations are used to generate s duplicate feature maps for the original map in Y' , and the average kernel size of each linear operation is $d \times d$. The theoretical speedup ratio when using the Ghost module to upgrade ordinary convolution is computed by Eq. 1. The magnitude of $d \times d$ is similar to $k \times k$ and $s \ll c$. The compression ratio of the parameter is computed by Eq. 2. The compression ratio of the parameter is approximately equal to the speedup ratio.

$$r_s = \frac{n \times h' \times w' \times c \times k \times k}{\frac{n}{s} \times h' \times w' \times c \times k \times k + (s-1) \times \frac{n}{s} \times h' \times w' \times d \times d} \quad (1)$$

$$= \frac{c \times k \times k}{\frac{1}{s} \times c \times k \times k + \frac{s-1}{s} \times d \times d} \approx \frac{s \times c}{s + c - 1} \approx s$$

$$r_c = \frac{n \times c \times k \times k}{\frac{n}{s} \times c \times k \times k + (s-1) \times \frac{n}{s} \times d \times d} \approx \frac{s \times c}{s + c - 1} \approx s \quad (2)$$

The Lightweight YOLOv4 Model Structure The Improvement of the YOLOv4 Model Framework

The Ghost module is applied to generate the same number of feature maps as the ordinary convolutional layer. It can easily replace the convolutional layer and integrate it into the existing designed neural network structure to reduce the computational cost. The Ghost module is utilized to build a Ghost bottleneck structure to replace the Resblock_body bottleneck structure in the YOLOv4 network model, which can further eliminate feature redundancy.

The Ghost bottleneck constructed using the Ghost module concept is shown in Figure 4. Similar to the basic residual block in ResNet, it integrates multiple convolutional layers and shortcuts.

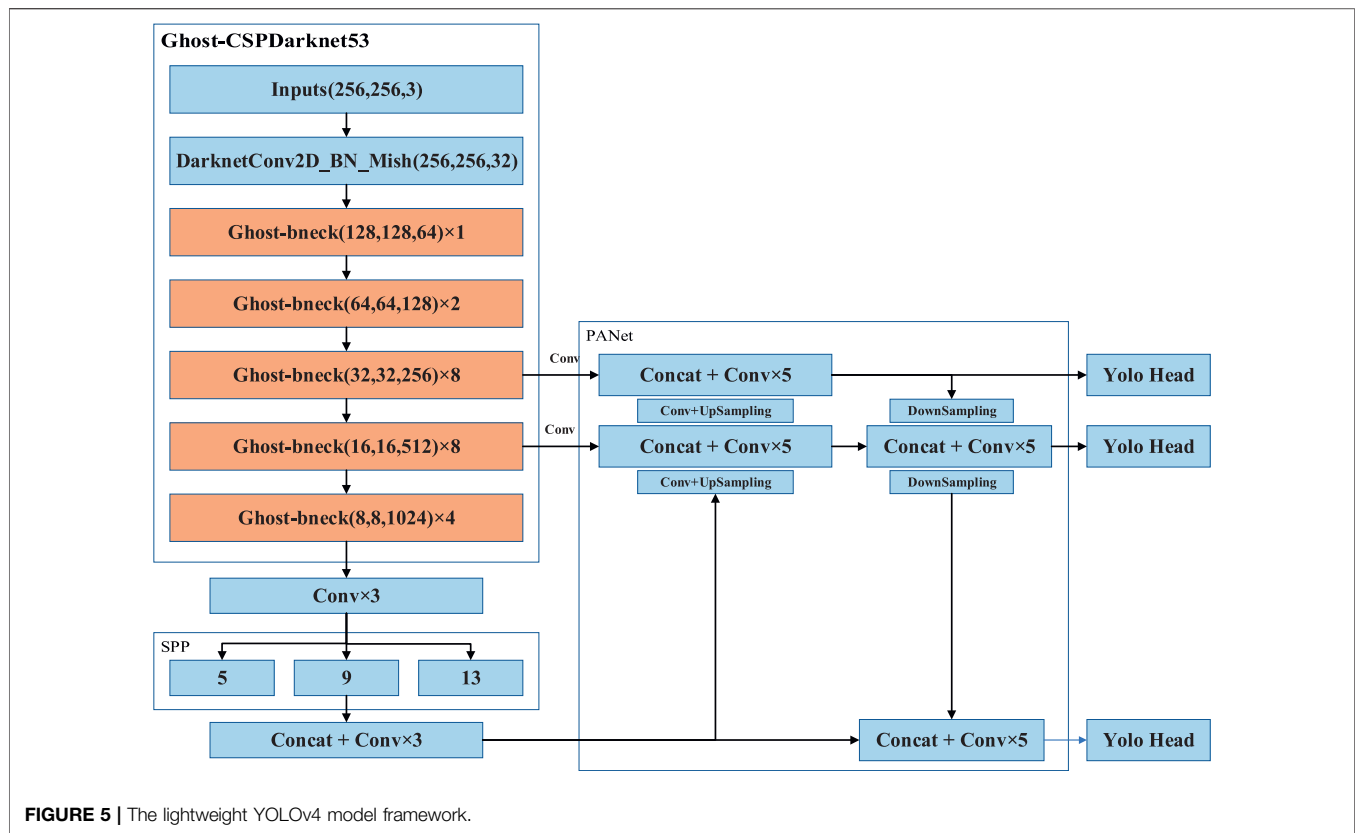


FIGURE 5 | The lightweight YOLOv4 model framework.

The Ghost bottleneck structure is mainly constructed by two stacked Ghost modules. The first Ghost module is used as an extension layer which increases the number of channels. The second one reduces the number of channels to match the shortcut path. The shortcut is then used to connect the input and output of the two Ghost modules, and the MobileNetv2 module concept is used for reference. The ReLU structure is not used after the second Ghost module. For the Ghost module with stride = 2, the shortcut path is implemented by the separable convolution of the downsampling layer and stride = 2.

In this section, following the advantages of the basic SPP and PANet architecture in the YOLOv4 module, the Ghost bottleneck is used to replace the Resblock_body structure in the YOLOv4 module. The specific replacement network structure is shown in **Figure 5**.

The Fast Non-Maximum Suppression Algorithm

The traditional Non-Maximum Suppression (NMS) (Neubeck and Gool, 2006) algorithm arranges items in descending order according to the confidence scores of the detected target boxes. It sets an Intersection over Union (IoU) threshold and removes bounding boxes larger than the threshold. Until all the prediction boxes are traversed, the remaining bounding boxes are taken as the final target detection result. Since it is a sequential traversal, each category needs to be sorted and filtered, which will result in a loss of algorithm speed. In this study, considering the image characteristics of the concrete surface cracks, parallel processing is adopted to screen and retain each boundary box in parallel.

Firstly, all unfiltered network prediction boxes are input, and are arranged in descending order according to the confidence scores. Only the first N detection results are selected. The IoU for the crack prediction results is then calculated to obtain the IoU matrix. The diagonal elements and the lower triangle are self-intersecting and recalculating, and are set to 0. The maximum value of the IoU matrix is calculated, and the boxes outside the threshold limit are filtered out. As a result, the final screening result is the final recognition result.

THE CONCRETE CRACK DETECTION MODEL IN FOG

With the frequent occurrence of adverse weather such as haze, the collected images will be degraded by low image resolution and the loss of detailed information. The YOLOv4 network model lacks some practicability when applied to crack detection in clear image scenes, and its detection performance will decrease. This section focuses on a series of degradation phenomena in image acquisition and the low detection rate of cracks in adverse weather. Dark channel prior and the Inception module are used for reference to integrate into the network model. The image crack features are extracted at multiple scales, and BReLU bilateral constraints are adopted to maintain local linearity. The clear crack scene is restored based on the atmospheric scattering model, and the crack structure is effectively detected by combining with the improved YOLOv4 network model.

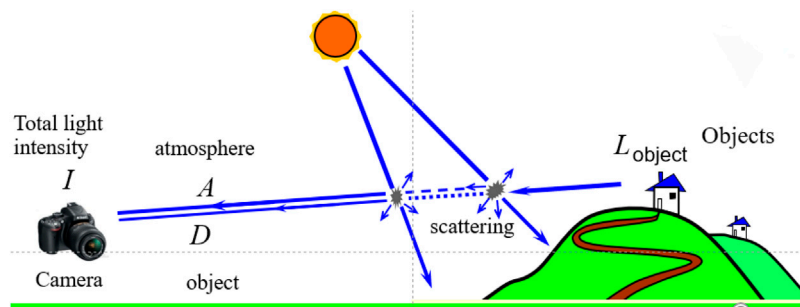


FIGURE 6 | Atmospheric scattering imaging link.

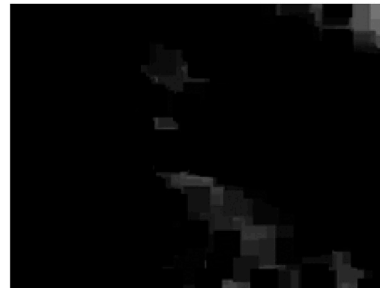
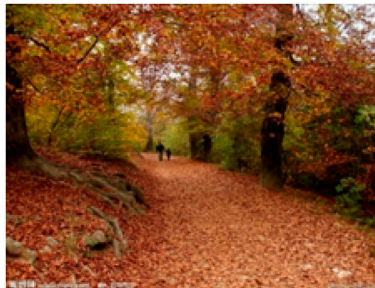


FIGURE 7 | Clear image and dark channel image.

Atmospheric Scattering Model

There are two main factors leading to image degradation in hazy weather. One is that the atmospheric light is scattered by the atmospheric haze particles to produce stray light, which affects the image resolution. The other is that the light reflected from the target will cause light attenuation through the absorption and scattering of suspended particles, which usually results in blurred image details and decreased contrast. Based on these two factors, Nayar and Narasimhan proposed an atmospheric scattering model (Nayar and Narasimhan, 2002). The imaging link is shown in Figure 6. The mathematical expression is shown in Eq. 3.

$$I = L^{object} \cdot t + A = L^{object} \cdot e^{-\beta d} + A_{\infty}(1 - e^{-\beta d}) \quad (3)$$

where I and L^{object} represent the light intensity of foggy images and sunny images, respectively; t represents the atmospheric transmittance; A represents the atmospheric light intensity; A_{∞} represents the atmospheric light intensity at infinity; β represents the extinction coefficient of scattering and absorption; d represents the distance between the target and the imaging system. Eq. 3 reveals that two parameters must be reconstructed if a clear image is to be restored: the atmospheric transmittance t and the atmospheric light intensity at infinity A_{∞} .

Dark Channel Prior

Dark channel prior (Kaiming et al., 2011) is a prior theory obtained from the statistics of a large number of fog-free

images. In most local areas of fog-free images, there are always one or more pixels whose gray value is close to 0. The mathematical expression is shown in Eq. 4.

$$J_{dark}^{object} = \min_{y \in \Omega(x)} \left\{ \min_{c \in \{r, g, b\}} [L_c^{object}] \right\} \rightarrow 0 \quad (4)$$

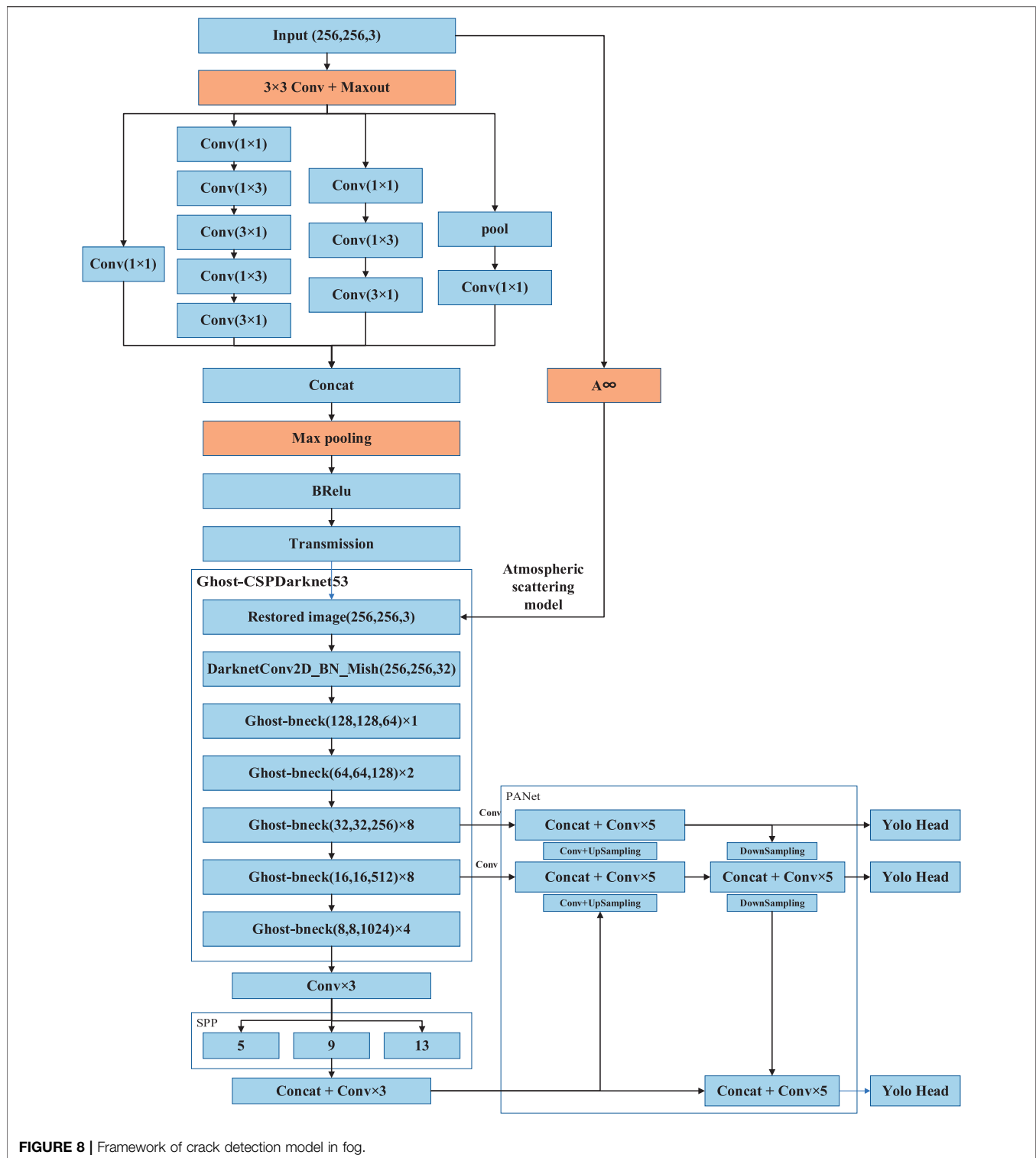
$$t(i, j) \rightarrow 1 - \min_c \left(\min_{y \in \Omega(x)} \left(\frac{I(i, j)}{A_{\infty}} \right) \right) \quad (5)$$

where $\Omega(x)$ is the local area of the fog-free image; L_c^{object} and J_{dark}^{object} represent the original image and the image processed by dark channel, respectively. Figure 7 presents a dark channel image of a fog-free image. The atmospheric transmittance t can be obtained quickly by substituting the dark channel concept of Eq. 4 into the atmospheric scattering model, after which the clear image can be restored. The mathematical expression is presented as Eq. 5 Drawing lessons from the characteristics of the dark channel concept and integrating them into the neural network model is helpful for restoring clear images, and provides a higher detection rate for detecting cracks on concrete surfaces.

Framework of Crack Detection Model

The Improvement of the Model Framework

In this section, the YOLOv4 model architecture is improved to complete the crack detection on concrete surfaces in fog. The input data structure is the RGB concrete fog image, and the transmittance map of the corresponding fog image is expected to



be output in the middle. The position information of the image pixels remains unchanged, and the atmospheric light intensity at infinity is then estimated. The atmospheric scattering model is used to restore the image, and the cracks on the concrete surface are detected in combination with the lightweight YOLOv4 model

structure. The specific improved network model is shown in **Figure 8**.

The first layer of the network is the feature extraction layer, which can effectively extract the features of foggy images. Combined with the dark channel prior method, the activation

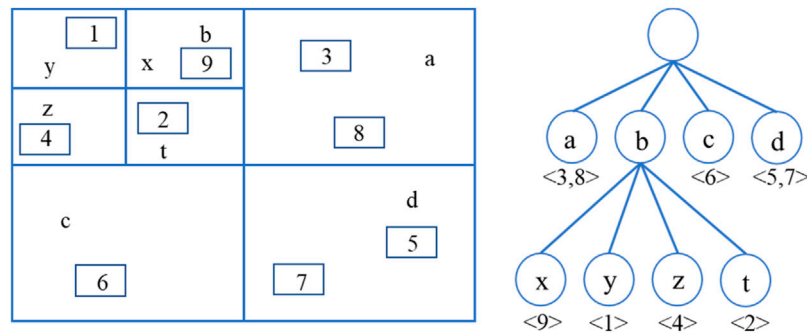


FIGURE 9 | The principle of the quadtree spatial index.

TABLE 1 | The method for estimating atmospheric light intensity at infinity.

Input image : Original foggy image I and Dark channel image I_{dark}

- (1) Perform median filtering on I : $I_{median} = \text{median}(I_{dark})$
- (2) Perform quadtree segmentation on I_{median} . The image area information is stored in four leaf nodes
- (3) The leaf node score is defined as: $I_{score}(\Omega) = \text{ave}\{I_{median}(\Omega)\}$;
- (4) Select the leaf node with the largest score Ω
- (5) Loop 2–5 steps until the area Ω is smaller than the threshold area size ψ of the adaptive image resolution. The threshold area is defined as: $\psi = 0.04 \times \min(\text{raw}, \text{col})$
- (6) Calculate the average value of the corresponding coordinate area in the original foggy image I as the atmospheric light intensity at infinity: $A_{\infty} = \text{ave}\{I(\Omega)\}$

function of convolution and Maxout is used as the first layer of the network. Firstly, the input foggy image is composed of 16 filters with a convolution kernel size of 3×3 . Subsequently, based on the idea of image dark channel, the Maxout nonlinear activation function is selected to realize the local minimum filtering function, and the extracted feature map is output.

Maxout divides the feature map z extracted by convolution into groups with k values, after which the Maxout unit outputs the largest element among them. It is defined as $h = z_j$. It can be seen that the Maxout activation function achieves the fitting of the convex function by separating the k terminal and taking its maximum value. On the basis of the Maxout unit, the first layer of the network is designed as shown in Eq. 6.

$$F_1^i(x) = \max_{j \in [1,k]} f_1^{ij}(x), \quad f_1^{ij} = W_1^{ij} \times I + B_1^{ij} \quad (6)$$

where W_1^{ij} is an inverse filter with a center value of -1 and a size of 3×3 . This means that the maximum output after the Maxout activation function is the minimum color channel value, which is the idea of the dark channel. The automatic learning of dark channel features is realized through feature extraction of the first layer.

In the second layer, a multi-scale convolution neural network is used to extract the features of the target. To improve the robustness of the feature extraction under different resolutions, the multi-scale extraction capability of the Inceptionv3 module structure is utilized, and the adaptability to the network width

and depth is increased. It can be seen that the spatial filters (5×5 , 7×7) with larger computing power are replaced by a convolution kernel (3×3) with smaller computing power in the second layer network structure, which not only reduces the number of parameters, but also speeds up the computations. Cross-channel information integration can be realized by designing the dimension reduction structure of a 1×1 convolution kernel followed by a 3×3 convolution kernel. The outputs of the adjacent activation responses are highly correlated, and the local representation ability is not reduced when reducing the number of these activation effects before aggregation. At the same time, the 3×3 convolution kernel is decomposed into two one-dimensional convolution kernels 1×3 and 3×1 by the convolution kernel decomposition design. Not only can this speed up the computations, but it can also increase the depth and nonlinearity of the network.

In the third layer, space invariance is achieved by selecting the maximum value of the neighborhood. Moreover, the local extremum is also consistent with the assumption that the medium transmission is locally constant in foggy weather, and the noise in the transmission image can be suppressed. In the fourth layer, inspired by the ReLU and Sigmoid activation functions, the BReLU activation function is used for nonlinear activation. The range of atmospheric transmittance t is $0-1$, which cannot be infinite or infinitesimal. Both local linearity and bilateral restrictions are maintained through a 3×3 convolution kernel. The transmittance image of the atmosphere can be mapped end to end. Ultimately, the input fog image is used to estimate the atmospheric light intensity at infinity, and the clear image can be restored. The lightweight YOLOv4 network model is utilized to detect concrete surface cracks.

The Estimation of Atmospheric Light Intensity at Infinity A_{∞}

According to the atmospheric scattering model of Eq. 3, the accuracy of the atmospheric light intensity estimation at infinity is analyzed. It directly determines the clarity of the restored target. Consequently, the atmospheric light intensity at infinity is directly related to the image clarity. In this paper, based on the dark channel of the haze image and combined with the quadtree spatial index principle, the atmospheric light

TABLE 2 | The initial parameters of the first stage.

Parameter	Value
Base_LR	10^{-3}
Batch_Size	16
Train_Epoch	100
Weight_decay	5×10^{-4}
Lr_scheduler_Max_iterations	5
Lr_scheduler_Minimum_lr	10^{-5}

TABLE 3 | The initial parameters of the second stage.

Parameter	Value
Base_LR	10^{-4}
Batch_Size	16
Train_Epoch	500
Weight_decay	5×10^{-4}
Lr_scheduler_Max_iterations	5
Lr_scheduler_Minimum_lr	10^{-5}

intensity at infinity is estimated. **Figure 9** illustrates the principle of the quadtree spatial index. The specific method of estimation is shown in **Table 1**.

The atmospheric light intensity at infinity is estimated by the above method, and the transmission image is reconstructed with the neural network. Through combination with the atmospheric scattering model of **Eq. 3**, a clear concrete crack image can be recovered, and by combination with the lightweight YOLOv4 network model framework, the crack training and detection can then be carried out.

The Construction of the Network Loss Function

The loss function of the network model is composed of the following parts: the transmittance estimation loss, the regression loss, the confidence loss and the classification loss. The regression loss of the prediction box adopts the CIOU loss function of the YOLOv4 network model. The mathematical expression is shown in **Eqs. 7–9**.

$$L_{CIOU} = 1 - IoU + \frac{d^2}{c^2} + \alpha v \quad (7)$$

$$v = \frac{4}{\pi^2} \left(\arctan \frac{w^{gt}}{h^{gt}} - \arctan \frac{w}{h} \right)^2 \quad (8)$$

$$\alpha = \frac{v}{1 - IoU + v} \quad (9)$$

where d represents the Euclidean distance between the center points of the two prediction boxes and c represents the diagonal distance of the closed area of the prediction box.

The confidence loss function adopts cross entropy and is divided into two parts: obj and noobj. In order to reduce the contribution weight of the noobj calculation part, the loss of noobj increases the weight coefficient λ_{noobj} . It is shown in **Eq. 10** The classification loss function adopts cross entropy. When the j th anchor box of the i th network is responsible for a real target, the bounding box generated by this anchor box will

calculate the classification loss function. This is shown in **Eq. 11** The loss of transmittance estimation learns the mapping relationship between the input image and transmittance by minimizing the loss function between the estimated transmittance and the actual transmittance. The mean square error between actual transmittance and predicted transmittance is defined as the loss function. The loss function is defined as **Eq. 12**.

$$L_{conf} = \sum_{i=0}^{K \times K} \sum_{j=0}^M I_{ij}^{obj} \left[\hat{C}_i \log(C_i) + (1 - \hat{C}_i) \log(1 - C_i) \right] - \lambda_{noobj} \sum_{i=0}^{K \times K} \sum_{j=0}^M I_{ij}^{noobj} \left[\hat{C}_i \log(C_i) + (1 - \hat{C}_i) \log(1 - C_i) \right] \quad (10)$$

$$L_{classes} = \sum_{i=0}^{K \times K} I_{ij}^{obj} \sum_{c \in classes} \left[\hat{p}_i(c) \log(p_i(c)) + (1 - \hat{p}_i(c)) \log(1 - p_i(c)) \right] \quad (11)$$

$$L_{trans} = \left[\frac{1}{m} \sum_{i=1}^m \left(\frac{1}{2} \| h_{w,b}(x) - y \|^2 \right) \right] + \frac{\lambda}{2} \sum_{l=1}^{n_l-1} \sum_{i=1}^{s_l} \sum_{j=1}^{s_l+1} (w_{ji}^{(l)})^2 \quad (12)$$

In **Eq. 12**, The first term on the right side of the equation is the mean square error term, and the second term is the regular term. The regular term has nothing to do with the bias $b_i^{(l)}$ and can only control the size of the weight, so it is also called the weight attenuation term. The weight decay parameter λ in the weight decay term can be used to determine the proportion of the two items in the loss function. The key of training is to obtain the minimum cost function by continuously adjusting the weight $w_{ij}^{(l)}$ and bias $b_i^{(l)}$.

In this section, the loss function of the crack detection model framework in fog is defined as:

$$L_{total} = L_{CIOU} + L_{conf} + L_{classes} + L_{trans} \quad (13)$$

EXPERIMENTS

Image Database Creation

A smartphone is used for image acquisition. For the purpose of collecting images of small cracks on a concrete surface, all images are taken from a distance of 0.1 m between the smartphone and concrete surface. 2000 original images ($3,024 \times 3,024$ pixels) are extracted from the surfaces of concrete buildings. Each original image can be cropped to generate 139 images (256×256 pixels). However, some cropped images do not include cracks. As a result, the images with cracks are meticulously selected from the cropped image set. Finally, 10,000 images conforming to requirements are selected to create the database.

The actual transmittance of the defogging images needs to be obtained as a label for training. Since the shooting target in actual fog needs to be aligned with the pixel position of the shooting target on a sunny day, there can be no shooting error, and the construction is too arduous. Accordingly, in this paper, images taken on sunny days are manually fogged to build the database.

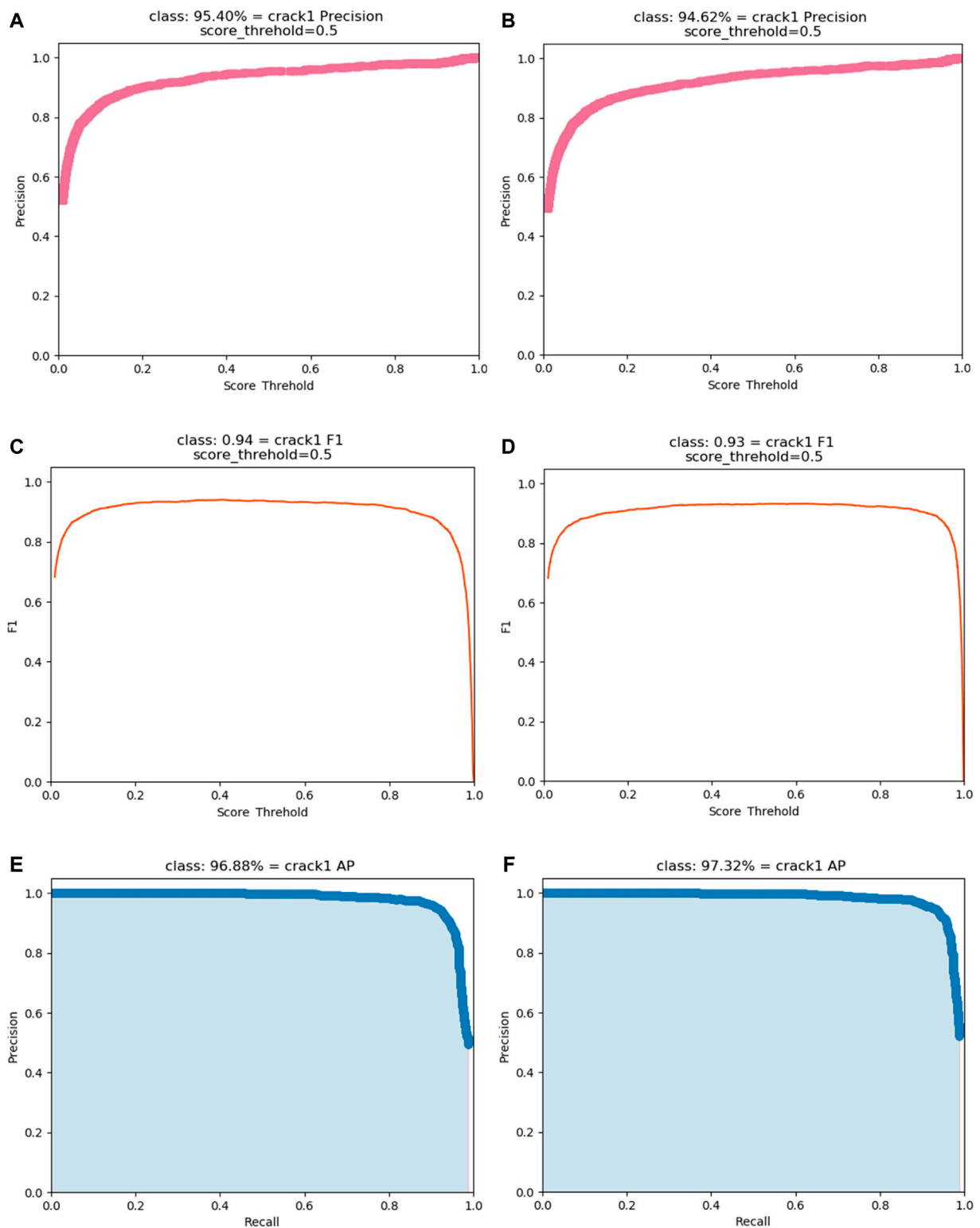
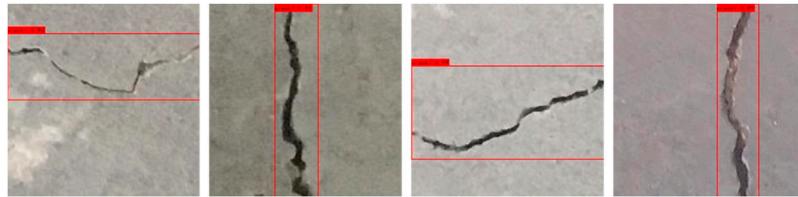


FIGURE 10 | The indices of the original YOLOv4 model and the lightweight YOLOv4 model: **(A)** Precision of the original YOLOv4 model **(B)** Precision of the lightweight YOLOv4 model **(C)** F₁ of the original YOLOv4 model **(D)** F₁ of the lightweight YOLOv4 model **(E)** AP of the original YOLOv4 model **(F)** AP of the lightweight YOLOv4 model.

TABLE 4 | The performance comparison of the lightweight YOLOv4 model with the original YOLOv4 model and the YOLOv3 model.

Algorithm	mAP (%)	Parameters (M)	FLOPs (GMacs)
The YOLOv3 model	93.13	234	32.8
The YOLOv4 model	97.32	244	29.9
The lightweight YOLOv4 model	96.88	121	1.95

**FIGURE 11 |** The detection results of the concrete surface cracks.

Matlab is used to realize by adding different degrees of white noise to the image pixel by pixel. Furthermore, with reference to the Mosaic data enhancement method of YOLOv4, four images are randomly selected from the database, randomly scaled, and then randomly distributed for stitching. Not only can this greatly expand the original database, but it can also enrich the background of the images. When performing random cropping, if a part of the label box in the sample is cropped, it will be discarded and the intact label box will be retained after cropping. In the process of random scaling, many small targets are added to balance the scale problem of the original database, and the robustness of the network is better. Another benefit of Mosaic data enhancement is that the data of four pictures can be directly calculated during training, and the batch size can be improved in disguise. Therefore, the Mini-batch size set during training does not need to be large, which reduces the training difficulty of the model.

For the purpose of assessing the generalization ability of the proposed model, 10,000 images are divided into five parts based on the fivefold cross-validation principle, among which 80% are used to train and validate the model and the remaining 20% are used to test. More precisely, 8,000 images are randomly selected from the 10,000 images, among which 7,000 images are used to generate a training set and 1,000 images are used to create a validation set. The remaining 2,000 images not selected for training and validation are used to build a testing set.

Model Initialization

In the process of network training, in order to improve efficiency and better save computing resources and time, this paper adopts the training strategy of freezing some layers. The whole training process is divided into two stages. In the first stage, only the Backbone network structure is trained; in the second stage, the overall network structure is trained. In the training process, the Cosine Annealing learning rate strategy is adopted, and the hyperparameters are optimized according to the genetic

algorithm. The initial parameter settings of the first stage and the second stage are shown in **Tables 2, 3**, respectively.

Evaluation Metrics of Accuracy

For the purpose of assessing the accuracy of any object detection technique, many evaluation criteria are proposed and adopted. The most frequently-used metric for object detection is the mean Average Precision (mAP) which is currently used to measure how the labeling methods perform on a task. Before introducing the mAP, it is necessary to introduce the commonly-used metrics in the field of object detection, such as Intersection over Union (IoU), Precision and Recall. IoU is the ratio of the intersection and union of the candidate bound and the ground truth bound, which is also called the Jaccard index. The classification problem generally sorts the concerned classes into positive classes and other classes into negative classes. The prediction results of the testing set may be correct or wrong, and these results can be divided into four categories: True Positive (TP), True Negative (TN), False Positive (FP) and False Negative (FN). The accuracy refers to the number of correct recognitions of all samples predicted to be positive. According to the above classification, **Eqs. 14–15** define the precision and recall, respectively.

$$\text{Precision} = \frac{TP}{TP + FP} \quad (14)$$

$$\text{Recall} = \frac{TP}{TP + FN} = \frac{TP}{P} \quad (15)$$

where P is the number of positive samples in the testing set. The Recall reflects the missing rate of the model. The Precision and Recall are independent of each other. High precision means that the FP rate is low, which can lead to a high missing rate. **Eq. 16** defines the comprehensive evaluation value F_1 . Taking the recall as the horizontal axis and the precision as the vertical axis, the P-R curve can be obtained and the Average Precision (AP) can be calculated. In

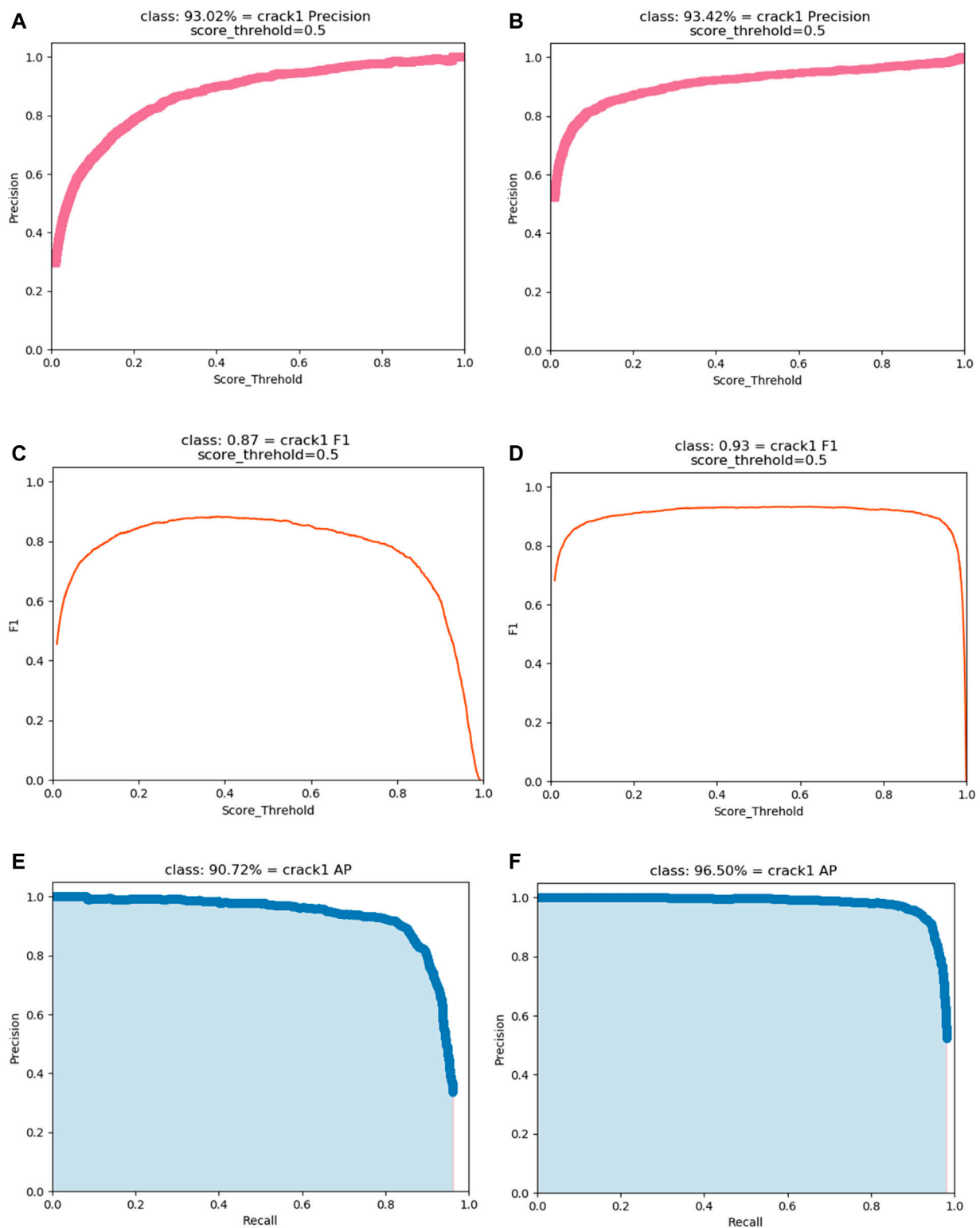


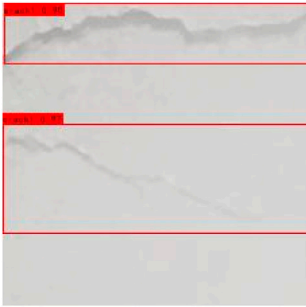


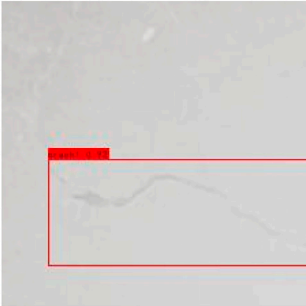

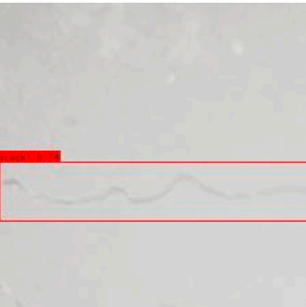
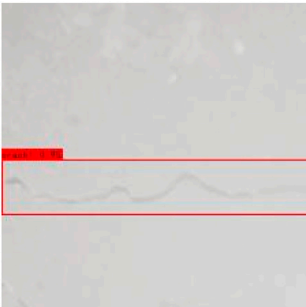


FIGURE 12 | The indices of the lightweight YOLOv4 model and the improved model in fog: **(A)** Precision of the lightweight YOLOv4 model **(B)** Precision of the improved model in fog **(C)** F_1 of the lightweight YOLOv4 model **(D)** F_1 of the improved model in fog **(E)** AP of the lightweight YOLOv4 model **(F)** AP of the improved model in fog.

TABLE 5 | The performance comparison between the lightweight YOLOv4 model and the improved model in fog.

Algorithm	mAP (%)	Parameters (M)	FLOPs (GMacs)
The lightweight YOLOv4 model	90.72	121	1.95
The improved model in fog	96.50	132	2.24

TABLE 6 | The input and output of the lightweight YOLOv4 model and the improved model in fog in concrete surface crack detection.

Original image	Prediction by the lightweight YOLOv4 model	Prediction by the improved model in fog
		
		
		

short, this is for calculating the mean value of precision on the P-R curve. **Eqs. 17, 18** are the formulas for AP and mAP, respectively.


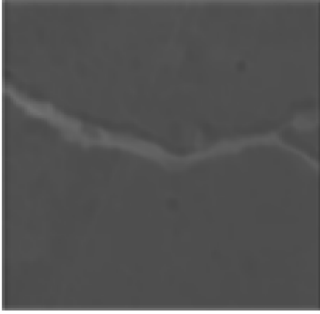




$$F_1 = \frac{2 \times P \times R}{P + R} \quad (16)$$

$$AP = \int_0^1 p(r) dr \quad (17)$$

$$mAP = \frac{1}{|Q_R|} \sum_{q=1}^{Q_R} AP(q) \quad (18)$$

In this paper, in addition to the mAP, the model size and computational complexity FLOPs are used to evaluate the model compression algorithm. The model's size is closely related to its parameters, which can be used to measure the simplification of the YOLOv4 model. FLOPs reflects the calculation amount of the algorithm. The unit of FLOPs is GMacs, which is short for Giga

TABLE 7 | The haze removal results of the concrete surface cracks.

Original image	Transmittance image	Restoration image
		
		

Multiply-Accumulation operations per second. It represents the floating-point operations per second, which can reflect the algorithm's calculation performance.

RESULTS AND DISCUSSIONS

The Lightweight YOLOv4 Model

To verify the concrete surface crack detection performance of the lightweight YOLOv4 model proposed in this paper, the experimental results are compared with those of the original YOLOv4 model. The detection rate (precision), comprehensive evaluation value F_1 and AP are used for evaluation, as shown in **Figure 10**.

Figure 10 shows that the detection performance of the lightweight YOLOv4 model is basically consistent with that of the original YOLOv4 model, and the curves of the precision, F_1 and AP are similar. It can be concluded that there is basically no loss in performance after the model is simplified. The model size and FLOPs are used to verify the simplification effect of the model. **Table 4** shows the performance comparison of the lightweight YOLOv4 model with the original YOLOv4 model and the YOLOv3 model. **Table 4** shows that in the lightweight YOLOv4 model, the weight is reduced by 50% and the FLOPs is reduced by 93.5%. Compared with the YOLOv3 model, the performance of the lightweight YOLOv4 model has certain advantages in terms of the mAP, the weight and the FLOPs. To demonstrate the detection performance of the proposed model more intuitively, some images shown in **Figure 11** were randomly selected from the database for testing.

The Crack Detection Model in Fog

To verify the performance of the improved YOLOv4 model when detecting concrete surface cracks in fog, the lightweight YOLOv4 model and the improved model in fog were trained with the same experimental conditions, the same foggy database and the same optimization algorithm. As shown in **Figure 12**, the precision, F_1 and AP are used for evaluation.

Figure 12 illustrates that the lightweight YOLOv4 model does not perform well in fog, while the improved model performs better. It can be seen that the AP has a higher improvement, which proves that the performance of the improved network model in detecting concrete surface cracks in fog exhibits a certain improvement. The model size and FLOPs are used to verify the performance of the improved model. **Table 5** shows the performance comparison between the lightweight YOLOv4 model and the improved model in fog.

Table 5 shows that the improved model in fog is slightly higher than the lightweight YOLOv4 model in terms of weight and FLOPs, but has a greater benefit in the mAP than the lightweight model. In order to more intuitively show the performance of the improved model in detecting concrete surface cracks in fog, some images were randomly selected from the database for testing, as shown in **Table 6**.

It can be seen intuitively from **Table 6** that the detection result of the lightweight YOLOv4 model in the first image is not accurate, and some of the crack features are not recognized. The improved model in fog has a better recognition effect. In the second image, due to the heavy fog, the thin crack structure and the inconspicuous features, the lightweight YOLOv4 model fails to make a correct identification, while the improved network model is accurate. Both algorithms can correctly detect cracks in the third image. In order to intuitively show

the effect of crack scene restoration in the middle layer of the improved model, several test images are selected to illustrate the effect of haze removal, as shown in **Table 7**. It can be seen that the results of restoring the crack structure using this paper's improved model are clearer and more obvious than the original fog image, which is more conducive to feature extraction by the subsequent lightweight YOLOv4 model.

CONCLUSION

A crack detection method based on the YOLOv4 algorithm is proposed, which provides a more accurate, efficient and intelligent method for the detection of cracks on concrete surfaces. A smartphone is used for collecting 2000 raw images ($3,024 \times 3,024$ pixels) from the surfaces of concrete buildings. To reduce the computation of the training process, the collected images are cropped to 256×256 pixels. 7,000, 1,000 and 2,000 images are used for training, validation and testing, respectively. The YOLOv4 architecture described in detail in **Section 2.3** was simplified for crack detection. The lightweight YOLOv4 model achieved an mAP of 96.88% with 121 M and 1.95 GMacs. The results showed that the proposed method can provide good crack detection results with a lower trained model weight. In this paper, images taken on sunny days are manually fogged to build the database. The lightweight YOLOv4 model was modified to have better performance for crack detection in fog, which is described in detail in **Section 3.3**. The improved model for crack detection in fog achieved an mAP of 96.50% with 132 M and 2.24 GMacs. The results showed that the improved method can provide better crack detection results with only a slightly higher trained model weight. The detection performance of the proposed model has been improved in both subjective vision and objective evaluation metrics, and is more effective at detecting concrete surface cracks in fog.

Though the proposed method in this paper exhibits good performance, there is still a long way to go for engineering

applications. In the experiment, there are several directions we found that may be tried and improved. Firstly, to reduce the computation of the training process, the model only uses small pixel images (256×256 pixels). If a large number of images must be processed, the images shall be cropped or scaled. It is absolutely not a fundamental solution to the problem. It is worth exploring approaches to improve the algorithm to adapt it to larger image inputs. Secondly, many hyper-parameters need to be artificially adjusted when applying the method. We must still carry out plenty of experiments to thoroughly explore the impact of these hyper-parameters on the performance of the model. Finally, more types of defect images across more complex backgrounds should be collected to enlarge the database, thus improving the accuracy and robustness of the proposed method.

DATA AVAILABILITY STATEMENT

The raw data supporting the conclusions of this article will be made available by the authors, without undue reservation.

AUTHOR CONTRIBUTIONS

All authors listed have made a substantial, direct, and intellectual contribution to the work and approved it for publication.

FUNDING

This work was supported by the National Natural Science Foundation of China (51608074), the Fundamental Research Funds for the Central Universities (2020CDJQY-A067), and the National Key Research and Development Project (2019YFD1101005).

REFERENCES

- Beck, A., and Teboulle, M. (2009). Fast Gradient-Based Algorithms for Constrained Total Variation Image Denoising and Deblurring Problems. *IEEE Trans. Image Process.* 18, 2419–2434. doi:10.1109/TIP.2009.2028250
- Bochkovskiy, A., Wang, C. Y., and Liao, H. (2020). "YOLOv4: Optimal Speed and Accuracy of Object Detection," in 2020 IEEE/CVF Conference on Computer Vision and Pattern Recognition (CVPR), Seattle, WA, USA, June 14–19 (Seattle, WA: arXiv:2004.10934v1).
- Cha, Y.-J., Choi, W., Suh, G., Mahmoudkhani, S., and Büyüköztürk, O. (2018). Autonomous Structural Visual Inspection Using Region-Based Deep Learning for Detecting Multiple Damage Types. *Computer-Aided Civil Infrastructure Eng.* 33, 731–747. doi:10.1111/mice.12334
- Chen, F.-C., and Jahanshahi, M. R. (2018). NB-CNN: Deep Learning-Based Crack Detection Using Convolutional Neural Network and Naïve Bayes Data Fusion. *IEEE Trans. Ind. Electron.* 65, 4392–4400. doi:10.1109/tie.2017.2764844
- Chen, M., Tang, Y., Zou, X., Huang, K., Li, L., and He, Y. (2019). High-accuracy Multi-Camera Reconstruction Enhanced by Adaptive point Cloud Correction Algorithm. *Opt. Lasers Eng.* 122, 170–183. doi:10.1016/j.optlaseng.2019.06.011
- Choi, J.-I., Lee, Y., Kim, Y. Y., and Lee, B. Y. (2017). Image-processing Technique to Detect Carbonation Regions of concrete Sprayed with a Phenolphthalein Solution. *Construction Building Mater.* 154, 451–461. doi:10.1016/j.conbuildmat.2017.07.205
- Cireşan, D., Meier, U., Masci, J., and Schmidhuber, J. (2012). Multi-column Deep Neural Network for Traffic Sign Classification. *Neural Networks* 32, 333–338. doi:10.1016/j.neunet.2012.02.023
- Dung, C. V., and Anh, L. D. (2019). Autonomous concrete Crack Detection Using Deep Fully Convolutional Neural Network. *Automation in Construction* 99, 52–58. doi:10.1016/j.autcon.2018.11.028
- Girshick, R., Donahue, J., Darrell, T., and Malik, J. (2014). Rich Feature Hierarchies for Accurate Object Detection and Semantic Segmentation. *IEEE Comp. Soc.* doi:10.1109/CVPR.2014.81
- Girshick, R. (2015). "Fast R-CNN," in IEEE International Conference on Computer Vision (ICCV), Santiago, CHILE, December 11–18 (IEEE), 1440–1448. doi:10.1109/ICCV.2015.169
- Guan, J., Yang, X., Ding, L., Cheng, X., Lee, V. C. S., and Jin, C. (2021). Automated Pixel-Level Pavement Distress Detection Based on Stereo Vision and Deep Learning. *Automation in Construction* 129, 103788. doi:10.1016/j.autcon.2021.103788
- Han, K., Wang, Y., Tian, Q., Guo, J., and Xu, C. (2020). "GhostNet: More Features from Cheap Operations," in 2020 IEEE/CVF Conference on Computer Vision and Pattern Recognition (CVPR), Seattle, WA, USA, June 14–19 (Seattle, WA: arXiv:1911.11907), 1577–1586. doi:10.1109/cvpr42600.2020.00165

- He, K., Sun, J., and Tang, X. (2011). Single Image Haze Removal Using Dark Channel Prior. *IEEE Trans. Pattern Anal. Mach. Intell.* 33 (12), 2341–2353. doi:10.1109/TPAMI.2010.168
- He, K., Zhang, X., Ren, S., and Sun, J. (2015). Spatial Pyramid Pooling in Deep Convolutional Networks for Visual Recognition. *IEEE Trans. Pattern Anal. Mach. Intell.* 37, 1904–1916. doi:10.1109/TPAMI.2015.2389824
- Ji, A., Xue, X., Wang, Y., Luo, X., and Xue, W. (2020). An Integrated Approach to Automatic Pixel-Level Crack Detection and Quantification of Asphalt Pavement. *Automation in Construction* 114, 103176. doi:10.1016/j.autcon.2020.103176
- Jiang, Y., Pang, D., and Li, C. (2021). A Deep Learning Approach for Fast Detection and Classification of concrete Damage. *Automation in Construction* 128, 103785. doi:10.1016/j.autcon.2021.103785
- Koziarski, M., and Cyganek, B. (2017). Image Recognition with Deep Neural Networks in Presence of Noise - Dealing with and Taking Advantage of Distortions. *Ica* 24, 337–349. doi:10.3233/ica-170551
- Krizhevsky, A., Sutskever, I., and Hinton, G. E. (2017). ImageNet Classification with Deep Convolutional Neural Networks. *Commun. ACM* 60, 84–90. doi:10.1145/3065386
- Laofor, C., and Peansupap, V. (2012). Defect Detection and Quantification System to Support Subjective Visual Quality Inspection via a Digital Image Processing: A Tiling Work Case Study. *Automation in Construction* 24, 160–174. doi:10.1016/j.autcon.2012.02.012
- Lecun, Y., Bengio, Y., and Hinton, G. (2015). Deep Learning. *Nature* 521, 436–444. doi:10.1038/nature14539
- Li, S., Zhao, X., and Zhou, G. (2019). Automatic Pixel-Level Multiple Damage Detection of concrete Structure Using Fully Convolutional Network. *Computer-Aided Civil Infrastructure Eng.* 34, 616–634. doi:10.1111/mice.12433
- Lin, Y.-Z., Nie, Z.-H., and Ma, H.-W. (2017). Structural Damage Detection with Automatic Feature-Extraction through Deep Learning. *Computer-Aided Civil Infrastructure Eng.* 32, 1025–1046. doi:10.1111/mice.12313
- Liu, W., Anguelov, D., Erhan, D., Szegedy, C., Reed, S., Fu, C.-Y., et al. (2016). “SSD: Single Shot MultiBox Detector,” in 2016 14th European Conference on Computer Vision, Amsterdam, The Netherlands, October 8–10, 21–37. doi:10.1007/978-3-319-46448-0_2
- Mei, Q., and Gül, M. (2020). A Cost Effective Solution for Pavement Crack Inspection Using Cameras and Deep Neural Networks. *Construction Building Mater.* 256, 119397. doi:10.1016/j.conbuildmat.2020.119397
- Nayar, S. K., and Narasimhan, S. G. (1999). “Vision in Bad Weather,” in Proceedings of the Seventh IEEE International Conference on Computer Vision, Kerkira, Greece, September 20–27 (IEEE), 820–827. doi:10.1109/ICCV.1999.790306
- Neubeck, A., and Van Gool, L. (2006). “Efficient Non-maximum Suppression,” in International Conference on Pattern Recognition, Hong Kong, China, August 20–24, 850–855. doi:10.1109/icpr.2006.479
- Nishikawa, T., Yoshida, J., Sugiyama, T., and Fujino, Y. (2012). Concrete Crack Detection by Multiple Sequential Image Filtering. *Computer-Aided Civil Infrastructure Eng.* 27, 29–47. doi:10.1111/j.1467-8667.2011.00716.x
- Oh, J.-K., Jang, G., Oh, S., Lee, J. H., Yi, B.-J., Moon, Y. S., et al. (2009). Bridge Inspection Robot System with Machine Vision. *Automation in Construction* 18, 929–941. doi:10.1016/j.autcon.2009.04.003
- Peng, C., Yang, M., Zheng, Q., Zhang, J., Wang, D., Yan, R., et al. (2020). A Triple-Thresholds Pavement Crack Detection Method Leveraging Random Structured forest. *Construction Building Mater.* 263, 120080. doi:10.1016/j.conbuildmat.2020.120080
- Redmon, J., and Ali, F. (2018). “YOLOv3: An Incremental Improvement,” in 2018 IEEE/CVF Conference on Computer Vision and Pattern Recognition (CVPR), Salt Lake City, UT, USA, June 19–21 (Salt Lake City, UT: arXiv:1804.02767).
- Ren, S., He, K., Girshick, R., and Sun, J. (2017). Faster R-CNN: Towards Real-Time Object Detection with Region Proposal Networks. *IEEE Trans. Pattern Anal. Mach. Intell.* 39, 1137–1149. doi:10.1109/TPAMI.2016.2577031
- Salman, M., Mathavan, S., Kamal, K., and Rahman, M. (2013). “Pavement Crack Detection Using the Gabor Filter,” in 2013 16th International Ieee Conference on Intelligent Transportation Systems, The Hague, NETHERLANDS, 6–9 Oct. 2013 (IEEE), 2039–2044. doi:10.1109/ITSC.2013.6728529
- Sun, Y., Yang, Y., Yao, G., Wei, F., and Wong, M. (2021). Autonomous Crack and Bughole Detection for Concrete Surface Image Based on Deep Learning. *IEEE Access* 9, 85709–85720. doi:10.1109/access.2021.3088292
- Szegedy, C., Vanhoucke, V., Ioffe, S., Shlens, J., and Wojna, Z. (2016). “Rethinking the Inception Architecture for Computer Vision,” in 2016 IEEE/CVF Conference on Computer Vision and Pattern Recognition (CVPR), Seattle, WA, June 27–30 (IEEE), 2818–2826. doi:10.1109/CVPR.2016.308
- Tang, Y., Feng, W., Chen, Z., Nong, Y., Guan, S., and Sun, J. (2021b). Fracture Behavior of a Sustainable Material: Recycled concrete with Waste Crumb Rubber Subjected to Elevated Temperatures. *J. Clean. Prod.* 318, 128553. doi:10.1016/j.jclepro.2021.128553
- Wei, F., Yao, G., Yang, Y., and Sun, Y. (2019). Instance-level Recognition and Quantification for concrete Surface Bughole Based on Deep Learning. *Automation in Construction* 107, 102920. doi:10.1016/j.autcon.2019.102920
- Wei, W., Ding, L., Luo, H., Li, C., and Li, G. (2021). Automated Bughole Detection and Quality Performance Assessment of concrete Using Image Processing and Deep Convolutional Neural Networks. *Construction Building Mater.* 281, 122576. doi:10.1016/j.conbuildmat.2021.122576
- Yao, G., Sun, Y., Wong, M., and Lv, X. (2021). A Real-Time Detection Method for Concrete Surface Cracks Based on Improved YOLOv4. *Symmetry* 13, 1716. doi:10.3390/sym13091716
- Yao, G., Wei, F., Yang, Y., and Sun, Y. (2019). Deep-Learning-Based Bughole Detection for Concrete Surface Image. *Adv. Civil Eng.* 2019, 1–12. doi:10.1155/2019/8582963
- Yeum, C. M., and Dyke, S. J. (2015). Vision-Based Automated Crack Detection for Bridge Inspection. *Computer-Aided Civil Infrastructure Eng.* 30, 759–770. doi:10.1111/mice.12141
- Yunchao, T., Zheng, C., Wanhui, F., Yumei, N., Cong, L., and Jieming, C. (2021a). Combined Effects of Nano-Silica and Silica Fume on the Mechanical Behavior of Recycled Aggregate concrete. *Nanotechnology Rev.* 10, 819–838. doi:10.1515/ntrev-2021-0058
- Zalama, E., Gómez-García-Bermejo, J., Medina, R., and Llamas, J. (2014). Road Crack Detection Using Visual Features Extracted by Gabor Filters. *Computer-Aided Civil Infrastructure Eng.* 29, 342–358. doi:10.1111/mice.12042
- Zhang, W., Li, H., Li, Y., Liu, H., Chen, Y., and Ding, X. (2021). Application of Deep Learning Algorithms in Geotechnical Engineering: a Short Critical Review. *Artif. Intell. Rev.* 54, 5633–5673. doi:10.1007/s10462-021-09967-1

Conflict of Interest: The authors declare that the research was conducted in the absence of any commercial or financial relationships that could be construed as a potential conflict of interest.

Publisher’s Note: All claims expressed in this article are solely those of the authors and do not necessarily represent those of their affiliated organizations, or those of the publisher, the editors and the reviewers. Any product that may be evaluated in this article, or claim that may be made by its manufacturer, is not guaranteed or endorsed by the publisher.

Copyright © 2021 Yao, Sun, Yang and Liao. This is an open-access article distributed under the terms of the Creative Commons Attribution License (CC BY). The use, distribution or reproduction in other forums is permitted, provided the original author(s) and the copyright owner(s) are credited and that the original publication in this journal is cited, in accordance with accepted academic practice. No use, distribution or reproduction is permitted which does not comply with these terms.



Experimental Study on Preparation and Performance of Concrete With Large Content of Fly Ash

Changyong Li^{1,2*}, Haibin Geng^{1,2}, Siyi Zhou¹, Manman Dai¹, Baoshan Sun³ and Fenglan Li^{1,2*}

¹International Joint Research Lab for Eco-building Materials and Engineering of Henan, School of Civil Engineering and Communications, North China University of Water Resources and Electric Power, Zhengzhou, China, ²Collaborative Innovation Center for Efficient Utilization of Water Resources, North China University of Water Resources and Electric Power, Zhengzhou, China, ³Henan Fifth Construction Group, Zhengzhou, China

OPEN ACCESS

Edited by:

Xijun Shi,
Texas State University, United States

Reviewed by:

Ionut Ovidiu Toma,
Gheorghe Asachi Technical University
of Iasi, Romania

Jiaqing Wang,
Nanjing Forestry University, China

*Correspondence:

Changyong Li
lichang@ncwu.edu.cn
Fenglan Li
liff64@ncwu.edu.cn

Specialty section:

This article was submitted to
Structural Materials,
a section of the journal
Frontiers in Materials

Received: 26 August 2021

Accepted: 26 November 2021

Published: 06 January 2022

Citation:

Li C, Geng H, Zhou S, Dai M, Sun B
and Li F (2022) Experimental Study on
Preparation and Performance of
Concrete With Large Content of
Fly Ash.
Front. Mater. 8:764820.
doi: 10.3389/fmats.2021.764820

Producing concrete with large content of fly ash attracts increasing attention in low carbon building materials. In this paper, the fly-ash concrete (FAC) with a content of fly ash no less than 50% total weight of binders was developed. The adaptability of fly ash used for concrete was firstly examined by testing the water requirement of normal consistency and the setting time for cement fly-ash paste, and the strengths of cement fly-ash mortar at the curing age of 7 and 28 days. The factors of water-to-binder ratio from 0.3 to 0.5, the content of fly-ash from 40% to 80%, and the excitation measures with additional $\text{Ca}(\text{OH})_2$ and steam curing at initial were considered. After that, the FAC was designed by adding an excessive content of fly ash to reduce the water-to-binder ratio from 0.50 to 0.26, and the content of fly-ash varied from 52% to 60%. Results show that the cement fly-ash paste presented a reduction of water requirement and an elongation of setting time with the increased content of fly ash. This provides a foundation of maintaining the workability of fresh FAC with a decreased water-to-binder ratio by adding the excessive content of fly ash. The cement fly-ash mortar had a lower early strength due to the slow reaction of fly-ash with $\text{Ca}(\text{OH})_2$, which could be improved by steam curing at the initial 24 h due to the excitation of fly-ash activity. At curing age of 28 days, the FAC had the expected axial compressive strength and modulus of elasticity, but the tensile strength was lower than predicted. At the curing age of 56 days, all the basic mechanical properties of FAC reached the prediction. The resistances of FAC to chloride ion penetration and carbonization were realized at a very high level as specified in codes.

Keywords: concrete with large content of fly-ash, activity of fly-ash, mechanical property, strength development, chloride ion penetration, carbonization

INTRODUCTION

Fly ash is a by-product of coal combustion in power stations, which presents as tiny grains with a certain pozzolanic activity. As one of the industrial solid wastes, fly ash has attracted much more attention on its comprehensive utilization to protect the environment (Wu and Lian, 1999; Choi et al., 2015; Amran et al., 2021). Based on its chemical composition, grain fineness, and pozzolanic activity, fly ash is classified into different types and is most widely used as a mineral admixture of cement and concrete (Wu and Lian, 1999; Li et al., 2013; GB/T1596-2017, 2017). Normally, fly ash admixed in concrete is no more than 40% of the total binder to improve the workability of fresh mix

and get a better reliability of concrete, ensuring its strength (Liu et al., 2013a; Zhao et al., 2013; GB/T1596-2017, 2017; Zhao et al., 2018; Ding et al., 2020; Liu et al., 2021). Based on technique specifications (JGJ55-2011, 2011; JGJ/T281-2012, 2012; GB/T50164-2014, 2014), the limit content of fly ash is 35%–40% for the concrete with common Portland cement used for reinforced concrete structures when the water-to-binder ratio is no larger than 0.40 and should be reduced by 5% when the water-to-binder ratio is larger than 0.40. In order to control the early strength and reduce the loss of prestress caused by shrinkage and creep of concrete, the limit content of fly ash for the concrete used for prestressed concrete structures should be reduced by 10%–15% on the same condition to reinforce concrete structures. Because no mineral admixtures are admixed for the Portland cement, the limit content of fly ash can be increased by 5%–10% at the same above condition if the concrete is made with Portland cement.

The decreased strength of fly-ash concrete (FAC) especially at an early age is a drawback which confined the content of admixed fly ash. Normally, the FAC with content of fly ash larger than 30%–40% has an elongated setting time of fresh mix and presents a lower strength before the standard curing age of 28 days, although the strength continuously increased later (Malhotra and Paintert, 1989; Sun G. W. et al., 2019; Olivia et al., 2019). To solve this problem, excitation measures for the activity of fly ash have been studied. One is addition of other alkaline admixtures such as calcium hydrate, sodium silicate, and calcium carbonate, which makes the crystalline silicon and aluminum compounds of fly ash converse into active soluble compounds (Gunasekara et al., 2016; Hefni et al., 2018; Singh and Subramaniam, 2019; Promsawat et al., 2020). The second is the admixture of other high-activity admixtures such as silica fume, nano silica, and metakaolin. This accelerates the hydrations of both fly ash and cement, decreases the porosity and total pore volume, and improves the microstructure of the interface transition zone (Mei et al., 2018; Nežerka et al., 2019; Anjos et al., 2020). The third is the grounding of the fly ash into much more fineness. With the changes in particle morphology and distribution of irregular grains from broken spherical particles, fly ash behaves with higher pozzolanic activity and tiny-aggregate filling effect on the improvement of composite strength (Ma et al., 2021). The fourth is making of the fly-ash composites at a high-temperature environment; this accelerates the hydration of both cement and fly ash (Hefni et al., 2018; Mei et al., 2018; Singh and Subramaniam, 2019; Yang et al., 2021). However, some of the measures are debatable due to the lack of convenience of engineering application, high energy consumption, and/or low economic benefit.

To achieve economic benefits from effective utilization of fly ash, studies have been done to improve the applicability of FAC with large content of fly ash. With the replacement of 50% cement by fly ash containing 6.49% calcium oxide, the high-fluidity FAC was made by admixing the superplasticizer and air-entraining agent; the early strength was ensured by decreasing the water dosage and increasing the content of binders, and then the strength at the curing age of 28 days reached the target (Choi

et al., 2015). In case of the replacement of 20%–80% cement by fly ash, the flowability of fly ash cement composites is improved at paste and concrete level (Thiyagarajan et al., 2018). The self-compacting FAC with strength around 30 MPa at the curing age of 28 days was made with the replacement of 50% cement by class-C fly ash of 14.1% calcium (Wardhono, 2021). The FAC was produced with the replacement of 50% cement by fly ash containing 14.6% calcium oxide; the compressive strength was 45 MPa at the curing age of 56 days (Solikin and Setiawan, 2017). The FACs were prepared with the replacement of 40%–70% cement by fly ash containing 8.75% calcium oxide. Due to critical controls of the dilution and the pozzolanic effects of fly ash on cement hydration, the compressive strength of FAC was lower at the early age with decreased heat release of hydration, while it developed faster beyond the curing age of 28 days; the FAC with 40% replacement of cement by fly ash showed comparable compressive strength to the control concrete at the curing age of 28 days, while those with 55% and 70% fly ash reduced by 30.9% and 52.7%, respectively (Sun J. et al., 2019). By lowering the water-to-binder ratio at 0.2 and properly combining raw materials, the FAC with adequate strength and workability was developed even when 80% of the cement was replaced by fly ash. In this case, the content of fly ash had no obvious effect on the cementing efficiency of fly ash. When the content of fly ash further increased, the cementing efficiency of fly ash decreased significantly. Meanwhile, adding a small amount of silica fume could improve the mechanical properties and the penetration performance of FAC (Yu et al., 2017). The concrete with 56% fly ash of binders was examined to have good long-term strength development accompanied with high resistance of chloride ion penetration (Sivasundaram et al., 1990). Due to the positive effects of fly ash on refinement of pores, filling macro pores and improving the microstructure of the interface transition zone, the concrete with large content of fly ash behaves with ideal resistances to chloride ion penetration and carbonation (Aruhan and Yan, 2011; Li et al., 2014; Amran et al., 2021).

Generally, the above studies provide a sound foundation for the understanding of the effect of fly ash on performance of FAC. In practice, considering the effective utilization of long-term strength of concrete and the control of early tensile stress due to the heat release of cement hydration, the large content of fly ash no less than 40% can be used for the large volume concrete structures, and the limit content of fly ash can be taken as 65% for the roller compacted concrete dam (JGJ55-2011, 2011; JGJ/T281-2012, 2012; GB/T50164-2014, 2014). However, lack of FAC with large content of fly ash over 50% is applied in reinforced concrete structures, and few studies have been done on the relationships of different basic mechanical properties which are needed in the structural design (Li et al., 2012; Liu et al., 2013b).

Aiming to provide sufficient proof for the application of FAC with large content of fly ash in reinforced concrete structures, an experimental study was carried out in this paper. To provide a foundation of FAC with the content of fly ash over 50%, tests for the activity of fly ash were firstly examined to verify the effects of

TABLE 1 | Physical and mechanical properties of cement.

Setting time (min)		Compressive strength (MPa)			Flexural strength (MPa)			Specific surface area (m ² /kg)	Apparent density (kg/m ³)
Initial	Final	3 days	7 days	28 days	3 days	7 days	28 days		
170	215	27.5	39.2	58.5	5.4	6.8	8.3	360	3,090

TABLE 2 | Physical properties of fly ash.

Fineness: residual on sieve of 45 μm (%)	Water demand ratio (%)	Loss on ignition (%)	Activity index at 28 days (%)	Apparent density (kg/m ³)
21.7	84	2.6	73.3	2,340

TABLE 3 | Test results of the amount of oxides in cement and fly ash (%).

Materials	SiO ₂	Al ₂ O ₃	Fe ₂ O ₃	CaO	MgO	SO ₃	f-CaO
Cement	20.81	5.99	3.28	60.1	2.13	2.23	0.67
Fly-ash	55.91	17.31	5.91	6.59	3.82	1.93	0.26

fly-ash content on the workability and strength of cement fly-ash mortar and determine the efficiency of activity excitation by calcium hydroxide and steam curing. After that, the mixed proportion of FAC was designed by using the method of replacing cement with excessive fly ash to decrease the water-to-binder ratio (Li et al., 2012; Li et al., 2014). The workability of fresh mix, the mechanical properties at the curing age of 7–56 days, and the resistances to chloride ion penetration and carbonization of hardened FAC with content of fly ash from 52% to 60% were experimentally studied. Test results are discussed and evaluated with the comparisons to specifications of current codes.

RAW MATERIALS

Grade 42.5 common Portland cement and second-class fly ash produced by Henan Mengdian Cement Co. Ltd. (Zhengzhou, China) were used as binders. The physical and mechanical properties are presented in **Tables 1, 2**, which met the specifications of China codes (GB175-2007, 2007; GB/T1596-2017, 2017). The amounts of oxides in cement and fly ash were detected by the methods specified in the China code (GB/T176-2017, 2017); test results are presented in **Table 3**.

According to the specifications of China codes (GB/T14684-2011, 2011; GB/T14685-2011, 2011), the properties of fine and coarse aggregates were measured. The fine aggregate was manufactured sand with fineness modulus of 2.6, apparent density of 2,690 kg/m³, and mud content of 1.2%. The coarse aggregate was crushed limestone with apparent density of 2,800 kg/m³, closed-packing density of 1,745 kg/m³, crushed index in cylindrical tube of 4.8%, and mud content of 3.2%.

The water reducer was of high-performance polycarboxylic acid type with water reduction of 35%. The alkali activator for fly ash was Ca(OH)₂. The mix water was tap water.

TESTS FOR ACTIVITY OF FLY ASH

Properties of fresh cement fly-ash paste

Tests of the water requirement of normal consistency and the setting time for cement fly-ash paste were carried out according to the specification of the China code (GB/T1346-2011, 2011), the binder was 500 g in total, and the percent of fly ash changed from 40% to 80%. Concretely, the content of fly ash was 200, 250, 300, 350, and 400 g, respectively. Test results are presented in **Figure 1**. With the increasing content of fly ash, the water requirement of normal consistency reduced linearly, while the setting time was directly elongated. When the content of fly ash was 40%, the water requirement of normal consistency decreased by 7.7%, the initial setting time increased by 10.1%, and the final setting time increased by 4.1%. After that, with the content of fly ash increased by 10%, the water requirement of normal consistency decreased by about 1.5%, and the initial and final setting time increased by about 9.4% and 13.4%. This indicates that the flow friction of cement grains was decreased by the fly ash with a smooth surface of spherical particles, and the hydration process of cement was reduced by the dilution of fly ash with lesser cement. In fact, the hydration process of cement controls the setting time of binder paste; the reaction of fly ash with cement hydration product Ca(OH)₂ is a little bit in the early age (Li et al., 2013; Li et al., 2021). This indicates that the replacement of cement by excessive content of fly ash is applicable to maintain the workability of fresh cement fly-ash mortar with content over 40% of fly ash.

Strength of cement fly-ash mortar

The cement fly-ash mortar was designed referencing to the specifications for the determination of cement strength and the strength activity index of fly ash in China codes (GB/T1596-2017, 2017; GB/T17671-2020, 2020); the dosage of the binder was 450 kg/m³; the water-to-binder ratio was 0.3, 0.4, and

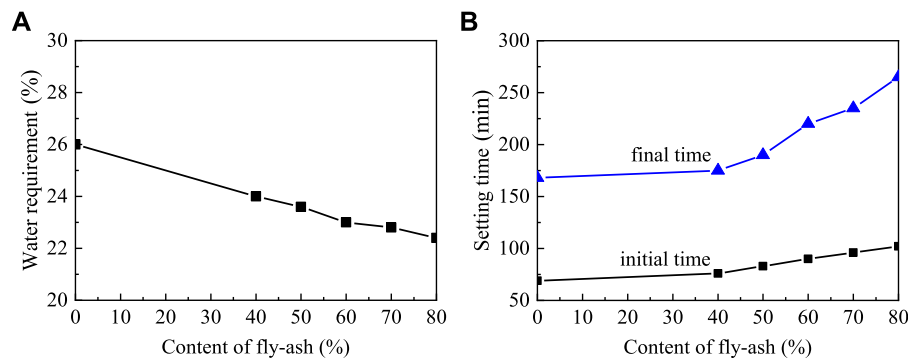


FIGURE 1 | Test results of cement fly-ash paste: **(A)** water requirement of normal consistency; **(B)** setting time.

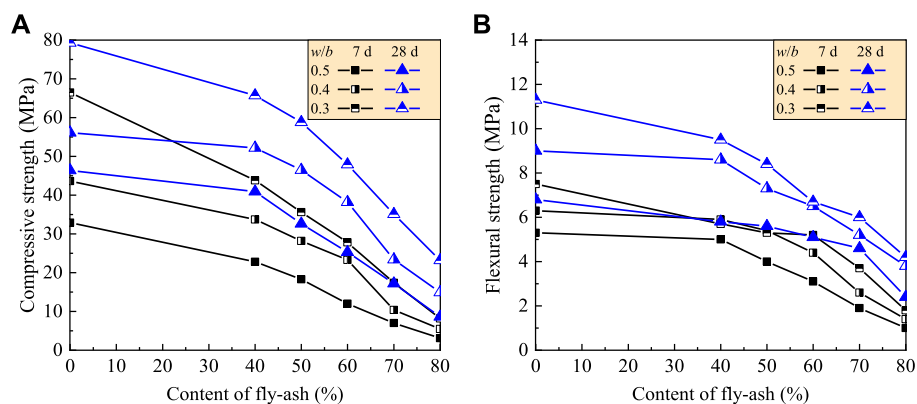


FIGURE 2 | Changes in strength with content of fly ash: **(A)** compressive strength; **(B)** flexural strength.

0.5, respectively, and the content of fly ash in weight of total binders changed from zero to 80%. Based on the test method of China codes (JGJ/T70-2009, 2009), the flowability of the test mortars was within 170–220, 180–220, and 210–280 mm with the change of the water-to-binder ratio. The compressive and flexural strengths were measured on a cement mortar testing machine with specimens of 40 mm × 40 mm × 160 mm at the curing age of 7 and 28 days. For each test, three specimens were made as a group. Test results are presented in **Figure 2**.

The influence of fly ash on the strength of mortar was related to the water-to-binder ratio and the curing age in a complex relationship. At a lower water-to-binder ratio, the compressive strength and flexural strength decreased rapidly with the increasing content of fly ash, while the decrease at the early age of 7 days was larger than that at the age of 28 days. In the case of the cement fly-ash mortar with the content of fly ash at 40% and the water-to-binder ratio of 0.40, the compressive and flexural strengths decreased by 6.9% and 4.4% at the curing age of 28 days, although a relatively large decrease took place at the curing age of 7 days. Comparatively, the compressive strength decreased by 11.9% and 17.2%, and the flexural strength decreased by 14.7% and 15.9% at the curing age of 28 days when the water-to-binder ratio was 0.30 and 0.50,

respectively. When the content of fly ash was over 40%, the compressive and flexural strengths tended to be decreased fast. With the content of fly ash changing from 50% to 60%, the compressive strength of mortar at the curing age of 28 days decreased by 25.8–39.6%, 17.1–31.9%, and 29.7–45.4%, while the flexural strength decreased by 25.6–40.7%, 18.9–27.8%, and 17.6–25.0%, corresponding to the water-to-cement ratios of 0.3, 0.4, and 0.5. Therefore, in this test, the water-to-binder ratio of 0.40 was optimal, and the content of fly ash at 40% was almost the boundary to produce the mortar with less decrease in strength. To further improve the strength of cement fly-ash mortar with large content of fly ash over 40%, other measures should be adopted to excite the activity of fly ash in mortar.

Activity excitation of fly ash by calcium hydroxide and steam curing

A test for the pozzolanic activity of fly ash excited by calcium hydroxide $\text{Ca}(\text{OH})_2$ and steam curing was designed referencing to the specifications of China codes (GB/T1596-2017, 2017; GB/T17671-2020, 2020). The water-to-binder ratio was selected as 0.4 based on the above experiment, and the content of fly ash

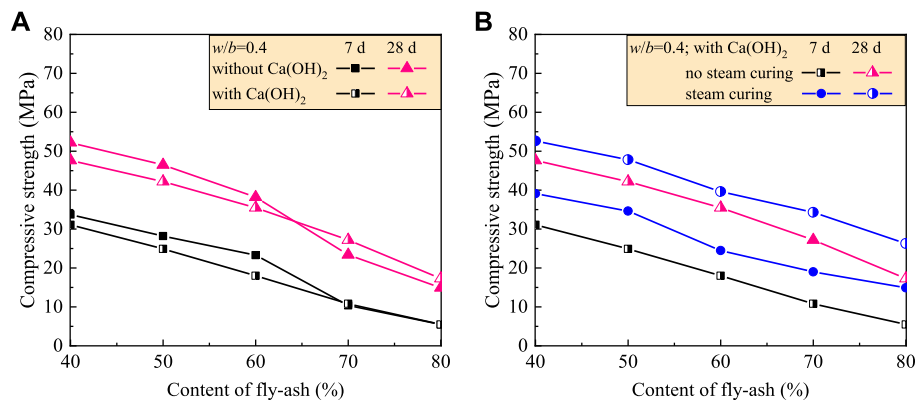


FIGURE 3 | Comparisons for the changes of compressive strength of test mortars: **(A)** with and without Ca(OH)_2 excitation; **(B)** cured in different conditions.

changed from zero to 80%. The content of Ca(OH)_2 was 25.8% by weight of the binder based on the study reported (Gunasekara et al., 2016; Gunasekera et al., 2017); the compressive strength of the test mortar was measured on a testing machine with the specimens of 40 mm × 40 mm × 160 mm at the curing age of 7 and 28 days. Each test had three specimens as a group. For specimens by steam curing, they were steam cured at a temperature of 80°C and relative humidity of 95% for 24 h and then cured at standard curing room before testing (Mei et al., 2018; Yang et al., 2021). The comparisons of compressive strength of the test mortar with or without Ca(OH)_2 excitation and those with Ca(OH)_2 excitation at different curing conditions are presented in **Figure 3**.

No obvious excitation of Ca(OH)_2 appeared on the strength of the cement fly-ash mortar. This indicates that the reaction of fly ash with Ca(OH)_2 was a slow process although the concentration of Ca(OH)_2 was increased by the addition (Wu and Lian, 1999; Li et al., 2014). When the content of fly ash was over 60%, less content of Ca(OH)_2 was produced by the hydration of cement. The excitation effect of additional Ca(OH)_2 began to present to make the cement fly-ash mortar reach about 16% higher compressive strength.

Because the solubility of Ca(OH)_2 increases obviously with the rise in temperature (Hefni et al., 2018; Singh and Subramaniam, 2019), and the solubility of silica increased by about one-third when exposed to water vapor (Iler, 1979), the reaction of fly ash with Ca(OH)_2 can be excited by steam curing at the start. This leads to a rapid reaction between silica and calcium hydroxide or calcium silicates and promotes the subsequent formation of hydrated calcium silicate. Finally, the reactions benefit the mechanical properties of the mortar after steam curing. When the content of fly ash was no larger than 60%, the compressive strength of the mortar increased by about 33% at the early age of 7 days and by about 12% at the age of 28 days. When the content of fly ash was larger than 60%, the compressive strength of the mortar increased by about 123% at the early age of 7 days and by about 39% at the age of 28 days. This indicates that the excitation effect of steam curing at the start contributed much more on the early strength of the mortar and tended obviously with the increasing content of fly ash especially higher than 60%.

TESTS FOR FAC

Mix proportion

With reference to the specification of the China code (JGJ 55-2011, 2011), the mix proportion of FAC was designed by the method of absolute volume of concrete. The reference mix was designed with the basic content of fly ash corresponding to the water-to-binder ratio w/b of 0.30, 0.34, 0.42, and 0.50, respectively. The excessive weight of fly ash was selected as 10%, 20%, and 30% of the basic content, and all the binders were counted in the w/b (Li et al., 2012; Liu et al., 2013a). The results of the mix proportion of FAC are presented in **Table 4**. Four groups of FAC were produced for tests. The content of fly ash changed from 51.9% to 60.2%, and the w/b varied from 0.26 to 0.50.

Workability of fresh FAC

Tests for fresh FAC were carried out according to the specification of the China code (GB/T 50080-2002, 2002). Good workability presented with the slump of concrete in 50–95 mm and the water retention without separation of aggregates from paste. This coincides with the test results of the properties of fresh cement fly-ash paste and ensures the workability of FAC, with a lower water-to-binder ratio.

Mechanical properties of FAC

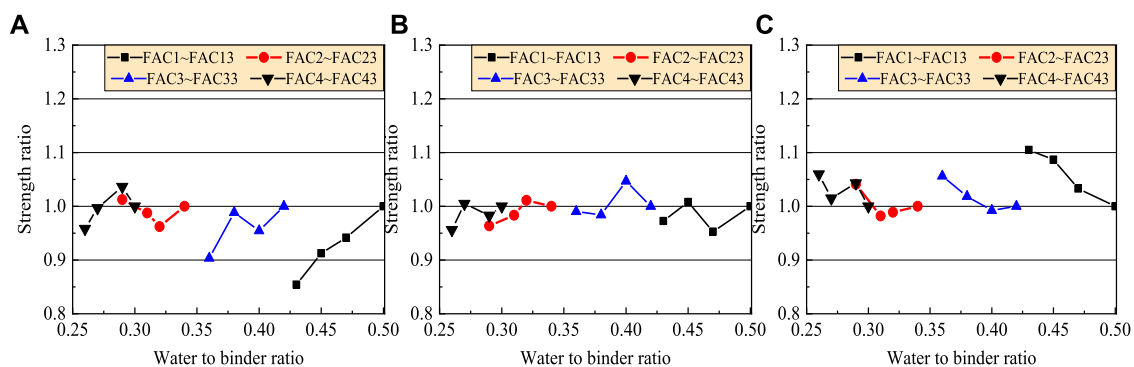
Tests for the basic mechanical properties of FAC were carried out in accordance with the China code (GB/T 50081-2002, 2002). The cubic specimens with a dimension of 100 mm were cast for the cubic compressive strength and splitting tensile strength; the prism specimens of 100 mm × 100 mm × 300 mm were cast for the axial compressive strength and the modulus of elasticity. For each test, three specimens were made as a group. The test results of compressive strength for specimens cured at standard curing room for 7, 28, and 56 days are presented in **Table 5**. On the test data, the strength ratio in each group of the FAC with excessive fly ash to the FAC with basic content of fly ash is computed and presented in **Figure 4**.

TABLE 4 | Mix proportion of FAC.

No	w/b	Content of fly ash (%)	Dosage of raw materials (kg/m ³)					Water reducer (%)
			Cement	Fly ash	Water	Sand	Stone	
FAC1	0.50	51.9	125	135	130	790	1,171	0.5
FAC11	0.47	54.4	125	149	130	783	1,160	0.5
FAC 12	0.45	56.4	125	162	130	777	1,157	0.5
FAC 13	0.43	58.5	125	176	130	771	1,143	0.5
FAC 2	0.42	53.0	140	158	125	779	1,155	0.8
FAC 21	0.40	55.4	140	174	125	772	1,144	0.8
FAC 22	0.38	57.6	140	190	125	767	1,132	0.8
FAC23	0.36	59.4	140	205	125	761	1,126	0.8
FAC3	0.34	53.8	170	198	125	761	1,127	1.0
FAC31	0.32	56.2	170	218	125	752	1,113	1.0
FAC32	0.31	58.3	170	238	125	743	1,098	1.0
FAC33	0.29	60.2	170	257	125	734	1,086	1.0
FAC4	0.30	52.5	190	210	120	742	1,100	1.2
FAC41	0.29	54.9	190	231	120	733	1,085	1.2
FAC42	0.27	57.0	190	252	120	723	1,070	1.2
FAC43	0.26	59.0	190	273	120	714	1,055	1.2

TABLE 5 | Cubic compressive strength of FAC at different curing ages.

No	Cubic compressive strength (MPa)			No	Cubic compressive strength (MPa)		
	7 days	28 days	56 days		7 days	28 days	56 days
FAC1	13.7	25.5	33.4	FAC2	17.6	29.8	38.7
FAC11	12.9	24.3	34.5	FAC21	16.8	31.2	38.4
FAC12	12.5	25.7	36.3	FAC22	17.4	30.7	39.1
FAC13	11.7	24.8	36.9	FAC23	15.9	30.4	41.3
FAC3	23.8	35.8	45.1	FAC4	30.1	41.0	53.6
FAC31	22.9	36.2	44.6	FAC41	31.2	40.3	55.9
FAC32	23.5	35.2	43.8	FAC42	31.1	41.2	54.4
FAC33	24.1	34.5	45.6	FAC43	29.8	39.2	56.8

**FIGURE 4** | Changes of the strength ratio with the water-to-binder ratio at the curing age of (A) 7 days; (B) 28 days; and (C) 56 days.

The effect of excessive fly ash on the strength of FAC was obvious with the increasing water-to-binder ratio at the early curing age of 7 days. The compressive strength of the four groups of FAC reduced in maximum by 4.2%, 3.8%, 9.7%, and 14.6%, respectively. With the time going on, the negative effect of fly ash became weaker and weaker with the increased excessive fly ash.

At the curing age of 28 days, the negative effect basically disappeared with the strength ratio in the same group changing from 0.953 to 1.046. At the curing age of 56 days, the positive effect was remarkable especially for the FAC with the $w/b = 0.42$ and 0.50 with the strength ratio ranging from 1.105. This reflects the long-term hydration process of fly ash

TABLE 6 | Cubic compressive strength of FAC affected by relative humidity of the curing room.

No	Cubic compressive strength at 7 days (MPa)			Cubic compressive strength at 28 days (MPa)		
	40%RH	60%RH	95%RH	40%RH	60%RH	95%RH
FAC1	15.0	15.2	13.7	21.3	27.4	25.5
FAC22	18.4	18.6	17.4	28.6	29.4	30.7
FAC4	32.2	30.8	30.5	41.2	44.2	43.4

TABLE 7 | Basic mechanical properties of FAC at different curing ages.

No	Axial compressive strength (MPa)			Tensile strength (MPa)			Modulus of elasticity (GPa)		
	7 days	28 days	56 days	7 days	28 days	56 days	7 days	28 days	56 days
FAC1	11.9	23.1	27.6	1.1	2.1	3.4	25.8	26.7	28.6
FAC22	15.1	24.2	28.5	1.3	2.4	3.6	28.2	34.0	39.1
FAC4	26.0	40.7	48.3	2.2	3.0	4.0	26.8	38.0	40.3

which reacted with the hydration product $\text{Ca}(\text{OH})_2$ to form the calcium silicate hydrate gel (Wu and Lian, 1999; Li et al., 2014). With a higher water-to-binder ratio and less cement content of $125\text{--}140\text{ kg/m}^3$, the hydration of cement is slowed down by the lower temperature rise with the increasing content of fly ash. This needs a long-term development of strength with the hydration of cement (Li et al., 2014; Hefni et al., 2018; Anjos et al., 2020). Finally, a higher increment of strength is gained with sufficient hydration of fly ash (Ding et al., 2016; Zhao et al., 2017). Meanwhile, the compactness of FAC can be further increased by the filling of tiny grains of excessive fly ash (Li et al., 2014). Therefore, by using the excessive fly ash to reduce the water-to-binder ratio, the compressive strength of FAC can reach the target at the standard curing age of 28 days.

According to the China code (JGJ 55-2011, 2011), the cubic compressive strength of FAC at the curing age of 28 days reached $24.3\text{--}41.2\text{ MPa}$, which corresponds to the strength grades of C15 to C30. The cubic compressive strength of FAC at the curing age of 56 days reached $33.4\text{--}56.8\text{ MPa}$, which corresponds to the strength grades of C20 to C45. Therefore, if the structure is not subject to early loads except weight itself, the strength of FAC can be controlled at a longer curing age such as 56 days to obtain the economic benefit of fly-ash utilization.

To explore the effect of curing relative humidity (RH) on the strength of FAC, three FACs FAC1, FAC22, and FAC4 were cured at curing RH of 40%, 60%, and 95%. The test results of cubic compressive strength at 7 and 28 days are presented in Table 6. Due to sufficient supply of water for the hydration at the early age of 7 days, the FACs cured at lower RH got higher strength than those cured at RH of 95%; however, the increment was below 10.9% and tended to decrease with the decreasing water-to-binder ratio. With the curing time going on, the curing RH needed to be increased not less than 60% due to the needs of humidity condition for hydration to get the higher strength of FAC. Therefore, it is better to adjust the curing RH in stages, combined with the water-to-binder ratio of FAC.

As specified in the China code (GB 50010-2010, 2010), the cubic compressive strength is used for the express of strength

grade, axial compressive strength, splitting tensile strength, and modulus of elasticity used for structural design which should be converted from the cubic compressive strength. Therefore, the above three FACs were also tested for the basic mechanical properties. The curing age of specimens was 7, 28, and 56 days, respectively, before testing. The results are presented in Table 7. This indicates a fast development of the basic mechanical properties of FAC before the curing age of 28 days, after which the increases become slow (Sivasundaram et al., 1990; Ding et al., 2016; Zhao et al., 2017). For the conversion, test data presented in Tables 5, 7 should successively multiply the coefficients of 0.95, 0.95, and 0.85 corresponding to standard specimens with sectional dimensions of 150 mm (GB/T 50081-2002, 2002).

Based on the relationship of the conventional concrete, a direct proportion exists between axial compressive strength and cubic compressive strength; the tensile strength (f_t) and the modulus of elasticity (E_c) of FACs at the curing age of 28 days in this study can be calculated with following formulas. The ratio of the test to calculated results is presented in Figure 5A).

$$f_t = 0.395 f_{cu}^{0.55} \quad (1)$$

$$E_c = 10^5 / (2.2 + 34.7/f_{cu}) \quad (2)$$

where f_{cu} is the cubic compressive strength of concrete (MPa).

The ratio of axial compressive strength to cubic compressive strength varies from 0.788 to 0.992, which is higher than the coefficient of 0.76 for conventional concrete at the curing age of 28 days. Meanwhile, the ratio of tensile strength varies from 0.783 to 0.861, and the ratio of the modulus of elasticity varies from 0.951 to 1.158. Therefore, FAC has a higher axial compressive strength, a lower tensile strength, and an almost equal modulus of elasticity compared to conventional concrete with the same strength grade. This is different from the fact that the FAC with content of fly ash no larger than 40% has equal tensile strength to conventional concrete (Liu et al., 2013b).

Making the above analyses on the FACs at the curing age of 56 days, the ratios are presented in Figure 5B. The ratio of axial

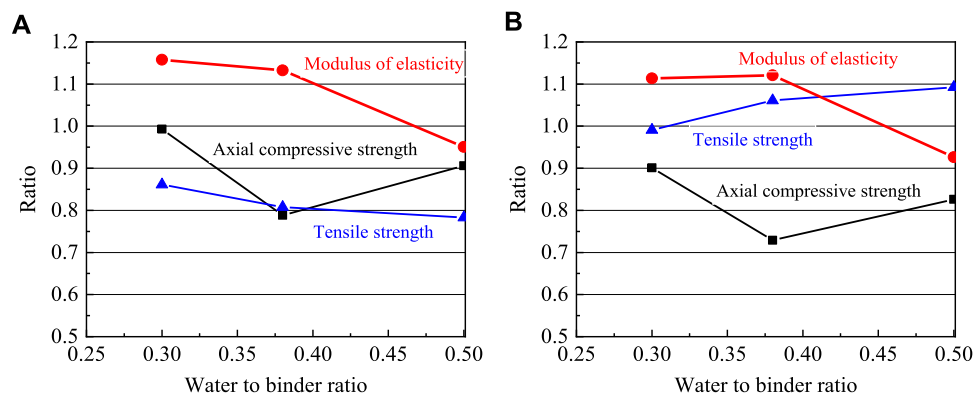


FIGURE 5 | Ratios of test to computed results for the mechanical properties at the curing age of (A) 28 days and (B) 56 days.

compressive strength to cubic compressive strength varies from 0.729 to 0.901, the ratio of tensile strength varies from 0.991 to 1.093, and the ratio of modulus of elasticity varies from 0.926 to 1.121. This shows a higher adaptability of the above relationships for the FAC at the curing age of 56 days. The changes in ratios reflect the changes in FAC microstructure with the increasing curing age. The FAC behaves better in compression due to the tiny aggregate effect of fly ash on the microstructure of FAC with refined pores and dense texture, while the splitting tensile strength of FAC mainly relies on the calcium silicate hydrate gel that came from the hydration of cement and the continuous hydration of fly ash. This depends much more on the hydration process with the increasing curing age (Sivasundaram et al., 1990; Ding et al., 2016).

Resistance to chloride-ion penetration of FAC

The electric flux test was carried out for the chloride ion penetration of FAC in accordance with the China code (GB 50082-2009, 2009), which is similar to the test method specified in ASTM C1202-19 (2019). The samples of $\phi 100$ mm \times 50 mm were cut from the specimen of $\phi 100$ mm \times 200 mm. The specimens were cured at standard curing room for 56 days before testing. Each test had three specimens as a group. The measured total electric flux (Q_{100}) was converted to be the value (Q_s) of a standard sample with diameter of 95 mm. Three FACs identified in Table 4 as FAC1, FAC22, and FAC4 were tested, and the test results of Q_s are 821 C, 516 C, and 413 C, successively. This indicates that the resistance of the test FAC to chloride penetration was basically positive to the water-to-binder ratio and the strength of FAC.

According to the China code for durability assessment of concrete (JGJ/T 193-2009, 2009), the grade of resistance to chloride penetration of test FACs belongs to Q-IV with the Q_s of 1,000–500 C. Therefore, the test FACs are good at resisting the penetration of chloride ion. In view that the cubic compressive strength of test FACs was only 15.2–30.8 MPa, the high-level resistance to chloride ion penetration came mainly from the admixing of large content of fly ash. The pores of concrete are

filled with tiny particles of fly ash and refined by the reaction of fly ash with the hydration product $\text{Ca}(\text{OH})_2$; a denser microstructure forms to block the osmotic path of chloride ion (Wu and Lian, 1999; Li et al., 2014). This lets chloride ion penetration in FAC to be at a very low level.

Carbonization of FAC

The fast carbonization test was carried out for the carbonization of FAC in accordance with the China code (GB 50082-2009, 2009). The cubic specimens with the dimension of 150 mm were cured at standard curing room for 56 days before testing in the carbonization chamber. The chamber was operated with the concentration of CO_2 at $(20 \pm 3)\%$, the temperature at $(20 \pm 5)^\circ\text{C}$, and the relative humidity at $(70 \pm 5)\%$. Each test had three specimens as a group. After being carbonized for 7 days, the specimens were splitting in two pieces on test machine, and the carbonized depth was measured.

The FACs used for the carbonization test were the same as those used for the chloride ion penetration test. The carbonized depth was 7.3, 3.2, and 0.4 mm for the three FACs identified as FAC1, FAC22, and FAC4, successively. This indicates that the carbonized depth decreased obviously with the decreasing water-to-binder ratio, due to the dense microstructure of FAC which blocks the diffusion of CO_2 (Wu and Lian, 1999; Zhao et al., 2013). According to the specification of the China code for the durability assessment of concrete (JGJ/T 193-2009, 2009), the resistance of test FACs to carbonization belonged to T-IV with 10–0.1 mm of the carbonized depth. This is a very high level of the resistance of concrete to carbonization.

CONCLUSION

- 1) The water requirement of normal consistency decreased, and the setting time elongated with the increase in fly-ash content in cement fly-ash paste. This provides a good flowability of building mortar and FAC with large content of fly ash.
- 2) The optimal content of fly ash for mortar was related to the water-to-binder ratio. In the case of the mortar with a water-to-binder ratio of 0.40 and the content of fly ash at 40%, the

compressive and flexural strengths decreased by 6.9% and 4.4% at the curing age of 28 days. When the content of fly ash was over 40%, the decrease in the compressive and flexural strengths tended to be fast. The decrease in the water-to-binder ratio benefited to the contribution of pozzolanic activity of fly ash to the strength of mortar.

- 3) There was no excitation of $\text{Ca}(\text{OH})_2$ on the early strength of the mortar with large content of fly ash, except for the less increase in the strength of the ones with fly ash over 60% at the curing age of 28 days. Steam curing for 24 h at the start presented the strengthening effect on the compressive strength of the mortar at the curing age of 7 and 28 days.
- 4) The mix proportion of FAC with large content of fly ash over 50% can be reasonably designed by the absolute volume method with excessive fly ash. With the increase in the water-to-binder ratio, it seems reasonable to adjust the curing RH from low to high with the increased curing age to ensure the hydration of cement and fly ash at a proper wet environment.
- 5) A higher decrease in cubic compressive strength of FAC took place at the curing age of 7 days. The cubic compressive strength of FAC maintained closely with the increase in fly ash content at the curing age of 28 days and tended to increase with the increase in fly-ash content at the curing age of 56 days. The strength grade of FAC at the curing age of 56 days can be raised to one to three grades over that at the curing age of 28 days. The relationships of axial compressive strength, tensile strength, and modulus of elasticity with cubic compressive strength of FAC at the curing age of 56 days are similar to those of conventional concrete at the curing age of 28 days. Therefore, it is more reasonable to evaluate the strength of FAC at the curing age of 56 days.
- 6) FAC with large content of fly ash from 51.9% to 57.6% presented super resistances to chloride ion penetration and

carbonization. The resistances increased with the decrease in the water-to-binder ratio and reached a very high level of current specifications.

DATA AVAILABILITY STATEMENT

The original contributions presented in the study are included in the article/supplementary material; further inquiries can be directed to the corresponding authors.

AUTHOR CONTRIBUTIONS

CL, BS, and FL contributed to the methodology, writing of the review, and funding acquisition; HG, SZ, and MD were involved in the tests, data interpretation, and writing of the original draft.

FUNDING

This research was funded by the Henan Provincial Special Project of Key Sci-Tech Research and Development Promotion, China (grant number 202102310272); Attracting Foreign Talents Fund of Henan, China (grant number YWZ 2018-6-HS2); and Innovative Sci-Tech Team of Eco-building Material and Structural Engineering of Henan Province, China (grant number YKRZ-6-066).

ACKNOWLEDGMENTS

Thanks are given to the supervision of Dr. David W. Law at RMIT University, Australia.

REFERENCES

- Amran, M., Debbarma, S., and Ozbakkaloglu, T. (2021). Fly Ash-Based Eco-Friendly Geopolymer concrete: a Critical Review of the Long-Term Durability Properties. *Construction Building Mater.* 270, 121857. doi:10.1016/j.conbuildmat.2020.121857
- Anjos, M. A. S., Camões, A., Campos, P., Azeredo, G. A., and Ferreira, R. L. S. (2020). Effect of High Volume Fly Ash and Metakaolin with and without Hydrated Lime on the Properties of Self-Compacting concrete. *J. Building Eng.* 27, 100985. doi:10.1016/j.jobe.2019.100985
- Aruhanand Yan, P. Y. (2011). Carbonation Characteristics of concrete with Different Fly-Ash Contents. *J. Chin. Ceram. Soci.* 39 (1), 7–12. doi:10.14062/j.issn.0454-5648.2011.01.022
- ASTM C1202-19 (2019). *Standard Test Method for Electrical Indication of Concrete's Ability to Resist Chloride Ion Penetration*. West Conshohocken, PA, USA: ASTM International.
- Choi, Y., Park, M., Choi, B., and Oh, S. A. (2015). Study on the Evaluation of Field Application of High-Fluidity concrete Containing High Volume Fly Ash. *Adv. Mater. Sci. Eng.*, 507018. doi:10.1155/2015/507018
- Ding, X., Li, C., Xu, Y., Li, F., and Zhao, S. (2016). Experimental Study on Long-Term Compressive Strength of concrete with Manufactured Sand. *Construction Building Mater.* 108, 67–73. doi:10.1016/j.conbuildmat.2016.01.028
- Ding, X., Zhao, M., Li, J., Shang, P., and Li, C. (2020). Mix Proportion Design of Self-Compacting SFRC with Manufactured Sand Based on the Steel Fiber Aggregate Skeleton Packing Test. *Materials* 13, 2833. doi:10.3390/ma13122833
- GB 175-2007 (2007). *Common Portland Cement*. Beijing, China: China Standard Press.
- GB 50082-2009 (2009). *Standard for Test Methods of Long-Term Performance and Durability of Ordinary Concrete*. Beijing, China: China Building Industry Press.
- GB 50010-2010 (2010). *Code for Design of Concrete Structures*. Beijing, China: China Building Industry Press.
- GB/T 1346-2011 (2011). *Test Methods for Water Requirement of Normal Consistency, Setting Time and Soundness of the Portland Cement*. Beijing, China: China Standard Press.
- GB/T 14685-2011 (2011). *Pebble and Crushed Stone for Construction*. Beijing, China: China Standard Press.
- GB/T 1596-2017 (2017). *Fly Ash Used for Cement and Concrete*. Beijing, China: China Standard Press.
- GB/T 176-2017 (2017). in *Cement - Test Methods -Part 1: Analysis by Wet Chemistry, NEQ* (Beijing, China: China Standard Press). *Methods for Chemical Analysis of Cement (ISO29581-1:2009)*
- GB/T 17671-2020 (2020). *Methods of Testing Cements: Determination of Strength (ISO679:2009 Cement Test Methods- Determination of Strength, MOD)*. Beijing, China: China Standard Press.
- GB/T 50080-2002 (2002). *Standard for Test Methods on Performance of Ordinary Fresh Concrete*. Beijing, China: China Building Industry Press.
- GB/T 50081-2002 (2002). *Standard for Test Methods on Mechanical Properties of Ordinary Concrete*. Beijing, China: China Building Industry Press.
- GB/T 50164-2014 (2014). *Technique Code for Application of Fly Ash Concrete*. Beijing, China: China Standard Press.

- GBT 14684-2011 (2011). *Sand for Construction*. Beijing, China: China Standard Press.
- Gunasekara, C., Law, D. W., and Setunge, S. (2016). Long Term Permeation Properties of Different Fly Ash Geopolymer Concretes. *Construction Building Mater.* 124, 352–362. doi:10.1016/j.conbuildmat.2016.07.121
- Gunasekara, C., Setunge, S., and Law, D. W. (2017). Correlations between Mechanical Properties of Low-Calcium Fly Ash Geopolymer Concretes. *J. Mater. Civ. Eng.* 29 (9), 04017111. doi:10.1061/(asce)mt.1943-5533.0001916
- Hefni, Y., Zaher, Y. A. E., and Wahab, M. A. (2018). Influence of Activation of Fly Ash on the Mechanical Properties of concrete. *Construction Building Mater.* 172, 728–734. doi:10.1016/j.conbuildmat.2018.04.021
- Iler, R. K. (1979). *The Chemistry of Silica: Solubility, Polymerization, Colloid and Surface Properties, and Biochemistry*. New York: John Wiley & Sons.
- JGJ 55-2011 (2011). *Specification for Mix Proportion Design of Ordinary Concrete*. Beijing, China: China Building Industry Press.
- JGJ/T 193-2009 (2009). *Standard for Inspection and Assessment of Concrete Durability*. Beijing, China: China Building Industry Press.
- JGJ/T 281-2012 (2012). *Technique Specification for Application of High Strength Concrete*. Beijing, China: China Building Industry Press.
- JGJ/T 70-2009 (2009). *Standard for Test Method of Performance on Building Mortar*. Beijing, China: China Building Industry Press.
- Li, C. Y., Jiang, L., Liu, Y., and Xu, Z. M. (2013). Experimental Study on Activity of Fly Ash Replacing Cement in concrete. *Amm* 438-439, 46–49. doi:10.4028/www.scientific.net/amm.438-439.46
- Li, C., Zhang, X., Zhang, B., Tan, Y., and Li, F. (2021). Reuse of Sintered Sludge from Municipal Sewage Treatment Plants for the Production of Lightweight Aggregate Building Mortar. *Crystals* 11, 999. doi:10.3390/cryst11080999
- Li, F. L., Liu, C., Pan, L. Y., and Li, C. Y. (2014). *Manufactured Sand Concrete*. Beijing, China: China Waterpower Press.
- Li, F. L., Zeng, Y., and Li, C. Y. (2012). Review of Mix Proportion Design Methods for Fly Ash concrete with Machine-Made Sand. *Adv. Mater. Res.* 418-420, 441–444.
- Liu, C. J., Jia, C. Y., and Li, C. Y. (2013a). Evaluation of Relations Among Basic Mechanical Properties of Fly-Ash Concrete with Machine-Made Sand. *Amm* 438-439, 15–19. doi:10.4028/www.scientific.net/amm.438-439.15
- Liu, C. J., Xu, Y. Y., and Zhang, X. Y. (2013b). Study on Durability of concrete with Machine-Made Sand Part I: Time-dependent Chloride Penetration. *Amm* 438-439, 3–9. doi:10.4028/www.scientific.net/amm.438-439.3
- Liu, S., Zhu, M., Ding, X., Ren, Z., Zhao, S., Zhao, M., et al. (2021). High-Durability Concrete with Supplementary Cementitious Admixtures Used in Corrosive Environments. *Crystals* 11 (2), 196. doi:10.3390/cryst11020196
- Ma, J., Wang, D., Zhao, S., Duan, P., and Yang, S. (2021). Influence of Particle Morphology of Ground Fly Ash on the Fluidity and Strength of Cement Paste. *Materials* 14 (2), 283. doi:10.3390/ma14020283
- Malhotra, V. M., and Painter, K. E. (1989). Early-age Strength Properties, and Freezing and Thawing Resistance of concrete Incorporating High Volumes of ASTM Class F Fly Ash. *Int. J. Cement Composites Lightweight Concrete* 11 (1), 37–46. doi:10.1016/0262-5075(89)90034-1
- Mei, J., Ma, B., Tan, H., Li, H., Liu, X., Jiang, W., et al. (2018). Influence of Steam Curing and Nano Silica on Hydration and Microstructure Characteristics of High Volume Fly Ash Cement System. *Construction Building Mater.* 171, 83–95. doi:10.1016/j.conbuildmat.2018.03.056
- Nežerka, V., Bílý, P., Hrbek, V., and Fládr, J. (2019). Impact of Silica Fume, Fly Ash, and Metakaolin on the Thickness and Strength of the ITZ in concrete. *Cem. Concr. Compos.* 103, 252–262. doi:10.1016/j.cemconcomp.2019.05.012
- Olivia, M., Wibisono, G., and Saputra, E. (2019). Early Strength of Various Fly Ash Based concrete in Peat Environment. *MATEC Web Conf.* 276, 01022. doi:10.1051/mateconf/201927601022
- Promsawat, P., Chatveera, B., Sua-iam, G., and Makul, N. (2020). Properties of Self-Compacting concrete Prepared with Ternary Portland Cement-High Volume Fly Ash-Calcium Carbonate Blends. *Case Stud. Construction Mater.* 13, e00426. doi:10.1016/j.cscm.2020.e00426
- Singh, G. V. P. B., and Subramaniam, K. V. L. (2019). Influence of Processing Temperature on the Reaction Product and Strength Gain in Alkali-Activated Fly Ash. *Cement and Concrete Composites* 95, 10–18. doi:10.1016/j.cemconcomp.2018.10.010
- Sivasundaram, V., Carette, G. G., and Malhotra, V. M. (1990). Long-term Strength Development of High-Volume Fly Ash concrete. *Cement and Concrete Composites* 12 (4), 263–270. doi:10.1016/0958-9465(90)90005-i
- Solikin, M., and Setiawan, B. (2017). The Effects of Design Strength, Fly Ash Content and Curing Method on Compressive Strength of High Volume Fly Ash concrete: a Design of Experimental. *MATEC Web Conf.* 103, 01003. doi:10.1051/mateconf/201710301003
- Sun, G. W., Tang, Q. Q., Zhang, L. J., and Wang, C. H. (2019a). Early Activation Effect and Mechanism of High Volume Fly Ash. *J. Harbin Eng. Univ.* 40 (3), 540–547. doi:10.11990/jheu.201711102
- Sun, J., Shen, X., Tan, G., and Tanner, J. E. (2019b). Compressive Strength and Hydration Characteristics of High-Volume Fly Ash concrete Prepared from Fly Ash. *J. Therm. Anal. Calorim.* 136, 565–580. doi:10.1007/s10973-018-7578-z
- Thiyagarajan, H., Mapa, M., and Kushwaha, R. (2018). Investigation on the Rheological Behavior of Fly Ash Cement Composites at Paste and concrete Level. *J. Inst. Eng. India Ser. A.* 99 (2), 295–301. doi:10.1007/s40030-018-0284-9
- Wardhono, A. (2021). Flowability and Strength Properties of High Volume of Fly Ash Material on Self-Compacting concrete. *J. Phys. Conf. Ser.* 1747, 012033. doi:10.1088/1742-6596/1747/1/012033
- Wu, Z. W., and Lian, H. Z. (1999). *High-performance Concrete*. Beijing, China: China Railway Press.
- Yang, J., Hu, H., He, X., Su, Y., Wang, Y., Tan, H., et al. (2021). Effect of Steam Curing on Compressive Strength and Microstructure of High Volume Ultrafine Fly Ash Cement Mortar. *Construction Building Mater.* 266, 120894. doi:10.1016/j.conbuildmat.2020.120894
- Yu, J., Lu, C., Leung, C. K. Y., and Li, G. (2017). Mechanical Properties of green Structural concrete with Ultrahigh-Volume Fly Ash. *Construction Building Mater.* 147, 510–518. doi:10.1016/j.conbuildmat.2017.04.188
- Zhao, M., Zhao, M., Chen, M., Li, J., and Law, D. (2018). An Experimental Study on Strength and Toughness of Steel Fiber Reinforced Expanded-Shale Lightweight concrete. *Construction Building Mater.* 183, 493–501. doi:10.1016/j.conbuildmat.2018.06.178
- Zhao, S. B., Li, Y. T., and Xu, Y. Y. (2013). Study on Durability of concrete with Machine-Made Sand Part II: Long-Term Carbonization. *Amm* 438-439, 10–14. doi:10.4028/www.scientific.net/amm.438-439.10
- Zhao, S., Ding, X., Zhao, M., Li, C., and Pei, S. (2017). Experimental Study on Tensile Strength Development of concrete with Manufactured Sand. *Construction Building Mater.* 138, 247–253. doi:10.1016/j.conbuildmat.2017.01.093

Conflict of Interest: Author BS was employed by the company Henan Fifth Construction Group.

The remaining authors declare that the research was conducted in the absence of any commercial or financial relationships that could be construed as a potential conflict of interest.

Publisher's Note: All claims expressed in this article are solely those of the authors and do not necessarily represent those of their affiliated organizations, or those of the publisher, the editors and the reviewers. Any product that may be evaluated in this article, or claim that may be made by its manufacturer, is not guaranteed or endorsed by the publisher.

Copyright © 2022 Li, Geng, Zhou, Dai, Sun and Li. This is an open-access article distributed under the terms of the Creative Commons Attribution License (CC BY). The use, distribution or reproduction in other forums is permitted, provided the original author(s) and the copyright owner(s) are credited and that the original publication in this journal is cited, in accordance with accepted academic practice. No use, distribution or reproduction is permitted which does not comply with these terms.



Corrosion Experimental Research on Local Damage of Epoxy-Coated Steel Bars in Concrete Under Marine Environment

Hongfei Cao^{1,2*}, Zhongda Lyu^{2,3*}, Wei Dong^{4,5}, Zhuo Zhao^{2,3}, Weizhong Gan^{2,3} and Yonggang Wang¹

¹Faculty of Mechanical Engineering and Mechanics, Ningbo University, Ningbo, China, ²School of Civil and Transportation Engineering, Ningbo University of Technology, Ningbo, China, ³Engineering Research Center of Industrial Construction in Civil Engineering of Zhejiang, Ningbo University of Technology, Ningbo, China, ⁴China Highway Engineering Consulting Corporation, Road and Bridge Design and Research Institute Branch, Wuhan, China, ⁵School of Highway, Chang'an University, Xi'an, China

OPEN ACCESS

Edited by:

Zhigang Zhang,
Chongqing University, China

Reviewed by:

Fengjiang Qin,
Chongqing University, China
Yang Zou,
Chongqing Jiaotong University, China

*Correspondence:

Hongfei Cao
caohongfei92@163.com
Zhongda Lyu
lzd01@189.cn

Specialty section:

This article was submitted to
Structural Materials,
a section of the journal
Frontiers in Materials

Received: 24 November 2021

Accepted: 15 December 2021

Published: 26 January 2022

Citation:

Cao H, Lyu Z, Dong W, Zhao Z, Gan W
and Wang Y (2022) Corrosion
Experimental Research on Local
Damage of Epoxy-Coated Steel Bars in
Concrete Under Marine Environment.
Front. Mater. 8:821716.
doi: 10.3389/fmats.2021.821716

Epoxy coating has been proven to protect steel bars from corrosion. However, the damage of epoxy coating is inevitable, and this may lead to more serious corrosion of steel bar. In order to study the corrosion resistance of steel bars with damaged epoxy coating, two groups of coating-damaged bar and one group of coating-intact rebar were designed, and six specimens were made. The influence of electrolyte concentration on the corrosion rate of steel bars was studied by setting different concentrations. After 30 days of accelerated corrosion, electrochemical data were recorded by the electrochemical workstation. The experimental result shows that the steel bars with coating damage have obvious polarization curve characteristics of corrosion, and corrosion resistance decreases obviously. According to the corrosion current and potential, the larger the damaged area of the coating, the faster will be the corrosion rate. According to the polarization curve data, the polarization resistance is modified, and the result is closer to the real polarization resistance value. The calculated corrosion rate shows that the corrosion rate of reinforcement is affected by both electrolyte concentration and coating damage area, and electrolyte concentration has a greater influence on the corrosion rate.

Keywords: corrosion, epoxy-coated steel bar, accelerated corrosion, linear polarization, marine environment

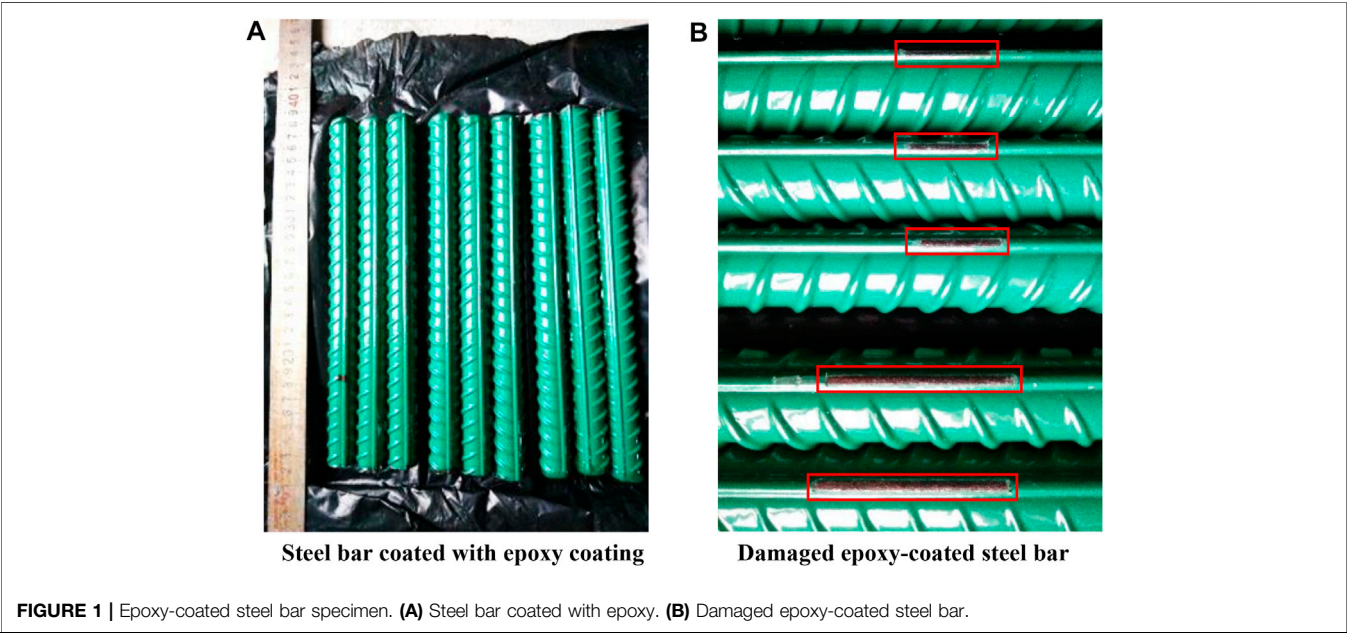
INTRODUCTION

As the bridge is gradually extended to the deep sea, the bridge not only needs to bear more complex loads but also will meet more severe durability problems of concrete structures. The mechanical failure of the concrete structure usually begins with material failure. For deepwater structures, corrosion, crack, breakage, and other problems of basic materials will lead to attenuation of structural resistance and affect the long-term bearing capacity, service safety, and reliability of the structure.

Additional measures on existing structures can reduce the probability of corrosion, such as coating concrete surfaces, corrosion inhibitors, electrochemical dechlorination, cathodic protection, high corrosion-resistant steel materials, and various coated steel bars. Because of its convenience, reinforcement-protective coating has been used in engineering (Stratmann et al., 1994; Grundmeier et al., 2000). In order to study the effectiveness of epoxy-coated steel bars, many

TABLE 1 | Parameters of test block.

Concrete strength grade	Size of test block (cm)	Concentration of NaCl solution	Epoxy-coated steel bars (HRB400)	
C40	15*15*30	0.1 mol/L	S1	Without damage
			S2	The damaged area was 0.5 cm ² , and the length of damage was 2 cm
			S3	The damaged area was 1 cm ² , and the length of damage was 4 cm
		1 mol/L	S4	Without damage
			S5	The damaged area was 0.5 cm ² , and the length of damage was 2 cm
			S6	The damaged area was 1 cm ² , and the length of damage was 4 cm

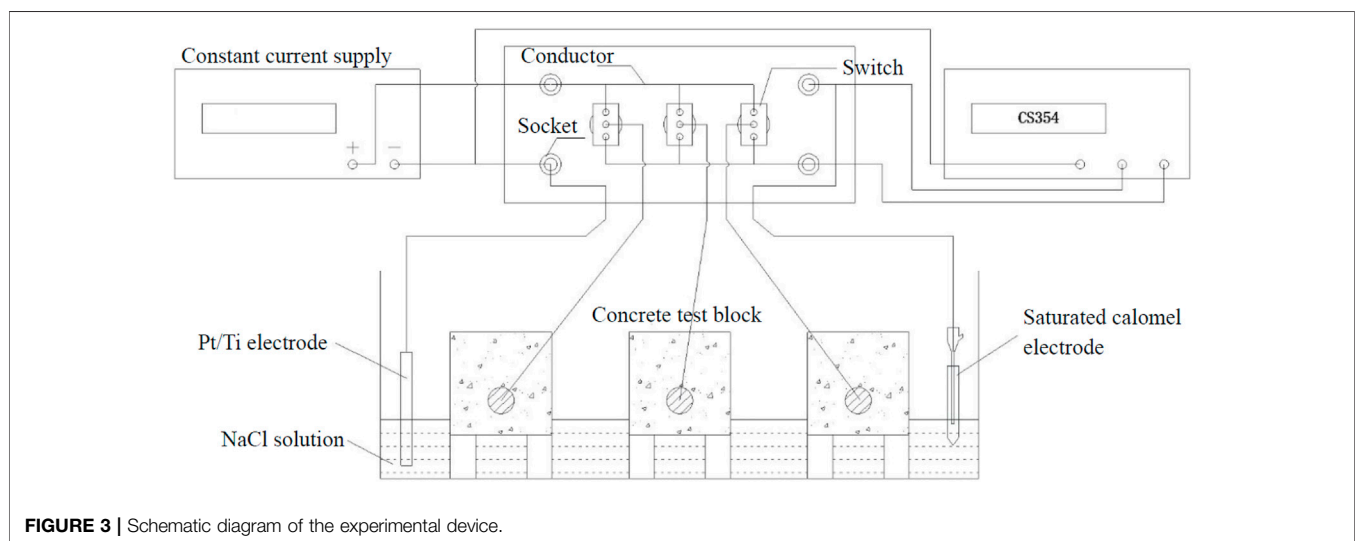
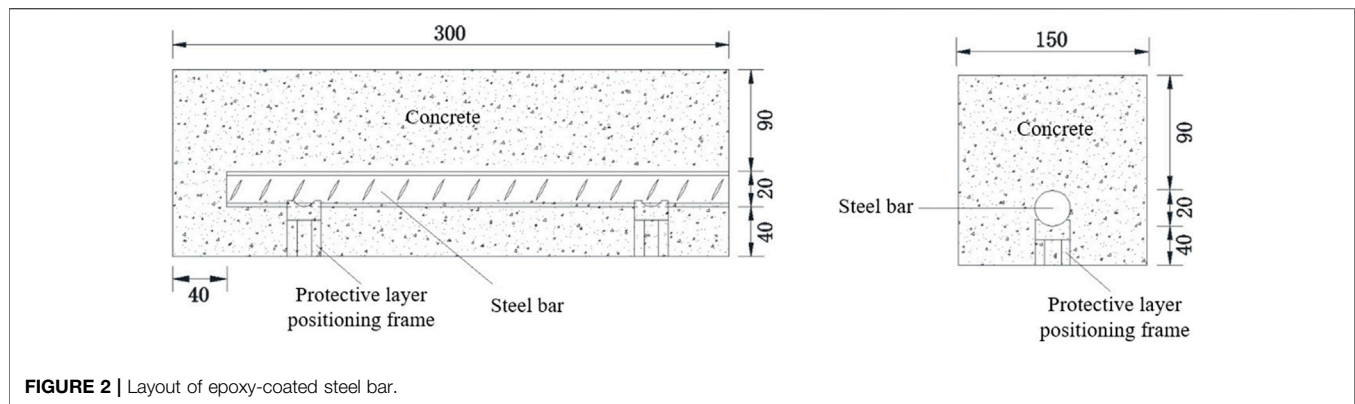


corrosion experiments and investigations had been carried out (Atilgan et al., 2018; Clear et al., 1995; Smith and Virmani, 1996; Manning, 1996; Weyers et al., 1997; Pyc', 1998; Montes et al., 2004; Venkatesan et al., 2006). The effectiveness of epoxy-coated steel bars was verified. However, some studies only considered the influence of environmental factors, ignoring the influence of construction quality, integrity of epoxy coating, and other factors, so the effect of epoxy coating could not be accurately analyzed.

Through the experiment and technical improvement, the protection performance of epoxy coating on steel bars has been continuously improved (Nguyen and Martin, 2004; Singh and Ghosh, 2005; Selvaraj et al., 2009; Caldoni et al., 2021). By changing the material and structure of the coating, the integrity performance of the reinforced concrete structure which is composed of epoxy-coated steel bars, and concrete has been verified and improved (Kim and Andrawes, 2019; Zhang et al., 2020; Shang et al., 2021). Epoxy coating can provide protection for steel bars even in the case of poor concrete quality (Darwin and Scantlebury, 2002). The corrosion protection of steel bars depends on the integrity of the epoxy coating, and its protection is always suspected once the epoxy coating is damaged (Manning,

1996; Darwin and Scantlebury, 2002; Kobayashi and Takewaka, 1984; Bautista and González, 1996; Gowripalan and Mohamed, 1998; Bellezze et al., 2006; Erdoğan et al., 2001). The damage of epoxy coating may be caused by many reasons, such as bumping during construction and transportation, structural deformation, damage during use, and chemical reaction with surrounding substances (Wang et al., 2015; Wang and Gao, 2016; Zhao et al., 2021). Corrosion may not occur in the short term due to the alkaline environmental protection provided by concrete (Bellezze et al., 2006), but its long-term performance may have a great impact (Elleithy et al., 1998).

In this study, the corrosion electrochemical characteristics of epoxy rebars with damaged surface coating are studied. In order to speed up the process of the experiment, the impressed current (IC) technique was used to accelerate the corrosion of steel bar (Li et al., 2021). Six epoxy-coated rebar specimens were manufactured with different degrees of breakage and placed in NaCl solution to simulate corrosion under the marine environment. The corrosion of epoxy-coated rebars was tested using the linear polarization method. According to the obtained electrochemical parameters, the corrosion of steel bars was quantitatively analyzed, and the influence of coating damage



on steel bar corrosion could be obtained. The research results of this study could provide theoretical support for the application of epoxy-coated steel bars under the marine environment.

EXPERIMENTAL DESIGN

Specimen Design

In this experiment, the influence of different damage degrees of epoxy coating on steel bars corrosion was mainly considered. Therefore, three groups of concrete blocks containing epoxy-coated steel bars with different damage levels were designed. **Table 1** summarizes the design parameter details of the tested epoxy-coated steel bars and blocks.

The epoxy-coated steel bar was an HRB400 steel bar with a diameter of 20 mm. The specimen of steel bar was cut to 26 mm in length. The epoxy coating was a Valspar product. After blending the coating and curing agent in a ratio of 5:1, epoxy was evenly coated on the surface of the steel bar. To simulate the damage of the epoxy rebar, part of the coating from the surface of

the steel bar was removed with a file (**Figure 1**). The protective layer positioning frame was secured to the steel bar, and the uncoated end of the steel bar was attached to the die in order to connect the wires (**Figure 2**). After connecting the wire, the exposed steel bar at the end was sealed with epoxy adhesive.

Experimental Apparatus

The experimental apparatus was mainly composed of four parts, as shown in **Figure 3**.

- (1) Current stable supply: This part was mainly composed of single-channel adjustable DC power supply and external wire.
- (2) Switch box (**Figure 4**): The constant current power supply and the CS354 electrochemical workstation were connected to the switch box through a socket, so the test process could be controlled through the switch. By flipping the switch on the switch box, the corrosion of the steel bar could be accelerated, and the electrochemical information such as resistance and potential of the steel bar in the sample

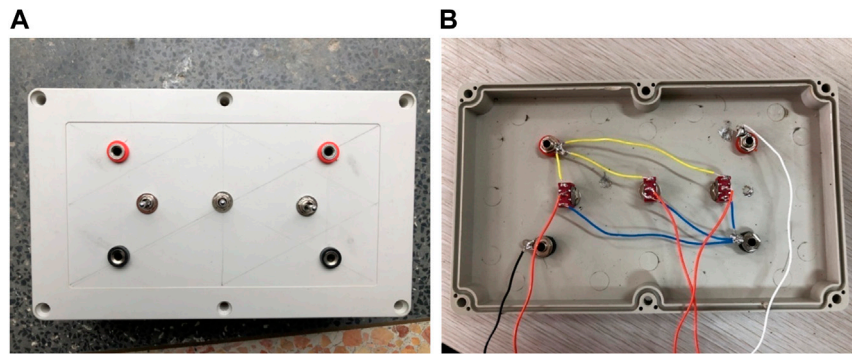


FIGURE 4 | Switch box. **(A)** Surface of the switch box. **(B)** Inside of the switch box.



FIGURE 5 | Accelerated corrosion method and measurement of electric polarization parameter.

could be measured. By using this equipment, the artificial test error caused by multiple measurements was reduced.

- (3) The CS354 electrochemical workstation: This part was mainly composed of workstations and external wires. The CS354 electrochemical workstation could complete electrodynamic potential or dynamic current scanning, electrochemical impedance spectroscopy, and other electrochemical testing functions, which could meet the requirements of this test (Guan, 2007).
- (4) Specimen test box: This part was composed of concrete test blocks, saturated calomel electrode, Pt/Ti electrode, NaCl solution, platinum cathode electrode, and conductors. Concrete test blocks were padded with wooden blocks and shelved in test boxes. A certain amount of NaCl solution was poured into the test box, and the reference electrode and

platinum electrode were placed in NaCl solution. NaCl solution was used as a corrosion medium to simulate the marine environment.

Experimental Process

Due to the protection of concrete and epoxy coating, the corrosion rate of the steel bar under natural conditions is slow. In order to speed up the process of the experiment, the electrochemical accelerated corrosion method was used to accelerate the corrosion rate of the steel bar. In order to avoid the obvious error between the corrosion caused by accelerated corrosion and the corrosion results produced in the natural environment due to excessive current density, the recommended critical value of $2000 \mu\text{A}/\text{cm}^2$ was used in this experiment (Wu, 2016; Feng et al., 2021). The steel bar in each concrete test block was connected to the switch box in parallel. It was calculated that the current provided to the steel bar block should be about 28.84 mA, so the output current of this experiment was set to 30 mA.

The current stable supply was connected to the switch box, and then the power supply was switched on to start galvanizing corrosion and control the galvanizing time and current size, as shown in Figure 5. The polarization curves were measured in different time periods, and the corrosion rates of steel bars at the damaged parts of the coating were calculated.

RESULT AND DISCUSSION

Analysis of Polarization Curve

After accelerated corrosion of each test block, the polarization curves of the specimens at different times were measured and plotted, as shown in Figure 6. As can be seen from the polarization curve in Figure 6A, the polarization curve slope of the epoxy steel bar with no surface damage in the test block after electrochemical accelerated corrosion is very large, without typical polarization curve characteristics, showing obvious low corrosion characteristics. In Figure 6B, after accelerated corrosion lasts for 30 days, corrosion current appears in the circuit, indicating that corrosion begins to occur in the epoxy steel bar. The cause may be slight damage to the epoxy coating

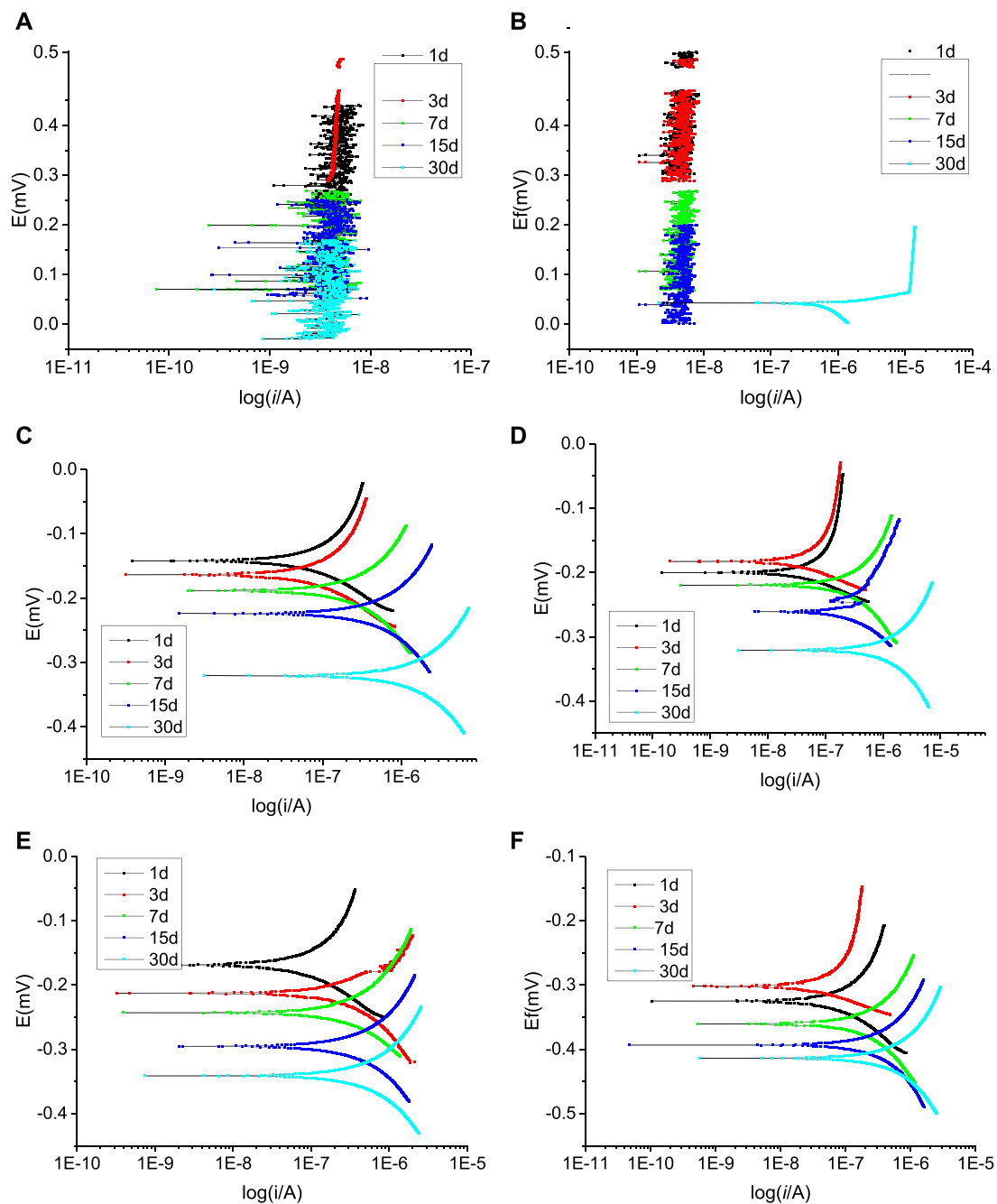


FIGURE 6 | Polarization curves of different specimens **(A)** S1, **(B)** S4, **(C)** S2, **(D)** S5, **(E)** S3, and **(F)** S6.

when assembling the specimen or pouring the concrete, resulting in a weak current in the circuit.

As can be seen from the polarization curves in **Figure 6C**, the steel bars show obvious corrosion characteristics. With the development of corrosion, the polarization curves gradually move to the lower right direction, that is, the corrosion rate (I_{corr}) increases and the corrosion potential (E_{corr}) decreases. Since the damage length of coating is relatively small, the

change in polarization current in the system has a greater impact on corrosion. As can be seen from **Figure 6D**, compared with the electrolyte solution of 0.1 mol/L, the polarization curve of the anode rises faster. The increase in electrolyte concentration promotes the corrosion of steel bars, accelerates the activation state of epoxy steel bars with damaged surfaces in concrete specimens, and accelerates the corrosion reaction.

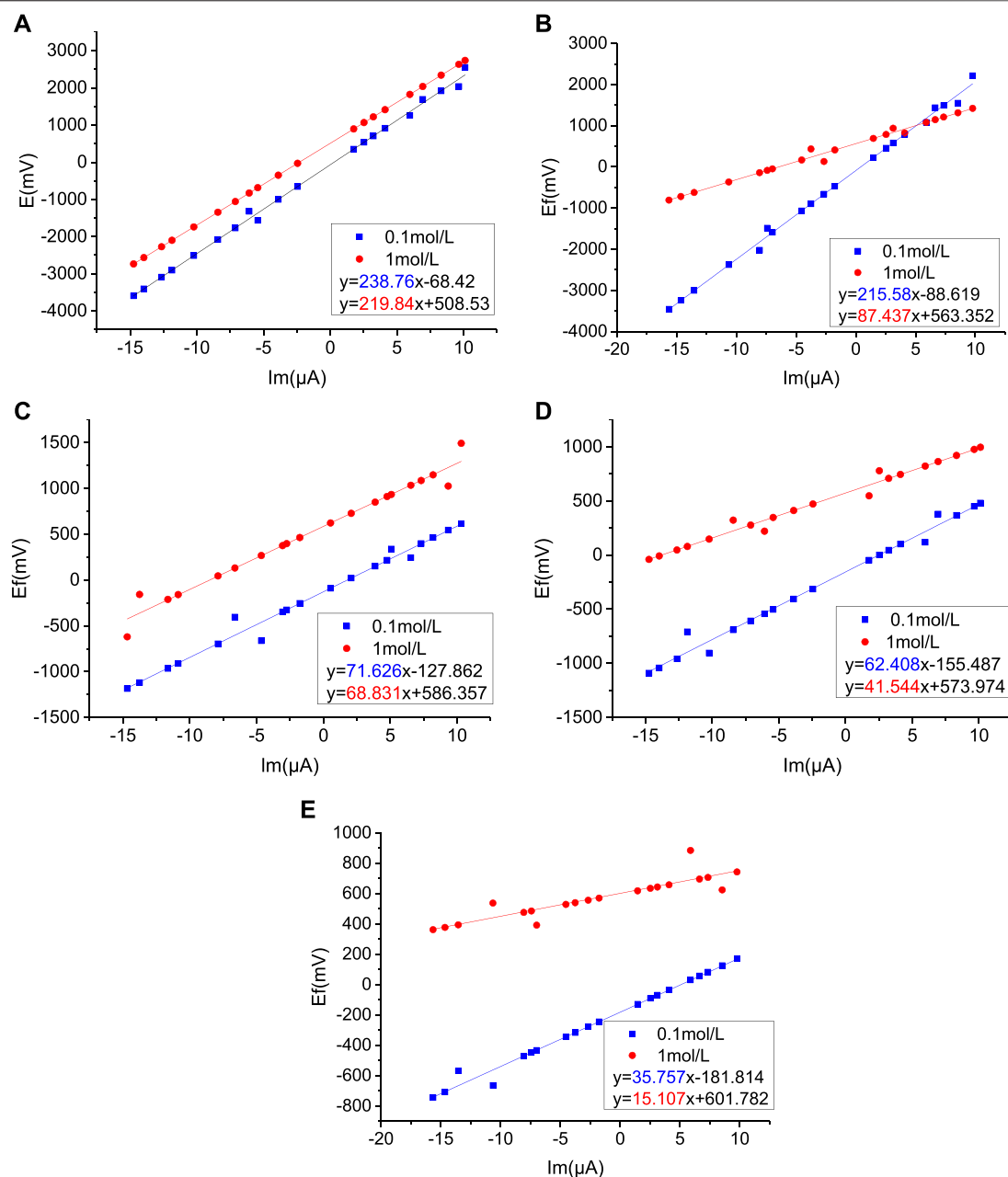


FIGURE 7 | Fitted polarization resistance of S2 and S5 at different times (A) 1d, (B) 3d, (C) 7d, (D) 15d, and (E) 30d.

Figure 6F shows the polarization curve of the steel bar at different corrosion times when the concentration of NaCl solution is 1 mol/L, and the surface coating is damaged by 4 cm. Compared with the case of coating damage of 2 cm under the same other conditions, the increase in the anodic polarization curve in this part is slower, indicating that the self-corrosion current (I_{corr}) is higher and the self-corrosion potential (E_{corr}) is lower after changing this parameter.

The polarization curve of the epoxy steel bar varies according to the degree of corrosion. Generally speaking, if

the electrode is polarized from the cathode to the anode, the equilibrium potential of the polarization curve will move in the negative direction. If the steel bar is passivated, the offset increases significantly. As shown in **Figure 6**, the cathode polarization curves are very stable on the third day. However, the anode polarization curves rise rapidly, and the Tafel slope is very large. The anode reaction process is very difficult. Based on the principle of corrosion potential, it can be known that the steel bar in the damaged area of the coating may be passivated.

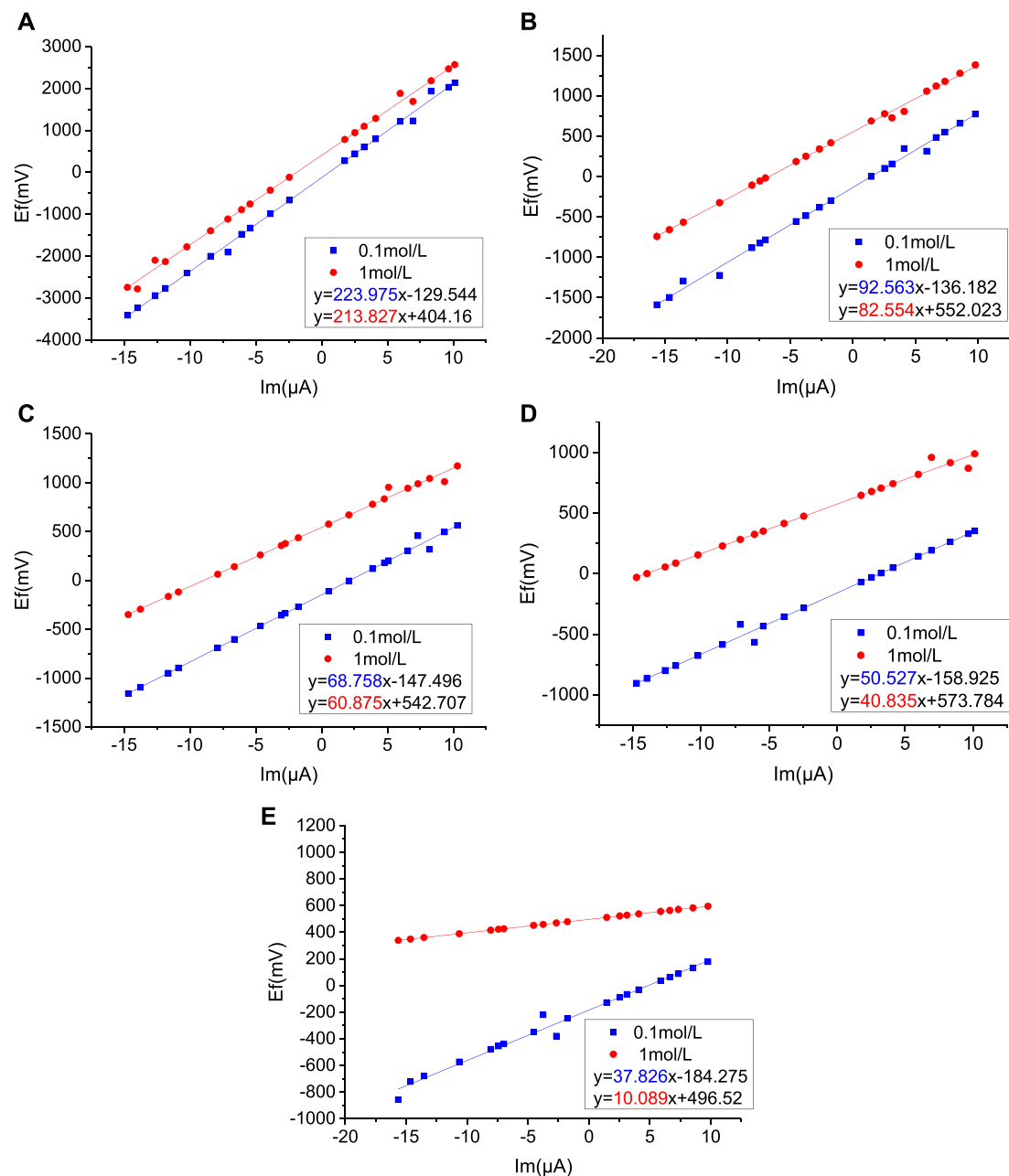


FIGURE 8 | Fitted polarization resistance of S3 and S6 at different times (A) 1d, (B) 3d, (C) 7d, (D) 15d, and (E) 30d.

With the development of corrosion, the range of negative and anode zone becomes smaller, indicating that the passivation state of the steel bar is not stable. The aforementioned phenomenon shows that the pitting resistance of epoxy-coated steel bars is getting weaker. It can be seen from **Figure 6E** that the partial area of the anode showed fluctuations, which may be due to the micro-cracks on the surface of the epoxy-coated steel bar and then re-passivation. Then the passivation layer broke again under the action of the corrosion solution, resulting in the fluctuation of the corrosion current.

After 30 days of accelerated corrosion, the polarization curve of the anode becomes more stable and β_a becomes smaller. It can be seen that the reaction of the anode is good, and the steel bar at the damaged site is highly involved in the reaction.

As can be seen from the characteristics of the polarization curve, the steel bar appears passivated on the third day, while the passivation film gradually disappears on the seventh day. With the concentration of NaCl solution is 1 mol/L, β_a of the anodic curve of the steel bar with damaged surface coating goes to infinity on the third day of corrosion, indicating that a dense

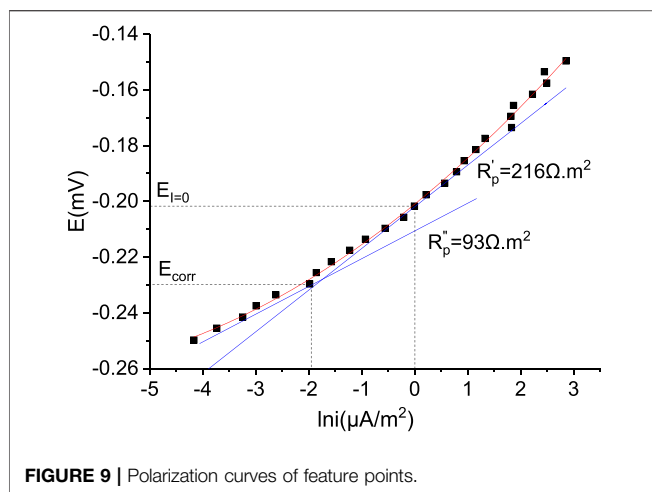


FIGURE 9 | Polarization curves of feature points.

TABLE 2 | Effect of scanning rate on potential offset.

Scanning rate (mV/s)	R_p' ($\Omega\cdot m^2$)	R_p'' ($\Omega\cdot m^2$)	R_p'/R_p''	$E_{corr} - E_{I=0}$ (mV)
0.10	268	298	0.90	2.7
0.25	127	184	0.69	3.8
0.50	20	37	0.55	4.2

passivation layer has been formed on the surface. At this time, the polarization current is mainly controlled by the cathode reaction.

Corrosion Potential

Figures 6A,B show the corrosion potential E_{corr} of the epoxy steel bar without surface damage maintained at about 0.25 mV after the accelerated corrosion test. It shows that the probability of steel bar corrosion is low. For epoxy steel bars without surface damage, 30 days of accelerated corrosion do not increase the risk of corrosion. For damaged steel bars, according to the change in corrosion potential, it can be seen that the corrosion of steel bars has been developing, and the corrosion potential continues to decrease.

By comparing the corrosion potential in different concentrations of the solution, it can be seen that the higher the concentration of the solution, the greater the negative value of corrosion potential. In addition, at the same electrolyte concentration, the greater the damage degree of epoxy coating, the faster will be the corrosion rate.

The disturbance of the electrode is excluded, and the effect of the ion diffusion rate on the electrode reaction is considered. With the progress of corrosion, Cl^- in the coat-damaged area of the steel bar gradually accumulates, and the reaction rate of the anode area is faster and faster. When the O_2 diffusion rate of the anode region is less than the corrosion reaction rate, the reaction rate of the anode is mainly determined by the O_2 diffusion rate.

TABLE 3 | Analysis of the anode polarization curve.

T/d	ω (NaCl)/(mol/L)	d/cm	$R_p/(\Omega\cdot cm^2)$	\bar{i}_{corr} (mA/cm²)	\bar{V}_{corr} (mm/a)
1	0.1	0	147,3382	1.00E-06	9.85E-06
		2	238,760	7.46E-05	7.34E-04
		4	223,975	8.03E-05	7.89E-04
	1	0	756,681	1.02E-06	1.01E-05
		2	219,840	8.27E-05	8.13E-04
		4	213,827	8.36E-05	8.22E-04
3	0.1	0	818,352	1.23E-06	1.21E-05
		2	215,580	8.44E-05	8.29E-04
		4	92,563	1.74E-04	1.71E-03
	1	0	534,289	5.87E-06	5.45E-05
		2	387,437	1.93E-05	1.90E-05
		4	382,554	1.96E-05	1.92E-05
7	0.1	0	427,320	4.15E-05	4.08E-04
		2	71,626	2.38E-04	2.34E-03
		4	68,758	2.45E-04	2.41E-03
	1	0	361,146	6.04E-05	5.94E-04
		2	68,831	2.57E-04	2.53E-03
		4	60,875	2.66E-04	2.61E-03
15	0.1	0	379,450	6.05E-05	5.95E-04
		2	62,408	2.68E-04	2.64E-03
		4	50,527	3.22E-04	3.17E-03
	1	0	350,747	6.38E-05	6.27E-04
		2	41,544	3.87E-04	3.81E-03
		4	40,835	4.03E-04	3.96E-03
30	0.1	0	382,073	6.39E-05	6.29E-04
		2	35,757	5.54E-04	4.23E-03
		4	37,826	4.36E-04	4.29E-03
	1	0	256,817	7.32E-05	7.19E-04
		2	15,107	1.07E-03	1.05E-02
		4	10,089	2.13E-03	2.06E-02

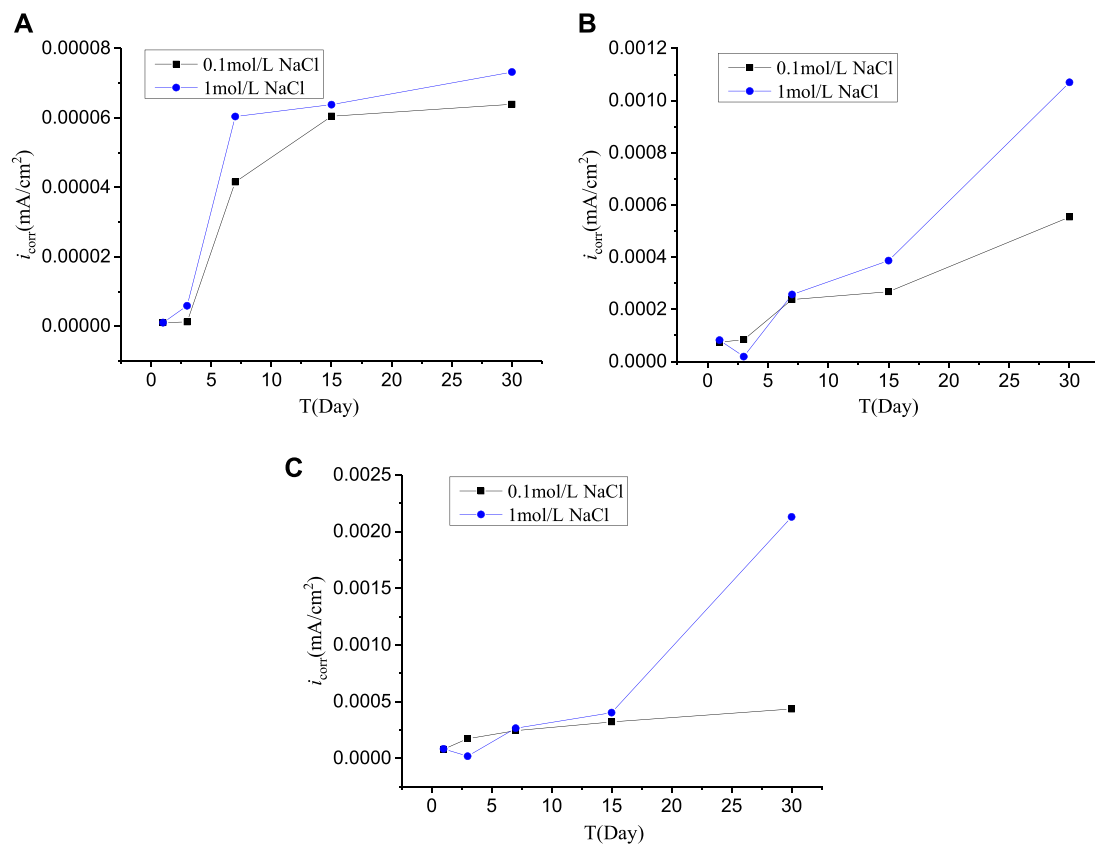


FIGURE 10 | Corrosion current density (A) S1 and S4; (B) S2 and S5; (C) S3 and S6.

It can be seen from **Figures 6D,F** that the equilibrium potential increases on the third day, and the polarization curve of the anode region changes faster than that of the cathode region. The reason may be that the corrosion reaction is under O_2 diffusion control, which leads to a decrease in the corrosion current density, thus slowing down the anodic polarization rate and making the slope of the anodic polarization curve large.

Polarization Resistance

Thirty days of accelerated corrosion tests were carried out on coated steel specimens, and the experimental data of 1st, 3rd, 7th, 15th, and 30th days were recorded. After testing by electrochemical workstation, the polarization resistance of each steel bar is obtained by fitting, as shown in **Figures 7, 8**. Under the condition that the concentration of NaCl solution is 0.1 mol/L and the surface coating is damaged 2 cm, the anodic polarization resistance of the steel specimens at different times is 238,760, 215,580, 71,626, 62,408, and 35,757 $\Omega \text{ cm}^2$. The polarization resistance of epoxy steel bars after accelerated corrosion has decreased much, indicating that the reaction rate of the steel bar surface has largely increased. As the corrosion continues, the polarization resistance becomes smaller and smaller, and the corrosion rate becomes higher

and higher. By comparing the polarization resistance values of 1 mol/L NaCl solution, it can be seen that the duration of acceleration has a great influence on the corrosion effect, while the difference in polarization resistance values at the same time is small.

Compared with the 0.1 mol/L concentration group, the polarization resistance value of concrete specimens after accelerated corrosion is reduced twice, indicating that the increase in NaCl solution concentration promotes corrosion. However, for 1 mol/L NaCl solution, there will be a sudden increase in polarization resistance on the third day, indicating that a passivation layer is produced on the steel bar at this time and then the passivation layer slowly disappears in a longer corrosion time.

By comparing the polarization resistance value of epoxy coating damaged 2 and 4 cm, it can be seen that the polarization resistance value of steel bars damaged 4 cm is lower after the accelerated corrosion at the same time, indicating that the larger the coating damage, the faster will be the corrosion.

It is found that polarization resistance measured by the electrochemical workstation can be affected by potential deviation, and it is difficult to determine the error value. Therefore, the mean value data of the specimen with 1 mol/L NaCl solution and 4-cm damaged surface coat are selected as the

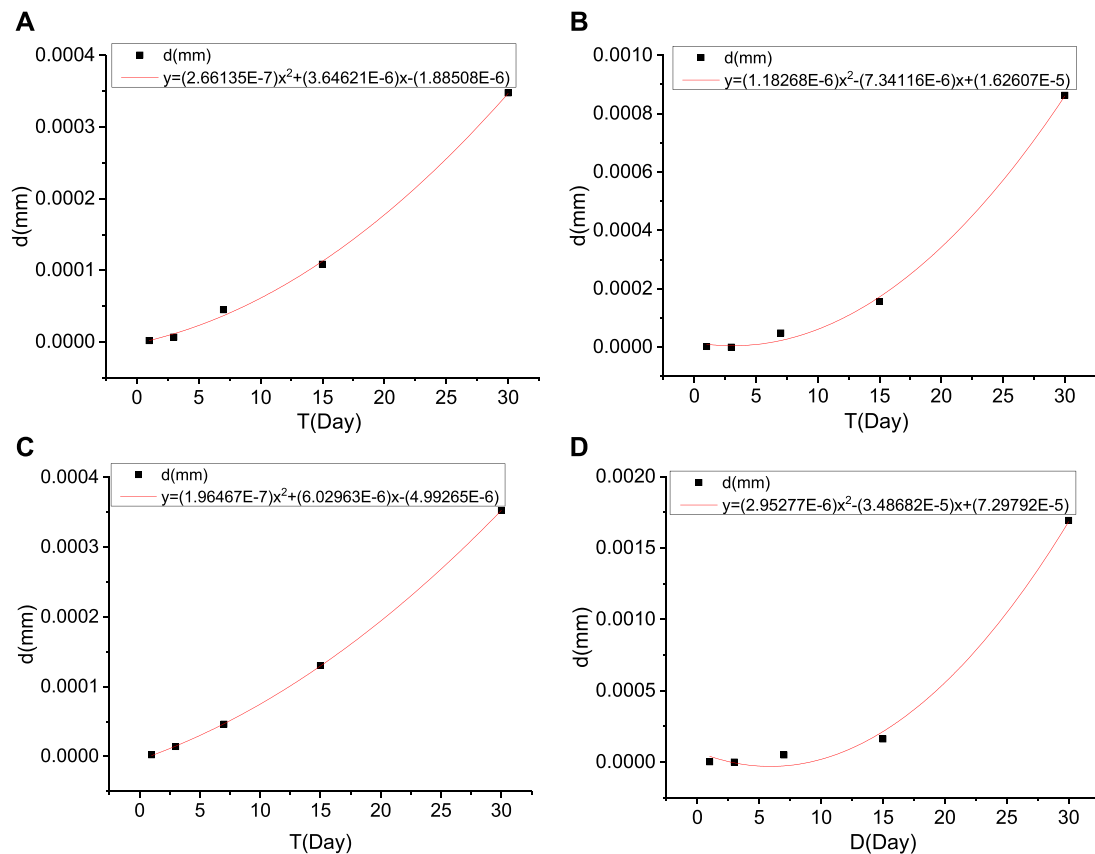


FIGURE 11 | Fitting curve of corrosion quantity (A) S2, (B) S5, (C) S3, and (D) S6.

research object. A section of polarization curve near $E_i = 0$ and E_{corr} is selected. First, the polarization curve is fitted, and then the tangent lines corresponding to $E_i = 0$ and E_{corr} are drawn, respectively (Figure 9). It can be found that the slope (polarization resistance) is different. We suspect that actual polarization resistance may lie somewhere between these two curves.

It is difficult to calculate the exact value of the polarization resistance, and R_p can be modified by the following formula to obtain a more realistic value:

$$R_p = \frac{R'_p + R''_p}{2}, \quad (1)$$

$$R'_p = \left(\frac{\partial \Delta E}{\partial I} \right)_{I=0, dE/dt \rightarrow 0}, \text{ and} \quad (2)$$

$$R''_p = \left(\frac{\partial \Delta E}{\partial I} \right)_{E=E_{\text{corr}}, dE/dt \rightarrow 0}. \quad (3)$$

The corrosion potential changes and corresponding polarization resistance values of epoxy steel bars at different scanning rates were measured and obtained and are given in Table 2. As the scanning speed decreases, the R'_p/R''_p value gradually approaches 1, and when the scanning speed

decreases to 0.10 mV/s, $R'_p/R''_p = 0.90$ shows that the value of R'_p and R''_p is very close.

Corrosion Current Density

The corrosion current and current density of each test block were recorded at days 1, 3, 7, 15, and 30, and the current density diagram is drawn as shown in Figure 10. Compared with the initial corrosion current density of epoxy steel bars, the corrosion current density sometimes decreases after accelerated corrosion. This may be due to the passivation of the surface of steel bars during the electrification process of accelerated corrosion, leading to a decrease in the polarization area, so the reaction shows a slight decrease in the corrosion current density. By comparing the current density of the 2-cm group and 4-cm group corroded by epoxy steel bar coating in electrolytes with different concentrations, it can be seen that the difference in corrosion current density between the two groups becomes larger and larger after accelerated corrosion, indicating that the concentration of electrolyte solution plays a dominant role in the later stage of corrosion.

Calculation of Corrosion Rate

The corrosion rate is calculated according to the following equation:

$$MPY = \frac{i_{corr} \times n \times 393.7 \times 365 \times 24 \times 3600}{\rho \times 96500}, \quad (4)$$

where MPY is the corrosion rate (mil/a), n is the relative atomic mass, ρ is the density of iron, and i_{corr} is the corrosion current density, which is calculated from the measured corrosion current. Through fitting calculation, the corrosion rate of steel bars under different corrosion durations, electrolyte solution concentrations, and coating damage degrees can be obtained (Table 3).

Comparing these three groups of independent variables, it is found that in the case of coating damage, the accelerated corrosion duration is the primary influencing factor in this experiment. In contrast, the concentration of the solution has a greater effect on the corrosion rate than the damaged area of the coating in this experiment.

Through the analysis of experimental data, the corrosion curves of steel bars under different corrosion areas and Cl^- concentration are fitted, and then the numerical relationship between corrosion quantity and corrosion time is obtained by curve fitting (Figure 11).

As can be seen from Figure 11, after local corrosion of steel bars, the higher Cl^- concentration, the will be the second derivative of the corrosion curve, indicating that when the coated steel bars are damaged, the Cl^- concentration will have a greater influence on the long-term corrosion of steel bars. For the corrosion of 2- and 4-cm coatings, the corrosion rate of steel bars at 4 cm is almost twice as high as that at 2 cm.

CONCLUSION

Based on the linear polarization theory principle, the electrochemical behavior of damaged epoxy-coated steel bars was analyzed using an accelerated corrosion test. The effects of the accelerated corrosion duration and electrolyte solution concentration on steel bar corrosion were analyzed through the check experiment. Finally, the following conclusions were drawn:

- (1) When the epoxy coating is not damaged, the polarization curve is chaotic and there is no obvious electrochemical reaction characteristic. When the coating is damaged, the

polarization curve has obvious change characteristics, through which the electrochemical reaction can be judged.

- (2) With different solution concentrations, the development process of steel bar corrosion is different. In the early stage of the corrosion reaction, the slope of the anode polarization curve of the steel bar in 1 mol/L electrolyte may be very large. The reason is the difficulty of electrochemical reaction caused by electrode passivation. In the long term, the development trend of corrosion is that the corrosion rate increases and the corrosion potential decreases.
- (3) According to the polarization curve near the characteristic points, the true value of the polarization resistance needs to be corrected. The polarization resistance calculated by the modified formula is closer to the real value.
- (4) According to the corrosion current density and the corrosion rate of steel bar, the higher the electrolyte solution concentration, the larger will be the damaged area of the coating and the faster will be the reaction. In comparison, the concentration of the electrolyte has a greater effect on corrosion.

DATA AVAILABILITY STATEMENT

The original contributions presented in the study are included in the article/Supplementary Material, and further inquiries can be directed to the corresponding authors.

AUTHOR CONTRIBUTIONS

HC worked on the conception and design of this study, and derived relevant formulas. WD analyzed the data and charted it. ZL and ZZ made important revisions to the manuscript. WG and YW participated in the writing and revision of the manuscript.

FUNDING

This work is supported by the major special science and technology project (2019B10076) of “Ningbo science and technology innovation 2025” and the scientific research project (2018035) of Zhejiang Provincial Department of Transportation.

REFERENCES

- Atilgan, A., Yurdakul, Ş., Erdogdu, Y., and Güllüoğlu, M. T. (2018). DFT Simulation, Quantum Chemical Electronic Structure, Spectroscopic and Structure-Activity Investigations of 4-acetylpyridine. *J. Mol. Struct.* 1161, 55–65. doi:10.1016/j.molstruc.2018.01.080
- Bautista, A., and González, J. A. (1996). Analysis of the Protective Efficiency of Galvanizing against Corrosion of Reinforcements Embedded in Chloride Contaminated concrete. *Cement Concrete Res.* 26 (2), 215–224. doi:10.1016/0008-8846(95)00215-4
- Bellezze, T., Malavolta, M., Quaranta, A., Ruffini, N., and Roventi, G. (2006). Corrosion Behaviour in concrete of Three Differently Galvanized Steel Bars. *Cement and Concrete Composites* 28 (3), 246–255. doi:10.1016/j.cemconcomp.2006.01.011

- Caldona, E. B., Wipf, D. O., and Smith, D. W. (2021). Characterization of a Tetrafunctional Epoxy-Amine Coating for Corrosion protection of Mild Steel. *Prog. Org. Coat.* 151, 106045. doi:10.1016/j.porgcoat.2020.106045
- Clear, K. C., Hartt, W. H., McIntyre, J., and Lee, S. K. (1995). *Performance of Epoxy-Coated Reinforcing Steel in Highway Bridges*. NCHRP Report 370. Washington, DC: National Cooperation Highway Research Program.
- Darwin, A. B., and Scantlebury, J. D. (2002). Retarding of Corrosion Processes on Reinforcement Bar in concrete with an FBE Coating. *Cement and Concrete Composites* 24, 73–78. doi:10.1016/S0958-9465(01)00028-2
- Elleithy, W. M., Sharif, A. M., Al-Amoudi, O. S. B., Maslehuiddin, M., and Kalam Azad, A. (1998). Effect of Holidays and Surface Damage to FBEC on Reinforcement Corrosion. *Construction Building Mater.* 12 (4), 185–193. doi:10.1016/S0950-0618(98)00004-X
- Erdogdu, S., Bremner, T. W., and Kondratova, I. L. (2001). Accelerated Testing of plain and Epoxy Coated Reinforcement in Simulated Seawater and Chloride

- Solutions. *Cement Concrete Res.* 31, 861–867. doi:10.1016/S0008-8846(01)00487-2
- Feng, W., Tarakbay, A., Ali Memon, S., Tang, W., and Cui, H. (2021). Methods of Accelerating Chloride-Induced Corrosion in Steel-Reinforced concrete: a Comparative Review. *Construction Building Mater.* 289 (2), 123165. doi:10.1016/j.conbuildmat.2021.123165
- Gowripalan, N., and Mohamed, H. M. (1998). Chloride-ion Induced Corrosion of Galvanized and Ordinary Steel Reinforcement in High-Performance concrete. *Cement Concrete Res.* 28 (8), 1119–1131. doi:10.1016/S0008-8846(98)00090-8
- Grundmeier, G., Schmidt, W., and Stratmann, M. (2000). Corrosion protection by Organic Coatings: Electrochemical Mechanism and Novel Methods of Investigation. *Electrochimica Acta* 45 (15–16), 2515–2533. doi:10.1016/S0013-4686(00)00348-0
- Guan, X. (2007). *The Study and Design on the Electrochemical Power Measurement Workstation Based on Dsp* (Harbin: Harbin University of Science and Technology). MA thesis.
- Kim, K.-H. E., and Andrawes, B. (2019). Exploratory Study on Bond Behavior of Textured Epoxy-Coated Reinforcing Bars. *J. Mater. Civ. Eng.* 31 (8), 04019151. doi:10.1061/(ASCE)MT.1943-5533.0002799
- Kobayashi, K., and Takewaka, K. (1984). Experimental Studies on Epoxy Coated Reinforcing Steel for Corrosion protection. *Int. J. Cement Composites Lightweight Concrete* 6 (2), 99–116. doi:10.1016/0262-5075(84)90039-3
- Li, Q., Jin, X., Yan, D., Fu, C., and Xu, J. (2021). Study of Wiring Method on Accelerated Corrosion of Steel Bars in concrete. *Construction Building Mater.* 269 (3), 121286. doi:10.1016/j.conbuildmat.2020.121286
- Manning, D. G. (1996). Corrosion Performance of Epoxy-Coated Reinforcing Steel: North American Experience. *Construction Building Mater.* 10 (5), 349–365. doi:10.1016/0950-0618(95)00028-3
- Montes, P., Bremner, T. W., and Kondratova, I. (2004). Eighteen-year Performance of Epoxy-Coated Rebar in a Tunnel Structure Subjected to a Very Aggressive Chloride-Contaminated Environment. *Corrosion* 60 (10), 974–981. doi:10.5006/1.3287832
- Nguyen, T., and Martin, J. W. (2004). Modes and Mechanisms for the Degradation of Fusion-Bonded Epoxy-Coated Steel in a marine concrete Environment. *J. Coat. Technol. Res.* 1 (2), 81–92. doi:10.1007/s11998-004-0002-6
- Pyc', W. A. (1998). *Field Performance of Epoxy-Coated Reinforcing Steel in Virginia Bridge Decks* (Virginia: Faculty of the Virginia Polytechnic Institute and State University). Ph.D. thesis.
- Selvaraj, R., Selvaraj, M., and Iyer, S. V. K. (2009). Studies on the Evaluation of the Performance of Organic Coatings Used for the Prevention of Corrosion of Steel Rebars in concrete Structures. *Prog. Org. Coat.* 64 (4), 454–459. doi:10.1016/j.porgcoat.2008.08.005
- Shang, H., Shao, S., and Wang, W. (2021). Bond Behavior between Graphene Modified Epoxy Coated Steel Bars and concrete. *J. Building Eng.* 42, 102481. doi:10.1016/j.jobbe.2021.102481
- Singh, D. D. N., and Ghosh, R. (2005). Unexpected Deterioration of Fusion-Bonded Epoxy-Coated Rebars Embedded in Chloride-Contaminated Concrete Environments. *Corrosion* 61 (8), 815–829. doi:10.5006/1.3278216
- Smith, J. L., and Virmani, Y. P. (1996). Performance of Epoxy-Coated Steel Bars in Bridge Decks. *Public Roads* 60 (2), 6–12.
- Stratmann, M., Feser, R., and Leng, A. (1994). Corrosion protection by Organic Films. *Electrochimica Acta* 39 (8–9), 1207–1214. doi:10.1016/0013-4686(94)E0038-2
- Venkatesan, P., Palaniswamy, N., and Rajagopal, K. (2006). Corrosion Performance of Coated Reinforcing Bars Embedded in concrete and Exposed to Natural marine Environment. *Prog. Org. Coat.* 56 (1), 8–12. doi:10.1016/j.porgcoat.2006.01.011
- Wang, X.-H., Chen, B., Gao, Y., Wang, J., and Gao, L. (2015). Influence of External Loading and Loading Type on Corrosion Behavior of RC Beams with Epoxy-Coated Reinforcements. *Construction Building Mater.* 93 (15), 746–765. doi:10.1016/j.conbuildmat.2015.05.101
- Wang, X.-H., and Gao, Y. (2016). Corrosion Behavior of Epoxy-Coated Reinforced Bars in RC Test Specimens Subjected to Pre-exposure Loading and Wetting-Drying Cycles. *Construction Building Mater.* 119, 185–205. doi:10.1016/j.conbuildmat.2016.05.066
- Weyers, R. E., Pyc, W., Zemajtis, J., Liu, Y., Mokarem, D., and Sprinkel, M. M. (1997). Field Investigation of Corrosion-protection Performance of Bridge Decks Constructed with Epoxy-Coated Reinforcing Steel in Virginia. *Transportation Res. Rec.* 1597, 82–90. doi:10.3141/1597-11
- Wu, F. (2016). *Study on the Bond-Slip Constitutive Relation between Corroded Steel Bar and concrete under the Coupling Action of Load and Environment* (Chongqing: Chongqing Jiaotong University). MA thesis.
- Zhang, Z., Jung, D., and Andrawes, B. (2020). Evaluation of Surface Roughness and Bond-Slip Behavior of New Textured Epoxy-Coated Reinforcing Bars. *Construction Building Mater.* 262 (2), 120762. doi:10.1016/j.conbuildmat.2020.120762
- Zhao, Q., Zhang, D., Zhao, X.-L., and Sharma, S. (2021). Modelling Damage Evolution of Carbon Fiber-Reinforced Epoxy Polymer Composites in Seawater Sea Sand concrete Environment. *Composites Sci. Techn.* 215, 108961. doi:10.1016/j.compscitech.2021.108961

Conflict of Interest: WD was employed by the China Highway Engineering Consulting Corporation Road and Bridge Design and Research Institute Branch.

The remaining authors declare that the research was conducted in the absence of any commercial or financial relationships that could be construed as a potential conflict of interest.

Publisher's Note: All claims expressed in this article are solely those of the authors and do not necessarily represent those of their affiliated organizations, or those of the publisher, the editors, and the reviewers. Any product that may be evaluated in this article, or claim that may be made by its manufacturer, is not guaranteed or endorsed by the publisher.

Copyright © 2022 Cao, Lyu, Dong, Zhao, Gan and Wang. This is an open-access article distributed under the terms of the Creative Commons Attribution License (CC BY). The use, distribution or reproduction in other forums is permitted, provided the original author(s) and the copyright owner(s) are credited and that the original publication in this journal is cited, in accordance with accepted academic practice. No use, distribution or reproduction is permitted which does not comply with these terms.



Numerical Simulation on Cement Hydration and Microstructure Development in Repair-Substrate Interface

Mingzhang Lan^{1*}, Jian Zhou², Hui Li^{2*} and Ying Wang³

¹College of Materials Science and Engineering, Beijing University of Technology, Beijing, China, ²School of Civil and Transportation Engineering, Hebei University of Technology, Tianjin, China, ³School of Civil Engineering, Tianjin Chengjian University, Tianjin, China

OPEN ACCESS

Edited by:

Zhigang Zhang,
Chongqing University, China

Reviewed by:

Zhidong Zhang,
ETH Zürich, Switzerland
Peng Zhang,
National Natural Science Foundation
of China, China

*Correspondence:

Mingzhang Lan
lanmingzhang@bjut.edu.cn
Hui Li
hla_zyj@hebut.edu.cn

Specialty section:

This article was submitted to
Structural Materials,
a section of the journal
Frontiers in Materials

Received: 06 December 2021

Accepted: 14 January 2022

Published: 03 February 2022

Citation:

Lan M, Zhou J, Li H and Wang Y (2022)
Numerical Simulation on Cement
Hydration and Microstructure
Development in Repair-
Substrate Interface.
Front. Mater. 9:829743.
doi: 10.3389/fmats.2022.829743

One of the key parameters for the performance of concrete repairs is the quality of the interface between the repair material and concrete substrate, which is determined by cement hydration and microstructure development. The moisture exchange between the repair material and concrete substrate plays an important role in the cement hydration and porosity of cementitious repair materials. To better understand the influence of moisture exchange on the hydration of cementitious repair materials, this paper presents a numerical simulation of cement hydration and microstructure development of repair materials, considering moisture exchange. The simulation results reveal that the moisture exchange between the repair material and concrete substrate results in a water content change in two parts. Before the repair material setting, the water absorption of an unsaturated concrete substrate causes a reduction in the w/c ratio in the repair material, decreasing the hydration rate of the repair material. After the repair material setting, the water migrates from the concrete substrate to the repair material to provide additional water to accelerate the hydration of unhydrated cement in the repair material.

Keywords: numerical simulation, concrete repair, cement hydration, microstructure, moisture transport

1 INTRODUCTION

Concrete is the most popular structural material in the world today due to its excellent resistance to water, low cost and so on (Mehta and Monteiro, 2014; Xie et al., 2018). However, concrete structures are vulnerable to deterioration resulting from mechanical and environmental effects (Hobbs, 2001; Yin et al., 2020). Most of these concrete structures need repair after their deterioration. The bond between the concrete substrate and repair material usually shows a weak link in the repaired concrete structure (Momayez et al., 2005; Wang et al., 2021). Therefore, for good concrete repair work, sufficient bond strength between the concrete substrate and repair material is required to withstand the stresses in the interface (Emmons and Vaysburd, 1994; Gadri and Guettala, 2017; Garbacz et al., 2017; Abo Sabah et al., 2019; Gomaa et al., 2020). For cementitious repair materials, cement hydration and microstructure evolution play an important role in the bonding properties of the interface between the repair materials and concrete substrate (Courard, 2000; Shi et al., 2021). Courard and Degeimbre (2003), Courard (2005) and Lukovic and Ye (2016) suggested that cement hydration and microstructure development in concrete repairs is influenced by the moisture

exchange between the repair material and concrete substrate. Xue et al. (2021) suggested that water exchange typically occurs in the first 8 h after casting repair mortar. In the first 4 h of hydration, the free water transfers from the repair mortar to the old mortar. With the development of hydration (in 4–8 h), capillary pores are produced in the repair mortar, and the capillary pores absorb water from the old mortar. In addition, Zhou et al. (2016) studied the hydration process and microstructure development in concrete repairs. They proposed that after placing repair materials on the concrete substrate, moisture exchange between these two materials takes place. Moisture exchange changes the water content in the repair material and affects cement hydration and the microstructure at the interface. Therefore, it must affect the hydration process of the repair material.

This paper aims to develop a numerical model to understand better the influence of moisture exchange on the cement hydration process and microstructure development of cementitious repair materials. The HYMOSTRUC model is used to simulate the hydration process and to evaluate the pore structure characteristics in the repair materials. A model based on Darcy's law simulates the water exchange between the repair material and concrete structure in the developed numerical model. The proposed model is then used to simulate the hydration process and porosity development of repair mortar. The simulation results are compared with experimental results to verify the model and study the influence of water exchange on the microstructure development of repair materials during hydration.

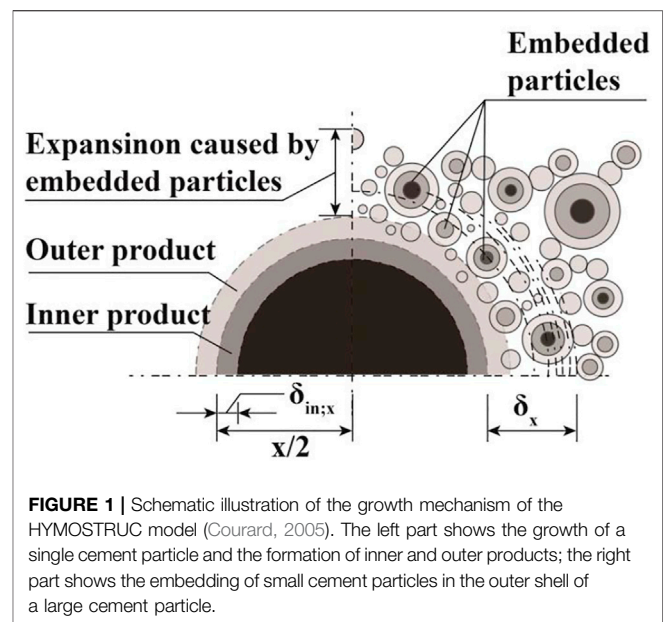
2 THEORETICAL BACKGROUND OF THE SIMULATION MODEL

Cement hydration in cementitious repair material consumes water, while moisture exchange causes water redistribution in the repair material. These two processes may lead to a change in water content. The change in water content can, therefore, be calculated by summing those caused by cement hydration and moisture exchange:

$$\frac{\partial \theta}{\partial t} = \frac{\partial \theta_{hy}}{\partial t} + \frac{\partial \theta_{mx}}{\partial t} \quad (1)$$

where $\partial \theta / \partial t$ is the change rate of the water content and $\partial \theta_{hy} / \partial t$; and $\partial \theta_{mx} / \partial t$ are the water change rates due to cement hydration and moisture exchange, respectively.

The hydration process of cement mainly depends on the water content (water-cement ratio) in the fresh mixture. When some water moves out from the fresh cement paste, the water left in the paste and the water-cement ratio decrease, decreasing the hydration rate (i.e., leading to a lower hydration degree). Conversely, if some water moves into the hydrating cement paste, the inflow water increases the water content (water-cement ratio), increasing the hydration rate. Therefore, the moisture exchange between the repair mortar and concrete substrate needs to be considered for hydration simulation.



Cement hydration influenced by moisture exchange is described in **Section 2.1**.

As cement hydration proceeds, water is gradually consumed, and hydration products grow into the pore structures. Cement hydration, therefore, has two effects on moisture transport. Firstly, the water consumption due to continuous hydration leads to a decrease in the water content in repair material. Secondly, since the hydration products occupy more space than the cement particles that have hydrated, the formation of hydration products decreases the porosity in the matrix and changes the size of the pores. The water content decrease and pore structure evolution affect capillary pressure, and unsaturated permeability is discussed in **Sections 2.2, 2.3**.

2.1 Cement Hydration

2.1.1 Cement Hydration and HYMOSTRUC Model

The HYMOSTRUC model was established by van Breugel (1991) to simulate the hydration process of cement and evaluate the microstructure in hardened cement-based materials. This model was further developed by Koenders (1997) and Ye (2003). Subsequent studies have confirmed that HYMOSTRUC has advantages in simulating cement hydration (Ye et al., 2003; Zhao et al., 2019).

In the HYMOSTRUC model, the cement particles are treated as a series of spheres with different diameters. For a given water-cement ratio, the number of cement particles with determined diameters is constant, and the particles are randomly distributed in the model space. As shown in **Figure 1**, the hydration of cement is simulated as the growth of the cement particles, consisting of a growing shell of hydration products and a shrinking unhydrated cement core. As the shell of hydration products grows outwardly, the smaller cement particles, located in the vicinity of the larger cement particles, become embedded in the outer shell of the larger cement particles. The stable structure has formed as the hydration shells are linked with each other.

The basic formula for determining the rate of hydration of an individual cement particle in the HYMOSTRUC model is described as (Van Breugel, 1991):

$$\frac{\partial \delta_{in,x}}{\partial t} = K_0 \times \Omega_1 \times \Omega_2 \times \Omega_3 \times F_1 \times \left(F_2 \times \left(\frac{\delta_{tr}}{\delta_x} \right)^{\beta_1} \right)^\lambda \quad (2)$$

where $\delta_{in,x}$ is the thickness of the inner hydration products in cement particle x ; K_0 is the basic rate factor constant depending on the cement composition and the degree of hydration; and Le et al. (2013) proposed a series of formulas to calculate the values of K_0 of C_3S , C_2S , C_3A and C_4AF . Since the volume fraction of the cement components of the cement used in this study is $C_3S:C_2S:C_3A:C_4AF = 0.65:0.18:0.11:0.06$, the average basic rate factor constant K_0 is taken to be $0.428 \mu\text{m/h}$; Ω_i ($i = 1, 2, 3$) are the reduction factors accounting for the different effects of water; F_i ($i = 1, 2$) are the temperature-related factors accounting for the effect of curing temperature; δ_x is the total thickness of the hydration products (i.e., the thickness of the hydration shell shown in **Figure 1**); δ_{tr} is the transition thickness equal δ_x time that the controlling mechanism changes from the “phase-boundary” stage ($\beta_1 = 0$ and $\delta_{tr}/\delta_x \leq 1$) to the “diffusion” stage ($\beta_1 = 1$ and $\delta_{tr}/\delta_x > 1$); β_1 is a constant; λ is the factor depending on the rate-controlling mechanism. The three water-related factors Ω_1 , Ω_2 and Ω_3 are water content-dependent parameters, which are affected by moisture exchange during cement hydration. The details about the relationship between these three factors and moisture exchanged during hydration are described in **Supplementary Appendix A1**.

The hydration degree of cement particle x can be calculated by dividing the incrementally decreased volume by the initial volume of the cement particle:

$$\alpha_x = 1 - \left(1 - \frac{\delta_{in,x}}{0.5d_{0,x}} \right)^3 \quad (3)$$

where α_x is the hydration degree of the cement particle x and $d_{0,x}$ is the initial diameter of the cement particle x .

Then, the overall degree of hydration α can be expressed by the average hydration degree of all cement particles, as expressed by

$$\alpha = \frac{1}{G(x-1)} \sum_{z=x_{\min}}^{x-1} \alpha_z \times W(z) \quad (4)$$

where $W(z)$ is the initial mass of cement particle z .

2.1.2 Water Consumed by Cement Hydration

For a given w/c ratio ω_0 , the volume ratio of water and cement can be expressed by $\omega_0 \rho_{ce}/\rho_w$, and the initial volume of cement particles in a unit volume of cement paste $V_{0,ce}$ can then be calculated as:

$$V_{0,ce} = \frac{1}{\omega_0 \frac{\rho_{ce}}{\rho_w} + 1} = \frac{\rho_w}{\rho_w + \rho_{ce} \omega_0} \quad (5)$$

where ρ_{ce} is the density of cement, which is 3.15 g/cm^3 ; ρ_w is the density of water, which is 1 g/cm^3 .

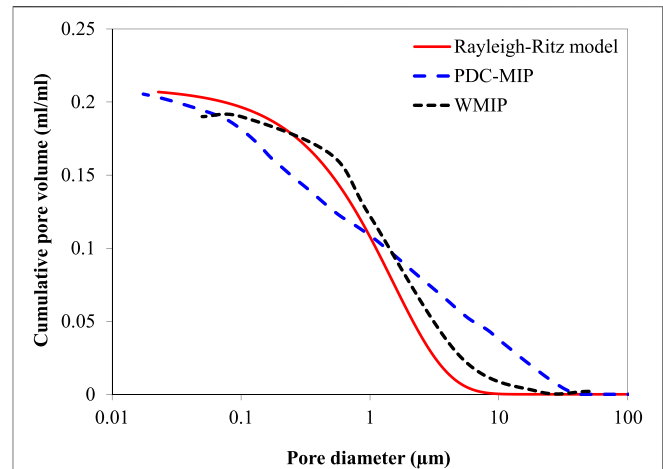


FIGURE 2 | Pore size distributions simulated by the Rayleigh-Ritz model and measured by PDC-MIP [after Zhou et al. (2010)] and WMIP (after Willis et al. (1998)).

According to Powers' model (Taylor, 1997), the amount of water consumed by cement hydration can be approximately calculated as:

$$\frac{\partial \theta_{hy}}{\partial t} = -\beta V_{0,ce} \frac{\partial \alpha}{\partial t} \quad (6)$$

where β is the volume of the water consumed by the hydration of per unit volume cement; α is the degree of hydration.

The fully hydrated cement contained two types of water, named non-evaporable water and gel water (Taylor, 1997). Non-evaporable water includes chemically bound and interlayer water in hydration products such as C-S-H and AFm (Taylor, 1997). The gel water is the water lost from the C-S-H upon passing from the saturated to the D-dry condition. It comprises part of the gel pore water plus an arbitrarily defined fraction of the interlayer water (Taylor, 1997). The hydration product contains, per g of cement, approximately 0.22 g of non-evaporable water and 0.21 g of gel water (Neville, 1995). Power and Brownyard (1946) proposed that the complete hydration of 1 g cement consumes approximately 0.4 g water. Therefore, considering the gel water in gel pores, β can be calculated as:

$$\beta = 0.4 \times \frac{\rho_{ce}}{\rho_w} \quad (7)$$

2.2 Pore Structure

According to Mindess and Young (1981), the porosity in hardened cement paste can be divided into capillary and gel porosity. Capillary porosity influences the strength and moisture transport of hardened cement paste, while gel porosity influences the shrinkage and creep properties. This study focuses on the influence of moisture transport from repair materials to concrete substrates on the hydration of repair materials. Therefore, this study considers only the capillary porosity, and the gel porosity is neglected for simplicity. The capillary porosity can be calculated

by subtracting the volumes of the unhydrated cement and the hydration products from the total volume of the hardened cement paste. Powers (Powers and Brownyard, 1946) proposed a model to calculate the porosity in hardened cement paste, given as:

$$\phi(\alpha) = 1 - \frac{\rho_w}{\rho_w + \rho_{ce}\omega_0} (1 + 1.1\alpha) \quad (8)$$

The Rayleigh-Ritz distribution (Chaube et al., 1999) is used to predict the size distribution of pores in cement-based materials. It reveals the relationship between the fraction of pores V and the pore radius r . **Figure 2** compares the pore size distribution simulated by the Rayleigh-Ritz model and measured by pressurization-depressurization cycling Mercury intrusion porosimetry (PDC-MIP) and Wood's metal intrusion porosimetry (WMIP). The calculation of the pore size distribution based on the Rayleigh-Ritz model can be expressed as:

$$V = 1 - \exp(-Br) \quad (9)$$

$$dV = Br \exp(-Br) dr \quad (10)$$

where B is the Rayleigh-Ritz pore size distribution constant, representing the peak pore size distribution on a logarithmic scale.

2.3 Moisture Transport

Moisture transport occurs in porous media in the forms of liquid and vapor. At low relative humidity, water exists mainly in the form of vapor. At high relative humidity, capillary action dominates moisture transport. Capillary action is much faster and in a larger quantity than vapor diffusion. Crausse et al. (1981) suggested that when the relative humidity in the pore system exceeds 4%, the contribution of the vapor phase to overall moisture transport is negligible. In cement paste and concrete, the relative humidity is normally higher than 75% (Neville, 1995). This research, therefore, focuses on capillary action rather than vapor diffusion.

Darcy's law is used to describe the water transport in cement-based materials, expressed as (Dullien, 1992):

$$q = -K_\theta \nabla p_t \quad (11)$$

where q is the volumetric flux of water; K_θ is the water permeability, depending on the water content θ and saturation of the pores in the matrix; p_t is the pressure that causes the water transport, which is the sum of the capillary pressure p and the hydraulic pressure p_h .

The rate of the water content changes due to moisture transport $\partial\theta_{mx}/\partial t$ can be calculated as:

$$\frac{\partial\theta_{mx}}{\partial t} = \nabla \cdot q \quad (12)$$

The definitions of the water permeability K_θ and the capillary pressure p are described in detail in **Supplementary Appendix A3**.

2.4 General Equation

Substituting Eqs 6–12 into Eq. 1, the equation for describing the water content change in repair materials can be expressed as:

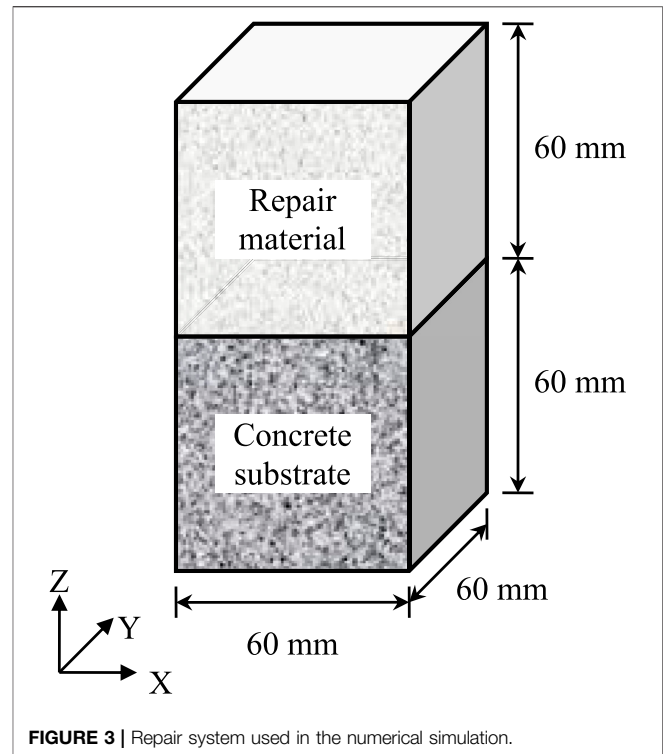


FIGURE 3 | Repair system used in the numerical simulation.

$$\frac{\partial\theta}{\partial t} = -\beta V_{0,ce} \frac{\partial\alpha}{\partial t} - \nabla \cdot (K_\theta \nabla p_t) \quad (13)$$

3 NUMERICAL SIMULATION PROCESS

The model for simulating cement hydration and moisture transport in repair materials is programmed using MATLAB. The numerical simulation is described in detail in this section.

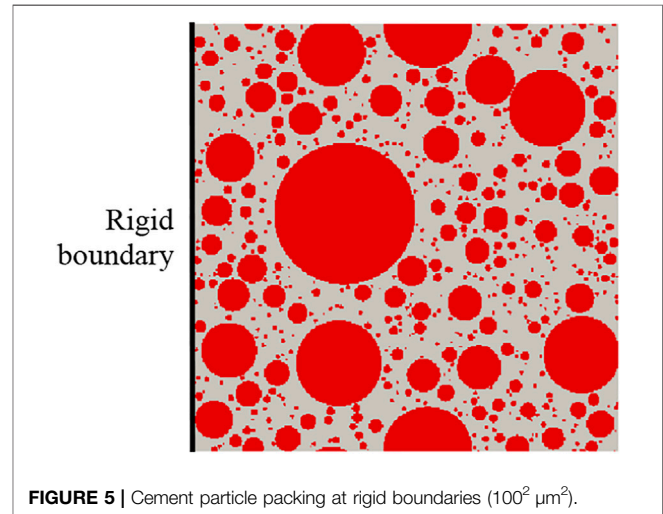
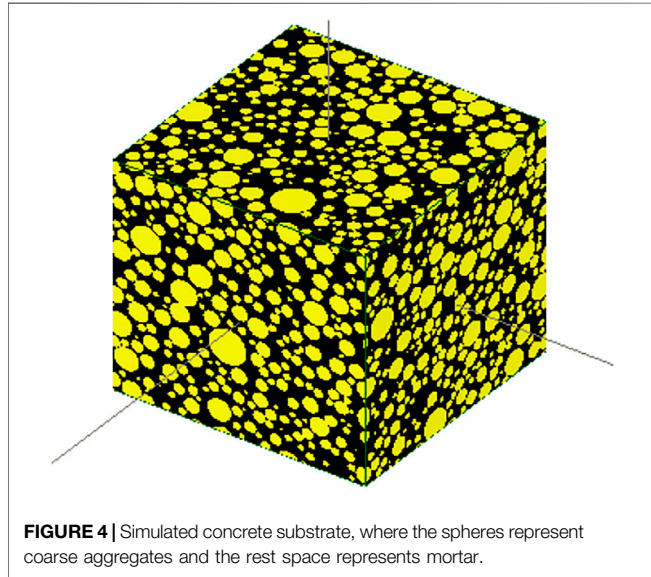
3.1 Repair System

Previous work has been done to experimentally study the hydration process and microstructure evaluation in concrete repairs with cementitious repair materials (Courard and Degeimbre, 2003). For comparison, this numerical study investigates the same repair cement paste (as shown in **Figure 3**) with the same material composition. The thicknesses of the repair material and the concrete substrate are both 60 mm. The repair material is ordinary Portland cement paste with a cement-to-water ratio of 0.4. The chemical composition of Portland cement is listed in **Table 1**. Assume that the concrete substrate consists of two phases, coarse aggregates and mortar. The coarse aggregates are modeled as spheres with given size distribution and randomly distributed in the cube specimen shown in **Figure 4**. The detailed proportions and coarse aggregates in the concrete substrate are listed in **Tables 2, 3**.

The coarse aggregates occupy 44.4% of the volume of concrete, while the mortar occupies 55.6% of the volume of concrete. The

TABLE 1 | Chemical composition of Portland cement.

Composition	CaO	SiO ₂	Al ₂ O ₃	Fe ₂ O ₃	MgO	K ₂ O	Na ₂ O	SO ₃
Weight (%)	64.1	20.1	4.8	3.2	1.2	0.5	0.3	2.7

**TABLE 2** | Mix composition of the substrate concrete.

Coarse aggregate (kg/m ³)	Fine aggregate (kg/m ³)	Cement (kg/m ³)	Water (kg/m ³)	W/c ratio (-)
1,177.2	633.9	375.0	187.5	0.5

TABLE 3 | Proportion of the coarse aggregates in the concrete substrate.

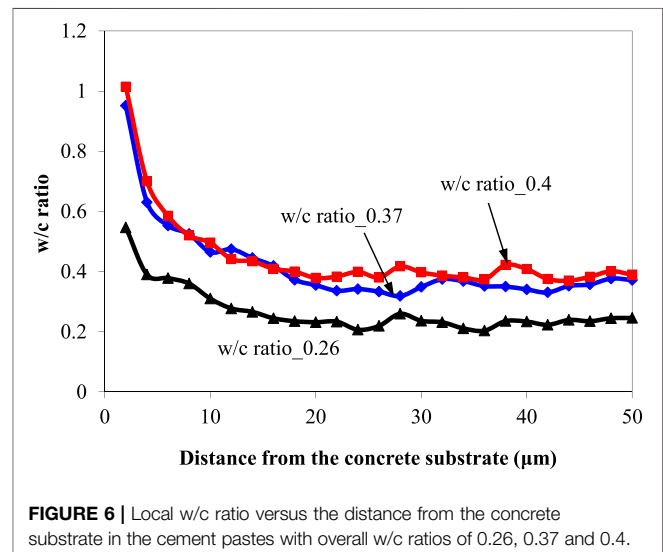
Aggregate size (mm)	Weight content (kg/m ³)
2–4	271.6
4–8	362.1
8–16	543.2

coarse aggregates have very low porosity, and their porosity is neglected. The porosity of the mortar is 14.7%. The degree of saturation of the concrete substrate is 14.4%.

3.2 Repair-Substrate Interface

Due to the “wall effect”, the cement particles have a loose packing at the surface of the concrete substrate. The w/c ratio is, therefore, locally increased. In the simulation, the cement particles are considered a group of spheres. The distribution of these spheres on a rigid boundary is used to simulate the packing of cement particles at the surface of the concrete substrate, as shown in **Figure 5**. The w/c volume ratio from the rigid boundary can be calculated by dividing the number of voxels of cement by that of water. The w/c volume ratio is then converted to the w/c ratio by dividing the w/c density ratio.

Figure 6 shows the local w/c ratio over the distance from a rigid boundary obtained by the numerical model. Close to the



rigid boundary, the local w/c ratio is very high. As the distance from the concrete substrate increases, the local w/c ratio decreases. The results indicate that the thickness of the interfacial zone is approximately 20 μm when the w/c ratio of

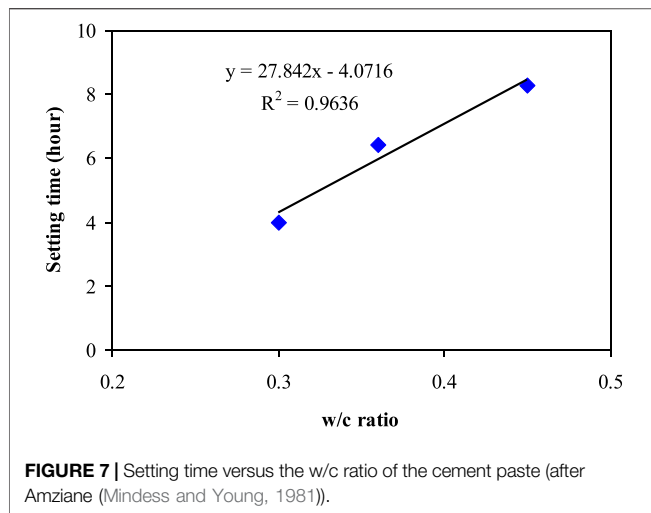


FIGURE 7 | Setting time versus the w/c ratio of the cement paste (after Amziane (Mindess and Young, 1981)).

repair cement paste ranges from 0.26 to 0.4. This value agrees well with the experimental results of BSE image analysis (Zhou et al., 2016). In the following discussion, the 20 μm -thick interfacial zone is called the “interface”, distinguished from the “bulk repair material”.

3.3 Water Absorption by the Concrete Substrate and Resultant w/c Ratio

After the repair material is placed on the concrete substrate, the repair material needs several hours to harden. A previous study (Zhou et al., 2016) revealed that an unsaturated concrete substrate absorbs water from a fresh repair material. As mentioned above, the water absorption is driven by the capillary pressure and the hydraulic pressure generated by the gravity force of the fresh repair material. Before the repair material setting, the solid phases, i.e., the cement particles and a small amount of the hydration products, are suspended in water and isolated from each other. Due to the gravitation of cement paste, the free water is pushed out from the repair cement paste to migrate into the concrete substrate. Consequently, the hydraulic pressure can be calculated as follows:

$$p_h = \rho_c g h_r = \frac{(\omega_0 + 1)\rho_{ce}^2}{\rho_w + \omega_0\rho_{ce}} g h_r \quad (14)$$

where h_r is the thickness of the repair material; and g is the acceleration of gravity.

The loss of water in the repair material reduces the w/c ratio, called the resultant w/c ratio. The resultant w/c ratio $\omega_{res}(x, y, z)$ can be calculated as follows:

$$\omega_{res}(x, y, z) = \omega_0 \left(1 - \frac{V_{ab}(x, y, z)}{V_{0,w}} \right) \quad (15)$$

where $V_{ab}(x, y, z)$ is the volumetric water loss in the repair material due to the water absorption of the concrete substrate.

The setting time of the repair material depends on the w/c ratio. As shown in **Figure 7**, when the w/c ratio is between 0.3 and

0.5, the setting time is approximately proportional to the w/c ratio of the repair material (Amziane, 2006). The setting time t_{set} can, therefore, be determined as:

$$t_{set} = 27.8 \times \omega_{res} - 4.1 \quad (16)$$

3.4 Cement Hydration and Moisture Transport After the Setting of the Repair Material

After the repair material setting, a solid framework has formed in the repair material. The loss of water cannot reduce the w/c ratio of the repair material in this stage. The driving force for moisture exchange becomes the capillary gradient in these two materials, and the moisture exchange process can be calculated using **Eq. 11**. In the simulation, further cement hydration and the change in the porosity in the concrete substrate are not considered. The degree of hydration and the porosity of the repair cement paste cured at 20°C for 28 days are calculated using (**Eqs 4–8**), respectively.

4 SIMULATION RESULTS

4.1 Water Absorption by the Concrete Substrate

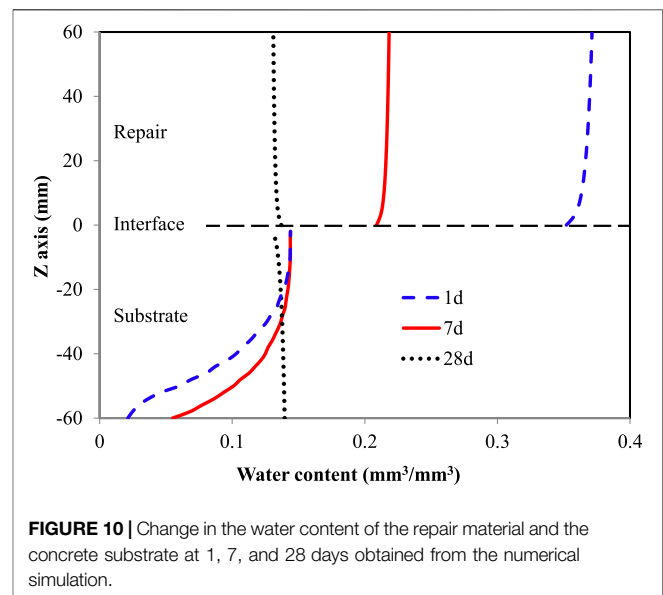
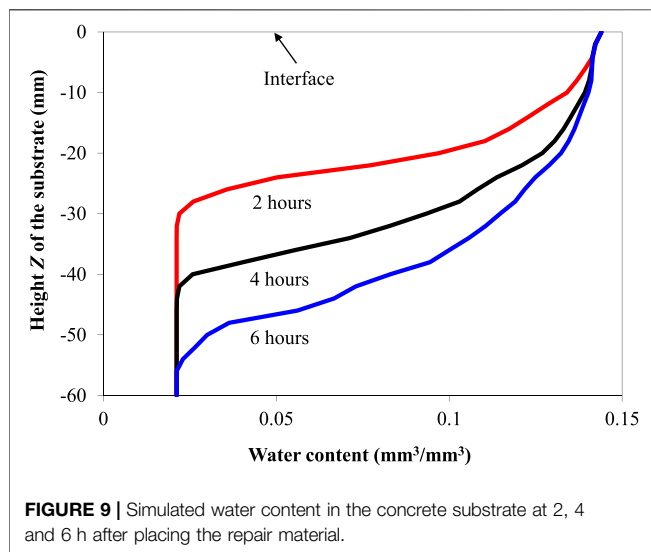
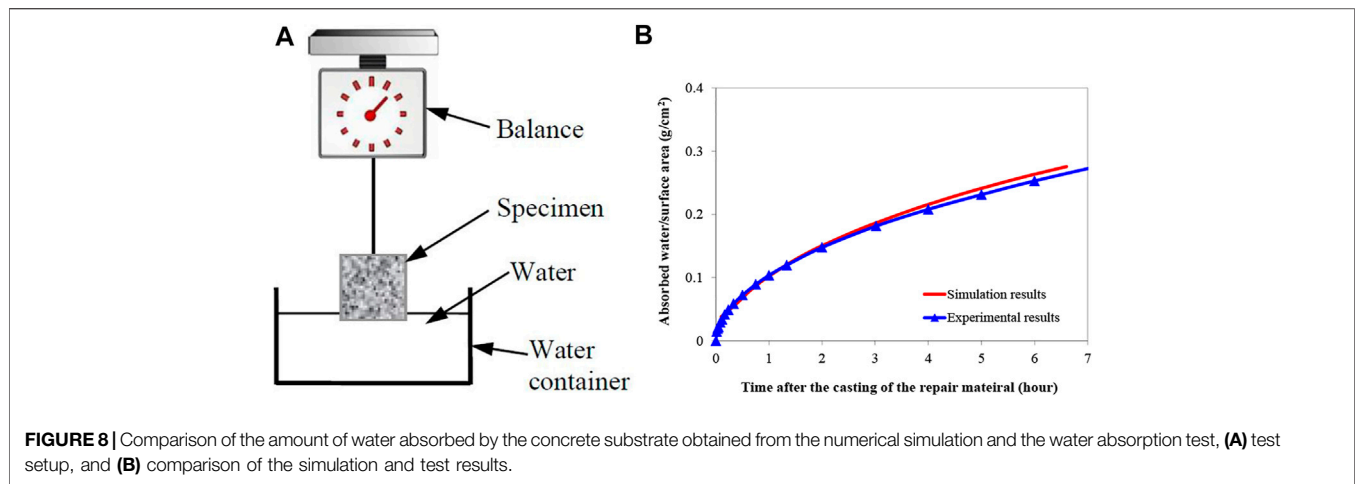
First, the unsaturated concrete substrate's water absorption behavior is studied using numerical simulations and experiments. The experimental method follows the European standard EN 480-5 (2005). The concrete specimen prepared based on the mix proportion listed in **Table 2** is a cylinder with a diameter of 60 mm and a thickness of 60 mm. The porosity of the specimen is tested by MIP and is 0.144. The specimens are coated with a thin layer of epoxy to prevent water penetration from the side surfaces of the cylinder specimen. After the epoxy hardened, the specimens were suspended on balance and then immersed in water, as shown in **Figure 8A**. The immersed level is 5 mm. After the specimen comes in contact with water, water is absorbed into the specimen, and the weight of the specimens increases continuously. The weight change of the specimen was measured for 10 h. Three parallel measurements are done.

The numerical model is used to simulate the absorbed water behavior of the concrete substrate based on the same conditions as the test. The comparison of simulation and test results is drawn in **Figure 8B**. The good agreement between the two curves indicates that the simulation gives a good prediction of the water absorption process of the concrete substrate.

Figure 9 shows the simulated change in the water content profile in the concrete substrate due to water absorption. The water absorption results in an increase in the water content of the concrete substrate. Water in the concrete substrate gradually moves from the surface exposed to the repair material to the bottom.

4.2 Resultant w/c Ratio in the Bulk Repair Material and at the Interface

The water absorption of the concrete substrate causes a reduction in the w/c ratio in the bulk repair material and at the interface.



The concrete substrate absorbs 0.28 g/cm^2 , and the resultant w/c ratio in the bulk repair is 0.37. The simulated resultant w/c ratio agrees well with the value obtained from BSE image analysis, which is 0.36 (Courard and Degeimbre, 2003). Due to the “wall effect”, the interface has a relatively loose particle packing and a higher resultant w/c ratio of 0.53.

4.3 Moisture Exchange Between the Repair Material and the Concrete Substrate

Figure 10 shows the water content profile in the repair material and the concrete substrate at curing ages of 1, 7, 21 and 28 days obtained from the simulation. As time elapses, the total water content in the repair material and the concrete substrate decreases. The reason is that cement hydration consumes a part of the water in the repair material.

At 1 and 7 days, in the concrete substrate, the closer to the interface, the higher the water content is. In the repair material, the closer to the interface, the lower the water content is. These

results imply that some water moves from the repair material to the concrete substrate driven by the capillary gradient.

At 21 days, the concrete substrate became fully saturated, while the water content of the repair material decreased. The water content distribution in the repair material becomes more uniform, and the water content close to the interface is slightly lower than that at the top. These results imply that the moisture transport process becomes slower, and the repair-substrate system approaches the balanced condition in capillary potential. At 28 days, the water content in the concrete substrate decreases when approaching the repair-substrate interface. In the repair material, the water content close to the interface becomes higher than that at the top. The reason is that as cement hydration proceeds, the water content decreases and the pore sizes decrease. The capillary pressure, therefore, increases. When the capillary pressure in the repair material exceeds that in the concrete substrate, water is forced to flow from the concrete substrate to the repair material.

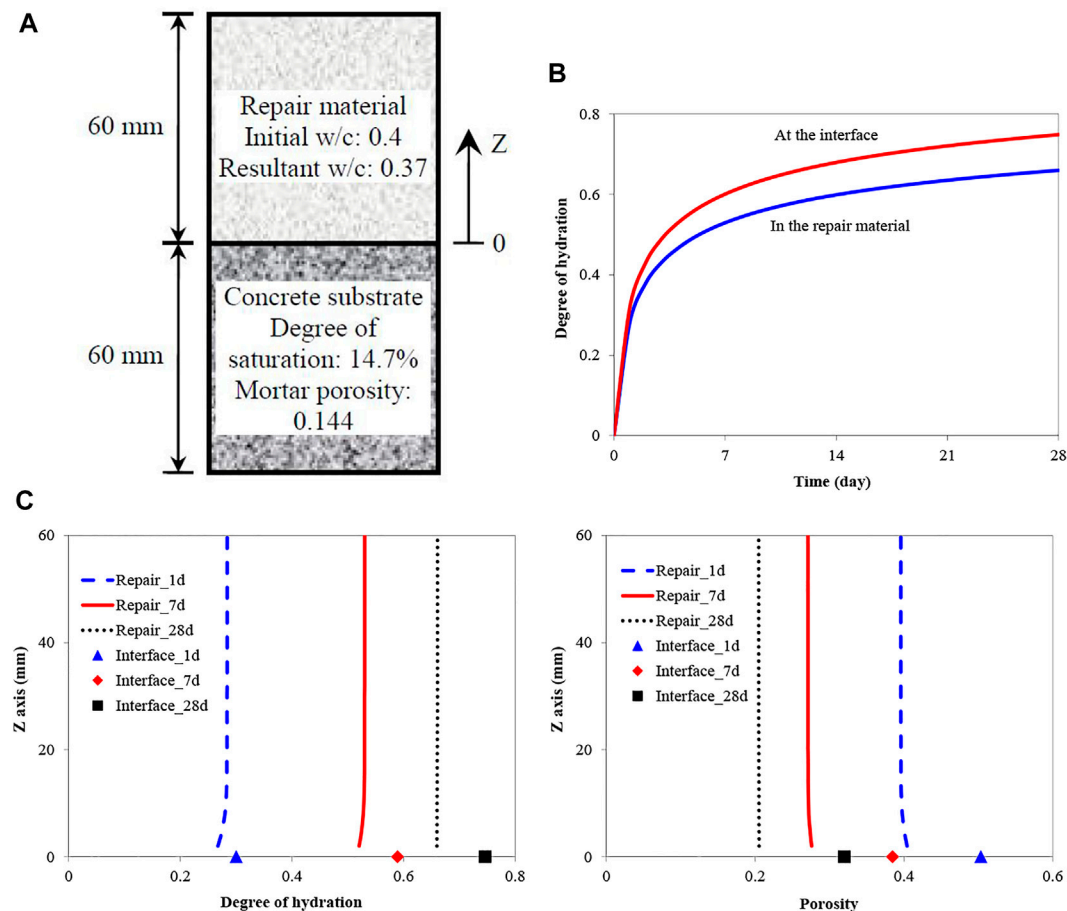


FIGURE 11 | Degree of hydration in the bulk repair material and at the interface. **(A)** In the first 28 days obtained from the simulation, **(B)** the degree of hydration at 1, 7 and 28 days, **(C)** porosity at 1, 7 and 28 days.

4.4 Simulated Degree of Hydration and Porosity of the Bulk Repair Material and the Interface

The hydration degree and porosity of the bulk repair material and the interface are evaluated by simulation and experiment. For experimental research, the initial w/c of repair cement paste is 0.4 (the components are listed in **Table 1**), and the concrete substrate is prepared using the mix proportion listed in **Table 2**. The test specimen dimensions are shown in **Figure 11A**. After curing, small pieces were taken from the specimen to test the hydration degree and porosity. The hydration degree of bulk repair materials with different curing ages is determined by measuring their non-evaporable water content. The porosities of the repair material and the concrete substrates are measured using MIP. The detailed test procedures follow those proposed in Zhou (2011).

The numerical model is used to simulate the hydration process of the repair cement mortar based on the same conditions as the test. The comparison of the simulation and experimental results are listed in **Table 4**. In general, the simulation results agree well with the experimental results. The good agreement between the

simulation results and experimental results indicates that the numerical model can accurately simulate the cement hydration process and microstructure development in the repair system.

Now, the numerical model is used to simulate the hydration process of the repair cement paste. The condition and dimension of the repair system used in the simulation are shown in **Figure 11A**. **Figure 11B** shows the evolution of the degree of hydration in the bulk repair material (at half height) and at the interface in the first 28 days obtained from the simulation. Due to the “wall effect”, the interface has a higher w/c ratio than the bulk repair material. Therefore, the cement paste shows a higher degree of hydration at the interface.

Figure 11C shows the degree of hydration of the bulk repair material and the interface at 1, 7 and 28 days obtained from the simulation. Since the interface has a higher resultant w/c ratio than the bulk repair material, its hydration rate is higher than that of the bulk repair material. Therefore, the hydration degree of the interface is higher than that of bulk repair material with the same curing age. The results indicate that cement hydration proceeds slower in the bulk repair material closer to the interface, where the bulk repair material loses more water at the early stage. Later, the hydration process in the bulk repair material close to the interface

TABLE 4 | Comparison between the simulation results and experimental results (Zhou et al., 2016) of the degree of hydration and porosity in the bulk repair material and at the interface.

Location	Degree of hydration			Porosity	
	Simulation	Non-evaporable water test	BSE image analysis	Simulation	MIP
Repair	0.659	0.671	0.654	0.200	0.206
Interface	0.747	—	0.764	0.318	—

becomes relatively fast since some water flows back to the bulk repair material from the substrate concrete to provide additional water for cement hydration.

Figure 11D shows the simulated porosity of the bulk repair material and the interface at 1, 7 and 28 curing days. Since the interface has a higher resultant w/c ratio than the bulk repair material, the porosity is higher than that in the bulk repair material. In the first 28 days, the porosity of the interface is approximately 1.5 times higher than that of the bulk repair material, which may reduce the bonding strength between the repair material and concrete substrate.

5 CONCLUSION

This paper presents a numerical study on the cement hydration and microstructure development of repair materials influenced by moisture exchange. Based on the simulation results, the following conclusions can be drawn:

- The moisture exchange between the repair material and concrete substrate results in a change in the water content in two parts, which affects the cement hydration process and microstructure development in the repair system.
- Before the repair material setting, the water absorption of an unsaturated concrete substrate causes a reduction in the w/c ratio in the repair material, called the resultant w/c ratio. The resultant w/c ratio in the repair material greatly influences the cement hydration and porosity of the repair material.
- After the repair material setting, the cement hydration works as a “motor”. It generates the driving force for moisture transport in the two materials, while water acts

as “fuel”, which consumes the “motor” and influences the efficiency of the “motor”.

DATA AVAILABILITY STATEMENT

The original contributions presented in the study are included in the article/**Supplementary Material**, further inquiries can be directed to the corresponding authors.

AUTHOR CONTRIBUTIONS

ML: Numerical simulation and experimental verification JZ: Establish numerical model HL: Model modification and validation analysis YW: Data curation, Writing-original draft.

ACKNOWLEDGMENTS

The authors gratefully acknowledge the financial support of the National Natural Science Foundation of China (Project No. 5217083356), the Natural Science Foundation of Beijing Municipality (Project No. KZ202010005013) and the Scientific Research Program of Tianjin Municipal Education Commission (Project No. 20140913).

SUPPLEMENTARY MATERIAL

The Supplementary Material for this article can be found online at: <https://www.frontiersin.org/articles/10.3389/fmats.2022.829743/full#supplementary-material>

REFERENCES

- Abo Sabah, S. H., Hassan, M. H., Muhamad Bunnori, N., and Megat Johari, M. A. (2019). Bond Strength of the Interface between normal concrete Substrate and GUSMRC Repair Material Overlay. *Construction Building Mater.* 216, 261–271. doi:10.1016/j.conbuildmat.2019.04.270
- Amziane, S. (2006). Setting Time Determination of Cementitious Materials Based on Measurements of the Hydraulic Pressure Variations. *Cement Concrete Res.* 36, 295–304. doi:10.1016/j.cemconres.2005.06.013
- Chaube, R., Kishi, T., and Maekawa, K. (1999). *Modelling of concrete Performance: Hydration, Microstructure and Mass Transport*. first ed. London: CRC Press.
- Courard, L. (2005). Adhesion of Repair Systems to concrete: Influence of Interfacial Topography and Transport Phenomena. *Mag. Concrete Res.* 57, 273–282. doi:10.1680/mac.2005.57.5.273
- Courard, L., and Degeimbre, R. (2003). A Capillary Action Test for the Investigation of Adhesion in Repair Technology. *Can. J. Civ. Eng.* 30, 1101–1110. doi:10.1139/l03-061
- Courard, L. (2000). Parametric Study for the Creation of the Interface between concrete and Repair Products. *Mat. Struct.* 33, 65–72. doi:10.1007/bf02481698
- Crausse, P., Bacon, G., and Bories, S. (1981). Etude fondamentale des transferts couples chaleur-masse en milieu poreux. *Int. J. Heat Mass Transfer* 24, 991–1004. doi:10.1016/0017-9310(81)90130-7
- Dullien, F. A. (1992). *Porous Media: Fluid Transport and Pore Structure*. Second ed. Salt Lake City: Academic Press.
- Emmons, P. H., and Vaysburd, A. M. (1994). Factors Affecting the Durability of concrete Repair: the Contractor's Viewpoint. *Construction Building Mater.* 8, 5–16. doi:10.1016/0950-0618(94)90003-5
- EN 480-5 (2005). *Admixtures for Concrete, Mortar and Grout - Test Methods - Part 5*. London: Determination of Capillary Absorption (in British).

- Feldman, R. (1986). *Pore Structure, Permeability and Diffusivity as Related to Durability*. Rio de Janeiro: 8th International Congress on Chemistry of Cement, 336–356. (in Brazil).
- Gadri, K., and Guettala, A. (2017). Evaluation of Bond Strength between Sand concrete as New Repair Material and Ordinary concrete Substrate (The Surface Roughness Effect). *Construction Building Mater.* 157, 1133–1144. doi:10.1016/j.conbuildmat.2017.09.183
- Garbacz, A., Piotrowski, T., Courard, L., and Kwaśniewski, L. (2017). On the Evaluation of Interface Quality in concrete Repair System by Means of Impact-echo Signal Analysis. *Construction Building Mater.* 134, 311–323. doi:10.1016/j.conbuildmat.2016.12.064
- Gomaa, E., Gheni, A., and ElGawady, M. A. (2020). Repair of Ordinary Portland Cement concrete Using Ambient-Cured Alkali-Activated concrete: Interfacial Behavior. *Cement Concrete Res.* 129, 105968. doi:10.1016/j.cemconres.2019.105968
- Hobbs, D. W. (2001). Concrete Deterioration: Causes, Diagnosis, and Minimising Risk. *Int. Mater. Rev.* 46, 117–144. doi:10.1179/0950666001101528420
- Koenders, E. (1997). *Simulation of Volume Changes in Hardening Cement-Based Materials*. Delft: Delft University of Technology.
- Le, N. L. B., Stroeve, M., Sluys, L. J., and Stroeve, P. (2013). A Novel Numerical Multi-Component Model for Simulating Hydration of Cement. *Comput. Mater. Sci.* 78, 12–21. doi:10.1016/j.commatsci.2013.05.021
- Lukovic, M., and Ye, G. (2016). Effect of Moisture Exchange on Interface Formation in the Repair System Studied by X-ray Absorption. *Materials* 9, 2. doi:10.3390/ma9010002
- Mehta, P. K., and Monteiro, P. J. (2014). *Concrete: Microstructure, Properties, and Materials*. fourth ed. New York: McGraw-Hill Education.
- Mindess, S., and Young, J. F. (1981). *Concrete*. First ed. Englewood Cliffs: Prentice-Hall.
- Momayez, A., Ehsani, M. R., Ramezaniapour, A. A., and Rajaie, H. (2005). Comparison of Methods for Evaluating Bond Strength between concrete Substrate and Repair Materials. *Cement Concrete Res.* 35, 748–757. doi:10.1016/j.cemconres.2004.05.027
- Neville, A. M. (1995). *Properties of Concrete*, 4. London: Longman.
- Powers, T. C., and Brownyard, T. L. (1946). Studies of the Physical Properties of Hardened Portland Cement Paste. *J. Am. Concrete Inst.* 43, 101–132.
- Shi, C., Wang, P., Ma, C., Zou, X., and Yang, L. (2021). Effects of SAE and SBR on Properties of Rapid Hardening Repair Mortar. *J. Building Eng.* 35, 102000. doi:10.1016/j.job.2020.102000
- Taylor, H. F. W. (1997). *Cement Chemistry*, 2. London: Thomas Telford.
- Van Breugel, K. (1991). *Simulation of Hydration and Formation of Structure in Hardening Cement-Based Materials*. Delft: Delft University of Technology.
- Wang, Y. S., Peng, K. D., Alrefaei, Y., and Dai, J. G. (2021). The Bond between Geopolymer Repair Mortars and OPC concrete Substrate: Strength and Microscopic Interactions. *Cement and Concrete Composites* 119 (2021), 103991. doi:10.1016/j.cemconcomp.2021.103991
- Willis, K. L., Abell, A. B., and Lange, D. A. (1998). Image-based Characterization of Cement Pore Structure Using Wood's Metal Intrusion. *Cement Concrete Res.* 28, 1695–1705. doi:10.1016/S0008-8846(98)00159-8
- Xie, T., Gholampour, A., and Ozbakkaloglu, T. (2018). Toward the Development of Sustainable Concretes with Recycled concrete Aggregates: Comprehensive Review of Studies on Mechanical Properties. *J. Mater. Civ. Eng.* 309, 04018211. doi:10.1061/(ASCE)MT.1943-5533.0002304
- Xue, S., Zhang, P., Lehmann, E. H., Hovind, J., and Wittmann, F. H. (2021). Neutron Radiography of Water Exchange across the Interface between Old and Fresh Mortar. *Measurement* 183, 109882. doi:10.1016/j.measurement.2021.109882
- Ye, G. (2003). *Experimental Study and Numerical Simulation of the Development of the Microstructure and Permeability of Cementitious Materials*. Delft: Delft University of Technology.
- Ye, G., van Breugel, K., and Fraaij, A. L. A. (2003). Three-dimensional Microstructure Analysis of Numerically Simulated Cementitious Materials. *Cement Concrete Res.* 33, 215–222. doi:10.1016/S0008-8846(02)00889-X
- Yin, G.-J., Zuo, X.-B., Li, X.-N., and Zou, Y.-X. (2020). An Integrated Macro-Microscopic Model for concrete Deterioration under External Sulfate Attack. *Eng. Fracture Mech.* 240, 107345. doi:10.1016/j.engfracmech.2020.107345
- Zhao, H., Liu, J., Yin, X., Wang, Y., and Huang, D. (2019). A Multiscale Prediction Model and Simulation for Autogenous Shrinkage Deformation of Early-Age Cementitious Materials. *Construction Building Mater.* 215, 482–493. doi:10.1016/j.conbuildmat.2019.04.225
- Zhou, J. (2011). *Performance of Engineered Cementitious Composites for Concrete Repairs*. Delft: Delft University of Technology.
- Zhou, J., Ye, G., and van Breugel, K. (2016). Cement Hydration and Microstructure in concrete Repairs with Cementitious Repair Materials. *Construction Building Mater.* 112, 765–772. doi:10.1016/j.conbuildmat.2016.02.203
- Zhou, J., Ye, G., and van Breugel, K. (2010). Characterization of Pore Structure in Cement-Based Materials Using Pressurization-Depressurization Cycling Mercury Intrusion Porosimetry (PDC-MIP). *Cement Concrete Res.* 40, 1120–1128. doi:10.1016/j.cemconres.2010.02.011

Conflict of Interest: The authors declare that the research was conducted in the absence of any commercial or financial relationships that could be construed as a potential conflict of interest.

Publisher's Note: All claims expressed in this article are solely those of the authors and do not necessarily represent those of their affiliated organizations, or those of the publisher, the editors and the reviewers. Any product that may be evaluated in this article, or claim that may be made by its manufacturer, is not guaranteed or endorsed by the publisher.

Copyright © 2022 Lan, Zhou, Li and Wang. This is an open-access article distributed under the terms of the Creative Commons Attribution License (CC BY). The use, distribution or reproduction in other forums is permitted, provided the original author(s) and the copyright owner(s) are credited and that the original publication in this journal is cited, in accordance with accepted academic practice. No use, distribution or reproduction is permitted which does not comply with these terms.



Experimental Study on Bearing Capacity of Corroded Reinforced Concrete Arch Considering Material Degradation

Jingzhou Xin^{1,2}, Jieyun Wang^{1*}, Zengwu Liu², Xing You² and Jianting Zhou²

¹Guangxi Communications Investment Group Corporation Ltd., Nanning, China, ²State Key Laboratory of Mountain Bridge and Tunnel Engineering, Chongqing Jiaotong University, Chongqing, China

OPEN ACCESS

Edited by:

Zhigang Zhang,
Chongqing University, China

Reviewed by:

Yu Wang,
Tsinghua University, China
Krzysztof Woloszyk,
Gdansk University of Technology,
Poland

*Correspondence:

Jieyun Wang
wangjyx@126.com

Specialty section:

This article was submitted to
Structural Materials,
a section of the journal
Frontiers in Materials

Received: 01 January 2022

Accepted: 17 January 2022

Published: 04 February 2022

Citation:

Xin J, Wang J, Liu Z, You X and Zhou J
(2022) Experimental Study on Bearing
Capacity of Corroded Reinforced
Concrete Arch Considering
Material Degradation.
Front. Mater. 9:847193.
doi: 10.3389/fmats.2022.847193

To study the bearing capacity of a corroded reinforced concrete (RC) arch and analyze the deterioration mechanism of an in-service RC arch bridge, a deterioration simulation under the coupling effect of the environment and load was performed by employing non-immersion energization, and considering the dead load on the arch, single point loading tests of the arch models were carried out; the crack development, structural deformation, and ultimate bearing capacity of a corroded RC arch under service stress were studied; the failure mode of the corroded arch was explored; and a bearing capacity prediction model considering dual deterioration effects of reinforcement corrosion deterioration and arch axis deterioration was established. Results indicated that the spacing of cracks caused by a load on the non-corroded arch was more uniform, and the number and distribution range of load-induced cracks in the corroded arch was smaller, while the maximum crack width was larger. Corrosion significantly reduced the strength of the arch rib; for the deteriorated arch with a corrosion rate of 7.62%, the cracking load and the bearing capacity decreased by 28.57 and 9.84%, respectively. Corrosion weakened structural stiffness, while it does not convert the failure mode of the arch. Only considering section resistance degradation may underestimate the damaging effects of corrosion on the arch structure.

Keywords: reinforced concrete arch, corrosion, static loading test, bearing capacity, mechanism of performance degradation

INTRODUCTION

Reinforced concrete (RC) arch bridges are widely used in China, especially in mountainous areas, because of their high structural stiffness, beautiful appearance, and economy advantage (Deng et al., 2019; Li et al., 2021). However, the performance degradation of RC structures has become acute as time goes on due to the coupling effect of the external service environment and internal materials degradation (Fu et al., 2017; Castorena-González et al., 2020; Fang, 2020). Accurate assessment of the carrying capacity of RC arch bridges in service is of great scientific significance and has a high engineering application value in order to carry out scientific management, as well as reduce the maintenance costs.

According to engineering experience, arch bridges are generally considered to have better durability than girder bridges (Shao et al., 2021). The reason is that on the one hand, service

areas of an RC arch bridge are mainly located in the southwest region of China, accounting for about 60% of the total, and the atmospheric environment in the southwest region of China is less corrosive to the service structures than the chloride environment in the coastal area. On the other hand, all sections of the main arch ring are subjected to compressive stress, and compared with the beam structures, the cracks are less, which reduce the migration rate of chloride and other erosion factors, and the durability of the structure is less prominent than that of the beam structures (Fu et al., 2020; Qiu et al., 2021). Therefore, the research on the performance of corroded concrete members mainly focuses on flexural members (Liu et al., 2016; Dong et al., 2017; Dai et al., 2019), while the research on RC arch bridges mainly focuses on intact structures; for example, Huang and Chen (2009) conducted an experiment on a RC box arch under two loads asymmetrically in-plane and analyzed the non-linear behavior and its influence on the ultimate load-carrying capacity. Du and Chen (2013) performed model tests on two reactive powder concrete arches subjected to concentrated loads. The load–displacement curves, cracks, strains, failure modes, and ultimate load capacities of the arches were analyzed and compared with the results of conventional RC model arches. Zhang et al. (2017) carried out a 1:7.5 scale model test on the world's largest span stiff skeleton concrete arch bridge to investigate the structural behavior during the construction process.

However, it is an inevitable developmental law of any physical system that the structural performance will be degraded with an extension in service years. The existing literature shows that with the increase in service life, the bearing capacity degradation of arch structures caused by materials degradation is non-negligible (Zhang et al., 2007). Several studies have been carried out around the performance degradation of RC arch bridges; for instance, Petryna et al. (2002) proposed the time-variant reliability assessment method of deteriorating RC structures under fatigue conditions, and reliability estimates were obtained within the response surface method using the important/adaptive sampling techniques and the time-integrated approach. Based on the field measurement results and numerical simulation, Zanardo et al. (2004) studied the static and seismic performance of the existing short span RC arch bridges, before and after strengthening interventions. Zhang et al. (2007) evaluated the residual bearing capacity of two arch ribs removed from a 28-year-old bridge based on full-scale tests. Tang et al. (2005) presented a tensorial damage theory and an isotropic application to the arch ribs of a real bridge. The damage theory-additional load-finite element method was developed to numerically simulate the failure process of RC structures. Based on the similarity theory of model design, Fan et al. (2007) examined the effects of the damage extent and location on the static and dynamic responses of the scaled damaged arch bridge model fabricated by organic glasses; the prototype of the scale was a 43-year-old RC arch bridge. Ma et al. (2016) investigated the effect of corrosion-induced cracking damage on the static behavior of RC arch ribs based on an experimental method; the reduction rate in the ultimate bearing capacity of arch ribs caused by rust expansion could

reach 60% by their results. Overall, there are relatively few experimental studies on RC arch bridges. In these few experimental studies, researchers poured more attention on the damage evolution mechanism of the intact arch structure during loading, and the failure process and behavior evolution of the statically indeterminate system are the main concerns. Research works on the adverse effects of various deterioration factors on the bearing capacity of an RC arch brought by a long-term service are relatively scarce.

The present study is an extension of the research on the performance degradation mechanism of RC arch bridges but with the following substantial differences. First, the coupling effects of load and corrosion on the arch were considered in this experiment. Second, a bearing capacity prediction model of the RC arch considering the two-dimensional deterioration effect of transverse and longitudinal directions was proposed. Note that corrosion of practical bridges often occurs under the stress state. Consequently, the present study has superior practical significance.

The rest of this article is organized as follows. In the *Experimental Program* section, experiments on arch models are elaborated, including the specimen design, the accelerated corrosion test program, the instrumentation, and the loading manner. In the *Result and Discussion* section, critical results are presented and then discussed. In the *Prediction Model of Bearing Capacity for Corroded RC Arch* section, a new prediction method of bearing capacity is put forward. On the basis of considering the influence of unfavorable factors caused by corrosion on the resistance, the increasing effect of the load caused by the deflection of the arch axis is also considered. Finally, the main conclusions are summarized in the *Conclusion* section.

EXPERIMENTAL PROGRAM

Specimen Design

The model design referred to a real bridge; the clear span of the catenary model arch was 4,200 mm, the rise was 840 mm, and the arch axis coefficient was 1.67. According to Li (2012), for arch bridges with rectangular sections, the section height is about 0.0167–0.025 times of the span and the section width is about 0.5–2.0 times of the section height. In addition, the width to span ratio should not be less than 1/20, considering the lateral stability. Considering the aforementioned factors comprehensively, the section size was determined as 120 mm × 240 mm.

Other details of specimens are as follows: all RC ribs were symmetrically reinforced with six longitudinal bars of 12 mm diameter and 6 mm stirrups with 100 mm spacing; the average yield strength of the virgin longitudinal bar and the stirrup was 400 and 335 MPa, respectively. The elastic modulus of steel bars was 210 GPa, and the thickness of the concrete cover at both tension and compression sides was 24 mm.

Simulation of In-Service Stress State of Model Arch

In order to make the stress condition of the model close to the real arch bridge, the influence of the load on the arch should be

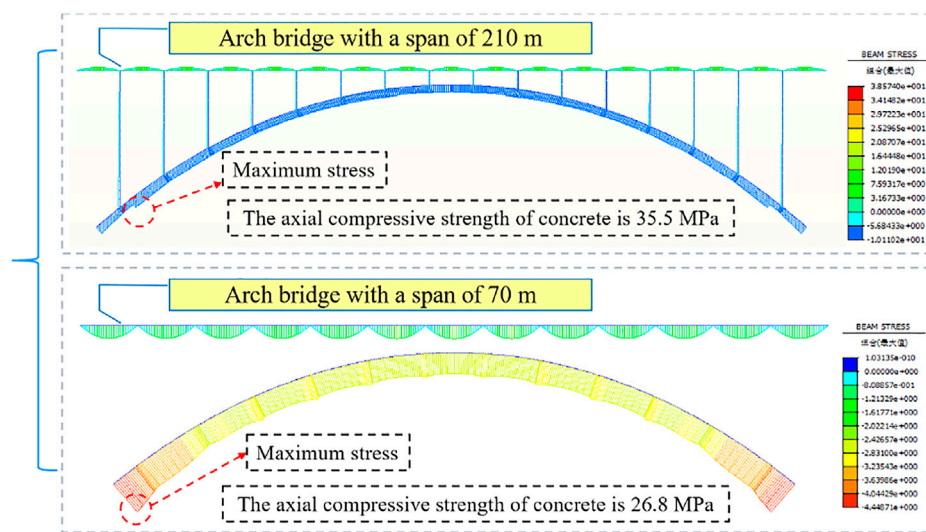


FIGURE 1 | Stress state of the real bridges under the dead load (MPa).

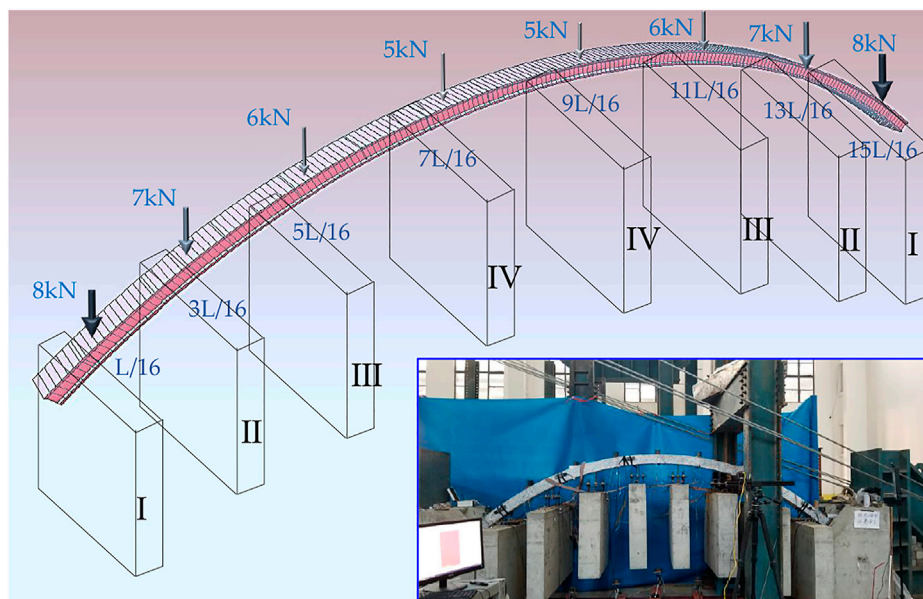


FIGURE 2 | Stress state simulation of the arch model under the dead load.

considered. Taking RC arch bridges with a main span of 70 and 210 m as references, this study calculated the internal force distribution and stress state of the main arch ring of real bridges under the dead load. As shown in **Figure 1**, the longitudinal stress distribution on the main arch ring of the real bridge was relatively uniform, and all sections were in compression. The maximum compressive stress on the arch bridge with the span of 210 m was 10.1 MPa, which was 28.5% of the axial compressive strength of the bridge concrete with Chinese specifications for grade C55. The maximum stress of the 70 m span arch bridge was 4.5 MPa, which was 16.8 % of the axial

compressive strength of the bridge concrete with Chinese specifications for grade C40.

In order to simulate the stress distribution and level of the real bridge, the test utilized a counterweight to simulate the load on the arch. The counterweight location and load are shown in **Figure 2**. Note that the stability of the counterweight load and the limitation of the test site were considered in this design. In this study, the scheme of lever loading was excluded as the later stage of it had unsatisfactory stability, the load was easy to deviate from the arch axis, and the requirements for the space were higher. The stress state of the model arch under a counterweight load is shown in **Figure 3** and **Table 1**.

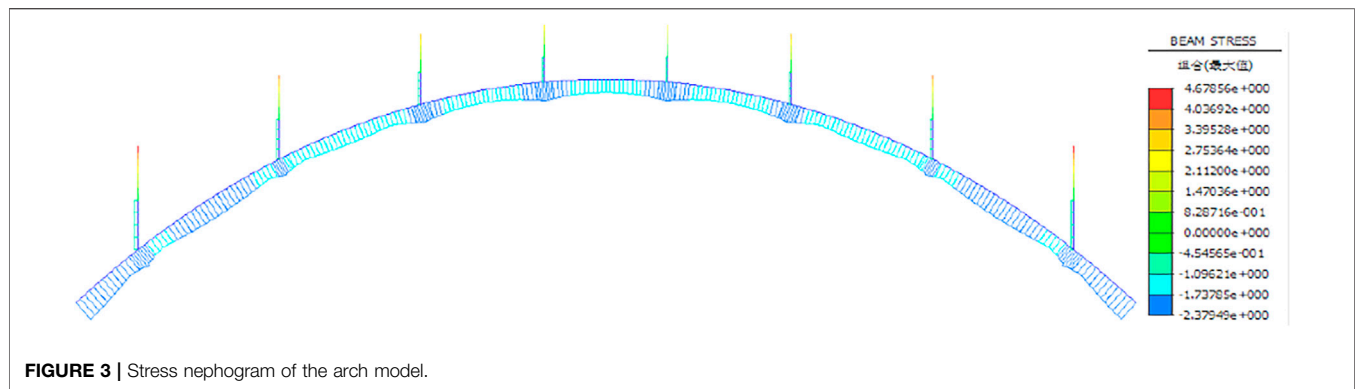


FIGURE 3 | Stress nephogram of the arch model.

TABLE 1 | Comparison of the stress state between real bridges and the arch model.

Object	Materials	Sections	Combined stress (MPa)	Stress level (%)	Section height (cm)	Axial force (kN)	Bending moment (kN · m)	Eccentricity (cm)	Eccentricity Section height (%)
Arch model	C30	0	-2.38	11.84	12	-39.31	-0.58	1.48	12.33
		L/4	-1.08	5.37		-30.71	-0.01	0.03	0.27
		L/2	-1.16	5.77		-28.50	-0.10	0.35	2.92
Arch bridge with a span of 210 m	C55	0	-8.67	24.42	350	-82,486.39	-34,039.50	41.27	11.79
		L/4	-7.64	21.52		-64,953.08	-1,341.59	2.07	0.6
		L/2	-7.35	20.70		-60,586.70	13,228.60	-21.83	6.24
Arch bridge with a span of 70 m	C40	0	-4.45	16.60	160	-25,286.97	-4,623.15	18.28	11.43
		L/4	-2.68	10.04		-20,499.85	457.72	2.62	1.64
		L/2	-2.56	9.55		-18,613.89	938.49	5.04	3.15

It can be seen from **Figure 3** and **Table 1** that the counterweight load conformed to the mechanical characteristics of a catenary arch bridge, that is, the load decreases gradually from the spring to the vault, the stress distribution in the longitudinal direction was relatively uniform, the maximum compressive stress was observed at the spring, about 2.38 MPa, which was 11.84% of the concrete axial compressive strength, and the ratio of eccentricity to the height of the arch ring was similar to that of real bridges. Therefore, the simulation effect of the model arches on the stress state of an existing RC arch bridge was satisfactory.

Two specimens were crafted, specimen 0# was the non-corrosion arch rib, and specimen 1# was the corroded one. When the arch rib was fabricated, the screw was embedded at the corresponding position of the counterweight, and the embedded bar and transverse and longitudinal reinforcement were welded to form the portal frame to enhance the bearing capacity of the screw. The axial compressive strength of specimen 0# and specimen 1# were 33.08 and 30.21 MPa, respectively.

Accelerated Corrosion Under Stress

Previous studies show that corrosion products, corrosion characteristics, and concrete expansion forms under the conditions of electrified corrosion, and natural corrosion were distinctive because of the difference in the electrochemical process (Zhang et al., 2009; Kashani et al., 2013; Fu et al., 2018; Zhou et al., 2020). The performance degradation caused

by corrosion of reinforcement in a concrete structure could be divided into two parts at the material level: the first is the loss of the reinforcement section and the degradation of mechanical properties, and the second is expansion cracking of concrete cover and bond degradation. The former is mainly related to geometric characteristics of steel bars after corrosion, while the latter is mainly affected by the composition of corrosion products; the volumetric expansion rates of different corrosion products are different. Therefore, even under the same corrosion degree, the deterioration degrees in a concrete structure caused by different corrosion modes are diverse.

In order to reduce the inaccuracy of the assessment of the adverse effects of corrosion damage caused by the difference between the accelerated corrosion and natural corrosion, the accelerated corrosion program, which is different from the scheme of Ma et al. (2016), was adopted in this study (**Figures 4, 5**). The arch rib was divided into nine corroded regions according to the position of the counterweight. Each region was connected to the cathode and anode of the power supply separately. For the sake of safety, the surface of counterweight screw shall be treated with antirust coating, and the distance between the edge of each corrosion section and screw should be 5 cm. The stainless steel mesh and sponge were wrapped on the surface of the model arch from inside to outside. The anode of the constant direct current power supply was connected with the internal longitudinal reinforcement of the concrete, and the cathode was connected with the stainless

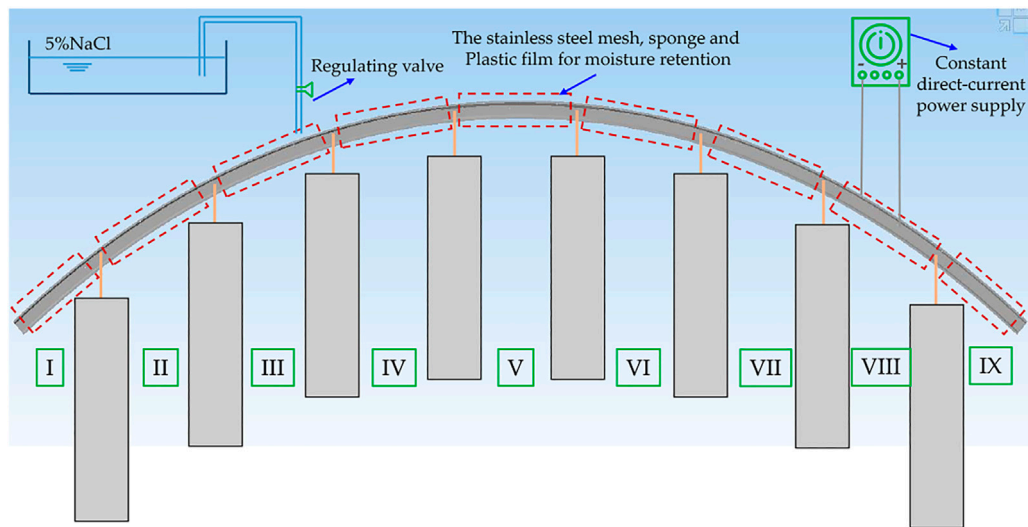


FIGURE 4 | Corrosion diagram of the arch model.



FIGURE 5 | Actual corrosion process of the arch model.

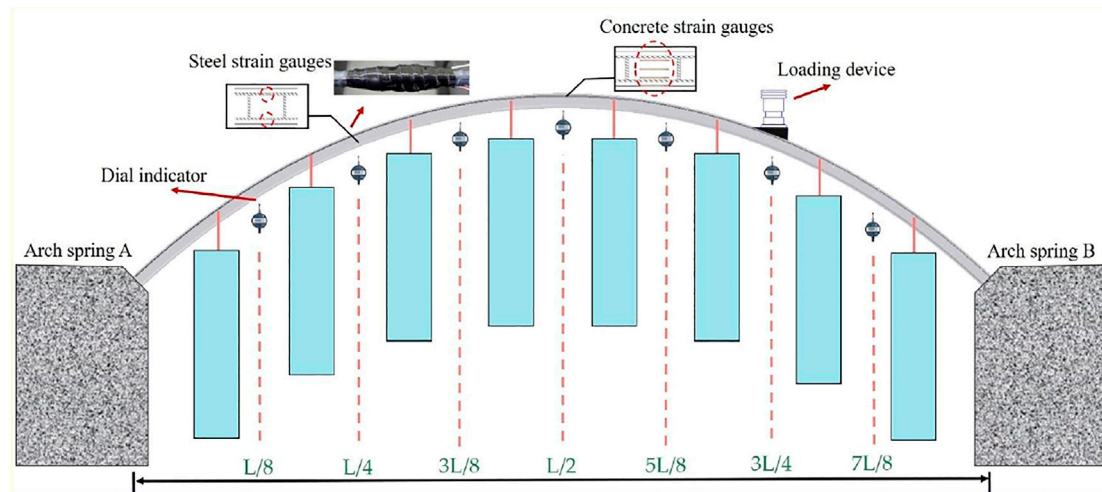


FIGURE 6 | Arrangement of measuring points and the loading device.

steel mesh. Before electrolytic corrosion, the specimen was immersed in 5% sodium chloride solution for several days to facilitate the corrosion process by allowing chloride ions to permeate into concrete cover. To prevent the loss of water in the process of corrosion, the outer side of the sponge was sealed with a plastic cloth. At the same time, an infusion pipe was used to drip 5% sodium chloride solution into the sponge at a constant speed to keep the chloride concentration constant. The corrosion current is 1.5 A, the current density is 1.5 mA/cm², and the power on time is 10.948 d.

Compared with the previous corrosion scheme, the advantages of this scheme could be summarized as follows: first, the corrosion process was carried out under conditions similar to the stress state of real bridges; second, the corrosion products were easy to be brought out by the solution during immersion accelerated corrosion, which reduced the damage of the corrosion products to the structure, and the non-immersion method adopted in this study evaded this issue; finally, it does not require a large electrolytic cell, and consequently, the corrosion of large components is easier to achieve.

Loading and Measuring Points Arrangement

In the loading test, the arch ribs were subjected to a single point load applied at the quarter point, and the wedge concrete block was set at the loading position so that the loading surface was plane; the calibrated pressure sensor was used to control the load.

Several details critical to the success in the experiment are explained as follows. A 3-cm-thick steel plate was placed on the wedge block to prevent local damage of concrete caused by stress concentration. Two reaction frames were symmetrically fixed by the laboratory ground anchor to ensure that there is no displacement in the longitudinal direction of the arch abutments. A U-shaped steel sleeve was reserved on the arch base, and cast *in situ* epoxy concrete was used to ensure the

consolidation of the springs after the arch rib was hoisted on the arch abutments.

Seven dial indicators were applied along the longitudinal direction of the arch rib to measure the vertical deflection: L/8, L/4, 3L/8, L/2, 5L/8, 3L/4, and 7L/8. The layout of measuring points and loading point is shown in **Figure 6**. A preloading test was conducted to check all the instruments and measurement devices. The load monotonically increased at a rate of 2 kN/min, with a 5-min holding time for technicians to mark all cracks on the surfaces. The load-induced transverse cracks and corrosion-induced longitudinal cracks mapping were monitored by using a crack width observation instrument with an accuracy of 0.01 mm.

RESULTS AND DISCUSSION

Steel Corrosion Rate and Distribution of Corrosion Cracks

In this study, the quality loss rate η_s was used to quantify the corrosion level. After the loading test, the steels in different sections were cut and immersed into oxalic acid solution. After the derusting, the specimens were taken away from the acid solution, washed in water to remove the acid, and dried by a dryer. At last, the steels were weighed on an electronic scale. The percentage gravimetric mass loss of steel could be calculated by the following equation:

$$\eta_s = \frac{m_0 - m_c}{m_0} \times 100\%, \quad (1)$$

where m_0 and m_c are the mass of uncorroded steel and corroded steel, respectively.

Figure 7 shows the corrosion rate of the reinforcement in different corrosion regions. From **Figure 7**, it can be concluded that the corrosion scheme adopted in this study was satisfactory. The average corrosion rate of each corrosion section had little difference, and the average corrosion rate of the whole arch was 6.85%. More detailed comparative findings are explained as follows. The

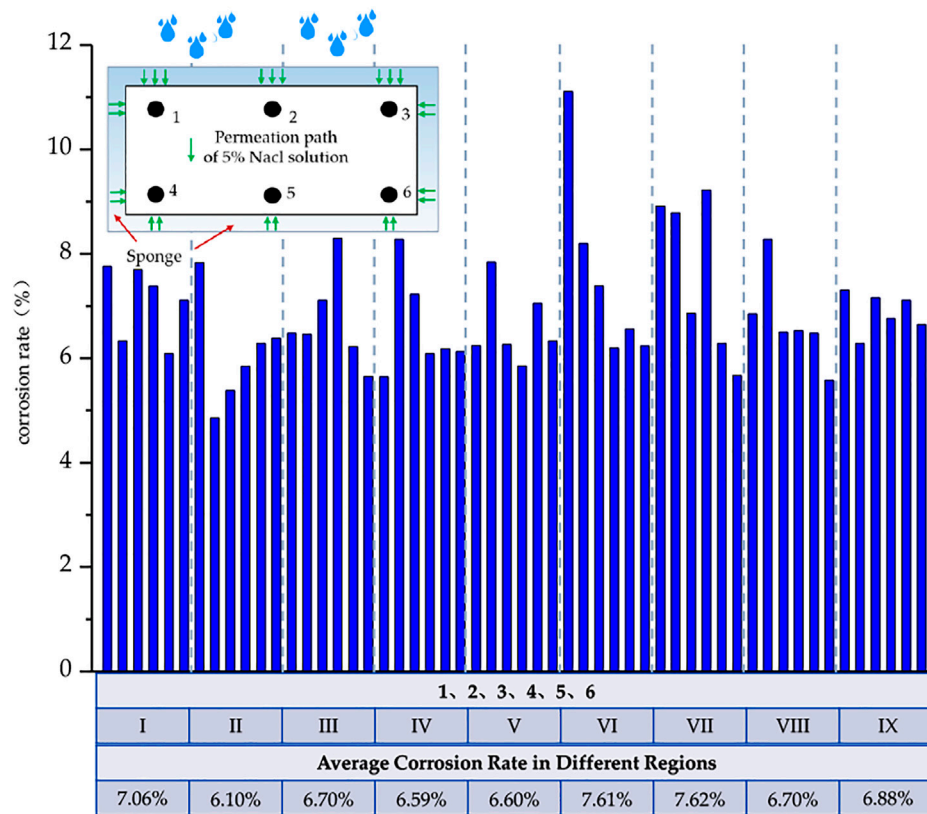


FIGURE 7 | Corrosion rate of reinforcement in each corrosion section.

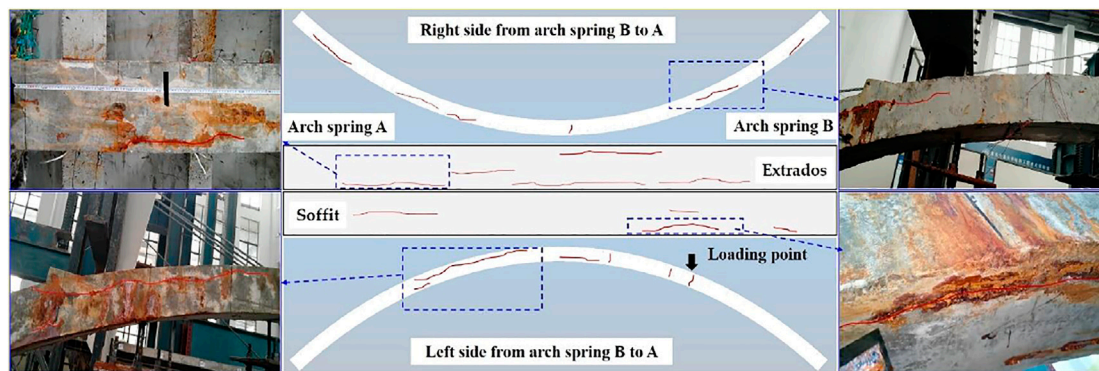


FIGURE 8 | Distribution of corrosion-induced cracks.

corrosion rate of the steel on the extrados was generally higher than that on the soffit. This phenomenon shows that there is a strong correlation between the corrosion rate of reinforcement and the concentration of chloride ion solution. In the corrosion method adopted in this study, sodium chloride solution diffused into concrete from top to bottom. Compared with the lower concrete, the infiltration effect of chloride and moisture in the upper concrete was more sufficient, and the corrosion current appeared earlier; thus, the upper reinforcement was corroded first. After that, the corrosion

rate of the upper and lower sides of the concrete tended to be the same as the concrete in the corrosion section was fully saturated, so difference of the corrosion rate between the upper and lower sides of the same region was not distinctive.

Figure 8 shows the distribution of corrosion-induced cracks in arch 1#. As plotted in **Figure 8**, there were many longitudinal corrosion-induced cracks, especially on the extrados. The cracks of corner steel bars (1#, 3#, 4#, and 6#) were more than those of middle steel bars (2# and 5#), which mainly resulted from the

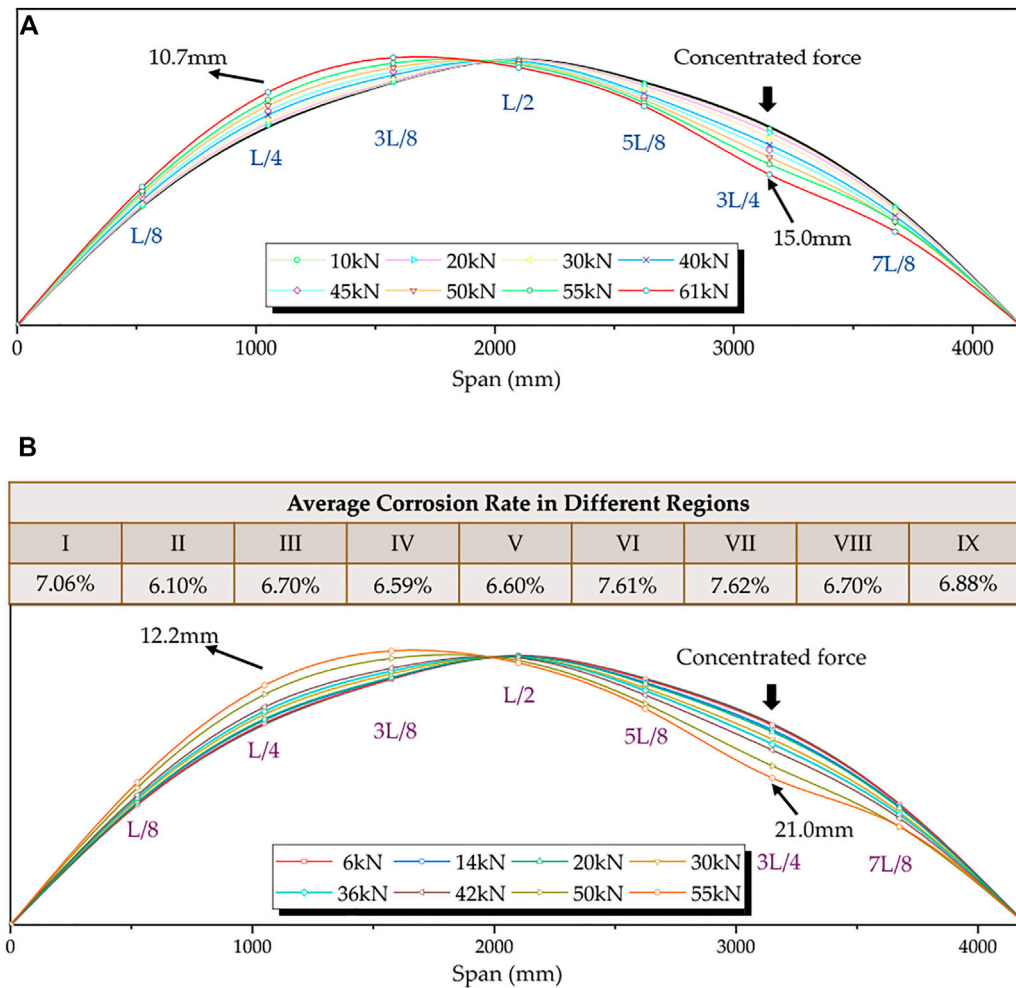


FIGURE 9 | Load-deflection curve of arch ribs: (A) arch 0# and (B) arch 1#.

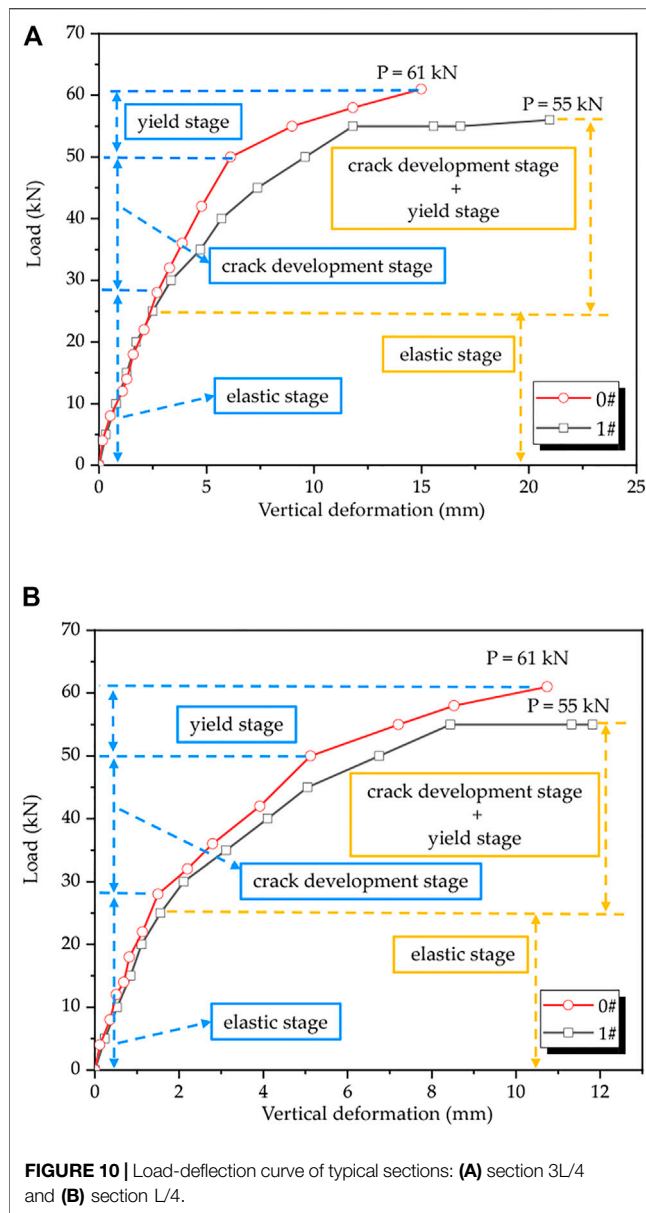
presence of more solution penetration paths in corner reinforcement than that in middle reinforcement. There were a certain number of vertical cracks caused by stirrup corrosion; the maximum crack width is 0.18 mm, appearing in region VI.

Relationship Between Load and Deflection

Figure 9 shows the vertical displacement curves of the arch ribs in different loading stages, and the spline curve was employed to fit the deflection measurement point data under graded loading. As shown in Figure 9, the deflection evolution trend of the two arch ribs was basically the same. During the loading process, the deflection of the arch ribs under quarter point loading was approximately antisymmetric. The deformation at section $L/4$ was less than that at section $3L/4$ (loading point), and the former was about 58.1~71.3% of the latter. The antisymmetric center was close to the vault, near the $L/4$ side, and the deformation at the vault position was small, with the deflection of arch 0# and 1# being 0.6 and 0.8 mm, respectively. The corrosion-induced cracks reduced the stiffness of arch rib, and the deflection of corroded arch was larger than the non-corrosion one bearing the same load. The maximum deformations of arch 0# and

arch 1# were 15.0 and 21.0 mm, respectively, and both of them appeared at the loading point position.

Figures 10A,B show the load–deflection curves for sections $3L/4$ and $L/4$, respectively. It can be seen from Figure 10 that the mechanical process of corroded arch was similar to that of non-corrosion one, with obvious non-linear evolution characteristics, and it could be roughly divided into three stages: elastic stage, crack development stage, and steel bar yield stage. The end point of the elastic stage corresponded to the cracking load, that is, once the transverse crack caused by loading appears, the structure immediately enters the crack development stage, in which the slope of the load vertical deformation curve increases and the development rate of the vertical deformation of the structure increases. The three stages of the two sections were divided synchronously. The three stages of the non-corrosion arch were clearly divided, while the crack development stage and the yield stage of the corroded arch were not easy to separate. In the elastic stage, the slope of load–deflection curve of the corroded arch was similar to that of the non-corrosion one, but the elastic stage of the corroded arch was shorter, which was mainly due to the



longitudinal cracking of concrete cover caused by the expansive stress, which weakened the strength contribution of concrete and reduced the cracking load.

Crack Development During Loading

The crack distribution caused by the load on arch 0# and arch 1# is shown in **Figures 11A,B**, respectively. For the non-corrosion arch rib, when the load reached 28 kN, the first transverse crack of the structure appeared in the soffit at the loading point. With the increase in load, the extrados of the arch spring near the loading point and section L/4 cracked one after another; and the crack height, width, and distribution range increased with the increase in load. The cracks were concentrated in three areas, that is, the arch spring near the loading point, sections L/4 and 3L/4, and the crack width in the soffit of section 3L/4; the extrados of the arch spring

near the loading point was obviously larger than that in section L/4. When the single hinge was formed, the maximum crack width of arch 0# was 2.80 mm, which was located at the extrados of the loading point; the maximum length of the crack distribution area was 47 cm, which was between the L/4 and L/2 spans. The law of crack propagation of the corroded arch was similar to that of the non-corrosion arch in the loading process. The cracking load of the corroded arch was reduced to 20 kN. In addition, the crack spacing of the intact arch was relatively uniform. In contrast, the number and distribution range of cracks in corroded arch were smaller, while the maximum crack width increased.

Failure Mode

Figures 12A,B show the failure modes of the non-corrosion arch and the corroded arch, respectively. It can be seen from **Figure 12** that the failure of the two arch ribs occurred at the loading point, and both of them showed obvious compression-bending failure. Before the loading process, all the sections of the arch rib were compressed under the dead load of the counterweight. With the application of the concentrated force at the section 3L/4, the tension trend of soffit at section 3L/4 was developed, while the compressive stress of extrados was further increased. As the load increased further, the concrete in the soffit cracked. The development of cracks made the tensile stress of steel bars in the tension area to increase rapidly and reach the yield strength. Then the neutral axis moved to the upper edge of the section; when the concrete cracked to 0.7 times of the sectional height, the steel bars in the compression zone yielded, the concrete in the extrados reached the ultimate compressive strain and was crushed, and the structure was destroyed.

Although corrosion did not transform the failure mode of the arch rib, the section resistance of the arch rib was reduced. The corrosion-induced longitudinal cracks were connected with load-induced transverse cracks, which accelerated the failure process. The failure load of arch 0# and 1# were 61 and 55 kN, respectively, that is, the ultimate bearing capacity of the arch decreased by 9.84% with the corrosion level of 7.62%.

Note that the failure mode of the structure is determined by the priority of different failure paths. The consistency of the failure mode before and after corrosion showed that the quantitative weakening degree of corrosion to the compression-bending failure and shear failure of the arch rib is not distinct. In addition, the ultimate load obtained in this study corresponded to the state of single hinge failure at the loading point, that is, the bearing capacity mentioned in this study was the section bearing capacity. Therefore, the corrosion rate here was the average corrosion rate of the loading point area, and the following theoretical bearing capacity was calculated accordingly.

PREDICTION MODEL OF BEARING CAPACITY FOR CORRODED REINFORCED CONCRETE ARCH

Bearing Capacity Model Considering Section Resistance Degradation

An arch is a member mainly carrying the bending moment and axial force. Based on the principle of equivalent beam-column,

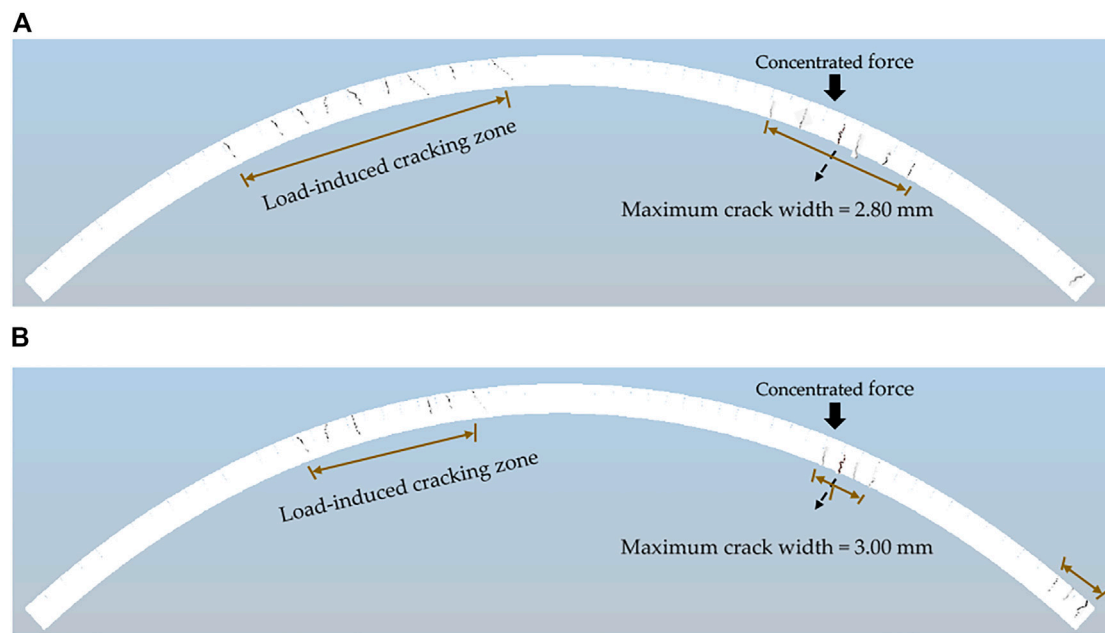


FIGURE 11 | Distribution of transverse cracks caused by loading: **(A)** arch 0# and **(B)** arch 1#.

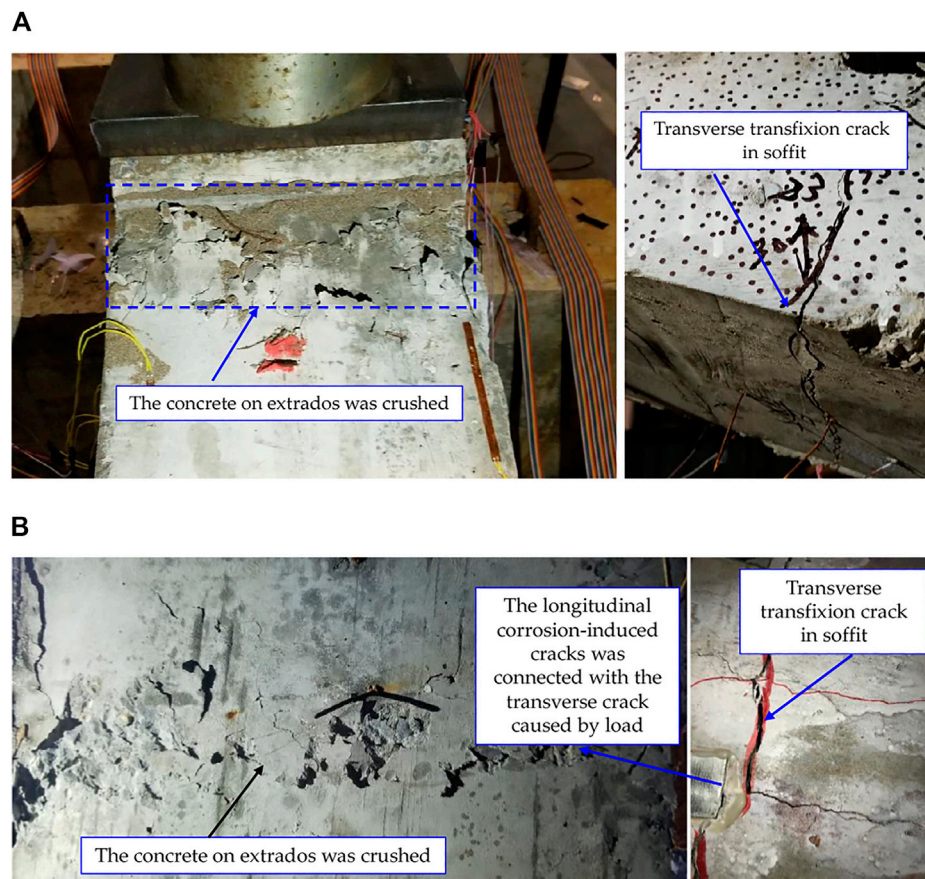
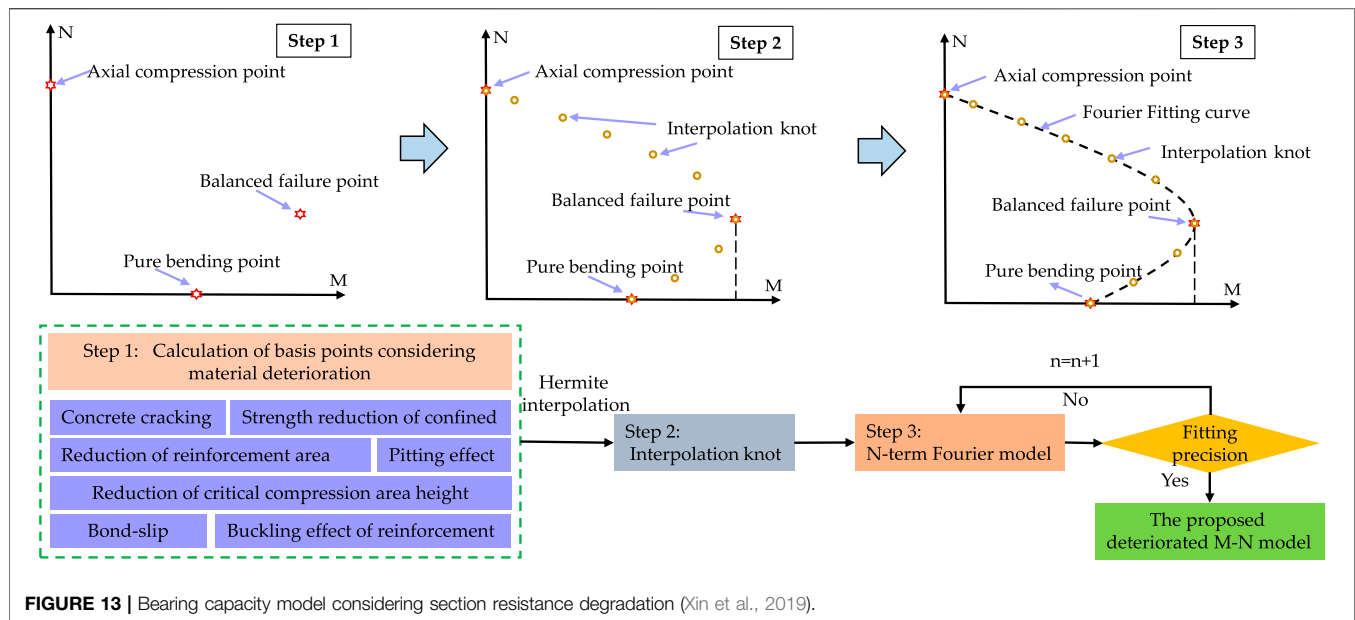


FIGURE 12 | Failure mode: **(A)** arch 0# and **(B)** arch 1#.

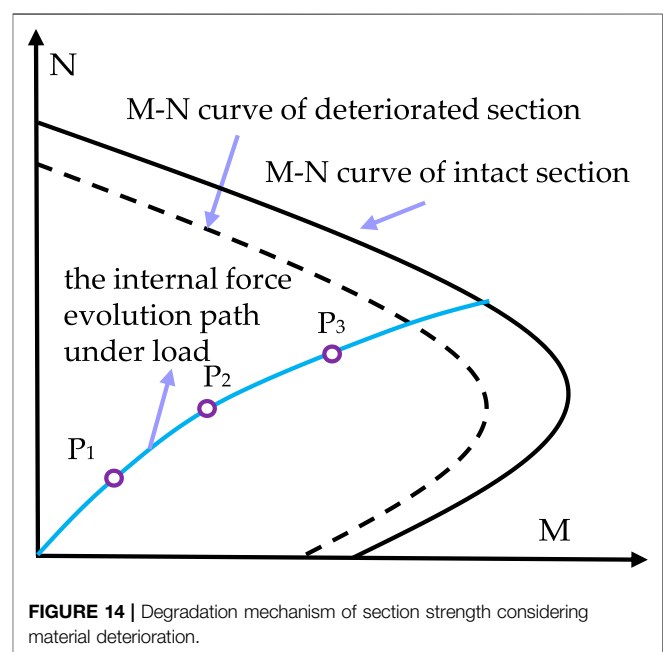


the bearing capacity of arches could be calculated as eccentric compression columns. A continuous moment–axial force (M–N) curve was the complete expression of the bearing capacity of the eccentric compression members.

For RC members whose sectional dimensions, reinforcement arrangement, and materials strength are determined, pure compression and pure bending can be regarded as two ultimate states of eccentric compression. From a continuum mechanics point of view, the transition between three mechanical states of pure compression, eccentric compression, and pure bending should be continuous. The curves of eccentric compression members should be smooth without breaking points. Based on the aforementioned properties, our previous study presented a bearing capacity evaluation model of deteriorated eccentric members based on a unified formula (Xin et al., 2019), which is shown in **Figure 13**. First, the axial compression point, the pure bending point, and the balanced failure point were selected as the basic points because of the definite stress states. The deteriorated strength of the basic points was calculated by considering various deterioration factors caused by steel corrosion. Second, the interpolation points were generated by the piecewise cubic Hermite interpolating polynomial (PCHIP). Third, the explicit expression of the interpolation points fitting function was realized by the trigonometric Fourier series model. The flowchart of the proposed model is shown in **Figure 13**. The validity and accuracy of the model had been proved by comparing the existing test data and models (Xin et al., 2019; Zhang et al., 2019).

Model Modification Considering the Deterioration Effect of Arch Axis

The essence of the bearing capacity model of corroded RC members considering the influence of various deterioration factors proposed in *Bearing Capacity Model Considering*



Section Resistance Degradation was the resistance correction of the transverse section of the arch rib. This correction occurred in the transverse direction. Correspondingly, the internal force development paths of different sections were different under the same load in the longitudinal plane of the structure. In **Figure 14**, P_i ($i = 1, 2, 3$) represents the internal force point caused by external load and $P_1 < P_2 < P_3$. The black solid line and dotted line are the resistance curves of the non-corrosive structure and corroded structure, respectively. The blue curve represents the internal force evolution path of any section under load without considering corrosion damage. As seen in **Figure 14**,

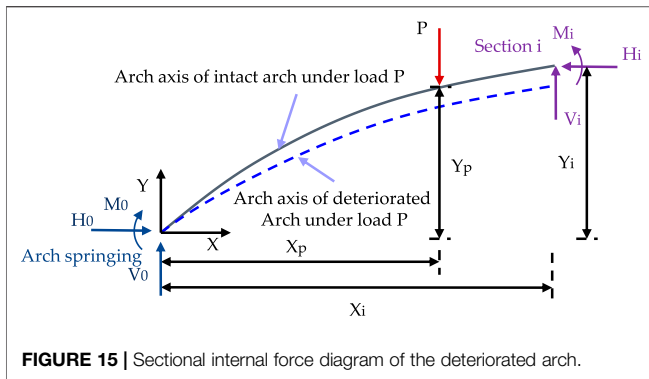


FIGURE 15 | Sectional internal force diagram of the deteriorated arch.

the internal force value of the section increases continuously with the increase of the load. When the internal force development curve intersects the resistance curve, it is considered that the section is damaged. Consequently, for the arch structure, the ultimate load is not only determined by the structural resistance but also related to the internal force development path caused by the load. The influence of internal force evolution path should be considered in the prediction of the ultimate load, which is also the main difference between the arch and ordinary eccentric compression members.

According to the principle of structural mechanics, the internal force of the arch structure is mainly related to the position of the load and the structural parameters of longitudinal plane such as rise, span, and arch axis coefficient. In Figure 15, the segment of the hingeless arch rib between the arch springing section and any section i was taken as the isolation body, where the solid line was the longitudinal axis of the non-corrosion arch under load, and the dotted line was the longitudinal axis of the corroded arch under the same load. The coordinate origin was located at the arch spring; the horizontal direction was defined as X -axis, while the vertical direction was defined as Y -axis; and P represents the external load.

According to the static equilibrium condition, the internal force of the section i of the hingeless arch could be obtained by the following equations:

$$M_i = M_0 + V_0 X_i - H_0 Y_i - P(X_i - X_p), \quad (2)$$

$$H_i = H_0, \quad (3)$$

$$V_i = P - V_0, \quad (4)$$

where M_0 , V_0 , and H_0 represent the bending moment, vertical reaction force, and horizontal thrust of the arch spring, respectively; M_i , V_i , and H_i represent the bending moment, vertical reaction force, and horizontal thrust of section i , respectively; X_i and Y_i are the horizontal distance and vertical distance from section i to coordinate origin; and X_p and Y_p are the horizontal distance and vertical distance from the loading section to the coordinate origin, respectively.

For the catenary arch bridge (Figure 16), the arch axis equation can be expressed as follows:

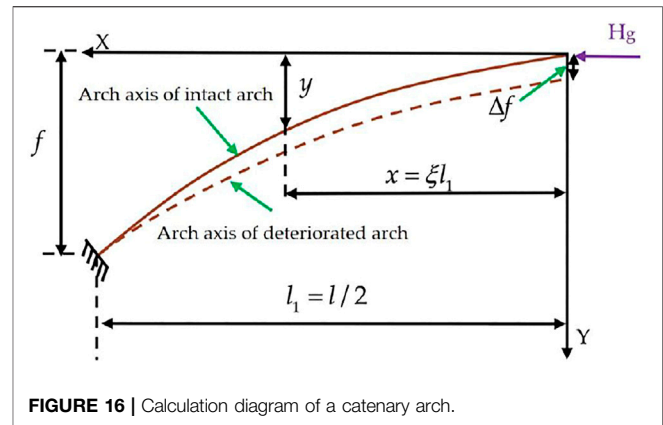


FIGURE 16 | Calculation diagram of a catenary arch.

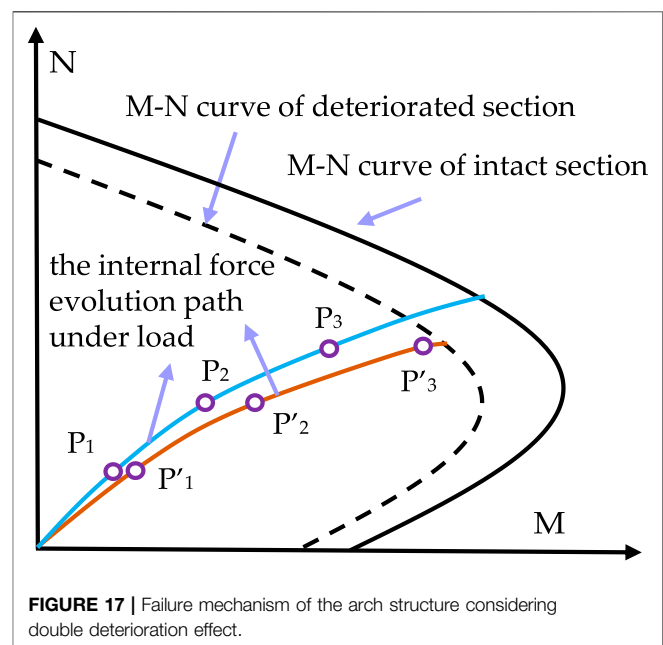


FIGURE 17 | Failure mechanism of the arch structure considering double deterioration effect.

$$y = \frac{f}{m-1} (\text{ch} k \xi - 1), \quad (5)$$

where ξ is the coordinate coefficient and $\xi = \frac{x}{l_1}$, with $l_1 = l/2$, where l is the computational span; m is the arch axis coefficient, $m = \frac{g_j}{g_d}$, where g_j and g_d are dead load intensity at the vault and arch spring, respectively; and f is the calculated vector height.

For the arch springing section, $\xi = 1$ and $y = f$, and according to the Eq. 5, $\text{ch} k = m$ can be obtained; then

$$k = \text{ch}^{-1} m = \ln(m + \sqrt{m^2 - 1}). \quad (6)$$

The horizontal thrust of the catenary arch can be calculated by the following equation:

$$H_g = \frac{l^2 g_d}{4k^2 f} (m - 1). \quad (7)$$

TABLE 2 | Bearing capacity of the arch model.

Specimen	Test value (kN)	Predicted value considering the resistance degradation (kN)	Predicted value considering double deterioration effect (kN)
Arch 0#	61	50	50
Arch 1#	55	44	41
Reduction rate	9.84%	12%	18%

After deterioration, the stiffness of the arch decreases and the deformation increases. The axial equation of the arch can be expressed by the following:

$$y = \frac{f - \Delta f}{m - 1} (\text{chk}\xi - 1) + \Delta f. \quad (8)$$

H_g^d is the horizontal thrust of the deteriorated arch, and the change rate of the horizontal thrust deduced from Eq. 6 can be calculated as follows:

$$\frac{H_g^d - H_g}{H_g} = \frac{\frac{g_d(m-1)}{4k^2} \left(\frac{l^2}{f - \Delta f} - \frac{l^2}{f} \right)}{\frac{g_d(m-1)}{4k^2} \frac{l^2}{f}} = \frac{f}{f - \Delta f} - 1 = \frac{\Delta f}{f - \Delta f}. \quad (9)$$

In general, the deformation of the deteriorated arch is very small compared with the rise in height, which is close to 0, so it is assumed that the internal force of the arch foot will not change after the deformation of the deteriorated arch. Then the bending moment of section i of the deteriorated arch can be calculated as follows:

$$M_i' = M_0 + V_0(X_i + u_i) - H_0(Y_i - v_i) - P[(X_i + u_i) - (X_p + u_p)], \quad (10)$$

$$M_i' = M_i + V_0 u_i + H_0 v_i - P(u_i - u_p), \quad (11)$$

where v_i and u_i are the vertical and horizontal displacement of section i , respectively; v_p and u_p are the vertical and horizontal displacement of loading position.

As shown in Eq. 11, under the same load, the deteriorated arch has additional bending moment in the same section compared with the intact arch, and the local limit state of the deteriorated arch is easier to achieve, as shown in Figure 17, P_i' ($i = 1, 2, 3$) represents the internal force point after considering the additional bending moment.

The horizontal compression displacement is not considered in this study. For the section at the loading point, $u_i = u_p$, $v_i = v_p$; the actual bending moment of the loading point section after considering the deterioration of the arch axis should be obtained by the following equation:

$$M_p' = M_p + H_0 v_p. \quad (12)$$

Comparison Between Predicted Strength and Test Data

Table 2 shows the calculation and test results of the ultimate bearing capacity of arch 0# and arch 1#. It can be seen from Table 2 that the

calculation results based on the equivalent beam-column method were smaller than the model test results, and the calculation result was conservative, which was consistent with the research conclusion of Lin and Chen (2016). The bearing capacity reduction rate obtained from the test was in good agreement with the theoretical value, which was 9.84 and 12%, respectively. Compared with the bearing capacity model only considering the section resistance degradation, the predictive value considering double deterioration effect of section resistance degradation and arch axis degradation was smaller, and only considering the section resistance degradation may underestimate the adverse effect of corrosion on the arch structure, which was more unsafe.

CONCLUSION

The existing studies pay insufficient attention to the durability deterioration of reinforced concrete arch bridges. To address this deficiency, an experiment on an RC arch rib under the coupling action of a load and corrosion was carried out in this study, and a theoretical prediction method of ultimate load considering the effect of resistance degradation and arch axis degradation was employed. Some concluding remarks can be summarized as follows.

- 1) The spacing of load-induced cracks in the non-corrosion arch was relatively uniform. In contrast, the number and distribution range of load-induced cracks in corroded arch were smaller, while the maximum crack width increased. The mechanical performance of the arch rib was sensitive to corrosion damage.
- 2) Corrosion significantly reduced the bearing capacity of the arch rib. Compared with the non-corrosion arch rib, when the corrosion level was 7.62%, the cracking load and bearing capacity of the corroded arch decreased by 28.57 and 9.84%, respectively.
- 3) Corrosion weakened the stiffness of the structure, and the deformation of the corroded arch was larger than that of the non-corrosion arch under the same load. Corrosion does not transform the failure mode of the arch rib, and both of arch models showed obvious compression-bending failure.
- 4) Compared with the bearing capacity model only considering the section resistance degradation, the calculation value considering double deterioration effect was smaller, and the theoretical design of bearing capacity prediction model based on dual deterioration effects was more comprehensive; only considering the section resistance deterioration effect may underestimate the detrimental effect of corrosion on the arch structure, which was unsafe.

This study takes the equivalent beam-column method as the underlying theoretical basis, and the equivalent beam-column theory is proposed from the straight column research results. As the stress characteristics of the arch is closer to the curved bar, the accuracy of the equivalent beam-column theory decreases with the breakthrough of the arch bridge span. Future studies should focus on new simplified computational methods to enhance bearing capacity prediction accuracy of long span arch bridges from the basic method level.

DATA AVAILABILITY STATEMENT

The original contributions presented in the study are included in the article/Supplementary Material; further inquiries can be directed to the corresponding author.

REFERENCES

- Castorena-González, J. H., Martin, U., Gaona-Tiburcio, C., Núñez-Jáquez, R. E., Almeraya-Calderón, F. M., Bastidas, J. M., et al. (2020). Modeling Steel Corrosion Failure in Reinforced Concrete by Cover Crack Width 3D FEM Analysis. *Front. Mater.* 7, 41. doi:10.3389/fmats.2020.00041
- Dai, L., Wang, L., Bian, H., Zhang, J., Zhang, X., and Ma, Y. (2019). Flexural Capacity Prediction of Corroded Prestressed concrete Beams Incorporating Bond Degradation. *J. Aerosp. Eng.* 32 (4), 04019027. doi:10.1061/(ASCE)AS.1943-5525.0001022
- Deng, K., Yan, G., Yang, H., and Zhao, C. (2019). RC Arch Bridge Seismic Performance Evaluation by Sectional N-M Interaction and Coupling Effect of Brace Beams. *Eng. Structures* 183, 18–29. doi:10.1016/j.engstruct.2019.01.013
- Dong, J., Zhao, Y., Wang, K., and Jin, W. (2017). Crack Propagation and Flexural Behaviour of RC Beams under Simultaneous Sustained Loading and Steel Corrosion. *Construction Building Mater.* 151, 208–219. doi:10.1016/j.conbuildmat.2017.05.193
- Du, R. Y., and Chen, B. C. (2013). Experimental Research on the Ultimate Load Capacity of Reactive Powder concrete Arches. *Eng. Mech.* 30 (5), 42–48. doi:10.6052/j.issn.1000-4750.2011.11.0783
- Fan, Y. F., Zhou, J., Hu, Z. Q., and Zhu, T. (2007). Study on Mechanical Response of an Old Reinforced concrete Arch Bridge. *Struct. Control. Health Monit.* 14 (6), 876–894. doi:10.1002/stc.184
- Fang, S. (2020). Axial Compressive Performance of Corroded Concrete Columns Strengthened by Alkali-Activated Slag Ferrocement Jackets. *Front. Mater.* 7, 567777. doi:10.3389/fmats.2020.567777
- Fu, C., Jin, N., Ye, H., Jin, X., and Dai, W. (2017). Corrosion Characteristics of a 4-year Naturally Corroded Reinforced concrete Beam with Load-Induced Transverse Cracks. *Corrosion Sci.* 117, 11–23. doi:10.1016/j.corsci.2017.01.002
- Fu, C., Jin, N., Ye, H., Liu, J., and Jin, X. (2018). Non-uniform Corrosion of Steel in Mortar Induced by Impressed Current Method: An Experimental and Numerical Investigation. *Construction Building Mater.* 183, 429–438. doi:10.1016/j.conbuildmat.2018.06.183
- Fu, C., Ye, H., Jin, N., and Huang, Y. (2020). Chloride Penetration in Reinforced Concrete Beams under Combined Sustained Loading and Drying-Wetting Cycles. *J. Mater. Civ. Eng.* 32 (4), 04020025. doi:10.1061/(ASCE)MT.1943-5533.0003076
- Huang, Q. W., and Chen, B. C. (2009). Experimental Research on Whole Process Behaviors of Reinforced concrete Box Arch under In-Plane Loads. *J. Fuzhou Univ. (Natural Sci. Edition)* 37 (3), 394–400. CNKI:SUN:FZDZ.0.2009-03-023.
- Kashani, M. M., Crewe, A. J., and Alexander, N. A. (2013). Use of a 3D Optical Measurement Technique for Stochastic Corrosion Pattern Analysis of Reinforcing Bars Subjected to Accelerated Corrosion. *Corrosion Sci.* 73, 208–221. doi:10.1016/j.corsci.2013.03.037
- Li, J. (2012). *Research on Moment Increasing Coefficient of Reinforced concrete Arch Bridge*. [D]: [Doctoral Dissertation]. [Chengdu]. Southwest Jiaotong University.

AUTHOR CONTRIBUTIONS

JX conceived and wrote this manuscript. JW offered useful suggestions for the preparation and writing the manuscript. XY collected the data. ZL advised on data analysis and manuscript organization. JZ was involved in manuscript writing.

FUNDING

This work was supported by the National Natural Science Foundation of China (51908094, U20A20314), the Natural Science Foundation of Chongqing (cstc2020jcyj-msxmX0532), and the Scientific and Technological Research Project of Chongqing Education Commission (KJQN202001211).

- Li, X., Zhou, J., Wu, Y., Wang, Z., and Li, X. (2021). Structural Analysis and Improvement for a New Form Traveler in Long-Span Cantilever-Casting Arch Bridge. *Adv. Mech. Eng.* 13 (4), 168781402110099. doi:10.1177/1687814021100999
- Lin, S. S., and Chen, B. C. (2016). Calculation of Load-Carrying Capacity of Reinforced concrete Arch Basing on Equivalent Beam-Column Method. *J. Fuzhou Univ. (Natural Sci. Edition)* 44 (1), 110–114.
- Liu, Y., Jiang, N., Deng, Y., Ma, Y., Zhang, H., and Li, M. (2016). Flexural experiment and Stiffness Investigation of Reinforced concrete Beam under Chloride Penetration and Sustained Loading. *Construction Building Mater.* 117, 302–310. doi:10.1016/j.conbuildmat.2016.04.110
- Ma, Y., Xu, F., Wang, L., Zhang, J., and Zhang, X. (2016). Influence of Corrosion-Induced Cracking on Structural Behavior of Reinforced concrete Arch Ribs. *Eng. Structures* 117, 184–194. doi:10.1016/j.engstruct.2016.03.008
- Petryna, Y. S., Pfanner, D., Stangenberg, F., and Krätzig, W. B. (2002). Reliability of Reinforced concrete Structures under Fatigue. *Reliability Eng. Syst. Saf.* 77 (3), 253–261. doi:10.1016/s0951-8320(02)00058-3
- Qiu, J., Zhang, H., Zhou, J., and Zhang, W. (2021). An SMFL-Based Non-destructive Quantification Method for the Localized Corrosion Cross-Sectional Area of Rebar. *Corrosion Sci.* 192, 109793. doi:10.1016/j.corsci.2021.109793
- Shao, X., He, G., Shen, X., Zhu, P., and Chen, Y. (2021). Conceptual Design of 1000 M Scale Steel-UHPFRC Composite Truss Arch Bridge. *Eng. Structures* 226, 111430. doi:10.1016/j.engstruct.2020.111430
- Tang, X. S., Zhang, J. R., Li, C. X., Xu, F. H., and Pan, J. (2005). Damage Analysis and Numerical Simulation for Failure Process of a Reinforced concrete Arch Structure. *Comput. Struct.* 83 (31), 2609–2631. doi:10.1016/j.compstruc.2005.03.017
- Xin, J., Zhou, J., Zhou, F., Yang, S., and Zhou, Y. (2019). Bearing Capacity Model of Corroded RC Eccentric Compression Columns Based on Hermite Interpolation and Fourier Fitting. *Appl. Sci.* 9 (1), 24. doi:10.3390/app9010024
- Zanardo, G., Pellegrino, C., Bobisut, C., and Modena, C. (2004). Performance Evaluation of Short Span Reinforced concrete Arch Bridges. *J. Bridge Eng.* 9 (5), 4245–4434. doi:10.1061/(ASCE)1084-0702(2004)9:5(424)
- Zhang, D., Zeng, Y., Fang, M., and Jin, W. (2019). Service Life Prediction of Precast concrete Structures Exposed to Chloride Environment. *Adv. Civil Eng.* 2019 (1), 1–14. doi:10.1155/2019/3216328
- Zhang, J., Li, C., Xu, F., and Yu, X. (2007). Test and Analysis for Ultimate Load-Carrying Capacity of Existing Reinforced Concrete Arch Ribs. *J. Bridge Eng.* 12 (1), 4–12. doi:10.1061/(asce)1084-0702(2007)12:1(4)
- Zhang, R., Castel, A., and François, R. (2009). The Corrosion Pattern of Reinforcement and its Influence on Serviceability of Reinforced concrete Members in Chloride Environment. *Cement Concrete Res.* 39 (11), 1077–1086. doi:10.1016/j.cemconres.2009.07.025
- Zhang, S. Y., Zhao, R. D., Jia, Y., Wang, Y. B., and Xie, H. Q. (2017). Model Test Study on Long-Span Railway Concrete Arch Bridge with Rigid Skeleton.

J. Southwest. Jiaotong Univ. 52 (6), 1088–1096. doi:10.3969/j.issn.0258-2724.2017.06.008

Zhou, H., Chen, S., Du, Y., Lin, Z., Liang, X., Liu, J., et al. (2020). Field Test of a Reinforced concrete Bridge under marine Environmental Corrosion. *Eng. Fail. Anal.* 115, 104669. doi:10.1016/j.engfailanal.2020.104669

Conflict of Interest: JX and JW were employed by Guangxi Communications Investment Group Corporation Ltd.

The remaining authors declare that the research was conducted in the absence of any commercial or financial relationships that could be construed as a potential conflict of interest.

Publisher's Note: All claims expressed in this article are solely those of the authors and do not necessarily represent those of their affiliated organizations, or those of the publisher, the editors, and the reviewers. Any product that may be evaluated in this article, or claim that may be made by its manufacturer, is not guaranteed or endorsed by the publisher.

Copyright © 2022 Xin, Wang, Liu, You and Zhou. This is an open-access article distributed under the terms of the Creative Commons Attribution License (CC BY). The use, distribution or reproduction in other forums is permitted, provided the original author(s) and the copyright owner(s) are credited and that the original publication in this journal is cited, in accordance with accepted academic practice. No use, distribution or reproduction is permitted which does not comply with these terms.



Structural Design and Analysis for a Timber-Concrete Hybrid Building

Xiaoyue Zhang^{1,2,3}, Lu Xuan^{1,2,3}, Wanru Huang^{1,2,3}, Lin Yuan⁴ and Pengcheng Li^{1,2,3*}

¹School of Civil Engineering, Chongqing University, Chongqing, China, ²The National Centre for International Research of Low-Carbon and Green Buildings, Ministry of Science and Technology, and the Joint International Research Laboratory of Green Buildings and Built Environments, Ministry of Education, Chongqing, China, ³Key Laboratory of New Technology for Construction of Cities in Mountain Area, Chongqing University, Chongqing, China, ⁴School of Arts, Guizhou Normal University, Guiyang, China

The benefits of using wood in tall and commercial construction are undisputed, namely reducing the carbon footprint, shortening construction times, and enhancing seismic and building physics performance. The international market for wood as a structural material in tall and non-residential construction, however, is still relatively untapped. China is home to the world's largest population and the largest construction sector worldwide, yet wood products are only used in a small fraction of buildings. The main reasons for this situation are the fire regulations and lack of guidelines for novel wood-based structural systems. This paper describes the design of a 10-storey timber-concrete business hotel which will be erected in the Guizhou province of China. The foundation design, gravity system design, lateral load resisting system design, seismic analysis and the fire resistance design were conducted, and the procedure provided appropriate information to the technological feasibility to promote the development of timber-based hybrid high-rise construction systems in China.

Keywords: tall timber-concrete hybrid building, glulam column, structural design, ground motion, seismic analysis

INTRODUCTION

Background

Wood, as one of the most attractive construction materials due to its renewability and carbon sequestration, has always been an essential part of the built environment (Foliente, 2000). Multiple studies (Buchanan et al., 2012; De Wolf et al., 2017; Andersen et al., 2021; Ryberg et al., 2021) demonstrated when compared to concrete or steel, using wood or its engineered wood product derivatives, e.g. Glued-Laminated Timber (GLT), Cross Laminated Timber (CLT), Laminated Veneer Lumber (LVL) and so on, as building materials present a favourable environmental balance. Wood contains a lot of solar energy, only a small amount of fossil fuel is needed in the production process, that is generally pollution-free in the production process. Modern wood structures produce little construction waste, which can improve the utilization efficiency of materials. Moreover, wood waste can be burned as renewable energy instead of fossil fuel to reduce energy consumption. The carbon dioxide released by wood combustion is the solar energy stored in the wood itself, which is part of the natural cycle and will not lead to the increase of greenhouse gases (Buchanan, 2007). According to Ritter et al., the proper installation and use of wood products in houses often reduce the greenhouse gases produced by products, and the environmental burden is lower than other building materials with the same function (Ritter et al., 2011). According to the case of tall wooden buildings, it is found that the cost of a 20-storey CLT building with the same function is roughly the same as that of a concrete building (Robertson et al., 2012). With the proposal of sustainable development goals and the increasing

OPEN ACCESS

Edited by:

Qian Zhang,
FAMU-FSU College of Engineering,
United States

Reviewed by:

Zhibin Ling,
Suzhou University of Science and
Technology, China
Yingyang Liu,
Zhengzhou University, China

*Correspondence:

Pengcheng Li
lipengcheng@cqu.edu.cn

Specialty section:

This article was submitted to
Structural Materials,
a section of the journal
Frontiers in Materials

Received: 28 December 2021

Accepted: 24 January 2022

Published: 25 February 2022

Citation:

Zhang X, Xuan L, Huang W, Yuan L
and Li P (2022) Structural Design and
Analysis for a Timber-Concrete
Hybrid Building.
Front. Mater. 9:844398.
doi: 10.3389/fmats.2022.844398



FIGURE 1 | Sketch of 10 storey timber-concrete hybrid building.

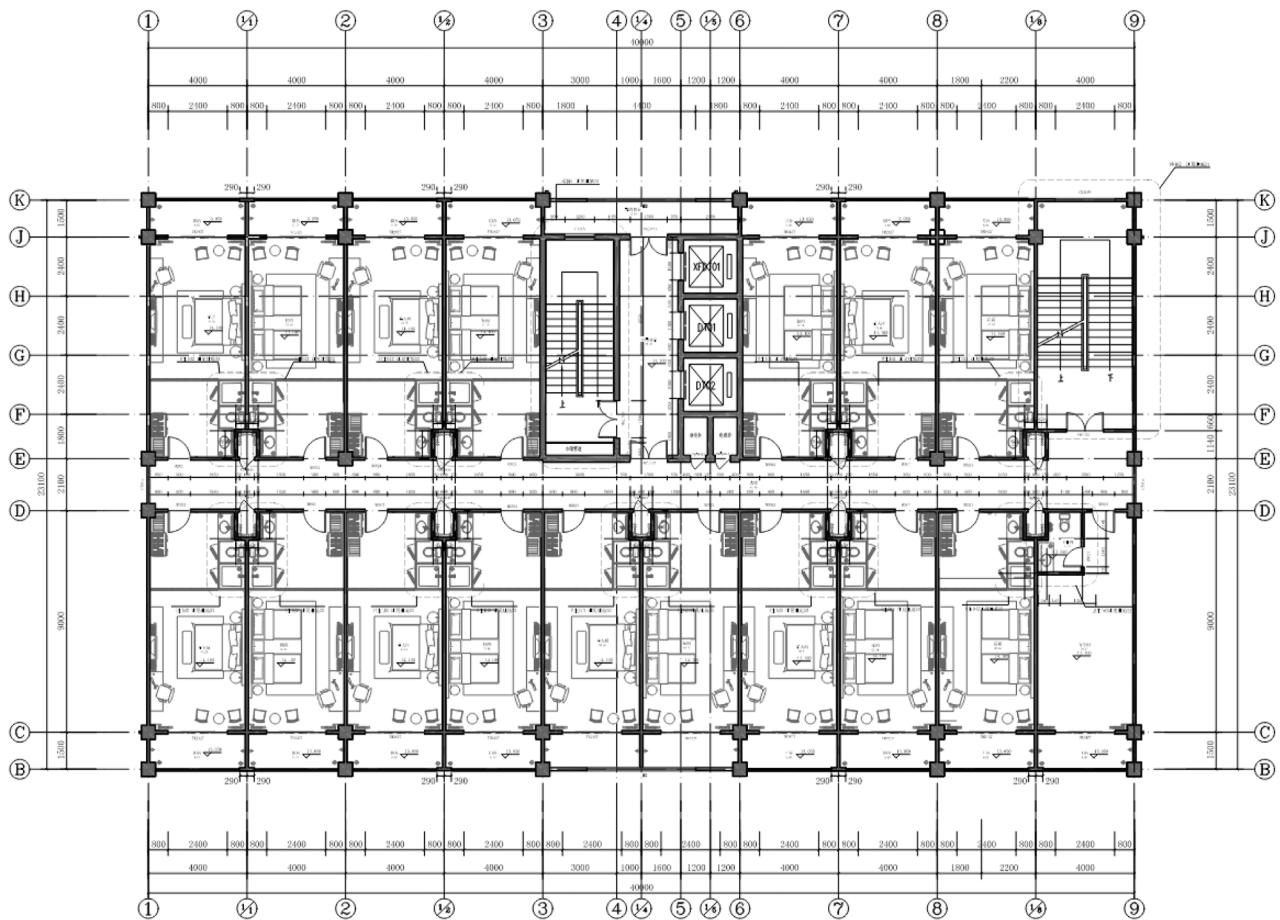


FIGURE 2 | Typical floor plan of the hybrid building.

awareness of environmental protection, the positive attributes of wood are gradually highlighted, making it become the preferred green building material to replace steel and concrete.

Although the application of wood in building systems has a good performance record, the international market for wood as a structural material in tall and commercial construction is still relatively small and the building regulations all over the world

limit the building height and area of wood in high-rise buildings, especially in China, where the relative research on the timber-based structure is backward.

Tall and Hybrid Timber Construction

With the rapidly increasing human population and the corresponding pressures on land resources, it has been

TABLE 1 | Structural member specifications and material parameters (GB T 50708, 2012) (GB 50010-2012: Code for design of concrete structures, 2015).

Member	Material	Grade	Material properties				
			f_m (MPa)	f_c (MPa)	f_t (MPa)	f_v (MPa)	E (MPa)
Glulam beam	Douglas fir	TC _T 21	21	—	—	2.2	11,700 ^a
Glulam column	Douglas fir	TC _T 21	21	20	15	—	8,000
Structural core	Concrete	C45	—	21.1	1.8	2.8	33,500

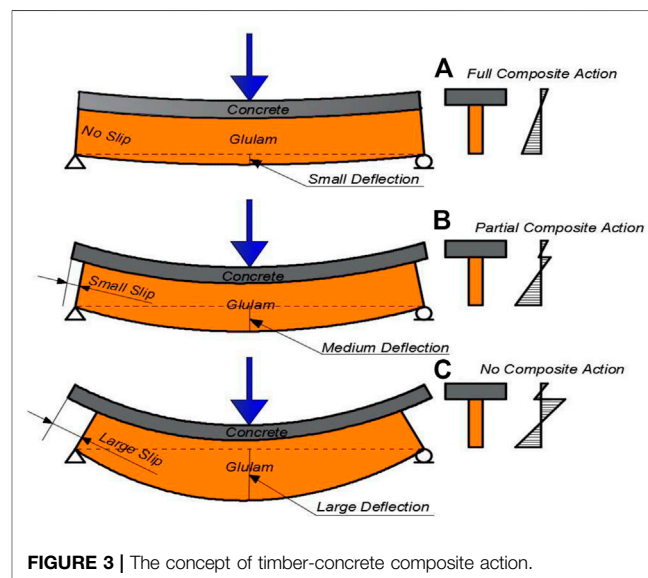
^aThe Glulam Beam is locally manufactured by YF, its elasticity modulus is obtained based on their tested results.

TABLE 2 | Glulam beam design.

Glulam beam design		
Label	GB1:Glulam Girder	GB2:Glulam Secondary Beam
Beam size	290×2–290 mm	240 × 400 mm
Ratio of resistance vs. demand for the member with maximum force loaded		
Shear	45.8%	28.4%
Moment	46.4%	58.0%
Shear (1-h fire)	42.1%	92.4%
Moment (1-h fire)	61.2%	28.1%
Natural frequency of vibration	8.0 Hz	5.7 Hz

argued that it is a matter of urgency to find a way to expand the possibilities of using wood as an efficient solution for large-scale tall buildings (Green and Karsh, 2012). Therefore, timber high-rise or timber-hybrid buildings are attracting more and more attention worldwide. Many studies have confirmed that timber and timber-hybrid buildings have enormous potential to reach higher heights with desired structural and environmental performance (Foster et al., 2016; Ramage et al., 2017; Wimmers, 2017; Zhang et al., 2021). Over the last decade, North America, Europe and other countries have begun to study the new system of building multi-storey and high-rise timber hybrid structures with other materials, for example, the concrete or the steel (He et al., 2016; Zhang et al., 2017; Zhang et al., 2018). Several feasibility studies for innovative tall timber-based hybrid structural systems were carried out, and many prototype buildings were tested (Kuilen et al., 2011; Hristovski et al., 2013; Zhang et al., 2016; Izzi et al., 2018). Meanwhile, several tall timber and timber-hybrid buildings, e.g., the 18-story Brock Commons in Canada (Tannert and Moudgil, 2017) and the 18-story Mjøstårnet in Norway (Abrahamsen, 2017), have been successfully built and are operating well, which demonstrates great competitiveness in the aspects of structural performance, environmental friendliness, and construction speed.

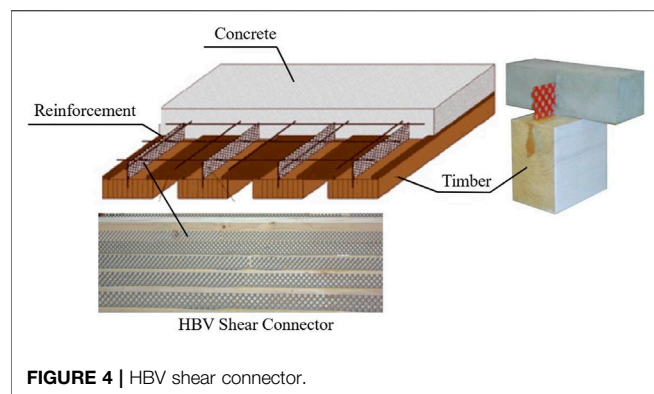
Timber-concrete hybrid building refers to the structure form dominated by wood structure and concrete structure. The most common type of tall wood hybrid structures is combining a case-in-place concrete core that resists the lateral loads, with the timber structure carrying the reminder of the gravity load and diaphragm loads. According to relevant research, timber concrete hybrid structure gives full play to the best performance of wood and concrete, and has higher bearing capacity, fire resistance and

**FIGURE 3 |** The concept of timber-concrete composite action.

seismic performance compared with pure wood structure (Poirier et al., 2016).

Timber Construction in China

Building tall structures with wood in China is not new - pagodas built hundreds of years ago are still standing despite exposure to seismic events, strong winds, and high-moisture environments (Lam et al., 2008). However, due to the shortage of wood resources and fire safety considerations, the government set strict rules to limit the use of timber and more attention was paid on the study and construction of steel and concrete



structures (Li et al., 2016; Karol et al., 2018; Li and Wang, 2021). Thus, the timber construction decreased rapidly and there have height and area limitations on it (timber structures were once limited to no more than three storeys in China, and the height was limited to no more than 10 m) (GB50016-2014: Code for Building Design on Fire protection, 2018).

Thanks to the advances in fire separation/fire-stopping system technology and the production of engineered wood products in worldwide, especially the global integration of low-carbon economy, increasing attention has been paid to using and researching structural timber in China in the past 2 decades. Imported dimension timber, glued-laminated timber and cross-laminated timber have recently been used to build homes, schools, shopping malls and stadiums, and substantial research has been undertaken on novel timber-based hybrid structures (Li et al., 2018).

Since the long construction periods for reinforced concrete buildings cause serious on-site noise and dust pollution, the Chinese government recently proposed a reform of the national approach to building systems and an implementation of the industrialization of buildings. Efforts are made to promote and develop prefabricated buildings which also include wood

constructions. With the growing interest in using timber for structures and in expanding the tall wood building sector, there is a desire to develop design guidance for timber high-rises under consideration of the very strict fire resistance requirements in China. One approach, and currently the most feasible for China, to overcome the height and scale limitations in building codes is to use wood in combination with non-combustible materials. The timber-concrete hybrid building is one of the good options to provide a good balance for people's living quality, environmental conservation, and fire protection.

Objective

The Objective of this study is to provide appropriate information on developing a timber concrete hybrid high rise building in China. Case studies of a 10-storey glulam timber frame with the concrete core business hotel are provided to present its structural design details and seismic performance.

STRUCTURAL DESIGN OF THE TIMBER-STEEL HYBRID BUILDING

Overview

A 10-storey timber-concrete hybrid building, proposed by the Guizhou Jianhe Yuanfang Forestry Investment & Explore Co., Ltd. (YF for short). was designed by Equilibrium Consulting Inc. The building was proposed for the location Jianhe County, Guizhou province of China and is designed for occupation as a luxury business hotel.

The building consists of a concrete core, concrete base and a Glulam frame system, shown in **Figure 1**, the first concrete floor is the parking lot, top nine stories of mass-timber superstructure, carrying all gravity loads, rest on the concrete core that act as both the wind and seismic lateral load-resisting systems. As shown in **Figure 2**, The 10-storey building has a typical inter-storey height of 3.9 m, a total building height of 46.43 m to the top of the timber roof, a typical storey floor area of 924 m² (23.1 × 40 m), a total

TABLE 3 | Timber concrete composite (TCC) beam design.

Timber concrete composite beam design

Label	TCC ₁	TCC ₂	TCC ₃	TCC ₄	
Beam Size		290mm×2–290 mm			
Shear Connection	3-HBV 1000 × 120 at 1350	2-HBV 1000 × 120 at 1350	1-HBV 1000 × 120 at 1350	3-HBV 1000 × 120 at 1100	
Ratio of resistance vs. demand for the member with maximum force loaded					
Shear	Concrete	84.9%	51.6%	15.9%	89.7%
	Timber	41.3%	24.1%	7.8%	43.2%
	HBV	92.1%	66.4%	50.1%	96.7%
Moment	Concrete	32.3%	20.8%	37.5%	28.4%
	Timber	48.6%	39.1%	46.8%	17.9%
Shear (1-h fire)	Concrete	74.6%	44.5%	14.3%	77.8%
	Timber	52.3%	33.2%	10.5%	44.1%
	HBV	80.0%	56.2%	46.9%	83.2%
Moment (1-h fire)	Concrete	37.3%	22.9%	43.5%	36.4%
	Timber	70.5%	55.2%	68.1%	63.7%
Vibration Frequency of Vibration		9.6hz	9.6hz	20.6hz	7.0hz

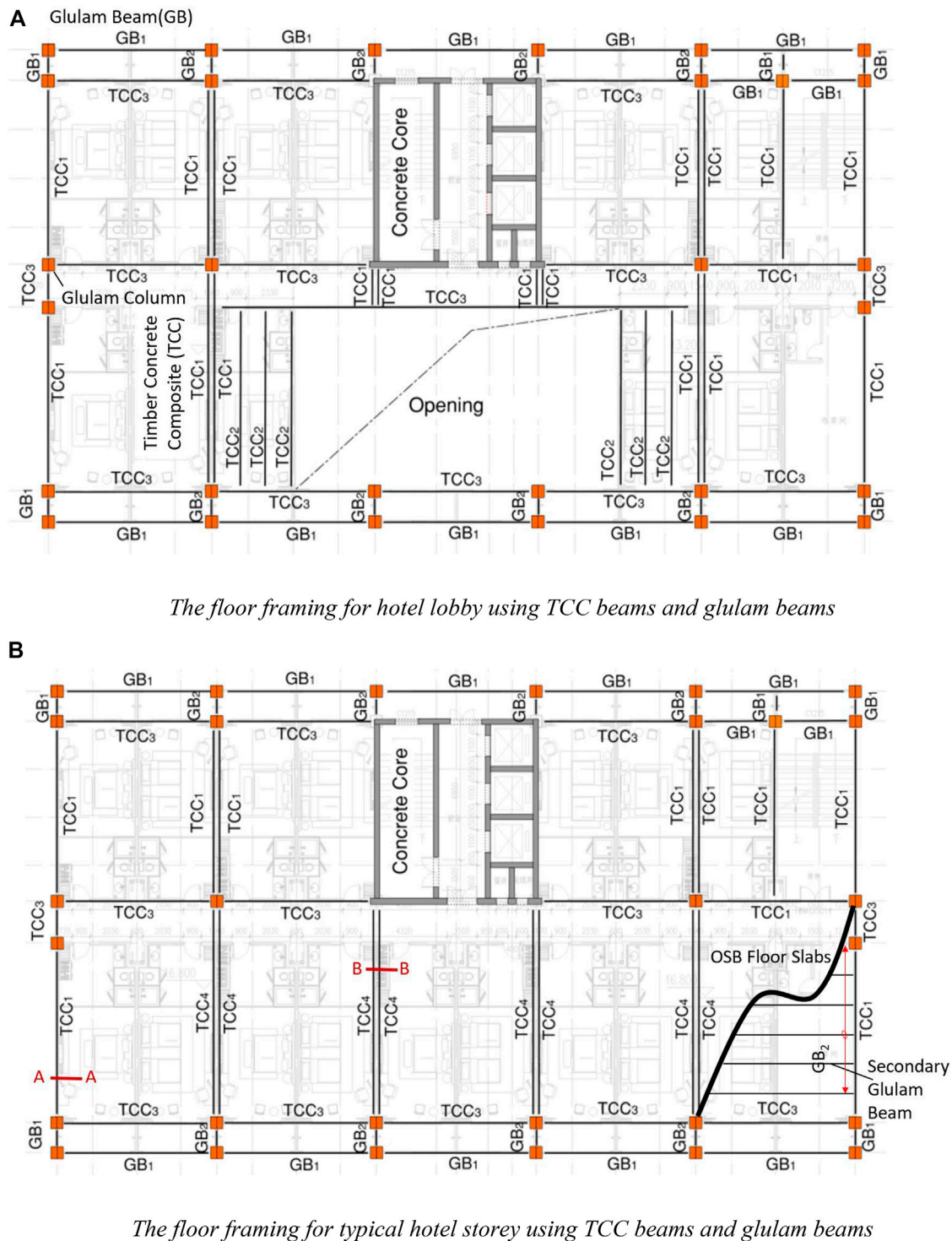


FIGURE 5 | Floor flaming for TCC beam and design details.

10,000 m² building area and provides lobbies, hotel rooms, and recreation clubs on floors 2–10. As it will be erected in China, the whole structure was designed mostly in accordance with the current structural design codes and technical standards of the

People's Republic of China. For some key connections or components design which lacks of Chinese code, like the timber - concrete composite (TCC) beam design, Eurocode 5 (Steer, 2001) will be used as a reference.

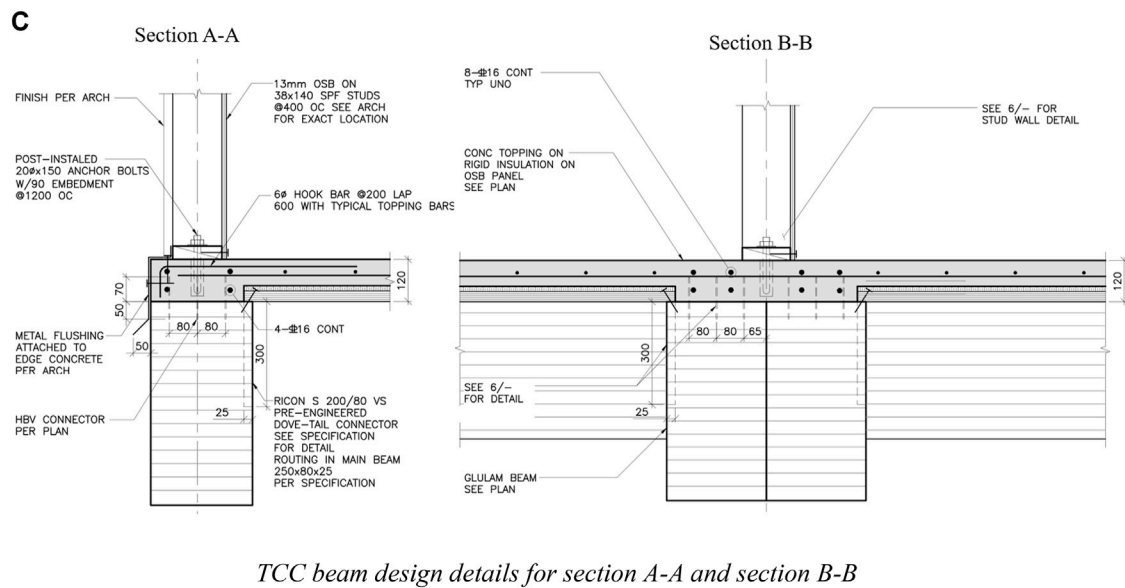


FIGURE 5 | (continued).

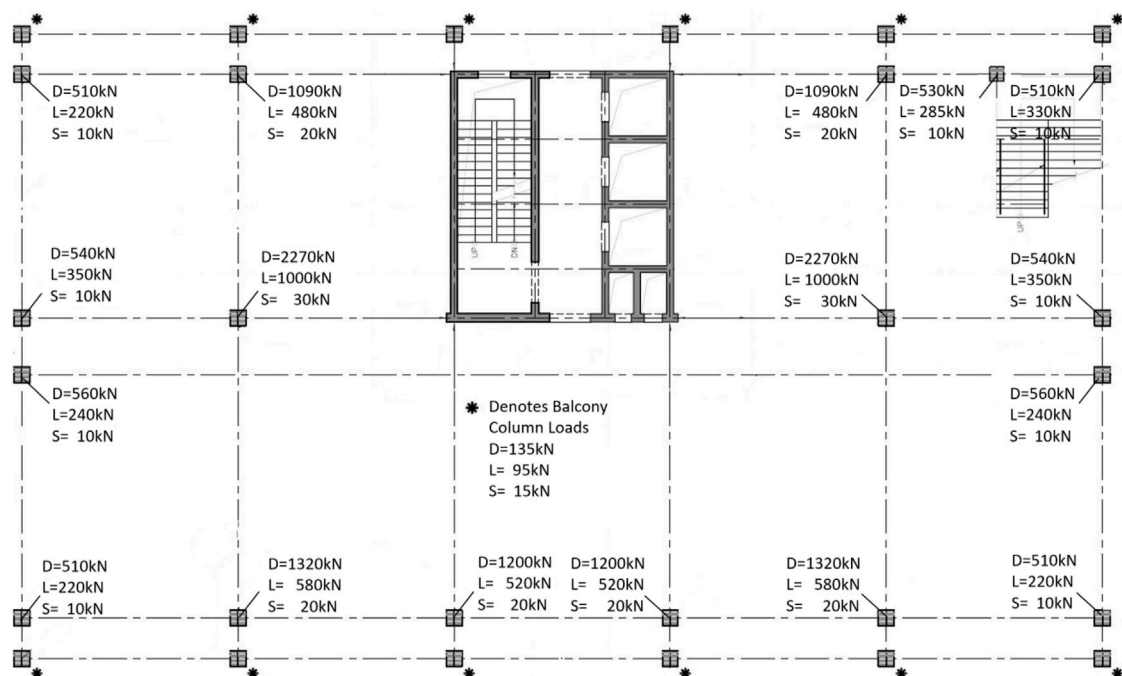


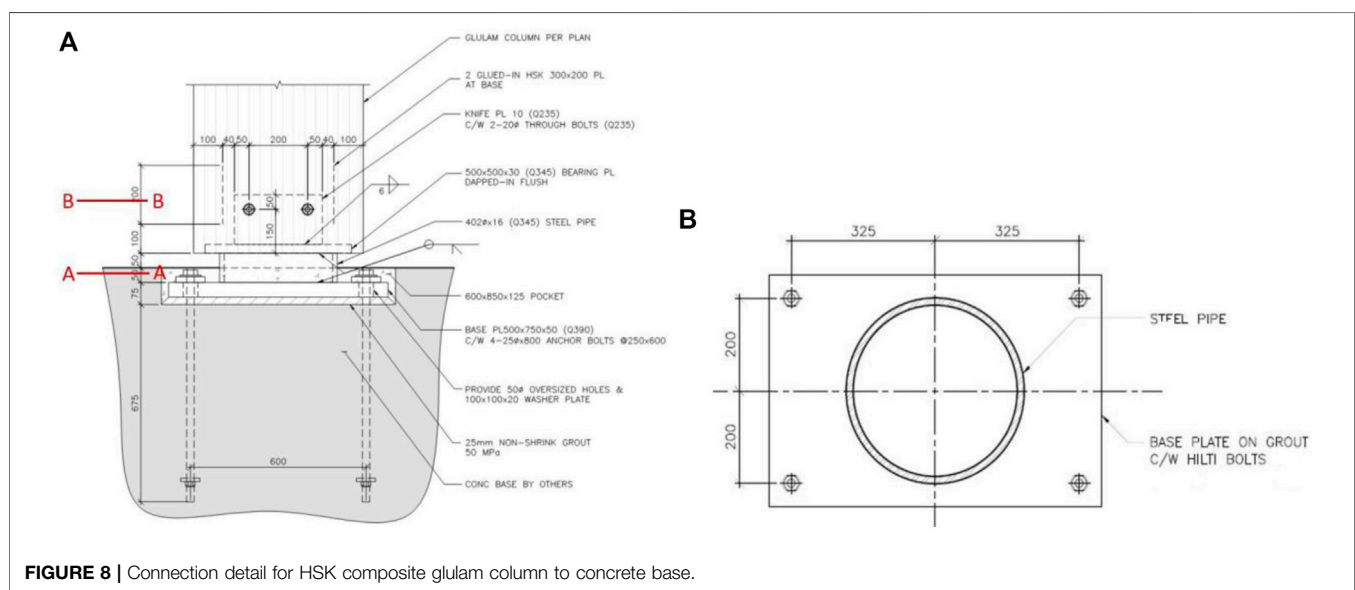
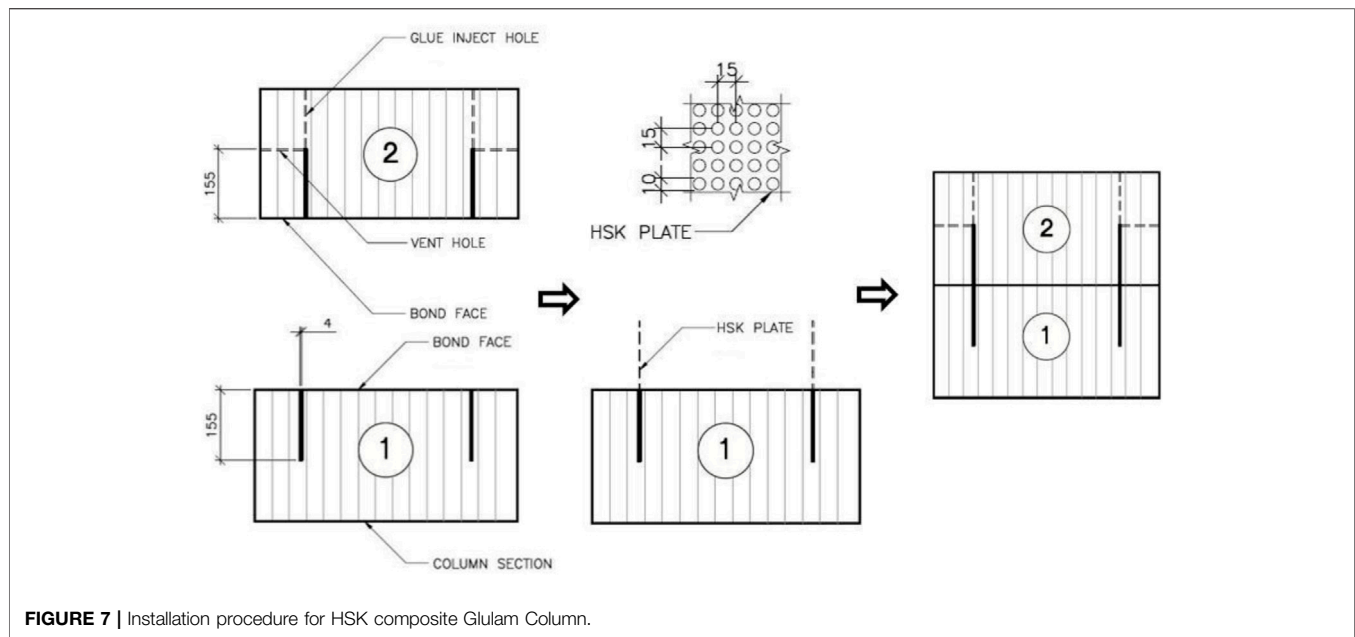
FIGURE 6 | Design loads for glulam column.

Foundation

Foundation design depends on the several factors like site location and soil conditions. Guizhou is a mountainous province with higher altitudes at the eastern end of the Yungui Plateau. According to Geotechnical Engineering Investigation Code of China (GB50021-2001 Code for Geotechnical engineering Investigation, 2002), the subsurface soil conditions at the

proposed development site consisted of miscellaneous filling soil (Q_4^{ml}) and moderately weathered argillaceous-siliceous rock, which are selected as the foundation bearing layer based on the geological investigation report.

Shallow foundations are recommended for most concrete columns as they located on rocks. The columns in the southwest corner adopt traditional manual hole digging pile



because of the soft fill dirt. Raft footing are utilized for foundation of cores on the base and rock bolts are applied at critical locations to provide adequate anti-overturning moment. The reinforced cast-in-place concrete sheets are placed on top of layered compacted soil, and sufficient soft fill dirt is substituted in the southwest corner in order to reduce the uneven settlement.

Gravity Load Resisting System

Glulam Beam and Timber-Concrete Composite Beam

The timber-concrete hybrid building was designed for seismic precautionary intensity 7 with a basic acceleration of ground motion 0.1 g according to the GB50011-2010 (GB50011-2010 Code for Seismic Design of Buildings, 2016) for a site class II in

Guizhou, China. The dead load for typical timber floor was 2.5 kPa, for concrete floor was 5.0 kPa and for timber roof was 1.5 kPa respectively. On the roof, the live load was considered as 0.5 kPa. In the typical floors, the live load for the guest rooms was 2.0 kPa, for public space (including balcony, corridors, lobby, tea room and private room) was 2.5 kPa, for stairs was 3.5 kPa, for mechanical/electrical space was 7 kPa, and for partition was 1.0 kPa respectively. The reference snow pressure and reference wind pressure with a 50-year return period was 0.2 and 0.3 kPa respectively. All the load values were obtained based on GB 50009-2012 (GB 50009-2012 Load code for the design of building structures, 2012) and they are typical for Chinese hotels.

The gravity system for this 10-storey timber-concrete hybrid structure adopts Glulam frame system as shown in **Figure 1**. The

Load Combination For Each Storey															
Floor Level	Floor Height [m]	(Short-D) [kN]	(Long-D+0.5L) [kN]	(Short-D) [kN]	(Long-D+0.5L) [kN]	(Short-D) [kN]	(Long-D+0.5L) [kN]	(Short-D) [kN]	(Long-D+0.5L) [kN]	(Short-D) [kN]	(Long-D+0.5L) [kN]	(Short-D) [kN]	(Long-D+0.5L) [kN]	(Short-D) [kN]	(Long-D+0.5L) [kN]
9	3.9	278.2	366.5	278.2	366.5	278.2	366.5	278.2	366.5	278.2	366.5	278.2	366.5	278.2	366.5
8	3.9	351.0	469.4	351.0	469.4	351.0	469.4	351.0	469.4	351.0	469.4	351.0	469.4	351.0	469.4
7	3.9	310.8	403.8	310.8	403.8	310.8	403.8	310.8	403.8	310.8	403.8	310.8	403.8	310.8	403.8
6	3.9	310.8	403.8	310.8	403.8	310.8	403.8	310.8	403.8	310.8	403.8	310.8	403.8	310.8	403.8
5	3.9	310.8	403.8	310.8	403.8	310.8	403.8	310.8	403.8	310.8	403.8	310.8	403.8	310.8	403.8
4	3.9	310.8	403.8	310.8	403.8	310.8	403.8	310.8	403.8	310.8	403.8	310.8	403.8	310.8	403.8
3	3.9	310.8	403.8	310.8	403.8	310.8	403.8	310.8	403.8	310.8	403.8	310.8	403.8	310.8	403.8
2	5.1	201.0	301.5	201.0	301.5	201.0	301.5	201.0	301.5	201.0	301.5	201.0	301.5	201.0	301.5
Floor Built		2~9		3~9		4~9		5~9		6~9		7~9		8~9	

Glulam Column Shortening for Individual Storey															
Floor Level	Floor Height [m]	(Short-D) [mm]	(Long-D+0.5L) [mm]	(Short-D) [mm]	(Long-D+0.5L) [mm]	(Short-D) [mm]	(Long-D+0.5L) [mm]	(Short-D) [mm]	(Long-D+0.5L) [mm]	(Short-D) [mm]	(Long-D+0.5L) [mm]	(Short-D) [mm]	(Long-D+0.5L) [mm]	(Short-D) [mm]	(Long-D+0.5L) [mm]
9	3.9	0.276	0.531	0.276	0.531	0.276	0.531	0.276	0.531	0.276	0.531	0.276	0.531	0.276	0.531
8	3.9	0.348	0.680	0.348	0.680	0.348	0.680	0.348	0.680	0.348	0.680	0.348	0.680	0.348	0.680
7	3.9	0.308	0.585	0.308	0.585	0.308	0.585	0.308	0.585	0.308	0.585	0.308	0.585	0.308	0.585
6	3.9	0.308	0.585	0.308	0.585	0.308	0.585	0.308	0.585	0.308	0.585	0.308	0.585	0.308	0.585
5	3.9	0.308	0.585	0.308	0.585	0.308	0.585	0.308	0.585	0.308	0.585	0.308	0.585	0.308	0.585
4	3.9	0.308	0.585	0.308	0.585	0.308	0.585	0.308	0.585	0.308	0.585	0.308	0.585	0.308	0.585
3	3.9	0.308	0.585	0.308	0.585	0.308	0.585	0.308	0.585	0.308	0.585	0.308	0.585	0.308	0.585
2	5.1	0.260	0.571	0.260	0.571	0.260	0.571	0.260	0.571	0.260	0.571	0.260	0.571	0.260	0.571
Floor Built		2~9		3~9		4~9		5~9		6~9		7~9		8~9	

Total Shortening for Each Storey		
Floor Level	(Short-D) [mm]	(Long-D+0.5L) [mm]
9	0.276	0.531
8	0.623	1.211
7	0.921	1.796
6	1.239	2.382
5	1.547	2.967
4	1.855	3.552
3	2.163	4.137
2	2.424	4.708

(Short Term-Dead)	
E _c	11700 [Mpa]

Column Size	
b	580 [mm]
h	580 [mm]

(Long Term-Dead+0.5Live)	
E _c	8000 [Mpa]

FIGURE 9 | Shortening of the glulam column.

TABLE 4 | Comparison of base shear under equivalent static method (ESM) and mode-superposition method in ETABS.

Direction	Fundamental period (s)	ESM (kN)	ETABS (kN)	ESM/ETABS
East-West (X-X)	0.59	2,474	3,158	0.78
South-North (Y-Y)	0.49	2,954	3,759	0.79

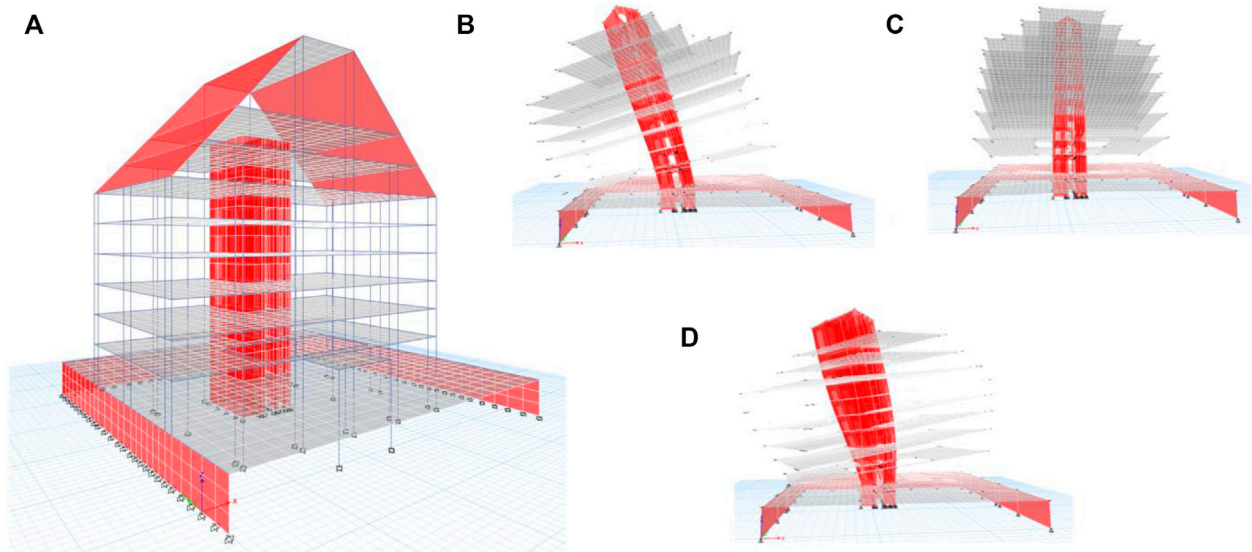


FIGURE 10 | Model Shapes of the LLRS: (A) ETABS Mode of the LLRS; (B) First Mode: Translation in East-West; (C) Second Mode: Translation in South-North; (D) Third Mode: Torsion.

material properties of the glulam timber in this research are based on the products supplied by YF, the structural member specifications and material parameters are shown in Table 1.

The glulam girders are the main framing beams which play a role in overall stability of the structure frame. They span between 9 and 11.1 m in north-south direction with secondary glulam

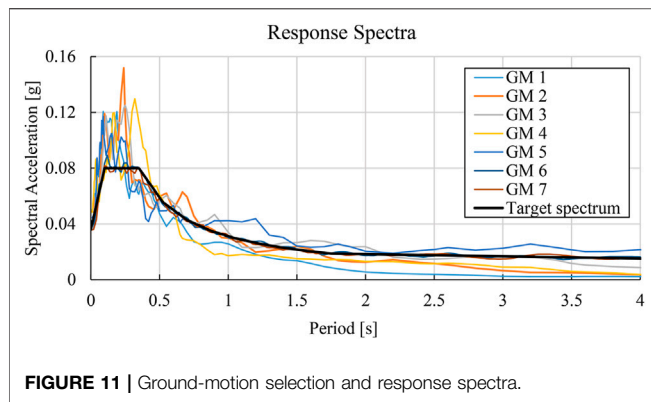


FIGURE 11 | Ground-motion selection and response spectra.

beams placed on top in east-west direction to support the OSB floor slabs and the depth of girders is considered as 580 mm in order to satisfy the structural clearance requirements.

According to the design loads and the tributary-area design methods, the 290×2-290 mm cross section was selected for the glulam beam girders and 240 × 400 mm cross section was selected for secondary glulam beams. **Table 2** summarizes the glulam beam sizes with corresponding utilizations as ratio of resistance vs. demand.

For some main girders which support high design loads with the span-depth ratio of 19 exceeds the common usage of glulam beams (normally round 12~14), the timber (glulam)—concrete composite (TCC) beams are used to meet the structural strength, stiffness, and vibration performance requirements.

The applied TCC beams focus on optimizing performance and material requirements by engineering a structural connection between glulam and concrete components. Structural efficiency is gained by creating composite action between these two materials. The efficiency of TCC beams depends strongly on the shear connection employed and can be expressed as a coefficient between 0 and 1. If the two materials work together perfectly as one beam and no slip between the contacting surfaces, the coefficient can be assumed to be 1, in this case, composite sections can be evaluated based on Euler-Bernoulli beam theory that plane sections remain plane, as shown in **Figure 3A**; if the two materials work separately and there is no composite action, the coefficient is assumed to be 0, as shown in **Figure 3C**. For most engineered TCC beams, partial composite action can be achieved, as shown in **Figure 3B**, with more rigid shear connections, leading to higher coefficients closer to 1. To guarantee sufficient stiffness

and strength of the glulam-concrete composite beam, the glued-in Holz-Beton-Verbund (HBV) shear connector (TiComTec Technical dossier HBV-systems, 2011), as shown in **Figure 4**, is used.

The HBV system consists of an expanded steel mesh with 2.5 mm thickness that is glued into a saw cut in the timber member and then concrete is cast on top. The adhesive and the concrete fill the voids in the mesh creating a mechanical “adhesive dowel” connection, which, if designed properly, will lead to the steel mesh yielding before adhesive failure (Gerber and Tannert, 2015). Glued in rebar, both angled and straight, can help push the failure into the timber beam after full plasticization of the connectors (Ceccotti et al., 2007). The HBV has been successfully tested and approved and maintains a high degree of stiffness and load bearing capacity even through an unsupported separation layer (Lehringer and Gabriel, 2014). The composite coefficient for HBV system is as high as 0.85 and the stiffness of the TCC beams using this type of connector can reach more than three times of traditional glulam beam. The design of the timber-concrete composite beam is based on Eurocode 5 (Steer, 2001), the capacity of the concrete, timber and the HBV connector components that constitute the TCC beam all need to be checked. As shown in **Table 3**, there are four different types of the TCC beam that are marked as TCC₁ to TCC₄, the location of the TCC beams in the floor framing and their design details are presented in **Figure 5**.

HSK Composite Glulam Columns

Similar to the glulam beams, the size selection for glulam columns are also based on the Chinese timber building designing codes (GB 50009-2012 Load code for the design of building structures, 2012) (GB 50005-2017: Standard for design of timber structures, 2017; GB 50206-2012 Code for construction quality acceptance of timber structures, 2012; GB T 50329 2002, 2002). Based on the vertical load take-off, the design loads for the glulam column on the bottom floor are shown in **Figure 6**, typical column size is designed accordingly as 580 × 580 mm, the ratio of compression resistance versus Demand in the ultimate limit state is 63.3%, 71.6% in 1-hour fire resistance and 99.5% in 2-hour fire resistance respectively.

Considering the limitation of manufacturing technology, two 290 × 580 mm glulam columns are designed and combined using Holz-Stahl-Komposit (HSK) connector as one single column. The HSK connector is based on adhesively bonded perforated steel plates. The holes in the plate are filled by the adhesive after

TABLE 5 | Selected ground motions.

Type	Result ID	RSN	Scaling factor	Earthquake name	Year	Station name	Magnitude	Rrup (km)
Historical	GM 1	72	0.275	San Fernando	1971	Lake Hughes #4	6.6	25.07
	GM 2	1006	0.132	Northridge-01	1994	LA - UCLA Grounds	6.7	22.49
	GM 3	4205	0.674	Niigata_ Japan	2004	NIG015	6.6	40.14
	GM 4	4870	0.265	Chuetsu-oki_ Japan	2007	Horinouchi Uonuma City	6.8	34.51
	GM 5	5750	1.001	Iwate_ Japan	2008	YMT007	6.9	58.12
Artificial	GM 6	AR221_932_1	1.000	n/a	n/a	n/a	n/a	n/a
	GM 7	AR221_932_2	1.000	n/a	n/a	n/a	n/a	n/a

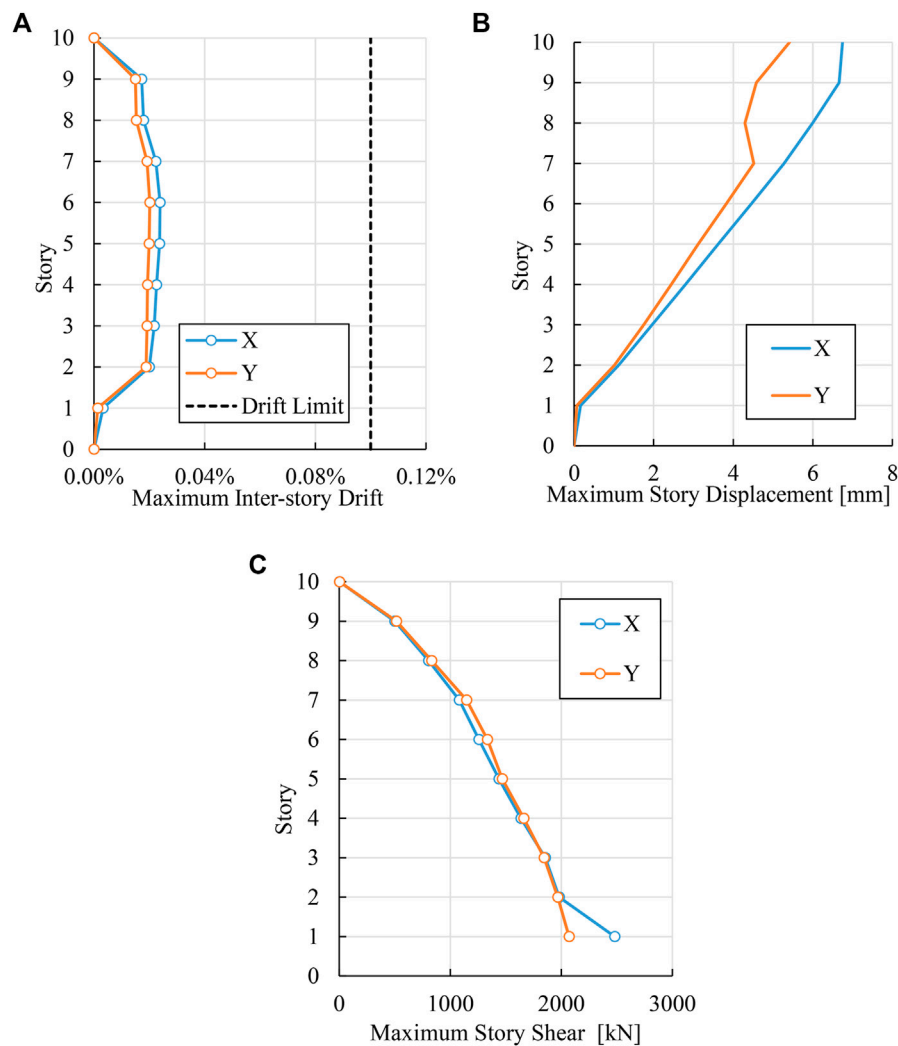


FIGURE 12 | Seismic Response, (A) maximum inter-story drift; (B) maximum story displacement; (C) maximum story shear.

inserting it into the wood, forming so-called “Adhesive Dowels”. The “bond capacity” is based on the sum of the individual adhesive dowel capacities which has been proved to equal 0.8kN (Bathon et al., 2014). As long as enough adhesive dowels are provided, the connection can be very stiff and the two glulam columns can perfectly work together as a whole.

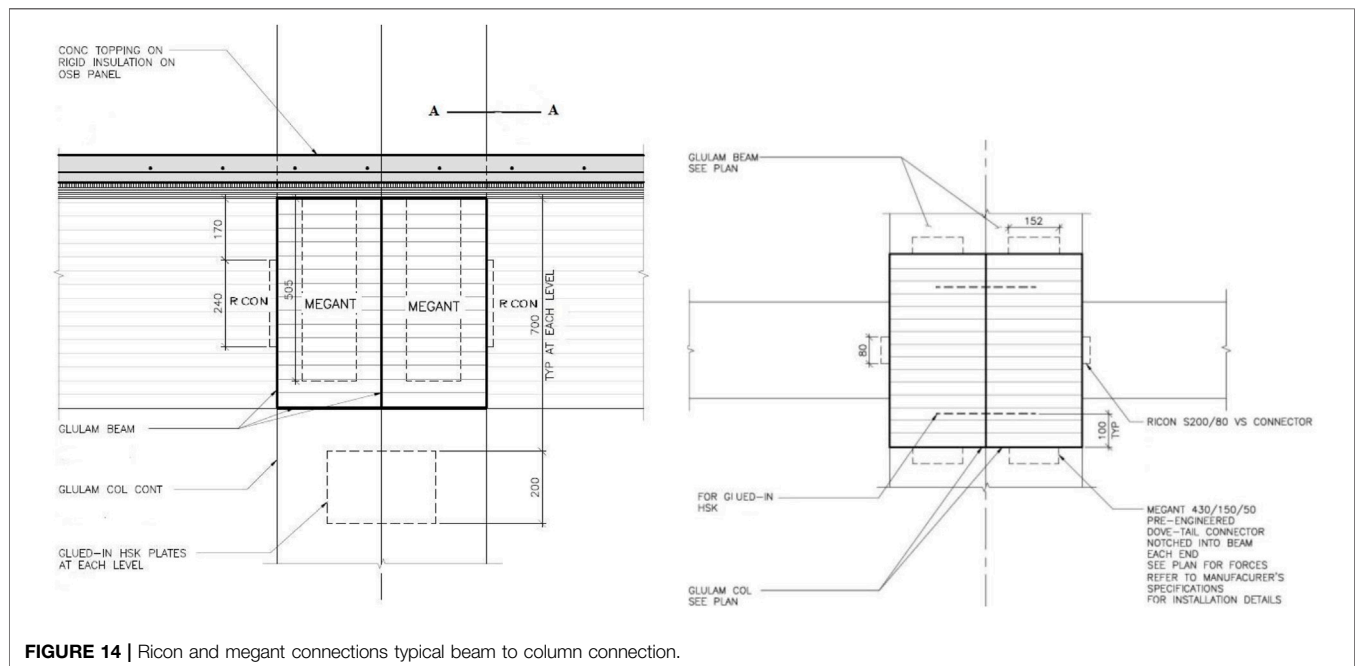
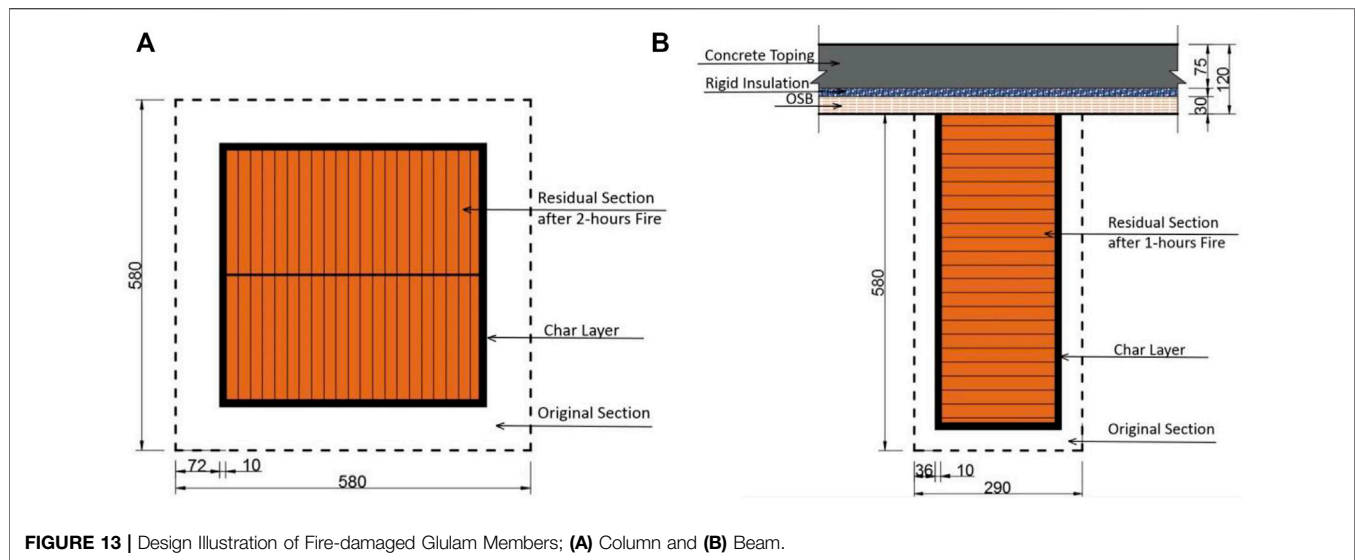
As shown in **Figure 7**, the manufacturing process includes three steps. Firstly, providing slot at the composite face of each segment column; secondly, injecting glue in segment 1 slots and inserting HSK plats; thirdly, combing segment 1 and 2 to form a composite column, injecting glue via holes in segment 2 until glue comes out from vent holes. **Figure 7** shows the connection detail for the HSK composite glulam column to the concrete base.

Aside from the calculation of axial compression capacity and stability, the shortening of the glulam column under the compression force should also be taken into account, because the differential shortening between columns and concrete core walls will cause additional stresses on the members.

Figure 9 presents the detailed shortening calculation of the glulam column which carries the largest compression force. The results shows that the maximum axial shortening of the column under long term loading is only around 5 mm. As the concrete core walls are very stiff, the long-term deformation can be ignored. The distance between them is around 8 m, that results in the slop changes of the floor is only around 0.6% and the stress influence on the floor slab can be ignored.

Lateral Load Resisting System Design and Seismic Analysis

The concrete core walls for this 10-storey business hotel act as the Lateral Load Resisting System (LLRS) to resist the seismic and wind loads. In seismic design, the core together with the fundamental concrete walls are modelled in ETABS and verified with the hand calculation based on the Equivalent Static Method (ESM).



The calculation of ESM for seismic design is simple, while it is only suitable for building less than 40 m based on seismic design code (GB50011-2010 Code for Seismic Design of Buildings, 2016). As the height of this 10-storey business hotel (47 m) exceeds the limitation, and the mode analysis in ETABS is needed. The mode-superposition method is a linear dynamic-response procedure which evaluates and superimposes free-vibration mode shapes to characterize displacement patterns. Mode shapes describe the configurations into which a structure will naturally displace. The obtained base shears for these two methods were compared in **Table 4**.

The linear dynamic analysis in ETABS considered twelve vibration modes, the model mass participation ratio reaches 95% which meets the code requirements. The dynamic analysis shows that the fundamental vibration mode contributes the majority of the base shear and the higher-mode effect on the seismic responses can be ignored for this timber-based hybrid tall building.

The first three vibration modes are shown in **Figure 10**. The fundamental and second vibration modes are translational motion and the third one is torsion. As the torsional stiffness of the concrete core is large, the torsional deformation is controllable. Also, the calculated torsional sensitivity ratio

equals 1.1 which is smaller than 1.7 limitation in the seismic design code, that means torsional effects can be ignored for this structure.

A total of seven ground motion records, including five historical strong earthquake records and two artificial records, were selected for the analyses. According to the GB50011-2010 (GB50011-2010 Code for Seismic Design of Buildings, 2016), for the Jianhe County in Guizhou with 7 seismic fortification and peak ground acceleration of 0.1g, the maximum seismic influence coefficient α_{\max} is set as 0.08 and the corresponding target spectrum is plotted in **Figure 11**. Those five earthquake records were selected from the Pacific Earthquake Engineering Research (PEER) database (PEER, 2013), as summarized in **Table 5**. All the selected records were linearly scaled so that their response spectra matched to the target design spectrum of the building site, as shown in **Figure 11**.

Figure 12 shows the mean seismic response results where the blue line represents the translation response in East-West (E-W) direction (X) and red line represents the North-South (N-S) direction (Y). Overall the building exhibited adequate seismic resistance that the maximum inter-story drifts were 0.024 and 0.020% for both directions, which were below the drift limit of 1/1000. The building had a maximum roof displacement of 6.8 and 5.4 mm in the E-W and NS directions, respectively, with a base shear of 2,480 and 2070 kN.

With regard to wind resisting analysis, the calculated maximum wind design force is in the south-west direction and equals 1758kN, which is only 71% of seismic design load in that direction. Therefore, the seismic load governs the design of the LLRS. Besides, as the fundamental period is less than 1s, the structural lateral response (displacement and acceleration) resulting from the wind almost has no effect to the comfort of living.

Fire Design

The fire design is of great importance for this project as the fire resistance requirements for timber buildings in China are very strict. To meet these requirements, the following strategy was chosen. First, the concrete topping on the floor slabs is an effective fire and smoke barrier. The 30 mm thick OSB floor slab belongs to category of heavy timber which also has some extent of fire protection. Even it burns, the 75 mm thick reinforced concrete topping can provide additional protection during a fire. Besides, as the main components of the gravity system, the glulam columns are designed for 2-hour fire-resistance, and the glulam girders and secondary glulam beams are designed for 1-hour fire resistance. The charring rate is considered 0.6 mm/min and 10 mm addition char layer is reduced to obtain the residual cross section for load capacity calculation (Karacabeyli and Desjardins, 2011). The design illustration of fire-damaged glulam members is shown in **Figure 13**.

Another fire protection consideration is using concealed connections, RICON and MEGANT connections. The RICON connector is a pre-engineered post-to-beam connector, a system manufactured from mild steel with a welded collar bolt. It consists

of two identical parts, one installed in the primary timber member and the other in the secondary member. The MEGANT connector is also a pre-engineered post-to-beam connector, a system manufactured from aluminum with connector plates and threaded rod to secure the connection. These two types of connections have been tested for the North American mass timber market and are applied in the girder to secondary beam joints and girder to column joints in this project, as shown in **Figure 14**.

Figure 14 gives the connection application detail in glulam beam to column joints. The RICON and MEGANT, as the pre-engineered connections, can be installed fully concealed or visible and provide large shear capacity, not only suitable for timber to timber, but also can be used for connecting the timber element to the concrete core walls.

CONCLUSION

This paper presented the design detail of a 10-storey timber-concrete hybrid building in China. The procedure includes foundation design, gravity system design, lateral load resisting system design, seismic analysis and the fire resistance design. It meets the requirements of Chinese building code with the advanced timber design technology and the structural analysis results proved the accuracy of the design, it can serve as guidance for subsequent timber-based hybrid high-rise structures and will promote the development of novel construction systems in China.

DATA AVAILABILITY STATEMENT

The original contributions presented in the study are included in the article/supplementary material, further inquiries can be directed to the corresponding author.

AUTHOR CONTRIBUTIONS

XZ: conceptualization, methodology, validation, analysis, writing-original draft, LX: validation, analysis, WH: validation, investigation, YL: conceptualization, validation, PL: conceptualization, investigation, writing-review and editing.

FUNDING

The authors would like to thank the National Key R&D Program of China (Grant Nos. 2021YFF0500804), the National Natural Science Foundation of China (Grant Nos. 52108192); the OEICDI fund (Grant Nos. B13041); the Entrepreneurship and Innovation Support Program for Overseas-educated student in Chongqing China (Grant Nos. CX2021085); This study also received funding from MITCAS Canada through an Elevate grant with Equilibrium Consulting Inc.

REFERENCES

- Abrahamsen, R. (2017). "Mjøstårnet-Construction of an 81 M Tall Timber Building," in *Internationales Holzbau-Forum IHF*, 1–12.
- Andersen, J. H., Rasmussen, N. L., and Ryberg, M. W. (2021). Comparative Life Cycle Assessment of Cross Laminated Timber Building and Concrete Building with Special Focus on Biogenic Carbon. *Energy and Buildings*, 111604.
- Bathon, L., Bletz-Mühlendorfer, O., Schmidt, J., and Diehl, F. (2014). *Fatigue Design of Adhesive Connections Using Perforated Steel Plates*. Quebec, CA: World Conference for Timber Engineering.
- Buchanan, A. (2007). Energy and CO₂ Advantages of Wood for Sustainable Buildings. *New Zealand Timber Des. J.* 15 (1), 11. doi:10.1016/j.soilbio.2014.05.017
- Buchanan, A. H., John, S., and Love, S. (2012). LCA and Carbon Footprint of Multi-Storey Timber Buildings Compared with Steel and concrete Buildings. *World* 15, 19
- Ceccotti, A., Fragiocomo, M., and Giordano, S. (2007). Long-term and Collapse Tests on a Timber-concrete Composite Beam with Glued-In Connection. *Mater. Struct.* 40 (1), 15–25. doi:10.1617/s11527-006-9094-z
- De Wolf, C., Pomponi, F., and Moncaster, A. (2017). Measuring Embodied Carbon Dioxide Equivalent of Buildings: A Review and Critique of Current Industry Practice. *Energy and Buildings* 140, 68–80. doi:10.1016/j.enbuild.2017.01.075
- E. Karacabeyli and R. Desjardins (Editors) (2011). *CLT Handbook* (Vancouver: FP Innovations).
- Foliente, G. C. (2000). "History of Timber Construction," in *Wood Structures: A Global Forum on the Treatment, Conservation, and Repair of Cultural Heritage* (ASTM International).
- Foster, R. M., Reynolds, T. P. S., and Ramage, M. H. (2016). Proposal for Defining a Tall Timber Building. *J. Struct. Eng.* 142 (12), 02516001. doi:10.1061/(asce)st.1943-541x.0001615
- Gb 50009-2012 Loadcodeforthedesigntofbuildingstructures (2012). *National Standards ofthePeople's Republic ofChina* ,Ministry ofConstruction ,PRC. Beijing: China Building Industry Press.
- GB 50010-2012: Code for design of concrete structures (2015). *National Standards of the People's Republic of China, Ministry of Construction*, PRC. Beijing: China Building Industry Press.
- Gb 50206-2012 Code for construction quality acceptance of timber structures (2012). *National Standards of the People's Republic of China, Ministry of Construction*, PRC. Beijing: China Building Industry Press.
- Gb T 50329 2002 (2002). *Technical Standard for Methods Testing of Timber Structures*. Beijing: China Building Industry Press.
- Gb T 50708 (2012). *Technical Standard for glued laminated timber structures*. Beijing: China Building Industry Press.
- GB50011-2010 Code for Seismic Design of Buildings (2016). *National Standards of the People's Republic of China, Ministry of Construction*, PRC. Beijing: China Building Industry Press.
- GB50016-2014: Code for Building Design on Fire protection (2018). *National Standards of the People's Republic of China, Ministry of Construction*, PRC. China Building Industry Press, Beijing.
- Gb50021-2001 Code for Geotechnical engineering Investigation (2002). *National Standards of the People's Republic of China, Ministry of Construction*, PRC. Beijing: China Building Industry Press.
- Gb5005-2017: Standard for design of timber structures (2017). *National Standards of the People's Republic of China, Ministry of Construction*, PRC. Beijing: China Building Industry Press.
- Gerber, A., and Tannert, T. (2015). "Timber-concrete Composites Using Flat-Plate Engineered wood Products," in *ASCE Structures Congress (USA)* (Portland). doi:10.1061/9780784479117.201
- Green, M., and Karsh, J. E. (2012). *Tall wood -The Case for Tall wood Buildings*. Vancouver: Wood Enterprise CoalitionCanada.
- He, M., Tao, D., and Li, Z. (2016). Research Progress of Multi-story and High-Rise Timber and Timber Hybrid Structures. *J. Building Structures* 37 (10), 1–9. doi:10.14006/j.jzjgxb.2016.10.001
- Hristovski, V., Dujic, B., Stojmanovska, M., and Mircevka, V. (2013). Full-scale Shaking-Table Tests of XLam Panel Systems and Numerical Verification: Specimen 1. *J. Struct. Eng.* 139 (11), 2010–2018. doi:10.1061/(asce)st.1943-541x.0000754
- Izzi, M., Casagrande, D., Bezzi, S., Pasca, D., Follesa, M., and Tomasi, R. (2018). Seismic Behaviour of Cross-Laminated Timber Structures: A State-Of-The-Art Review. *Eng. Structures* 170, 42–52. doi:10.1016/j.engstruct.2018.05.060
- Karol, S., Jianli, H., Isaac, G., Weiqi, X., Subo, W., and Zitong, C. (2018). July)Feasibility Study on Further Utilization of Timber in ChinaIOP Conference Series: Materials Science and Engineering. *IOP Conf. Ser. Mater. Sci. Eng.* 383 (No. 1), 012029. doi:10.1088/1757-899x/383/1/012029
- Kuilen, J. W. G. V. D., Ceccotti, A., Xia, Z., and He, M. (2011). Very Tall Wooden Buildings with Cross Laminated Timber. *Proced. Eng.* 14, 1621–1628. doi:10.1016/j.proeng.2011.07.204
- Lam, F., He, M., and Yao, C. Example of traditional tall timber buildings in China the Yingxian pagoda. *Struct. Eng. Int.* 18, 126–129. doi:10.2749/101686608784218743
- Lehringer, C., and Gabriel, J. (2014). Review of Recent Research Activities on One-Component PUR-Adhesives for Engineered wood Products. *Mater. joints timber structures*, 405–420. doi:10.1007/978-94-007-7811-5_37
- Li, B., Cai, L., Wang, K., and Zhang, Y. (2016). Prediction of the Residual Strength for Durability Failure of concrete Structure in Acidic Environments. *J. Wuhan Univ. Technol.-Mat. Sci. Edit.* 31 (2), 340–344. doi:10.1007/s11595-016-1373-0
- Li, P., and Wang, H. (2021). A Novel Strategy for the Crossarm Length Optimization of PSSCs Based on Multi-Dimensional Global Optimization Algorithms. *Eng. Structures* 238, 112238. doi:10.1016/j.engstruct.2021.112238
- Li, Z., Zhou, R., He, M., and Sun, X. (2018). August)Modern Timber Construction Technology and Engineering Applications in ChinaProceedings of the Institution of Civil Engineers-Civil Engineering. *Thomas Telford Ltd* 172 (5), 17. doi:10.1680/jcienv.18.00024
- Peer (2013). *Pacific Earthquake Engineering Research (PEER) NGA-West 2 Database*. Berkeley, CA, USA.
- Poirier, E., Moudgil, M., Fallahi, A., Staub-French, S., and Tannert, T. (2016). *Design and Construction of a 53-Meter-Tall Timber Building at the university of British Columbia*. Vienna, Austria: Proceedings of WCTE.
- Ramage, M., Foster, R., Smith, S., Flanagan, K., and Bakker, R. (2017). Super Tall Timber: Design Research for the Next Generation of Natural Structure. *The J. architecture* 22 (1), 104–122. doi:10.1080/13602365.2016.1276094
- Ritter, M., Skog, K., and Bergman, R. (2011). *Science Supporting the Economic and Environmental Benefits of Using wood and wood Products in green Building constructionGeneral Technic Report FPL-GTR-206*. Washington, D.C.: Unites States Department of Agriculture, Forest Service, Forest Products Laboratory.
- Robertson, A., Lam, F., and Cole, R. (2012). A Comparative Cradle-To-Gate Life Cycle Assessment of Mid-rise Office Building Construction Alternatives: Laminated Timber or Reinforced Concrete. *Buildings* 2012 (2), 245–270. doi:10.3390/buildings2030245
- Ryberg, M. W., Ohms, P. K., Möller, E., and Lading, T. (2021). Comparative Life Cycle Assessment of Four Buildings in Greenland. *Building Environ.* 204, 108130. doi:10.1016/j.buildenv.2021.108130
- Steer, P. J. (2001). EN1995 Eurocode 5: Design of Timber structuresProceedings of the Institution of Civil Engineers-Civil Engineering. *Proc. Inst. Civil Eng. - Civil Eng.* 144 (6), 39–43. doi:10.1680/cien.2001.144.6.39
- Tannert, T., and Moudgil, M. (2017). Structural Design, Approval, and Monitoring of a UBC Tall wood Building. *Structures Congress*, 541–547. doi:10.1061/9780784480410.045
- TiComTec Technical dossier Hbv-systems (2011). Retrieved from <https://ticomtec.de/en/hbvsystems/>.

- Wimmers, G. (2017). Wood: a Construction Material for Tall Buildings. *Nat. Rev. Mater.* 2 (12), 1–2. doi:10.1038/natrevmats.2017.51
- Zhang, X., Azim, M. R., Bhat, P., Popovski, M., and Tannert, T. (2017). Seismic Performance of Embedded Steel Beam Connection in Cross-Laminated Timber Panels for Tall-wood Hybrid System. *Can. J. Civ. Eng.* 44 (8), 611–618. doi:10.1139/cjce-2016-0386
- Zhang, X., Fairhurst, M., and Tannert, T. (2016). Ductility Estimation for a Novel Timber–Steel Hybrid System. *J. Struct. Eng.* 142 (4), E4015001. doi:10.1061/(asce)st.1943-541x.0001296
- Zhang, X., Pan, Y., and Tannert, T. (2021). The Influence of Connection Stiffness on the Dynamic Properties and Seismic Performance of Tall Cross-Laminated Timber Buildings. *Eng. Structures* 238, 112261. doi:10.1016/j.engstruct.2021.112261
- Zhang, X., Shahnewaz, M., and Tannert, T. (2018). Seismic Reliability Analysis of a Timber Steel Hybrid System. *Eng. Structures* 167, 629–638. doi:10.1016/j.engstruct.2018.04.051

Conflict of Interest: This study received funding from Equilibrium Consulting Inc. The funder had the following involvement with the study: the gravity system design, lateral load resisting system design and the fire design.

Publisher's Note: All claims expressed in this article are solely those of the authors and do not necessarily represent those of their affiliated organizations, or those of the publisher, the editors and the reviewers. Any product that may be evaluated in this article, or claim that may be made by its manufacturer, is not guaranteed or endorsed by the publisher.

Copyright © 2022 Zhang, Xuan, Huang, Yuan and Li. This is an open-access article distributed under the terms of the Creative Commons Attribution License (CC BY). The use, distribution or reproduction in other forums is permitted, provided the original author(s) and the copyright owner(s) are credited and that the original publication in this journal is cited, in accordance with accepted academic practice. No use, distribution or reproduction is permitted which does not comply with these terms.



Effect of Extracted Titanium Tailing Slag on the Properties of Alkali-Activated Fly Ash-Ground Blast Furnace Slag Binder

Shuping Wang¹, Jingjing Li¹, Xiaoxin Yun¹, Xuwei Lv¹, Yujie Zhao² and Zhigang Zhang^{3*}

¹College of Materials Science and Engineering, Chongqing University, Chongqing, China, ²Pangang Group Engineering Technology Co., Ltd, Panzhihua, China, ³School of Civil Engineering, Chongqing University, Chongqing, China

OPEN ACCESS

Edited by:

Kequan Yu,
Tongji University, China

Reviewed by:

Jun Liu,
Shenzhen University, China
Lili Kan,
University of Shanghai for Science and
Technology, China

*Correspondence:

Zhigang Zhang
zhangzg@cqu.edu.cn

Specialty section:

This article was submitted to
Structural Materials,
a section of the journal *Frontiers in
Materials*

Received: 18 December 2021

Accepted: 29 December 2021

Published: 28 February 2022

Citation:

Wang S, Li J, Yun X, Lv X, Zhao Y and
Zhang Z (2022) Effect of Extracted
Titanium Tailing Slag on the Properties
of Alkali-Activated Fly Ash-Ground
Blast Furnace Slag Binder.
Front. Mater. 8:838736.
doi: 10.3389/fmats.2021.838736

The extracted titanium tailings slag (TS) is a by-product of titanium extraction from the blast furnace slag. Its chemical composition is similar to that of ground granulated blast furnace slag (GGBS), but the relatively lower reactivity limited its utilization as a supplementary cementitious material. In this study, the reactivity of TS was improved by mechanical grinding, and the optimum property of finely ground TS was selected to replace fly ash (FA) in the alkali-activated FA-GGBS binder. The influence of TS content on the fluidity, setting time, and compressive strength of the ternary binder was investigated. X-Ray diffraction, Fourier-transform infrared spectroscopy, and scanning electron microscopy were used to analyze the effect of TS on the reaction process. Results showed that the optimum reactivity index of TS was 81.18% at 28 days when it was ground for 15 min in a ball mill. The highest compressive strength of the alkali-activated ternary binder was achieved when the replacement of FA by ground TS was 40%, and its 28-day compressive strength was 49.3 MPa, approximately 22% higher than the binder without TS. The addition of the TS would accelerate the reaction process of binder to form more products, including C-(A)-S-H and gismondine.

Keywords: alkali-activated material, extracted titanium tailings slag, reactivity, mechanical strength, reaction process

1 INTRODUCTION

The extracted titanium tailings slag (TS) was produced from titanium extraction blast furnace slag with high TiO₂ content by a process of high-temperature carbonization and low-temperature selective chlorination (Wang et al., 2008). It is mainly produced in the southwestern area of China, and the annual emission is approximately 90,000 tons at present (Sun et al., 2022). The main elements of TS are Ca, Mg, Al, Fe, Si, and Ti, and its chemical compositions are similar to those of ground granulated blast-furnace slag (GGBS). TS has a glassy structure with latent hydraulic property, indicating the potential application prospect in the field of building materials. However, it also contains mineral phases such as perovskite and diopside, causing a lower reactivity than that of GGBS (Zhang 2018; Yao 2019). Therefore, the utilization is limited.

To improve the utilization, some efforts have been made to prepare building materials including tetracalcium aluminoferrite cement (Hong 2014), porous heat insulation materials (Li et al., 2010), and bricks (Zhu et al., 2010). A few researchers focused on the mechanical grinding to improve the reactivity of industrial wastes due to the mechanical-chemical effect of breaking the Si-O and Al-O

bonds (Mucsi et al., 2015; Kumar et al., 2017). When TS was ground for 30 min, the reactivity index can reach 84% at 150 days. It was also reported that the microstructure of cement paste was more compacted by adding the ground TS, and the amount of $\text{Ca}(\text{OH})_2$ can be reduced attributed to the pozzolanic effect; thus, the interface between $\text{Ca}(\text{OH})_2$ and other hydration products was not so obvious and the durability of concrete was improved (Zhu et al., 2011).

Alkali activation is also considered as an effective method to produce cementitious materials from latent hydraulic industrial byproducts with substantial mechanical properties, and the emission of CO_2 is thought to be lower than Portland cement (Bumanis et al., 2017; Ameri et al., 2019; Moghadam et al., 2019; Beltrame et al., 2020; Biricik et al., 2021). Meanwhile, alkali-activated cementitious material is more durable than Portland cement when attacked by chemical substances. Many investigations have been conducted on the alkali-activated fly ash (FA), alkali-activated GGBS, and the hybrid binders (Moghadam et al., 2019; John et al., Giriya 2021). However, the alkali-activated FA usually showed long setting time and a low strength development rate (Temuujin et al., 2010; Pavithra et al., 2016; Soutsos et al., 2016), while the alkali-activated GGBS exhibits fast setting, high early strength but large drying shrinkage (Liu et al., 2016). In this case, the alkali-activated FA-GGBS, which generally has better performance, is in consideration, and some other types of industrial wastes and chemical agents were also applied to optimize the performance (Nath and Sarker 2014; Kuri et al., 2021; Nishanth and Patil 2021). Zhang et al. (2021) found that the flexural and compressive strength of alkali-activated FA mortars was improved by adding TS at 28 days. The values were 6.8 and 63.2 MPa, respectively, when 20% FA was substituted by TS, showing that TS is effective in promoting the mechanical properties of alkali-activated FA.

In the review, seldom investigation has focused on the influence of TS on the properties of alkali-activated FA-GGBS binders. The fluidity, setting time, strength development, and TS action mechanism in the alkali-activated materials is still unclear. This study aims to improve utilization of TS by mechanical grinding and alkali activation through preparing alkali-activated ternary binder. Since TS has a positive effect in alkali-activated cementitious system, FA was replaced by different contents of TS. The effects of TS content on the setting and hardening properties of alkali-activated ternary system were investigated. Furthermore, X-ray diffraction (XRD), Fourier-transform infrared (FTIR) spectroscopy, and scanning electron microscopy (SEM) were carried out to evaluate the microstructure evolution of the binder.

2 MATERIALS AND METHODS

2.1 Raw Materials

In this study, the fly ash was provided by a local power company. Its density was 2.54 g/cm^3 , the specific surface area was $405 \text{ m}^2/\text{kg}$, and the 28-day reactivity index was 86.8%. GGBS was supplied by a mineral admixture-making

TABLE 1 | Chemical composition of raw materials (wt.%)

	SiO_2	Al_2O_3	CaO	Na_2O	Fe_2O_3	MgO	Cl	TiO_2
FA	42.7	27.1	3.3	2.5	5.8	2.7	—	—
GGBS	35.06	14.42	38.66	0.43	0.34	7.93	—	—
TS	30.75	13.61	29.12	0.42	1.7	8.55	4.98	10.89

company in Hebei (China). The density was 2.88 g/cm^3 , the specific surface area was $431 \text{ m}^2/\text{kg}$, and 28-day reactivity index was 103%. TS was obtained from a local titanium dioxide-producing plant. Before being used, TS was oven dried at 105°C for 24 h until the free water was removed, followed by grinding at a ball mill for 15, 30, 45, and 60 min, respectively. Coarse particles larger than 0.075 mm were removed by sieving and the residues were adopted in this study. The chemical composition tested by X-ray fluorescence is listed in **Table 1**. The particle size distribution of materials was analyzed and the results are shown in **Figure 1A**. The D_{50} values of FA, GGBS, and TS were 27.75, 14.03, and $58.56 \mu\text{m}$, respectively. Their mineral phases were carried out by using X-ray diffraction (XRD) (**Figure 1B**). It can be seen that all these raw materials were mainly composed of glassy structure that the diffused peaks of TS and SG ranged from 23.5 to $34.9^\circ 2\theta$, and it appeared at 2θ of 23.3 – 36.9° for FA. In addition, TS contained crystalline structure including wuestite (d-spacings of 0.248, 0.215, and 0.152 nm). Quartz (d-spacings of 0.333 nm) and mullite (d-spacings of 0.537, 0.342, 0.338, and 0.269 nm) were involved in FA, and zoisite was contained in GGBS.

The alkali activator used for preparation of the alkali-activated cementitious material was water glass (sodium silicate solution) with moduli (n , $\text{SiO}_2/\text{Na}_2\text{O}$ molar ratio) of 1.2.17.57 g sodium hydroxide (NaOH) tablets that were dissolved directly into 100 g commercial water glass with modulus of 2.57 to adjust the modulus to 1.2. The content of Na_2O , SiO_2 , and H_2O of the original water glass was 11.91, 29.64, and 33.19%, respectively. The amount of water, which should be added to the water glass, was determined by the Na_2O equivalent content (mass ratio of Na_2O to solid materials = 12%) and the water to solid mass ratio ($w/s = 0.4$) of the paste. These materials were mixed homogeneously and kept for more than 24 h to make the alkali solution equivalently.

2.2 Experimental Methods

2.2.1 Preparation of Alkali-Activated Materials

The alkali-activated cementitious material was prepared by mixing the solid materials and alkali solution. In terms of the reference sample, the weight ratio between FA and GGBS was 7:3. The solid materials were mixed homogeneously for approximately 1 min before alkali solution was added in the mixture to prepare a paste. FA was replaced by TS with weight ratios ranging from 10 to 70% to investigate its influence on the setting and hardening properties of the paste. The paste was poured into cubic molds with a size of $40 \times 40 \times 40 \text{ mm}$ and cured at the standard condition with temperature of $20 \pm 2^\circ\text{C}$ and relative humidity (RH) $\geq 95\%$.

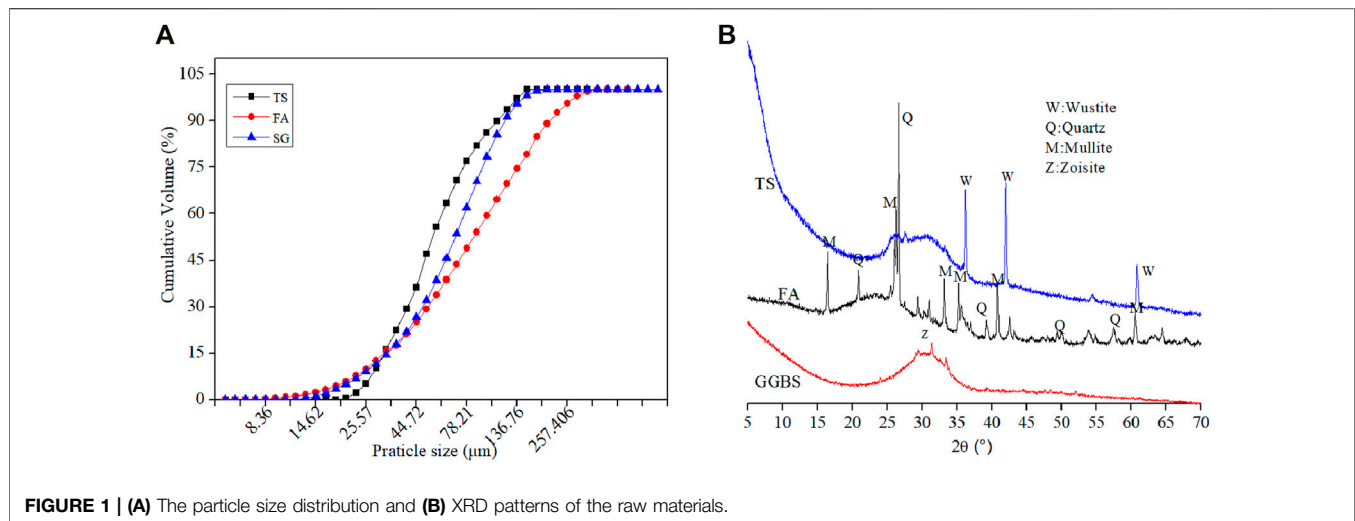


FIGURE 1 | (A) The particle size distribution and **(B)** XRD patterns of the raw materials.

2.2.2 Performance Test

The particle size distribution of FA, GGBS, and TS was analyzed using a Mastersizer 2000 laser diffraction analyzer. The specific surface area was measured by Blaine specific surface area tester according to the Chinese Standard GB/T 8074-2008 (GB/T 8074, 2008). The reactivity of these materials was measured following the Standard GB/T 1596-2017 (GB/T 1596, 2017). It was evaluated by the compressive strength ratios of blended cement mortar (70% Portland cement blended with 30% TS) to the Portland cement mortar at 7 and 28 days of curing, respectively. Setting time of the alkali-activated cementitious material was measured at $20 \pm 2^\circ\text{C}$ complying with GB/T 1346-2011 (GB/T 1346, 2011). The initial setting time was determined when the penetration depth of the initial setting needle was 36 ± 1 mm. The fluidity of alkali-activated cementitious material was tested according to GB/T 8077-2000 (GB/T 8077, 2000). The paste was poured into a mini-slump cone, and then the cone was lifted to allow the paste to flow freely for 30 s. The diameters of the spread were measured in two perpendicular directions, and the average value was the fluidity. Compressive strength of the hardened paste being cured at $20 \pm 2^\circ\text{C}$ with $\text{RH} \geq 95\%$ for 1, 3, and 28 days was measured by a hydraulic universal testing machine following the Standard GB/T 17671-1999 (GB/T 17671, 1999).

2.2.3 Microstructure Characterization

The sample at different curing ages was collected and immersed in ethanol for 7 days to stop its hydration. Humid samples were then dried at 45°C in a vacuum for 7 days before the microstructure analysis. The dried samples were ground in an agate bowl by hand, and the ground powders smaller than 0.075 mm were retained for XRD and FTIR testing. The mineral phases of the alkali-activated cementitious materials were analyzed by X-ray powder

diffraction (XRD; PANalytical X'Pert Powder). The scanning range of 2θ was from 5 to 70° , and the scanning rate was $2^\circ/\text{min}$ with a step of 0.02° . The functional groups of the hydration products of the alkali-activated cementitious material were characterized by FTIR spectroscopy (Nicolet iS50). SEM (Quattro S) was applied to investigate the morphology of the alkali-activated cementitious material. Before measurement, the dried samples were coated in gold with a thickness of approximately 20 nm to improve the electronic conductivity.

3 RESULTS AND DISCUSSIONS

3.1 Influence of Mechanical Grinding on the Performance of TS

3.1.1 Particle Size

The influence of mechanical grinding on the particle size distribution of TS is shown in Figure 2. Initially, the fineness of the extracted titanium tailings slag was increased with increasing grinding time, followed by an obvious decrease. The minimum particle size of TS was achieved when the grinding time was 15 min. The particle sizes of D_{10} , D_{25} , D_{50} , D_{75} , and D_{90} were 23.69, 31.91, 48.31, 69.16, and $82.89 \mu\text{m}$, respectively.

3.1.2 Reactivity

The reactivity index of the TS in Figure 3 showed a similar tendency that the value increased first and then decreased with increasing grinding time. When the grinding time was 15 min, the reactivity index was greatly improved and the values of 7- and 28-day reactivity index were 42.60 and 81.18%, respectively. However, when the grinding time increased to 60 min, the values of 7- and 28-day reactivity index decreased to 34.65 and 63.75%. The initial increase in reactivity can be

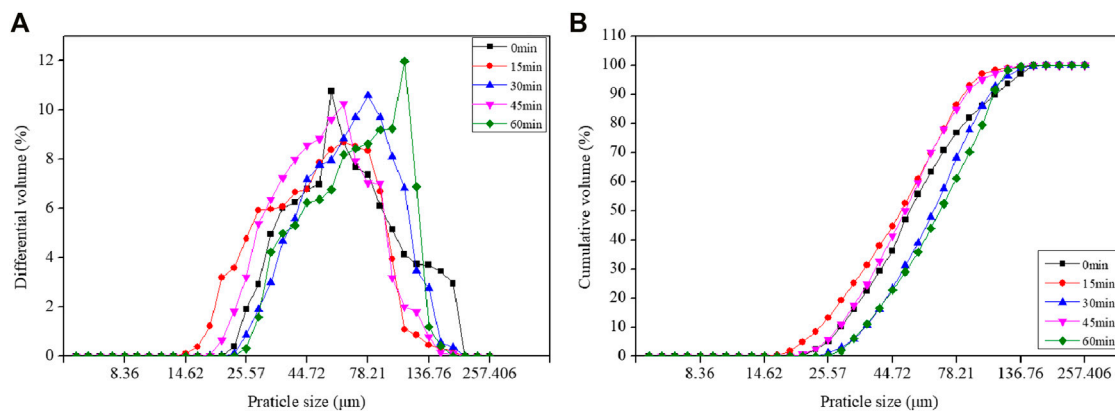


FIGURE 2 | Influence of different grinding times on the (A) differential volume and (B) cumulative volume of TS.

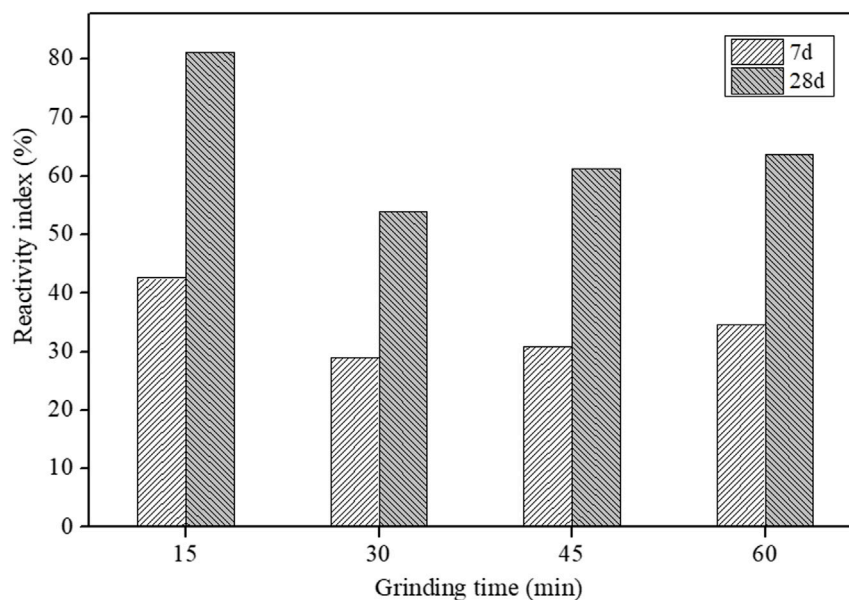


FIGURE 3 | Effect of grinding time on the reactivity of TS.

attributed to the mechanical grinding of refined particles and optimization of the particle gradation in cement paste. In addition, the glassy structure was destroyed and the surface area of TS particles involved in the chemical reaction increased, which is beneficial to silicon and aluminum dissolving and ion penetration in the cementitious system. In addition, the particle lattice was distorted with breakage of the Si–O and Al–O bonds in the network, the structure became disordered, and the number of charged particles increased, and as a consequence, the reactivity increased. The decrease in the reactivity when the grinding time exceeded 15 min was probably due to the aggregation of fine particles into coarser size by further grinding. With respect to the energy

consumption during grinding, therefore, the grinding time of 15 min was applied on TS for the preparation of alkali-activated binder in this study.

3.2 The Effect of TS on the Properties of Alkali-Activated FA-GGBS Binder

3.2.1 Fluidity

It can be seen from **Figure 4** that TS played an important role in changing the fluidity of the binder. The initial fluidity (L0 in the figure) of the reference sample (without TS) was 265 mm, and it increased by 5.7% to 280 mm as the content of TS in the alkali-activated materials increased to 40%. An apparent decrease of the

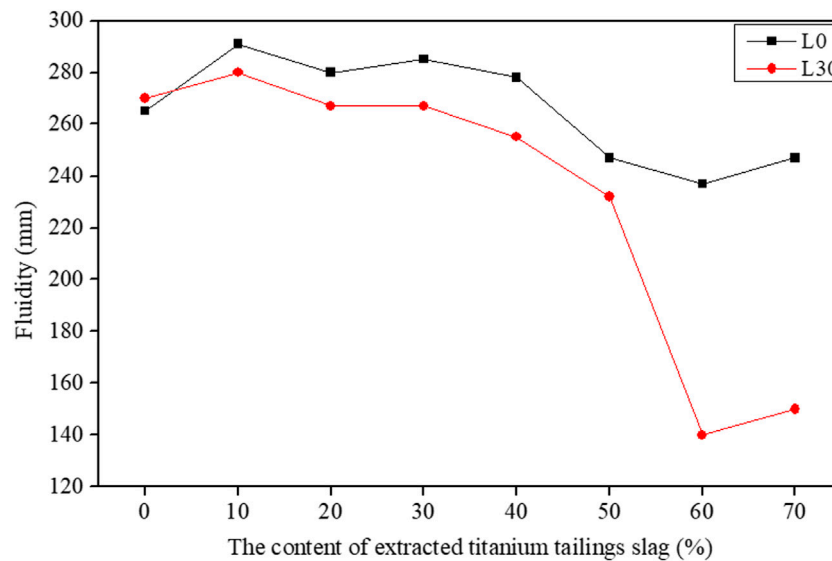


FIGURE 4 | Influence of TS content on the fluidity of the alkali-activated ternary binders.

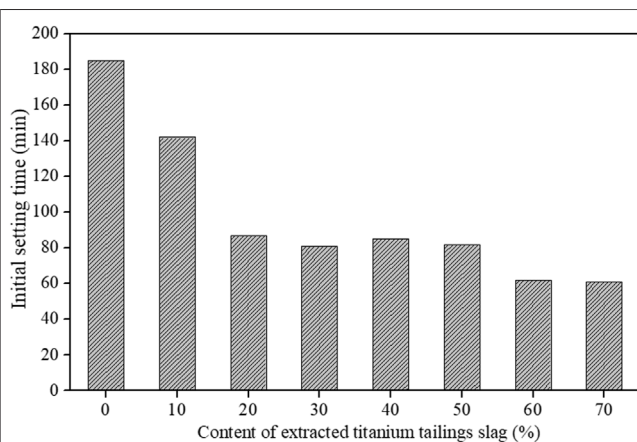


FIGURE 5 | Influence of TS content on the setting time of the alkali-activated ternary binders.

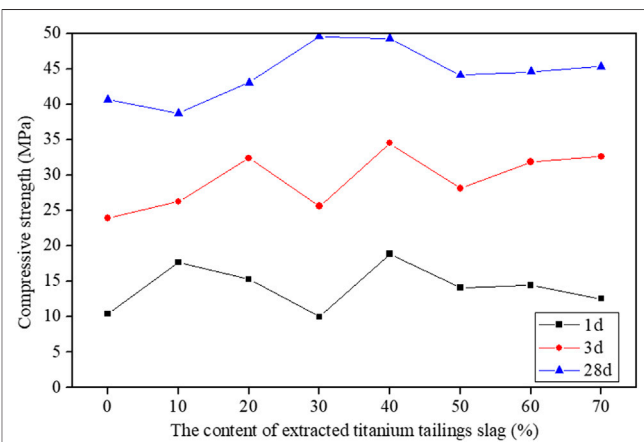


FIGURE 6 | Influence of TS content on the compressive strength of alkali-activated ternary binders.

initial fluidity was observed when the TS content increased from 40 to 70%. In terms of the fluidity at 30 min (L30 in the figure), a slight increase occurred when TS content increased to 10%, followed by a subtle decrease with increasing TS content to 40%. The value of fluidity at 30 min (without TS) was 270 mm, and it decreased by 5.5% to 255 mm at the TS content of 40%. The substantial decrease appeared as the TS content increased from 40 to 70%. The increase in the fluidity at a relatively lower content of TS was likely due to the smaller specific surface area of TS than FA, which reduced the water demand of the mixture. In this case, the amount of free water and the thickness of water film on the particles increased, and thereby the fluidity of the mixture was improved (Xiang et al., 2019). Compared with that of the reference sample, the alkali-activated materials with 60% TS had the lowest values of the initial fluidity

and fluidity at 30 min, which was decreased by 11 and 48% to 240 and 140 mm, respectively. A probable reason was that the increased amount of Ca^{2+} in the TS accelerated the reaction process, and the gelation of the binder was accelerated to form calcium silicate hydrate gel (C-S-H) and calcium aluminosilicate hydrate gel (C-A-S-H) (Yip et al., 2005; Rakngan et al., 2018; Song et al., 2019).

3.2.2 Setting Time

Figure 5 shows the influence of TS content on initial setting time of alkali-activated ternary binders. It can be seen that adding TS can shorten initial setting time evidently. Generally, the initial setting times decreased with the increment of TS content. The setting time of alkali-activated ternary binder decreased sharply as the content of TS increased to 40%. The initial setting time was

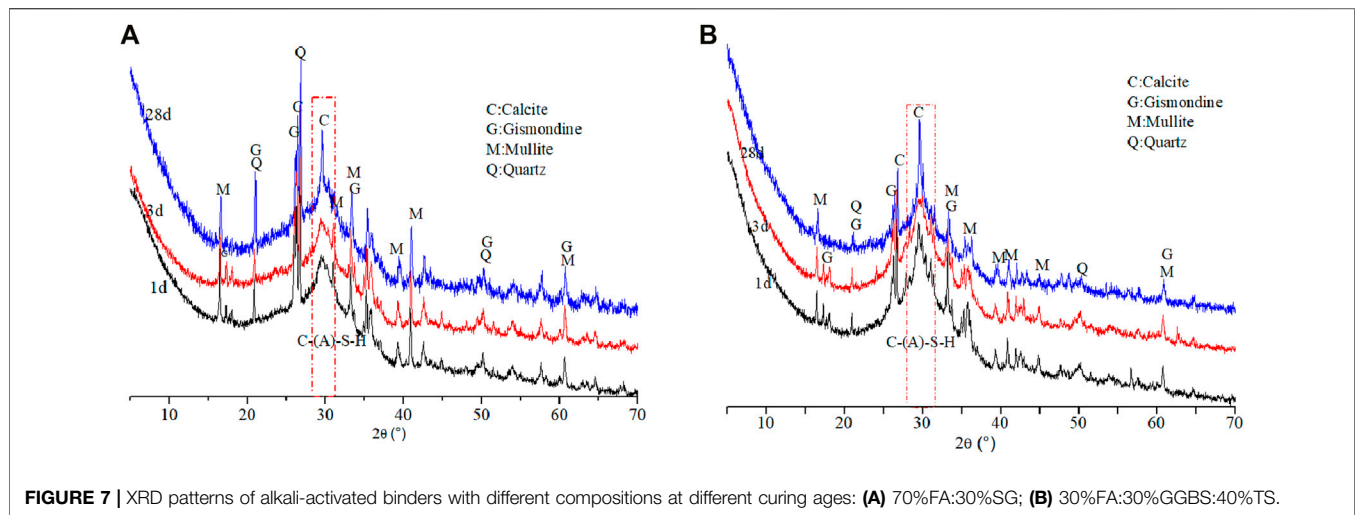


FIGURE 7 | XRD patterns of alkali-activated binders with different compositions at different curing ages: **(A)** 70%FA:30%SG; **(B)** 30%FA:30%GGBS:40%TS.

185 min without TS, and it decreased by 54% to 85 min at the TS-to-FA replacement ratio of 40%. When the TS content in the binder was higher than 40%, a slight diminishment was observed in initial setting time, and the value was 61 min at 70% TS. That is because the setting time is highly related to the amount of reaction products, such as C-A-S-H or C-S-H gels (Chindaprasirt et al., 2011; Cui et al., 2017). Increasing the amount of TS was equivalent to increase the content of calcium oxide in the ternary system, thus accelerating the formation of C-S-H and C-A-S-H gel, and subsequently shortening the setting time (Nath and Sarker 2014; Nath et al., 2015; Nishanth and Patil 2021).

3.2.3 Compressive Strength

The effect of TS on the compressive strength of the alkali-activated ternary binder is shown in **Figure 6**. It can be seen that the replacement of FA by TS generally improved the compressive strength of alkali-activated material, and the compressive strength increased first and then decreased with increasing TS content. The maximum compressive strength of the binder at early ages was achieved as TS content is 40%. Its compressive strength at 1, 3, and 28 days was 18.9, 34.5, and 49.3 MPa, respectively, which was increased by 80.77, 30.72, and 21.18%, respectively, as compared with reference samples without TS addition. This mixture was deemed to have the optimum particle gradation that forms a more compacted structure than the other mixtures, which contributes to the gaining of compressive strength. Apart of the sodium aluminosilicate hydrate gel (N-A-S-H) formed from the reaction between FA and alkali solution, the replacement of FA by TS in the binder system is likely to incorporate more Ca^{2+} ions to produce C-(A)-S-H gel. The combination of C-(A)-S-H and N-A-S-H gels tends to the optimization of pore structure, and resulted in the growth of compressive strength. However, excessive amount of TS was negative to the compressive strength of binder, which is mainly because the reaction between solid materials and alkali solution was accelerated, and subsequent superfluous C-(A)-S-H gel

formed in a relatively shorter time. It is likely to initiate cracks in the specimens as a result of the easy loss of gel water, which adversely affected the strength development (Cui et al., 2017).

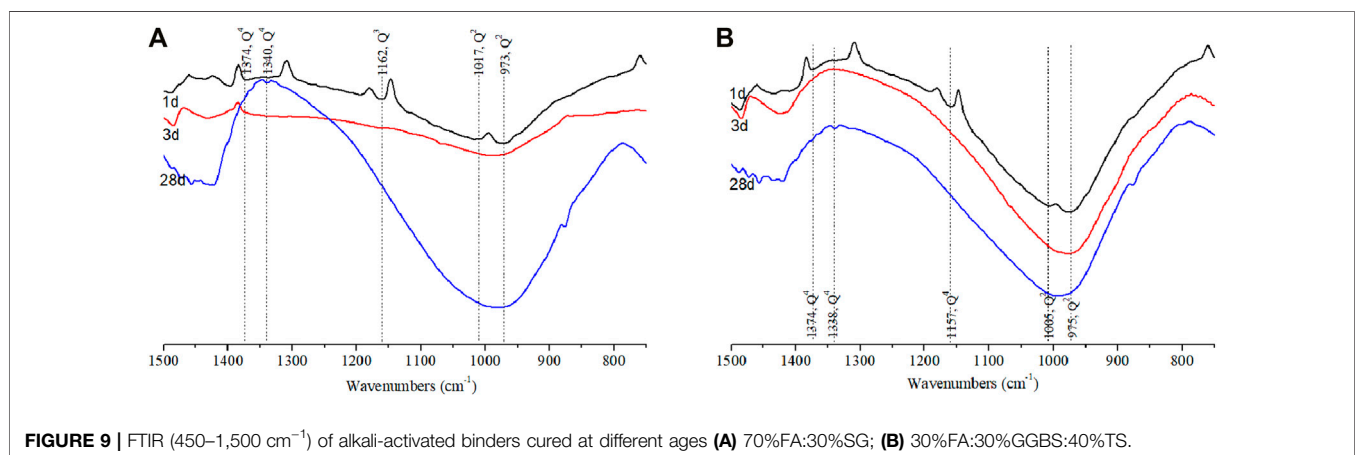
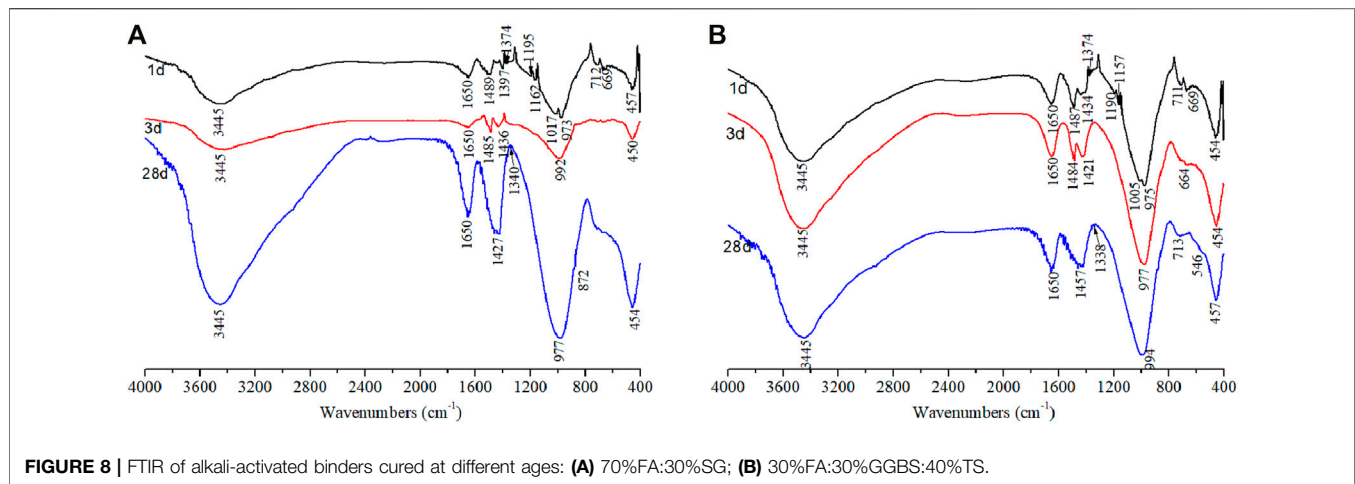
3.3 Microstructure Analysis

3.3.1 XRD Analysis

The XRD patterns of specimens at different ages are shown in **Figure 7**. It can be seen that the main reaction products were C-(A)-S-H gel with diffused peak ranging from 25 to 35° 2θ and gismondine (d-spacings of 0.427, 0.334, and 0.299 nm) (Chindaprasirt et al., 2012). Mullite (d-spacings of 0.534, 0.287, and 0.269 nm) and quartz (d-spacings of 0.537, 0.342, and 0.338 nm) derived from the raw materials were still present in all the samples at different ages. In addition, calcite (d-spacings of 0.386, 0.303, and 0.283 nm) was also detected, which was probably due to the carbonation of C-(A)-S-H gel. The peak intensity of mullite and quartz decreased with the increase of curing age. Meanwhile, the peak intensity of reaction products (e.g., C-(A)-S-H and gismondine) were stronger and sharper, suggesting the formation of new phase due to the occurrence of reaction between the raw materials and alkali solution. Furthermore, it is found that the peak intensity of mullite and quartz of the samples with addition of TS in **Figure 7B** became weaker than that of reference sample (**Figure 7A**), which is ascribed to the decreased amount of FA, while the peak intensity of C-(A)-S-H in the former sample were stronger and sharper. It indicates that the replacement of FA by TS can promote the formation of C-(A)-S-H gels, and reaction process proceeded with the increase of curing age.

3.3.2 FTIR Spectrum

Figure 8 shows the FTIR spectrum of the alkali-activated binder with different compositions. The bands at the region of 1,600–4,000 cm^{-1} were an indication of hydrogen stretching vibration groups (Si–O–H). The vibration at 3,445 and 1,647 cm^{-1} was attributed to the bending of the hydroxyl band. These bands indicated the presence of bound water molecules from the reaction products. For the reference sample (**Figure 8A**), the



increased vibration intensity in the region of 2,000–4,000 cm^{-1} indicated the increased amount of C-(A)-S-H over the curing age. It was low at 1 and 3 days, but increased dramatically at 28 days, indicating a relatively low reaction rate at early ages, and the reaction improved at a later age, whereas a slight increase of intensity in the hydrogen bond vibration was observed with TS addition. The bands at the region of 1,400–1,500 cm^{-1} were the signal of asymmetric stretching vibration of CO_3^{2-} . In addition, the band position at 872 cm^{-1} is due to the bending vibration of the C–O bond of carbonates. The bands positioned at 700–950 cm^{-1} and 400–500 cm^{-1} were the signals of $[\text{AlO}_4]^{5-}$ tetrahedron and $[\text{AlO}_6]^{9-}$ octahedron, respectively.

The most important bands positioned in the range of 750–1,400 cm^{-1} are related to the stretching vibration of Si–O–T (where T = Si, Al, Ti, and Na etc.) (Liu et al., 2020), as illustrated in **Figure 9**. The band at 950–970 cm^{-1} was ascribed to the Q^2 units of Si–O–Si (Lodeiro et al., 2009). The vibration at about 1,160 cm^{-1} derived from quartz and mullite disappeared at 3 and 28 days, indicating the consumption of raw materials by chemical activation. A weak band appeared at 1,374 cm^{-1} in the samples cured for 1 day, which was ascribed to Q^4 units of Si–O–Si derived from FA. This band shifted to a lower wavenumber (1,340 cm^{-1}) when the samples were cured for 28 days, implying a lower

polymerization degree with curing age forward. This phenomenon became more visible as shown in **Figure 9B** as adding TS to the alkali-activated binder system, suggesting the alteration of the structure of reaction products. Q^2 units appeared at 977 cm^{-1} at 28 days of curing for the sample without TS, but it shifted to a higher wavenumber (994 cm^{-1}), indicating the higher degree of geopolymerization of the structure. From the aforementioned, it can be concluded that the substitution of TS to FA caused the promotion of the reaction of binder (Lee and van Deventer 2002).

3.3.3 SEM Morphology

Figure 10 exhibits the morphology of alkali-activated binder at 28 days of curing. For the reference sample without TS, the products with petal-like shape with the size of 2 μm were observed, and these particles were loosely packing (**Figure 10A**). When TS was added, plate-like structure was developed, and some unreacted fly ash particles were also observed (**Figure 10B**). It indicates that the consumption of TS particles was faster than that of FA particles as the binder was activated by alkali solution, providing more reaction products with a denser structure, therefore leading to a higher compressive strength of binder. However, several micro-cracks with approximately 2 μm in width were observed in the sample containing TS. This may be ascribed to the fact that the

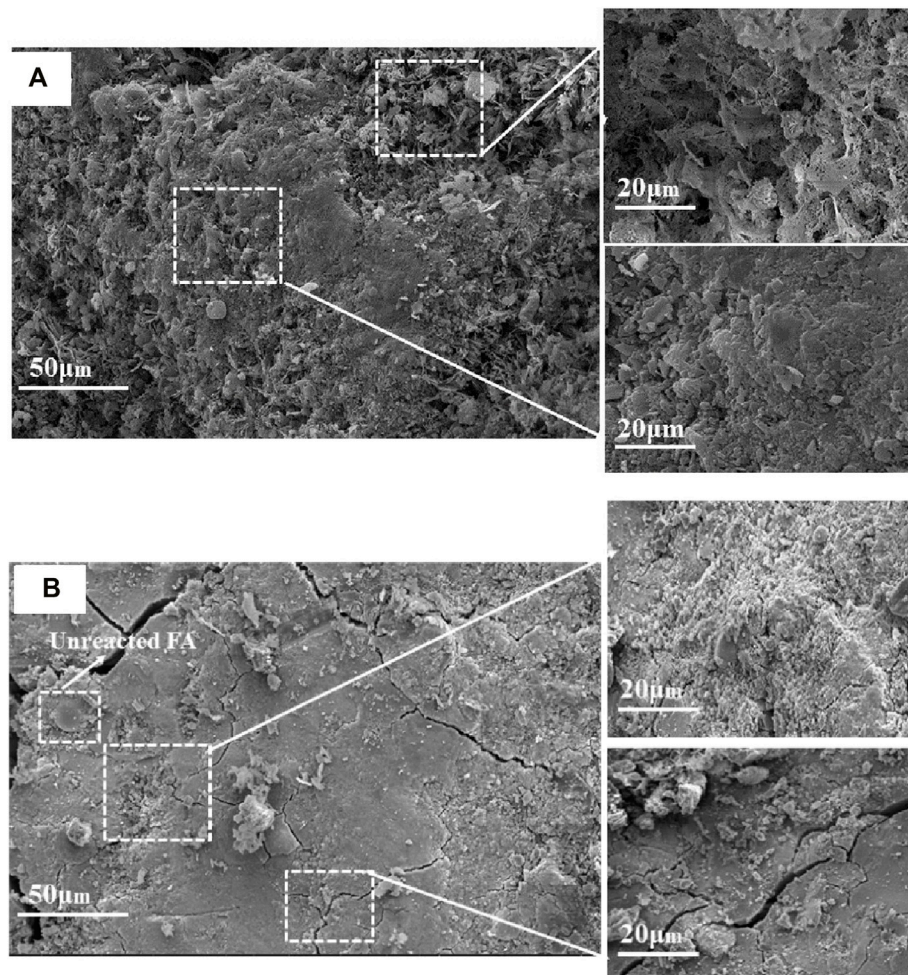


FIGURE 10 | SEM of alkali-activated binders with different compositions at different curing ages: **(A)** 70%FA:30%SG; **(B)** 30%FA:30%GGBS:40%TS.

addition of TS accelerated the reaction process of binder and promoted the formation of micro-cracks. Furthermore, the presence of TS produced a higher amount of C-(A)-S-H gel, which contained more adsorbed water molecules to maintain its shape. The drying shrinkage of the binder occurred after the removal of water molecules during the drying process, and it caused the formation of micro-cracks.

4 CONCLUSION

In this study, the reactivity of the extracted titanium tailings slag was improved by mechanical grinding, and the influence of the ground extracted titanium tailings slag on the setting and hardening properties of the alkali-activated FA-GGBS was investigated. The conclusions can be drawn as follows.

The particle size distribution of extracted titanium tailings slag (TS) can be optimized via mechanical grinding; as a result, the specific surface area and reactivity index were improved. The

highest 28-day reactivity index was achieved at 15 min of grinding, and the value was 81.18%. Its average grain diameter of D_{50} and D_{90} were 48.31 and 82.89 μm , respectively.

No notable reduction in the fluidity of the alkali activated binder appeared as the replacement ratio of TS to FA increased to 40%, but it decreased dramatically at a higher replacement ratio.

The setting time of alkali-activated FA-GGBS was greatly reduced by the addition of TS due to the increased calcium content in the ternary binder, while the compressive strength of alkali-activated cementitious materials was increased first and then decreased with the increase of TS content. When the TS content was 40%, the early strength of the binder developed rapidly to 18.8 MPa, increased by 80.77% compared with the binder without TS, and the compressive strength at 28 days increased by 21.18% to 49.3 MPa.

The replacement of FA by TS could accelerate the reaction process and the main reaction products were C-(A)-S-H and gismondine. Adding TS in the binder increased the amount of C-(A)-S-H and improved the polymerization degree of hydration products. Meanwhile, the structure became more compacted, and thus the compressive strength of the binder was improved.

DATA AVAILABILITY STATEMENT

The original contributions presented in the study are included in the article/Supplementary Material; further inquiries can be directed to the corresponding author.

AUTHOR CONTRIBUTIONS

SW: conceptualization, methodology, writing—original draft. JL: validation, data curation. XY: methodology, validation. YZ: preparation of raw materials. XL: writing—original draft. ZZ: methodology, supervision, writing—review and editing.

REFERENCES

- Ameri, F., Shoaie, P., Zareei, S. A., and Behforouz, B. (2019). Geopolymers vs. Alkali-Activated Materials (AAMs): A Comparative Study on Durability, Microstructure, and Resistance to Elevated Temperatures of Lightweight Mortars. *Construction Building Mater.* 222, 49–63. doi:10.1016/j.conbuildmat.2019.06.079
- Beltrame, N. A. M., Angulski da Luz, C., Perardt, M., and Hooton, R. D. (2020). Alkali Activated Cement Made from Blast Furnace Slag Generated by Charcoal: Resistance to Attack by Sodium and Magnesium Sulfates. *Construction Building Mater.* 238, 117710. doi:10.1016/j.conbuildmat.2019.117710
- Biricik, H., Kirgiz, M. S., Galdino, A. G. d. S., Kenai, S., Mirza, J., Kinuthia, J., et al. (2021). Activation of Slag through a Combination of NaOH/NaS Alkali for Transforming it into Geopolymer Slag Binder Mortar - Assessment the Effects of Two Different Blaine Fines and Three Different Curing Conditions. *J. Mater. Res. Tech.* 14, 1569–1584. doi:10.1016/j.jmrt.2021.07.014
- Bumanis, G., Vitola, L., Bajare, D., Dembovska, L., and Pundiene, I. (2017). Impact of Reactive SiO₂/Al₂O₃ Ratio in Precursor on Durability of Porous Alkali Activated Materials. *Ceramics Int.* 43, 5471–5477. doi:10.1016/j.ceramint.2017.01.060
- Chindaprasirt, P., Chareerat, T., Hatanaka, S., and Cao, T. (2011). High-Strength Geopolymer Using Fine High-Calcium Fly Ash. *J. Mater. Civ. Eng.* 23, 264–270. doi:10.1061/(ASCE)MT.1943-5533.0000161
- Chindaprasirt, P., De Silva, P., Sagoe-Crentsil, K., and Hanjitsuwan, S. (2012). Effect of SiO₂ and Al₂O₃ on the Setting and Hardening of High Calcium Fly Ash-Based Geopolymer Systems. *J. Mater. Sci.* 47, 4876–4883. doi:10.1007/s10853-012-6353-y
- Cui, C., Peng, H., Liu, Y., Zhang, J., Cai, C., and Peng, A. (2017). Influence of GGBFS Content and Activator Modulus on Curing of Metakaolin Based Geopolymer at Ambient Temperature. *J. Build Mater.* 20, 535–542. doi:10.3969/j.issn.1007-9629.2017.04.008
- García Lodeiro, I., Macphee, D. E., Palomo, A., and Fernández-Jiménez, A. (2009). Effect of Alkalies on Fresh C-S-H Gels. FTIR Analysis. *Cement Concrete Res.* 39, 147–153. doi:10.1016/j.cemconres.2009.01.003
- GB/T 1346 (2011). *Technical Specification for Test Methods for Water Requirement of normal Consistency, Setting Time and Soundness of the Portland Cement*. Beijing: China standard press.
- GB/T 1596 (2017). *Technical Specification for Fly Ash Used for Cement and concrete*. Beijing: China standard press.
- GB/T 17671 (1999). *Technical Specification for Method of Testing Cements-Determination of Strength*. Beijing: China standard press.
- GB/T 8074 (2008). *Technical Specification for Testing Method for Specific Surface of Cement-Blaine Method*. Beijing: China standard press.
- GB/T 8077 (2000). *Technical Specification for Methods for Testing Uniformity of concrete Admixture*. Beijing: China standard press.

FUNDING

This study was supported by the Natural Science Foundation Project of Chongqing (cstc2020jcyj-msxmX0954, cstc2020jcyj-msxmX0901), 111 Project of China (B18062), the National Natural Science Foundation of China (52078083), and the Fundamental Research Funds for the Central Universities (2020CDJ-LHZZ-088, 2021CDJQY-008).

ACKNOWLEDGMENTS

The authors gratefully appreciate the support from the Electron Microscope Center of Chongqing University (202103150147) and the project of Leading Talent of Science and Technology Innovation in Chongqing.

- Hong, Y. (2014). *Preparation and Properties of Alum Inoferrite Cement Clinker Based on the Slag of Ti-Si-V-Fe alloy-making from Titania-Rich BF Slag*. Wuhan: Wuhan University of Science and Technology. doi:10.7666/d.Y2657482
- John, S. K., Nadir, Y., and Girija, K. (2021). Effect of Source Materials, Additives on the Mechanical Properties and Durability of Fly Ash and Fly Ash-Slag Geopolymer Mortar: A Review. *Construction Building Mater.* 280, 122443. doi:10.1016/j.conbuildmat.2021.122443
- Kumar, S., Mucsi, G., Kristály, F., and Pekker, P. (2017). Mechanical Activation of Fly Ash and its Influence on Micro and Nano-Structural Behaviour of Resulting Geopolymers. *Adv. Powder Tech.* 28, 805–813. doi:10.1016/j.apt.2016.11.027
- Kuri, J. C., Khan, M. N. N., and Sarker, P. K. (2021). Fresh and Hardened Properties of Geopolymer Binder Using Ground High Magnesium Ferronickel Slag with Fly Ash. *Construction Building Mater.* 272, 121877. doi:10.1016/j.conbuildmat.2020.121877
- Lee, W. K. W., and van Deventer, J. S. J. (2002). The Effects of Inorganic Salt Contamination on the Strength and Durability of Geopolymers. *Colloids Surf. A: Physicochemical Eng. Aspects* 211, 115–126. doi:10.1016/S0927-7757(02)00239-X
- Li, S., Li, Y., Xing, L., Ke, C., and Li, N. (2010). Porous Ceramics of Calcium Hexaluminate-Magnesia Alumina Spinel Prepared by Titanium Recovering Slag. *Refractories* 44, 100–103. doi:10.3969/j.issn.1001-1935.2010.02.006
- Liu, W., Lin, L., Wang, S., Peng, X., Wu, B., Sun, K., et al. (2020). Setting and Hardening Behaviour of Alkali-Activated Landfilled Fly Ash-Slag Binder at Room Temperature. *Materials* 13, 3130. doi:10.3390/ma13143130
- Liu, Y., Zhu, W., and Yang, E.-H. (2016). Alkali-activated Ground Granulated Blast-Furnace Slag Incorporating Incinerator Fly Ash as a Potential Binder. *Construction Building Mater.* 112, 1005–1012. doi:10.1016/j.conbuildmat.2016.02.153
- Moghadam, M. J., Ajalloeian, R., and Hajiannia, A. (2019). Preparation and Application of Alkali-Activated Materials Based on Waste Glass and Coal Gangue: A Review. *Construction Building Mater.* 221, 84–98. doi:10.1016/j.conbuildmat.2019.06.071
- Mucsi, G., Kumar, S., Csöke, B., Kumar, R., Molnár, Z., Rácz, Á., et al. (2015). Control of Geopolymer Properties by Grinding of Land Filled Fly Ash. *Int. J. Mineral Process.* 143, 50–58. doi:10.1016/j.minpro.2015.08.010
- Nath, P., and Sarker, P. K. (2014). Effect of GGBFS on Setting, Workability and Early Strength Properties of Fly Ash Geopolymer concrete Cured in Ambient Condition. *Construction Building Mater.* 66, 163–171. doi:10.1016/j.conbuildmat.2014.05.080
- Nath, P., Sarker, P. K., and Rangan, V. B. (2015). Early Age Properties of Low-Calcium Fly Ash Geopolymer Concrete Suitable for Ambient Curing. *Proced. Eng.* 125, 601–607. doi:10.1016/j.proeng.2015.11.077
- Nishanth, L., and Patil, D. N. N. (2021). Experimental Evaluation on Workability and Strength Characteristics of Self-Consolidating Geopolymer concrete Based on GGBFS, Flyash and Alccofine. *Mater. Today Proc.* doi:10.1016/j.matpr.2021.10.200

- Pavithra, P., Srinivasula Reddy, M., Dinakar, P., Hanumantha Rao, B., Satpathy, B. K., and Mohanty, A. N. (2016). A Mix Design Procedure for Geopolymer concrete with Fly Ash. *J. Clean. Prod.* 133, 117–125. doi:10.1016/j.jclepro.2016.05.041
- Rakngan, W., Williamson, T., Ferron, R. D., Sant, G., Juenger, M. C. G., and Juenger, G. (2018). Controlling Workability in Alkali-Activated Class C Fly Ash. *Construction Building Mater.* 183, 226–233. doi:10.1016/j.conbuildmat.2018.06.174
- Song, W., Zhu, Z., Peng, Y., Wan, Y., Xu, X., Pu, S., et al. (2019). Effect of Steel Slag on Fresh, Hardened and Microstructural Properties of High-Calcium Fly Ash Based Geopolymers at Standard Curing Condition. *Construction Building Mater.* 229, 116933. doi:10.1016/j.conbuildmat.2019.116933
- Soutos, M., Boyle, A. P., Vinai, R., Hadjierakleous, A., and Barnett, S. J. (2016). Factors Influencing the Compressive Strength of Fly Ash Based Geopolymers. *Construction Building Mater.* 110, 355–368. doi:10.1016/j.conbuildmat.2015.11.045
- Sun, K. K., Xuan, D. X., Li, J. J., Ji, G. X., Poon, C. S., Wang, S. P., et al. (2022). Effect of the Ti-extracted Residue on Compressive Strength and Microstructural Properties of Modified Cement Mortar. *Constr. Build Mater.* 320. doi:10.1016/j.conbuildmat.2021.126190
- Temuujin, J., van Riessen, A., and MacKenzie, K. J. D. (2010). Preparation and Characterisation of Fly Ash Based Geopolymer Mortars. *Construction Building Mater.* 24, 1906–1910. doi:10.1016/j.conbuildmat.2010.04.012
- Wang, P., Han, B., Han, Y., Ke, C., and Li, N. (2008). Research on Hydration Capability of Panzhihua Iron and Steel CO.BF Slag after Silicon-Titanium Alloy. *B Chin. Ceram. Soc.* 27, 1208–1211. doi:10.16552/j.cnki.issn1001-1625.2008.06.029
- Xiang, J., Liu, L., Cui, X., He, Y., Zheng, G., and Shi, C. (2019). Effect of Fuller-fine Sand on Rheological, Drying Shrinkage, and Microstructural Properties of Metakaolin-Based Geopolymer Grouting Materials. *Cement and Concrete Composites* 104, 103381. doi:10.1016/j.cemconcomp.2019.103381
- Yao, Y. (2019). *Study on Effect of Chloride Ion Curing in High Chlorine Extraction Titanium Tailings*. Anshan: University of Science and Technology Liaoning.
- Yip, C. K., Lukey, G. C., and van Deventer, J. S. J. (2005). The Coexistence of Geopolymeric Gel and Calcium Silicate Hydrate at the Early Stage of Alkaline Activation. *Cement Concrete Res.* 35, 1688–1697. doi:10.1016/j.cemconres.2004.10.042
- Zhang, J. (2018). *Investigation on Utilization of Ti-Extracted Residues and Red Gypsum for the Preparation of Construct Ion and Building Materials*. Mianyang: Southwest University of Science and Technology.
- Zhang, J., Pan, G., and Yan, Y. (2021). Early Hydration, Mechanical Strength and Drying Shrinkage of Low-Carbon Alkali-Activated Ti-Extracted Residues-Fly Ash Cement and Mortars. *Construction Building Mater.* 293, 123517. doi:10.1016/j.conbuildmat.2021.123517
- Zhu, H., Wang, P., Zhang, J., and Wang, B. W. (2011). Effects of Chlorination Titanium Blast Furnace Slag on Strength and Microstructure of Mortar. *J. Build Mater.* 14, 443–446. doi:10.3969/j.issn.1007-9629.2011.04.002
- Zhu, H., Wang, P., Zhang, J., and Wang, B. W. (2010). Preparation of Bricks by Using Titanium-Extracted Pangang BF Waste Slag. *New Build Mater.* 37, 31–33. doi:10.3969/j.issn.1001-702X.2010.06.009

Conflict of Interest: YZ is employed by Pangang Group Engineering Technology Co., Ltd.

The remaining authors declare that the research was conducted in the absence of any commercial or financial relationships that could be construed as a potential conflict.

Publisher's Note: All claims expressed in this article are solely those of the authors and do not necessarily represent those of their affiliated organizations, or those of the publisher, the editors, and the reviewers. Any product that may be evaluated in this article, or claim that may be made by its manufacturer, is not guaranteed or endorsed by the publisher.

Copyright © 2022 Wang, Li, Yun, Lv, Zhao and Zhang. This is an open-access article distributed under the terms of the Creative Commons Attribution License (CC BY). The use, distribution or reproduction in other forums is permitted, provided the original author(s) and the copyright owner(s) are credited and that the original publication in this journal is cited, in accordance with accepted academic practice. No use, distribution or reproduction is permitted which does not comply with these terms.



A Unified Model for Fibers With Divergent Pullout Behaviors in Strain Hardening Cementitious Composites (SHCC)

Peiyun She, Jiajie Wang, Zhiming Pang and Cong Lu*

School of Civil Engineering, Southeast University, Nanjing, China

OPEN ACCESS

Edited by:

Zhigang Zhang,
Chongqing University, China

Reviewed by:

Junxia Li,
Institute of Materials Research and
Engineering (A*STAR), Singapore
Yao Ding,
Chongqing University, China

*Correspondence:

Cong Lu
conglu@seu.edu.cn

Specialty section:

This article was submitted to
Structural Materials,
a section of the journal
Frontiers in Materials

Received: 22 January 2022

Accepted: 15 February 2022

Published: 08 March 2022

Citation:

She P, Wang J, Pang Z and Lu C
(2022) A Unified Model for Fibers With
Divergent Pullout Behaviors in Strain
Hardening Cementitious
Composites (SHCC).
Front. Mater. 9:860113.
doi: 10.3389/fmats.2022.860113

Strain Hardening Cementitious Composites (SHCC) are materials exhibiting high tensile ductility with the formation of multiple cracks. Since the mechanical properties of SHCC members are governed by the interfacial characteristics between fibers and matrix, understanding the mechanism of single fiber pullout behavior is crucial for SHCC material design. Existing model was set up based on Polyvinyl Alcohol (PVA) fibers, making it inapplicable to other kinds of synthetic fibers those exhibit divergent pullout behaviors. As a result, the simulated curves cannot agree well with the tested results of SHCC made with other fibers or hybrid fibers. In this study, a unified single fiber pullout model was proposed to take divergent kinds of fiber pullout behavior into account. Five parameters were defined to describe the single fiber pullout behavior, where the frictional strength during the pullout stage and the blocking length of fiber under pulley force were for the first time introduced. For verification purpose, fiber-pullout samples with Polyethylene terephthalate (PET) and PVA fibers were tested and the results agree well with the simulated curves from proposed model. The stochasticity of each parameters were then analyzed and described by normal distribution, through which fibers with various random pullout behaviors can be incorporated into a larger scale modelling. Therefore, the fiber-bridging constitutive law for a single crack was calculated and compared with the single crack test results, which confirmed again the validity of the proposed model.

Keywords: physical model, SHCC, fiber pullout, PET fiber, PVA fiber

INTRODUCTION

Due to the quasi-brittle nature, traditional cementitious materials are vulnerable to cracking (Li et al., 2003; Jun et al., 2006; Zhigang, 2020a). Hence, fibers are added to control the cracks and improve toughness (Graybeal, 2006). With moderate fiber content added, Strain Hardening Cementitious Composites (SHCC) was developed in the 1990s (Li and Leung, 1992; Li and Wu, 1992; Victor and Forii, 1993; Leung, 1996; Li et al., 2001; Li, 2011; Victor and Li, 2012; Zhigang, 2021), which exhibits strain hardening behavior accompanied by the formation of multiple cracks and ensures the high ductility and durability of the structure.

In order to explain the strain hardening behavior in SHCC, the design criterion for SHCC including fiber, matrix and interface parameters have been proposed by Li first (Victor and Li, 2012). The most fundamental property of SHCC is the fiber bridging constitutive law which can be derived from modeling a single fiber pullout behavior against the surrounding matrix. Since the initial fiber

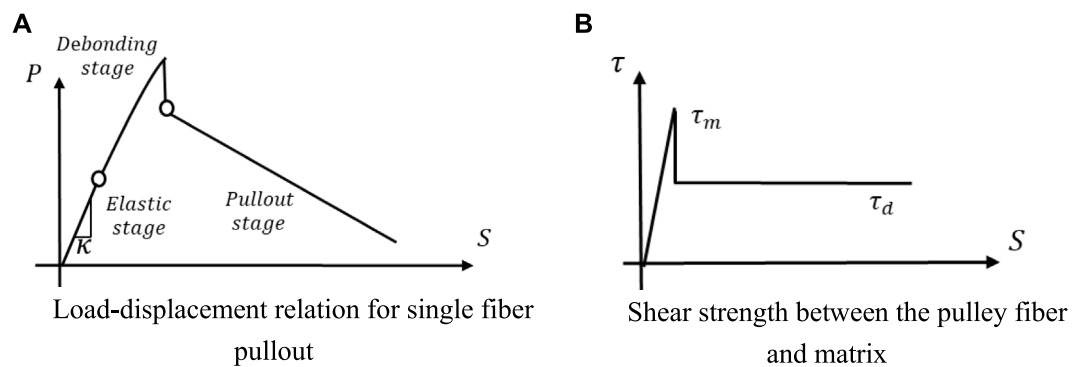


FIGURE 1 | Load-displacement relation for single fiber pullout and shear strength diagram. **(A)** Load-displacement relation for single fiber pullout. **(B)** Shear strength between the pulley fiber and matrix.

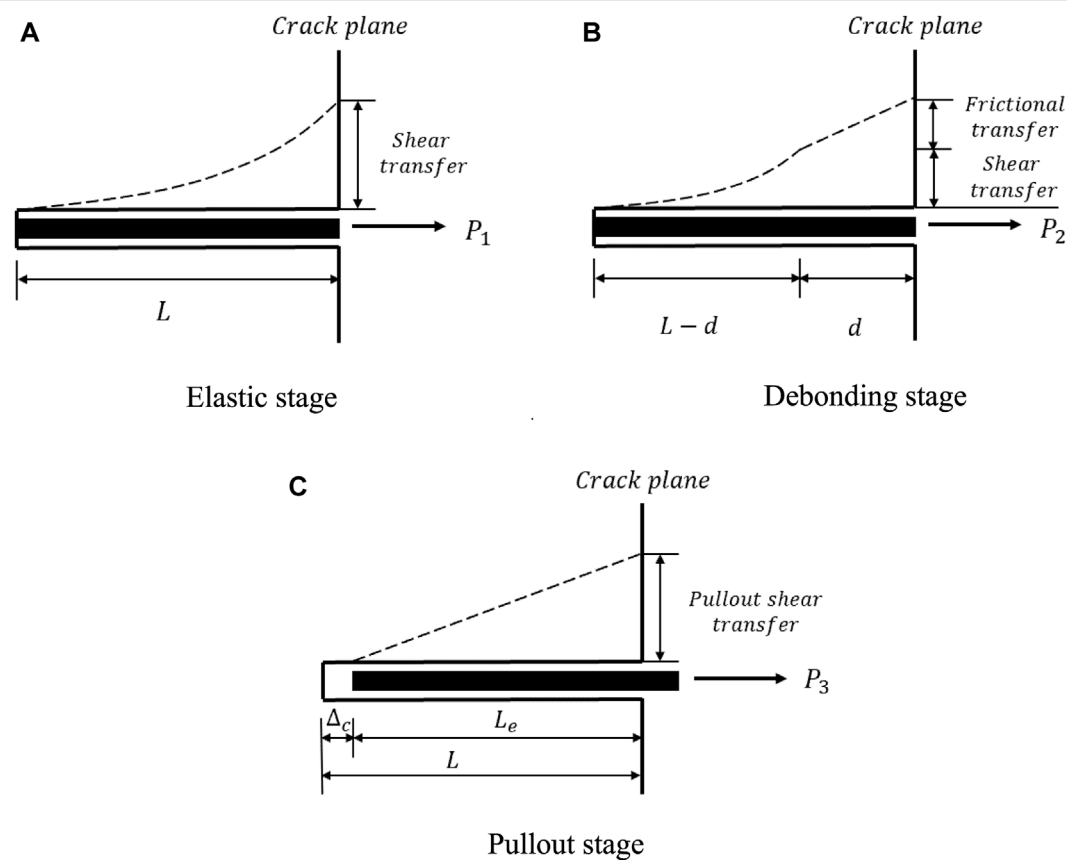
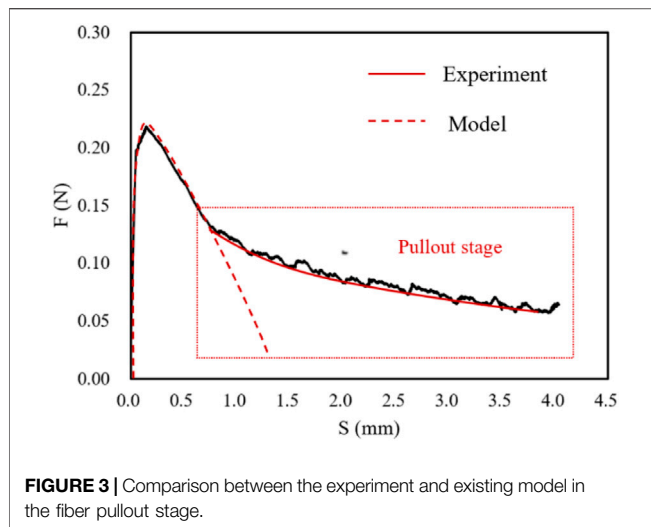


FIGURE 2 | Schematic force distribution at fiber-matrix interface in different single fiber pullout stages. **(A)** Elastic stage. **(B)** Debonding stage. **(C)** Pullout stage.

bridging constitutive law only considered the friction between fiber and matrix (Kanda and Li, 1998), new mechanisms of fiber/matrix interactions including slip hardening (Ochi et al., 2007), fiber rupture (Lin and Li, 1997), chemical bonding (Maalej et al., 1995) and two-way fiber debonding (Yang et al., 2008) were taken into account to improve the accuracy of crack opening prediction.

Above studies were mainly based on PVA fibers which exhibit high tenacity and good adhesion with cement. Flashbacking to the invention of SHCC in the 1990s, high-modulus polyethylene (PE) fibers were firstly used as the bridging fibers by Li et al. (Li, 1998), which are greatly more expensive than the other fibers. To reduce the high cost of fibers, SHCC with polyvinyl alcohol (PVA) fibers were introduced by



Kanda and Li (Kanda and Li, 1998). However, its application in construction is limited because the price is still relatively high for large-scale construction use (Pan et al., 2015). Therefore, cheaper substitute for PVA fibers is strongly in demand. By far, there have been many studies with other inexpensive synthetic fibers such as Polypropylene (PP) fibers, Polyacrylonitrile (PAN) fibers and polyethylene terephthalate (PET) fibers (Pereira et al., 2012; Pakravan et al., 2016; Lu et al., 2018; Zhigang, 2020b). The properties of different fibers vary widely, and even the same kind of fibers show completely different properties due to the different surface treatment processes (Foti, 2016), which directly results in differentiated performance of fibers when they are pulled out from the matrix. For example, PE and PVA fibers exhibit strong slip hardening characteristic (Li, 1998; Pan et al., 2015), while PAN and PET fibers show clear slip softening trend (Pereira et al., 2012; Lu et al., 2018). Therefore, it is not enough to establish a single fiber pullout model exclusively for PVA fibers. A unified model needs

to be developed to describe the single fiber pullout behavior of different fibers.

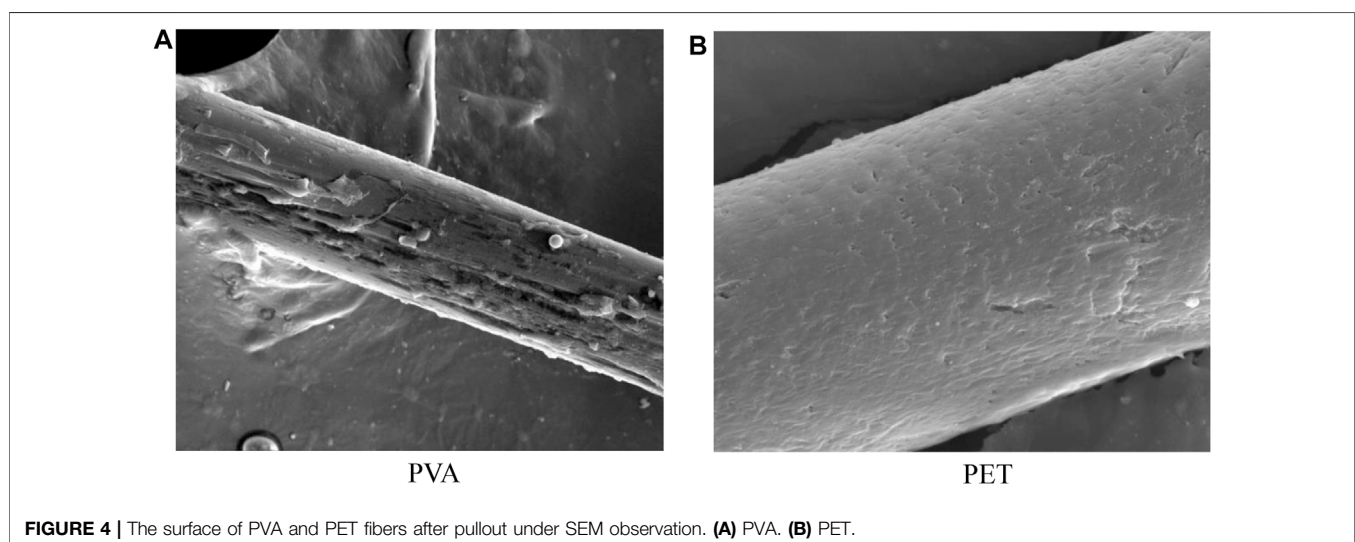
This paper aims at establishing a unified fiber bridging model of SHCC, applying to different kinds of fibers which may show different surface bonding properties. PVA fibers and PET fibers are taken as typical examples which show slip hardening and slip softening behavior, respectively. Modeling a single fiber pullout behavior against the surrounding matrix will be firstly conducted. Two new parameters including frictional strength during the pullout stage and the blocking length of fiber under pulley force are introduced to simulate the single fiber pullout behavior. In the following part, the stress-crack opening relation for a bridged crack is simulated based on the stochastic parameters derived from the single fiber pullout model. The revised fiber bridging model is then compared with the curve acquired from the experiment to confirm the validity.

MODELING OF SINGLE FIBER PULLOUT

Existing Theory

The pullout behavior of single fiber has been modelled in the literature (Lin and Li, 1997; Kanda and Li, 1999). In these existing models, when the fiber is subjected to a pullout force P , three stages are considered including elastic, debonding and pullout stage with different range of the slip S as shown in **Figure 1**. When the load is small, the local shear stress τ appears linear correlation with slip S and κ is the slope of the τ - S curve in elastic stage. When the shear stress exceeds the maximum shear strength τ_m , the debonding of the fiber is initiated and the frictional strength is defined as a constant value τ_d . After debonding reaches the embedded end of the fiber, the interface is purely governed by the frictional force and the fiber is assumed to be pulled out from the matrix, which is determined as pullout stage.

The model is established based on the static equilibrium requirement (Naaman et al., 1991; Li et al., 2003), and the tensile force in the fiber F is transferred to the matrix M



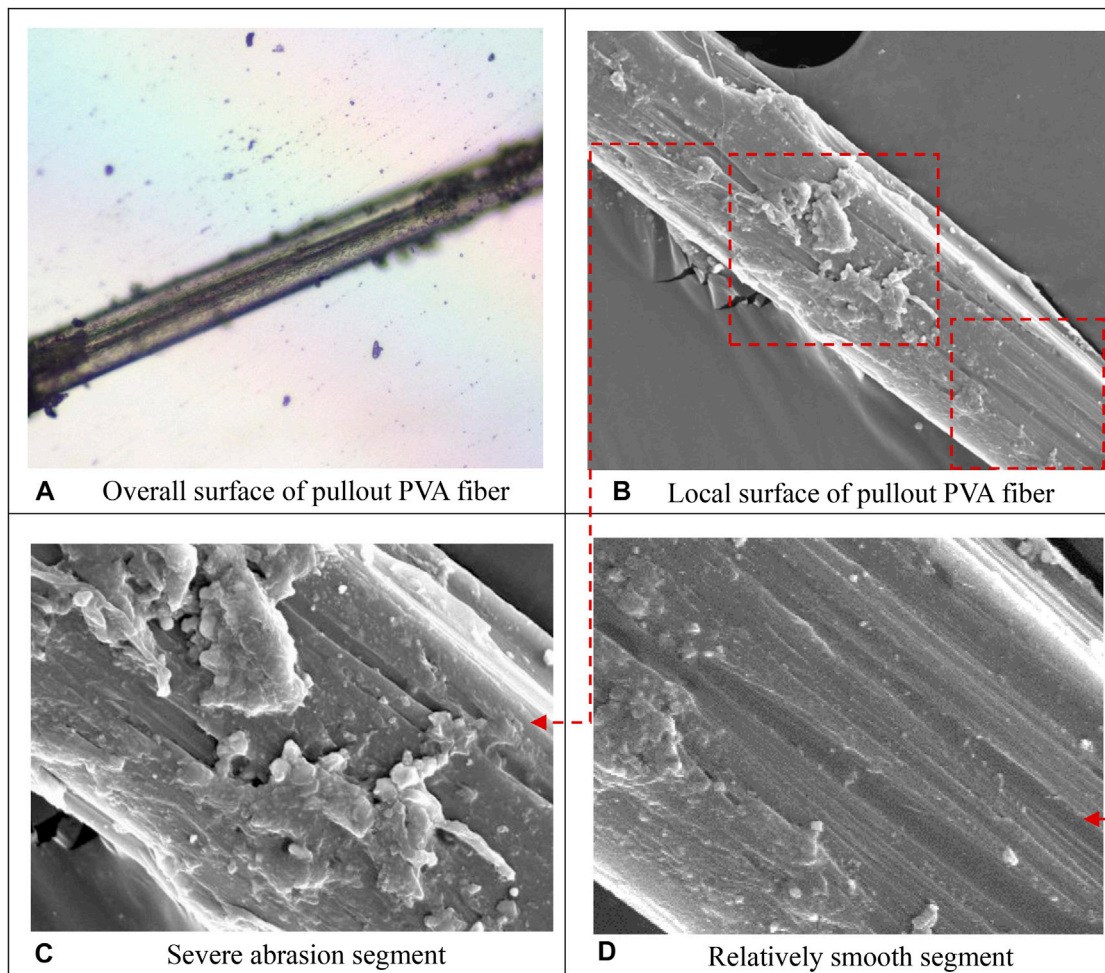


FIGURE 5 | Various segments of the pullout PVA fiber surface under observation. **(A)** Overall surface of pullout PVA fiber. **(B)** Local surface of pullout PVA fiber. **(C)** Severe abrasion segment. **(D)** Relatively smooth segment.

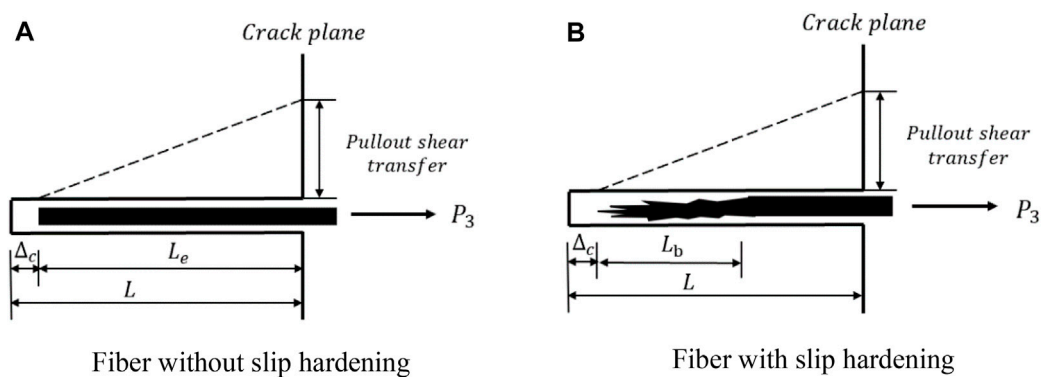
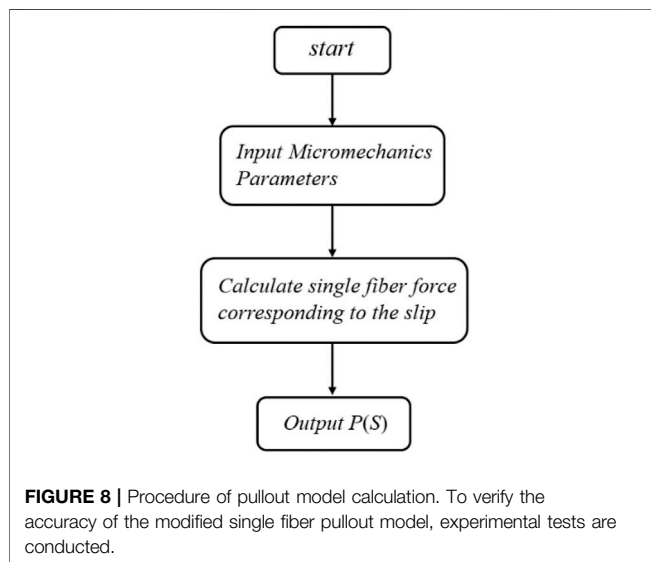
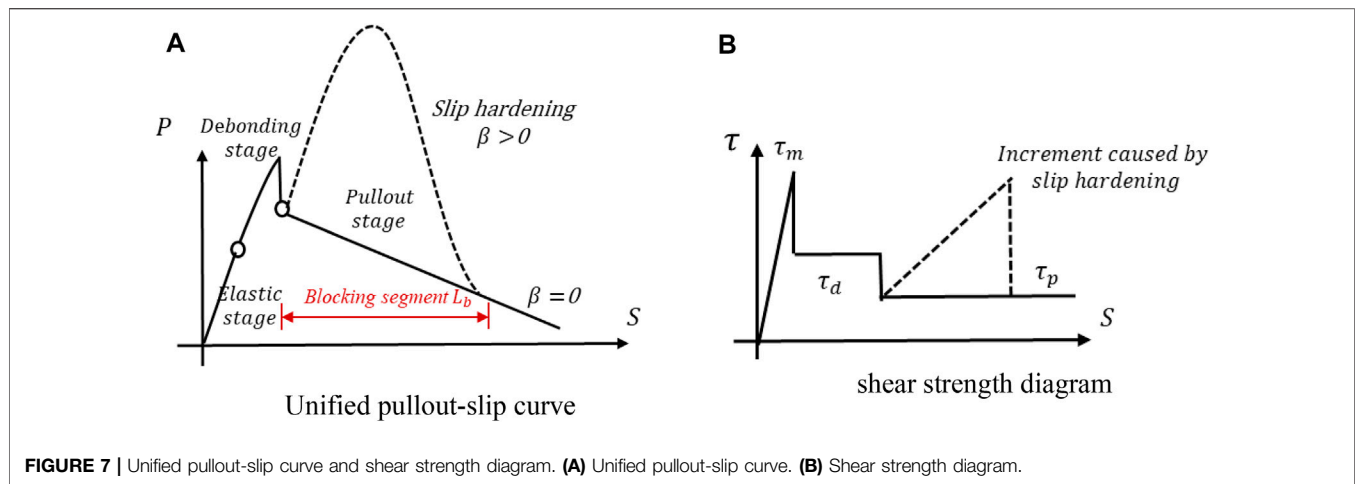


FIGURE 6 | Schematic diagram of introducing parameter blocking segment L_b into fiber pullout stage. **(A)** Fiber without slip hardening. **(B)** Fiber with slip hardening.



through the interface. This relationship expressed in the differential form is

$$\frac{dF}{dx} = -\frac{dM}{dx} = \psi\tau \quad (1)$$

where ψ = equivalent circumference of the fiber; and τ = shear stress at fiber-matrix interface.

When the fiber and matrix are fully bonded as shown in **Figure 2A**, the relationship between slip S_1 and the bonded load P_1 can be formulized as

$$S_1 = \frac{P_1 Q}{\eta \sinh(\eta L)} [\cosh(\eta L) - 1] \quad (2)$$

where $\eta^2 = \psi \kappa Q$ and slope κ is defined from the shear strength diagram, $Q = \frac{1}{A_y E_y} + \frac{1}{A_m E_m}$. When shear stress at $x = L$ reaches the maximum strength, the elastic stage is terminated and the maximum bonded load is calculated by

TABLE 1 | Properties of fibers.

Fibers	Diameter (μm)	Strength (MPa)	Modulus (GPa)
PVA	39	980	9.5
PET	20	900	6.0

The elastic modulus of the matrix is 20 GPa.

$$P_{1\max} = \frac{\tau_m \psi}{\eta} \tanh(\eta L) \quad (3)$$

When the shear stress exceeds the maximum shear strength τ_m , debonding for a length of d in **Figure 2B** is initiated, resulting in two separate regions, bonded and debonded. The shear strength of debonded stage decreases from τ_m to τ_d .

$$S_2 = \frac{P_{2\max} Q}{\eta} \frac{\cosh(\eta(L-d)) - 1}{\sinh(\eta(L-d))} + \frac{1}{2} Q d (\tau_d \psi d + 2P_{2\max}) \quad (4)$$

$$P_{2\max} = \frac{\tau_m \psi}{\eta} \tanh(\eta(L-d)) \quad (5)$$

It is assumed that at the time the fiber is completely debonded, the shear resistance still remains τ_d , leading to a simplified rigid body motion after sliding begins ($\Delta c > 0$) as shown in **Figure 2C**.

$$S_3 = -\frac{\tau_d \psi Q}{2} (L - \Delta c)^2 + P_{3,\text{nth}} Q (L - \Delta c) \quad (6)$$

$$P_3 = \tau_d \psi (L - \Delta c) \quad (7)$$

New Considerations in Single Fiber Pullout Stage

The above section illustrates the stress transfer via interface between the fiber and matrix when the fiber is being pulled out. However, due to the great divergency in the interface properties between various fibers, the previous model mentioned above cannot apply to different types of fibers. The limitations will be explained in detail in this section.

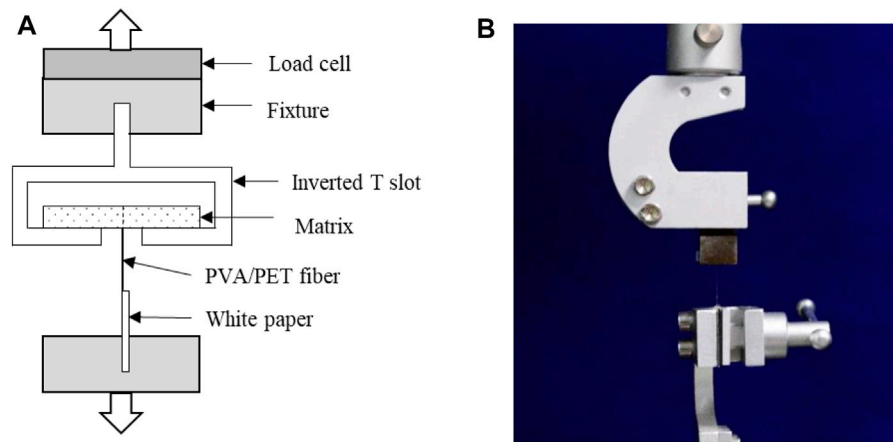


FIGURE 9 | Setup of single fiber pullout test. **(A)** Single fiber pullout specimen placement. **(B)** Single fiber pullout test instrument.

TABLE 2 | interfacial parameters for PVA and PET fiber pullout simulation.

PVA/ No	τ_m (MPa)	τ_d (MPa)	τ_p (MPa)	L_b (mm)	β	PET/No	τ_m (MPa)	τ_d (MPa)	τ_p (MPa)	L_b (mm)	β
1	1.20	0.55	0.32	1.70	0.20	1	0.80	0.52	0.36	0	0
2	0.90	0.60	0.34	1.5	0.32	2	0.65	0.50	0.30	0	0
3	0.80	0.70	0.38	1.50	0.34	3	1.15	0.60	0.36	0	0
4	0.90	0.90	0.30	2.20	0.45	4	0.95	0.65	0.46	0	0
5	0.95	0.90	0.33	2.60	0.48	5	0.80	0.70	0.36	0	0
6	0.90	0.90	0.32	2.20	0.46	6	0.80	0.58	0.38	0	0
7	1.10	1.10	0.40	2.50	0.46	7	1.05	0.70	0.42	0	0
8	1.10	1.10	0.51	1.90	0.5	8	1.10	0.85	0.58	0	0
9	1.40	1.20	0.95	1.90	0.16	9	0.90	0.73	0.52	0	0
10	0.90	0.85	0.75	2.00	0.22	10	1.20	1.10	0.70	0	0
11	1.30	1.20	0.90	1.95	0.28	11	1.15	1.05	0.80	0	0
12	1.10	1.00	0.65	2.20	0.22	12	1.20	1.10	0.70	0	0
13	1.60	1.40	0.50	1.56	0.43	13	0.90	0.85	0.48	0	0
14	1.60	1.50	0.60	1.45	0.37	14	1.00	0.93	0.62	0	0
15	1.40	1.30	0.50	1.55	0.45	15	1.20	1.10	0.60	0	0
16	1.10	1.00	0.50	1.30	0.52	16	0.80	0.73	0.50	0	0

Limitation 1: Inconsistency of Frictional Strength During Different Fiber Pullout Stages

According to the above assumption, the frictional strength used in the debonding and pullout stages is the same parameter τ_d shown in **Figure 1**. Nevertheless, this assumption is not completely consistent with the actual situation. As is shown in **Figure 3**, it is assumed that at the time the fiber is completely debonded, the shear resistance still remains τ_d in the previous model. However, in the experiment the force in the pullout stage descends at a slower rate compared to that in the debonding stage, which should be related to the difference of the static friction and dynamic friction (Sueki et al., 2007). Therefore, it is necessary to adopt different frictional strength in different stages according to the actual pullout situation.

Limitation 2: Varying Slipping Behaviors for Different Fibers

In the actual experimental observation, slipping behaviors for different fibers vary widely due to the completely different

interfacial properties between the matrix and the fibers. The possible slipping phenomena in the fiber pullout stage are compared between the PVA and PET fiber. When the PVA fibers slide along the interface tunnel between fiber and matrix, the pullout force suddenly increases due to abrasion and jamming. By scanning electron microscope (SEM), it can be seen that the surface of PVA fiber (**Figure 4A**) has serious abrasion, while the surface of PET fiber (**Figure 4B**) is relatively smooth after pullout from the matrix. Hence, the various pullout performance of PET and PVA due to the different surface properties of fibers should be considered.

Limitation 3: Partial Abrasion Surface of Single Fiber After Pullout

Moreover, by Scanning Electron Microscope (SEM) shown in **Figure 5**, the PVA fiber showed both severe abrasion and relatively smooth segments after pullout, indicating that only part of the fiber was worn during pullout stage. Therefore, the partial blocking segment should be introduced to simulate the actual pullout

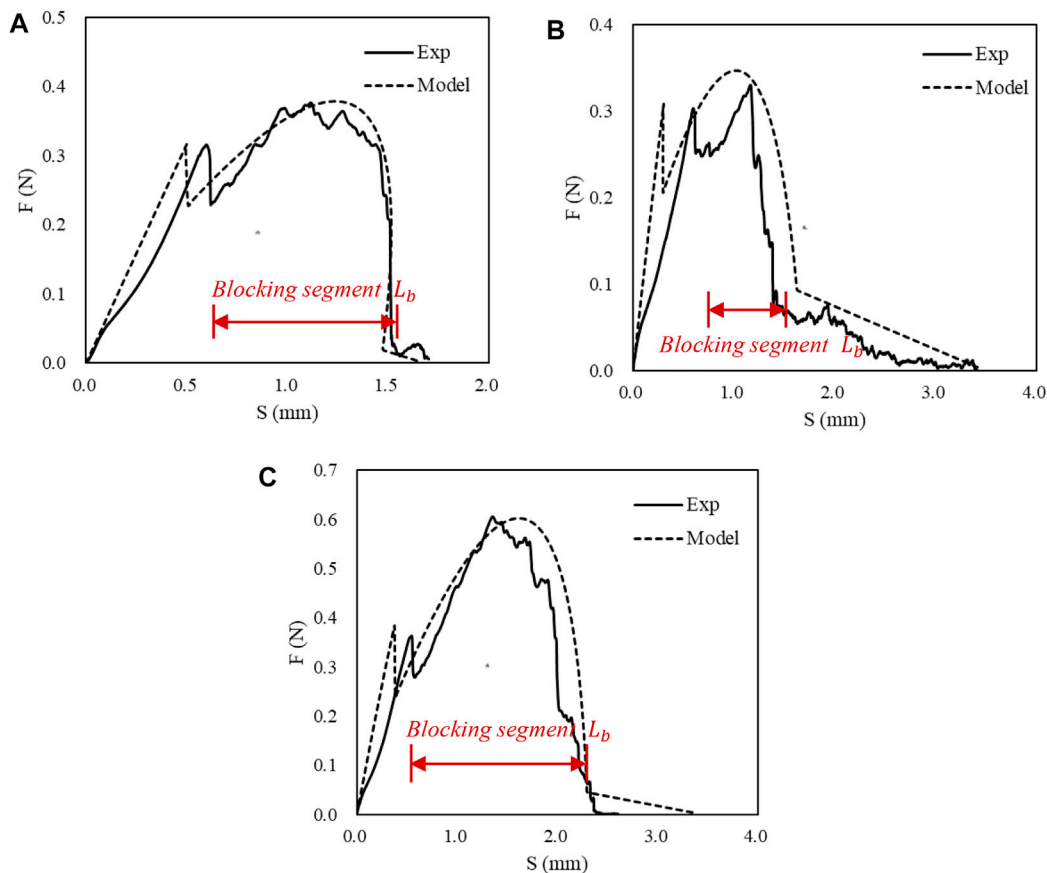


FIGURE 10 | Comparison of experiments and modified PVA fiber pullout simulation results.

process compared with the sliding hardening coefficient applied to the whole pullout process in the previous study (Yang et al., 2008).

Refined Single Fiber Pullout Model With New Considerations

To address the mentioned limitations of current model, a refined model for single fiber pullout is proposed in this section.

As mentioned before, the frictional strength varies in different fiber pullout stages, especially in the debonding and pullout stages. To account for this variation, a new parameter pullout frictional strength τ_p is adopted. During the fiber pullout process, fiber and matrix are fully bonded when the shear stress at interface is less than the maximum chemical strength τ_m . Along the debonded zone the frictional strength is constant as τ_d . Sliding begins right after the completion of debonding and the resisting frictional strength is assumed to drop to pullout strength τ_p . By introducing this new parameter, the overall trend of pullout stage will be flatter and more consistent with the experiment than the previous model.

Moreover, considering the surface of some fibers bonded with the matrix is partly worn under pulley force which results in obvious slip hardening phenomenon, the new parameter blocking segment L_b (as shown in **Figure 6**) and is introduced to describe different slipping phenomena.

The pulley force of fiber with slip hardening in the pullout stage can be expressed as

$$P_3 = \tau_p \left[(L_b - \Delta_d + \Delta_c) \left(1 + \frac{\beta(\Delta_d - \Delta_c)}{D} \right) + (L + \Delta_c - L_b) \right] \quad (8)$$

where, Δ_d represents the fiber displacement, slip hardening coefficient β represents the rate of frictional change, Δ_c represents the debonding length, and D represents fiber diameter.

By adding these new parameters, the fiber like PVA fiber which has obvious slip hardening phenomenon can be simulated more accurately, and the pullout phenomena of fibers with different properties can be unified through the processing of the pullout stage formula as shown in **Figure 7**.

Based on the analytical model established above, the curves obtained from the experiment can be simulated. The specific calculation process is summarized as follows in **Figure 8**.

Experimental Validation

In this section, the preparation and setup of single fiber pullout tests are introduced in detail. Moreover, parameters are fitted based on different experimental curves to obtain more accurate fiber bridging curve.

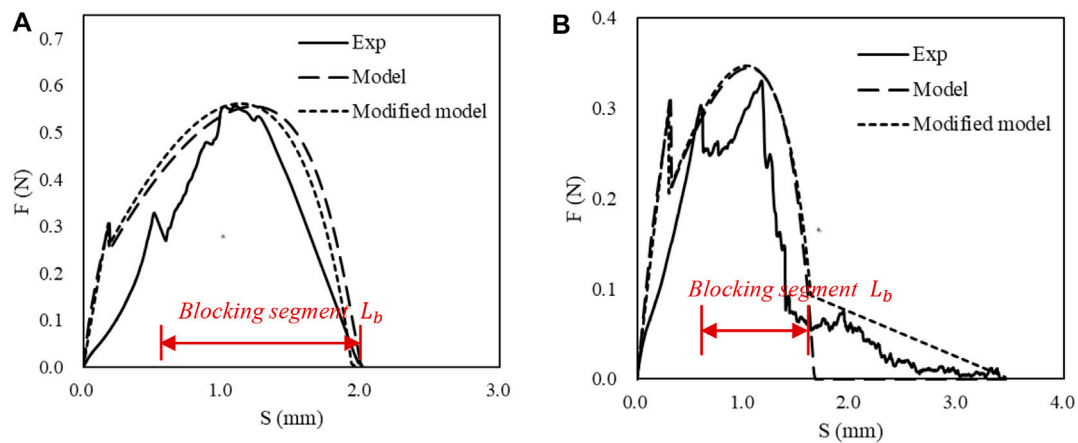


FIGURE 11 | Comparison of PVA fiber pullout model and modified PVA fiber pullout model with introduced parameter L_b . (A) The entire surface of the fiber was worn. (B) The partial surface of the fiber was worn.

Setup of Single Fiber Pullout Test

The main components of SHCC matrix materials used in the test are ordinary silicate 42.5 cement, F class I level fly ash, 80–100 mesh quartz sand and polycarboxylic acid water-reducing agent (PCA).

The fibers selected in the test are PET fiber and domestic PVA fiber. According to the actual measurement, the basic mechanical parameters are shown in **Table 1**.

Single fiber pullout test was performed to evaluate the interfacial bond between the PVA/PET fiber and the matrix. Then the experimental curve was fitted, respectively, to obtain the fitting parameters. In this test, the testing setup is shown in **Figure 9**. More details of the test can be found in Katz and Li (1996). As shown in **Figure 9A**, the fiber pullout specimen was placed on an inverted T slot. At the same time, the free end of PVA/PET fiber was glued to a piece of white paper, which was fixed with the lower fixture. The single fiber was pulled out under displacement control at the rate of 0.5 mm/min.

Results and Discussion on the Single Fiber Pullout Test

Simulation of single fiber pullout based on the new model is conducted on each individual tested specimen. The parameters including τ_m , τ_d , τ_p , L_b and β are estimated in order to find a match between the simulation and experiment. Nominal shear strength τ_n has been defined to estimate the value of τ_m and τ_d .

$$\tau_n = \frac{F_{max}}{\pi DL} \quad (8a)$$

where F_{max} = maximum load of experiment; D = diameter of a fiber; and L = embedded length of fiber.

τ_m controls the development rate of elastic stage, the value of which is higher than that of τ_n . τ_d is related to the maximum force of the debonding stage, the value of which tend to be lower

than that of τ_n . τ_p controls the development rate of pullout stage and its value is the minimum.

L_b and β are used to describe slip hardening phenomenon. L_b is obtained by calculating the difference between displacement at the end of slip hardening and that at the beginning of slip hardening. Based on the determined L_b , higher value of β means higher value of second peak. The parameters used for all specimens are listed in **Table 2** below.

It can be seen that in the PVA fiber pullout stage, the blocking segment for each fiber in **Figure 10** vary from each other, while the modified model can simulate well regardless of the length of the blocking segment. The modified model is consistent with the test results which show various lengths of blocking segment L_b . This proves that the introduction of new parameters can simulate the real situation more properly.

The previous model and the modified model both can fit well with the experimental curve when the entire surface of the fiber was worn under pulley force as shown in **Figure 11A**. However, when the surface of the fiber was partially worn, the previous model could not fit well with the experimental curve in the pullout stage. With the introduced parameter L_b , the modified single fiber pullout model can apply to the same fibers which show various lengths of blocking segment under pulley force.

Compared with PVA fibers which have obvious blocking segment, PET fibers show negligible slip-hardening in **Figure 12**. This difference is expected since the surface of PET fiber is smoother than that of the PVA fiber.

Overall, the proposed single fiber pullout model can fit well with the experimental results for both the PVA and PET fibers. It can be seen that different parameters derived from the pullout tests vary widely between different fibers in **Table 2**. Therefore, normal distribution is conducted based on the obtained parameters to better describe the stochasticity of fiber pullout characteristic.

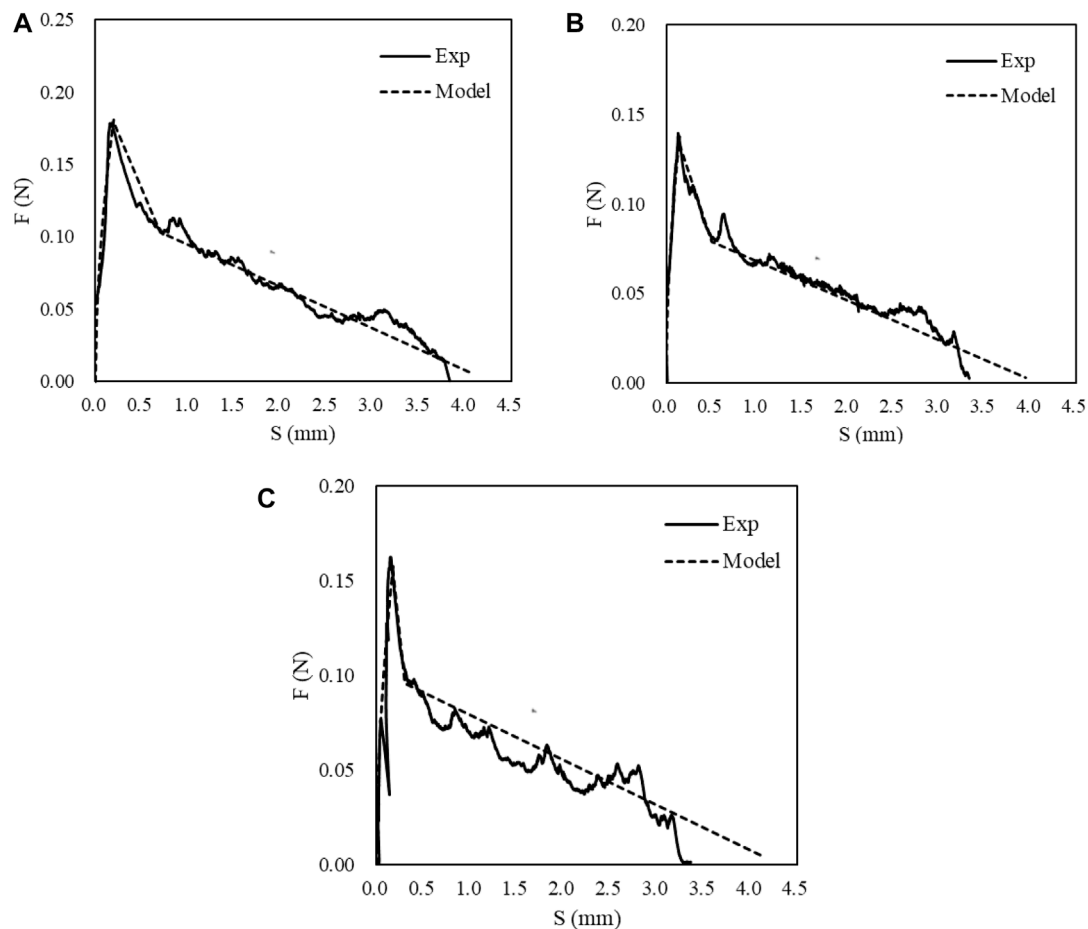


FIGURE 12 | Comparison of experiments and modified PET fiber pullout simulation results.

MODELING OF FIBER-BRIDGING CONSTITUTIVE LAW $\sigma(\delta)$

Description of the Stochasticity in the Fiber Pullout Behaviors

According to the parameter results obtained from single fiber pullout simulation above, even the same kind of fibers vary a lot in discreteness. Considering such difference, average values were used in the previous study to apply these parameters to a larger scale like simulation of fiber bridging curve. However, the randomness of interface parameters cannot be expressed completely by using the average values, so the parameters used in fiber bridging curve are obtained from normal distribution in this paper.

As illustrated in **Figure 13**, all parameters were randomized for PVA and PET fibers, respectively. Then a modified single crack model will be established based on the parameters

selected randomly from the probability distribution of these parameters.

Modeling Strategy of the $\sigma(\delta)$ Relation for Single Crack

Fiber-bridging constitutive law $\sigma(\delta)$ describes the relationship between the bridging stress σ transferred across a crack and the opening of this crack δ . On the one hand, this curve is related to the material microstructure. On the other hand, tensile strain-hardening behavior of composites is governed by this law. Therefore, to successfully design SHCC material properties, it is necessary to understand and simulate the $\sigma(\delta)$ curve with good accuracy.

For a fiber perpendicular to the interface between fiber and matrix, the parameters are selected randomly from the probability distribution of these parameters above in **Figure 13**. Therefore, a

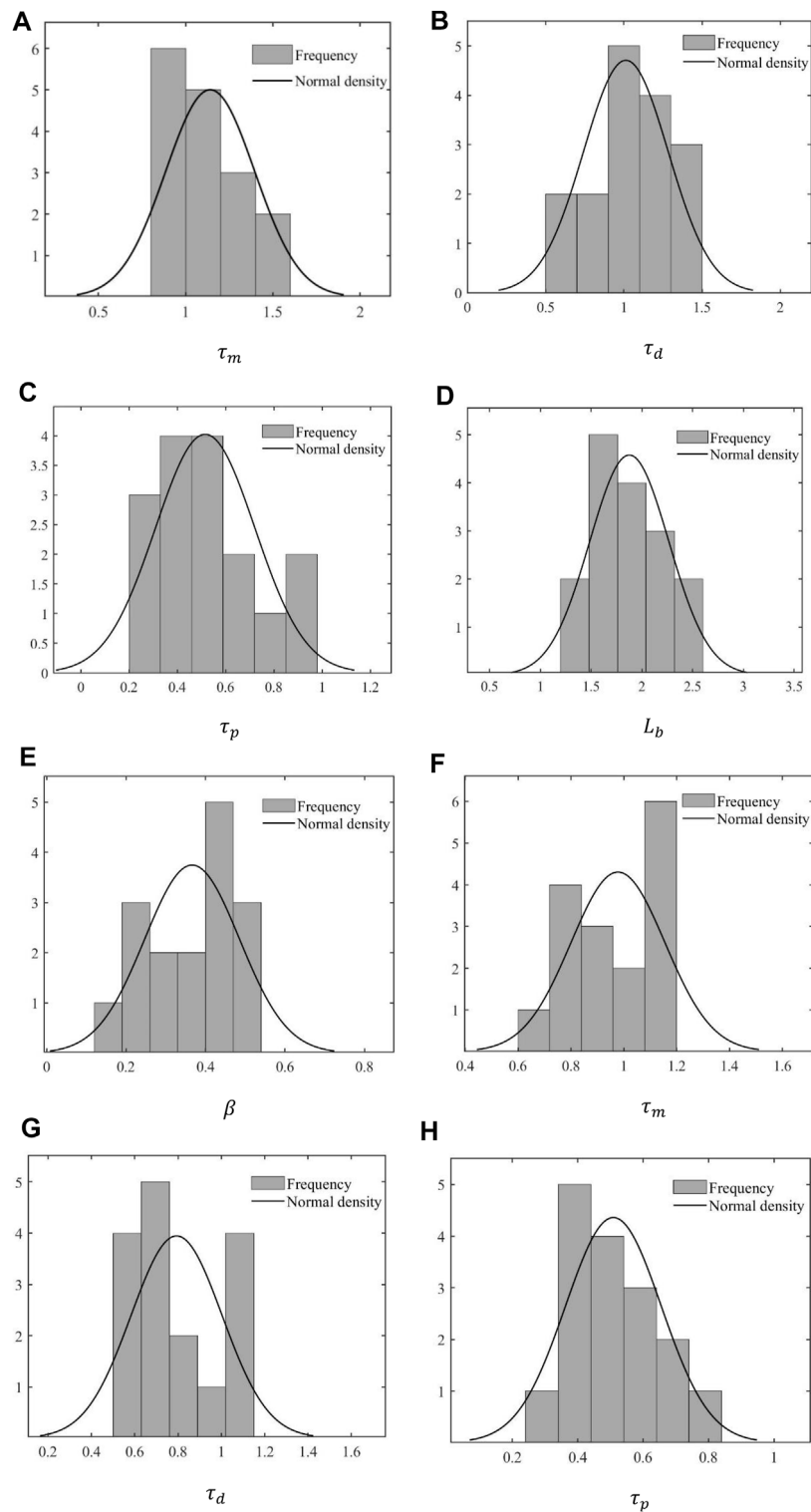


FIGURE 13 | Histogram of normal distribution: **(A–E)** in PVA fiber, **(F–H)** in PET fiber.

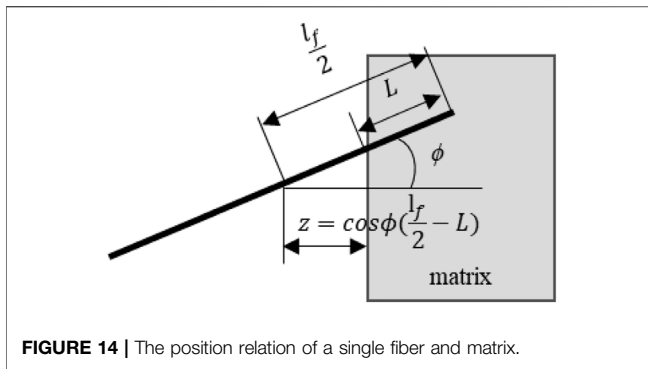


FIGURE 14 | The position relation of a single fiber and matrix.

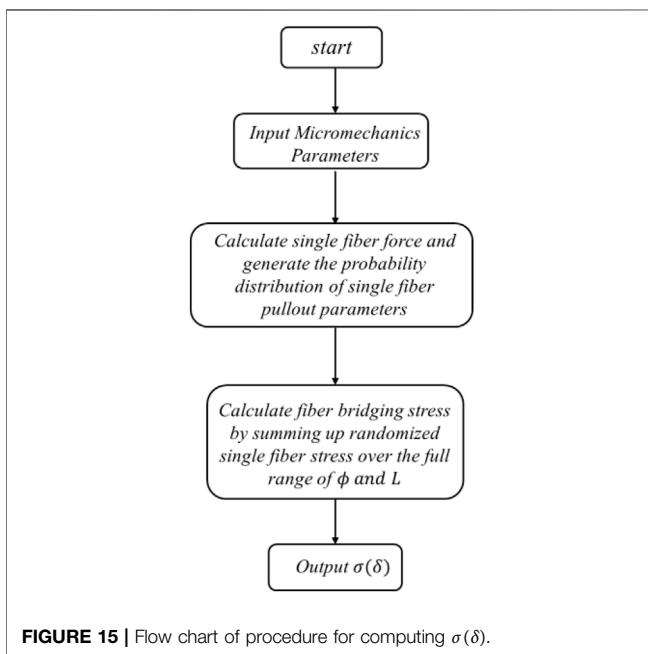


FIGURE 15 | Flow chart of procedure for computing $\sigma(\delta)$.

single fiber pullout force can be calculated when the orientation angle ϕ is 0. However, the bridging force is contributed by the fibers which are randomly distributed with different orientation angle ϕ and embedding length L . Hence, the fiber-bridging $\sigma(\delta)$ relation is available through assuming the force of fibers with different centroidal distance z and orientation angle ϕ on the crack plane. The position relation of a single fiber and matrix is shown in **Figure 14**.

Equation 9 shows the formulation of fiber-bridging $\sigma(\delta)$ relation.

$$\sigma(\delta) = \frac{1}{A_f V_f} \int P(z, \phi) p(z, \phi) dz d\phi \quad (9)$$

A_f and V_f are the cross-sectional area and volume fraction of fiber, respectively. $P(z, \phi)$ is the bridging force contributed by a single fiber with distance z and orientation angle ϕ . $p(z, \phi)$ is the probability density function of fiber with distance z and orientation angle ϕ .

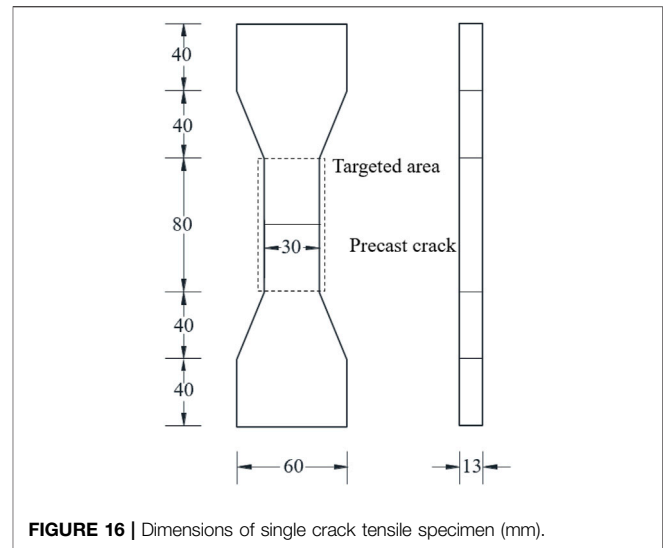


FIGURE 16 | Dimensions of single crack tensile specimen (mm).

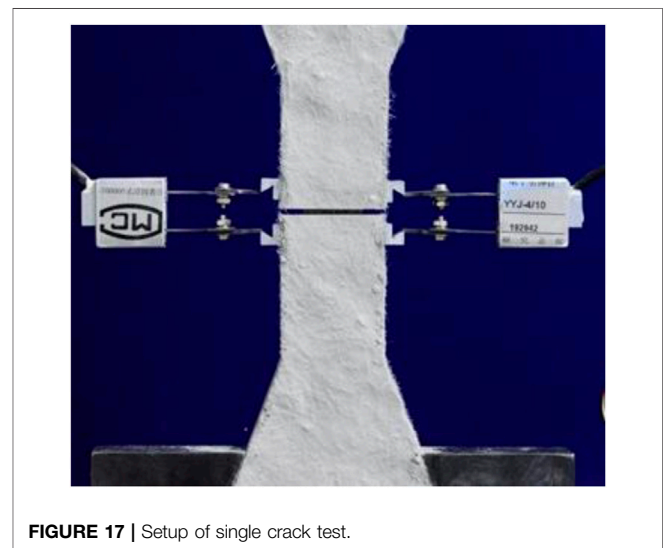


FIGURE 17 | Setup of single crack test.

The probability density functions of distance z and orientation angle ϕ are independent of each other. So $p(z, \phi)$ can be expressed as following

$$p(z, \phi) = p(z)p(\phi) \quad (10)$$

$$p(z) = \frac{2}{l_f}, 0 \leq z \leq \frac{l_f}{2} \quad (11)$$

$$p(\phi) = \sin(\phi), 0 \leq \phi \leq \frac{\pi}{2} \quad (12)$$

A discrete method was adopted to deal with such complex analytic expressions in previous studies (Lu and Leung, 2016), which divides the fibers according to the combination of their inclination and embedding length. Assuming that the fibers are randomly distributed, fibers with different embedment length are uniformly divided into 100 groups from 0 to $L/2$, and those at different inclination angles are divided into 100 groups from 0 to $\pi/2$. Hence, 10,000 different groups are

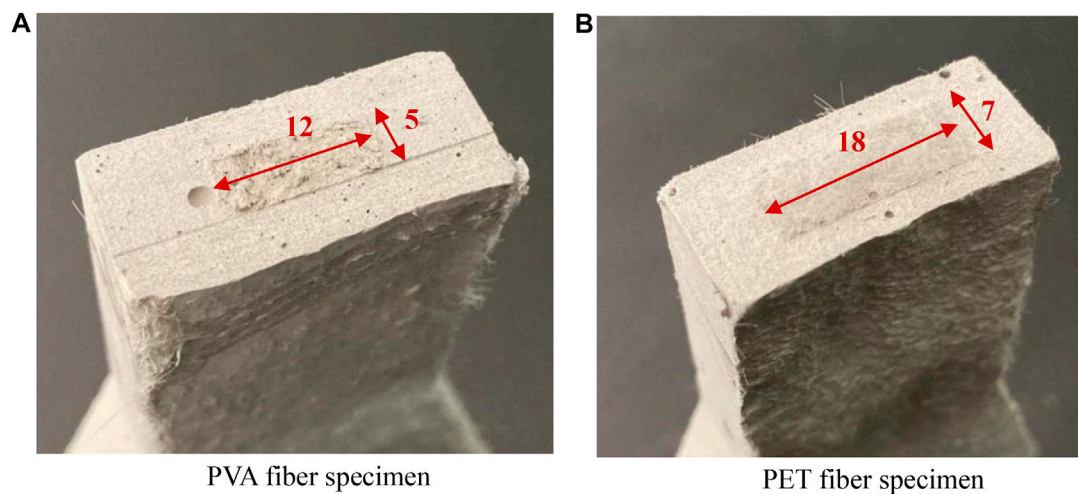


FIGURE 18 | The dimension of the cross section of PVA and PET fiber specimens. **(A)** PVA fiber specimen. **(B)** PET fiber specimen.

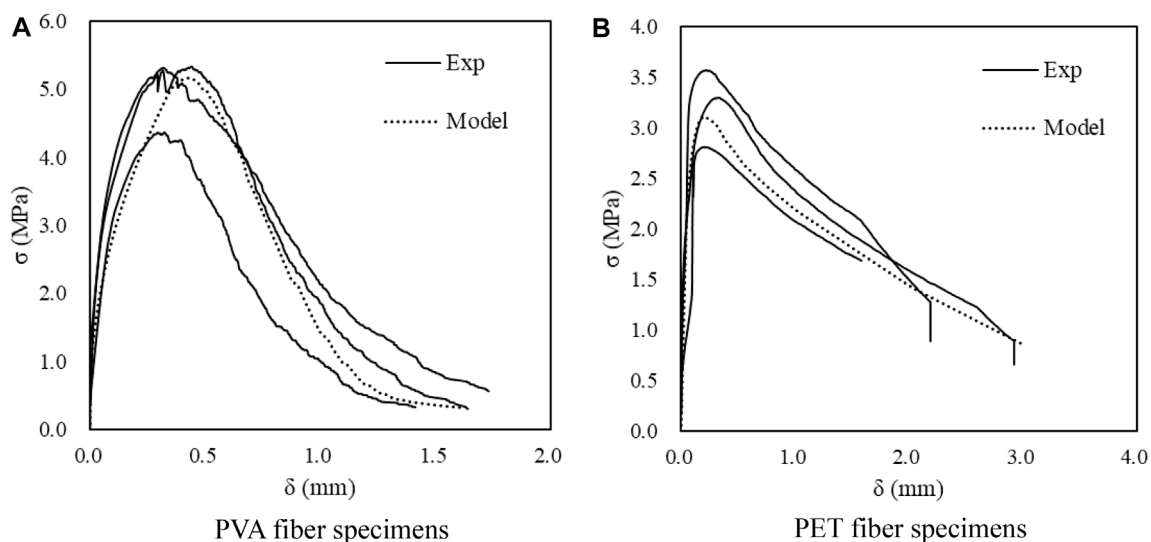


FIGURE 19 | Comparison of experiments and modified $\sigma(\delta)$ curve simulation results for PVA and PET fiber specimens. **(A)** PVA fiber specimens. **(B)** PET fiber specimens.

considered totally. Meanwhile, assuming that fibers with longer embedment length (from $L/2$ to L) have the same distribution as fibers with shorter embedment length and their lengths sum up to L . Therefore, when calculating the friction stress transfer with a certain embedment length, the frictional stress from both the long and short embedment side should be calculated and averaged.

Through this way, the stress-crack opening curves are simulated and compared with the experimental results. The specific calculation process is summarized in **Figure 15**.

Verification With Experimental Results

Single crack tensile test was conducted to compare with the simulation results. Dog-bone specimen is used according to the SHCC mechanical test specification, and the specific size is shown in **Figure 16**.

The test preparation is shown in **Figure 17**. The preparation of specimens mainly includes weighing, mixing, pouring, demolding and curing of raw materials. After curing, the middle section of the specimen was notched by a cutting

machine to prevent the phenomenon of multi-crack cracking during tensile test and the dimension of the cross section of PVA and PET fiber specimens are shown in **Figure 18**. For the test setup, the edge of electronic extensometer was glued on the side of the specimen, and the force arm of the extensometer was finally clamped and fixed on the tool edge.

It can be seen in **Figure 19** that the bridging stress reaches the peak stress at roughly 5 MPa in PVA fibers while PET fibers can only reach 3 MPa peak stress. Besides the peak bridging stress, the corresponding crack opening displacement δ for PVA fiber specimen is wider than that for PET fiber specimen, which means that PVA fibers may have better ductility. Meanwhile, due to the larger crack width, the durability of PVA fiber specimen may be not as good. Compared with the PVA fiber specimen, PET fibers can continue to bridge the matrix under a larger crack opening displacement more than 2 mm. It is likely due to the interfacial bond between PVA fiber and the matrix is stronger than that between PET fiber and the matrix. Due to the weaker bond with the matrix, PET fiber shows higher tendency to pull out, which accounts for the flatter decline trend of PET fiber in the pullout stage as shown in **Figure 19B**.

Overall, the single crack model which is built based on the proposed single fiber pullout model fits well with the test results so the validity is confirmed again.

CONCLUSION

In this study, a unified model for single fiber pullout was successfully developed with introduced parameters, which is

suitable for fibers with different interfacial properties, including PET and PVA fibers investigated in this paper. Single crack model based on the new single fiber pullout model was then developed, which takes into account the stochasticity of various pullout behaviors between different fibers. Experimental verification on single fiber pullout and single crack opening were conducted to show that the proposed model can agree well with the test results.

To conclude, this model is suitable not only for one specific fiber, but can apply to different kinds of fibers by one united form, which was verified by experiments in PVA and PET fiber systems. This revised fiber-bridging model can be utilized to predict the composite tensile ductility of SHCC with different fibers effectively, which will help the understanding and micro-mechanics-based design of SHCC materials.

DATA AVAILABILITY STATEMENT

The original contributions presented in the study are included in the article/Supplementary Material, further inquiries can be directed to the corresponding author.

AUTHOR CONTRIBUTIONS

PS was responsible for most experimental testing and model simulation work, CL put forward constructive suggestions for the revision of this paper, JW assisted in the simulation of single crack model and ZP offered help to scan the specimen by SEM.

REFERENCES

- Foti, D. (2016). Innovative Techniques for concrete Reinforcement with Polymers. *Construction Building Mater.* 112, 202–209. doi:10.1016/j.conbuildmat.2016.02.111
- Graybeal, B. A. (2006). *Material Property Characterization of Ultra-high Performance concrete Creep*.
- Jun, Z., Leung, C. K. Y., and Yin Nee, C. (2006). Flexural Performance of Layered ECC-concrete Composite Beam. *Composites Sci. Technol.* 66 (11–12), 1501. doi:10.1016/j.compscitech.2005.11.024
- Kanda, T., and Li, V. C. (1999). Effect of Fiber Strength and Fiber-Matrix Interface on Crack Bridging in Cement Composites. *J. Eng. Mech.* 125 (3), 290–299. doi:10.1061/(asce)0733-9399(1999)125:3(290)
- Kanda, T., and Li, V. C. (1998). Interface Property and Apparent Strength of High-Strength Hydrophilic Fiber in Cement Matrix. *J. Mater. civil Eng.* 10 (1), 5–13. doi:10.1061/(asce)0899-1561(1998)10:1(5)
- Katz, A., and Li, V. C. (1996). A Special Technique for Determining the Bond Strength of Micro-fibers in Cement Matrix by Pullout Test. *J. Mater. Sci. Lett.* 15 (20), 1821–1823. doi:10.1007/bf00275353
- Leung, C. K. Y. (1996). Design Criteria for Pseudoductile Fiber-Reinforced Composites. *J. Eng. Mech.* 122 (1), 10–18. doi:10.1061/(asce)0733-9399(1996)122:1(10)
- Li, V. C. (1998). Engineered Cementitious Composites - Tailored Composites through Micromechanical Modeling. *J. Adv. Concrete Techn.* 1(3).
- Li, V. C. (2011). *Engineered Cementitious Composites (ECC) – Material, Structural, and Durability Performance*.
- Li, V. C., Mishra, D. K., Naaman, A. E., Wight, J. K., and Inada, Y. (2003). On the Shear Behavior of Engineered Cementitious Composites. *Adv. Cement Based Mater.* 1 (3), 142. doi:10.1016/1065-7355(94)90045-0
- Li, V. C. (2012). On Engineered Cementitious Composites (ECC) A Review of the Material and its Applications. *Fiber reinforced Concrete Engineering Materials 2012 Summit Forum of China Association of Concrete and Cement Products*, 2164, 1–810.
- Li, V. C., Wang, S., and Wu, C. (2001). Tensile Strain-Hardening Behavior of Polyvinyl Alcohol Engineered Cementitious composite(PVA-ECC). *Acı Mater. J.* 98(6), 483.
- Li, V. C., and Leung, C. K. Y. (1992). Steady-State and Multiple Cracking of Short Random Fiber Composites. *J. Eng. Mech.* 118 (11), 2246–2264. doi:10.1061/(asce)0733-9399(1992)118:11(2246)
- Li, V. C., and Wu, H.-C. (1992). Conditions for Pseudo Strain-Hardening in Fiber Reinforced Brittle Matrix Composites. *Appl. Mech. Rev.* 45 (8), 390–398. doi:10.1115/1.3119767
- Lin, Z., and Li, V. C. (1997). Crack Bridging in Fiber Reinforced Cementitious Composites with Slip-Hardening Interfaces. *J. Mech. Phys. Sol.* 45 (5), 763–787. doi:10.1016/s0022-5096(96)00095-6
- Lu, C., and Leung, C. K. Y. (2016). A New Model for the Cracking Process and Tensile Ductility of Strain Hardening Cementitious Composites (SHCC). *Cement Concrete Res.* 79, 353–365. doi:10.1016/j.cemconres.2015.10.009
- Lu, C., Yu, J., and Leung, C. K. Y. (2018). Tensile Performance and Impact Resistance of Strain Hardening Cementitious Composites (SHCC) with Recycled Fibers. *Construction Building Mater.* 171, 566–576. doi:10.1016/j.conbuildmat.2018.03.108
- Maalej, M., Li, V. C., and Hashida, T. (1995). Effect of Fiber Rupture on Tensile Properties of Short Fiber Composites. *J. Eng. Mech.* 121 (8), 903–913. doi:10.1061/(asce)0733-9399(1995)121:8(903)
- Naaman, A. E., Namur, G. G., Alwan, J. M., and Najm, H. S. (1991). Fiber Pullout and Bond Slip. I: Analytical Study. *J. Struct. Eng.* 117.

- Ochi, T., Okubo, S., and Fukui, K. (2007). Development of Recycled PET Fiber and its Application as concrete-reinforcing Fiber. *Cement and Concrete Composites* 29 (6), 448–455. doi:10.1016/j.cemconcomp.2007.02.002
- Pakravan, H. R., Latifi, M., and Jamshidi, M. (2016). Ductility Improvement of Cementitious Composites Reinforced with Polyvinyl Alcohol-Polypropylene Hybrid Fibers. *J. Ind. Textiles* 45 (5), 637–651. doi:10.1177/1528083714534712
- Pan, Z., Wu, C., Liu, J., Wang, W., and Liu, J. (2015). Study on Mechanical Properties of Cost-Effective Polyvinyl Alcohol Engineered Cementitious Composites (PVA-ECC). *Construction Building Mater.* 78, 397–404. doi:10.1016/j.conbuildmat.2014.12.071
- Pereira, E. B., Fischer, G., and Barros, J. A. O. (2012). Effect of Hybrid Fiber Reinforcement on the Cracking Process in Fiber Reinforced Cementitious Composites. *Cement and Concrete Composites* 34 (10), 1114–1123. doi:10.1016/j.cemconcomp.2012.08.004
- Sueki, S., Soranakom, C., Mobasher, B., and Peled, A. (2007). Pullout-slip Response of Fabrics Embedded in a Cement Paste Matrix. *J. Mater. Civ. Eng.* 19 (9), 718–727. doi:10.1061/(asce)0899-1561(2007)19:9(718)
- Victor, C. L., and Forii, H. (1993). From Micromechanics to Structural Engineering the Design of Cementitious Composites for Civil Engineering Applications. *Doboku Gakkai Ronbunshu* 1993 (471), 1.
- Yang, E. H., Wang, S., Yang, Y., and Li, V. C. (2008). "Fiber-bridging Constitutive Law of Engineered Cementitious Composites". (Japan: Japan Concrete Institute).
- Zhigang, Z. (2020a). Effect of Sub-elevated Temperature on Mechanical Properties of ECC with Different Fly Ash Contents. *Construction Building Mater.* 262, 120096. doi:10.1016/j.conbuildmat.2020.120096
- Zhigang, Z. (2020b). SPEco-Friendly High Strength, High Ductility Engineered Cementitious Composites (ECC) with Substitution of Fly Ash by rice Husk Ash. *Cement Concrete Res.* 137, 106200. doi:10.1016/j.cemconres.2020.106200
- Zhigang, Z. (2021). Sustainable High Strength, High Ductility Engineered Cementitious Composites (ECC) with Substitution of Cement by rice Husk Ash. *J. Clean. Prod.* 317, 128379. doi:10.1016/j.jclepro.2021.128379

Conflict of Interest: The authors declare that the research was conducted in the absence of any commercial or financial relationships that could be construed as a potential conflict of interest.

Publisher's Note: All claims expressed in this article are solely those of the authors and do not necessarily represent those of their affiliated organizations or those of the publisher, the editors and the reviewers. Any product that may be evaluated in this article, or claim that may be made by its manufacturer, is not guaranteed or endorsed by the publisher.

Copyright © 2022 She, Wang, Pang and Lu. This is an open-access article distributed under the terms of the Creative Commons Attribution License (CC BY). The use, distribution or reproduction in other forums is permitted, provided the original author(s) and the copyright owner(s) are credited and that the original publication in this journal is cited, in accordance with accepted academic practice. No use, distribution or reproduction is permitted which does not comply with these terms.



Chromatic Aberration Identification of Fair-Faced Concrete Research Based on Multi-Scale Lightweight Structured Data Algorithm

Gang Yao^{1,2}, Wentong Sun¹, Yang Yang^{1,2*}, Yujia Sun¹, Liangjin Xu¹ and Jian Zhou¹

¹School of Civil Engineering, Chongqing University, Chongqing, China, ²Key Laboratory of New Technology for Construction of Cities in Mountain Area, Ministry of Education, Chongqing, China

OPEN ACCESS

Edited by:

Fangying Wang,
University of Nottingham,
United Kingdom

Reviewed by:

Anming She,
Tongji University, China
Yunchao Tang,
Guangxi University, China

*Correspondence:

Yang Yang
20121601009@cqu.edu.cn

Specialty section:

This article was submitted to
Structural Materials,
a section of the journal
Frontiers in Materials

Received: 10 January 2022

Accepted: 08 February 2022

Published: 11 March 2022

Citation:

Yao G, Sun W, Yang Y, Sun Y, Xu L and
Zhou J (2022) Chromatic Aberration
Identification of Fair-Faced Concrete
Research Based on Multi-Scale
Lightweight Structured Data Algorithm.
Front. Mater. 9:851555.
doi: 10.3389/fmats.2022.851555

Chromatic aberration is one of the quality defects in the appearance of fair-faced concrete (FFC). The mainly surface chromatic aberration identification (CAI) method being applied is manual observation, which is subjective and time-consuming. A multi-scale lightweight structured data algorithm (MSLSDA) for CAI in FFC is proposed in this manuscript. An unmanned aerial vehicle (UAV) is used for image acquisition. 2368 FFC sample images are collected to build the datasets. The FFC chromatic aberration features are identified by the improved Residual Network Convolutional Neural Network (CNN) framework to achieve chromatic aberration samples quantitative analysis. The method proposed in this manuscript can verify the generalization prediction ability of the MSLSDA for different building samples by generalization prediction set. The results show that the accuracy in CAI samples and chromatic aberration generalization prediction samples can achieve 92.1 and 99.6%, respectively. The FFC chromatic aberration detection platform (FFC-CADP) built by color space conversion, histogram equalization, image color recognition, image noise reduction and image mask algorithm is able to calculate boundary features, geometric parameter features (length and width), chromatic aberration ratio features, total chromatic aberration ratio and number of chromatic aberration.

Keywords: multi-scale feature fusion, structured data algorithm, fair-faced concrete chromatic aberration, algorithm hyperparameter optimization, lightweight algorithm

INTRODUCTION

Architects believe that FFC reveals the most essential architectural aesthetics (Coburn et al., 2019). Compared with ordinary concrete, FFC has been widely used in domestic and international buildings for its natural surface as a decorative surface, which has a high-quality appearance while satisfying mechanics and durability. The decorative surface of FFC reduces the increased costs associated with additional decorative surfaces, so the probability of budget changes during construction is low (Miranda et al., 2020). FFC has been applied and achieved positive results not only in transportation centers and commercial buildings such as Chongqing West Station, Raffles Chengdu and Raffles Chongqing, but also in modern religious buildings (Ribeiro and Xavier, 2019). The chromatic aberration control on the FFC decorative surface affects the overall effect of the building, so chromatic aberration is a key point in the control of FFC appearance. At present, the research on the

appearance quality of FFC is divided into two main directions, one is to study the factors affecting chromatic aberration and their improvements, and the other is to study the evaluation method of the FFC appearance quality.

The appearance quality of FFC is directly influenced by its own factors such as mix ratio and saturation. Studies have shown that the increase in cement saturation is beneficial to the appearance quality of FFC, but the mechanical properties of concrete decrease (Ajtayne Karolyfi and Papp, 2021). The self-compaction and appearance quality of FFC can be improved via adjusting the coarse aggregate gradation, but its application is limited due to the complex processes and high costs (Wu et al., 2021). The surface color and brightness of FFC are influenced by the cement content, water-cement ratio and sand ratio in that order (Mohammed et al., 2021). In the field of FFC apparent quality identification, there are more studies on crack identification and bubble identification. The diagnosis and repair of FFC surfaces can be performed by collecting images of the original FFC structure and combining them with machine vision techniques (Piferi, 2018), but there are still irreparable defects in the concrete appearance quality, and the diagnosis and repair work will be resource-intensive. This manuscript designs an experimental data acquisition method for FFC surface chromatic aberration based on UAV technology, it can rapidly acquire large area sample images, reduce the interference factors of image data, and improve the efficiency and quality of data acquisition. In addition, this method reduces the risk factor for staff.

The appearance quality of FFC is also indirectly influenced by factors in the production environment. Studies have shown that the effects of acid rain, haze, freeze-thaw and carbonation can cause significant chromatic aberrations in the facade of FFC buildings (Zhang et al., 2013). The dark chromatic aberration will destroy the surface appearance of FFC, and the dark chromatic aberration is more serious in the production process of outdoor FFC in winter (Chang et al., 2021). The process of removing the surface coating of FFC and mismatched release agents can lead to defects in the FFC appearance quality (Strehlein and Schiessl, 2008; Shyha et al., 2016). FFC buildings produce new chromatic aberrations in use, so it is necessary to study the identification and quantification of FFC chromatic aberration. The existing studies on the FFC surface CAI are few and cannot effectively quantify the FFC chromatic aberration.

Image processing technique can provide objective results quickly (Abouhamad et al., 2017; Mohan and Poobal, 2018; Payab et al., 2019; Chen et al., 2019; Tang et al., 2019). The identification and quantification of FFC by multi-intelligent body fuzzy systems (Payab and Khanzadi, 2021), the defects identification in the FFC appearance quality by laser point thermography (Scalbi et al., 2019), and the recording of the cracks beginning and development in combination with timelines (Prasanna et al., 2016) have been implemented. Scholars have identified the bubble contours on the FFC surface by extracting the grayscale values of the concrete surface images (Liu and Yang, 2017; Yoshitake et al., 2018). Scholars avoid the influence of subjectivity by predicting concrete performance through machine learning methods

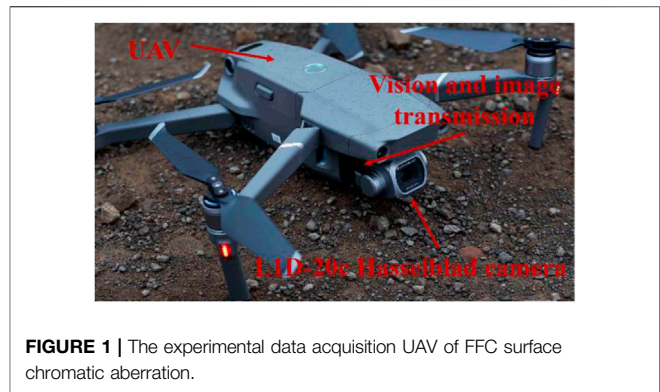


FIGURE 1 | The experimental data acquisition UAV of FFC surface chromatic aberration.

(Feng et al., 2022). This manuscript builds a FFC chromatic aberration identification model based on the optimized MSLSDA, avoids the problem of subjectivity in image processing techniques.

At present, the evaluation of the appearance quality of FFC is mainly through the image processing method (Liu et al., 2019), and the image data is segmented by selecting the appropriate threshold value (Yao et al., 2021). Therefore, the image processing process can only be applied to the current experimental data and lacks the ability to generalize to similar data (Li et al., 2020). Unlike cracks and bubbles on the surface of FFC, chromatic aberrations do not have clear boundaries and a fixed range of grayscale values, which cannot be quantified directly. This manuscript implements the FFC chromatic aberration quantization function through color space conversion, histogram equalization, image color recognition, image noise reduction and image mask operation.

A MSLSDA for FFC surface CAI is proposed in this manuscript. Firstly, the problem of subjectivity in CAI is solved by learning chromatic aberration features and classifying chromatic aberration by MSLSDA. Then, the surface chromatic aberration of FFC is quantitatively segmented by means of image processing, boundary features, geometric parameter features (length and width), chromatic aberration ratio features, total chromatic aberration ratio and number of chromatic aberration are calculated. Finally, the FFC-CADP is built to realize the prediction function and quantitative segmentation function of the FFC chromatic aberration.

CHROMATIC ABERRATION IMAGE ACQUISITION METHOD FOR FFC BASED ON UAV

FFC buildings often have a large project volume, making it difficult for inspectors to take samples and test them. Therefore, UAV is used for image acquisition in this study (Siebert and Teizer, 2014), as shown in **Figure 1**. The China Overseas HuanYu Art Center and Rail Transit R1 in Jinan are identified as sample buildings for experimental data through fieldwork, as shown in **Figure 2**. The image acquisition device is DJI Mavic two Pro, and the performance parameters are shown

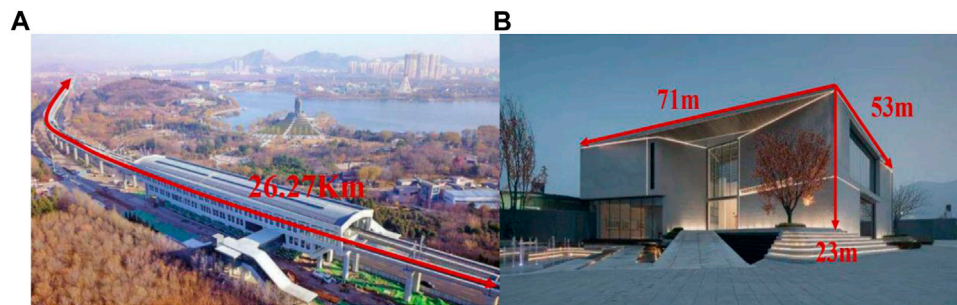


FIGURE 2 | Sample buildings of FFC chromatic aberration experimental data: **(A)** Rail Transit R1 (sub-sample) **(B)** China Overseas HuanYu Art Center (main sample).

TABLE 1 | UAV flight system and image transmission system configuration.

UAV		L1D-20c hasselblad camera		Vision and image transmission	
Technical parameters		Technical parameters		Technical parameters	
Endurance time	34 min	Image sensor	1/2-Inch CMOS	Precise front sight range	0.35–22.0 m
Hover time	33 min	Lens	Viewing angle: 84°Aperture: f/2.8	Precise range for rear view	0.37–23.6 m
Speed	72 km/h	Photo size	5,472 × 3,684	Downward-looking sensor	Binocular ToF
Wind resistance	Level 5 wind	Photo format	JPEG/DNG (RAW)	ToF accurate height measurement	0.1–8 m
Hovering accuracy	±0.1 m	Color mode	D-Cinelike	Obstacle avoidance system	APAS 3.0
On-board memory	8 GB	File system	FAT32 and exFAT	Graphical Transfer Solution	OcuSync2.0
		Digital zoom	Support	Distance	10 km

TABLE 2 | FFC appearance quality and testing methods (chromatic aberration).

Item	Normal FFC	Finished FFC	Inspection method
Chromatic aberration	No significant chromatic aberration	The color is basically the same and no significant chromatic aberration	5 m observation from the wall

in **Table 1**. UAV has high vertical hovering accuracy and horizontal hovering accuracy, L1D-20c Hasselblad camera lens angle can reach 84°, the nearest focus point 1m, the lens can achieve autofocus, can meet the observation requirements of 5 m from the wall. The photo resolution can reach 5,472*3,684, and the high pixel can meet the requirements of the experiment on the data amount. Positive endurance and stable flight speed can ensure the efficiency of image acquisition.

According to the current Technical Specification for Fair-faced Concrete Construction JGJ169-2009, the identification method for the FFC appearance quality shall conform to the provisions of **Table 2** (Kang and Cha, 2018). To ensure the consistency of the experimental data, the UAV is 5.0 m away from the target plane, the lens normal direction is always perpendicular to the target plane, and the shooting environment is naturally illuminated under normal weather. The combination of shooting angle and plane to be photographed include vertical flat surface, vertical curved surface, non-vertical flat surface and non-vertical curved surface. Currently, this study addresses the chromatic

aberration identification in the FFC vertical flat surface. The cases of vertical curved surface, non-vertical flat surface and non-vertical curved surface will be considered in further studies to improve the generalizability of the FFC chromatic aberration identification method.

The original image is taken by UAV at a distance of 5 m from the FFC vertical flat surface. Obstructions obscuring light rarely occurs during the original images acquisition. And we consciously avoid shooting original images with obstructions obscuring them. In the process of dataset production, we carefully screen and remove the sample images with obstructions obscuring them. However, the phenomenon of obstructions obscuring light and creating shadow area on the FFC does exist. The pixel value of the shadow area is affected by the light intensity and obstruction position, which we will try to solve in further studies.

In order to test the ability of the MSLSDA to generalize the FFC chromatic aberration problem, chromatic aberration data were collected from China Overseas HuanYu Art Center and Rail Transit R1 during the period of 12:30–14:30 on 22 March 2021, with 13:10–14:00 as the site transition period. China Overseas

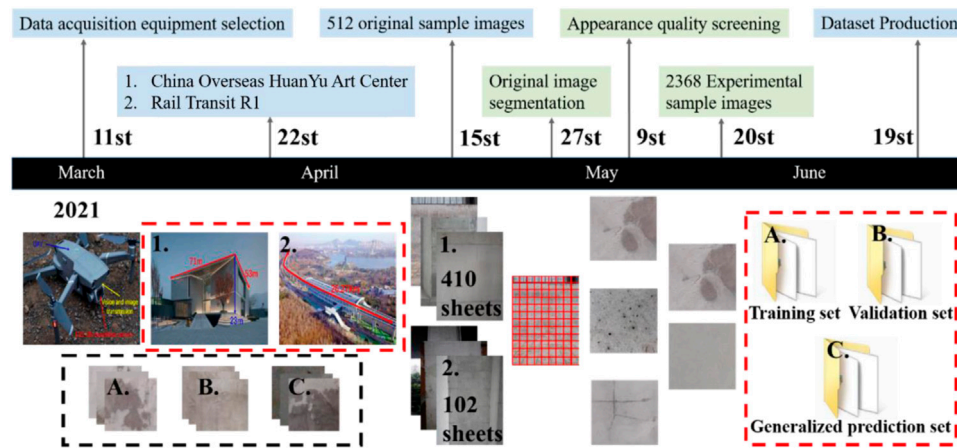


FIGURE 3 | FFC chromatic aberration experimental data acquisition, pre-processing and dataset production timeline.

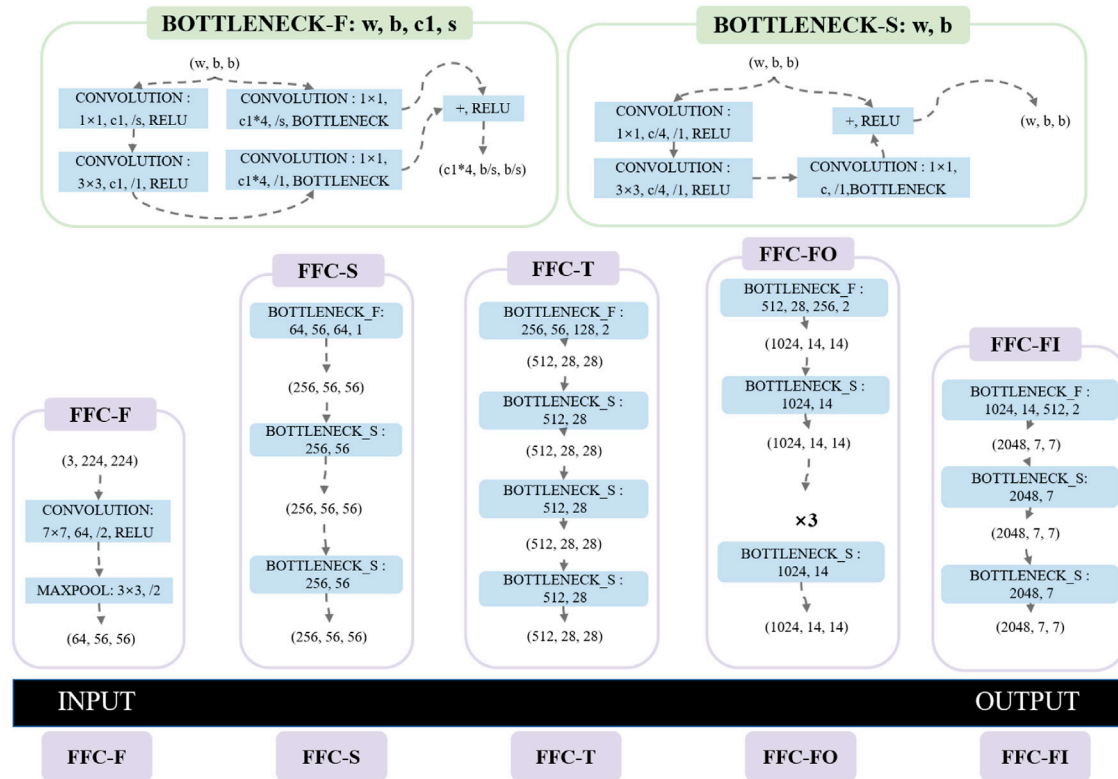
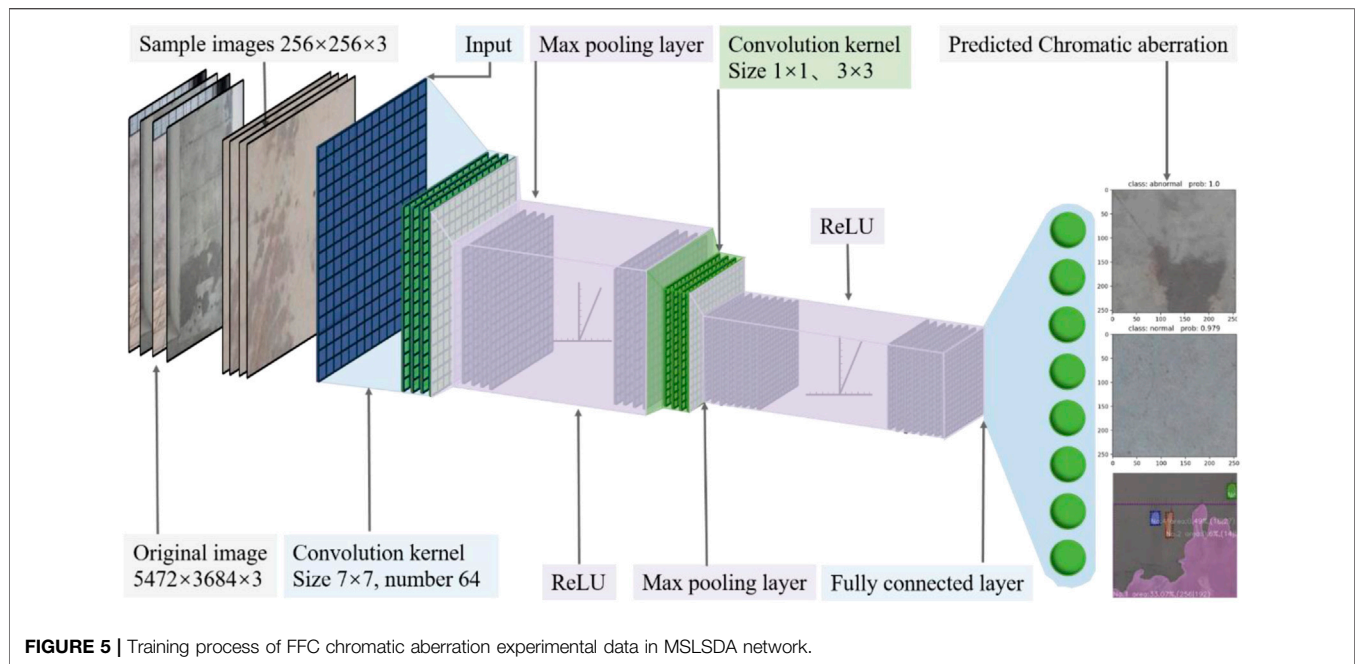


FIGURE 4 | Residual Network CNN framework and structured data propagation process.

HuanYu Art Center is the main sample building, and Rail Transit R1 is the sub-sample building. According to the sample buildings, 410 original images of the main sample buildings are used for the training set and validation set, and 102 original images of the sub-sample buildings are used for the generalized prediction set (Cha et al., 2017).

FFC IMAGE PRE-PROCESSING

In order to improve the training efficiency of MSLSDA, the original data is pre-processed in this study. The original image with a resolution of $5,472 \times 3,684$ is segmented into 306 sample images with a resolution of 256×256 . After excluding the images

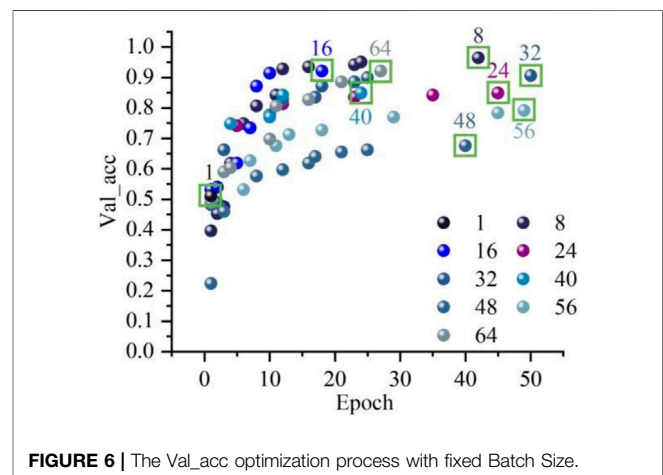


with non-chromatic appearance quality indicators from the segmented sample images, a total of 2,368 experimental sample images are obtained, as shown in **Figure 3**.

Among them, 1894 experimental sample images are selected from 410 original images of the main sample buildings, accounting for 80% of the total number of experimental sample images. The 474 experimental sample images are selected from the original images of 102 sub-sample buildings, accounting for 20% of the total number of experimental sample images. The 474 experimental sample images include 237 sample images without chromatic aberration and 237 sample images with chromatic aberration. 80% of the 1894 experimental sample images are randomly selected as the training set and the remaining 20% as the validation set. The validation set consists of 189 sample images without chromatic aberration and 189 sample images with chromatic aberration. The training set consists of 758 sample images without chromatic aberration and 758 sample images with chromatic aberration.

In this manuscript, generalization prediction experiments are designed to enhance the generalization ability of the MSLSDA for the FFC surface CAI problem. The optimized and trained MSLSDA will sequentially predict each experimental sample image in the generalized prediction set and output the identification result and probability value prod. The identification results are compared with the actual results to quantitatively evaluate the generalization prediction ability of the MSLSDA. The probability value prod can quantitatively evaluate the probabilistic reliability of the identification results.

Labeling and path standardization of the experimental samples are crucial to the process of producing the dataset. Firstly, input the experimental sample images and save the structured data into fixed channels and fixed dimensions. Then, the dataset form is saved as Numpy form and the



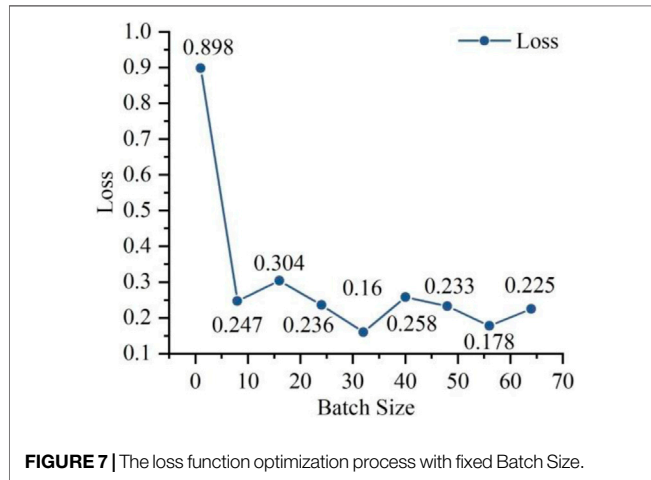
dataset is reordered. Finally, the 2,368 experimental sample images in the dataset are written to the corresponding paths in the images folder to complete the dataset.

MSLSDA HYPERPARAMETER OPTIMIZATION

Residual Network CNN's lightweight residual network structure allows for deeper learning of more features layer by layer, making the forward and backward propagation process smooth, and it is more suitable for mobile terminal environments. Therefore, the Residual Network CNN lightweight structured data algorithm framework is used to identify the surface chromatic aberration of FFC. The Residual Network CNN framework accomplishes two main tasks, including qualitative and confidence evaluation of

TABLE 3 | Batch Size optimization process with different loss function values.

Batch size	1	8	16	24	32	40	48	56	64
Val_acc (%)	0.511	0.964	0.921	0.849	0.906	0.849	0.676	0.791	0.921
Loss (%)	0.898	0.247	0.304	0.236	0.160	0.258	0.233	0.178	0.225

**FIGURE 7** | The loss function optimization process with fixed Batch Size.

classification accuracy on structured data. The goal of structured data qualitative is to classify the color status of sample images. Confidence is a criterion to judge whether the classification results satisfy the probability requirement or not.

Network Framework Construction

FFC-F is the first stage of Residual Network CNN framework, and its main function is to pre-process the input structured data. Same as the remaining four stages, FFC-F consists of bottleneck, but the number of bottleneck units is different. When the input channel, height and width are 3, 244 and 244, the 64 convolution kernels of FFC-F with 7×7 size will implement the convolution operation in step of 2. Then the 3×3 kernel max-pooling layer will also process the data further in step of 2. The input structured data will go through convolution layer, batch normalization layer, ReLU and max-pooling layer to get 64, 56, 56 output shapes. Where the 64 channel represents the number of convolutional kernels in the first convolutional layer, and 56 is the quotient of the input value and the corresponding step size, as in **Figure 4**.

Bottleneck is divided into Bottleneck-F and Bottleneck-S, the input channel is equal to output channel in Bottleneck-S, the input channel is unequal to output channel in Bottleneck-F. Bottleneck-F has four variable parameters, including the number of input channels w , the width b , the number of channels c_1 in the left 1×1 convolution layer and the step size s . $G(x)$ convolution layer is able to transform the dimensional difference between the input and the output.

Compared with Bottleneck-S, there is one more convolution block in Bottleneck-F, which is set as $G(x)$. The three convolution blocks in the Bottleneck-S module are $F(x)$, which contains the corresponding batch normalization layer and the ReLU. Bottleneck-S contains two variable parameters w and b , and the output shape data (w, b, b) of Bottleneck-S module can be obtained by adding $F(x)$ and x , as shown in **Eqs. 1, 2**.

$$\text{Bottleneck1: } (w, b, b) = [F_{BN}^{ReLU}(x) + G(x)] \quad (1)$$

$$\text{Bottleneck2: } (w, b, b) = [F_{BN}^{ReLU}(x) + (w, b, b)] \quad (2)$$

The convolution layer enables the forward propagation process of input samples and the backward propagation process of parameter estimation. The forward propagation of the convolution process starts when the samples x_n pass through the input layer into the first hidden layer. The L_i is the number of convolutional layers, $Z_l^{(j)}$ is the activation value of the j th neuron in layer l , w_l^{ji} is the weight of the i th neuron in the previous layer connected by the j th neuron in layer l , $b_l^{(j)}$ is the threshold value of the j th neuron in layer l and E is the loss function in the output layer. The forward propagation of any layer in a MSLSDA network is shown in **Eqs. 3–5**.

$$y_l^{(j)} = \text{ReLU}(Z_l^{(j)}) \quad (3)$$

$$Z_l^{(j)} = \sum_{i \in L_{l-1}} w_l^{ji} y_{l-1}^{(i)} + b_l^{(j)} \quad (4)$$

$$y_l = \text{ReLU}(w_l y_{l-1} + b_l) \quad (5)$$

After the convolution MSLSDA is constructed, the parameters can be estimated from back to front by the gradient descent strategy and the chain derivation rule, as shown in **Eq. 6**.

$$\begin{cases} \frac{\partial E}{\partial w_l^{ji}} = \frac{\partial E}{\partial y_l^{(j)}} \frac{\partial y_l^{(j)}}{\partial z_l^{(j)}} \frac{\partial z_l^{(j)}}{\partial w_l^{ji}} = \frac{\partial E}{\partial y_l^{(j)}} \text{ReLU}'(Z_l^{(j)}) y_{l-1}^{(i)} \\ \frac{\partial E}{\partial b_l^{(j)}} = \frac{\partial E}{\partial y_l^{(j)}} \frac{\partial y_l^{(j)}}{\partial z_l^{(j)}} \frac{\partial z_l^{(j)}}{\partial b_l^{(j)}} = \frac{\partial E}{\partial y_l^{(j)}} \text{ReLU}'(Z_l^{(j)}) \end{cases} \quad (6)$$

Max-Pooling Layer and Fully Connected Layer Settings

The max-pooling layer enables the dimensionality reduction of structured data, greatly reducing the number of parameters while retaining the main features, as shown in **Eq. 7**.

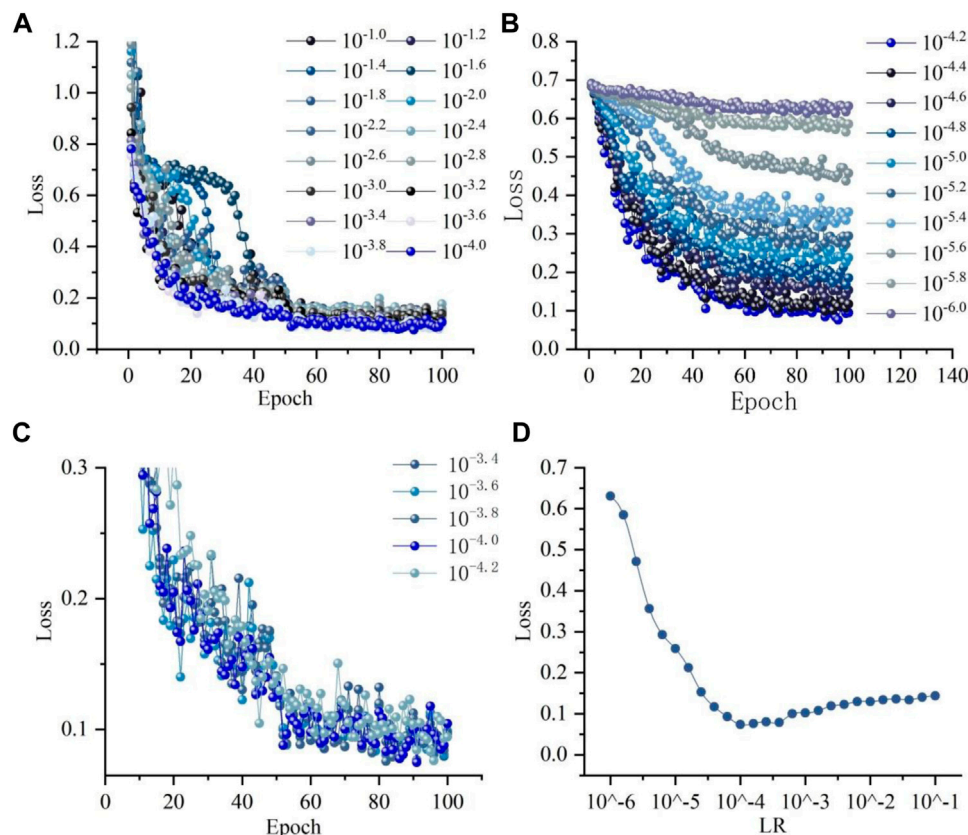


FIGURE 8 | MSLSDA LR optimization results of FFC chromatic aberration experimental data: **(A)** Experimental results before optimal LR **(B)** Experimental results after optimal LR **(C)** Experimental results near optimal LR **(D)** Optimization process of LR versus loss function on logarithmic scale.

$$\begin{cases} h_{out} = \left\lceil \frac{h_m + 2pad - kernel}{s} \right\rceil + 1 \\ w_{out} = \left\lceil \frac{w_{in} + 2pad - kernel}{s} \right\rceil + 1 \end{cases} \quad (7)$$

Where h is the input height parameter, pad is the edge expansion parameter and $kernel$ is the length and width parameter of the convolutional layer filter. The fully connected layer maps the currently available “distributed features” into the structured data notation space and performs a linear transformation of the feature space. After connecting the fully connected layer to the convolutional layer and the max-pooling layer, it corresponds to connecting all neurons of the previous layer. The fully connected layer matches the distinguishing local feature information processed by the convolutional layer and the max-pooling layer, and implants it into the softmax layer to finally realize the MSLSDA training, confidence assignment and loss function calculation, as in Figure 5.

Hyperparameter Optimization

The system environment configuration for the workstation includes Python 3.7, Pytorch 1.7.1 and Anaconda3-5.3.1. Write training code, validation code, prediction code and algorithm

code for MSLSDA via PyCharm. The MSLSDA uses a joint training strategy with a full training process of 230 epochs, including 30 epochs to tune the algorithm network head, 30 epochs to optimize the Batch Size hyperparameters, 80 epochs to optimize the learning rate (LR) hyperparameters, 40 epochs to optimize the Epoch hyperparameters, 20 epochs to train the test set, and 30 epochs to train the generalized prediction set and evaluate the MSLSDA generalization capability.

Hyperparameters including LR, Batch Size, Epoch, number of hidden layers, number of neurons and ReLU can control and influence the final parameters w and b . With the structured data algorithm selected, planning the values of LR, Batch Size, and Epoch is an effective way to achieve positive results in deep learning networks.

Batch Size is the total number of structured sample data contained in a batch. Due to the large amount of data in the FFC chromatic aberration dataset, the dataset is divided into multiple batches to pass the algorithm in order. Since the larger Batch Size value is, the higher GPU performance is required, and the value is an integer multiple of 8 (Dong et al., 2021). Therefore, the experiments set the Batch Size values to 1, 8, 16, 24, 32, 40, 48, 56, and 64 based on the actual workstation configuration. To ensure the reliability of the Batch Size hyperparameter optimization, the LR uniformly set to 0.001 and Epoch

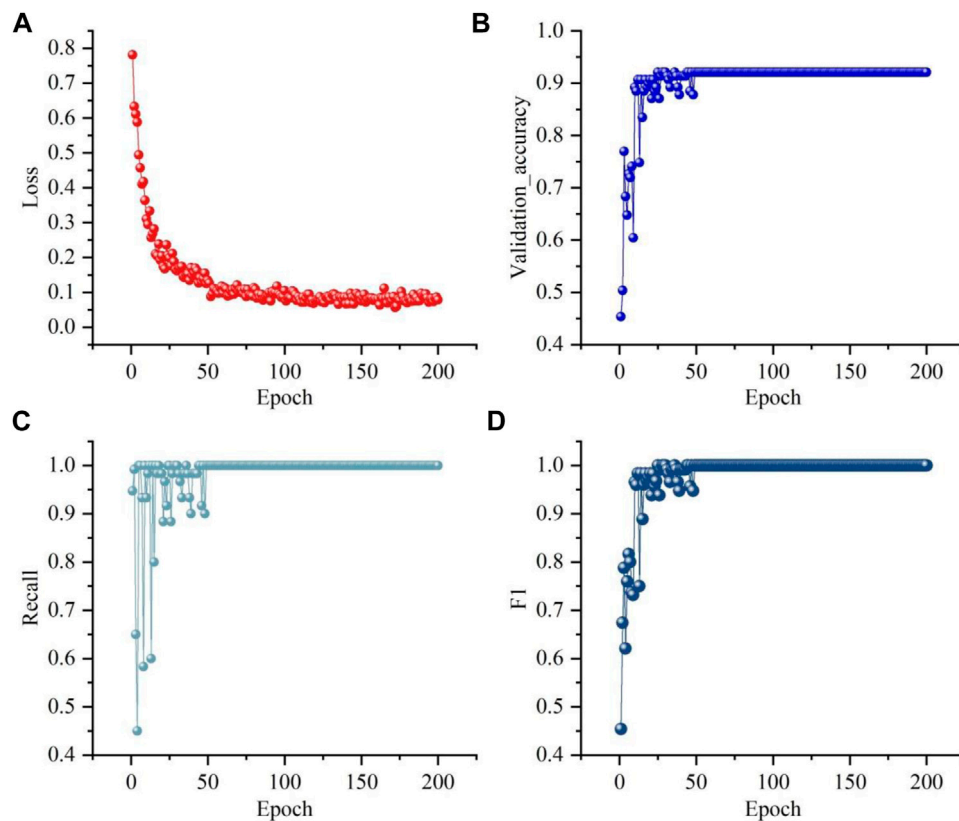


FIGURE 9 | The indices of optimized MSLSDA model for FFC chromatic aberration experimental data: **(A)** Experimental results of loss **(B)** Experimental results of Val_acc **(C)** Experimental results of recall **(D)** Experimental results of F₁.

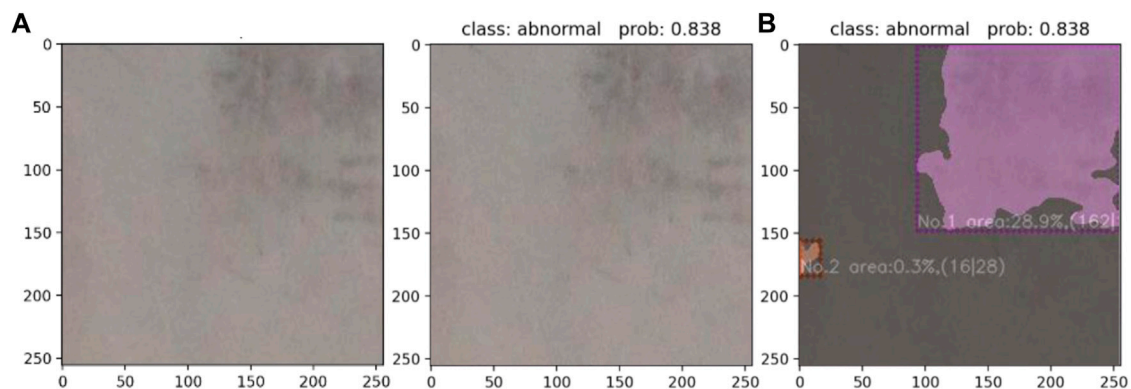


FIGURE 10 | Prediction and quantification results for mild chromatic aberration: **(A)** Original image **(B)** Prediction and quantification results.

uniformly set to 50. Each Batch Size generates a different number of weight files during training, and each weight file contains information on the loss function value, Epoch, and the weight value. To avoid duplicate recording of the same weight file, the basis for weight file generation is encoded as an increase in verification accuracy (Val_acc). The relationship between the Epoch, Val_acc and Batch Size is depicted in **Figure 6**. The

results show that only one Val_acc peak for different Batch Size within a finite epoch. The weight file corresponding to the Val_acc peak point is the optimal weight file under each Batch Size. For a more visual representation of the Val_acc sensitivity to different Batch Size, **Table 3** shows the statistical data.

Since the number of Batch Size_1 datasets is equal to the number of experimental sample images in the training

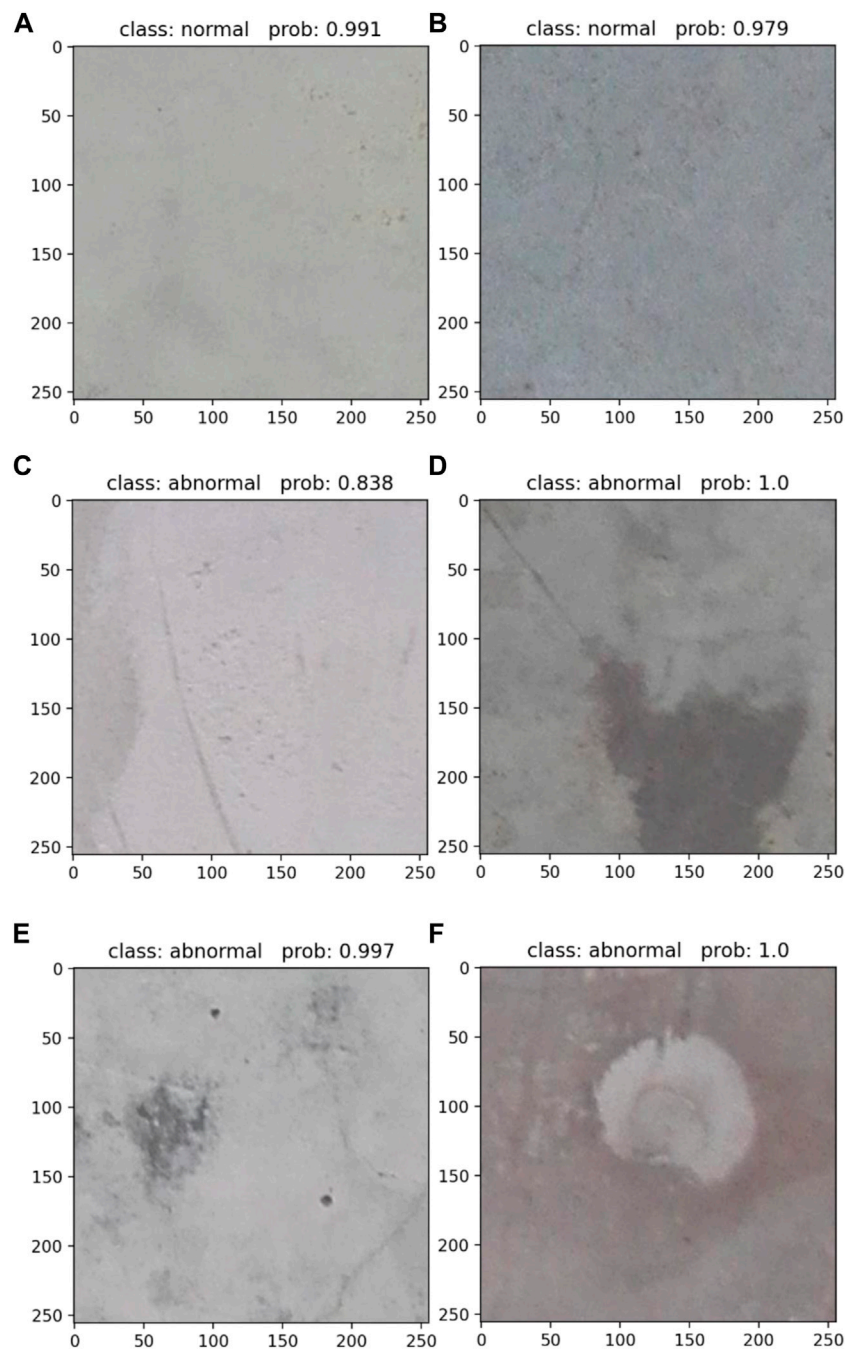


FIGURE 11 | Prediction results of different FFC chromatic aberration defects categories: **(A)** Light color without chromatic aberration output **(B)** Dark color without chromatic aberration output **(C)** Light color incomplete chromatic aberration output **(D)** Dark color incomplete chromatic aberration output **(E)** Light color complete chromatic aberration output **(F)** Dark color complete chromatic aberration output.

set, Val_acc does not converge in the range of 50 epochs, as in **Figure 7**. As the predicted probability of the validation set deviates from the actual labels, the loss function gradually increases. Therefore, the loss function value 0.160 corresponding to Batch Size_32 shows a high match between the predicted probability and the actual label.

The LR affects the convergence speed of structured data algorithms to regional minima. A suitable LR enables the algorithm to descend in the largest gradient direction with suitable step, and the LR value can be effectively optimized by the descending gradient of the loss function. In this manuscript, the LR range from $10^{-6.0}$ to $10^{-1.0}$, and the LR values are set sequentially in step of $10^{-0.2}$ (Mayr et al., 2018). The Batch Size

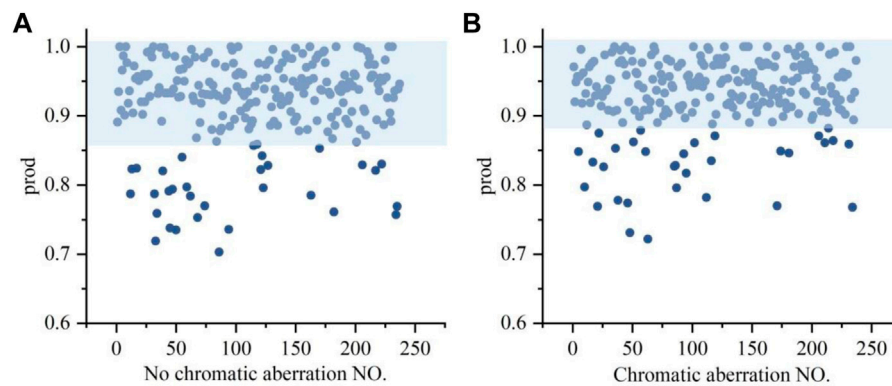


FIGURE 12 | Generalization prediction prod statistics results of FFC chromatic aberration experimental data: **(A)** No chromatic aberration prod **(B)** Chromatic aberration prod.

follows the optimal solution of the previous experiment three2 and the Epoch is set to 100, because the optimization of the LR needs to be performed when the loss function converges. **Figure 8** shows the convergence of the loss function for all LR values. The loss function curves with LR values in the range of $10^{-3.2}$ to $10^{-1.0}$ are initially agitated due to excessive LR values. When the LR takes the value of $10^{-3.6}$, the loss function decreases significantly faster than the other curves in the early stage, and it cannot be converged in the later stage due to the large LR. Although the loss functions with LR taking values of $10^{-3.4}$ and $10^{-3.8}$ converge in the later stages, there are clearly multiple oscillation points in the earlier stages. The loss function converges to larger values for LR ranging from $10^{-4.2}$ to $10^{-6.0}$, because of the small LR. The loss function with LR taking the value of $10^{-4.0}$ shows a uniform sliding decline. It means that the learning performance is better in less time.

Figure 8 plots the optimization process of LR versus loss function on logarithmic scale, and it shows the effect of LR on loss function convergence speed. The LR takes values from $10^{-6.0}$ to $10^{-1.0}$ asymptotically, and the loss function value stops decreasing and slowly increases at $10^{-4.0}$. With a fixed Epoch of 100, a small LR can slow down the training process by a factor proportional to the amount of LR reduction. This typical relationship between the training loss and the LR is expressed as an increasing trend of the loss function value when the LR is greater than the optimal value, and a decreasing trend vice versa. Therefore, the optimal LR in this study takes the value of $10^{-4.0}$.

The epoch indicates all batches of single training process in forward and backward propagation. In each epoch, all samples of the training set participating in training process. After each epoch, all the sample data need to be shuffled to the next epoch. In the Residual Network CNN framework, several epochs are performed to update the weight parameters of the structured data algorithm using a limited number of data and gradient descent. In order to find suitable epoch for the FFC chromatic aberration dataset, the epoch is set to 2000, the LR and Batch Size follow $10^{-4.0}$ and 32 from the previous experiment. The results of the loss, Val_acc, recall and F_1 parameters are shown in **Figure 9**.

A key metric for deep learning is to compare the gap between the learning results and the actual sample labels. During the whole training process, the loss function value starts to converge around 100 epochs, and reaches the minimum value of 0.061 for the first time in the whole learning process at the 755th epoch, and the Val_acc has converged to 0.921 at this time. Recall is the ratio of correctly identified number as chromatic samples in the validation set to all chromatic samples number in the validation set. As the epoch increases, recall finally converges to 0.990, which indicates that the MSLSDA has positive identification performance on the validation set. The equilibrium mean F_1 integrates the calculation results of precision and recall, and the F_1 value finally converges to 0.990 in the experiment, which indicates that this MSLSDA has positive accuracy in FFC surface CAI.

The traditional method of FFC surface CAI is observed by human eyes, which is subjective. Therefore, it is not easy to judge the chromatic aberration in **Figure 10A** by the human eyes. The coordinate axes of the sample images are in px. Compared with the traditional method, the FFC surface CAI method in this study can objectively identification chromatic aberration that are not easily judged by the human eyes, as shown in **Figure 10B**.

FFC CHROMATIC ABERRATION GENERALIZATION ANALYSIS

In order to test the generalization ability of the MSLSDA for FFC surface CAI, 474 sample images of sub-sample buildings are performed full-sample identification. The output sample images include light color without chromatic aberration (LW) output, dark color without chromatic aberration (DW) output, light color complete chromatic aberration (LCC) output, light color incomplete chromatic aberration (LIC) output, dark color complete chromatic aberration (DCC) output and dark color incomplete chromatic aberration (DIC) output, as shown in **Figure 11**. The first index is the result of CAI, abnormal indicates chromatic aberration in sample image and normal indicates uniform color of the sample image. The second

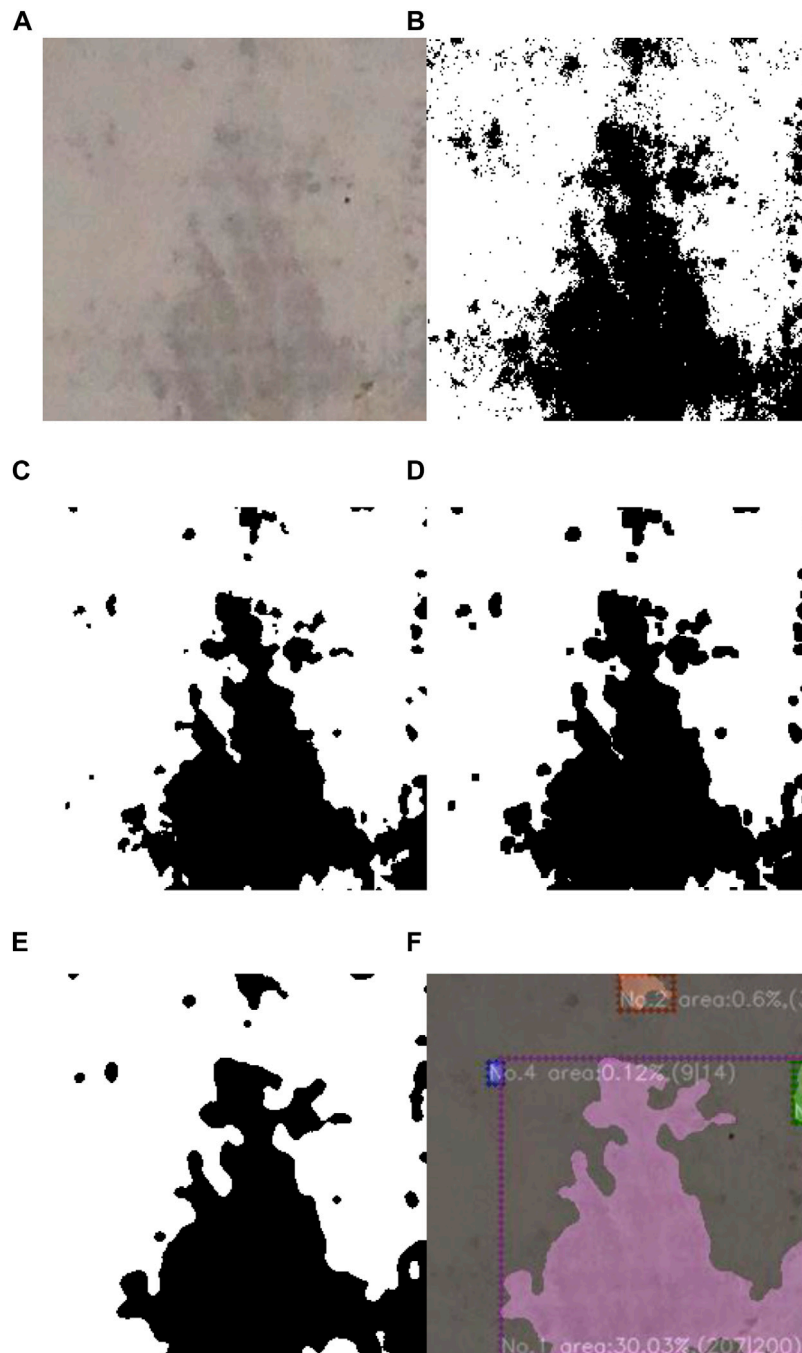


FIGURE 13 | Quantification process of FFC chromatic aberration experimental data: (A) Input (B) Color space recognition (C) Median filter noise reduction (D) Data open operation (E) Data closure operation (F) Quantitative segmentation.

index indicates the probability value prod of the target dimension, which illustrates the confidence of the CAI results.

The generalized prediction set contains four defect categories of light FFC, dark FFC, complete chromatic aberration and incomplete chromatic aberration. And it contains four comprehensive defect categories of LCC sample images, DCC sample images, LIC sample images and DIC sample images, but

the MSLSDA is still able to accomplish the CAI task. The two indexes show positive performance of FFC surface CAI. To represent the results of the generalization prediction experiments, the confidence data for the chromatic aberration and without chromatic aberration samples are labeled in **Figure 12**. It can be seen that the confidence range of the generalized prediction samples with chromatic aberration is

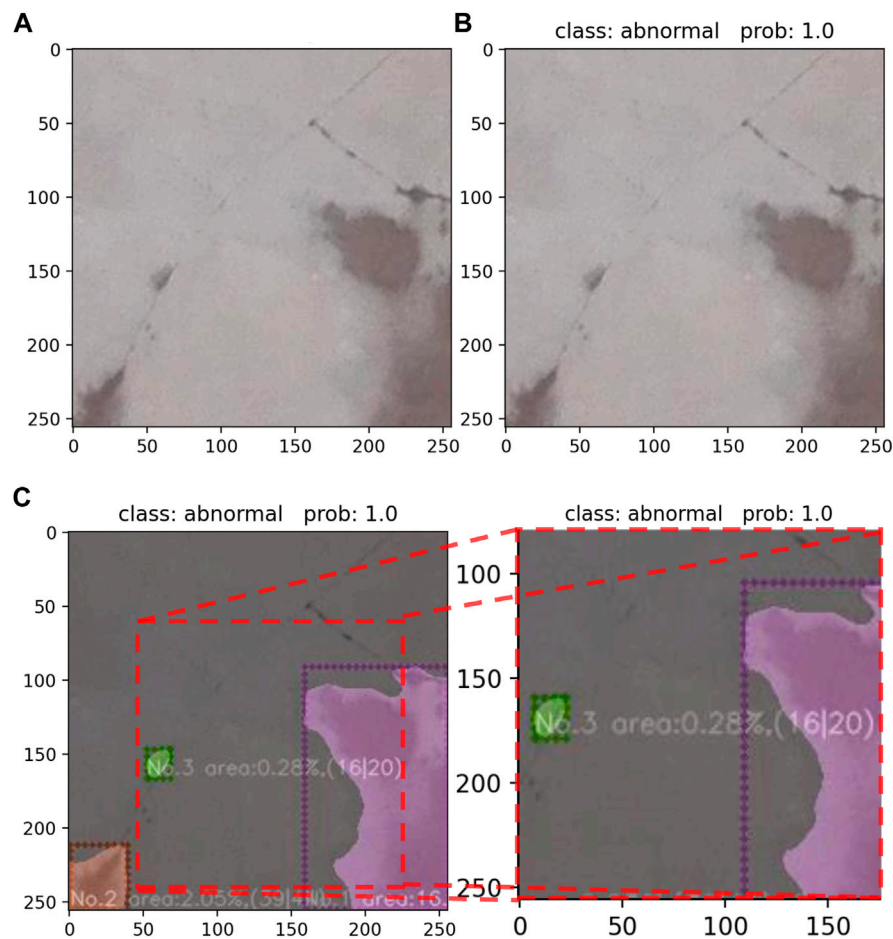


FIGURE 14 | Identification and quantification of FFC chromatic aberration experimental data: (A) Input (B) Experimental results of projection (C) Experimental results of quantitative segmentation.

almost between 0.88 and 1.00, and the confidence range of the generalized prediction samples without chromatic aberration is almost between 0.86 and 1.00. The accuracy of the chromatic aberration generalization prediction reaches 99.6%, which reflects the positive generalization prediction ability of the MSLSDA.

QUANTIFICATION OF CHROMATIC ABERRATION IN FFC

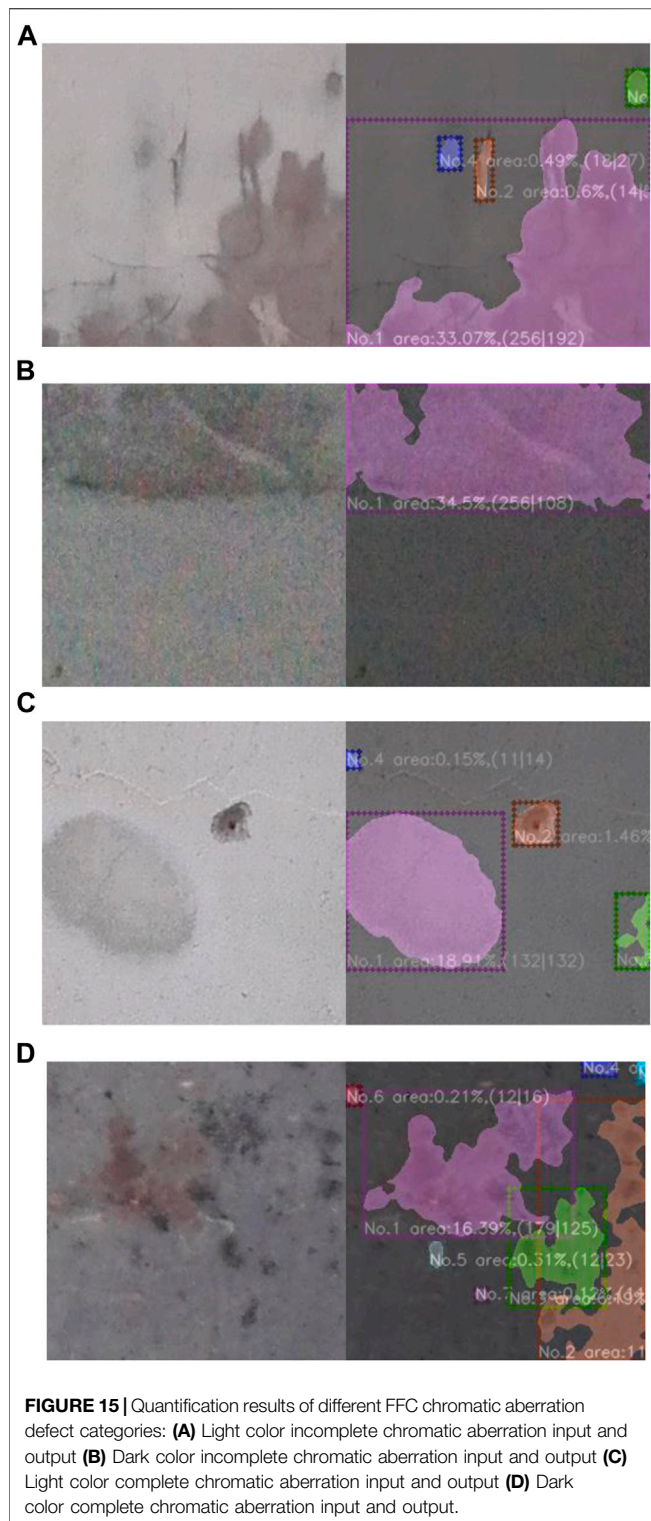
Through color space conversion, histogram equalization, image color recognition, image noise reduction and image mask operation, the multi-scale feature fusion of structured data is realized. The boundary features, geometric parameter features (length and width) and chromatic aberration ratio features of structured data are identified, as shown in Figure 13.

In order to perform histogram equalization of color sample images, the RGB color space of the structured data (shown in Figure 13A) is converted into an HSV color space that enables

efficient image processing. Then the Void InRange function is used to identification whether each pixel point of src image is between lowerb value and upperb value. The pixel points between lowerb value and upperb value are set to 255, and the rest of the pixel points are set to 0. The pixel values are finally saved in the dst image, which gives a binary image corresponding to the target color, as shown in Figure 13B.

To remove the pretzel noise points in the binary image, a median filter method is used, as shown in Figure 13C. To remove the scattered distribution of noisy pixel points from the binary image, an open operation of erosion followed by expansion is used, as shown in Figure 13D. In order to reduce the independence of chromatic aberration areas and enhance the connectivity of individual chromatic aberration blocks, a closed operation of expansion followed by erosion is used, as shown in Figure 13E. In order to extract structural features of chromatic aberration in sample images, similarity variables are used to detect structural features similar to image masks, as shown in Figure 13F.

As can be seen in Figure 14, the sample image can be calculated by the masking algorithm and output the chromatic



aberration mask index. The dimensional pixel values of the FFC chromatic aberration are more informative than the millimeter values during the inspection. Therefore, the mask algorithm trained in this manuscript directly outputs the pixel values of the chromatic aberration size. The index

contains the chromatic aberration block number, chromatic aberration ratio features and geometric parameter features (length and width), these three parts listed in order from left to right. The chromatic aberration block number is based on chromatic aberration ratio features, and each chromatic aberration block is coded in order from the largest to the smallest, which is helpful for the inspector to quickly determine the largest chromatic aberration block. The chromatic aberration ratio features represent the proportion of a single chromatic aberration to the sample image, and further the total chromatic aberration ratio of the whole sample image can be obtained, which provides an accurate quantitative evaluation basis for inspectors. The geometric parameter features (length and width) are also expressed as pixel values in parentheses at the end of the index, the chromatic aberration block length pixel value on the right and the width pixel value on the left, which provides the inspector with information on the degree of chromatic aberration coverage.

As shown in **Figure 15**, all chromatic aberration blocks in the figure are identified and quantified. It can be seen that the Residual Network CNN framework and the chromatic aberration mask algorithm have positive identification and quantization performance not only for LCC sample images (shown in **Figure 15A**), but also for LIC sample images (shown in **Figure 15B**), DCC sample images (shown in **Figure 15C**) and DIC sample images (shown in **Figure 15D**).

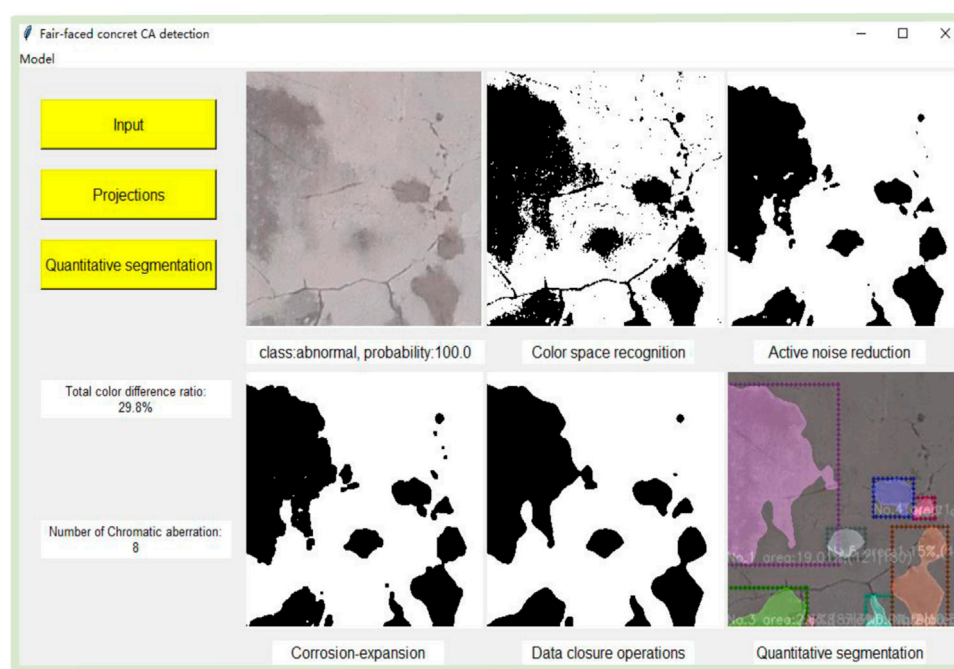
In order to illustrate the results of FFC identification and quantification in different states, The information of identification and quantification for different classes of experimental sample images in **Figure 15** is listed in **Table 4**.

The FFC-CADP (shown in **Figure 16**) implements an automated procedure for identification and quantification of chromatic blocks on the surface image of FFC. The hardware environment for developing platform includes Core i7 8750h, 6 GB of gtx1060 and 16 GB of RAM. The operating system used to develop platform is Windows 10 × 64. The environment used to develop platform is Anaconda3 and Pycharm. To improve the applicability of platform, it is coded to apply to Windows 10 × 64 and ubuntu 18.04 × 64 operating system. The supporting environment for platform operation includes Pytorch 1.7.1, Opencv4, Numpy and Matplotlib. This study builds platform through Python 3.7 programming language.

Click the input button to switch the interface to the images folder path, and select the sample images to be identified and quantified to complete the input operation. The sample image after input is displayed in the first output box in the first line for comparison with the quantized output results. Click the projections button, the CAI result and prod will be output below the input sample image. Click the quantitative segmentation button to get color space recognition output, active noise reduction output, corrosion-expansion output, data closure operations output and quantitative segmentation output in sequence. The quantitative segmentation output contains the boundary features, geometric parameter features (length and width),

TABLE 4 | FFC chromatic aberration data of different defect categories.

Chromatic aberration sample	Number	Area (%)	Width	Length	Total chromatic aberration	Total chromatic aberration ratio (%)
LIC	NO.1	33.07	256	192	4	34.75
	NO.2	0.6	14	54		
	NO.3	0.59	21	29		
	NO.4	0.49	18	27		
LCC	NO.1	18.91	132	132	4	21.44
	NO.2	1.46	32	30		
	NO.3	0.92	21	59		
	NO.4	0.15	11	14		
DIC	NO.1	34.5	256	108	1	34.5
DCC	NO.1	16.39	179	125	8	35.08
	NO.2	11.27	87	223		
	NO.3	6.19	81	104		
	NO.4	0.49	27	13		
	NO.5	0.31	12	23		
	NO.6	0.21	12	16		
	NO.7	0.12	11	13		
	NO.8	0.10	4	22		

**FIGURE 16** | FFC chromatic aberration detection platform.

chromatic aberration ratio features, total chromatic aberration ratio and number of chromatic aberration.

CONCLUSION

According to the actual working environment of FFC inspectors and combined with the demand of FFC surface CAI, the experimental data acquisition method of FFC surface

chromatic aberration based on UAV technology is designed. Compared with traditional data acquisition methods, this method can quickly collect sample images in a large area, and reduce the interference factors in image data. Besides it can reduce the risk factor of staff, improve the efficiency and quality of data acquisition.

Based on the optimized MSLSDA, a FFC chromatic aberration identification model is built. The model can complete the quantization of FFC chromatic aberration quickly and

accurately, and the quantization accuracy of the target reaches 92.1%.

The FFC-CADP is built to visualize the operation of identification and quantization on the FFC surface sample images. The calculations of the platform include image category return value, prod, boundary features, geometric parameter features (length and width), chromatic aberration ratio features, total chromatic aberration ratio and number of chromatic aberration.

Aiming at the problems of low efficiency and strong subjectivity in the quality inspection of FFC surface CAI, a method based on MSLSDA for FFC surface CAI is proposed. The method achieves the FFC chromatic aberration prediction function by FFC chromatic aberration identification model. The FFC chromatic aberration quantization function achieves by color space conversion, histogram equalization, image color recognition, image noise reduction and image mask operation.

This project will further investigate the performance and generalization prediction ability of different weight structured data algorithms for the FFC chromatic aberration dataset, and obtain the FFC surface CAI models suitable for different application scenarios.

REFERENCES

- Abouhamad, M., Dawood, T., Jabri, A., Alsharqawi, M., and Zayed, T. (2017). Corrosiveness Mapping of Bridge Decks Using Image-Based Analysis of Gpr Data. *Automation in Construction* 80, 104–117. doi:10.1016/j.autcon.2017.03.004
- Ajtayné Károlyfi, K., and Papp, F. (2021). Laboratory Study of the Effect of Saturation Degree on Quality of Fair-Faced concrete Surfaces. *Epitoanyag - JSBCM* 73, 115–118. doi:10.14382/epitoanyag-jsbcm.2021.17
- Cha, Y.-J., Choi, W., and Büyüköztürk, O. (2017). Deep Learning-Based Crack Damage Detection Using Convolutional Neural Networks. *Computer-Aided Civil Infrastructure Eng.* 32, 361–378. doi:10.1111/mice.12263
- Chang, H. L., Jin, Z. Q., Wang, P. G., Wang, J. H., and Liu, J. (2021). Comprehensive Resistance of Fair-Faced concrete Suffering from Sulfate Attack under marine Environments. *Construction Building Mater.* 277, 122312. doi:10.1016/j.conbuildmat.2021.122312
- Chen, M., Tang, Y., Zou, X., Huang, K., Li, L., and He, Y. (2019). High-Accuracy Multi-Camera Reconstruction Enhanced by Adaptive Point Cloud Correction Algorithm. *Opt. Lasers Eng.* 122, 170–183. doi:10.1016/j.optlaseng.2019.06.011
- Coburn, A., Kardan, O., Kotabe, H., Steinberg, J., Hout, M. C., Robbins, A., et al. (2019). Psychological Responses to Natural Patterns in Architecture. *J. Environ. Psychol.* 62, 133–145. doi:10.1016/j.jenvp.2019.02.007
- Dong, X., Shen, J., Wang, W., Shao, L., Ling, H., and Porikli, F. (2021). Dynamical Hyperparameter Optimization via Deep Reinforcement Learning in Tracking. *IEEE Trans. Pattern Anal. Mach. Intell.* 43, 1515–1529. doi:10.1109/TPAMI.2019.2956703
- Feng, W., Wang, Y., Sun, J., Tang, Y., Wu, D., Jiang, Z., et al. (2022). Prediction of Thermo-Mechanical Properties of Rubber-Modified Recycled Aggregate concrete. *Construction Building Mater.* 318, 125970. doi:10.1016/j.conbuildmat.2021.125970
- Kang, D., and Cha, Y.-J. (2018). Autonomous Uavs for Structural Health Monitoring Using Deep Learning and an Ultrasonic beacon System with Geo-Tagging. *Computer-Aided Civil Infrastructure Eng.* 33, 885–902. doi:10.1111/mice.12375
- Li, D., Liu, J., Feng, L., Zhou, Y., Liu, P., and Chen, Y. F. (2020). Terrestrial Laser Scanning Assisted Flatness Quality Assessment for Two Different Types of concrete Surfaces. *Measurement* 154, 107436. doi:10.1016/j.measurement.2019.107436
- Liu, B., and Yang, T. (2017). Image Analysis for Detection of Bugholes on Concrete Surface. *Construction Building Mater.* 137, 432–440. doi:10.1016/j.conbuildmat.2017.01.098

DATA AVAILABILITY STATEMENT

The raw data supporting the conclusions of this article will be made available by the authors, without undue reservation.

AUTHOR CONTRIBUTIONS

Conceptualization, GY and WS; methodology, WS and YY; software and formal analysis, WS and YY; writing—original draft preparation, WS and YS; review and editing, WS and JZ. All authors have read and agreed to the published version of the manuscript.

FUNDING

This work was supported by the National Natural Science Foundation of China (51608076, 51808074), the Fundamental Research Funds for the Central Universities (2020CDJQY-A067).

- Liu, J., Li, D., Feng, L., Liu, P., and Wu, W. (2019). Towards Automatic Segmentation and Recognition of Multiple Precast concrete Elements in Outdoor Laser Scan Data. *Remote Sensing* 11, 1383. doi:10.3390/rs11111383
- Mayr, A., Klambauer, G., Unterthiner, T., Steijaert, M., Wegner, J. K., Ceulemans, H., et al. (2018). Large-Scale Comparison of Machine Learning Methods for Drug Target Prediction on ChEMBL. *Chem. Sci.* 9, 5441–5451. doi:10.1039/c8sc00148k
- Miranda, J., Valença, J., Costa, H., and Júlio, E. (2020). Chromatic Design and Application of Restoration Mortars on Smooth Surfaces of white and GRAY concrete. *Struct. Concrete* 22, E535–E548. doi:10.1002/suco.202000054
- Mohammed, A., Rafiq, S., Sihag, P., Kurda, R., and Mahmood, W. (2021). Soft Computing Techniques: Systematic Multiscale Models to Predict the Compressive Strength of Hvf concrete Based on Mix Proportions and Curing Times. *J. Building Eng.* 33, 101851. doi:10.1016/j.job.2020.101851
- Mohan, A., and Poobal, S. (2018). Crack Detection Using Image Processing: A Critical Review and Analysis. *Alexandria Eng. J.* 57, 787–798. doi:10.1016/j.aej.2017.01.020
- Payab, M., and Khanzadi, M. (2021). State of the Art and a New Methodology Based on Multi-Agent Fuzzy System for concrete Crack Detection and Type Classification. *Arch. Computat Methods Eng.* 28, 2509–2542. doi:10.1007/s11831-020-09465-7
- Payab, M., Abbasina, R., and Khanzadi, M. (2019). A Brief Review and a New Graph-Based Image Analysis for Concrete Crack Quantification. *Arch. Computat Methods Eng.* 26, 347–365. doi:10.1007/s11831-018-9263-6
- Piferi, C. (2018). Materials and Innovative Methodologies for Restoring Fair Faced Concrete. *Techno-J. Technol. Architecture Environ.* 16, 258–269. doi:10.13128/Techno-23013
- Prasanna, P., Dana, K. J., Gucunski, N., Basily, B. B., La, H. M., Lim, R. S., et al. (2016). Automated Crack Detection on concrete Bridges. *IEEE Trans. Automat. Sci. Eng.* 13, 591–599. doi:10.1109/TASE.2014.2354314
- Ribeiro, C. M., and Xavier, D. J. (2019). The Revealing Role of Modern Religious Architecture in Sao Paulo: Fair-Faced concrete Finish in Religious Architecture and its Symbolology of the Sacred. *Rever* 19, 25–41. doi:10.23925/1677-1222.2018vol191a3
- Scalbi, A., Olmi, R., and Inglese, G. (2019). Evaluation of Fractures in a Concrete Slab by Means of Laser-Spot Thermography. *Int. J. Heat Mass Transfer* 141, 282–293. doi:10.1016/j.ijheatmasstransfer.2019.06.082
- Shyha, I., Richardson, A., Coventry, K., and Ponton, H. (2016). Mould Release Technologies with Regard to Concrete Surface Finish. *Mag. Concrete Res.* 68, 87–98. doi:10.1680/macrc.15.00067

- Siebert, S., and Teizer, J. (2014). Mobile 3d Mapping for Surveying Earthwork Projects Using an Unmanned Aerial Vehicle (Uav) System. *Automation in Construction* 41, 1–14. doi:10.1016/j.autcon.2014.01.004
- Strehlein, D., and Schiessl, P. (2008). Dark Discoloration of Fair-Face Concrete Surfaces-Transport and Crystallization in Hardening Concrete. *J. Adv. Concrete Technol.* 6, 409–418. doi:10.3151/jact.6.409
- Tang, Y., Li, L., Wang, C., Chen, M., Feng, W., Zou, X., et al. (2019). Real-Time Detection of Surface Deformation and Strain in Recycled Aggregate Concrete-Filled Steel Tubular Columns via Four-Ocular Vision. *Robot. Comput. Integr. Manuf.* 59, 36–46. doi:10.1016/j.rcim.2019.03.001
- Wu, M., Xiong, X., Shen, W., Huo, X., Xu, G., Zhang, B., et al. (2021). Material Design and Engineering Application of Fair-Faced Self-Compacting concrete. *Construction Building Mater.* 300, 123992. doi:10.1016/j.conbuildmat.2021.123992
- Yao, G., Sun, Y., Wong, M., and Lv, X. (2021). A Real-Time Detection Method for Concrete Surface Cracks Based on Improved YOLOv4. *Symmetry* 13, 1716. doi:10.3390/sym13091716
- Yoshitake, I., Maeda, T., and Hieda, M. (2018). Image Analysis for the Detection and Quantification of concrete Bugholes in a Tunnel Lining. *Case Stud. Construction Mater.* 8, 116–130. doi:10.1016/j.cscm.2018.01.002
- Zhang, X., Ma, X., Jin, L., and Li, X. (2013). Simulated Environment Test on Weather Fastness of Fair-Faced Concrete for Urban Bridge. *Appl. Mech. Mater.* 438–439, 1150–1155. doi:10.4028/www.scientific.net/amm.438-439.1150
- Conflict of Interest:** The authors declare that the research was conducted in the absence of any commercial or financial relationships that could be construed as a potential conflict of interest.
- Publisher's Note:** All claims expressed in this article are solely those of the authors and do not necessarily represent those of their affiliated organizations, or those of the publisher, the editors and the reviewers. Any product that may be evaluated in this article, or claim that may be made by its manufacturer, is not guaranteed or endorsed by the publisher.
- Copyright © 2022 Yao, Sun, Yang, Sun, Xu and Zhou. This is an open-access article distributed under the terms of the Creative Commons Attribution License (CC BY). The use, distribution or reproduction in other forums is permitted, provided the original author(s) and the copyright owner(s) are credited and that the original publication in this journal is cited, in accordance with accepted academic practice. No use, distribution or reproduction is permitted which does not comply with these terms.



Experimental Study of GFRP Reinforced Concrete Beams With U-Shaped CFRP Grid-Reinforced ECC Stay-in-Place Formwork

Chang Wu^{1,2}, Yanli Su¹, Pu Zhang^{3*}, Hong Zhu^{1,2}, Danying Gao³ and Shamim Ahmed Sheikh^{3,4}

¹School of Civil Engineering, Southeast University, Nanjing, China, ²Key Laboratory of Concrete and Prestressed Concrete Structures of Ministry of Education, Southeast University, Nanjing, China, ³School of Civil Engineering, Zhengzhou University, Zhengzhou, China, ⁴Department of Civil and Mineral Engineering, University of Toronto, Toronto, ON, Canada

OPEN ACCESS

Edited by:

Zhigang Zhang,
Chongqing University, China

Reviewed by:

Ali Raza,
University of Engineering and
Technology Taxila, Pakistan
Yang Zou,
Chongqing Jiaotong University, China

*Correspondence:

Pu Zhang
zhp@zhu.edu.cn

Received: 09 February 2022

Accepted: 24 February 2022

Published: 14 March 2022

Citation:

Wu C, Su Y, Zhang P, Zhu H, Gao D and Sheikh SA (2022) Experimental Study of GFRP Reinforced Concrete Beams With U-Shaped CFRP Grid-Reinforced ECC Stay-in-Place Formwork. *Front. Mater.* 9:872232. doi: 10.3389/fmats.2022.872232

Corrosion is a major concern for structures under the harsh environment. In this paper, ECC was applied as an alternative to concrete in tension zones, which was combined with FRP bars to develop a new type of composite beam with excellent durability. The flexural performance of glass fiber-reinforced polymer (GFRP)-reinforced concrete beams with U-shaped CFRP grid-reinforced ECC formwork was investigated. Five beams were designed, including one reference beam with full concrete, one composite beam with a coupon-shaped ECC permanent formwork at the bottom, and three composite beams with the proposed formwork. The effects of the application of the U-shaped ECC formwork, the formwork types, the application of CFRP grids, and the strength of the ECC were investigated. The test results showed that ECCs were an ideal material to improve the flexural behavior of FRP-reinforced concrete beams. The proposed formwork had a positive effect on crack resistance at the serviceability limit and substantially improved the cracking load by 78.57–85.71% and the ultimate load by 5.29–15.71% compared with those of the reference beam. Moreover, the proposed formwork improved the shear stiffness of the composite beam. The addition of CFRP grids improved the tensile strength of the ECC formwork and consequently contributed to the improvement in the load capacity of the composite beams.

Keywords: fiber-reinforced polymer (FRP), engineered cementitious composites (ECC), CFRP grids, u-shaped ECC formwork, flexural performance

INTRODUCTION

In the marine environment, strong corrosive ions penetrate concrete structures through cracks, which causes corrosion of steel reinforcement; accordingly, the mechanical properties of structures, such as the bearing capacity and stiffness, are reduced (Akiyama et al., 2012; Liu et al., 2020; Zhang et al., 2020). A feasible solution to avoid the structural failure caused by corrosion is to use fiber-reinforced polymer (FRP) bars instead of steel rebar as reinforcements due to the excellent corrosion resistance of FRP (Xu and Li, 2012; Dong et al., 2019). In addition, FRP bars have additional advantages, including high tensile strength, light weight and excellent fatigue resistance (Kazemi et al., 2020), and therefore have been used in concrete structures, such as those in bridge engineering (Zafari et al., 2016; Siwowski et al., 2018; Kim, 2019; Zou et al., 2021), geotechnical engineering

(Merwe and Hofmann, 2020) and traffic engineering (Al-Saoudi et al., 2021). However, compared with normal reinforced concrete structures, FRP reinforced concrete structures are characterized by higher deflection and larger crack widths due to their lower modulus and linear elasticity before fracture (no yield state) (Gar et al., 2018; Issa and Ismail, 2020; Liu et al., 2021); these factors hinders further promotion and application of FRP materials in the field of civil engineering (Barris et al., 2017; Dong et al., 2019; Ge et al., 2020).

Victor C. Li (Li and Leung, 1992) developed a new type of high-performance cementitious composite by adding randomly distributed short polymer fibers, named ECCs (engineered cementitious composites), which exhibit pseudostrain hardening behavior, ultrahigh toughness, ultrahigh ductility and pseudoductile characteristics (Liu et al., 2017; Zheng et al., 2018; Zhang et al., 2020; Zhang et al., 2021). The ultimate tensile strain of ECCs can reach values above 2–11%, which is several hundred times of concrete (Huang et al., 2021; Huang et al., 2021). The tensile crack widths of ECCs can be controlled within 0.1 mm, which effectively prevents the intrusion of harmful substances such as chloride ions into the material and consequently improves the durability (Zhang et al., 2020). In laboratory studies, some scholars (Li et al., 2002; Cai et al., 2017) have studied the flexural performance of ECC beams through numerical simulations and experiments. Existing studies have shown that the flexural strength and deformation capacity of pure ECC beams are greater than those of normal concrete beams. However, the cost of PVA-ECCs can be approximately 4.5 times that of normal concrete. As a result, ECCs should be properly used in the key part of a structure to achieve good performance and economy.

Many efforts have been made to investigate the mechanical performance of composite beams where normal concrete is partly replaced by ECCs. For example, Qiao et al. (2017) proposed a composite beam with U-shaped ECC formwork and designed three interfacial treatments to study the flexural behavior of the beam. The results showed that the bearing capacity and ductility of composite beams had been improved and that different interfacial treatments had little effect on the ultimate bearing capacity. Qin et al. (2020) studied the flexural behaviors of RC beams strengthened with high strength, high ductility ECCs (HSHD-ECCs). The test results showed that HSHD-ECCs can be an ideal strengthening material for improving the flexural performance of reinforced concrete beams.

Due to the great crack control ability of ECCs, the crack width is no longer a governing index for designing FRP reinforced components; this indicates that ECCs could be compatible with FRP reinforcing bars to improve the durability of structures. Moreover, FRP bars are not completely immune to the marine service environment. Researches have shown that FRP bars will still exhibit performance degradation in hot, humid and alkaline environments (Al-Salloum et al., 2013; Altalmas et al., 2015; Wang et al., 2017; Wang et al., 2017). Improving the impermeability of concrete cover could reduce the damage to the internal FRP bars (Zhang et al., 2021). Therefore, composite structures with combined ECC components and FRP reinforcement could be a suitable application in marine

environments, which require extremely high durability. Yuan et al. (2013) investigated six FRP-reinforced ECCs and ECC/concrete beams with an effect on the longitudinal/transverse reinforcement ratios and ECC thickness. The test results showed that the width of the cracks on the beam could be effectively controlled, while the ultimate load capacity and deformation of the composite beams were also improved. Ge et al. (2019) tested fifteen ECC-concrete composite beams to investigate the effects of the type of reinforcement, reinforcement ratio and ECC thickness on their flexural behaviors. The test results showed that the moment capacity and stiffness of the composite beams were improved compared with those of normal concrete beams.

However, it is worth nothing that research on FRP-reinforced ECC-concrete composite beams is not deep enough, and further research on their mechanical performance is needed. In this paper, a type of GFRP-reinforced composite beam that uses U-shaped CFRP grid-reinforced ECC permanent formwork was proposed to provide excellent durability under the harsh environment. Moreover, the CFRP grids were placed in the middle of the U-shaped ECC formwork to improve the bearing capacity of composite beams. The U-shaped CFRP grid-reinforced ECC formwork was designed to achieve the following objectives: 1) provide permanent formwork for rapid *in situ* casting of concrete beams in marine environments and 2) improve the flexural strength and ductility of composite beams. The flexural performance of the proposed beams was experimentally studied. The effects of the type of formwork, the addition of CFRP grids, and the ECC strength were investigated. Based on the test results, the crack patterns, failure modes, load-deflection behavior and strain response of composite beams were analyzed and discussed.

TEST PROGRAM

Specimen Details

A total of five beams were designed, including one reference beam with full concrete, one composite beam with an ECC plate as the bottom permanent formwork, and three composite beams with U-shaped ECC permanent formwork. The cross-sectional views and reinforcement details of the tested beams are shown in **Figure 1**. The beams have a cross-section of 150 mm × 250 mm, a total length of 2000 mm, and a clear span of 1800 mm, as seen in **Figure 1A**. All the beams were reinforced with two GFRP bars with a diameter of 14 mm in the tension zone, resulting in a reinforcement ratio of 0.95%. In the compression zone where the durability issue is recognized as not critical, two steel bars with a diameter of 10 mm were used to reduce the cost. Stirrups with a diameter of 6 mm were adopted at a center-to-center spacing of 100 mm in the shear spans, whereas no lateral reinforcement was used in the pure bending zone between the two loading points. Two types of ECC formwork were used: the bottom ECC formwork and the U-shaped ECC formwork (shown in **Figure 1B**). All the ECC formworks were designed to be 20 mm thick, while two

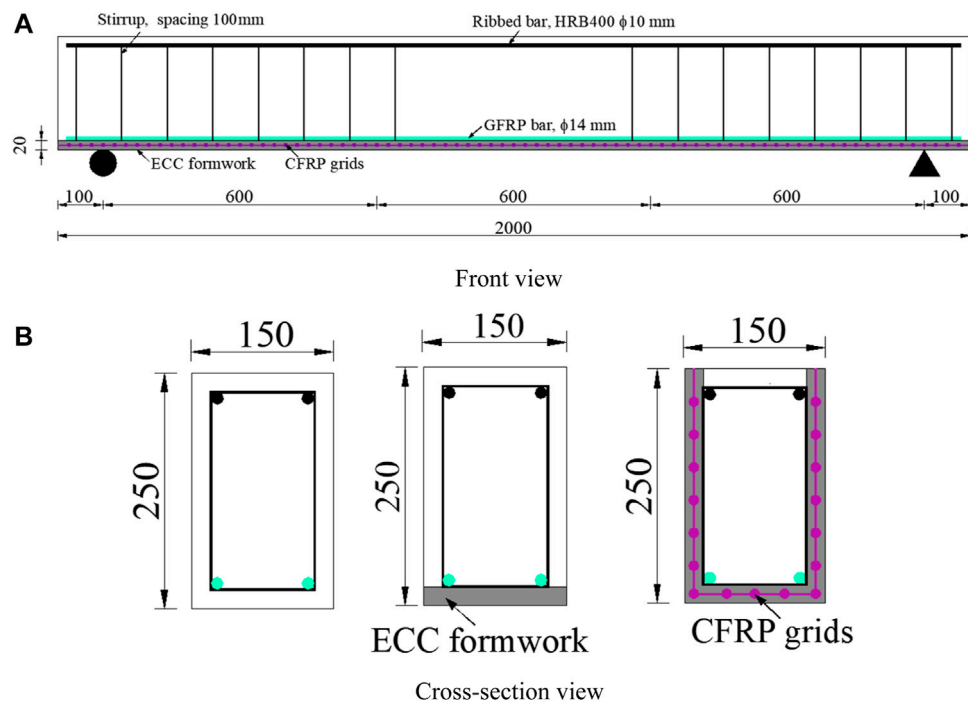


FIGURE 1 | Schematic diagram of a composite beam.

TABLE 1 | Test matrix of the composite beams.

Label	Formwork type	s/mm	A_g/mm^2	ECC strength grade
R	—	—	—	—
B	Bottom	—	—	C30
U	U-shaped	—	—	C30
UC-30	U-shaped	35	4	C30
UC-50	U-shaped	35	4	C50

Note: s is the grid spacing, mm; A_g is the cross-sectional area of the carbon fiber bundle, mm^2 .

U-shaped ECC formworks were reinforced with CFRP grids. The CFRP grids were posited in the middle of both bottom and side ECC formwork. The carbon fibers were arranged at a space of 35 mm center-to-center along the longitudinal and transverse direction, and the cross-sectional area of a single carbon fiber bundle used in the grid was 4 mm^2 . In addition, two ECC strength grades were used, including C30 and C50.

The information for the tested composite beams is shown in **Table 1**, where the formwork type, the CFRP grid reinforcement, and the ECC strength were taken into account as variables for investigation. In the designation of the tested beams, symbols “R”, “B”, and “U” represent the reference concrete beam, the composite beam with the bottom ECC formwork, and the composite beams with the U-shaped ECC formwork, respectively. In addition, “C” in the label indicates that CFRP grid reinforcements were applied, while “-30” and “-50” are labeled to distinguish the two ECC strength grades used in the specimens.

Specimen Preparation

The preparation process of the composite beams included the preparation of the ECC formwork and the casting of inner concrete. The U-shaped ECC formwork was first cast in an aluminum mold with inner dimensions of $150 \text{ mm} \times 250 \text{ mm} \times 2000 \text{ mm}$ (see **Figure 2A**). A 10 mm thick ECC layer was first poured in the bottom of the aluminum mold, and then a layer of CFRP grids was put on the ECC after casting and subsequently covered with another layer of 10 mm thick ECC mixture. A similar process was adopted in the preparation of the bottom ECC formwork. After casting the bottom of the U-shaped ECC formwork, a stuffing mold was placed inside the aluminum mold reserving two 20 mm gaps on both sides between the inner and exterior molds. Two CFRP grids were fixed in the middle of the gaps before pouring the rest of the ECC mixture for the formwork sides (see **Figure 2B**). The cased ECC formwork was cured at room temperature for 7 days.

After demolding the cured ECC formwork, a layer of 2 mm thick epoxy resin was brushed on the inner surfaces of the formwork (see **Figure 2C**), and the prepared reinforcement framework, including GFRP bars, steel bars and stirrups, was then placed into the permanent ECC formwork (see **Figure 2D**). Finally, the inner concrete mixture was poured and vibrated layer by layer, and the cast specimens were cured for 28 days (see **Figures 2E,F**).

Test Setup and Loading Pattern

As shown in **Figure 3A**, the composite beam was tested by a 100 kN hydraulic actuator with a four-point loading scheme. Per Chinese standard GB/T 50,152–2012 (China’ National Standard,

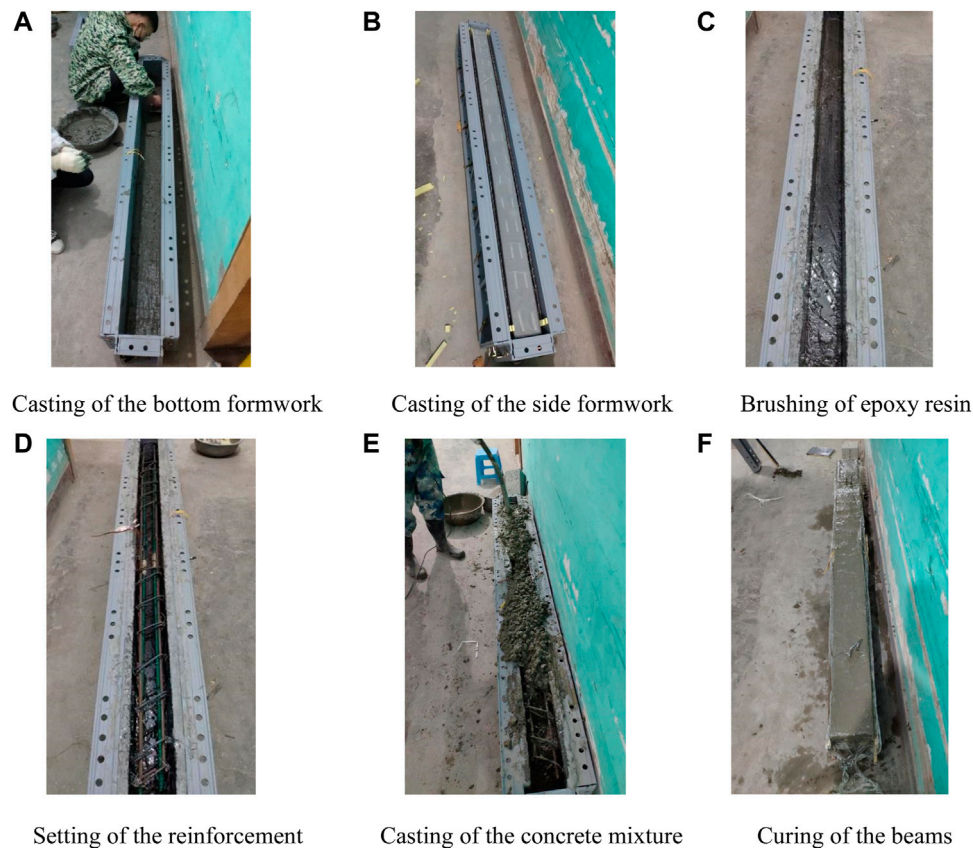


FIGURE 2 | Preparation of the composite beam specimens.

2012), the preloading force that was determined to be 60% of the estimated cracking load was applied to check the workability of measurement devices and eliminate gaps between the beam and supports. Formal loading was adopted as a multistage loading protocol. The load level was chosen as 5 kN before the cracking load and then changed to 10 kN until the test ended. At each load level, the applied load was sustained for approximately 5 min to measure and record any possible cracks and failure.

The measurement layout for the composite beams is shown in **Figure 3B**. The load applied by the hydraulic actuator was monitored by a load cell with a maximum capacity of 1,000 kN. The deflections at the loading points and supports were recorded by YWC-100-type displacement transducers with a displacement capacity of 100 mm and YWC-10-type displacement transducers with a displacement capacity of 10 mm, respectively. Strains across the mid-span were measured by 250 mm long handheld strain gauges at a spacing of 50 mm. In addition, BX120-5AA-type strain gauges were attached to GFRP bars and CFRP grids at the mid-span. Cracks were measured by a ZBL-F120-type crack width measuring device with a measurement range of 2 mm and a sensitivity coefficient of 0.02 mm. Once the crack widths exceeded 2 mm, they were recorded with a regular ruler by the naked eye. All load, displacement, and strain data were collected by a DH3816N static strain testing system at a frequency of 1 Hz.

Materials

The C30 concrete was composed of ordinary Portland cement labeled P. O 42.5, gravel with a particle size of 5–20 mm, river sand, and water. The mix proportion of the C30 concrete was cement: water: sand: gravel = 1:0.65:2.08:3.70. Per Chinese standard GB/T 50,081–2019 (China' National Standard, 2019), the concrete cubes were loaded on 3,000 kN hydraulic universal testing machine, and the loading rated is 0.8 MPa/s. Per Chinese standard GB 50010–2010 (China' National Standard, 2010), the 28-days compressive strength of the concrete was measured to be 34.2 MPa on average for 150 mm × 150 mm × 150 mm cubes under standard curing conditions (temperature $20 \pm 2^\circ\text{C}$ and relative humidity $\text{RH} \geq 95\%$). Two strength grades of ECC were prepared in this test, which consisted of P.O.42.5 cement, class I fly ash, amorphous ultrafine silica fume, quartz sand, PVA fiber, water, water reducer and additives. The mix proportions of the ECC are listed in **Table 2**. The water reducer was a polycarboxylate superplasticizer with a water reduction rate of 18–25%. The RECS15-type PVA fibers (dry bundled) were provided by Kuraray Co., Ltd, and the main material parameters are shown in **Table 3**. Per Chinese standard JGJ 70–2009 (China' National Standard, 2009), the material properties of the two ECCs with different strengths were tested, and the results are shown in **Table 4**.

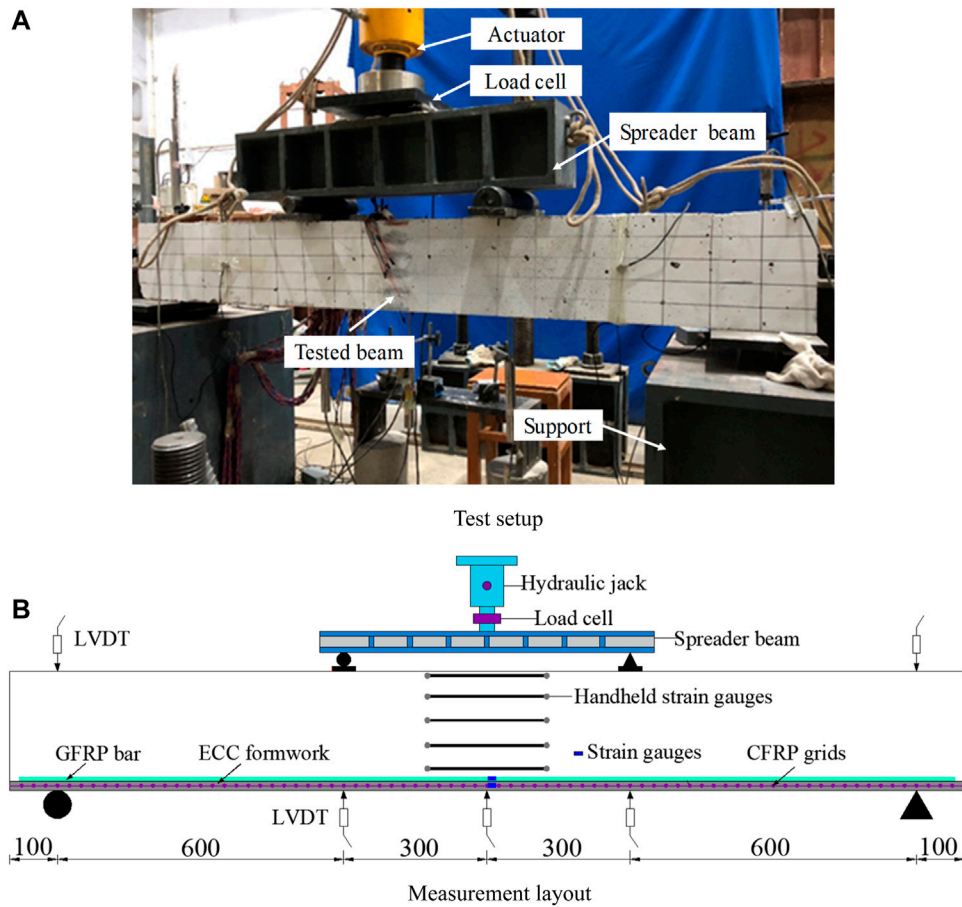


FIGURE 3 | Test setup and measurement layout for the composite beam.

TABLE 2 | ECC mix proportion.

Strength	Relative weight ratios to cement							PVA (volume fraction)
	(%)Cement	Fly ash	Silica fume	Quartz sand	Water	Water reducer	Additives (%)	
C30	1	3	0.1	0.4	0.992	0.003	0.31	2.00
C50	1	3	0.1	0.4	0.88	0.003	0.15	2.00

TABLE 3 | Material parameters of PVA fibers.

Density/(g/cm ³)	Elongation/%	Length/mm	Diameter/ μ m	Elastic modulus/GPa	Tensile strength/MPa
1.3	6.5	35	40	41	1,560

TABLE 4 | Material parameters of ECCs.

Grade	Elastic modulus /GPa	Compressive strength/MPa	Flexural strength/MPa	Tensile strength/MPa	Tensile strain/%
C30	14.8	36.2	18.9	4.8	1.72
C50	20.0	52.6	20.6	6.2	2.40

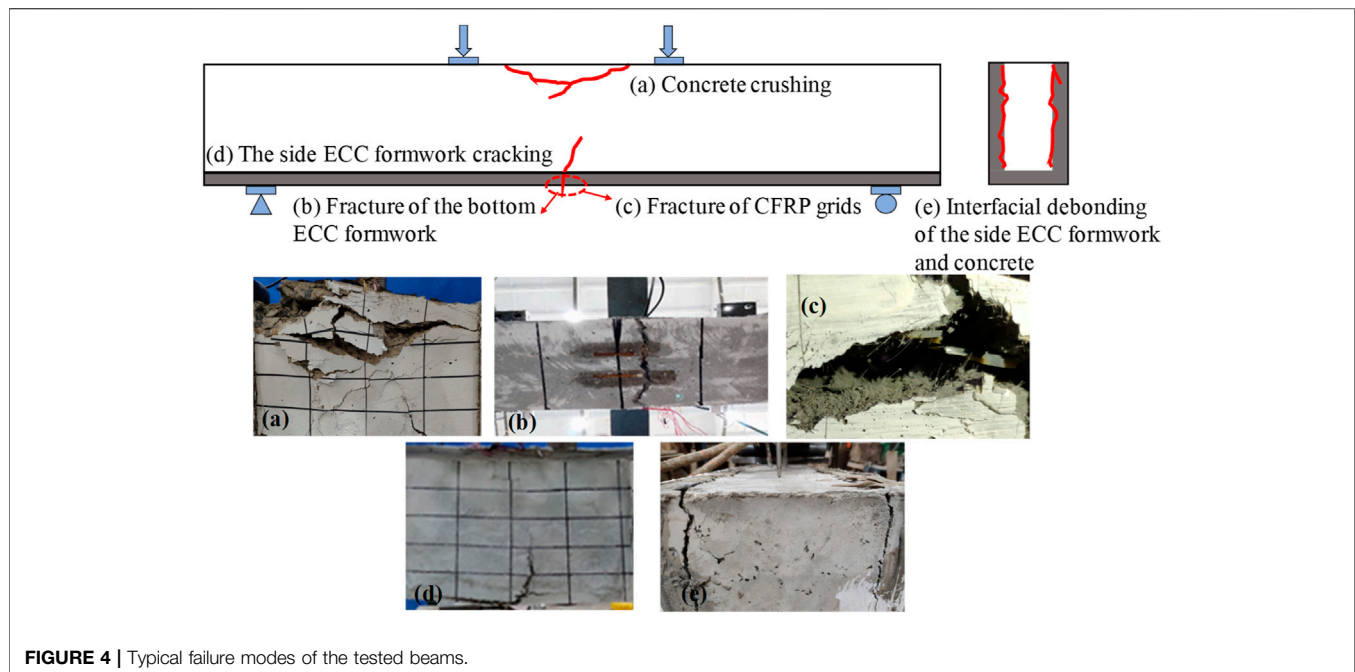


FIGURE 4 | Typical failure modes of the tested beams.

The GFRP bars were composed of glass fibers and epoxy resin that were obtained by the pultrusion process and manufactured by Nanjing Fenghui Composite Material Co., Ltd. The ultimate tensile strength and elastic modulus were measured to be 712.3 MPa and 59.3 GPa, respectively. HRB400 ribbed steel bars with diameters of 6 and 10 mm were used as the stirrups and top longitudinal reinforcement, respectively. For the 6 mm diameter steel bars, the yield strength, ultimate tensile strength, elastic modulus and ultimate elongation were 425 MPa, 610 MPa, 187 GPa and 29%, respectively. For the 10 mm diameter steel bars, the yield strength, ultimate tensile strength, elastic modulus and ultimate elongation were 435 MPa, 705 MPa, 205 GPa and 22%, respectively. CFRP grids were made of continuous carbon fibers impregnated with epoxy resin, provided by Carbon Composites (Beijing) Co., Ltd. The material properties of the CFRP grids with a 4-mm² cross-section were measured per ASTM-D882-2009 (Institute, 2009). The tensile strength and elastic modulus were 2,529 MPa and 190.2 GPa, respectively.

TEST RESULTS AND ANALYSIS

Crack Patterns and Failure Modes

Figure 4 shows the failure modes of all the tested beams. In the reference concrete beam R, the first crack was detected at a load of 14.4 kN, and its width was 0.107 mm. Typical V-shaped cracks could be observed on the beam sides, while both the crack number and width increased as the load increased. The concrete was crushed in the compression zone at an ultimate load of 140 kN (see **Figure 4A**), which indicated that the failure of the testing beam.

In beam B with bottom ECC formwork, the first crack with a width of 0.063 mm was observed on the bottom ECC at a load of 19.7 kN (0.13 M_u). Dense and fine cracks were observed on the ECC formwork, thereby indicating the excellent crack resistance

ability of the ECC, as shown in **Figure 5B**, which was different from the reference concrete beam R (see **Figure 5A**). The cracks extending from the bottom occurred first in the middle of the side concrete at a load of 30.0 kN and then extended in all areas along the beam length. At a load of 152.0 kN, the concrete was crushed in the compression zone, whereas no interfacial debonding between the ECC formwork and the concrete was observed.

Beam U with U-shaped ECC formwork first cracked (0.027 mm wide) at a load of 25.0 kN (0.19 M_u) (see **Figure 5B**). At the load of 79.0 kN (0.62 M_u), the ECC formwork fully fractured at both sides and the bottom, and interfacial debonding with a width of 3 mm occurred between the side ECC formwork and the core concrete, as seen in **Figure 4E**. At this time, the bearing capacity of beam U increased slowly, whereas the deflection increased rapidly. With increasing loading, the concrete in the compression zone inside the ECC formwork was crushed at a load of 128.7 kN.

The first crack with a width of 0.063 mm was observed in beam UC-30 with U-shaped CFRP grid-reinforced ECC formwork at a load of 25.0 kN (0.17 M_u). When beam UC-30 was loaded to 147.4 kN, the ECC formwork fractured at both sides and the bottom, as seen in **Figure 4D**, and then the load dropped suddenly to 135 kN. The test beam then entered the horizontal stage, i.e., the deflection increased continuously while the load remained basically unchanged. The crack width of the test beam was relatively uniform during loading. The concrete in the compression zone was crushed, and the CFRP grids were fractured (as seen in **Figure 4C**) until a load of 146.0 kN was reached, thereby demonstrating the failure of the beam. In beam UC-50 with the C50 ECC formwork, a crack with a width of 0.027 mm emerged at 26.0 kN (0.16 M_u). At a load of 147.0 kN (0.91 M_u), the bottom of the ECC formwork fractured. The CFRP grids at the bottom fractured at a load of 153.0 kN (0.95 M_u), and the CFRP grids at both sides also fractured with continued loading. The load fluctuated between 153.0 and 156.0 kN, while the deflection increased and the

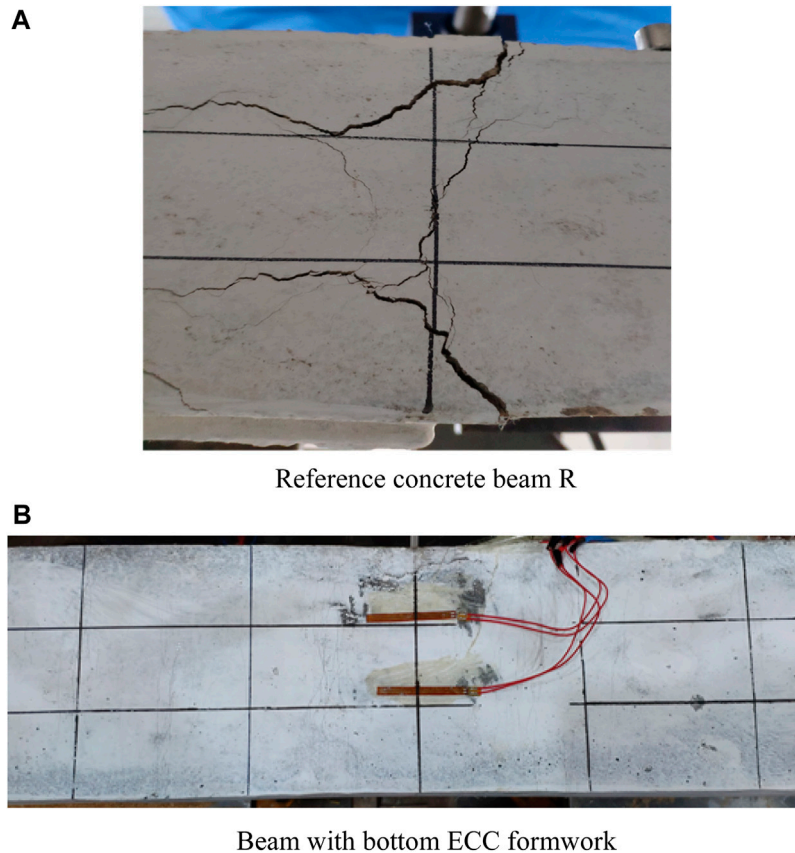


FIGURE 5 | Comparison of the crack distribution in the bottom of the beam.

TABLE 5 | Test results of all the tested beams.

Label	P_{cr} (kN)	D_{cr} (mm)	P_u (kN)	D_u (mm)	M_u (MPa)	Failure mode
R	14.4	0.6	140.0	41.5	42.0	Concrete crushing
B	19.7	0.9	152.0	41.2	45.6	Fracture of the ECC, concrete crushing
U	25.0	1.4	128.7	46.5	38.6	Fracture of the bottom and sides of the ECC, concrete crushing
UC-30	25.0	1.1	147.4	48.4	44.2	Fracture of the bottom and sides of the ECC, fracture of the CFRP grids, concrete crushing
UC-50	26.0	1.3	162.0	34.8	48.6	Fracture of the bottom and sides of the ECC, fracture of the CFRP grids, concrete crushing

Note: P_{cr} is the cracking load; D_{cr} is the cracking deflection corresponding to the cracking load; P_u is the ultimate load; D_u is the ultimate deflection; and M_u is the flexural strength. The failure mode is listed according to the actual failure order in the test observations.

concrete in the compression zone started to crush. At the ultimate load (161.9 kN), all the CFRP grids fractured, and the concrete crushed, thereby demonstrating the failure of the beam. In conclusion, the failure types of the composite beams can be summarized as: 1) concrete crushing; 2) fracture of the bottom ECC formwork; 3) fracture of CFRP grids; 4) fracture of the side ECC formwork; and 5) interfacial debonding of the side of the ECC formwork and core concrete.

Load-Deflection Behavior of Composite Beams

The test results of all beams are summarized in **Table 5**, while the load versus mid-span deflection curves of all the tested beams are

shown in **Figure 6**. Compared with that of beam R, the cracking strengths corresponding to the first crack observed for beams U, UC-30 and UC-50 with U-shaped ECC formwork increased within a range of 73.6 and 80.6%, whereas the cracking load observed in beam B with bottom ECC formwork only increased by approximately 36.8%. This phenomenon demonstrated that the application of the U-shaped ECC formwork greatly improved the cracking resistance of the composite beams, and their efficiency of improvement was better than that of the bottom ECC formwork. For the ultimate load, an increase between 5.3 and 15.7% could be achieved in beams UC-30 and UC-50 when compared with the reference concrete beam. In beam B and beam U, the ultimate load of the former was improved by 8.6%, whereas

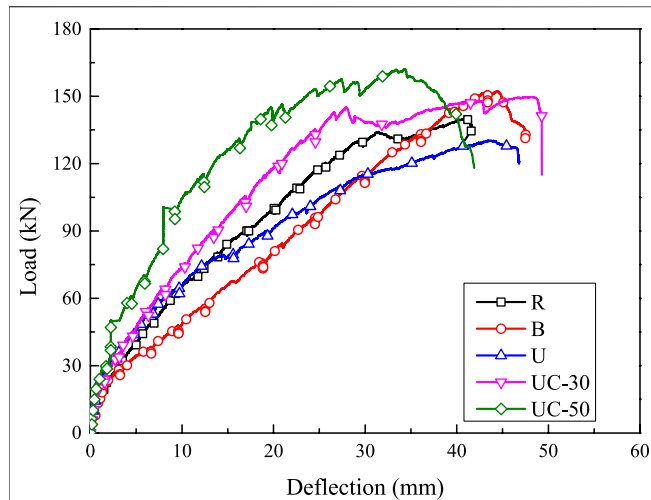


FIGURE 6 | Load versus mid-span deflection curves of all the tested beams.

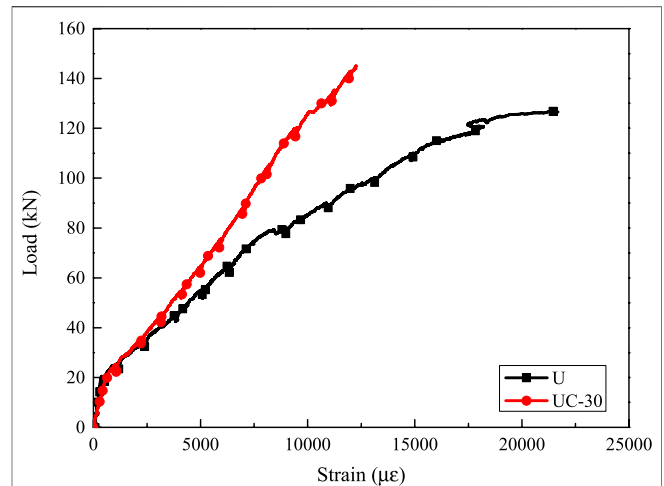


FIGURE 8 | Load versus strain curves of the GFRP bars.

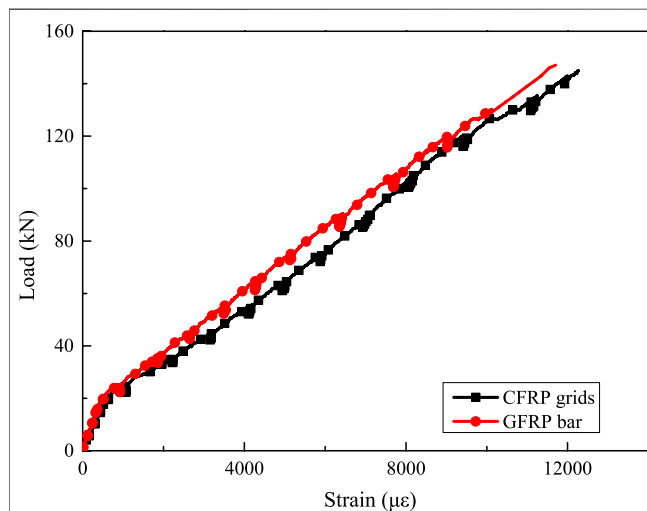


FIGURE 7 | Load versus strain curves of GFRP bars and CFRP grids (taken from beam UC-30).

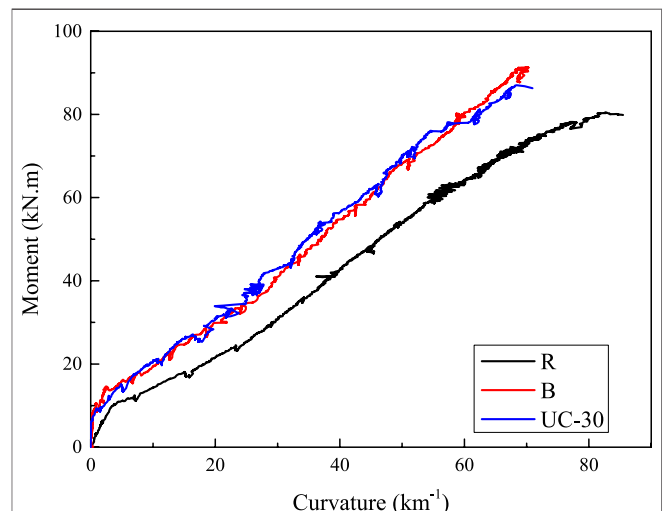


FIGURE 9 | Moment-curvature responses of composite beams.

that of the latter adversely decreased by 8.1%. The severe interfacial debonding between the U-shaped ECC formwork and the core concrete accounted for the above phenomenon. When the U-shaped ECC formwork was applied, the stiffness difference between the ECC and concrete resulted in interfacial debonding; accordingly, the ultimate load of composite beam U decreased.

Strain Response

Figure 7 shows the load versus strain curves of the GFRP bars and CFRP grids at the mid-span location, which are chosen from beam UC as an example. The load-strain behavior of both the GFRP bars and CFRP grids could be divided in two stages, i.e., 1) before cracking and 2) after cracking. Before

cracking, the strains of the GFRP bars and CFRP grids linearly increased with the load, and the strain development rates of the two materials were similar because the distances between the GFRP bars and CFRP grids were close. After cracking, the strain development rates of the GFRP bar and CFRP grids significantly increased, and the strain development was still approximately linear with increasing load because the two materials were both linear-elastic. **Figure 8** shows the load versus the GFRP bars in beam U with pure ECC formwork and UC-30 with CFRP grid-reinforced ECC formwork. The strain of the GFRP bars in beam U was smaller than that of beam UC-30 under the same level of loading, which indicated that the embedded CFRP grids effectively carried part of the tension force from the GFRP bars. It is obvious that the

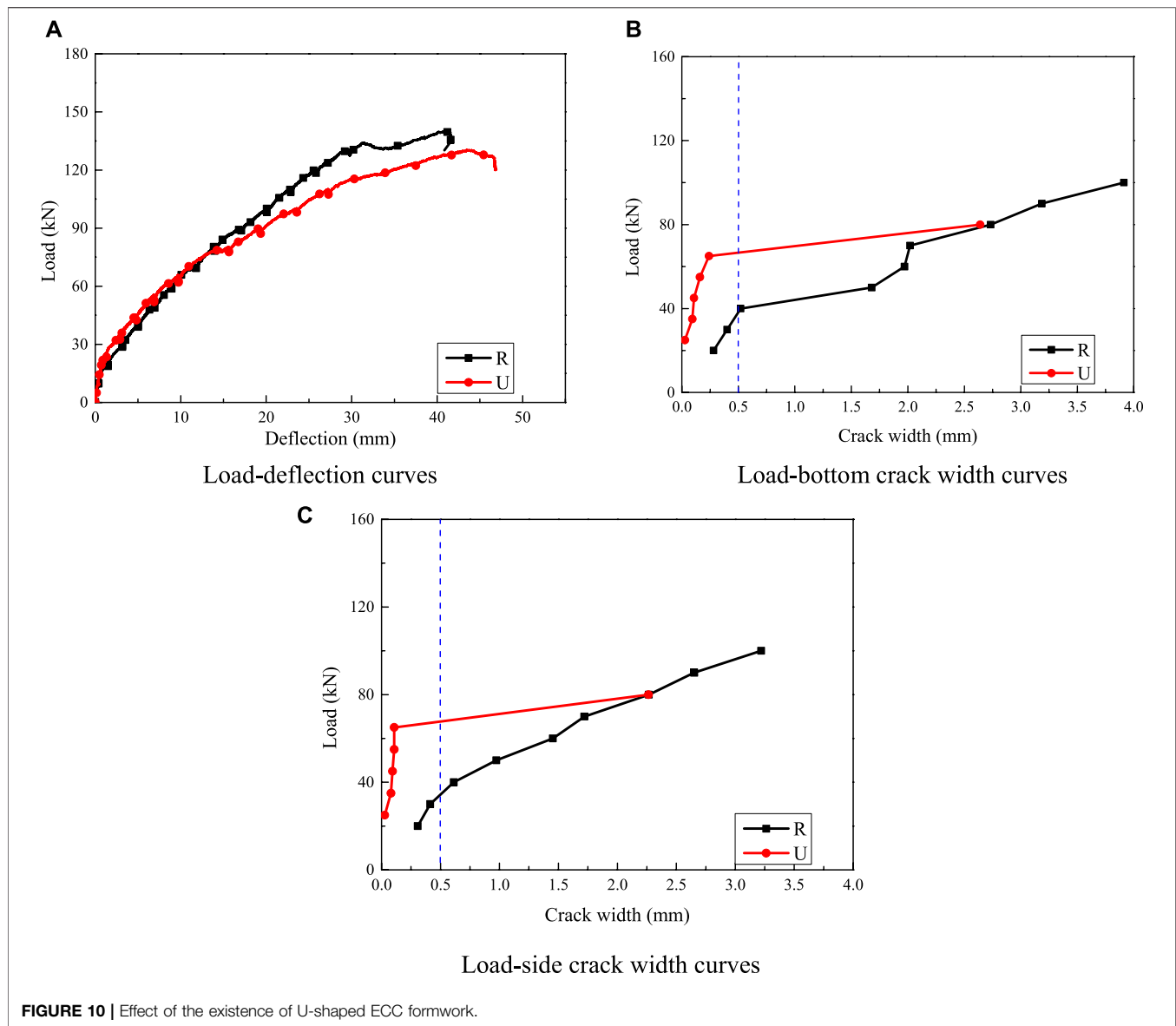


FIGURE 10 | Effect of the existence of U-shaped ECC formwork.

CFRP grids and GFRP bars contributed to the composite beam.

Moment-Curvature Response in the Pure Bending Section

Figure 9 shows the moment-curvature response in the pure bending section that is obtained from three typical beams. The slopes of the moment-curvature curves of beam B and beam UC-30 are almost the same, and both are larger than that of beam R. This indicates that the use of the ECC formwork can improve the sectional stiffness of the normal FRP reinforced concrete beam, whether the precracking stiffness or postcracking stiffness is considered. It is also evident that the ultimate moments of beam B and UC-30 are larger than that of beam R, thereby indicating that beams with ECC bottom or U-shaped ECC formwork can improve the bearing capacity. The

type of ECC formwork has little effect on the bearing capacity of the composite beams. The ultimate curvatures, defined as the curvatures corresponding to the peak moments, of beam B and UC-30 are 68.73 km^{-1} and 68.29 km^{-1} , respectively, whereas the ultimate deflection of beam B is smaller than that of beam UC-30, with a reduction of 14.88%. The above phenomenon can be explained as follows. The employment of CFRP grid-reinforced U-shaped ECC formwork may increase the shear stiffness of composite beams in the shear-span zone and consequently reduce the mid-span deflection. A similar conclusion was obtained by Dong (Dong et al., 2019).

DISCUSSION

The effects of the application of the U-shaped ECC formwork, the formwork types, the application of CFRP grids, and the strength

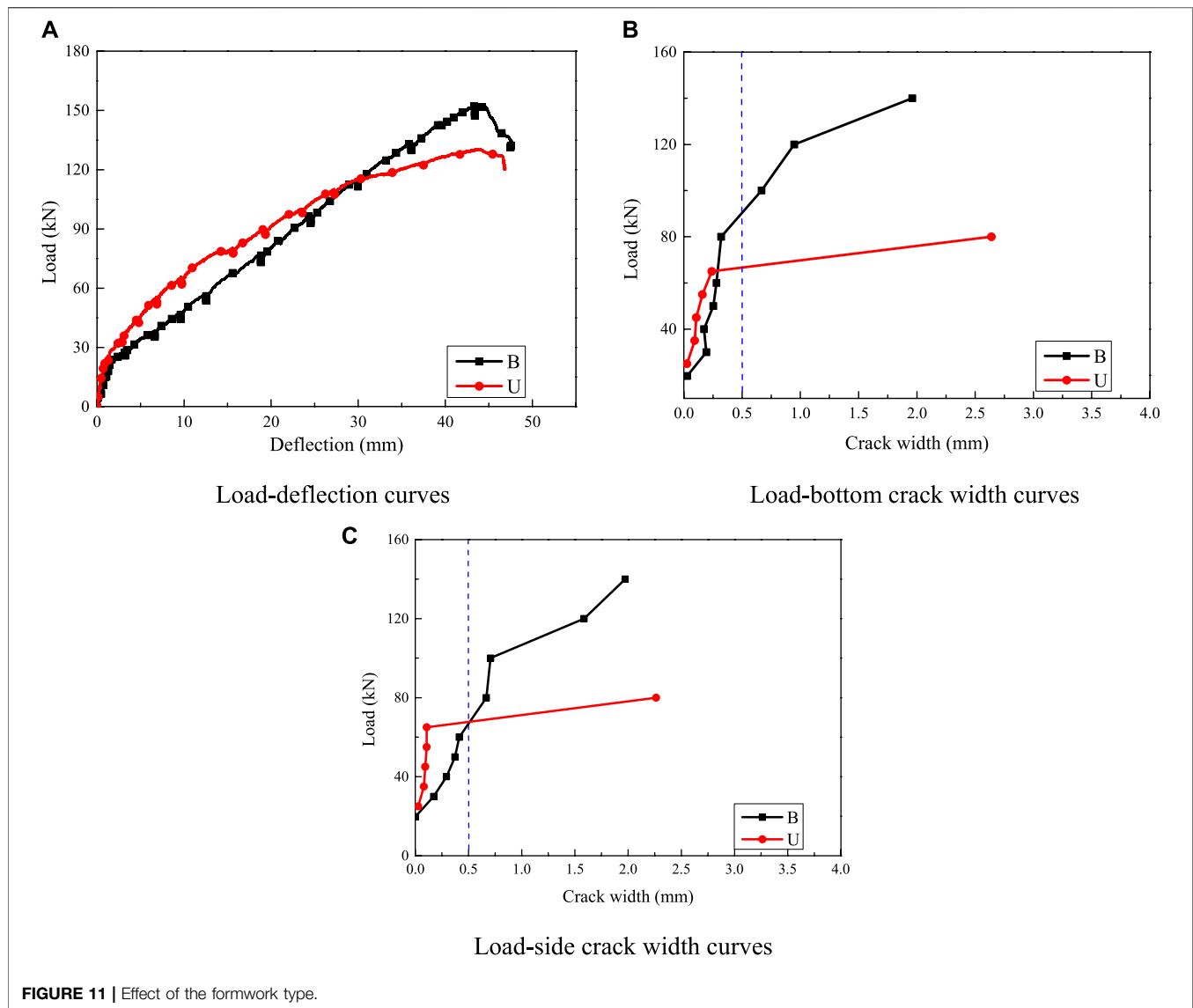


FIGURE 11 | Effect of the formwork type.

of the ECC were compared to study the cracking performance and mechanical behavior of the tested beams. The detailed analysis is provided below.

Effect of the U-Shaped ECC Formwork

Figure 10 shows the effect of the U-shaped ECC formwork on the load-deflection relationship and load-crack width behavior by comparing reference beam R to beam U with U-shaped ECC formwork. As shown in **Figure 10A**, the precracking and postcracking stiffnesses of beam R were 23.45 kN/mm and 4.87 kN/mm, respectively. The precracking stiffness of beam U was 7.3% larger than that of beam R, which indicated that the use of U-shaped ECC formwork could increase the precracking stiffness of the beam. Due to the interfacial debonding in beam U, the U-shaped ECC formwork and core concrete did not work together, and thereafter, the cross-sectional stiffness was significantly reduced to 2.25 kN/mm. Compared with the case of beam R, the cracking load in beam U increased by 73.6%

(**Table 5**), which indicates that the use of U-shaped ECC formwork can significantly improve the cracking strength. The ultimate load of beam U (128.7 kN) decreased compared to that of reference beam R (140.0 kN), with a reduction of 8.1%, which was mainly due to the interfacial debonding between the concrete and U-shaped ECC formwork. In this case, the following conclusion can be drawn: U-shaped ECC formwork had a positive effect on crack resistance due to the multicracking characteristic of ECCs, whereas a good interfacial bonding mechanism should be guaranteed. In addition, at the ultimate load, the mid-span deflection of beam U (46.5 mm) was larger than that of beam R (41.5 mm), which improved the ductility of the composite beam because of the application of the U-shaped ECC formwork.

The largest crack widths at the bottom and side of the ECC formwork were taken as the crack widths shown in **Figures 10B,C**, and crack widths larger than 4.0 mm were not recorded in the present study. Both the bottom and side crack

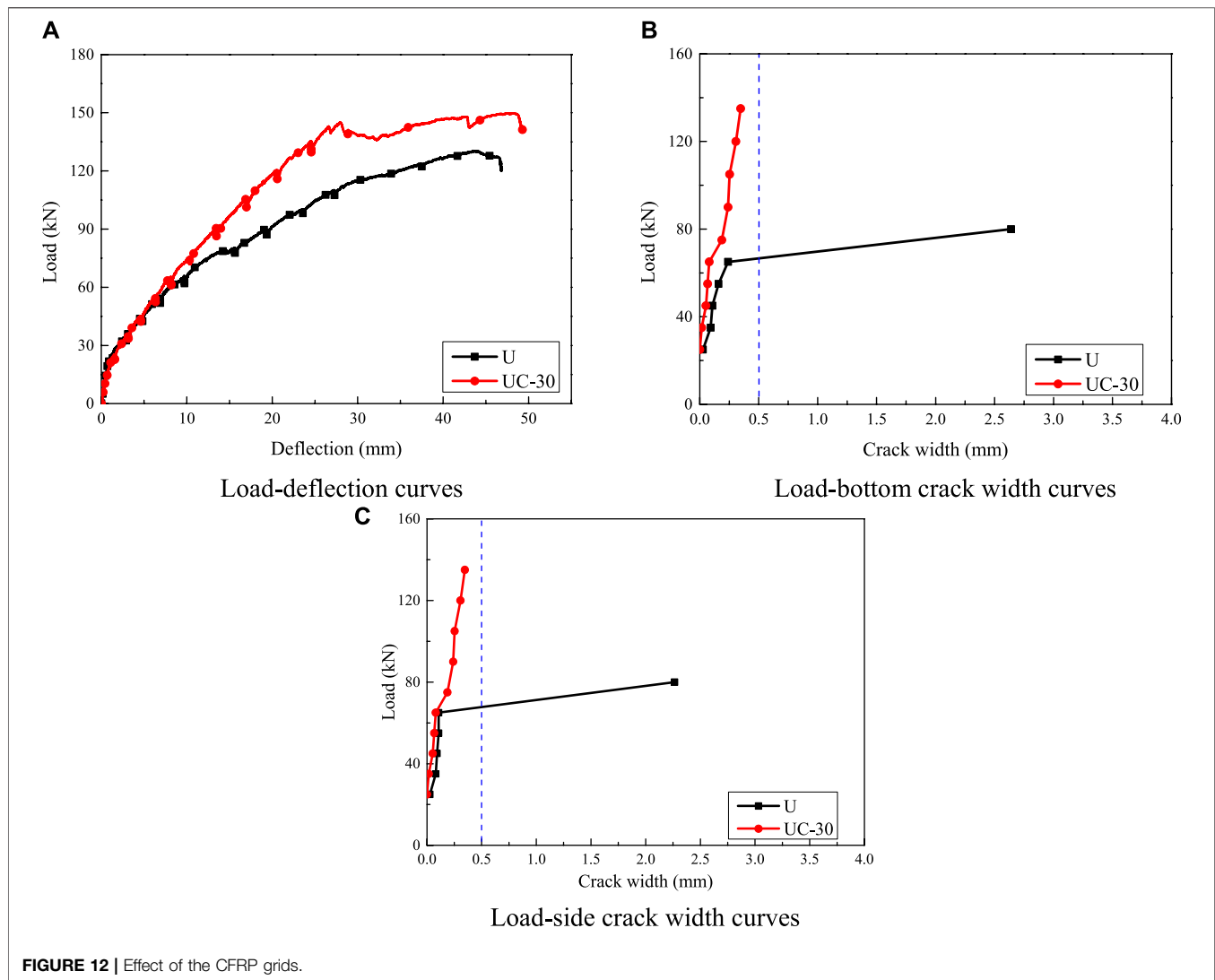


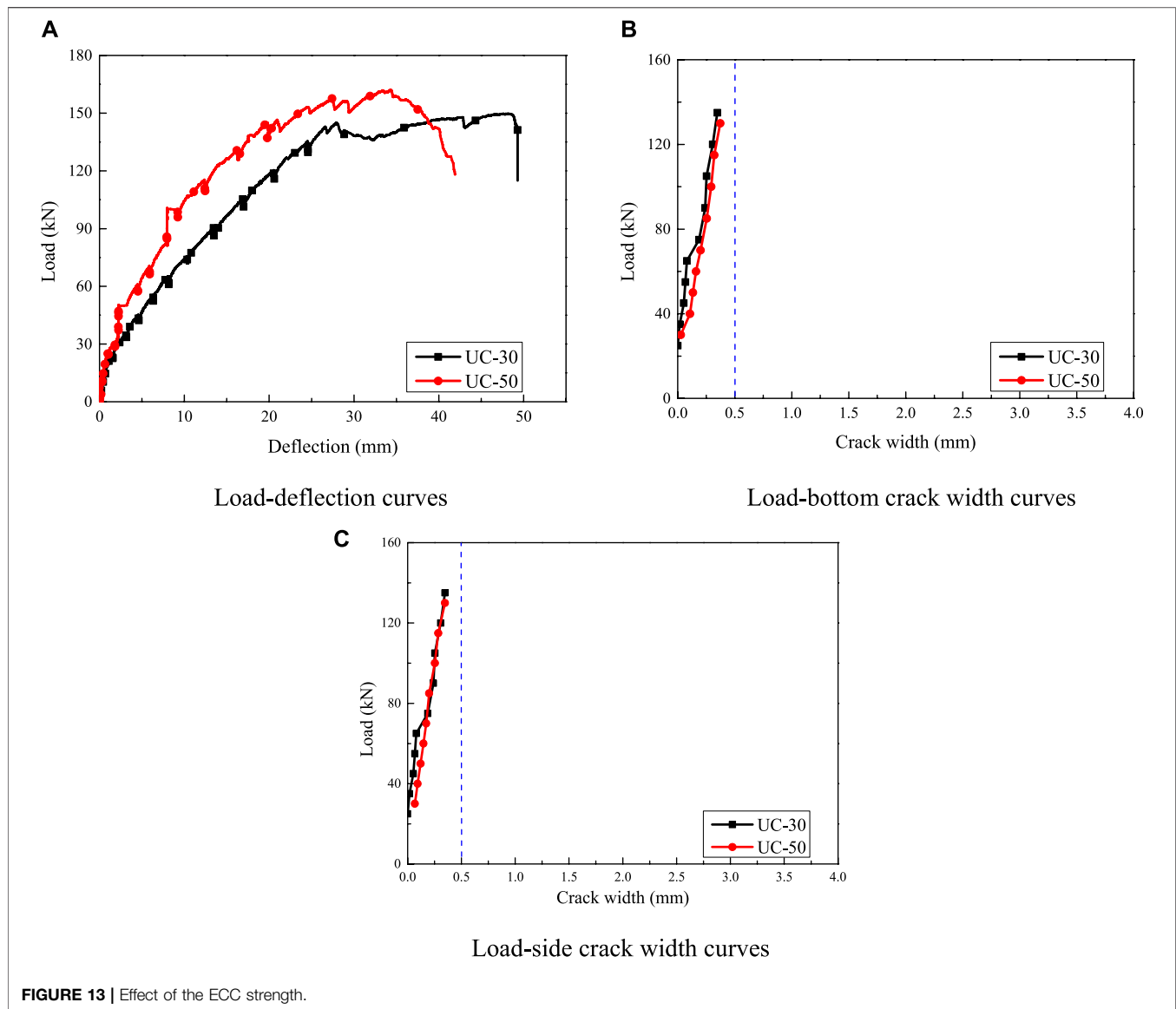
FIGURE 12 | Effect of the CFRP grids.

widths measured in beam U were much smaller than those in beam R under the same load before interfacial debonding between the ECC formwork and core concrete occurred (at a load of 79.0 kN); see **Figures 10B,C**. However, after interfacial debonding, the bottom and side crack widths in beam U developed extremely fast and exceeded 2.0 mm at the next data recording process. At the bottom crack width limit of 0.5 mm specified in the Chinese standard GB50608-2010 for the serviceability limit state (SLS) (China' National Standard, 2010), the loads obtained from beams R and U were 40.0 and 66.0 kN, corresponding to 0.29 M_u and 0.51 M_u , respectively. In beam R, only 29% of the ultimate load could be utilized at the SLS. However, in the case of U-shaped ECC formwork, the load bearing capacity corresponding to the SLS significantly improved to approximately half of the ultimate bearing capacity.

Effect of the Formwork Type

Figure 11 shows the effect of the formwork type on the load-deflection relationships and load-crack width by comparing

beam B with bottom ECC formwork and beam U with U-shaped ECC formwork. As shown in **Figure 11A**, the precracking stiffness of beam U (25.15 kN/mm) was 22.7% larger than that of beam B (21.89 kN/mm). Similarly, the postcracking stiffness of beam U (3.45 kN/mm) was smaller than that of beam B (4.45 kN/mm) before interfacial debonding was observed in beam U (79.0 kN). The above phenomenon demonstrated that the U-shaped ECC formwork improved the cross-sectional stiffness, as the elastic modulus of the ECC was larger than that of the concrete. After interfacial debonding, the cross-sectional stiffness measured from beam U decreased compared to that of beam B, and the postdebonding stiffness of beam U was only 2.25 kN/mm. The cracking load increased by 26.9% as the ECC formwork changed from the bottom type to the U-shaped type (see **Table 5**). The ultimate load of beam U was weakened due to interfacial debonding and even decreased compared to that of beam B. The ultimate deflection of beam U was 12.9% larger than that of beam B. This result indicated that



the beam with the U-shaped ECC formwork exhibited better ductility than the beam with the bottom ECC formwork.

The largest crack widths at the bottom and side of the ECC formwork were taken as the crack widths shown in **Figures 11B,C**. The development of the crack width was smaller in beam U than in beam B before interfacial debonding occurred at a load of 79.0 kN in beam U. Thus, a reasonable assumption can be drawn that the crack control ability was better in the composite beam with U-shaped ECC formwork. For beam B, the crack width developed relatively slowly before the load of approximately 80.0 kN was reached, and after that, the crack width grew fast. At the bottom crack width limit of 0.5 mm for the SLS, the loads of beams B and U were 65.6 and 66.0 kN, corresponding to $0.43 M_u$ and $0.51 M_u$, respectively. By changing the bottom ECC formwork to U-shaped ECC formwork, the bearing capacity corresponding to the SLS in beam U was improved by 18.6% compared with the case of beam B. For the side crack width in **Figure 11C**, the width of beam U was smaller than that of beam B

due to the existence of the side ECC formwork with a good effect on crack control.

Effect of the CFRP Grids

Figure 12 shows the effect of the CFRP grids on the load-deflection relationships and load-crack width by comparing beam U using the U-shaped ECC formwork and beam UC-30 using the U-shaped CFRP grid-reinforced ECC formwork. As shown in **Figure 12A**, the precracking stiffness and postcracking stiffness of beam UC-30 were 26.6 kN/mm and 5.33 kN/mm, respectively, which were both larger than those of beam U due to the existence of CFRP grids. This result indicated that using CFRP grids to strengthen the U-shaped ECC formwork had a good effect on improving the stiffness of the composite beam. The employment of CFRP grids had little effect on constraining the cracking development of the composite beam during loading. The cracking loads of beams U and UC-30 were both 25 kN. The

ultimate loads of beams U and UC-30 were 128.7 and 147.4 kN, respectively. An increase of 14.5% in the bearing capacity was observed in beam UC-30. This shows the enhancement effect of the U-shaped CFRP grid-reinforced ECC formwork on the beam. In addition, the ultimate deflection of beam U (46.5 mm) was smaller than that of beam UC-30 (48.4 mm).

The largest crack widths at the bottom and side of the ECC formwork were taken as the crack widths shown in **Figures 12B,C**, and crack widths larger than 4.0 mm were not recorded in the present study. It is obvious that the crack width in beam UC-30 was smaller than that in beam U under the same load during the entire loading history. At the bottom crack width limit of 0.5 mm for the SLS, the load of beam U was 66 kN, corresponding to 0.51 M_u , where the maximum bottom crack width in beam UC-30 was smaller than 0.5 mm during the entire loading process. In the case of using the CFRP grid-reinforced ECC formwork, the bearing capacity corresponding to the SLS improved significantly.

Effect of the ECC Strength

Figure 13 shows the effect of the concrete strength on the load-deflection relationships and load-crack width by comparing beam UC-30 with C30 ECC and beam UC-50 with C50 ECC. As shown in **Figure 13A**, the precracking stiffness of beam UC-50 (29.97 kN/mm) was 12.7% larger than that of beam UC-30 (26.6 kN/mm), and the postcracking stiffness of beam UC-50 (7.27 kN/mm) was also larger than that of beam UC-30 (5.33 kN/mm), as the elastic modulus of C50 concrete was larger than that of C30 concrete. The mid-span deflection of beam UC-50 decreased by 28.0% compared with that of beam UC-30 at the ultimate load. The cracking loads of beams UC-30 and UC-50 were similar, and the difference was less than 4%. Regarding the ultimate load, an increment of 9.9% was obtained in beam UC-50 using higher ECC strength compared with beam UC-30. The higher ECC strength could sustain more load in the composite beam.

The largest crack widths at the bottom and side of the ECC formwork were taken as the crack widths shown in **Figures 13B,C**. The crack widths developed at a similar rate in beams UC-30 and UC-50 during the entire loading history, where a relatively smaller crack width under the same load level was observed in beam UC-30, thereby indicating that the increased ECC strength showed a negative effect on the crack control ability. Both beams UC-30 and UC-50 satisfied the bottom crack width limit of 0.5 mm for the SLS during the entire loading history.

CONCLUSION

In this paper, the flexural performance of GFRP-reinforced composite beams with U-shaped CFRP grid-reinforced ECC stay-in-place formwork was studied through bending experiments. The application of U-shaped ECC formwork, different formwork types, the CFRP grids, and various ECC strengths served as the test variables. The failure modes, load-deflection and stain response were analyzed. Based on the experiments, the following results can be drawn:

- (1) ECCs could be an ideal strengthening material to improve the flexural performance of concrete beams. The cracking load and ultimate load of beam B with bottom ECC formwork were 36.81 and 8.57% larger than those of reference beam R. Moreover, the interfacial bond between the ECC and normal concrete performs well during loading.
- (2) The same failure modes were observed in GFRP-reinforced composite beams strengthened with ECC formwork and CFRP grid-reinforced ECC formwork at the ultimate load, where the concrete was crushed and GFRP bars were not fractured. Both the ECC formwork and CFRP grids at the bottom and sides were fractured in all the beams during the loading process.
- (3) The CFRP grids used could improve the cracking capacity and bearing capacity of composite structures. In terms of the composite beam with CFRP grid-reinforced U-shaped ECC formwork, the cracking load and bearing capacity were 78.57–85.71% and 5.29–15.71% larger than those of beam R. Moreover, the employment of CFRP grid-reinforced U-shaped ECC formwork can improve the shear stiffness.
- (4) The U-shaped ECC formwork exhibited better ductility and crack control effect than the beam with the bottom ECC formwork. In terms of different strength of U-shaped ECC formwork the increase in ECC strength from C30 to C50 was not obvious with the increase in the cracking load, and a higher ECC strength could increase the ultimate load of composite beams by 9.9%.
- (5) The employment of U-shaped ECC formwork had a positive effect on the crack resistance at the serviceability limit, which will be of great benefit to structural durability. The composite beams showed better performance of cracking load, stiffness and bearing capacity than those of reference beam corresponding to the SLS.

DATA AVAILABILITY STATEMENT

The original contributions presented in the study are included in the article/Supplementary Material, further inquiries can be directed to the corresponding author.

AUTHOR CONTRIBUTIONS

CW Conceptualization, Methodology, Writing- Original draft preparation. YS Investigation, Software, Visualization, Writing-Original draft preparation. PZ Conceptualization, Data curation, Writing- Reviewing and Editing. HZ Validation, Writing-Reviewing and Editing. DG Validation, Writing- Reviewing and Editing. SS Supervision.

FUNDING

This study was funded by financial support from the National Natural Science Foundation of China (U1904177, 51508519, 52108119), the Natural Science Foundation of Jiangsu Province (Grant Nos. BK20200376), and the Fundamental Research Funds for the Central Universities (Grant Nos. 2242021R10081).

REFERENCES

- Akiyama, M., Frangopol, D. M., and Suzuki, M. (2012). Integration of the Effects of Airborne Chlorides into Reliability-Based Durability Design of Reinforced concrete Structures in a marine Environment. *Struct. Infrastructure Eng.* 8, 125–134. doi:10.1080/15732470903363313
- Al-Salloum, Y. A., El-Gamal, S., Almusallam, T. H., Alsayed, S. H., and Aql, M. (2013). Effect of Harsh Environmental Conditions on the Tensile Properties of GFRP Bars. *Composites B: Eng.* 45 (1), 835–844. doi:10.1016/j.compositesb.2012.05.004
- Al-Saoudi, A., Kalfat, R., Al-Mahaidi, R., Cervenka, J., and Pryl, D. (2021). Numerical and Experimental Investigation into the Fatigue Life of FRP Bonded to concrete and Anchored with Bidirectional Fabric Patches. *Eng. Structures* 239, 112335. doi:10.1016/j.engstruct.2021.112335
- Altamas, A., El Refai, A., and Abed, F. (2015). Bond Degradation of basalt Fiber-Reinforced Polymer (BFRP) Bars Exposed to Accelerated Aging Conditions. *Construction Building Mater.* 81, 162–171. doi:10.1016/j.conbuildmat.2015.02.036
- Balandran, R. V., Rana, T. M., Maqsood, T., and Tang, W. C. (2002). Application of FRP Bars as Reinforcement in Civil Engineering Structures. *Struct. Surv.* 20, 62–72. doi:10.1108/02630800210433837
- Barris, C., Torres, L., Vilanova, I., Miàs, C., and Llorens, M. (2017). Experimental Study on Crack Width and Crack Spacing for Glass-FRP Reinforced concrete Beams. *Eng. Structures* 131, 231–242. doi:10.1016/j.engstruct.2016.11.007
- Cai, J., Pan, J., and Zhou, X. (2017). Flexural Behavior of basalt FRP Reinforced ECC and concrete Beams. *Construction Building Mater.* 142, 423–430. doi:10.1016/j.conbuildmat.2017.03.087
- China' National Standard (2010b). *GB 50010-2010 Code for Design of concrete Structures*. China.
- China' National Standard (2012). *GB/T 50152-2012 Standard for Test Method of concrete Structures*. China.
- China' National Standard (2010a). *GB50608-2010 Technical Code for Infrastructure Application of FRP Composites*. China.
- China' National Standard (2009). *JGJ/T70-2009 Standard for Test Method of Performance on Building Mortar*. China.
- Dong, H.-L., Zhou, W., and Wang, Z. (2019). Flexural Performance of concrete Beams Reinforced with FRP Bars Grouted in Corrugated Sleeves. *Compos. Structures* 215, 49–59. doi:10.1016/j.compstruct.2019.02.052
- Dong, Z., Wu, G., Zhao, X.-L., Zhu, H., and Shao, X. (2019). Behaviors of Hybrid Beams Composed of Seawater Sea-Sand concrete (SWSSC) and a Prefabricated UHPC Shell Reinforced with FRP Bars. *Construction Building Mater.* 213, 32–42. doi:10.1016/j.conbuildmat.2019.04.059
- Gar, S. P., Mande, J. B., and Hurlbaeus, S. (2018). Deflection of FRP Prestressed Concrete Beams. *J. Compos. Constr.* 22 (2), 1–11. doi:10.1061/(asce)cc.1943-5614.0000832
- Ge, W., Ashour, A. F., Cao, D., Lu, W., Gao, P., Yu, J., et al. (2019). Experimental Study on Flexural Behavior of ECC-concrete Composite Beams Reinforced with FRP Bars. *Compos. Structures* 208, 454–465. doi:10.1016/j.compstruct.2018.10.026
- Ge, W., Wang, Y., Ashour, A., Lu, W., and Cao, D. (2020). Flexural Performance of concrete Beams Reinforced with Steel-FRP Composite Bars. *Archiv.Civ.Mech.Eng* 20 (2), 1–17. doi:10.1007/s43452-020-00058-6
- Huang, B.-T., Weng, K.-F., Zhu, J.-X., Xiang, Y., Dai, J.-G., and Li, V. C. (2021). Engineered/strain-hardening Cementitious Composites (ECC/SHCC) with an Ultra-high Compressive Strength over 210 MPa. *Composites Commun.* 26, 100775. doi:10.1016/j.coco.2021.100775
- Huang, B.-T., Wu, J.-Q., Yu, J., Dai, J.-G., Leung, C. K. Y., and Li, V. C. (2021). Seawater Sea-Sand Engineered/strain-Hardening Cementitious Composites (ECC/SHCC): Assessment and Modeling of Crack Characteristics. *Cement Concrete Res.* 140, 106292. doi:10.1016/j.cemconres.2020.106292
- Institute (2009). *ASTM D882-2009 Standard Test Method for Tensile Properties of Thin Plastic Sheet*. United States.
- Issa, M. S., and Ismail, E.-S. (2020). Long-term Deflections of FRP Reinforced concrete Beams. *HBRC J.* 16 (1), 269–282. doi:10.1080/16874048.2020.1812897
- Kazemi, M., Li, J., Lahouti Harehdasht, S., Yousefieh, N., Jahandari, S., and Saberian, M. (2020). Non-linear Behaviour of concrete Beams Reinforced with GFRP and CFRP Bars Grouted in Sleeves. *Structures* 23, 87–102. doi:10.1016/j.istruc.2019.10.013
- Kim, Y. J. (2019). State of the Practice of FRP Composites in Highway Bridges. *Eng. Structures* 179, 1–8. doi:10.1016/j.engstruct.2018.10.067
- Li, V. C., and Leung, C. K. Y. Steady-State and Multiple Cracking of Short Random Fiber Composites. *J. Eng. Mech.* 118 (11), 2246–2264. doi:10.1061/(asce)0733-9399(1992)118:11(2246)
- Li, V. C., and Wang, S. and View Correspondence (2002). Flexural Behaviors of Glass Fiber-Reinforced Polymer (GFRP) Reinforced Engineered Cementitious Composite Beams. *Mj* 99 (1), 11–21. doi:10.14359/11311
- Li, V. C., Wu, C., Wang, S., Ogawa, A., and Saito, T. (2002). Interface Tailoring for Strain-Hardening Polyvinyl Alcohol-Engineered Cementitious Composite (PVA-ECC). *Mj* 99 (5), 463–472. doi:10.14359/12325
- Liu, H., Zhang, Q., Gu, C., Su, H., and Li, V. (2017). Influence of Microcrack Self-Healing Behavior on the Permeability of Engineered Cementitious Composites. *Cement and Concrete Composites* 82, 14–22. doi:10.1016/j.cemconcomp.2017.04.004
- Liu, J., Jiang, Z., Zhao, Y., Zhou, H., Wang, X., Zhou, H., et al. (2020). Chloride Distribution and Steel Corrosion in a Concrete Bridge after Long-Term Exposure to Natural Marine Environment. *Materials* 13 (17), 3900. doi:10.3390/ma13173900
- Liu, Y., Tafsirojjaman, T., Dogar, A. U. R., and Hückler, A. (2021). Bond Behaviour Improvement between Infra-lightweight and High Strength Concretes Using FRP Grid Reinforcements and Development of Bond Strength Prediction Models. *Construction Building Mater.* 270, 121426. doi:10.1016/j.conbuildmat.2020.121426
- Merwe, F. v. d., and Hofmann, P. (2020). Guidance on the Design and Use of Fibre-Reinforced Polymer (FRP) Soil Nails and Ground Anchors - Geotechnical Engineering. *Civil Eng.* 2020 (3), 56–63.
- Qiao, Z., Pan, Z., Leung, C. K. Y., and Meng, S. (2017). Experimental Study and Analysis of Flexural Behavior of ECC/RC Composite Beams. *J. Southeast University(Natural Sci. Edition)* 47 (4), 724–731.
- Qin, F., Zhang, Z., Yin, Z., Di, J., Xu, L., and Xu, X. (2020). Use of High Strength, High Ductility Engineered Cementitious Composites (ECC) to Enhance the Flexural Performance of Reinforced concrete Beams. *J. Building Eng.* 32, 101746. doi:10.1016/j.jobbe.2020.101746
- Siwowski, T., Kulpa, M., Rajchel, M., and Poneta, P. (2018). Design, Manufacturing and Structural Testing of All-Composite FRP Bridge Girder. *Compos. Structures* 206, 814–827. doi:10.1016/j.compstruct.2018.08.048
- Wang, Z., Zhao, X.-L., Xian, G., Wu, G., Singh Raman, R. K., and Al-Saadi, S. (2017). Durability Study on Interlaminar Shear Behaviour of basalt-, Glass- and Carbon-Fibre Reinforced Polymer (B/G/CFRP) Bars in Seawater Sea Sand concrete Environment. *Construction Building Mater.* 156, 985–1004. doi:10.1016/j.conbuildmat.2017.09.045
- Wang, Z., Zhao, X.-L., Xian, G., Wu, G., Singh Raman, R. K., Al-Saadi, S., et al. (2017). Long-term Durability of basalt- and Glass-Fibre Reinforced Polymer (BFRP/GFRP) Bars in Seawater and Sea Sand concrete Environment. *Construction Building Mater.* 139, 467–489. doi:10.1016/j.conbuildmat.2017.02.038
- Xu, J., and Li, Z. (2012). A Review on Ecological Engineering Based Engineering Management. *Omega* 40, 368–378. doi:10.1016/j.omega.2011.06.004
- Yuan, F., Pan, J., and Leung, C. K. Y. (2013). Flexural Behaviors of ECC and Concrete/ECC Composite Beams Reinforced with Basalt Fiber-Reinforced Polymer. *J. Compos. Constr.* 17 (5), 591–602. doi:10.1061/(asce)cc.1943-5614.0000381
- Zafari, B., Qureshi, J., Mottram, J. T., and Rusev, R. (2016). Static and Fatigue Performance of Resin Injected Bolts for a Slip and Fatigue Resistant Connection in FRP Bridge Engineering. *Structures* 7 (1), 71–84. doi:10.1016/j.istruc.2016.05.004
- Zhang, P., Su, Y., Liu, Y., Gao, D., and Sheikh, S. A. (2021). Flexural Behavior of GFRP Reinforced concrete Beams with CFRP Grid-Reinforced ECC Stay-In-Place Formworks. *Compos. Structures* 277, 114653. doi:10.1016/j.compstruct.2021.114653
- Zhang, W., François, R., Cai, Y., Charron, J.-P., and Yu, L. (2020). Influence of Artificial Cracks and Interfacial Defects on the Corrosion Behavior of Steel in concrete during Corrosion Initiation under a Chloride Environment. *Construction Building Mater.* 253, 119165. doi:10.1016/j.conbuildmat.2020.119165

- Zhang, Z., Liu, S., Yang, F., Weng, Y., and Qian, S. (2021). Sustainable High Strength, High Ductility Engineered Cementitious Composites (ECC) with Substitution of Cement by rice Husk Ash. *J. Clean. Prod.* 317, 128379. doi:10.1016/j.jclepro.2021.128379
- Zhang, Z., Qin, F., Ma, H., and Xu, L. (2020). Tailoring an Impact Resistant Engineered Cementitious Composite (ECC) by Incorporation of Crumb Rubber. *Construction Building Mater.* 262, 120116. doi:10.1016/j.conbuildmat.2020.120116
- Zhang, Z., Yang, F., Liu, J.-C., and Wang, S. (2020). Eco-friendly High Strength, High Ductility Engineered Cementitious Composites (ECC) with Substitution of Fly Ash by rice Husk Ash. *Cement Concrete Res.* 137, 106200. doi:10.1016/j.cemconres.2020.106200
- Zheng, Y., Zhang, L. F., and Xia, L. P. (2018). Investigation of the Behaviour of Flexible and Ductile ECC Link Slab Reinforced with FRP. *Construction Building Mater.* 166, 694–711. doi:10.1016/j.conbuildmat.2018.01.188
- Zou, X., Lin, H., Feng, P., Bao, Y., and Wang, J. (2021). A Review on FRP-concrete Hybrid Sections for Bridge Applications. *Compos. Structures* 262, 113336. doi:10.1016/j.compstruct.2020.113336

Conflict of Interest: The authors declare that the research was conducted in the absence of any commercial or financial relationships that could be construed as a potential conflict of interest.

Publisher's Note: All claims expressed in this article are solely those of the authors and do not necessarily represent those of their affiliated organizations, or those of the publisher, the editors, and the reviewers. Any product that may be evaluated in this article, or claim that may be made by its manufacturer, is not guaranteed or endorsed by the publisher.

Copyright © 2022 Wu, Su, Zhang, Zhu, Gao and Sheikh. This is an open-access article distributed under the terms of the Creative Commons Attribution License (CC BY). The use, distribution or reproduction in other forums is permitted, provided the original author(s) and the copyright owner(s) are credited and that the original publication in this journal is cited, in accordance with accepted academic practice. No use, distribution or reproduction is permitted which does not comply with these terms.



Numerical Investigation on the Dynamic Responses and Failure Criterion of RC Beam Under Impact

Jinlong Guo^{1,2,3}, Guoping Jiang¹, Zhengyu Wu^{1*}, An He² and Jian Cai²

¹School of Civil Engineering, Fujian Jiangxia University, Fuzhou, China, ²School of Civil and Transportation Engineering, South China University of Technology, Guangzhou, China, ³Institute of Infrastructural Protection in Fujian Jiangxia University, Fuzhou, China

During the period of service, the infrastructure is subjected to various forms of impact. To investigate the impact responses of a reinforced concrete (RC) beam, a numerical model of the RC beam under impact was developed by the finite element package LS-DYNA in this study. The numerical model was verified by using the drop hammer test on the RC beam. Using the numerical model, the midspan displacement of the RC beam is analyzed under the interaction of impact mass and impact velocity. The results show that the response surface of midspan displacement can be fitted as a binary power function of impact mass and impact velocity. The midspan displacement under various impact conditions with equal impulse or equal impact energy is different. Within the scope of a low-speed impact, the midspan displacement decreases with an increase in the impact mass under the equal impulse, while it increases with an increase in the impact mass under the equal impact energy. In addition, the impact failure of the RC beam is judged by the deformation criterion. The threshold value of the ductility coefficient is recommended to be set as 15 in the impact-resistant design for RC beams in civil engineering structures within the scope of a low-speed impact.

Keywords: RC beam, impact response, midspan displacement, response surface, failure criterion

OPEN ACCESS

Edited by:

Fangying Wang,
University of Nottingham,
United Kingdom

Reviewed by:

Guan Lin,
Hong Kong Polytechnic University,
Hong Kong SAR, China
Youxin Ma,
Nanyang Technological University,
Singapore

*Correspondence:

Zhengyu Wu
zhengyu_wu@fjxu.edu.cn

Specialty section:

This article was submitted to
Structural Materials,
a section of the journal
Frontiers in Materials

Received: 09 January 2022

Accepted: 17 February 2022

Published: 14 March 2022

Citation:

Guo J, Jiang G, Wu Z, He A and Cai J
(2022) Numerical Investigation on the
Dynamic Responses and Failure
Criterion of RC Beam Under Impact.
Front. Mater. 9:851301.
doi: 10.3389/fmats.2022.851301

1 INTRODUCTION

Compared with the static load, an impact releases a large amount of energy in a short period time, which often results in serious damage to structures. In recent years, dynamic responses of reinforced concrete (RC) members under impact have drawn much more attention. Some researchers have used the drop hammer device or the lateral impact device to carry out impact tests on reinforced concrete members (Fujikake et al., 2009; Sha and Hao, 2013; Zhao et al., 2017; Ye et al., 2021), and other researchers have used numerical simulation methods to carry out impact analysis on reinforced concrete members (Cai et al., 2017; Saleh et al., 2019; He et al., 2020; Tran et al., 2021). Several impact tests have primarily been performed to study the dynamic responses of RC beams under impact. Tachibana et al. (2010) carried out a drop hammer test on eight RC beams to investigate the influence of various beam spans, cross-sectional dimensions, and reinforcement ratios with characteristic values like the impact force and the energy absorbed by the beams. Zeng and Xu (2012), Xu and Zeng (2014) carried out a drop hammer test on six RC beams to investigate the effects of different impact masses and initial impact velocities on the dynamic responses. Some basic results have been obtained in these research studies, and the impact force is the main analysis content of the dynamic response. The impact force versus displacement curves are always analyzed to obtain the energy absorption of

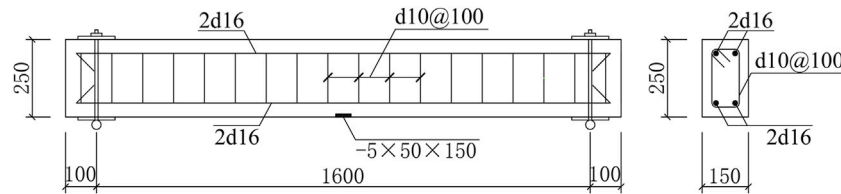


FIGURE 1 | Specimen dimensions and reinforcement layout of the beam (mm).

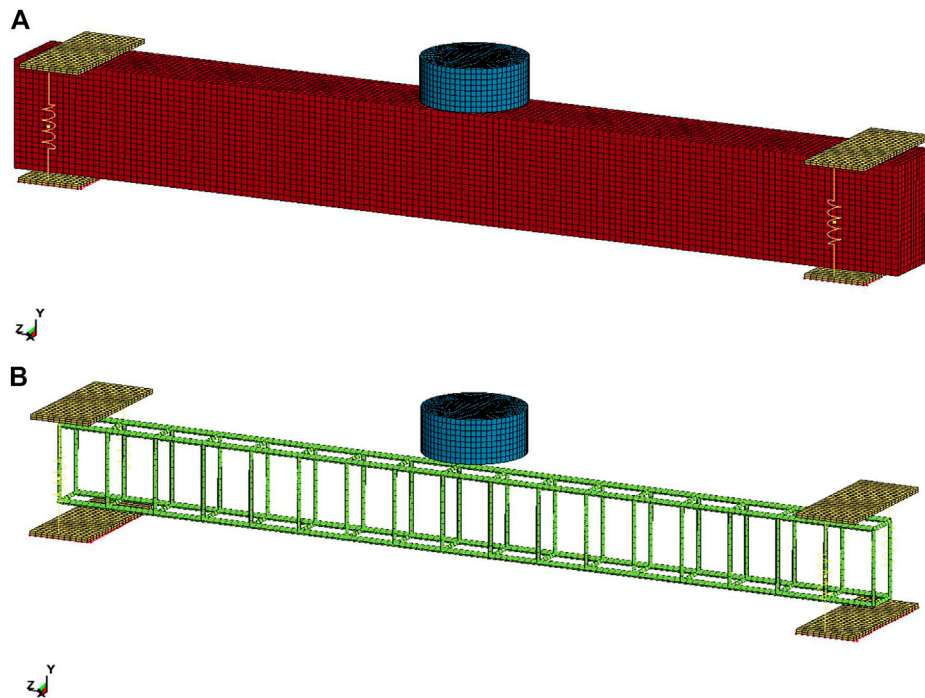


FIGURE 2 | 3-D numerical model of RC beam.

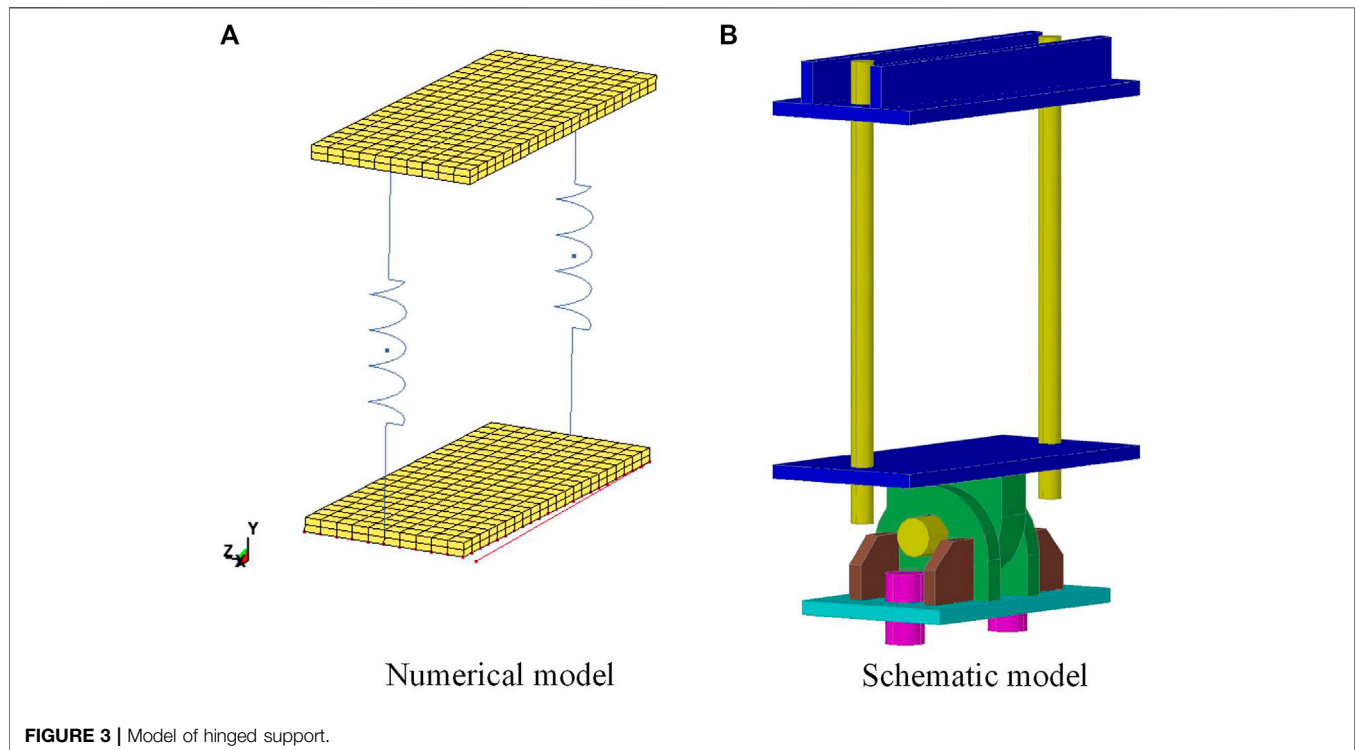
the RC members, and the peak impact force or the peak reaction force caused by the impact force is considered as the bearing capacity for the impact design of RC beams. However, these views would not be appropriate for RC members under impact. Ohnuma (1987) found that the peak impact force is considerably larger than the ultimate static bearing capacity of RC beams. From this result, we may deduce that the cross section would be unusually large if the impact force is taken as the design value. The reason may be that the inertial effect on the RC beam is significant, and a large portion of the impact force is applied to accelerate the beam and overcome the inertial force (Guo et al., 2017). In addition, the drop hammer test on 10 RC beams conducted by Soleimani et al. (2007) showed a time lag between the peak impact force and the peak support reaction, which means the force-based structural impact design is not suitable, and the peak impact force or the peak reaction force may not be directly used as the bearing capacity for the impact design of RC beams. Comparatively, a displacement-based design could be suitable for the impact design. Furthermore, the existing

studies almost consider the effects of impact mass and impact velocity on dynamic responses of RC beams independently. Therefore, it is of great significance to further analyze the impact responses of RC beams under the interaction of impact mass and impact velocity. A more reasonable failure criterion of the RC beam under impact is necessary, instead of the bearing force.

A displacement-based design is an effective design method, especially when the structure has large deformation. In this study, the displacement response of RC beams under impact, which provides a theoretical basis for the displacement-based structural impact design, is mainly analyzed under the interaction of impact mass and impact velocity. In order to achieve it, a numerical model is developed by the finite element package LS-DYNA. The numerical model is calibrated with the testing results of the drop hammer impact on the RC beam specimen. Using the calibrated numerical model, the midspan displacement of RC beams under equal impulse or equal impact energy, in which the impact condition, the impact mass, and impact velocity are varied

TABLE 1 | Material parameters for concrete.

ρ	IRATE	ERODE	RECOV	PRED	G	K	α	θ	λ	β
2.4×10^{-9}	1	1.05	0	0	1.196×10^4	1.595×10^4	15.32	0.321	10.5	1.929×10^{-2}
α_1	θ_1	λ_1	β_1	α_2	θ_2	λ_2	β_2	R	X_0	W
7.474×10^{-1}	9.443×10^{-4}	1.700×10^{-1}	6.213×10^{-2}	0.66	1.126×10^{-3}	0.16	6.213×10^{-2}	5	94.65	0.05
D_1	D_2	B	G_{fc}	D	G_{ft}	G_{fs}	pwrc	pwrt	pmod	η_{oc}
2.500×10^{-4}	3.490×10^{-7}	1.00×10^2	7.895	0.1	0.07895	0.07895	5	1	0	1.338×10^{-6}
N_c	η_{ot}	N_t	overc	overt	Srate	repow				
-0.763	0	0.48	25.02	25.02	1	1				

**FIGURE 3** | Model of hinged support.

simultaneously, is analyzed. In addition, the failure of RC beam is judged according to the deformation criterion.

2 BRIEF OF TEST

In the drop hammer impact test on the RC beam conducted by the authors, the beam specimen had 1,800 mm length, with a cross section of 250 mm in depth and 150 mm in width. As shown in **Figure 1**, the longitudinal reinforcements at both top and bottom sides were 16 mm, with the yield strength of 430 MPa and the ultimate strength of 578 MPa. The thickness of the longitudinal reinforcement protection layer was 35 mm, and the reinforcement ratio was 1.25%. The 10-mm bars spaced at 100 mm apart with the yield strength of 407 MPa and the ultimate strength of 594 MPa were used as stirrups. The stirrup reinforcement ratio was 1.05%. To avoid the measurement error caused by the concrete spalling, a flat steel plate with a size of $5 \times 50 \times 150$ was welded on the steel cage

at the bottom of the midspan to measure the displacement response. The hinge supports were arranged at both ends of the beam. Each support was composed of an upper cover plate, a lower bottom plate, and two pull rods between them, and the beam was clamped between the upper and lower plates. The beam specimen was impacted at the midspan by the impact mass, m , of 400 kg and the impact velocity, v , of 6 m/s.

3 NUMERICAL MODEL

3.1 Geometric and Element

A 3D numerical model of the RC beam is developed by the finite element package LS-DYNA to simulate the drop hammer impact test. To save the calculation cost, only half of the midspan symmetry specimen is established, and the span displacement of the node on the symmetric plane is constrained. As shown in **Figure 2**, the model is mirrored by the midspan plane.

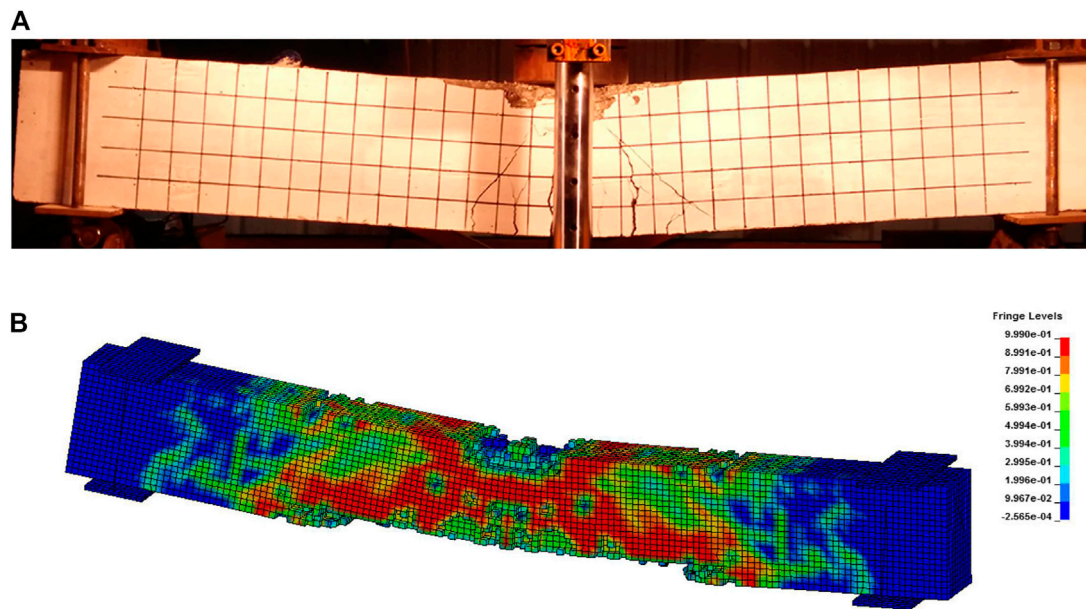


FIGURE 4 | Damage patterns of the beam.

The model consists of concrete, a reinforcement cage, a hinged support, and a drop hammer. The concrete is discretized into eight-node solid elements with one-point Gauss integration and viscous hourglass control. The longitudinal and transverse reinforcement bars are discretized into truss elements. The perfect bond between reinforcement and adjacent concrete is assumed, and common nodes are defined between the reinforcement elements and the concrete elements. Because of their small thickness, the upper and lower plates of the hinged supports are discretized into eight-node solid elements with complete integration to avoid the hourglass model. The pull rods are modeled by two-node discrete spring elements. The drop hammer is simplified and modeled as a cylinder, and the eight-node constant stress solid element is used to model it.

3.2 Material Model

3.2.1 Concrete

The material model plays an essential role when undertaking non-linear finite element analysis. A number of material models available in LS-DYNA can be used to model the behavior of the concrete material, of which the continuous surface cap model is commonly used in the analysis of concrete structures under low-speed impact. Both elastic deformation and failure of concrete used in structures when involved in a collision with an impactor have been implemented into the CSCM model (Murry, 2007). In this study, the CSCM model with a strain rate effect is used to predict the concrete performance. The dynamic compressive strength f_d can be expressed as follows:

$$f_d = f_s + E\eta_0\dot{\epsilon}^{(1-n)}, \quad (1)$$

where f_s is the unconfined static compression strength, E is the elastic modulus, $\dot{\epsilon}$ is the strain rate, and η_0 and n are the strain rate effect parameters, which are specified by the SHPB test.

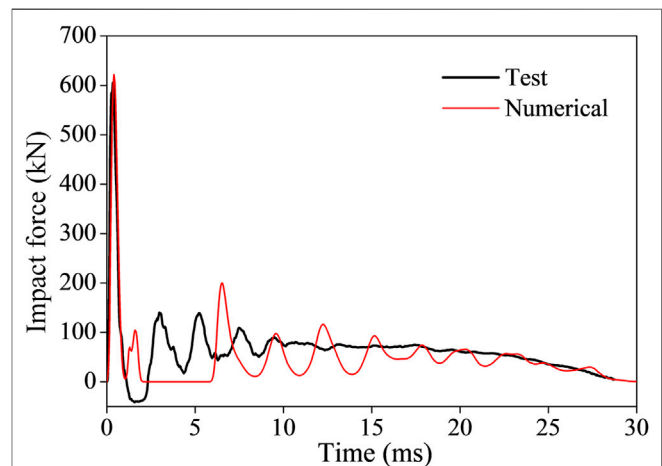


FIGURE 5 | Time history curves of impact force.

In the previous equation,

$$E = 4700\sqrt{f_s} \quad (2)$$

Ductile damage, $d(\tau_c)$, and brittle damage, $d(\tau_t)$, are introduced into the CSCM model to simulate the damage of a concrete element. Ductile damage accumulates when the pressure is compressive, which is defined as follows:

$$d(\tau_c) = \frac{d_{\max}}{B} \left[\frac{1+B}{1+B \cdot \exp[-A(\tau_c - \tau_{0c})]} - 1 \right], \quad (3)$$

where the parameters A and B set the shape of the softening curve plotted as stress–displacement or stress–strain, d_{\max} is the

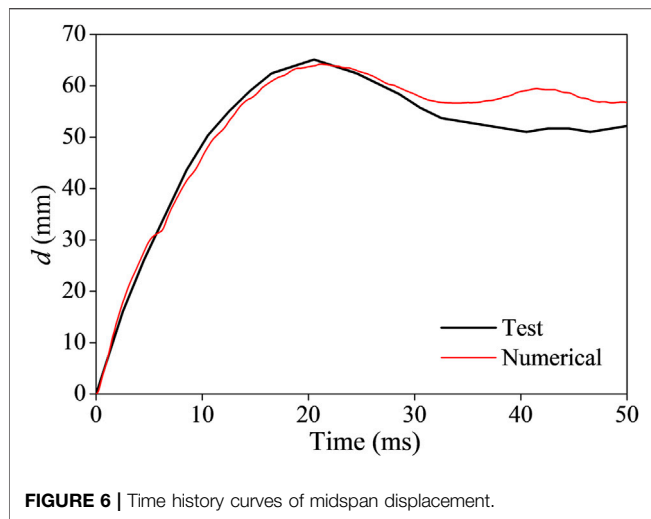


FIGURE 6 | Time history curves of midspan displacement.

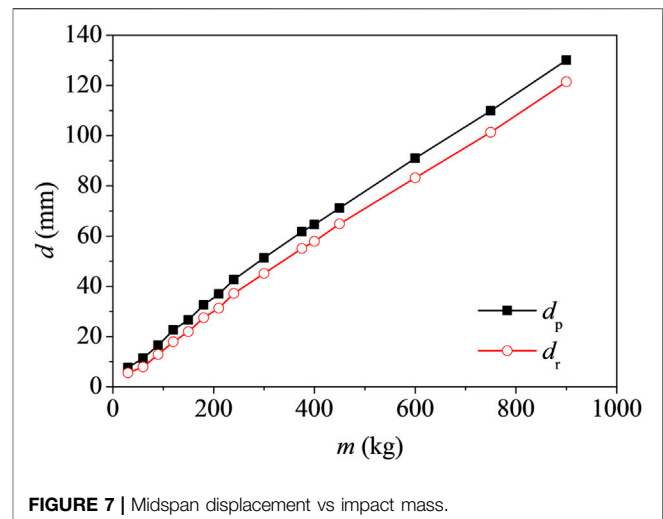


FIGURE 7 | Midspan displacement vs impact mass.

TABLE 2 | Comparison of dynamic responses.

	Test	Numerical	Error (%)
F_d (kN)	605.5	621.8	2.7
d_p (mm)	65.1	64.2	-1.4
d_r (mm)	54.4	57.9	6.4

maximum damage level, and τ_c is an energy-type term, which is defined as follows:

$$\tau_c = \sqrt{\frac{1}{2} \sigma_{ij} \varepsilon_{ij}}, \quad (4)$$

where σ_{ij} and ε_{ij} are the elasto-plastic stresses and strain. Ductile damage initiates when τ_d exceeds the initial threshold τ_{0c} .

Brittle damage accumulates when the pressure is tensile, which is defined as follows:

$$d(\tau_t) = \frac{0.999}{D} \left[\frac{1 + D}{1 + D \cdot \exp[-C(\tau_t - \tau_{0t})]} - 1 \right], \quad (5)$$

where the parameters C and D set the shape of the softening curve; energy-type term τ_t accumulation depends on the maximum principal strain, ε_{\max} , as follows:

$$\tau_t = \sqrt{E \varepsilon_{\max}^2} \quad (6)$$

The concrete element erodes when the damage parameter $d > 0.99$, which means it loses all its strength and stiffness. The detailed parameters of the CSCM model are shown in Table 1.

3.2.2 Reinforcement

The elastic-plastic model with kinematic hardening is employed for the reinforcement. The plastic hardening modulus is assumed as 1% of the elastic modulus, which is 2.1×10^5 MPa. The Poisson ratio is 0.3. The strain rate effect is taken into account by using the Cowper-Symonds model with the parameters given as $C = 40$ and

$p = 5$ (Cowper and Symonds, 1957). Thus, the yield stress of reinforcement can be expressed as follows:

$$\sigma_y = \left[1 + \left(\frac{\dot{\varepsilon}}{C} \right)^{\frac{1}{p}} \right] \sigma_0, \quad (7)$$

where σ_0 is the initial yield stress and $\dot{\varepsilon}$ is the strain rate.

The strain failure criterion is adopted to simulate the failure of reinforcement elements. It means the reinforcement element erodes when it exceeds the strain threshold value, ε_f , which is taken as 0.1 according to the percentage elongation of this material.

3.2.3 Hinged Support and Drop Hammer

The elastic model with elastic modulus 2.1×10^5 MPa is employed for the upper and lower plates of hinged support. The elastic spring model is employed for the pull rod between the upper and lower plates. Based on the geometry dimension of the pull rod with 18 mm in the cross-sectional diameter and 250 mm in length, the elastic stiffness of the spring is taken as follows:

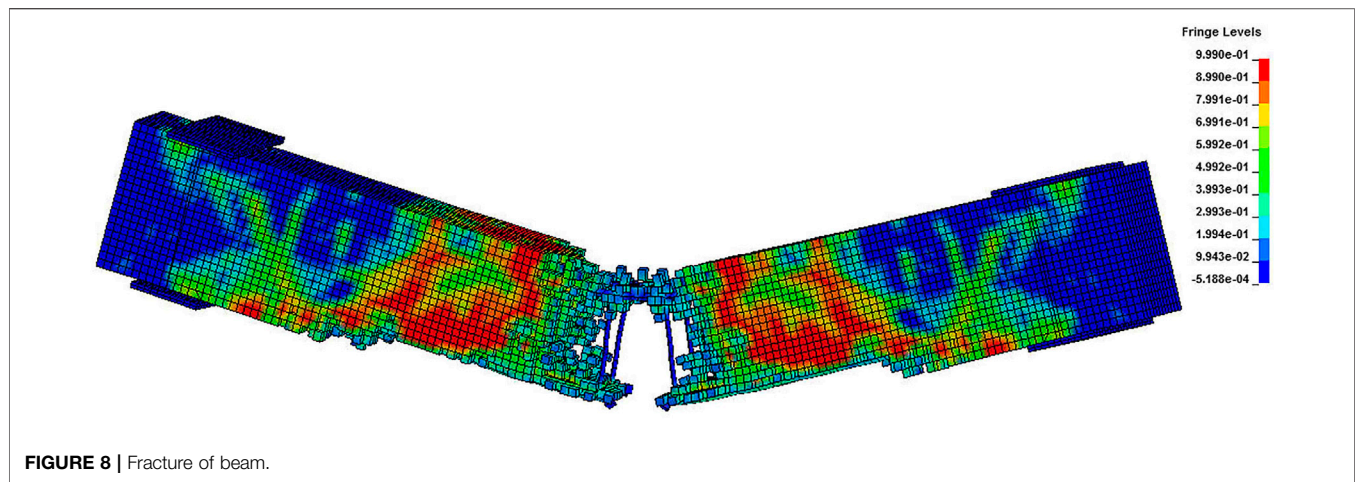
$$k = \frac{1}{250} \times 2.1 \times 10^5 \times \frac{\pi}{4} \times 18^2 = 213754 \text{ (N/mm)}. \quad (8)$$

The drop hammer is assumed as a rigid body due to its much higher stiffness than the beam specimen, and the total mass of the drop hammer is 400 kg by controlling its density in the numerical simulation.

3.3 Constraint and Boundary Condition

Considering the form of hinged support, all the nodes at the bottom of the lower plate are bound to the point 45 mm directly below the bottom side by using a NODAL_RIGID_BODY constraint. The point is located at the midpoint of the central axis of the bolt passing through the ear plate, as shown in Figure 3.

The automatic surface-to-surface contact with the default setting of the parameters, based on the penalty method, is employed to simulate the contacts between the beam specimen



and the cover plates of the hinged support, and between the drop hammer and the beam specimen. The beam is defined as a slave segment, and the cover plates and the drop hammer are defined as a master segment, respectively. No friction is assumed in the contact between the slave and master segments. The impact velocity of the drop hammer is taken as 6 m/s, and the initial distance between the drop hammer and the top surface of the beams is set as 10 mm to save computational cost. The hourglass mode is controlled by the Flanagan–Belytschko stiffness form.

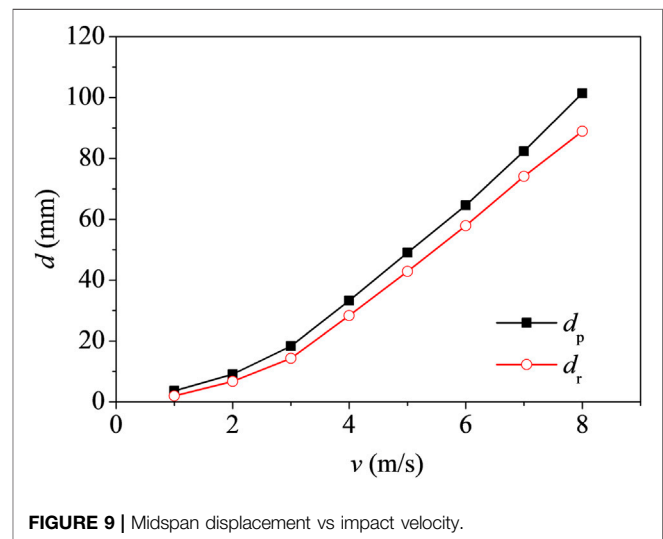
3.4 Mesh Convergence

The explicit integration method based on the central difference method is used to solve the motion equation of the structure. Considering the central difference method is conditionally stable, the time step should be smaller than the critical step, and the critical step of the model is as follows:

$$\Delta t = l/C, \quad (9)$$

where C is the stress wave velocity of the element, which depends on the material properties of the element, and l is the geometric size of the element, that is, the minimum height for the 8-node element and the length for the two-node element. It can be seen that if the model mesh is too fine and the value of l is small, the model critical step length Δt will be reduced, thereby increasing the computational cost. If the mesh of the model is too thick, it may cause the model stiffness to be too large, and the simulation result would be seriously inconsistent with the actual.

For the beam specimen, a mesh convergence test is carried out by reducing the mesh size. Three element sizes of 25 mm, 12.5 mm, and 10 mm are used in the main region of the concrete and reinforcement. The mesh convergence test results are listed as 56.5, 64.2, and 64.2 mm of the peak midspan displacement, correspondingly. It can be found that the results of midspan displacement for element sizes of 12.5 and 10 mm are quite close. Furthermore, element refinement will not improve the accuracy significantly, while the computational efficiency will largely decrease. Therefore, the optimum element size of 12.5 mm is adopted as the main element size in this study. In total, the total



semi-structural model consists of 21,232 solid elements, 632 truss elements, and two discrete spring elements.

3.5 Verification

To verify the numerical model, the damage pattern of the beam specimen under the drop hammer test is compared with the numerical result. The test result is shown in **Figure 4A**. The cracks of the beam are concentrated in the middle of the span, and the bending cracks in the middle of the span are well developed and close to the top of the beam. Obvious shear cracks are developed near the center of the span, and a local concrete crushing occurs on the upper surface of the beam, which is in contact with the drop hammer. The simulation failure mode is shown in **Figure 4B**. The numerical contour plots are indicated by the damage level ranging from 0 to 1. Flexural failure for the specimen is observed, and the eroded concrete element is mainly concentrated in the midspan of the beam, and results in vertical and oblique cracks at the bottom of the beam and local damage at the top. The numerical model can

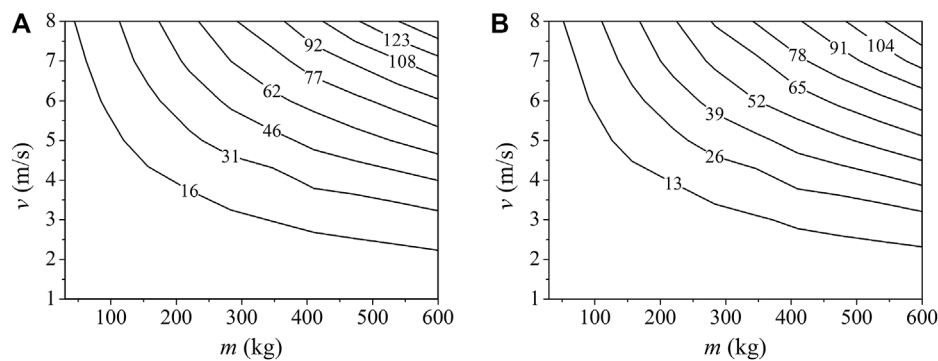


FIGURE 10 | Response surface of midspan displacement: **(A)** Peak value d_p ; **(B)** Residual value d_r .

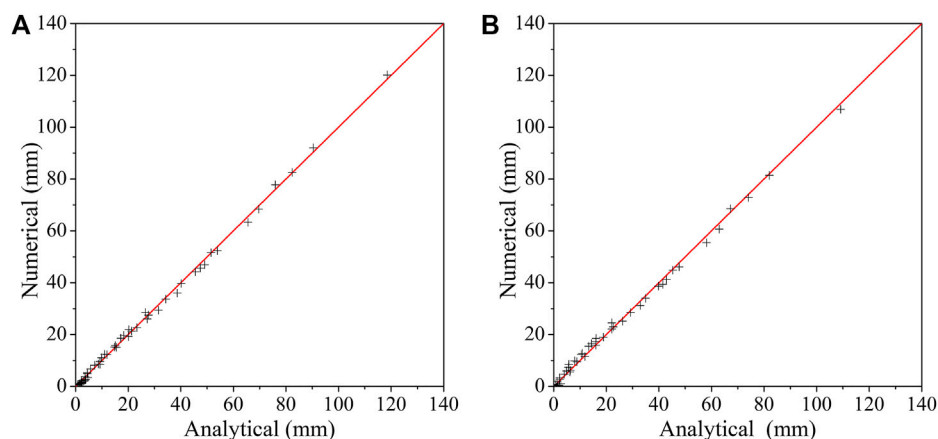


FIGURE 11 | Comparison of analytical and numerical simulation: **(A)** Peak value d_p ; **(B)** Residual value d_r .

simulate the damage pattern of the beam under impact accurately.

Figures 5, 6 present the comparisons between the numerical and the test results in terms of the impact force and the midspan displacement curves of the specimen. As shown in Figure 5, the peak impact force, F_d , and its duration time are simulated with accuracy. When the contact takes place, the drop hammer penetrates the beam immediately and causes the peak impact force. Following the peak impulse, the curve vibrates around the plateau value. This phenomenon may be attributed to the interaction between the drop hammer and the beam. Then, the beam deflects downward and tends to depart from the drop hammer; hence, the interaction between the two components decreases, and the impact force descends simultaneously. As shown in Figure 6, the curve of midspan displacement rises to the peak value, d_p , when the contact takes place, and then turns to descend to a residual value, d_r . As shown in Table 2, the results of dynamic responses between the test and the numerical simulation agree quite well.

Comparing the damage pattern, impact force, and midspan displacement response obtained from the test and numerical simulation, it is found that the numerical model in this study

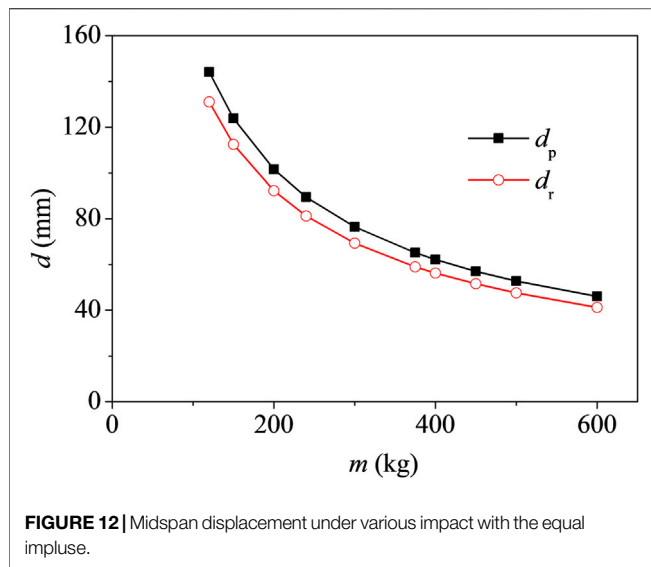
can provide an accurate simulation of impact responses of the RC beam.

4 DISPLACEMENT ANALYSIS

4.1 Response Surface of Midspan Displacement

Using the verified numerical model, the midspan displacement of the RC beam under the same impact velocity $v = 6$ m/s and different impact masses m is analyzed. The results are shown in Figure 7. It can be seen that the peak midspan displacement of the RC beam increases with the impact mass in a certain range. Beyond the range, the beam fractures are as shown in Figure 8. The residual displacement d_r also increases with the impact mass, and the value of d_r is relatively lower than d_p .

The midspan displacement of the RC beam under the same impact mass $m = 400$ kg and different impact velocities v is analyzed. The results are shown in Figure 9. It can be seen that similar to the variation law reflected in Figure 7, the peak and residual midspan displacements of the RC beam increase with the impact velocity in a certain range. Beyond the range, the beam fractures.



Based on the previous analysis, it can be concluded that both the impact mass and the impact velocity have effects on the midspan displacement of the RC beam. To investigate the integrated effects, the midspan displacement of the RC beam under the impact mass and impact velocity varies at the same time. The results are shown in **Figure 10**.

The power function is used to fit the response surface of midspan displacement, as shown in **Figure 10**. Thus, d_p and d_r can be expressed as **Eq. 10** and **Eq. 11**, in which the dimension is mm for d_p and d_r , and is kg and m/s for m and v , respectively. As shown in **Figure 11**, the analytical solution results of **Eq. 10** and **Eq. 11** are compared with the numerical results with the correlation coefficient R is 0.997 and 0.999, respectively. Therefore, it can be concluded that the impact mass and the impact velocity have integrated effects on the midspan displacement of the RC beam, and the response surface of the midspan displacement can be fitted as the binary power function of impact mass and impact velocity.

$$d_p(m, v) = 0.29 - 0.0043m^{0.94} - 0.043v^{1.65} + 0.012m^{0.94} \cdot v^{1.65} \quad (10)$$

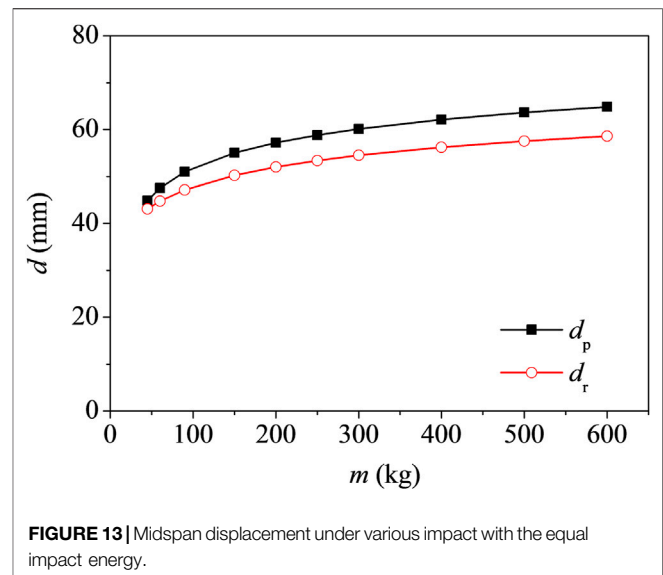
$$d_r(m, v) = -0.97 - 0.0074m^{0.93} - 0.00045v^{1.60} + 0.012m^{0.93} \cdot v^{1.60}, \quad (11)$$

where the units of m , v , and d are kg, m/s, and mm, respectively.

With the change in the RC beam parameters, such as the dimensions, the strengths of the reinforced bar and concrete, and the reinforcement ratio, the impact response surface of midspan displacement would be fitted as binary power functions with other constants.

4.2 Impact Analysis Under Equal Impulse or Equal Impact Energy

The point on the response surface shown in **Figure 10** represents the midspan displacement of the RC beam under various impact



mass and impact velocity combinations, and the isoline represents various impact combinations with the same midspan displacement response.

In the drop hammer test mentioned earlier, the RC beam specimen is subjected to the impact with the impulse $p = mv = 400 \times 6 = 2400$ N/s. The peak and residual displacement of the RC beam under various impact combinations with the equal impulse, 2,400 N/s, are analyzed within the scope of low-speed impact, in which the velocity is no more than 20 m/s. The value scope is on the basis of the impact accident occurring in structural engineering (Perry and Burns, 1965; Mainstone, 1966; Struck and Voggenreiter, 1975). From the analysis results shown in **Figure 12**, it can be seen that the midspan displacement response of the RC beam is different under various impact combinations, and it decreases with an increase in the impact mass under an equal impulse.

In the test, the RC beam specimen is subjected to the impact with the impact energy $E = 1/2mv^2 = 1/2 \times 400 \times 6^2 = 7,200$ J. The peak and residual displacement of the RC beam under various impact combinations with the equal impact energy, 7,200 J, are analyzed within the scope of a low-speed impact, and the results are shown in **Figure 13**. From the figure, it can be seen that the midspan displacement response of the RC beam increases with an increase in the impact mass under an equal impact energy.

From the aforementioned analysis, it can be concluded that the impulse or impact energy could not be used as an independent indicator of the impact.

4.3 Impact Failure

The deformation criterion can well reflect the main failure reason of the RC element in the non-linear stage, and it can concisely reflect the failure degree of the element (Moehle, 1992; Kowalsky et al., 1995; Chopra and Goel, 2001). Therefore, the deformation criterion is suggested to be used to judge the impact failure of the RC beam.

The deformation criterion takes the deformation exceeding the threshold value of the element as the criterion of failure and is usually expressed in the form of ductility coefficient μ as follows:

$$\mu \geq [\mu], \quad (12)$$

where $[\mu]$ is the threshold value of ductility coefficient, and μ can be expressed as follows:

$$\mu = d/d_y, \quad (13)$$

where d is the displacement of the RC beam and d_y is the yield one.

According to the section analysis, the yield displacement of the RC beam in the drop hammer test is 5 mm, and the residual displacement is $d_r = 54.4$ mm under the impact with the impact mass of 400 kg and the impact velocity 6 m/s. It is suggested that the threshold ductility coefficient, $[\mu]$, of the bending element in the protective structure under the chemical explosion should not exceed 10 referring to the literature (Tsinghua University, 1982). Thus, the RC beam failures under the impact based on the ductility coefficient $\mu = d_r/d_y = 54.4/5 = 10.88 \geq [\mu]$.

However, considering that the importance of common civil engineering structures is lower than the protective structures and that the adverse social effects caused by the soft impact are also relatively lower than those caused by the chemical explosion, the threshold value of ductility coefficient is set as 15 in this research. Thus, it can be concluded that the RC beam can resist the impact based on the ductility coefficient $\mu = 10.88 \leq [\mu]$. Compared to the literature (Tsinghua University, 1982), the threshold value used in this research would be more applicable for the RC beam because of the general integrity of the beam shown in **Figure 4**. Based on $[\mu] = 15$, the maximum allowable residual midspan displacement of the beam specimen in this study can be calculated as 75 mm. The beam specimen does not fracture and can resist the impact within the scope of a low-speed impact, while the larger residual midspan displacement would mean the beam fracture.

5 CONCLUSION

This study presents a numerical model to simulate the impact responses of the RC beam. The numerical model is calibrated using the drop hammer test on the RC beam specimen. Using the verified numerical model, the displacement response of the RC beam is

analyzed by considering the incorporation of the impact mass and impact velocity, and the impact failure of the RC beam is judged by the deformation criterion. The results are summarized as follows.

- 1) The impact mass and the impact velocity have integrated effects on the midspan displacement of the RC beam, and the response surface of the midspan displacement can be fitted as a binary power function of impact mass and impact velocity.
- 2) The midspan displacement response of the RC beam is different under various impact combinations with equal impulse, and it decreases with an increase in the impact mass, while it increases with an increase in the impact mass under various impact combinations with equal impact energy. The impulse or impact energy could not be used as an independent indicator of the impact.
- 3) The deformation criterion is recommended to be used to judge the impact failure of the RC beam, and the threshold value of the ductility coefficient is suggested to set as 15 in the impact-resistant design for RC beams in civil engineering structures within the scope of a low-speed impact.

DATA AVAILABILITY STATEMENT

The original contributions presented in the study are included in the article/Supplementary Material, further inquiries can be directed to the corresponding author.

AUTHOR CONTRIBUTIONS

JG performed the test and the data analyses and wrote the manuscript. GJ contributed to the data analyses. ZW contributed significantly to manuscript preparation. AH helped to perform the analysis with constructive discussions. JC contributed to the conception of the study.

ACKNOWLEDGMENTS

The authors would like to acknowledge Fujian Province Natural Sciences (2019J01885 and 2019J01884), and the Fujian Jiangxia University Scientific Foundation (JXZ2019003) for financial support to carry out this study.

REFERENCES

- Cai, J., Ye, J., Wang, Y., and Chen, Q. (2017). Numerical Study on Dynamic Response of Reinforced concrete Columns under Low-Speed Horizontal Impact Loading. *Proced. Eng.* 210, 334–340. doi:10.1016/j.proeng.2017.11.085
- Chopra, A. K., and Goel, R. K. (2001). Direct Displacement-Based Design: Use of Inelastic vs. Elastic Design Spectra. *Earthquake Spectra* 17, 47–64. doi:10.1193/1.1586166
- Cowper, G. R., and Symonds, P. S. (1957). *Strain-hardening and Strain-Rate Effects in the Impact Loading of Cantilever Beams*. Providence: Brown University.
- Fujikake, K., Li, B., and Soeun, S. (2009). Impact Response of Reinforced concrete Beam and its Analytical Evaluation. *J. Struct. Eng.* 135, 938–950. doi:10.1061/(asce)st.1943-541x.0000039
- Guo, J., Cai, J., and Chen, W. (2017). Inertial Effect on RC Beam Subjected to Impact Loads. *Int. J. Str. Stab. Dyn.* 17, 1750053. doi:10.1142/s0219455417500535
- He, Q. F., Li, J., Yue, L. Y., and Mao, J. W. (2020). Numerical Simulation on Impact Test of CFRP Strengthened Reinforced Concrete Beams. *Front. Mater.* 7, 252. doi:10.3389/fmats.2020.00252
- Kowalsky, M. J., Priestley, M. J. N., and Macrae, G. A. (1995). Displacement-based Design of RC Bridge Columns in Seismic Regions. *Earthquake Engng. Struct. Dyn.* 24, 1623–1643. doi:10.1002/eqe.4290241206

- Mainstone, R. (1966). Structural Tests on an Experimental Helicopter Platform. *Proc. Inst. Civil Eng.* 33, 65–91. doi:10.1680/iicep.1966.8959
- Moehle, J. P. (1992). Displacement-based Design of RC Structures Subjected to Earthquakes. *Earthquake spectra* 8, 403–428. doi:10.1193/1.1585688
- Murray, Y. D. (2007). Users Manual for LS-DYNA concrete Material Model 159. Available at: <https://www.fhwa.dot.gov/publications/research/infrastructure/pavements/05062/index.cfm> (Accessed 27.2.2022).
- Ohnuma, H. (1987). *Dynamic Response and Local Rupture of Reinforced concrete Beam and Slab under Impact Loading*. Tokyo: Transactions of the Japan Concrete Institute.
- Perry, E. S., and Burns, N. H. (1965). Simple Set up for Applying Impact Loads. *Mater. Res. Stand.* 5, 515–516.
- Saleh, Z., Sheikh, M. N., Remennikov, A. M., and Basu, A. (2019). Numerical Analysis of Behavior of Glass Fiber-Reinforced Polymer Bar-Reinforced concrete Beams under Impact Loads. *ACI Struct. J.* 116, 151–160. doi:10.14359/51715658
- Sha, Y., and Hao, H. (2013). Laboratory Tests and Numerical Simulations of Barge Impact on Circular Reinforced concrete Piers. *Eng. structures* 46, 593–605. doi:10.1016/j.engstruct.2012.09.002
- Soleimani, S. M., Banthia, N., and Mindess, S. (2007). *Behavior of RC Beams under Impact Loading: Some New Findings*. London: Taylor & Francis.
- Struck, W., and Voggenteiter, W. (1975). Examples of Impact and Impulsive Loading in the Field of Civil Engineering. *Mat. Constr.* 8, 81–87. doi:10.1007/bf02476326
- Tachibana, S., Masuya, H., and Nakamura, S. (2010). Performance Based Design of Reinforced concrete Beams under Impact. *Nat. Hazards Earth Syst. Sci.* 10, 1069–1078. doi:10.5194/nhess-10-1069-2010
- Tran, D. T., Pham, T. M., Hao, H., and Chen, W. (2021). Numerical Study on Bending Response of Precast Segmental concrete Beams Externally Prestressed with FRP Tendons. *Eng. Structures* 241, 112423. doi:10.1016/j.engstruct.2021.112423
- Tsinghua University (1982). *Underground Protective Structure*. Beijing: China Architecture and Building Press.
- Xu, B., and Zeng, X. (2014). Experimental Study on the Behaviors of Reinforced concrete Beams under Impact Loadings. *China Civil Eng. J.* 47, 41–51. doi:10.15951/j.tmgcxb.2014.02.010
- Ye, J.-B., Cai, J., Liu, X., Chen, Q.-J., Zuo, Z.-L., and He, B.-Q. (2021). Experimental Investigation of Inclined RC Pile Groups under Horizontal Static and Impact Loads. *Eng. Structures* 233, 111846. doi:10.1016/j.engstruct.2020.111846
- Zeng, X., and Xu, B. (2012). Experimental Study on the Impact-Resistant Behavior of RC Beams without Shear-Resistant Rebar. *China Civil Eng. J.* 45, 63–73. doi:10.15951/j.tmgcxb.2012.09.022
- Zhao, D. B., Yi, W. J., and Kunnath, S. K. (2017). Shear Mechanisms in Reinforced concrete Beams under Impact Loading. *J. Struct. Eng.* 9, 04017089. doi:10.1061/(ASCE)ST.1943-541X.0001818

Conflict of Interest: The authors declare that the research was conducted in the absence of any commercial or financial relationships that could be construed as a potential conflict of interest.

Publisher's Note: All claims expressed in this article are solely those of the authors and do not necessarily represent those of their affiliated organizations, or those of the publisher, the editors, and the reviewers. Any product that may be evaluated in this article, or claim that may be made by its manufacturer, is not guaranteed or endorsed by the publisher.

Copyright © 2022 Guo, Jiang, Wu, He and Cai. This is an open-access article distributed under the terms of the Creative Commons Attribution License (CC BY). The use, distribution or reproduction in other forums is permitted, provided the original author(s) and the copyright owner(s) are credited and that the original publication in this journal is cited, in accordance with accepted academic practice. No use, distribution or reproduction is permitted which does not comply with these terms.



Experimental Study on Axial Compression Performance of Thin-Walled Steel Tube Lightweight Concrete Columns With Composite Section

Yue Li^{1*}, Yong Yan¹, Xue Meng¹, Kechao Zhang^{2,3*}, Xiaorun Li⁴ and Chongming Gao¹

¹School of Civil Engineering, North China University of Technology, Beijing, China, ²Research Institute of Highway Ministry of Transport, Beijing, China, ³School of Civil Engineering, Chongqing University, Chongqing, China, ⁴Central Research Institute of Building and Construction Co., Ltd., MCC Group, Beijing, China

OPEN ACCESS

Edited by:

Fangying Wang,
University of Nottingham,
United Kingdom

Reviewed by:

An He,
South China University of Technology,
China
Yong Zhu,
Harbin Institute of Technology, China
Luciano De Lima,
Rio de Janeiro State University, Brazil

*Correspondence:

Yue Li
liyue@ncut.edu.cn
Kechao Zhang
kechao.zhang@ctvic.cn

Specialty section:

This article was submitted to
Structural Materials,
a section of the journal
Frontiers in Materials

Received: 20 January 2022

Accepted: 18 February 2022

Published: 15 March 2022

Citation:

Li Y, Yan Y, Meng X, Zhang K, Li X and
Gao C (2022) Experimental Study on
Axial Compression Performance of
Thin-Walled Steel Tube Lightweight
Concrete Columns With
Composite Section.
Front. Mater. 9:858935.
doi: 10.3389/fmats.2022.858935

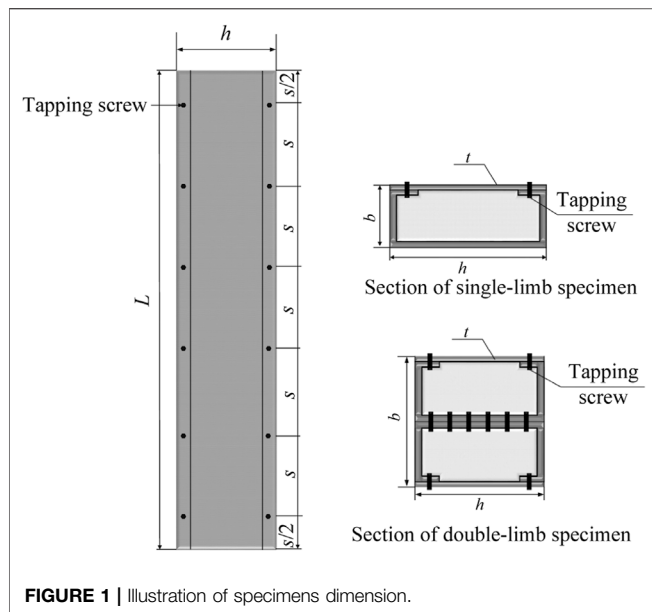
To provide references for the use of fabricated thin-walled cold-formed steel tubular lightweight concrete columns, the axial compression tests were conducted on single-limb and double-limb specimens. The results were compared with hollow specimens to analyze the effects of the cross-sectional size of the members, wall thickness, and steel ratio of the sections on the axial load-bearing capacity of the specimens. The test results show the following: 1) under the axial load, the typical damage of the specimens is local buckling of the steel tube and local crushing of the concrete. 2) The ultimate bearing capacity of the double-limb specimen is the highest. For the specimen with the sectional height-width ratio of 1.43, the ultimate bearing capacity of the double-limb specimen is 275.71% higher than that of the hollow steel tubular column and 241.49% that of single-limb specimens. 3) Based on the material superposition strength theory, the calculating method of the axial load-bearing capacity of thin-walled cold-formed steel tubular lightweight concrete columns was proposed and verified by comparing with the test results, which provides the design guidance for such members.

Keywords: thin-walled steel tube, lightweight concrete, composite section, axial compression performance, Experiment

1 INTRODUCTION

Compared with the traditional reinforced concrete structure, the fabricated thin-walled cold-formed steel tubular lightweight concrete columns have the advantages of high bearing capacity, ready construction, and good economic efficiency (Cai, 2003). The steel tube and concrete work together in the fabricated thin-walled cold-formed steel tubular lightweight concrete columns, which can effectively delay the buckling of the steel tube wall, enhance the ductility and load-bearing capacity of the members, and make the structures have good seismic performance. Therefore, the fabricated thin-walled cold-formed steel tubular lightweight concrete columns have been widely used in building and bridge engineering (Wright, 1993).

At present, the mechanical properties of thin-walled steel tube concrete columns have been studied to some extent. Ge and Usami (1992) conducted horizontal low cyclic load tests on thin-walled square steel tube concrete columns and hollow steel tubes to investigate the ultimate



bearing capacity and the deformation capacity of the thin-walled steel tube concrete structure. Mursi and Uy (2004) conducted experimental and numerical simulation studies on high-strength thin-walled steel tube concrete columns to investigate the main factors affecting the overall instability and local buckling of such members. Varma et al. (2004)

analyzed the effects of axial compression ratio and width-to-thickness ratio on the hysteretic properties of high-strength concrete columns with square steel tubes, and the results showed that the horizontal bearing capacity of the specimens decreased with the increase of axial compression ratio. Skalomenos et al. (2016) conducted horizontal load tests on circular thin-walled steel tube concrete columns and found that the yield strength of the steel had a significant effect on the ductility and horizontal bearing capacity of the specimens. Zhao et al. (2008) found that the steel tube had an obvious constraining effect on the core concrete and discussed the calculating conditions for the bearing capacity of concrete-filled cold-formed steel tubular columns by the axial compression formula of concrete-filled ordinary steel tubular columns. Li (2017) conducted the axial compression experiment of high-strength concrete-filled cold-formed steel tube columns and obtained the calculation formula of the bearing capacity. Islam et al. (2021) studied the effect of concrete strength, the width-to-thickness ratio, and the height-to-width ratio of the section on the bearing capacity and ductility of the cold-formed concrete-filled steel tubular columns. Zhang et al. (2005) analyzed the effect of concrete types on the load-bearing capacity of lightweight concrete steel tubular columns and found that the higher the concrete strength, the higher the load-bearing capacity of steel tube lightweight concrete columns. Chen (2007) found that the reinforcement ratio could improve the flexural performance of light aggregate

TABLE 1 | Main parameters of specimens.

Group	Specimen number	$b \times h \times t \times L$ (mm)	Yield stress f_y (MPa)	Steel elastic modulus E_s (MPa)	Concrete strength f_{cu} (MPa)	Concrete elastic modulus E_c (MPa)	h/b	Steel ratio (%)
Double-limb specimen	SR50-2.2	$100 \times 120 \times 2.2 \times 1,500$	390	206,000	16.7	19,100	1.20	13.9
	SR50-3.0	$100 \times 120 \times 3.0 \times 1,500$	390	206,000	16.7	19,100	1.20	19
	SR70-2.2	$140 \times 200 \times 2.2 \times 1,500$	390	206,000	16.7	19,100	1.43	9.1
	SR70-3.0	$140 \times 200 \times 3.0 \times 1,500$	390	206,000	16.7	19,100	1.43	12.4
Single-limb specimen	R50-2.2	$50 \times 120 \times 2.2 \times 1,500$	390	206,000	16.7	19,100	2.40	13.9
	R50-3.0	$50 \times 120 \times 3.0 \times 1,500$	390	206,000	16.7	19,100	2.40	19
	R70-2.2	$70 \times 200 \times 2.2 \times 1,500$	390	206,000	16.7	19,100	2.86	9.1
	R70-3.0	$70 \times 200 \times 3.0 \times 1,500$	390	206,000	16.7	19,100	2.86	12.4
Hollow specimen	R50-2.2-K	$50 \times 120 \times 2.2 \times 1,500$	390	206,000	—	—	2.40	—
	R50-3-K	$50 \times 120 \times 3.0 \times 1,500$	390	206,000	—	—	2.40	—
	R70-2.2-K	$70 \times 200 \times 2.2 \times 1,500$	390	206,000	—	—	2.86	—
	R70-3-K	$70 \times 200 \times 3.0 \times 1,500$	390	206,000	—	—	2.86	—

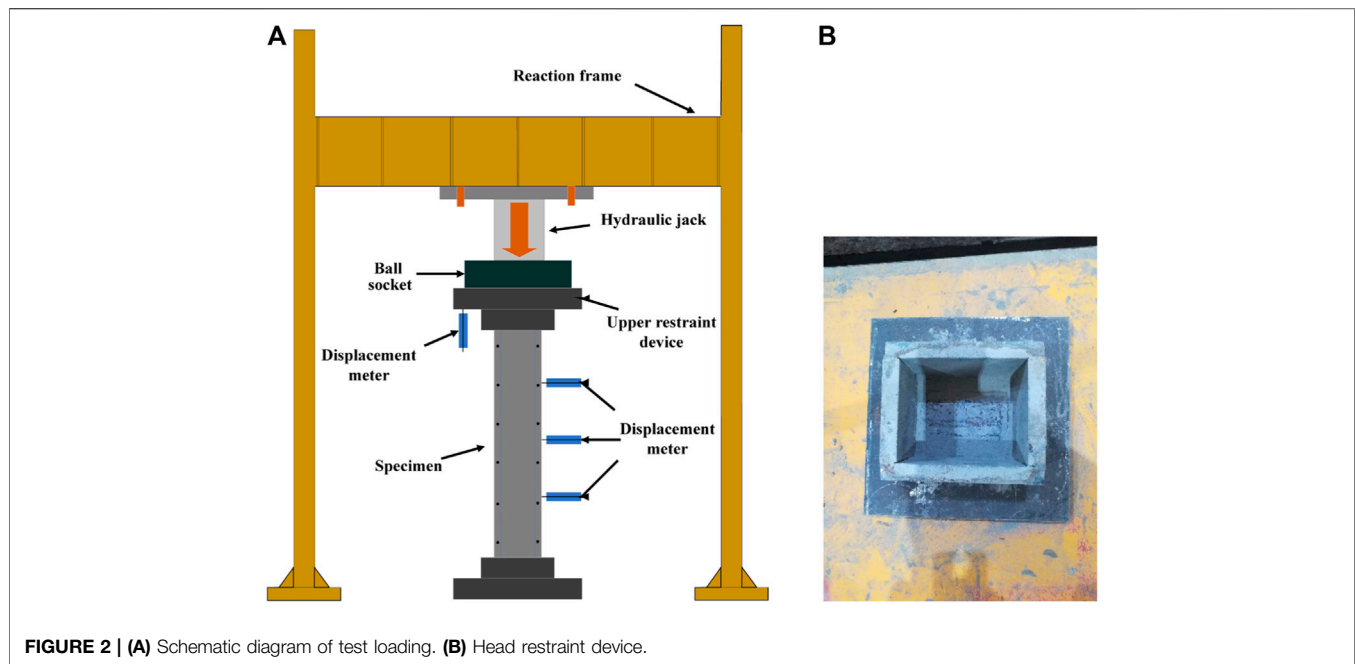


FIGURE 2 | (A) Schematic diagram of test loading. (B) Head restraint device.

concrete steel tubes. Li and Liu (2001) investigated the type of cross section on the constraint performance of the tube on the infilled concrete and found the round tube had the best performance.

The current research mostly focuses on steel tube concrete and thin-walled steel tube concrete structure members, while the research on the fabricated thin-walled cold-formed steel tubular lightweight concrete columns is not yet perfect, and the existing code lacks the relevant provisions for the design and calculation of such members. Therefore, the axial load test was carried out for the fabricated thin-walled cold-formed steel tubular lightweight concrete columns. The main factors affecting the bearing capacity of the members were analyzed, and the calculation method for the bearing capacity of the members was proposed, which would provide support for the application of such members.

2 DESIGN OF AXIAL COMPRESSIVE LOAD TEST

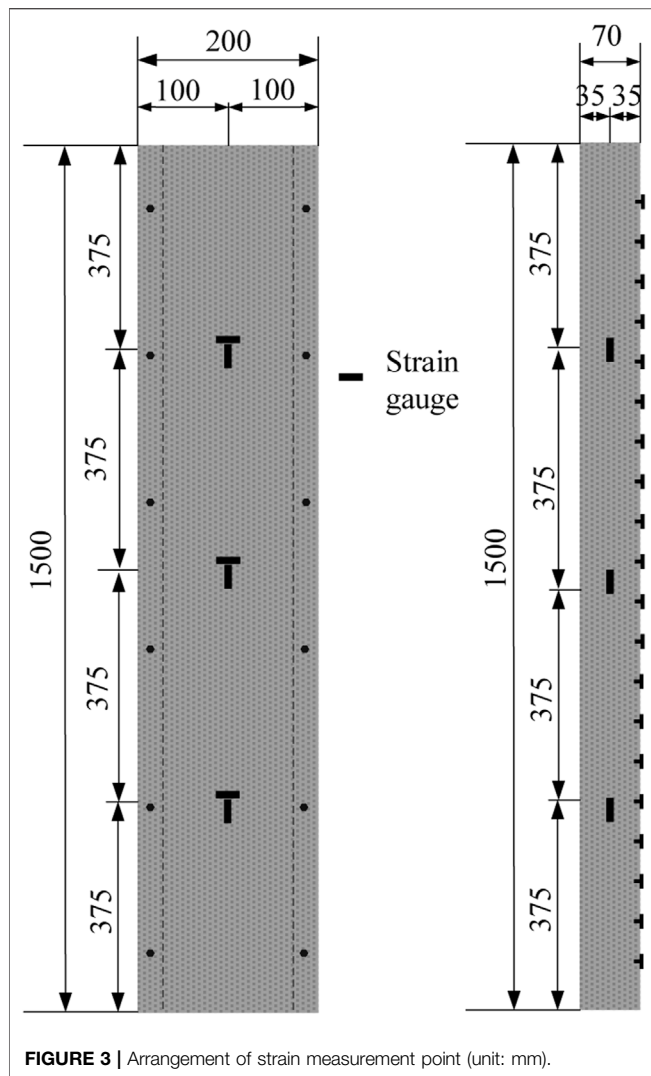
2.1 Specimen Design and Fabrication

According to the Chinese Technical Code GB50936 (Zha et al., 2014), the axial compressive load test of single-limb and double-limb specimens was designed and compared with the hollow specimens. The dimensions of the specimen are shown in Figure 1. The material characterization tests were performed in order to obtain the real mechanical properties of steel and concrete concerned in this work. The specimens were made of Q390 weathering steel with the yield stress f_y 390 MPa and the ultimate stress f_u 490 MPa, produced into C-shape by the plate bender. Then, the steel plate was connected to the C-shape steel with an ST4.8 tapping screw to form a closed tube. The coarse and

fine aggregates in the lightweight concrete were grade 900 spherical shale ceramic granules and expanded perlite granules, respectively, which were mixed with reference to the Chinese Technical Standard JGJ/T 12 (Ding et al., 2019). The concrete strength f_{cu} with 16.7 MPa was consistent with the C35 grade, which met the minimum concrete strength requirement of C30 in the Chinese Technical Code GB50936 (Zha et al., 2014). The steel ratio is the percentage of the steel area to the concrete area. The design parameters of the specimen are shown in Table 1.

2.2 Test Loading Scheme and Measurement Point Arrangement

The test was carried out on the electro-hydraulic servo testing machine. A pre-load 5 kN was imposed on the top of the specimen to eliminate tiny gaps between specimens and the loading machine firstly. After that, the displacement control model was used, and the loading rate was 0.5 mm/s during formal loading. In order to measure the axial compression deformation of the specimen and the deflection in the middle of the specimen, axial and transverse displacement gauges were arranged at the top and 1/2 height of the specimen, respectively. The test loading and displacement gauges were arranged as shown in Figure 2A. In order to ensure the uniform force at the end of the specimens and restrain the horizontal displacement, two customized head plates were installed at both ends, as shown in Figure 2B. The test was terminated when the load was reduced to 85% of the ultimate load or the specimen was seriously damaged. At the same time, strain gauges were arranged on the outer surface of the cold-formed thin-walled steel tube. The measurement points are shown in Figure 3.



3 ANALYSIS OF TEST RESULTS

3.1 Specimen Damage Phenomenon

Under the axial load, both the steel tube and the concrete of the specimens were subjected to axial pressure. As the load increases, the lateral deformation of the concrete increases continuously. Once the lateral deformation of the concrete exceeds that of the steel tube, the steel tube will constrain the core concrete, which will increase the transverse stress of the steel tube and the radial pressure of the concrete.

When the load was close to the ultimate bearing capacity of the single-limb specimen, the sealing steel plate buckled between the tapping screws at the upper end of the specimen. After reaching the ultimate load, the bearing capacity of the specimen dropped rapidly, the C-shape steel also bulged outward rapidly, and the test was terminated. In the bulging part of the specimen after being opened, it could be found that the concrete in the section was crushed, but the concrete on the center was not damaged. The rivets were not detached in the test. The damage phenomenon is shown in **Figure 4**.

For the double-limb column specimen, a small deformation of the sealing steel plate appeared first at the beginning of loading. When reaching the ultimate bearing capacity of the specimen, the bulging damage occurred at the top of the specimen. The steel plate was buckled outward and the rivets were pulled out. The damage of the specimen is shown in **Figure 5**.

The hollow specimen in the early loading stage had no obvious damage until close to the ultimate bearing capacity; the upper of the steel tube near the end caused rapid inward buckling. The test was terminated, and the rivets were not pulled out during the loading. The damage of the specimen is shown in **Figure 6**.

3.2 Load-Strain Curves of Specimens

Figure 7 shows the load-strain curves in the middle of specimens. At the beginning of loading, the specimens were uniformly compressed, and the strains increased simultaneously in the

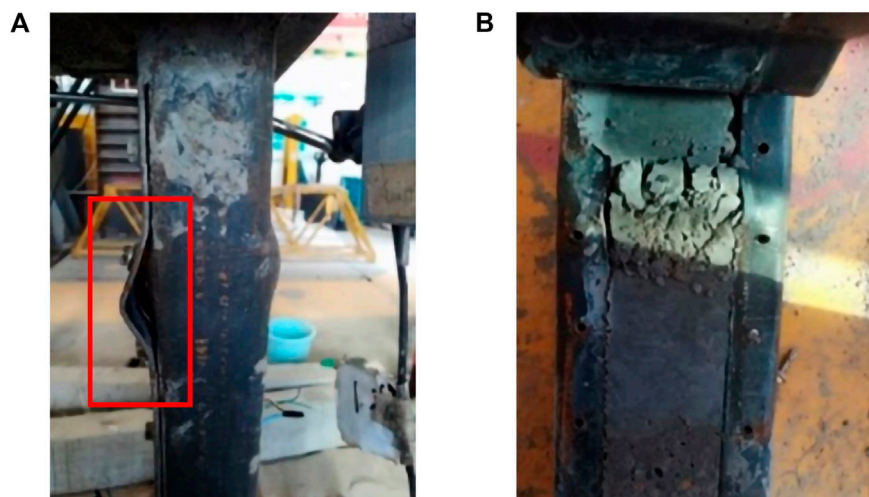


FIGURE 4 | (A) Local buckling on R50-2.2. (B) Crushed concrete in R50-2.2.

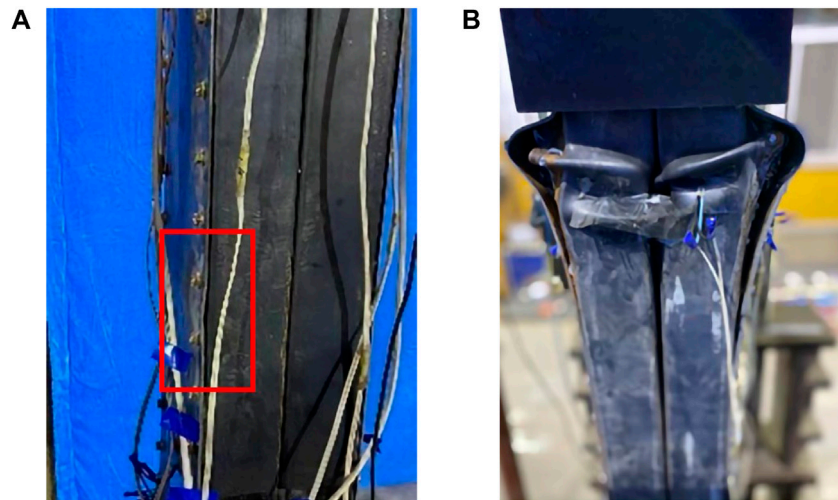


FIGURE 5 | (A) Local deformation of specimen steel plate of SR50-2.2. **(B)** Specimen buckling of SR50-2.2.

same direction with the load. As the load increases, local buckling appeared on the specimens before the ultimate damage of the specimens. At the same time, the bearing capacity of the double-limb specimen was greater than that of the single-limb specimen, which was greater than that of the hollow tubular specimen.

3.3 Load and Deformation Relationship of Specimens

Figure 8 shows the load-displacement curves of the specimens. It can be found that the ultimate bearing capacity of the double-limb specimen is about two times that of the single-limb specimen due to the restraint of the steel tube on the concrete and the inhibition of concrete on the buckling effect of the steel section. The specimen cross section size has a greater influence on the bearing capacity of

the same limb column. However, the greater the wall thickness, the higher the bearing capacity of the specimen. The bearing capacity of the hollow specimen is influenced by the wall thickness of the steel tube. When the wall thickness of the steel tube is larger, the local buckling damage of the specimen appears relatively late, and thus the bearing capacity continues to grow.

Meanwhile, the specimens were divided into four groups according to the steel ratio. The ductility coefficient μ (Yang, 2012) was used to express the deformation capacity of the specimens, which could be calculated according to

$$\mu = \frac{\varepsilon_{85\%}}{\varepsilon_u}, \quad (1)$$

where $\varepsilon_{85\%}$ is the average vertical strain when the load drops to 85% of the ultimate load-bearing capacity of the specimen and

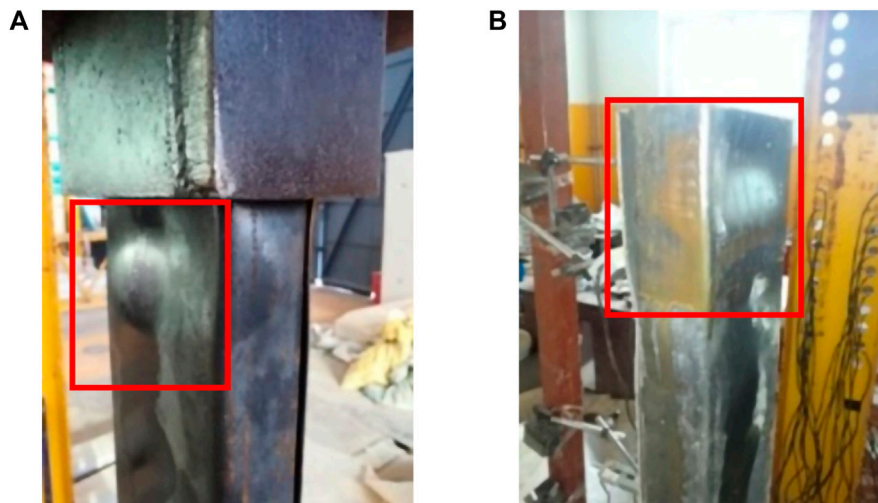
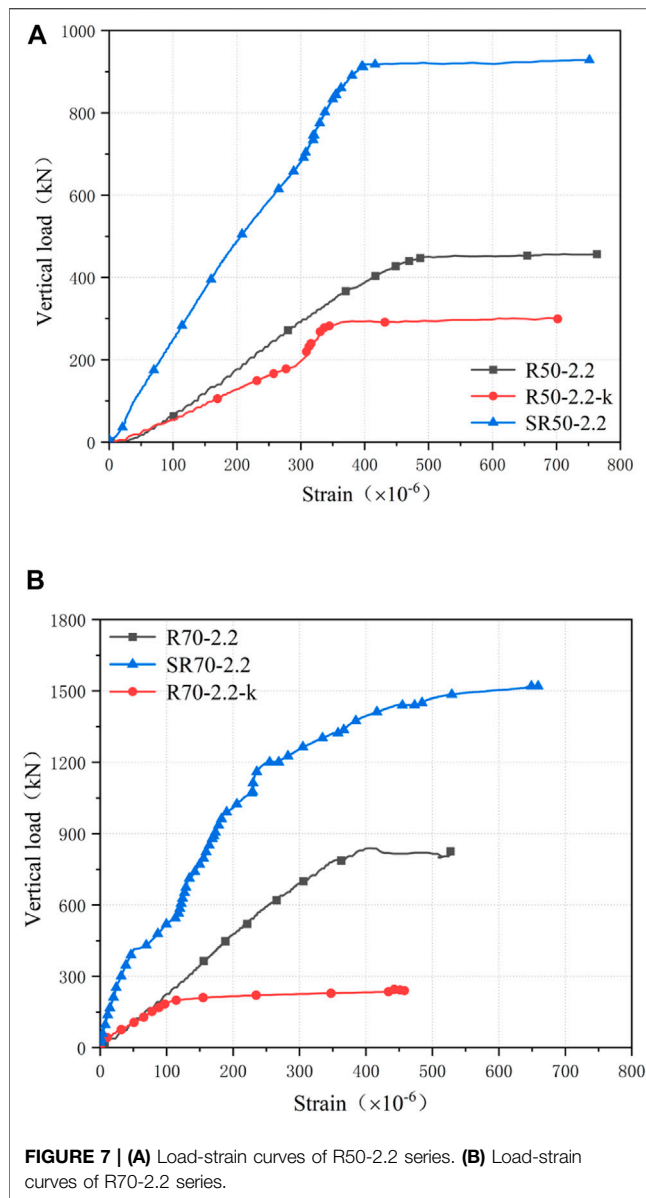
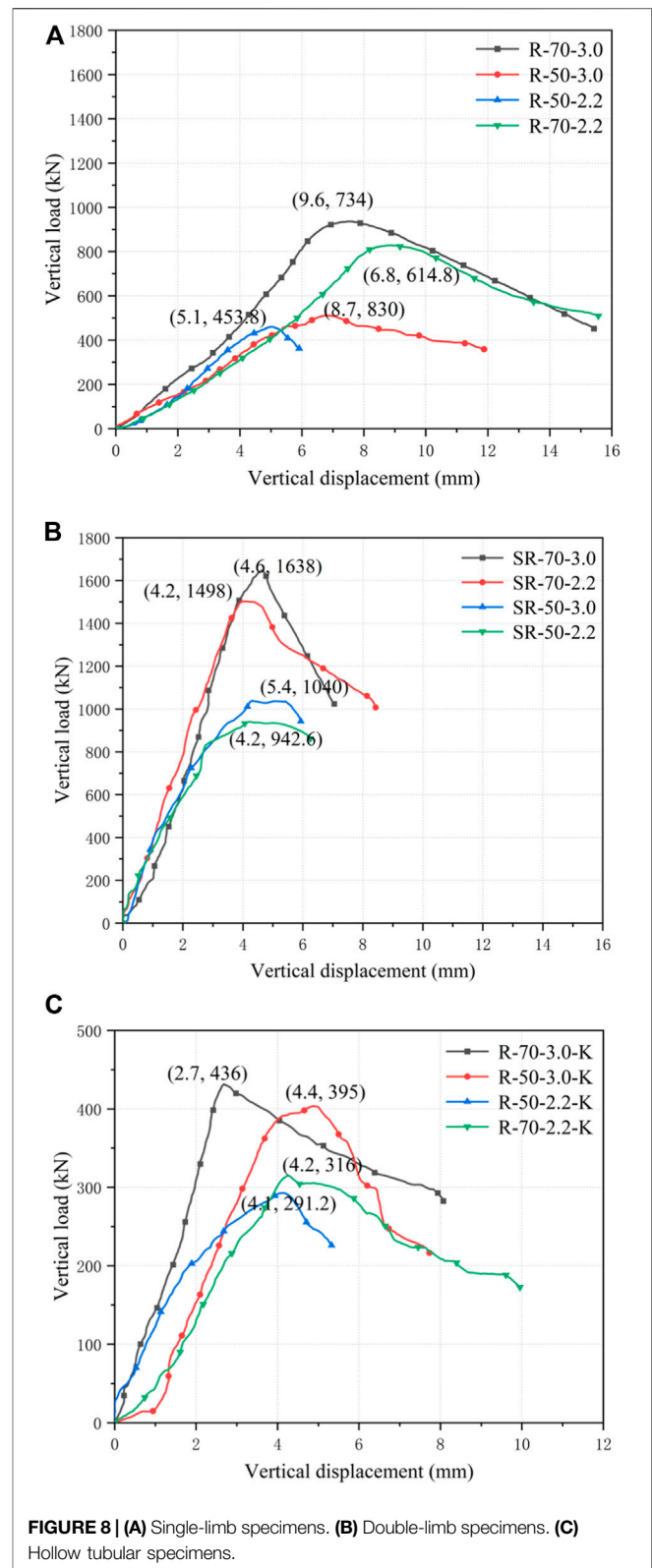


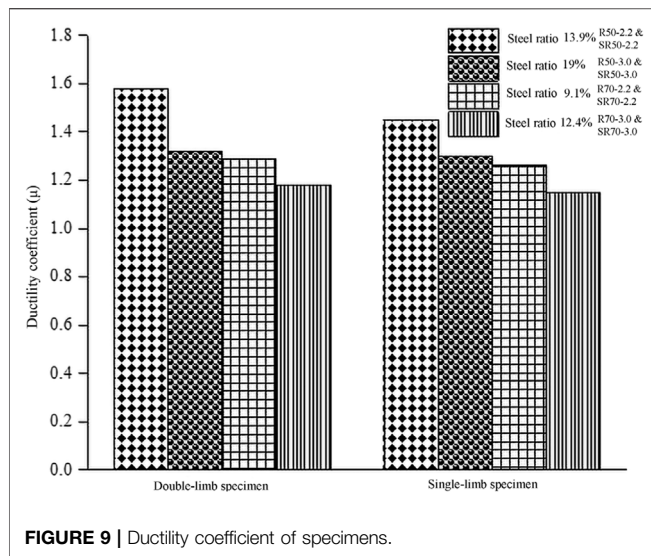
FIGURE 6 | (A) Local buckling of R50-2.2-K. **(B)** Buckling of the specimen at the end of R50-2.2-K.



ε_u is the average vertical strain when the load reaches the ultimate load-bearing capacity of the specimen. If the load did not drop to 85% of the peak load, the final failure point was defined as the symmetry point, which was reflected to 85% of the peak load in the rising part of the load-displacement curve (Lue et al., 2007).

The ductility coefficients of the specimens are shown in Figure 9. It can be found that the filled concrete greatly improves the ultimate bearing capacity of the specimen. For the specimens with the sectional height-width ratio of 1.43, the ultimate bearing capacity of the single-limb column specimen is 114.17% higher than that of the hollow steel tube





column, and the ultimate bearing capacity of the double-limb column specimen is 275.71% higher than that of the hollow steel tube column. The steel ratio has little effect on the ductility coefficient of the specimens with the same limb.

4 BEARING CAPACITY CALCULATION METHOD OF FABRICATED COLD-FORMED THIN-WALLED STEEL TUBULAR CONCRETE COLUMNS

The existing specification lacks provisions for the design of fabricated thin-walled cold-formed steel tubular lightweight concrete columns. Therefore, according to the comprehensive comparison of Japanese Design Code (AIJ, 1997), Chinese Design Code GJB4142-2000 (Wei et al., 2000), engineering construction standard of Fujian province DBJB-51-2003 (Tao et al., 2003), CECS159-2004 (Shen et al., 2004), and Chinese concrete-filled steel tubular structure code GB50936-2014 (Zha et al., 2014) on the calculation method of the bearing capacity of steel tube

TABLE 3 | Comparison of calculated and test results.

Specimen number	ξ	k_c	N_u	N_{exp}	N_u/N_{exp}
R50-2.2	2.11234	1.81206	418.53	453.83	0.92
R50-3.0	2.80042	1.81767	484.03	514.83	0.94
R70-2.2	2.33042	1.78281	781.70	830.53	0.94
R70-3.0	3.25521	1.83891	850.99	934.06	0.91
SR50-2.2	3.62101	1.84004	963.50	943.63	1.02
SR50-3.0	3.94958	1.85179	968.36	1,040.17	0.93
SR70-2.2	2.37059	1.80285	1,615.10	1,494.54	1.08
SR70-3.0	3.23025	1.79979	1,606.86	1,638.63	0.98

concrete under compression, the ultimate bearing capacities of the specimens in the test were compared with the design value of the specifications. The results are shown in **Table 2**. It can be found that the ultimate bearing capacities of the specimens were 2.55~4.26 times the design value of the concrete-filled steel tube (CFST) members. Compared with CFST, the cold-formed steel specimens have the advantages of lightweight, fewer welds, and convenient construction.

Based on the superimposed strength theory of steel tube concrete, the formula for calculating the design value of the cross-sectional bearing capacity is proposed when the fabricated thin-walled cold-formed steel tubular lightweight concrete columns are axially compressed as follows:

$$N_u = k_c f_c A_c + f_y A_s, \quad (2)$$

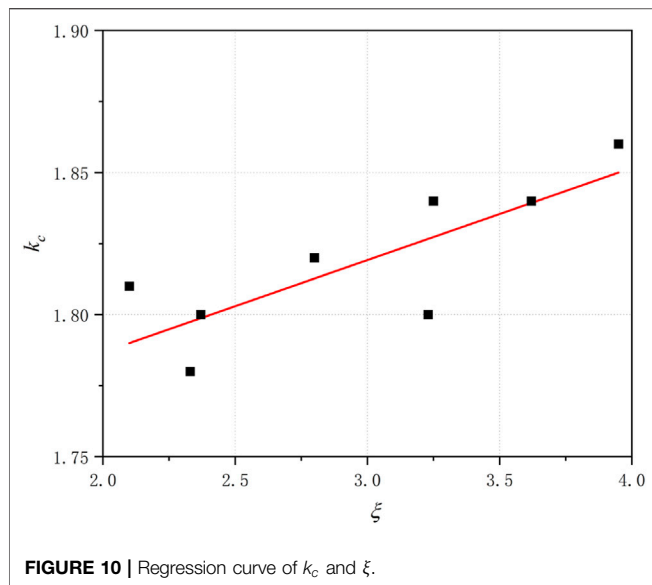
$$\xi = \alpha_{sc} \frac{f_y}{f_c}, \quad (3)$$

where k_c is the concrete strength correction factor, related to the casing hoop steel coefficient ξ . f_y and f_c are the design values of steel and concrete strengths, respectively. A_c and A_s are the core concrete and steel tube cross-sectional areas. α_{sc} is the steel ratio which is the percentage of the steel area to the concrete area.

The regression analysis of k_c and ξ (shown in **Figure 10**) was performed according to the test results to obtain the expression of the concrete strength reduction coefficient k_c , which is shown in **Eq. 4**, where the correlation coefficient $R^2 = 0.77$:

TABLE 2 | Comparison of calculated bearing capacity.

Specimen number	Measured ultimate bearing capacity (kN)	Bearing capacity in test/design bearing capacity				
		AIJ (1997)	GJB4142-2000	DBJB-51-2003	CECS159-2001	GB50936-2014
R50-2.2	453.83	1.24	1.76	1.79	1.67	2.55
R50-3.0	514.83	1.22	1.77	1.76	1.61	2.58
R70-2.2	830.53	1.47	1.94	2.02	1.83	4.26
R70-3.0	934.06	1.32	1.80	1.86	1.61	3.95
SR50-2.2	943.63	1.11	1.63	2.14	1.57	3.12
SR50-3.0	1,040.17	1.07	1.50	2.02	1.95	3.47
SR70-2.2	1,494.54	1.08	1.55	1.88	1.63	2.60
SR70-3.0	1,638.63	0.92	1.46	2.09	1.90	3.41
R50-2.2-K	291.67	1.04	—	—	—	—
R50-3-K	403.17	1.18	—	—	—	—
R70-2.2-K	316.67	0.89	—	—	—	—
R70-3-K	435.59	0.90	—	—	—	—



$$k_c = 0.0277\xi + 1.7363. \quad (4)$$

Therefore, the compressive bearing capacity of the fabricated thin-walled cold-formed steel tubular lightweight concrete columns can be calculated as follows:

$$N_u = (0.0277\xi + 1.7363)f_c A_c + f_y A_s. \quad (5)$$

The comparing results of the bearing capacity N_u obtained based on Eq. 5 with the test results N_{exp} are shown in Table 3. It can be found that the error N_u/N_{exp} is around 1, which indicates the calculation method is fitted.

5 CONCLUSION

The main factors affecting the bearing capacity and ductility performance of the combined columns were investigated through the axial compression load test on 12 fabricated thin-walled cold-formed steel tubular lightweight concrete

columns. Based on the existing steel tubular concrete column design code, the load-bearing capacity calculation formula adapted to the cold-formed thin-walled steel-lightweight concrete column was proposed. The main conclusions are as follows:

- (1) In the loading process, all specimens did not experience out-of-plane instability during the test. The local buckling is the main damage mode. The ultimate bearing capacity of the double-limb specimen is significantly higher than that of the single-limb specimen and hollow steel tube.
- (2) For the specimen with the height-to-width ratio of 1.43, the ultimate bearing capacity of the single-limb specimen is 114.17% higher than that of the hollow steel tube column, and the ultimate bearing capacity of the double-limb column is 275.71% higher than that of hollow steel tube column. For the specimens with the same limb, the steel ratio has a large influence on the bearing capacity and little influence on the ductility coefficient.
- (3) Based on the superimposed strength theory, the load-bearing capacity of the fabricated thin-walled cold-formed steel tubular lightweight concrete columns is proposed, which guides the design of such structure members.

DATA AVAILABILITY STATEMENT

The raw data supporting the conclusion of this article will be made available by the authors without undue reservation.

AUTHOR CONTRIBUTIONS

YL contributed to the conception and design of the study. KZ organized the database. XL performed the statistical analysis. YY wrote the first draft of the manuscript. CG wrote sections of the manuscript. All authors contributed to manuscript revision and read and approved the submitted version.

REFERENCES

- AIJ (1997). *Recommendations for Design and Construction of concrete Filled Steel Tubular structures* AIJ: 1997. Tokyo: Architectural Institute of Japan.
- Cai, S. H. (2003). *Modern Steel Tube and concrete Structures*. Beijing: People's Traffic Press.
- Chen, J. S. (2007). *Experimental Study and Theoretical Analysis of Flexural Performance of Lightweight Aggregate concrete Filled Steel Tubes*. Nanjing: Hehai University. [dissertation/master's thesis]. doi:10.7666/d.y1031016
- Ding, W., Zhu, A. P., and Wang, J. (2019). *Technical Standard for Application of Lightweight Aggregate concrete Ministry of Construction of the People's Republic of China*. JGJ/T 12-2019 (in Chinese).
- Ge, H., and Usami, T. (1992). Strength of Concrete-Filled Thin-Walled Steel Box Columns: Experiment. *J. Struct. Eng.* 118, 3036–3054. doi:10.1061/(asce)0733-9445(1992)118:11(3036)
- Islam, M. M., Ali, R. B., Begum, M., and Rahman, M. S. (2021). Experimental Study of Square Concrete-Filled Welded Cold-Formed Steel Columns under Concentric Loading. *Arab J. Sci. Eng.* 46, 4225–4237. doi:10.1007/s13369-020-04797-9
- Li, D. (2017). *Study on the Mechanical Properties of concrete Filled High Strength Cold-Formed Steel Tubular Columns*. Jingzhou City, Hubei Province (China): Yangtze University, 24–60. [dissertation/master's thesis]
- Li, G. C., and Liu, Z. Y. (2001). *Self-stressing Steel Tube Lightweight Aggregate concrete Structure*. Shenyang: North eastern University Press.
- Lue, D. M., Liu, J.-L., and Yen, T. (2007). Experimental Study on Rectangular CFT Columns with High-Strength concrete. *J. Constructional Steel Res.* 63 (1), 37–44. doi:10.1016/j.jcsr.2006.03.007
- Mursi, M., and Uy, B. (2004). Strength of Slender concrete Filled High Strength Steel Box Columns. *J. Constructional Steel Res.* 60 (12), 1825–1848. doi:10.1016/j.jcsr.2004.05.002
- Shen, Z. Y., Lv, X. L., He, B. K., Zhang, S. M., Cheng, Y. Y., Cheng, G. J., et al. (2004). *Technical Regulations for Rectangular Steel Tube concrete*

- Structures]. Shanghai City (China): China association of engineering construction standards. CECS159-2004(in Chinese).
- Skalomenos, K. A., Hayashi, K., and Nishi, R. (2016). Experimental Behavior of concrete-filled Steel Tube Columns Using Ultra High-Strength Steel. *J. Struct. Eng. J.* 45 (2), 285–288. doi:10.1061/(ASCE)ST.1943-541X.0001513
- Tao, Z., Chen, H., Yu, Q., Wang, Z. B., Lu, W. H., Lu, H., et al. (2003). *Technical Specification for Steel Tube concrete Structure*. Fuzhou City, Fujian Province (China): Department of housing construction of Fujian province. DBJB-51-2003 (in Chinese).
- Varma, A. H., Ricles, J. M., Sause, R., and Lu, L.-W. (2004). Seismic Behavior and Design of High-Strength Square Concrete-Filled Steel Tube Beam Columns. *J. Struct. Eng.* 130 (2), 169–179. doi:10.1016/S0143-974X(01)00099-210.1061/(asce)0733-9445(2004)130:2(169)
- Wei, Z. B., Han, L. H., Liu, X. L., Zhang, S. Y., Chen, H. F., Tao, Z., et al. (2000). *Wartime Military Port Emergency Repair Early-Strength Combined Structure Technical Regulations*, GJB4142. Beijing City (China): The General Logistics Department of the Chinese People's Liberation Army
- Wright, H. D. (1993). Buckling of Plates in Contact with a Rigid Medium. *Struct. Eng.* 71 (12), 209
- Yang, J. (2012). *Research on the Axial Compression Performance of Steel Tube-Recycled concrete Short Columns*. Quanzhou City, Fujian Province (China): Huaqiao University. [dissertation/master's thesis]. [Quanzhou(350000)]. doi:10.7666/d.D259861
- Zha, X. X., Xiao, C. Z., Zhong, S. T., Cai, S. H., Fan, X. Q., Wang, Q., et al. (2014). *Technical Code for concrete-filled Steel Tube Structure*. Beijing City (China): Ministry of housing and urban rural development of the People's Republic of China. GB50936- 2014 (in Chinese).
- Zhang, Y. C., Wang, Q. P., and Mao, X. Y. (2005). Experimental Study on the Axial Compression Performance of Thin-Walled concrete-filled Steel Tube Short Columns. *Building Struct.* 35 (1), 22
- Zhao, D. S., Zheng, Q., and Li, P. (2008). Calculation on Axial Bearing Capacity of concrete-filled Thin-Walled Cold-Formed Steel Box Punched. *Zhejiang Construction* 25 (7), 17. doi:10.3969/j.issn.1008-3707.2008.07.006
- Conflict of Interest:** Author XL was employed by the company Central Research Institute of Building and Construction Co., Ltd.
- The remaining authors declare that the research was conducted in the absence of any commercial or financial relationships that could be construed as a potential conflict of interest.
- Publisher's Note:** All claims expressed in this article are solely those of the authors and do not necessarily represent those of their affiliated organizations, or those of the publisher, the editors and the reviewers. Any product that may be evaluated in this article, or claim that may be made by its manufacturer, is not guaranteed or endorsed by the publisher.
- Copyright © 2022 Li, Yan, Meng, Zhang, Li and Gao. This is an open-access article distributed under the terms of the Creative Commons Attribution License (CC BY). The use, distribution or reproduction in other forums is permitted, provided the original author(s) and the copyright owner(s) are credited and that the original publication in this journal is cited, in accordance with accepted academic practice. No use, distribution or reproduction is permitted which does not comply with these terms.



Numerical Analysis of Structural Performance of Concrete-GFRP Composite I-Beam

Zhaohui Chen^{1,2}, Jiajie Xing^{1,2}, Qiwen Luo^{1,2,3} and Xiaoyue Zhang^{1,2*}

¹School of Civil Engineering, Chongqing University, Chongqing, China, ²Key Laboratory of New Technology for Construction of Cities in Mountain Area, Chongqing University, Chongqing, China, ³Quakesafe Technologies Co., Ltd, Kunming, China

OPEN ACCESS

Edited by:

Fangying Wang,
University of Nottingham,
United Kingdom

Reviewed by:

Jian Weng,
Building and Construction Authority,
Singapore
Weihong Qin,
Southeast University, China

*Correspondence:

Xiaoyue Zhang
xiaoyuezhong@cqu.edu.cn

Specialty section:

This article was submitted to
Structural Materials,
a section of the journal
Frontiers in Materials

Received: 28 December 2021

Accepted: 09 February 2022

Published: 16 March 2022

Citation:

Chen Z, Xing J, Luo Q and Zhang X
(2022) Numerical Analysis of Structural
Performance of Concrete-GFRP
Composite I-Beam.
Front. Mater. 9:844393.
doi: 10.3389/fmats.2022.844393

The concrete-GFRP composite beams have received extensive attention in civil engineering. However, the ambiguity of the fracture, debonding of the interface, and the GFRP profile limit the precise design of the composite beam. This article presents a comprehensive numerical study for the structural performance of composite pultruded GFRP beams to provide a better understanding of the mechanism of interfacial debonding and GFRP matrix fracture. The failure and delamination process of pultruded GFRP for anisotropy of materials is modeled using the Hashin criteria. The bond-slip behavior between the concrete slab and the top flange of the GFRP I-beam is simulated by the bilinear cohesive interface element. The availability and accuracy of the finite element model are verified by comparison with the four-point bending test results of the pure GFRP I-beam and composite beams as well. Based on the proposed comprehensive finite element model, the effects of the strength, thickness, and width of the concrete slab and the shear-span ratio of the beam on the structural behavior of the composite beam are studied. According to the parametric analysis, the excessive high strength of concrete, the width, and/or thickness of the concrete slab would lead to shear failure of the slab rather than significantly increasing the ultimate load of the composite beam. When having a small shear-span ratio, the matrix fracture and delamination will occur in the web of the GFRP profile. In addition, the height of the I-profile web has a significant effect on the stress and strain distribution of the composite beam. These parametric analyses could provide the numerical basis for the design of the GFRP composite beams.

Keywords: GFRP-concrete composite beam, Hashin failure criteria, bilinear cohesive model, bond-slip, anisotropy

INTRODUCTION

Nowadays, the fiber-reinforced polymer (FRP) pultruded profiles are widely used in engineering practice (Gand et al., 2013). Among the different kinds of fiber-reinforced polymer, GFRP which is made of glass fiber-reinforced polymer matrix is the most popular one due to its cost-effective, light weight, high strength, and durability compared with the traditional building materials, such as steel and reinforced concrete (Borowicz and Bank, 2009; Borowicz and Bank, 2011). The pultruded GFRP profiles with I- or box-shaped cross sections are commonly used. However, the high deformability of the pultruded GFRP I-beam resulting from low elastic modulus of materials also limits its application in engineering practice and has attracted research interest. In order to prevent the buckling of the GFRP beam and improve the stiffness of the structure, an economical and practical way is to bond the concrete slab at the upper flange of the GFRP profile and form a concrete-GFRP composite beam

by means of metallic studs and/or adhesive bonding, such as epoxy resin (Keller, 2001; Correia, et al., 2007; Zou et al., 2018). Lots of experimental and numerical research studies have been carried out on the mechanical performance and failure mechanism of this concrete-GFRP composite beam.

The experimental studies showed that the shear connection between the concrete slab and GFRP profile has a dominant effect on the synergistic of the composite beam (Neagoe et al., 2015). Among the shear connections, adhesive bonding is widely used to improve the bonding performance of the concrete slabs and GFRP profile (Gonilha et al., 2010). Nordin conducted the bending tests to compare the structural performance of the pure GFRP beam and concrete-GFRP composite beam (Nordin and Taeljsten, 2004). It has shown that with the effective adhesive bonding, the composite beam can prevent the premature buckling of the pure pultruded GFRP profile, thereby significantly increasing the ultimate load of the composite beam. However, as the load increases, the concrete debonds from the GFRP profile and the interface slips, resulting in a decrease in the stiffness of the composite beam. On the other hand, the significant increase in the ultimate load of the composite beam also makes the internal stress of the GFRP profile much larger than that of the pure GFRP beam which is prone to premature buckling. As a result, the composite beam will suffer from the matrix fracture of the GFRP profile.

The numerical simulation is also used to study the mechanism and failure process of the pultruded GFRP profile, which is beneficial for the design of the GFRP profile beam. Alnahal et al. (2008) treated GFRP and concrete as linear materials and assumed that the interface between concrete and GFRP has a perfect bonding performance. They gave the critical load for elastic buckling of the composite structure but failed to predict the ultimate load. According to Kong et al. (Kong et al., 2018), debonding occurs when the connection reaches shear strength. The research of Yuan et al. (Yuan and Hadi, 2017) showed that with the ignorance of the bond-slip of composite beams, the stiffness and ultimate load of the structure will be overestimated. Wang (Wang et al., 2015) highlights the debonding mechanism of the GFRP concrete composite beams theoretically, which is verified by the tests. Furthermore, Umberto (Umberto et al., 2021) used the cohesive model to simulate the bond-slip of FRP-strengthened concrete beams, and the results were in good agreement with the experimental results. Assuming the pultruded GFRP as a linear material, the composite beam would be damaged by the shear cracking of the concrete slab, which is quite different from the experiments. Thus, the fracture models of the composite material such as Tsai-Hill and Tsai-Wu are introduced to simulate the progressive damage of the pultruded GFRP that are prone to interlayer delamination.

In summary, the nonlinearities of the GFRP composite beam investigated through experimental studies are not adequately addressed in numerical analysis. Moreover, regarding the effects of geometric of the composite cross sections on the ultimate load and the mechanical behavior of the composite beam, more experiments are also required to be carried out. Thus, in this article, a comprehensive finite element model is established in order to provide a better understanding of the

progressive debonding and fracture of the composite GFRP beam. The numerical model is developed using the Hashin criteria for pultruded GFRP and a bilinear cohesive model for the adhesive interface of the concrete slab to the GFRP flange. The four-point bending experimental results of the pure GFRP I-beam and the concrete-GFRP composite I-beam provided by Nordin (Nordin H, Taeljsten B. 2004) were compared with the numerical simulations to verify the accuracy of the FE model. Furthermore, as a complement to the experimental research, the comprehensive FE model, which allows for a more in-depth study in terms of stress and strain distributions of the composite beam, is used for parametric analysis to investigate the effects of the concrete strength and the cross-section geometry of the composite beam on the mechanical performance of the composite beam. These parametric analyses can provide a numerical basis for the design of the concrete-GFRP composite beam in engineering practice.

GFRP FAILURE CRITERIA

Pultruded GFRP Constitutive Relationship

The pultruded GFRP profile is prone to premature buckling because of the small elastic modulus of the material. One way to improve the stiffness of pultruded GFRP profiles is to make GFRP laminates by gluing several GFRP sheets. In this case, the mechanical properties of the GFRP laminates depend on the fiber lay-up direction of the sheet. When all fiber directions are the same (Figure 1A), the GFRP sheet exhibits anisotropy, and the stress along the sheet thickness direction cannot be ignored. See $\sigma_3 \neq 0$, $\tau_{23} \neq 0$, and $\tau_{31} \neq 0$.

If the fibers of each GFRP sheet are intertwined (Figure 1B), the transverse isotropic on a macroscopic scale can be presented. The constitutive relationship can be simplified as follows:

$$\begin{bmatrix} \varepsilon_1 \\ \varepsilon_2 \\ \varepsilon_3 \\ \varepsilon_4 \\ \varepsilon_5 \\ \varepsilon_6 \end{bmatrix} = \begin{bmatrix} S_{11} & S_{12} & S_{13} & 0 & 0 & 0 \\ S_{12} & S_{11} & S_{13} & 0 & 0 & 0 \\ S_{13} & S_{13} & S_{33} & 0 & 0 & 0 \\ 0 & 0 & 0 & S_{44} & 0 & 0 \\ 0 & 0 & 0 & 0 & S_{44} & 0 \\ 0 & 0 & 0 & 0 & 0 & 2(S_{11} - S_{12}) \end{bmatrix} \begin{bmatrix} \sigma_1 \\ \sigma_2 \\ \sigma_3 \\ \sigma_4 \\ \sigma_5 \\ \sigma_6 \end{bmatrix}, \quad (1)$$

where the flexibility coefficient, S_{ij} , is expressed in terms of engineering elasticity constants as follows:

$$\begin{aligned} S_{11} &= \frac{1}{E_1}, S_{12} = -\frac{\nu_{12}}{E_2}, S_{13} = -\frac{\nu_{13}}{E_3}; \\ S_{33} &= \frac{1}{E_3}, S_{44} = \frac{1}{G_{23}}, \end{aligned} \quad (2)$$

where E_1 , E_2 , and E_3 are the elastic moduli along the directions 1, 2, and 3, respectively, G_{23} is the shear modulus, and ν_{12} and ν_{13} are the Poisson's ratios.

According to the principle of symmetry, Eq. 2 can be expressed as follows:

$$\frac{\nu_{ij}}{E_j} = \frac{\nu_{ji}}{E_i} \quad (i, j = 1, 2, 3, i \neq j) \quad (3)$$

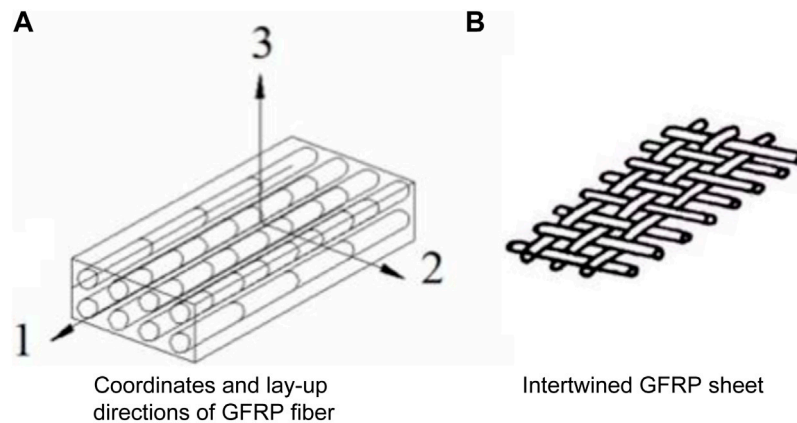


FIGURE 1 | Fiber lay-up directions of pultruded GFRP laminates. **(A)** Coordinates and lay-up directions of GFRP fiber **(B)** Intertwined GFRP sheet.

Failure Criteria of Pultruded GFRP

According to the three-dimensional Hashin failure criteria (Hashin and Rotem, 1973; Hashin, 1980; El-Hacha and Chen, 2012; Alnahhal et al., 2008) that can precisely simulate the progressive damage mode of the composite materials by reducing the material engineering elastic constants, the following four failure criteria can be established for the pultruded GFRP (Hashin and Rotem, 1973; Hashin, 1980):

- (1) Fiber tensile failure ($\sigma_1 \geq 0$)

$$\left(\frac{\sigma_1}{f_{1t}}\right)^2 + \left(\frac{\tau_{12}}{S_{12}}\right)^2 + \left(\frac{\tau_{13}}{S_{13}}\right)^2 = 1; \quad (4)$$

- (2) Fiber buckling failure ($\sigma_1 \leq 0$)

$$\left(\frac{\sigma_1}{f_{1c}}\right)^2 = 1; \quad (5)$$

- (3) Matrix tensile failure ($\sigma_2 + \sigma_3 > 0$)

$$\left(\frac{\sigma_2 + \sigma_3}{f_{2t}}\right)^2 + \frac{\tau_{23}^2 - \sigma_2\sigma_3}{S_{23}^2} + \frac{\tau_{12}^2}{S_{12}^2} + \frac{\tau_{13}^2}{S_{13}^2} = 1; \quad (6)$$

- (4) Matrix compression failure ($\sigma_2 + \sigma_3 \leq 0$)

$$\left[\left(\frac{f_{2c}}{2S_{12}}\right)^2 - 1\right] \frac{\sigma_2 + \sigma_3}{f_{2c}} + \left(\frac{\sigma_2 + \sigma_3}{2S_{12}}\right)^2 + \frac{\tau_{23}^2 - \sigma_2\sigma_3}{S_{23}^2} + \frac{\tau_{12}^2}{S_{12}^2} + \frac{\tau_{13}^2}{S_{13}^2} = 1, \quad (7)$$

where f_{1c} and f_{2c} are the compressive strength, f_{1t} and f_{2t} are the tensile strength at directions 1 and 2, σ_1 , σ_2 , and σ_3 are the principal stresses at directions 1, 2, and 3, respectively, and τ_{ij} is the shear stress.

In the numerical analysis, the degradation of material stiffness is considered when the failure criteria presented previously are met. The degradation process is simulated by reducing the stiffness coefficient of the material at the finite element integration point. However, the stiffness reduction

factors proposed by Tan (Tan, 2016), which are validated by experiments of composite materials (Feng and Aymerich, 2014; Hongliang et al., 2018), are used to model the damage in GFRP laminates, as shown in Table 1, where Q and Q_d represent the engineering elastic moduli in undamaged and damaged states, respectively.

BILINEAR COHESIVE MODEL OF THE ADHESIVE INTERFACE

The concrete slab and the upper flange of the GFRP I-profile are bonded with an adhesive, such as epoxy glue. According to the softening and fracture behavior of the adhesive interface between the concrete and GFRP, the bilinear cohesive model (Blackman et al., 2003; Wang, 2006) is introduced. It can be noticed that based on the cohesive traction–separation law, the mechanical behavior of the adhesive interface includes three stages: 1) Elastic stage: The cohesive stress increases linearly with the displacement until the initial failure criterion is satisfied; 2) Softening stage: After reaching the maximum cohesive strength, the adhesive stress decreases linearly to zero with the increase of the displacement; and 3) Debonding stage: The displacement continues to increase, but the cohesive stress remains zero. In the bilinear cohesive model, K_0 is the initial stiffness of the interface. Taking the quadratic nominal stress criterion as the initial damage criterion, the adhesive interface is destroyed when the following equation is satisfied:

$$\left\{\frac{\langle \sigma_n \rangle}{\sigma_n^{\max}}\right\}^2 + \left\{\frac{\sigma_s}{\sigma_s^{\max}}\right\}^2 + \left\{\frac{\sigma_t}{\sigma_t^{\max}}\right\}^2 = 1, \quad (8)$$

where σ_n , σ_s , and σ_t are the normal stress and tangential stress, respectively, and $\sigma_n^{\max}/\sigma_s^{\max}$ and σ_t^{\max} are the maximum normal stress and tangential stress, respectively. $\langle \cdot \rangle$ is the Macaulay brackets. It means that when $\sigma_n > 0$, $\langle \sigma_n \rangle = \sigma_n$; when $\sigma_n < 0$, $\langle \sigma_n \rangle > \sigma_n$.

The bilinear cohesive model can then be expressed as follows:

TABLE 1 | Stiffness degradation model of GFRP.

Damage mode	Matrix tensile failure	Matrix compression failure	Fiber tensile failure	Fiber buckling failure
Stiffness reduction factor	$Q_d = 0.2Q$ ($Q = E_2, G_{12}, G_{23}, \mu_{12}, \mu_{23}$)	$Q_d = 0.4Q$ ($Q = E_2, G_{12}, G_{23}, \mu_{12}, \mu_{23}$)	$Q_d = 0.07Q$ ($Q = E_1, G_{12}, G_{31}, \mu_{12}, \mu_{31}$)	$Q_d = 0.14Q$ ($Q = E_1, G_{12}, G_{31}, \mu_{12}, \mu_{31}$)

$$T_n = \begin{cases} \frac{\sigma_{\max}}{\delta_n^0} \delta & (\delta \leq \delta_n^0) \\ \sigma_{\max} \frac{\delta_n^f - \delta}{\delta_n^f - \delta_n^0} & (\delta > \delta_n^0) \end{cases}; \quad (9)$$

$$T_t = \begin{cases} \frac{\tau_{\max}}{\delta_t^0} \delta & (\delta \leq \delta_t^0) \\ \tau_{\max} \frac{\delta_t^f - \delta}{\delta_t^f - \delta_t^0} & (\delta > \delta_t^0) \end{cases}, \quad (10)$$

where T_n and T_t are the normal stress and tangential stress, σ_{\max} and τ_{\max} are the maximum normal stress and shear stress, δ_n^0 and δ_t^0 are the normal and slip displacement corresponding to the maximum normal stress and shear stress, δ_n^f and δ_t^f are the final normal and slip displacements of the cracking, respectively (Chen et al., 2019).

When the strain energy of the interface reaches the fracture energy, the failure at the interface occurs. The normal and tangential fracture energies are given as follows, respectively:

$$G_n^c = \frac{1}{2} \sigma_{\max} \cdot \delta_n^f, G_t^c = \frac{1}{2} \tau_{\max} \cdot \delta_t^f. \quad (11)$$

The damage phenomena of the concrete-GFRP interface are then quantified by the damage factor given as follows:

$$D = \frac{\delta_f (\delta_m - \delta_0)}{\delta_m (\delta_f - \delta_0)}, \quad (12)$$

where δ_m is the maximum cracking displacement, a variable that depends on the interfacial cracking process. In the softening stage, the damage factor D would vary from 0 (state of intact) to 1 (state of damage).

The key parameters of the bilinear cohesive model in the numerical simulation for the bond behavior of the adhesive interface are the initial shear stiffness K_0 , the maximum shear

stress τ_c , and the interfacial fracture energy G_c . The initial shear stiffness K_0 can be modeled as a sequence of the shear stiffness of the adhesive layer and the concrete, expressed as follows:

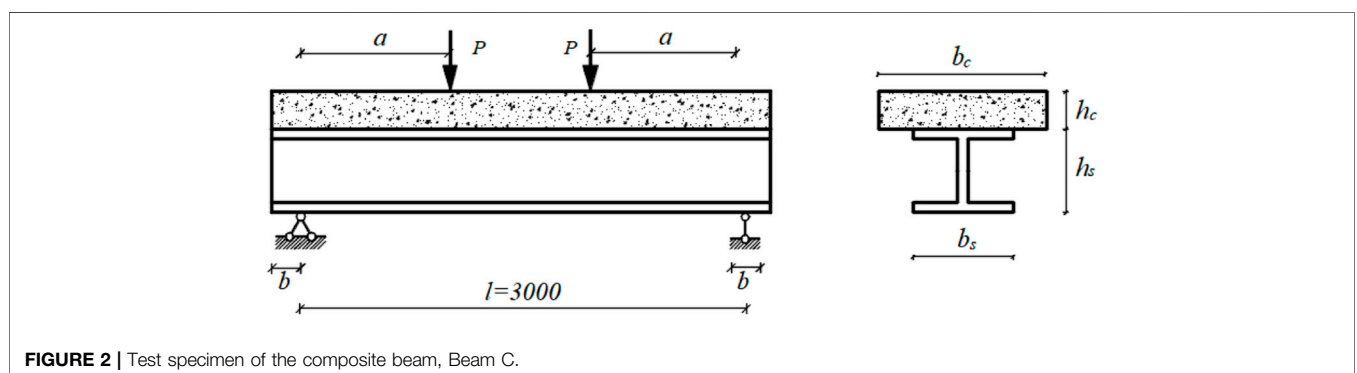
$$K_0 = K_a K_c / (K_a + K_c), \quad (13)$$

where the shear stiffness of the adhesive layer is $K_a = G_a/t_a$, the shear stiffness of concrete at the interface is $K_c = G_c/t_c$, while G_a and t_a are the shear modulus and the thickness of the adhesive layer, respectively, and G_c and t_c are the elastic shear modulus and the effective thickness of the concrete incorporating bond behavior at the interface, respectively, here $t_c = 5\text{mm}$. The maximum shear stress τ_c is dependent on the tension strength of concrete, $\tau_c = 1.5\beta_w f_t$, where β_w is a regression coefficient based on experimental results, $\beta_w = \sqrt{\frac{2.25-b_f/b_c}{1.25+b_f/b_c}}$, in which b_c and b_f are the width of the concrete slab and the flange of the GFRP I profile, respectively. The interfacial fracture energy G_c is statistically determined from experimental tests, $G_c = 0.308\beta_w^2 \sqrt{f_t} f(K_a)$ in the following analysis.

NUMERICAL SIMULATION

Overview of Experimental Tests

Comparative static loading tests were carried out by Nordin et al. (Nordin H, Taljsten B. 2004) for a pure GFRP I-beam, Beam A, and a concrete-GFRP composite beam, Beam C. The pure GFRP beam (Beam A) is reinforced with a 3-mm-thick CFRP sheet pasted on the bottom edge. These experiments are the basis for sophisticated numerical simulations and further analysis, to study the effects of material properties and geometric parameters on the mechanical performance of the composite beams. The test specimen subjected to four-point bending is shown in **Figure 2**, and the elastic moduli and strength of pultruded GFRP profile are represented in **Table 1A** in the Appendix. The spans for both Beam A and Beam C are $l = 3000\text{ mm}$ and

**FIGURE 2** | Test specimen of the composite beam, Beam C.

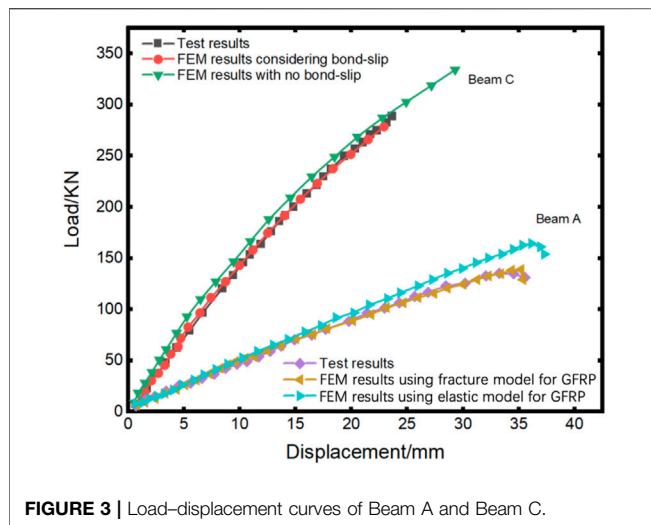


FIGURE 3 | Load–displacement curves of Beam A and Beam C.

the shear span $a = 1000$ mm, the width and thickness of the concrete slab of Beam C are $b_c = 120$ mm and $h_c = 115$ mm, respectively, the height of the GFRP web is $h_w = 240$ mm, and the total height of Beam C is h . Ribs are added at the loading point to avoid local buckling of GFRP I-profile.

In the loading test of Beam A, the concrete began to crack when it was loaded around 80 kN. At 100 kN, local buckling of the upper flange occurred. A strong fracture sound was heard at about 130 kN. Meanwhile, the buckling of the upper flange was increasing. Finally, when the load reached 133 kN, the beam slid off the support. In the loading test of Beam C, when a load of 90 kN was applied, micro cracks were generated at the bottom of the concrete slab, and the cracks were gradually visible as the load increased. At 250 kN, the tension cracks at the bottom of the concrete slab were obvious; when the load reached 292 kN, the concrete slab failed in the shear zone, while two-thirds of the concrete slabs were debonded with GFRP.

Finite Element Model

The tested beams with the concrete slab, GFRP profile, and adhesive layer between concrete and GFRP are all modeled as different elements in Abaqus. The web and flange of GFRP I-beam are discretized into spatial shell elements (S4R). Considering the anisotropy and softening behavior of pultruded GFRP laminates, the stiffness degradation model based on Hashin failure criteria proposed in **Section 2** is implemented by using VUMAT models in Abaqus. In order to simulate the debonding and slipping of the concrete-to-GFRP

interface, the interface elements (COH3D8) with zero-thickness by using the bilinear cohesive model are set between the bottom of the concrete slab and the upper flange of the GFRP I-beam. The concrete slab of the composite beam, Beam C, is modeled with linear solid elements (C3D8R), and the plastic damage constitutive model in terms of tensile and compressive damage factors proposed by Oller S, et al. (Oller et al., 1990) is used to simulate the stiffness degradation.

To take into account the contribution of shear deformation to the deflection of the beam, the shear modulus of GFRP, $G_{12} = G_{13} = 2800$ MPa, is obtained from the numerical simulation according to the load–displacement response of Beam C.

Obaidat et al. (Obaidat et al., 2010) showed that when CFRP is used for reinforcement, whether the material anisotropy of CFRP was considered or not, it had no significant effect on the results. Therefore, the CFRP reinforcement at the bottom of Beam A is assumed to be isotropic with a modulus of elasticity of 150 GPa. In addition, according to the loading test of Beam A, no damage was observed at the interface of CFRP and CFRP, so GFRP was bound to CFRP in the numerical simulation.

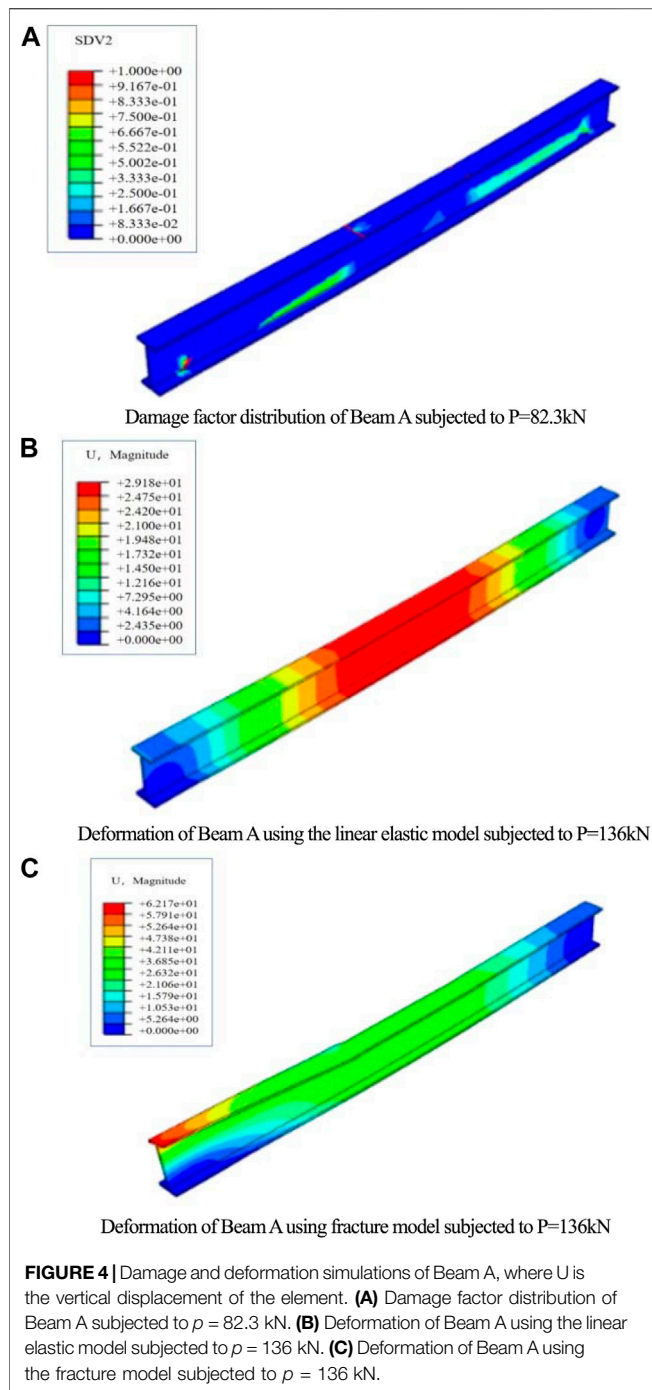
Numerical Simulation of the Testing Beams

The results of the experimental tests and FE models are shown in **Figure 3** and **Table 2**. In general, the numerical simulations are in good agreement with the experimental tests when considering the softening of GFRP and the bond–slip at the adhesive interface of the composite beam. For the pure GFRP beam, Beam A, the numerical simulations by using the elastic model and fracture model for GFRP are all consistent with the experimental results at the initial stage. As the load increased, the results using the elastic model for GFRP separated from the test result. On the other hand, considering the damage of GFRP and by using the fracture model, the slope of the load–displacement curve decreases slowly, which is still consistent with the experimental phenomenon. It can be seen from **Table 2** that when considering the fracture of the GFRP matrix, the relative error of the ultimate load and mid-span deflection with the test results is less than 4%. When ignoring the softening of GFRP, the numerical analysis will overestimate the ultimate load by 23.3% and the mid-span deflection is 7.4% higher than the test results.

Comparing the load–displacement curves for Beam A and Beam C, the flexural stiffness and ultimate load of the beam can be significantly improved by assembling the concrete slabs on the GFRP I-beam. The increase in ultimate load is even around 105%. Neglecting the softening of GFRP, the numerical analysis will overestimate the ultimate

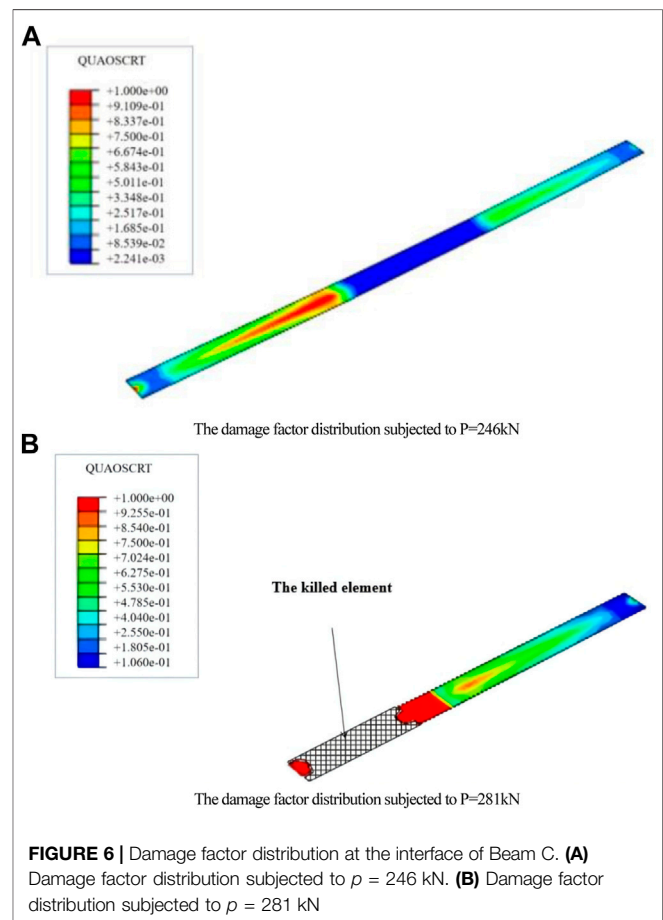
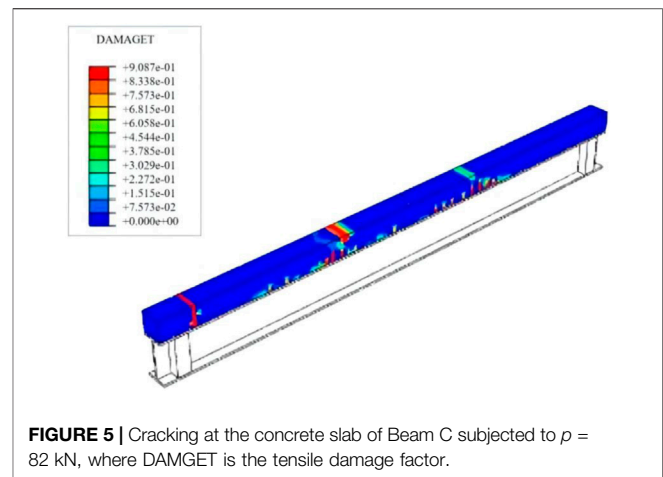
TABLE 2 | Comparison of FE results with experimental tests.

Beam A		Ultimate load/kN	Deflection/mm	Beam C		Ultimate load/kN	Deflection/mm
Test results		133	33.8	Test results		292	23.4
FE results	GFRPLinear elastic model	164 (23.3%)	36.3 (7.4%)	FE results	No bond–slip and GFRP damage	331 (13.4%)	28.8 (23.1%)
	GFRPFracture model using Hashin failure criteria	137 (3%)	34.7 (2.7%)		Considering bond–slip and GFRP damage	281 (3.8%)	24.2 (3.4%)

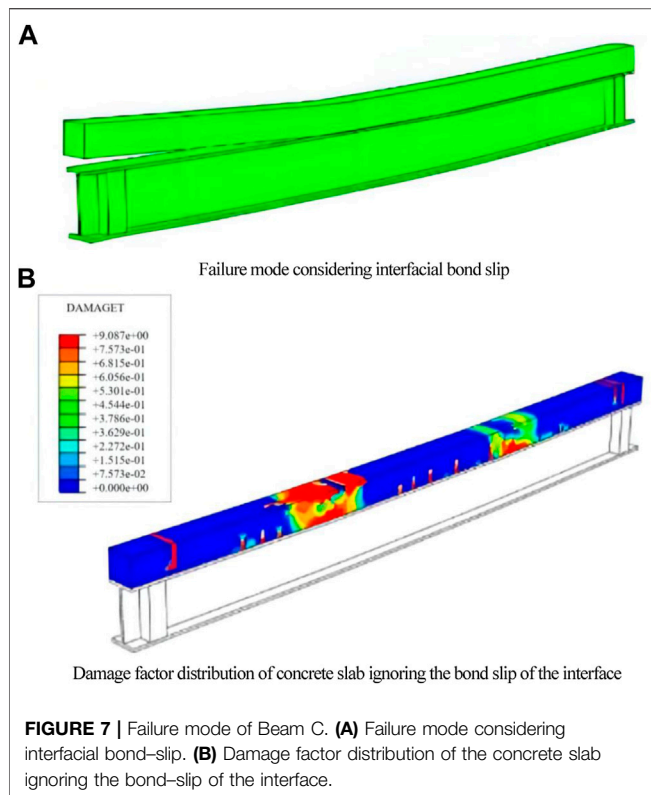


load with less effect on the stiffness of the beam. However, ignoring the bond-slip at the interface of the composite beam, Beam C, will overestimate the stiffness of the structure. According to Table 2, the relative error of the mid-span deflection is about 23.1%.

The damaged nephogram of the pure GFRP I-beam (Beam A) is shown in Figure 4A, where SDV2 is the compressive damage factor of the fiber matrix. The numerical analysis shows that the failure mechanism of Beam A is the buckling of the web and



upper flange of the GFRP I-profile. The analysis also illustrates that the bottom of the web at middle span of the shear zone of Beam A was in tension when the beam was loaded up to 82.3 kN, and the stress concentration took place at the loading point while the matrix of GFRP was cracking. This is why in the experimental tests, Beam A made a “split” sound when the beam was loaded to about 80 kN. The simulation results are consistent with the



experimental phenomenon, that is, when the beam was loaded to about 80 kN, buckling occurred at the GFRP flange.

Figures 4B,C clarify the influence of the nonlinear damage of GFRP on the deformation of Beam A. When approaching the ultimate load, it can be observed that the deformation of the beam with the considered material damage is no longer symmetric, and local buckling occurs at the loading point, while the deformation of the beam under the linear elastic models remains symmetrical. It can be seen from **Figures 3, 4** that the wooden ribs on the beam web strengthen the beam stiffness, resulting in the load still increasing after the upper flange of Beam A buckled.

The numerical analysis of Beam C shows that the micro-cracks appear first at the bottom of the concrete slab in the bending area and support area. As the load increases, concrete cracks continue to expand, as shown in **Figure 5**. However, few matrix damage of the GFRP web is found in the shear span, which has little effect on the bending stiffness of the composite beam. **Figure 6** shows the damage factor distribution at the interface of Beam C where “QUAOSCRT” represents the quadratic traction damage initiation criterion for cohesive surfaces. It can be seen that the interface damage starts from the end of the shearing spans and extends to the mid-span of the beam. When the cracking energy at the interface is reached, the concrete slab and the GFRP flange debonded. The debonding process is simulated using the element killing technology. During the nonlinear analysis, the adhesive element at the interface will be killed when its strain energy met the fracture energy of the bilinear cohesive model. Then, the killed element is removed directly, and the FE model is renumbered. As shown in **Figures 6, 7A**, the debonding extends

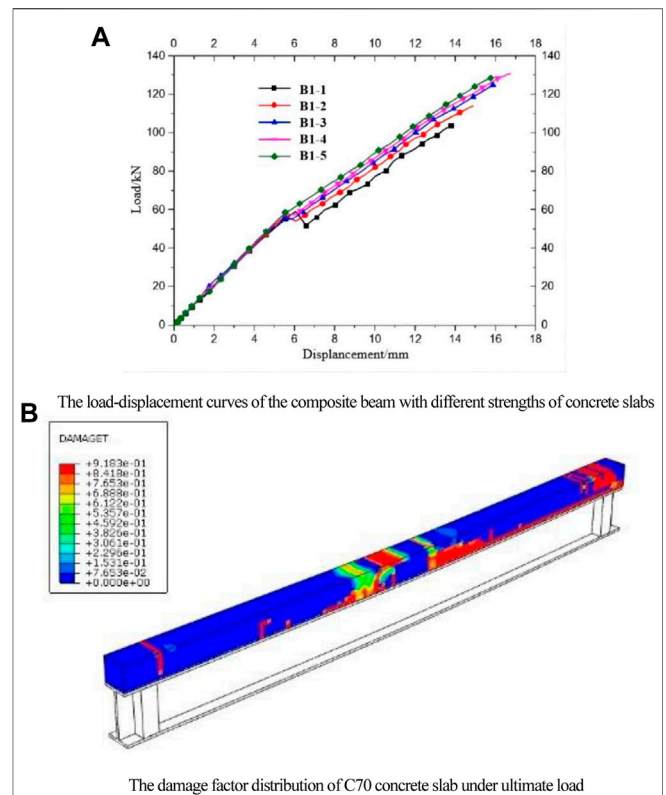


FIGURE 8 | Effect of concrete strength on the mechanical properties of the composite beam. **(A)** Load-displacement curves of the composite beam with different strengths of concrete slabs. **(B)** Damage factor distribution of the C70 concrete slab under ultimate load.

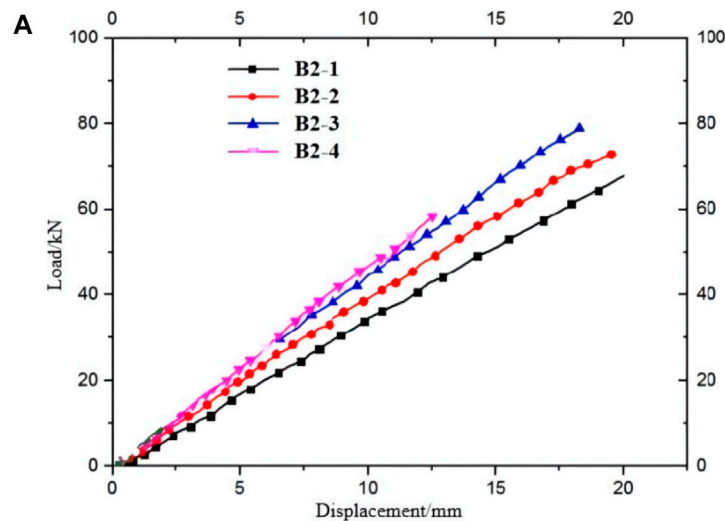
from the end of the concrete slab to the mid-span. The simulation results are consistent with the failure phenomena of composite beams observed by Nordin (**Figure 7** of Nordin, H., and Taeljsten, B., 2004).

Ignoring the interfacial bond-slip of the composite beam as well as the softening of GFRP, the damage factor distribution of the concrete slab is shown in **Figure 7B**. It can be seen that the shear failure occurred in the concrete slab eventually, and there is no debonding at the interface. The simulated result is different from the test.

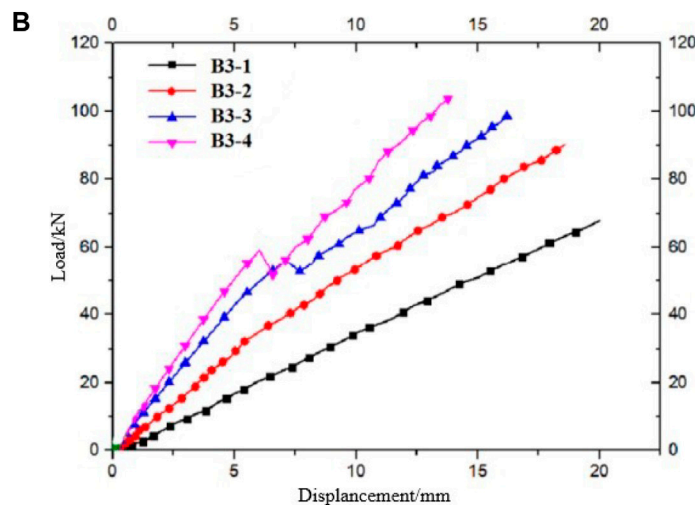
In conclusion, the softening and nonlinear damage of GFRP and the bond-slip of the interface have significant influence on the numerical simulation of concrete-GFRP composite beams. The good agreement between the aforementioned numerical analysis and the experimental tests indicates that the GFRP damage model used in this study based on the Hashin failure criterion and the cohesive element used for the concrete-to-GFRP interface can well simulate the mechanical properties of the concrete-GFRP composite beam.

PARAMETRIC ANALYSIS

The comparison between the numerical simulation and the experimental tests in **Section 4** has indicated the accuracy of



The load-displacement curves of the composite beam with different concrete slab thicknesses



The load-displacement curves of composite beams with different width ratio

FIGURE 9 | Effects of the width ratio and thicknesses of the concrete slab on the load performance of the composite beam. **(A)** Load–displacement curves of the composite beam with different concrete slab thicknesses. **(B)** Load–displacement curves of composite beams with different width ratios.

the finite element models for the composite beam. The parametric analysis, including the effects of the strength and thickness of the concrete slab, the width ratio of the concrete slab to the GFRP flange, the shear-span ratio of the composite beam, and the GFRP web height are further analyzed to provide basis for the design of the composite beam. The diagram of the composite beam for parametric analysis is similar to **Figure 2**.

Concrete Strength

A total of five concrete slabs with different compressive strengths of C30 (B1-1), C40 (B1-2), C50 (B1-3), C60 (B1-

4), and C70 (B1-5) are selected to analyze the effect of concrete strength on the mechanical properties of the composite beam, and the results are represented in **Figure 8**. The numerical results show that the increasing of the strength of the concrete slab has a limited influence on the stiffness and ultimate load of composite beams, as shown in **Figure 8A**. When having a low concrete strength, such as B1-1 with C30 and B1-2 with C40, the bonding stress at the interface between the concrete slab and GFRP flange leads to the bending failure of the concrete slab. Cracking at the bottom of the concrete slab results in an inflection point in the load–displacement curve. However, high compressive

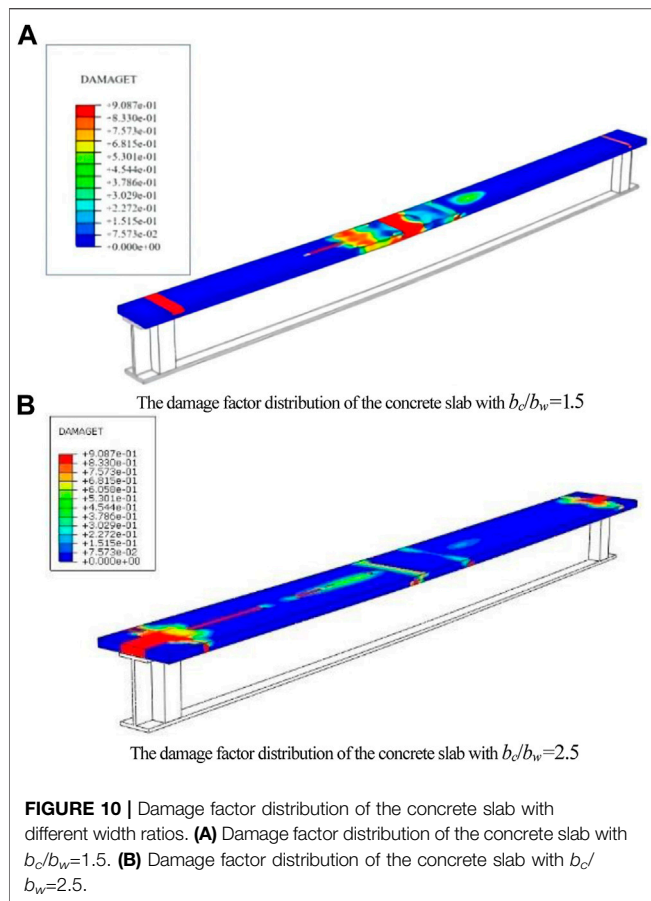


FIGURE 10 | Damage factor distribution of the concrete slab with different width ratios. **(A)** Damage factor distribution of the concrete slab with $b_c/b_w = 1.5$. **(B)** Damage factor distribution of the concrete slab with $b_c/b_w = 2.5$.

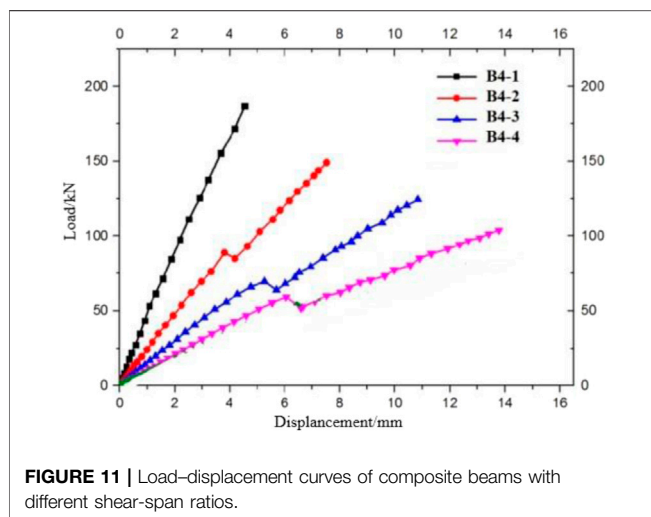


FIGURE 11 | Load-displacement curves of composite beams with different shear-span ratios.

strength may change the failure mode of composite beams, as shown in **Figure 8B**. When the strength of concrete is too high, such as C70, the concrete slab will undergo longitudinal shear failure in the shear-span area. Consequently, the neutral axis of the beam will move up, thereby reducing the ultimate load of the composite beam.

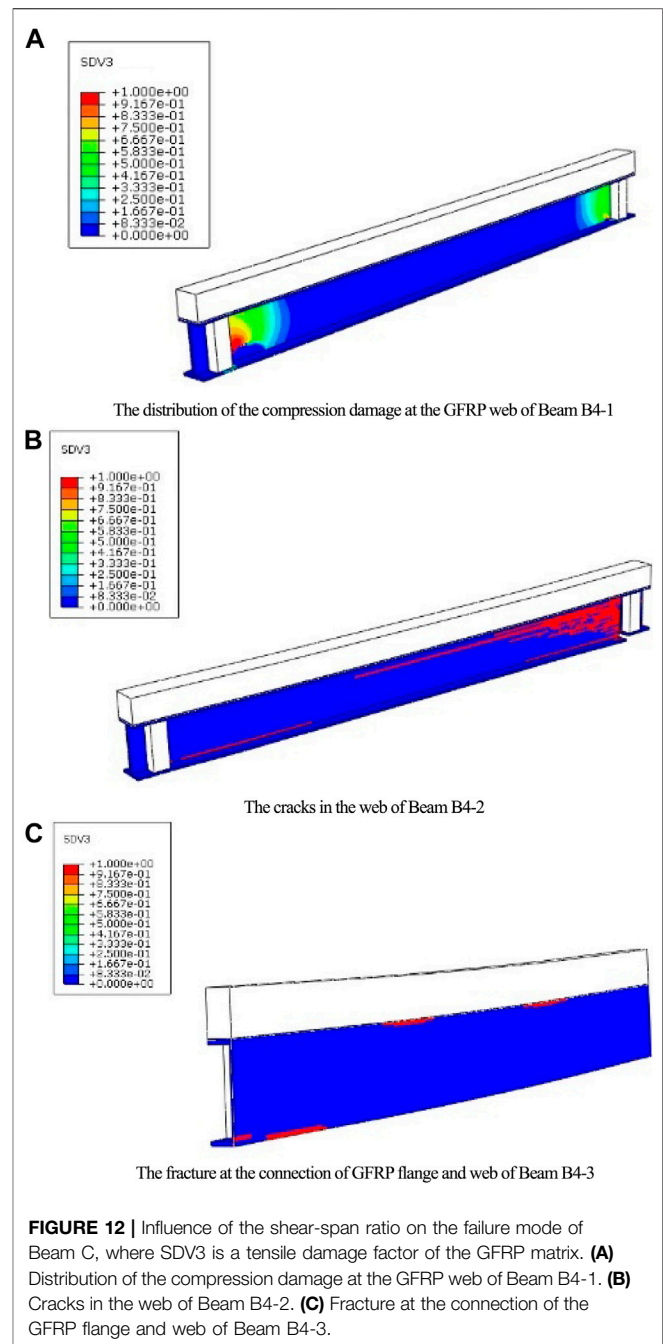


FIGURE 12 | Influence of the shear-span ratio on the failure mode of Beam C, where SDV3 is a tensile damage factor of the GFRP matrix. **(A)** Distribution of the compression damage at the GFRP web of Beam B4-1. **(B)** Cracks in the web of Beam B4-2. **(C)** Fracture at the connection of the GFRP flange and web of Beam B4-3.

Thickness of the Concrete Slab

The influence of the concrete slab thickness on the structural performance of the composite beam is shown in **Figure 9A**. In this figure, B2-1, 2, 3, and 4 represent slabs with thicknesses of 30, 60, 90, and 115 mm, respectively. It can be found that the thickness of the concrete slab has a significant impact on the flexural stiffness and the ultimate load of the composite beam comparing to the slab strength. In general, the load capacity increases with the thickness of the concrete slab. However, when the thickness of concrete is too large, such as B2-4 being 115 mm, the neutral axis of the cross section will move up to the concrete slab, resulting in the tension

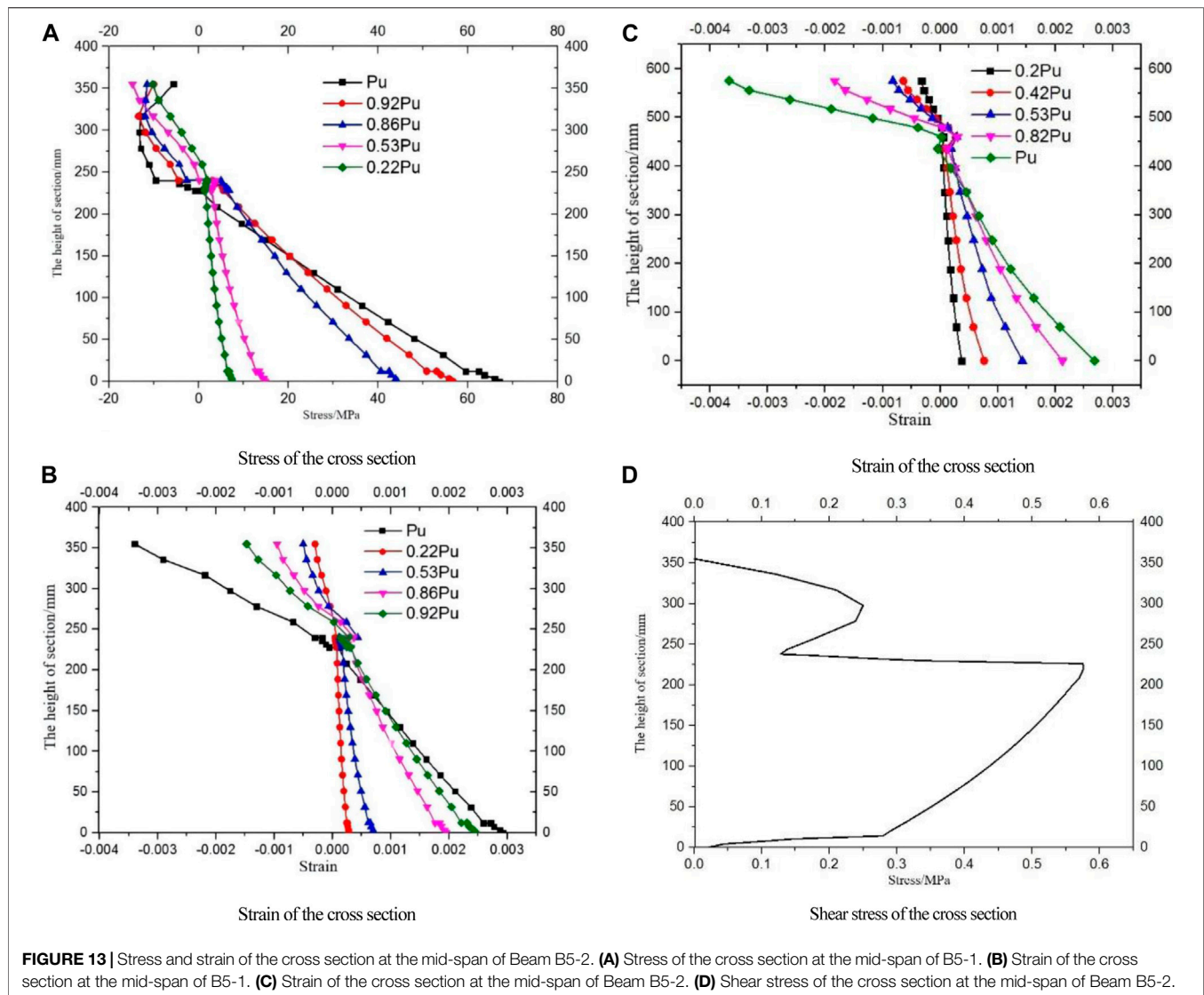


FIGURE 13 | Stress and strain of the cross section at the mid-span of Beam B5-2. **(A)** Stress of the cross section at the mid-span of B5-1. **(B)** Strain of the cross section at the mid-span of B5-1. **(C)** Strain of the cross section at the mid-span of Beam B5-2. **(D)** Shear stress of the cross section at the mid-span of Beam B5-2.

cracks in the slab. As a result, the bearing capacity of the composite beam is greatly reduced.

Width Ratio of the Concrete Slab to GFRP Flange

The influence of the width ratio of the concrete slab to the GFRP flange, b_c/b_w , on ultimate load is also investigated and shown in **Figure 9B**, where the values of b_c/b_w are 1, 1.5, 2, and 2.5 for B3-1, B3-2, 2 B3-3, and B3-4, respectively.

In **Figure 9B**, it can be seen that if $b_c/b_w \leq 2$, as the width ratio increases, the ultimate load and flexural stiffness of composite beams increase. As shown in **Figure 10A**, the flexural failure of the composite beams can be observed, that is similar to that of over-reinforced beams. If $b_c/b_w > 2$, as shown in **Figure 10B**, the transverse shear failure takes place on the concrete slab near the support area, and longitudinal shear failure can be found in the shear span. Compared with the width ratio $b_c/b_w = 2$, the ultimate load is reduced by about 7% when $b_c/b_w = 2.5$. It

can be concluded that the width ratio of the concrete slab to GFRP flange should be controlled within a reasonable range.

Shear-Span Ratio

The influence of shear-span ratio on the performance of the composite beams is also analyzed by varying the position of loading point a . The results are illustrated in **Figure 11**. In this figure, B4-1, 2, 3, and 4 represent the shear-span ratios of 0.84, 1.69, 2.52, and 3.36, respectively. It can be found that the ultimate loads of the composite beams decrease with the increase of the shear-span ratio, and there are inflexion points in all load-displacement curves, which express the first bending crack in the concrete slab.

As shown in **Figure 12**, when the composite beams reach the ultimate load, the concrete at the loading point is crushed. With the increase of the shear-span ratio, the failure mode of the composite beam changes from shear failure to bending failure. When the shear-span ratio is 0.84 (B4-1), the concrete slab suffers shear failure, and GFRP webs crack at the supports, as shown in **Figure 12A**. When the

shear-span ratio is 1.69 (B4-2), the composite beam undergoes interlaminar shear failure on the GFRP web, as shown in **Figure 12B**. Since the shear performance of the GFRP web is crucial for composite beams, it is beneficial in practice to strengthen the web by adding GFRP sheets along the web diagonal. According to **Figure 12C**, the increase of the shear-span ratio (B4-3) leads to the stress concentration at the connection between the flange and the web of the GFRP I-beam, resulting in the damage of the GFRP matrix in this area. This analysis explains why a continuous sound was heard in the GFRP profile when the load was close to the ultimate value during the experimental test. The sound was caused by the GFRP matrix fracture.

GFRP Web Height

Keeping the thickness of the concrete slab constant, such as 115 mm, the effect of the height of the GFRP web was investigated. The results are shown in **Figure 13**, where B5-1 and B5-2 are the composite beams with the web height of 276 and 336 mm, respectively. When the height of the GFRP I-beam web is small, such as B5-1 is 276 mm, with the increase of the load, the concrete slab gradually enters the plasticity, and the neutral axis of the section moves down. In addition, the stress distribution of the concrete slab is changing from linear to rectangular. At the same time, the bond-slip at the interface between the concrete slab and the GFRP flange causes the inflection points in both the stress and strain curves in **Figure 13**. Moreover, from **Figure 13B**, it can be inferred that the bending of the concrete slab is similar to that of the GFRP I-profile since the slope of the strain curve on the upper side of the deflection point is close to the lower side. This means that the plane section assumption of the Bernoulli-Euler beam is available for the composite beam with a small web height.

In contrast, the stress-strain distribution of the mid-span section of B5-2 with a web height of 336 mm is quite different from that of B5-1. As shown in **Figure 13C**, the curvature of the concrete slab is much larger than that of the GFRP I profile, and the plane section assumption no longer applies. As can be seen from **Figure 13D**, the web of the GFRP I-profile bears most of the shear stress of the entire section. Considering the height of the GFRP web, the additional deflection caused by shear deformation cannot be ignored. In addition, large shear stress will lead to shear failure of the GFRP web. As the shear stress increases, the GFRP web starts to crack from the left end of the support, and the crack expands from the edge of the beam to the mid-span of the beam. The composite beam is damaged due to the shear failure of the web, as shown in **Figure 1A** in Appendix.

CONCLUSION

A comprehensive FE model was proposed to investigate the structural behavior of concrete-GFRP composite I-beam. The Hashin failure criteria was used regarding the fracture and delamination of the pultruded GFRP matrix, and the bilinear cohesive model was adopted considering the bond-slip behavior of the interface between the concrete slab and the GFRP flange. The main conclusions can be drawn as follows:

- 1) The nonlinearities of GFRP and the interface have essential effects on the structural performance of composite beams. The

results when considering GFRP as a linear material do not agree with the experimental tests. However, the anisotropy softening and fracture procession of pultruded GFRP and the bond-slip behavior analysis of the concrete-to-GFRP interface developed in this article can effectively simulate the damage of GFRP and the degradation of adhesive interface.

- 2) Compared with concrete strength, increasing the thickness and width of the concrete slab can significantly improve the stiffness and ultimate load of composite beams. However, when the thickness and width of the concrete slab are too large, the slab will suffer shear failure, thereby reducing the bearing capacity of the composite beam. Therefore, reinforcement in the concrete slab should be considered in practical application.
- 3) When the shear-span ratio is small, the composite beams will be damaged by the shear failure of the concrete slab. As the shear-span ratio increases, the GFRP web is prone to cracking due to the weak interlaminar shear strength of the GFRP matrix. Therefore, it is recommended to improve the strength of the beam by reinforcing the GFRP web.
- 4) The height of the web has a significant influence on the shear stress distribution and deformation of the composite beam. The composite beam with smaller height can be considered satisfying the plane-section assumption. While, for beams with large height, the assumption is not applicable, and the additional deflection caused by shear deformation must be considered.

In summary, the numerical studies here have shown that the structural behavior of concrete-GFRP composite beams is related to the nonlinearity of pultruded GFRP and adhesive materials as well as the geometric parameters of the composite section and deserves further study. More experimental tests and comparisons with the numerical results are needed to improve the practical design accuracy of GFRP composite beams.

DATA AVAILABILITY STATEMENT

The raw data supporting the conclusion of this article will be made available by the authors, without undue reservation.

AUTHOR CONTRIBUTIONS

The authors confirm contribution to the article as follows: ZC and XZ: study conception and design; ZC and JX: analysis and interpretation of results; ZC and QL: formula derivation and programming and ZC and XZ: draft manuscript preparation. All authors reviewed the results and approved the final version of the manuscript.

FUNDING

This research was supported by the National Key R and D Program of China (Grant No. 2021YFF0500804).

REFERENCES

- Alnahhal, W., Aref, A., and Alampalli, S. (2008). Composite Behavior of Hybrid Frp-concrete Bridge Decks on Steel Girders. *Compos. Structures* 84 (1), 29–43. doi:10.1016/j.compstruct.2007.06.005
- Blackman, B., Hadavinia, H., Kinloch, A. J., and Williams, J. G. (2003). The Use of a Cohesive Zone Model to Study the Fracture of Fiber Composites and Adhesively-Bonded Joints. *Int. J. Fracture* 119 (1), 25–46. doi:10.1023/A:1023998013255
- Borowicz, D. T., and Bank, L. C. (2009). Behavior of Pultruded Fiber-Reinforced Polymer (FRP) Beams Subjected to Concentrated Loads in the Plane of the Web. *Second Official International Conference of International Institute for FRP in Construction for Asia-Pacific Region*, 13–18. Seoul.
- Borowicz, D. T., and Bank, L. C. (2011). Behavior of Pultruded Fiber-Reinforced Polymer Beams Subjected to Concentrated Loads in the Plane of the Web. *J. Composites Construction* 15 (2), 229–238. doi:10.1061/(ASCE)CC.1943-5614.0000082
- Chen, Z., Wei, C., and Luo, Q. (2019). Analysis on Mechanical Properties of FRP Retrofitted concrete Beam-Column Structure Using Cohesive Model[J]. *J. Building Structures* 201940 (09), 122–130.
- Correia, J. R., Branco, F. A., and Ferreira, J. G. (2007). Flexural Behaviour of GFRP-concrete Hybrid Beams with Interconnection Slip. *Compos. Structures* 77 (1), 66–78. doi:10.1016/j.compstruct.2005.06.003
- El-Hacha, R., and Chen, D. (2012). Behaviour of Hybrid FRP-UHPC Beams Subjected to Static Flexural Loading. *Composites B: Eng.* doi:10.1016/j.compositesb.2011.07.004
- Feng, D., and Aymerich, F. (2014). Finite Element Modelling of Damage Induced by Low-Velocity Impact on Composite Laminates. *Compos. Structures* 108 (feb.), 161–171. doi:10.1016/j.compstruct.2013.09.004
- Gand, A. K., Chan, T.-M., and Mottram, J. T. (2013). Civil and Structural Engineering Applications, Recent Trends, Research and Developments on Pultruded Fiber Reinforced Polymer Closed Sections: a Review. *Front. Struct. Civ. Eng.* 7 (3), 227–244. doi:10.1007/s11709-013-0216-8
- Gonilha, J. A., Aquino, A., Correia, J. R., and Branco, F. A. (2010). *Experimental Evaluation of the GFRP/ECC Connection – Shear Connection Tests: Phase 1. ICIST Internal Project Report A5.T4.IST.1*. Nanjing, China: Instituto Superior Técnico, Technical University of Lisbon.
- Hashin, Z. (1980). Fatigue Failure Criteria for Unidirectional Fiber Composites. *J. Appl. Mech.* 47. doi:10.1115/1.3153664
- Hashin, Z., and Rotem, A. (1973). A Fatigue Failure Criterion for Fiber Reinforced Materials. *J. Compos. Mater.* 7 (4), 448–464. doi:10.1177/002199837300700404
- Hongliang, T., Xiaoping, M. A., Zhixian, L. U., Aeronautics, S. O., University, N. P., and University, N. P. (2018). A Model for Low Velocity Impact Damage Analysis of Composite Laminates Based on Continuum Damage Mechanics. *Acta Materiae Compositae Sinica*. doi:10.13801/j.cnki.fhclxb.20180103.001
- Keller, T. (2001). Recent All-Composite and Hybrid Fiber-Reinforced Polymer Bridges and Buildings. *Prog. Struct. Eng. Mater.* 3. doi:10.1002/pse.66
- Kong, S. Y., Yang, X., and Lee, Z. Y. (2018). Mechanical Performance and Numerical Simulation of GFRP-concrete Composite Panel with Circular Hollow Connectors and Epoxy Adhesion. *Construction Building Mater.* 184 (SEP.30), 643–654. doi:10.1016/j.conbuildmat.2018.07.008
- Neagoe, C. A., Lluís, P., Marco, L., and Pérez, M. A. (2015). Experimental Study of GFRP-concrete Hybrid Beams with Low Degree of Shear Connection. *Construction Building Mater.* 101 (Dec.30 Pt.1), 141–151. doi:10.1016/j.conbuildmat.2015.10.024
- Nordin, H., and Täljsten, B. (2004). Testing of Hybrid FRP Composite Beams in Bending. *Composites Part B: Eng.* 35 (1), 27–33. doi:10.1016/j.compositesb.2003.08.010
- Obaidat, Y. T., Heyden, S., and Dahlblom, O. (2010). The Effect of CFRP and CFRP/concrete Interface Models when Modelling Retrofitted RC Beams with Fem. *Compos. Structures* 92 (6), 1391–1398. doi:10.1016/j.compstruct.2009.11.008
- Oller, S., Onate, E., Oliver, J., and Lubliner, J. (1990). Finite Element Nonlinear Analysis of concrete Structures Using a "Plastic-Damage Model". *Eng. Fracture Mech.* 35 (1-3), 219–231. doi:10.1016/0013-7944(90)90200-Z
- Tan, S. C. (2016). A Progressive Failure Model for Composite Laminates Containing Openings. *J. Compos. Mater.* doi:10.1177/002199839102500505
- Umberto, D. M., Fabrizio, G., Lorenzo, L., Paolo, N. B., and Andrea, P. (2021). An Investigation about Debonding Mechanisms in FRP-Strengthened RC Structural Elements by Using a Cohesive/volumetric Modeling Technique. *Theor. Appl. Fracture Mech.* 117. doi:10.1016/j.tafmec.2021.103199
- Wang, J. (2006). Cohesive Zone Model of Intermediate Crack-Induced Debonding of Frp-Plated concrete Beam. *Int. J. Sol. Structures* 43 (21), 6630–6648. doi:10.1016/j.ijsolstr.2006.01.013
- Wang, J., Zou, X., and Feng, Y. (2015). Bilinear Load-Deflection Model of Fiber-Reinforced Polymer-concrete Composite Beam with Interface Slip. *Adv. Mech. Eng.* 7 (7), 1687814015590312. doi:10.1177/1687814015590312
- Yuan, J. S., and Hadi, M. N. S. (2017). Bond-slip Behaviour between GFRP I-Section and concrete. *Composites Part B: Eng.* 130 (dec.), 76–89. doi:10.1016/j.compositesb.2017.07.060
- Zou, X., Feng, P., and Wang, Ji. (2018). Bolted Shear Connection of FRP-concrete Hybrid Beams. *J. Composites Construction*. doi:10.1061/(asce)cc.1943-5614.0000845

Conflict of Interest: The authors declare that the research was conducted in the absence of any commercial or financial relationships that could be construed as a potential conflict of interest.

Publisher's Note: All claims expressed in this article are solely those of the authors and do not necessarily represent those of their affiliated organizations, or those of the publisher, the editors, and the reviewers. Any product that may be evaluated in this article, or claim that may be made by its manufacturer, is not guaranteed or endorsed by the publisher.

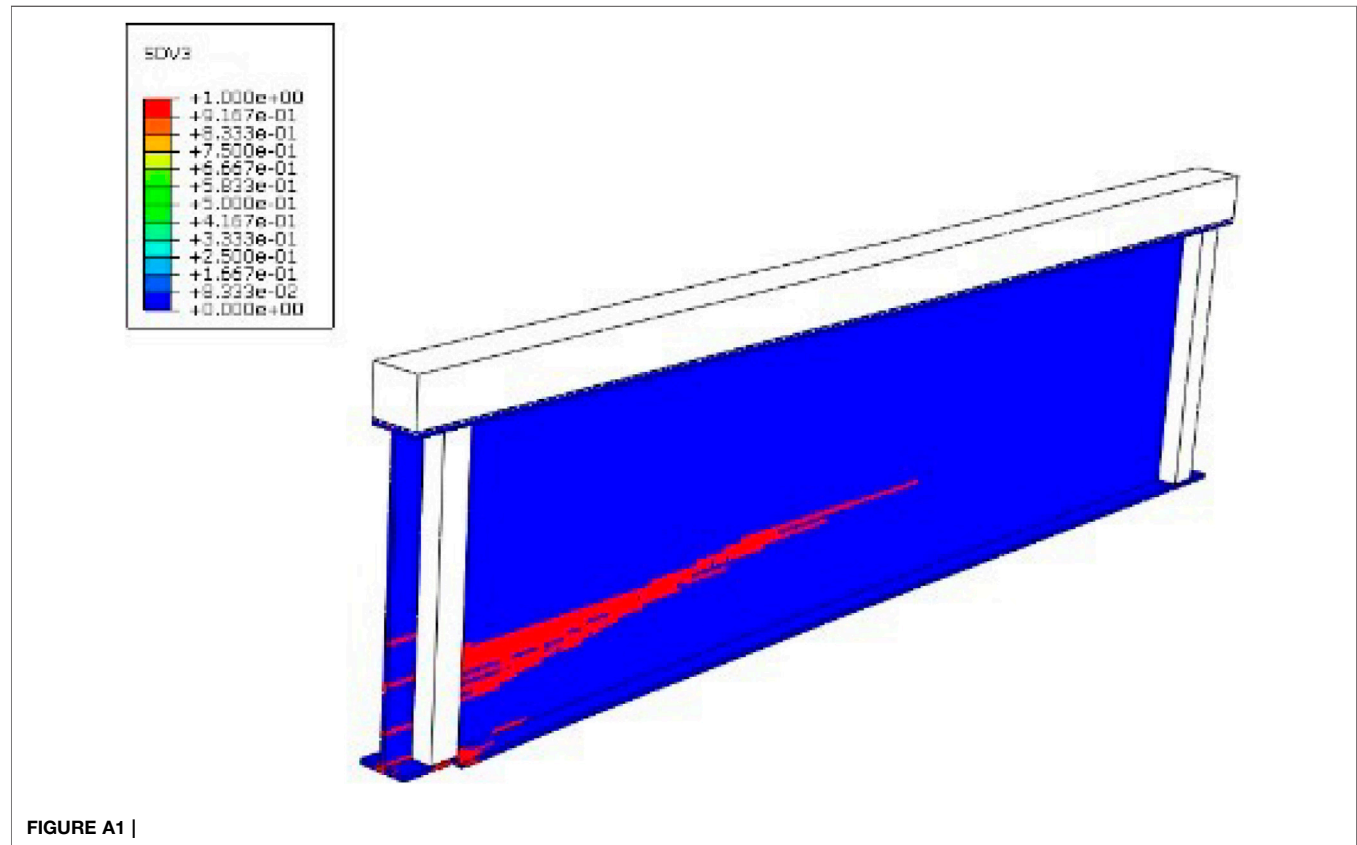
Copyright © 2022 Chen, Xing, Luo and Zhang. This is an open-access article distributed under the terms of the Creative Commons Attribution License (CC BY). The use, distribution or reproduction in other forums is permitted, provided the original author(s) and the copyright owner(s) are credited and that the original publication in this journal is cited, in accordance with accepted academic practice. No use, distribution or reproduction is permitted which does not comply with these terms.

APPENDIX A

TABLE A1: Elastic modulus and strength of the pultruded GFRP profile for the test beam.

FIGURE A1: Shear failure at the GFRP web of Beam B5-2.

E_1/GPa	$E_2 = E_3/\text{GPa}$	$G_{12} = G_{13}/\text{GPa}$	G_{23}/GPa	$\mu_{12} = \mu_{13}$	μ_{23}	f_{1t}/MPa	f_{1c}/MPa	f_{2t}/MPa	f_{2c}/MPa	S_{23}/MPa	S_{12}/MPa	S_{13}/MPa
23	8.5	2.8	1	0.18	0.25	240	180	50	30	20	30	30





Research on the Bonding Performance of UHPC–NC Interfaces With Different Sizes of Grooves

Jun Yang^{1,2}, Junrun Xia¹, Chongsheng Cheng¹, Jieyun Wang^{2*}, Jie Zhang³ and Gang Wang⁴

¹State Key Laboratory of Mountain Bridge and Tunnel Engineering, Chongqing Jiaotong University, Chongqing, China, ²Guangxi Communications Investment Group Corporation Ltd, Nanning, China, ³Guizhou Provincial Highway Bureau, Guizhou, China, ⁴Transportation Bureau of Tian Men City, Hubei, China

OPEN ACCESS

Edited by:

Xijun Shi,
Texas State University, United States

Reviewed by:

Shao-Bo Kang,
Chongqing University, China
Zehra Canan Girgin,
Yildiz Technical University, Turkey

*Correspondence:

Jieyun Wang
wangjywx@126.com

Specialty section:

This article was submitted to
Structural Materials,
a section of the journal
Frontiers in Materials

Received: 21 January 2022

Accepted: 28 February 2022

Published: 23 March 2022

Citation:

Yang J, Xia J, Cheng C, Wang J,
Zhang J and Wang G (2022) Research
on the Bonding Performance of
UHPC–NC Interfaces With Different
Sizes of Grooves.
Front. Mater. 9:859717.
doi: 10.3389/fmats.2022.859717

The interfacial treatment between normal concrete (NC) and ultra-high-performance concrete (UHPC) is crucial to ensure bonding strength. Grooving is an effective method to treat the UHPC–NC interface, but the shear properties and failure modes at the composite interface remain under-investigated. This study focuses on the bonding performance of different groove designs (width, spacing, and angle) at the UHPC–NC interface, and push-off tests with 15 specimens were carried out to evaluate the strength and stiffness. Furthermore, a finite element model (FEM) and calculation methods were validated with the experimental study to reveal the bonding strength, and a parametric study on the groove depth was also carried out. The interface treated by grooves increases 3.32 and 2.48 times in strength and stiffness compared with specimens bonded by epoxy resin adhesive. The results also show that failing at the interface and NC matrix made up a majority of the failure modes. The shear strength of the UHPC–NC interface increased with the width and decreased with the space between the grooves. Grooves with 10 mm width, 100 mm space, 25 mm depth, and right angle were recommended. This paper will lay a foundation for the surface preparation of UHPC strengthening NC bridges.

Keywords: bridge engineering, UHPC, bonding strength, bonding stiffness, grooved interface, finite element model

INTRODUCTION

Ultra-high-performance concrete (UHPC) is widely defined as a cement-based material with compressive strength of no less than 150 MPa and tensile strength of no less than 8 MPa (Yoo and Banthia, 2016; Li and Deng, 2021). In addition, UHPC exhibits long-term durability due to its great impermeability (Lian et al., 2021). The potential of using the cement-based material as a repair material for strengthening normal concrete (NC) bridges is promising (Feng et al., 2020; Qin et al., 2020; Zhang et al., 2021). For the concrete bridges strengthened by UHPC, the bonding performance of the UHPC–NC interface is critical to ensure the efficiency (Murthy et al., 2018; Yang et al., 2019). The literature showed that more than 50% of structures failed due to interfacial cracking after repair or reinforcement (Li, 2004). Thus, it is essential to utilize UHPC and NC together to delay cracking at the interface (Al-Osta et al., 2017; Tong et al., 2021).

Currently, many researchers have paid attention to the interfacial behaviors of UHPC and NC. Harris et al. (2011) studied the bonding performance applying varying stress configurations and environmental conditions. The roughness of concrete substrates, bonding age, freeze–thaw cycles, and the wetting conditions of the concrete substrate were considered. The results showed that the interfacial bonding between UHPC and NC exhibited good mechanical properties as the bonding

strength could be 69%–117% of the tensile strength of the NC substrate. Lee et al. (2007) evaluated the bonding durability between UHPC and NC using grooving through accelerated aging tests. Notably, the UHPC–NC interface had a relatively higher performance than the NC–NC interface during slant shear and pull-out tests. Hussein et al. (2016) and Hussein et al. (2017) researched the adhesion and friction of the UHPC–NC interface with different interfacial roughness, and the tensile strength and friction coefficient of the bonded interface were obtained. Moreover, they established a traction-separation model widely used in simulating the bond behaviors in the UHPC–NC composite structures (Zhu et al., 2020; Zhu et al., 2021). Tayeh et al. (2012) and Tayeh et al. (2013) carried out shear tests and tensile splitting tests to study the bonding ability between UHPC and NC. The test results showed that UHPC improves the microstructure of the transition zone, thus enhancing the bonding strength between the NC substrate and UHPC. To sum up, the good impermeability of the interface can significantly prolong the service life of the repaired structure. Most research focuses on the shear properties and failure modes of the UHPC–NC interfaces using different interfacial treatments.

Previous studies had shown that the shear strength increased greatly after grooved treatment. Zhang et al. (2020a) and Zhang et al. (2020b) applied 10 mm and 20 mm grooves for surface treatment, and it was found that the shear strength of the NC matrix with different strengths can be improved. Besides, the specimens showed significant ductility. The bearing capacity and ductility of the grooved interface were slightly lower than those of the interface with embedded studs. Wu and Zhang (2018) researched the bonding performance between the precast ultra-high-performance concrete repair layer and existing concrete. It is recommended that grooving is an effective way, before repairing, to make the interface in the state of shearing. Jiang et al. (2020) and Jiang et al. (2021) compared the vertical groove, groove formed by high-pressure water, and different depths. It was found that the interlocking effect of aggregates produced by the groove can improve the shear strength, and 20 mm depth showed better performance compared with 10 mm and 30 mm. Ganesh and Murthy (2020) predicted the maximum failure load by the numerical method through oblique shear, splitting tensile, and four-point bending tests. The research shows that the interface with grooves presented a uniform and good mechanical performance. The interface strength can be predicted by the relationship between stress and crack width. Guan et al. (2021) evaluated the interfacial shear performance between UHPC and NC. Dimensions of the grooves and the effect of dowel rebar were considered. The UHPC–NC interface with a depth of 10 mm groove had the best mechanical performance if no dowel rebar was applied. Larger grooves had higher shear resistances due to the interlocking effect. In sum, grooving is a common treatment method for the interface connection between NC and UHPC, which can significantly improve the shear strength and slip of the interface. Its specific shapes, sizes, and spaces can still be further optimized. However, failure mechanisms, numerical simulation, and calculation methods need to be further explored.

In view of the limited research on the mechanisms and shapes of grooves between UHPC and NC, this paper carried out the push-off experiment (EXP). Different widths (10 mm, 20 mm,

and 30 mm), spaces (50 mm, 75 mm, and 100 mm), and angles (-11° , 0° , and 11°) were considered. By comparing UHPC–NC bonded by epoxy resin adhesive, the influence on interface strength and stiffness with various shapes was discussed, and a recommended groove size was obtained. In addition, the finite element model (FEM) was established using the concrete damaged plasticity (CDP) model and then validated with the strength–slip curves obtained from the EXP. Calculation methods to obtain the strength of interface were provided. After that, a parametric analysis for different depths was conducted. The results can support the interface treatment of NC structures before repairing with UHPC.

EXPERIMENTAL PROGRAM

Description of Specimens

In order to explore the bonding performance of the UHPC–NC interface with grooves, Z-shaped specimens were selected for the push-off experiment. The design of specimens refers to the study by Wu and Zhang (2018). The pressure area is $100 \times 100 \text{ mm}^2$, the interfacial bonding area is $200 \times 100 \text{ mm}^2$, and detailed information is shown in **Figure 1**.

In this experiment, five groups of three specimens were designed, as shown in **Figure 1**. The depth of the groove is 10 mm, and the main parameters are shown in **Table 1**. The interfaces of the S5 group are bonded with epoxy resin adhesive, and the interfaces of the other four groups are treated with grooving. The groove width of the S1 group includes 10 mm, 20 mm, and 30 mm; the groove space of the S2 group includes 50 mm, 75 mm, and 100 mm. Different groove angles are considered in S3 and S4 groups. In addition, the width of the S3 group is 10 mm, and the width of the S4 group is 20 mm. After calculation, when the angle between the inclined edge of the trapezoidal groove and the normal direction of the bonding surface is less than 22° , the interfacial friction is greater than the tangential force along the inclined surface, which will prevent the interfacial slip in order to facilitate the fabrication of the specimens, and different angles including 11° , 0° , and -11° are chosen.

Epoxy resin adhesive is used for the S5 group as the bonding material. Its applicable temperature is -60°C to -120°C . The initial curing time is 2 h, and it gets completely cured after 24 h with shear strength $\geq 12 \text{ MPa}$.

Materials

The mix proportions of NC and UHPC are given in Supplementary **Table 1**. UHPC, which was mixed with flat steel fibers of 2% volume ratio, 8 mm length, and 0.12 mm diameter, was produced by Hunan Gu Li Engineering New Material Company, and the nominal tensile strength of the fiber was 2,700 MPa.

According to the relevant codes for concrete mechanical properties (GB/T 50081-2002 (2002) (Standard for Test Method of Mechanical Properties on Ordinary Concrete, 2002) for NC and GB/T 31387-2015 (2015) for UHPC, respectively) (Reactive Powder Concrete, 2015), the compressive strength of concrete was obtained by cubic specimens with dimensions of $150 \times 150 \times 150 \text{ mm}$ for NC

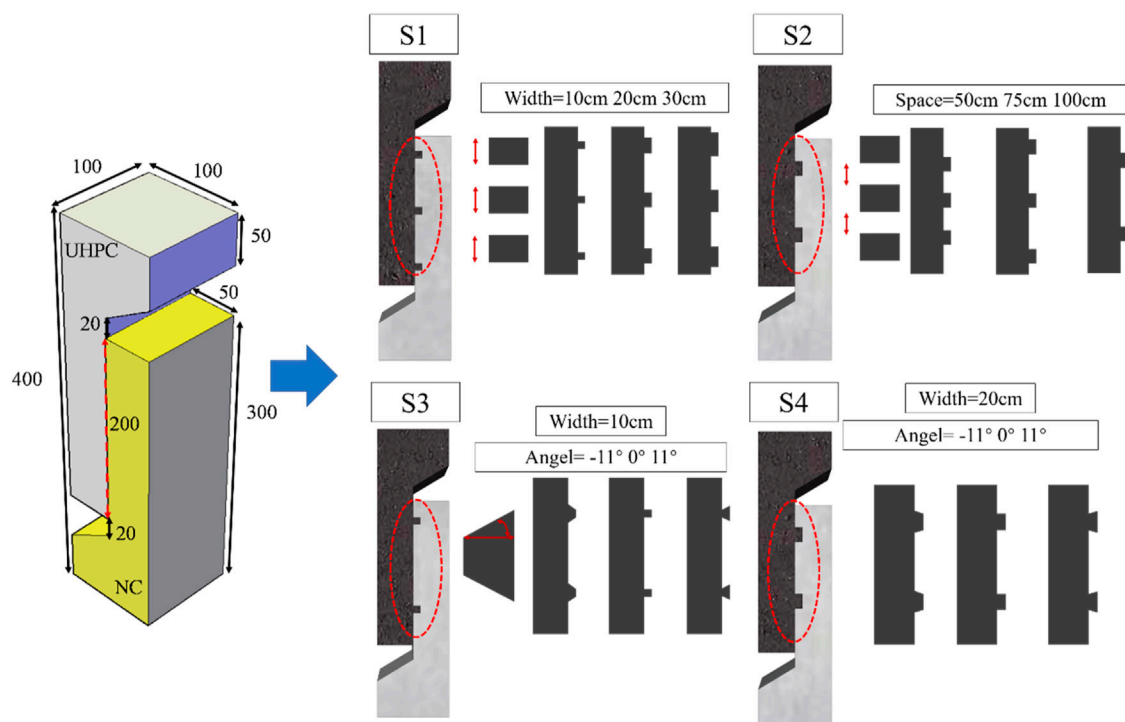


FIGURE 1 | Details of UHPC-NC push-off specimens.

TABLE 1 | Details of specimens.

Specimens	Numbers	Shape of the grooves		
		Width (mm)	Space (mm)	Angle (°)
S1	S1-1	10	75	0
	S1-2	20	75	0
	S1-3	30	75	0
S2	S2-1	20	50	0
	S2-2	20	75	0
	S2-3	20	100	0
S3	S3-1	10	100	-11
	S3-2	10	100	0
	S3-3	10	100	11
S4	S4-1	20	100	-11
	S4-2	20	100	0
	S4-3	20	100	11
S5	S5-1-3	Bonded by epoxy resin adhesive, S = 200 × 100 mm ²		

and 100 × 100 × 100 mm for UHPC. Prism specimens with dimensions of 150 × 150 × 300 mm for NC and 100 × 100 × 300 mm for UHPC were also fabricated to test the elastic modulus. All the mechanical properties are listed in **Table 2**. The stress-strain relationship of UHPC under compression and tension is provided in Supplementary **Figure 1**.

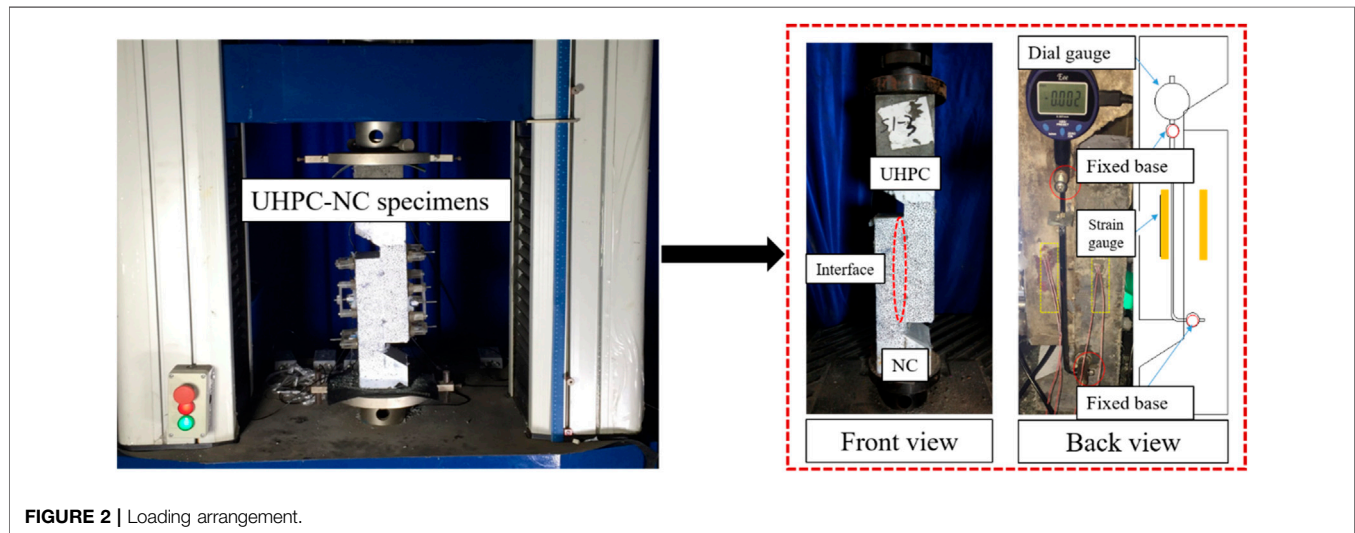
Mechanical Properties of NC and UHPC Manufacturing of the Specimens

The fabrication process of the specimens is shown in Supplementary **Figure 2**. The formwork was made

according to the design size (**Figure 2A**). After that, NC was poured into the formwork (**Figure 2B**). Twenty-eight days after the NC side was formed, the specimens were grooved with water cutting (**Figure 2C**). Then, the other side of the UHPC formwork was nailed to NC after cutting, and then the UHPC part was poured into it to finish the fabrication process (**Figure 2D**). In order to ensure the formwork can be fully and evenly filled with UHPC and enhance the bonding performance, the interface is kept wet during pouring UHPC. The formworks were removed after 24 h for normal temperature curing and steam-cured at 90°C

TABLE 2 | Mechanical properties of NC and UHPC.

Materials	Compressive strength (MPa)	Tensile strength (MPa)	Modulus of elasticity (MPa)
NC	42.5	2.3	32500
UHPC	145.1	7.6	47300

**FIGURE 2** | Loading arrangement.

for 48 h. After that, the specimens were allowed to cure for 7 days at normal temperature.

Loading Arrangement

The bond strength was measured using the single-side shear test method, as shown in **Figure 2**. All specimens were tested using the 200 kN MTS testing machine and preloaded with 5kN as the control load before formal loading. The loading was conducted at a rate of 6kN/min. When the crack or interface slip appeared, the loading transformed to control by displacement at 0.05 mm/min rate. The interfacial bonding strength was obtained by the MTS testing machine. A dial gauge was arranged at the back of the specimens to assist in measuring the bonding slip of the interface. This loading and test arrangement has been used by other researchers (Wu and Zhang, 2018).

FINITE ELEMENT MODELS

Commercial software ABAQUS was chosen to simulate the experiment. Considering that the loading rate of the experiment is slow, the standard (static general) solver is applied in ABAQUS. Detailed information on material properties, meshing, boundary conditions, and interactions is described in the following sections.

Constitutive Model of Materials

The concrete damaged plasticity (CDP) model in ABAQUS is based on the relations between stress and strain of concrete

materials under tension and compression. It characterizes the inelastic behavior of concrete through tension and compression damage theories, which shows different yield strengths in compression and tension (Shafieifar et al., 2017).

NC

The constitutive law of NC is obtained through the calculation equation defined in GB50010-2010 (Code for Design of Concrete Structures, 2011), and the concrete damaged plasticity model is used, as shown in Supplementary **Figure 3**.

For NC under compression, the stress-strain curves can be calculated through the following equations:

$$\sigma = (1 - d_c)E_c \varepsilon \quad (1)$$

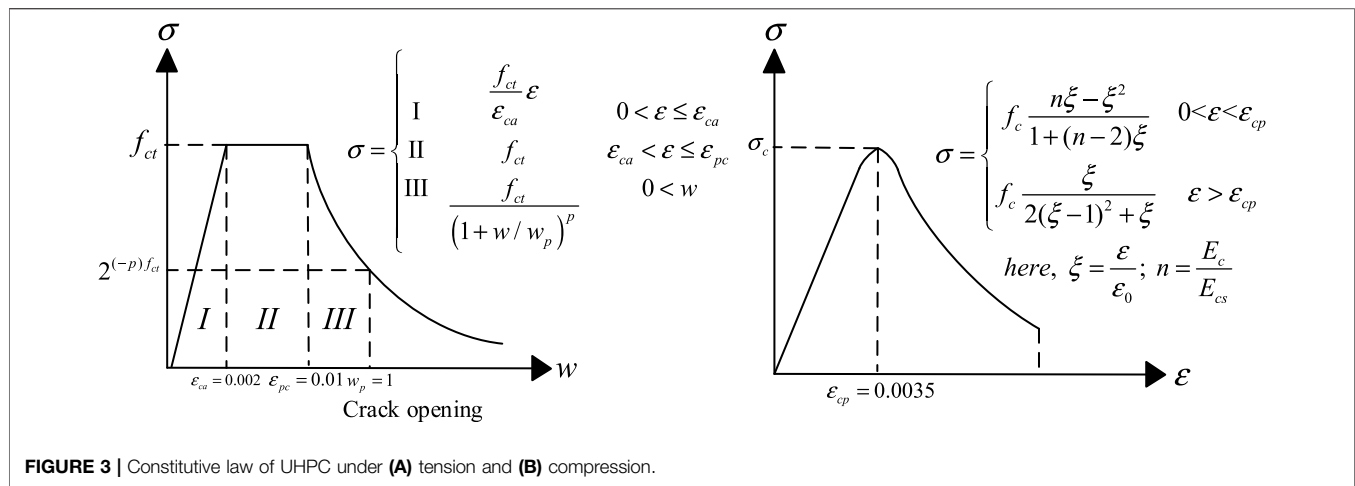
$$d_c = \begin{cases} 1 - \frac{\rho_c n}{n - 1 + x^n}, & x \leq 1 \\ 1 - \frac{\rho_c}{\alpha_c (x - 1)^2 + x}, & x > 1, \end{cases} \quad (2)$$

$$x = \frac{\varepsilon}{\varepsilon_{c,r}} \quad (3)$$

$$\rho_c = \frac{f_{c,r}}{E_c \varepsilon_{c,r}} \quad (4)$$

$$n = \frac{E_c \varepsilon_{c,r}}{E_c \varepsilon_{c,r} - f_{c,r}} \quad (5)$$

where d_c is the damage parameter of NC under compression, E_c is the elastic modulus of NC, $f_{c,r}$ is the standard compressive strength of NC, which is determined by the material test, $\varepsilon_{c,r}$



is the peak compressive strain, and α_c is the shape parameter for the drop stage, $\alpha_c = 0.94$.

The stress-strain curve can be calculated for NC under tension as

$$\sigma = (1 - d_t)E_c \varepsilon \quad (6)$$

$$d_t = \begin{cases} 1 - \rho_t [1.2 - 0.2x^5], & x \leq 1 \\ 1 - \frac{\rho_t}{\alpha_t (x - 1)^{1.7} + x}, & x > 1, \end{cases} \quad (7)$$

$$x = \frac{\varepsilon}{\varepsilon_{t,r}} \quad (8)$$

$$\rho_t = \frac{f_{t,r}}{E_c \varepsilon_{t,r}} \quad (9)$$

where d_t is the damage parameter of NC under tension, $f_{c,r}$ is the standard tensile strength of NC, which is determined by the material test, $\varepsilon_{c,r}$ is the peak tensile strain, and α_c is the shape parameter for the drop stage, $\alpha_c = 2.19$.

UHPC

The concrete damaged plasticity model in ABAQUS is used to represent the constitutive law of UHPC. The stress-strain relationship under tension and compression is based on the CDP model (Wang et al., 2019), as shown in **Figure 3**. In this relationship, E_c = initial elastic modulus of UHPC and E_{cs} = secant elastic modulus at the peak point. σ_c is 4.9 MPa, ε_{ca} is 120 $\mu\text{m/m}$, ε_{pc} is 750 $\mu\text{m/m}$, p is 0.95, w_p is 0.25mm, f_c is 120MPa, ε_0 is 3,500 $\mu\text{m/m}$, ε_u is 10000 $\mu\text{m/m}$, and n is 1.19. Poisson's ratio of UHPC is 0.2.

FE Meshing

Three-dimensional eight-node (C3D8R) elements were used to simulate UHPC and NC with reduced integration to avoid the locking phenomenon. These elements have three translational degrees of freedom in each node with linear interpolation for the displacement. Moreover, a general size mesh is applied for the models, and the scale is 5 mm to obtain independent results from the mesh. Details of FE meshing for models of push-off tests are depicted in Supplementary **Figure 4**.

Boundary Conditions and Interactions

According to the experimental scheme, rotations and displacements of the bottom of the push-off specimens were restrained in X-, Y-, and Z-directions. A reference point was coupled with the loading surface, as shown in **Figure 4**. The displacement-controlled loading is used in the finite element analysis to obtain the strength-slip curves. Besides, geometric non-linearity is considered.

Assuming that grooves fully connect the UHPC-NC interface, therefore, surface-to-surface contact can be applied for interaction. Finite sliding and no adjustment are chosen. The contact is characterized by tangential behavior and normal behavior. In ABAQUS, the penalty function is used to describe the relationship between the tangential friction and the relative slip of the interface. When the slip reaches the limit value of 1, the friction will remain constant. A friction coefficient was implemented in which finite slip was allowed between the contact surface of UHPC and NC. The value of friction coefficient was recommended by AASHTO, which is 0.6 for the NC surface without any roughness treatment (AASHTO, 2016). Normal behavior is mainly represented by the relationship between normal stress and opening. Hard contact was applied to depict the behavior of normal bonding. Separation is allowed after contact. That is to say, no penetration is allowed at each constraint location, and the surfaces transmit no contact pressure unless the nodes of the slave surface contact the master surface. Moreover, there is no limit to the magnitude of contact pressure transmitted when the surfaces are in contact. Finite sliding was set in normal behavior in ABAQUS (Chen and Graybeal, 2012; Nasrin and Ibrahim, 2018).

DISCUSSION OF THE RESULTS

Failure Modes

During the push-off tests, cracks appeared near the UHPC-NC interface and intersected or paralleled it. Most specimens did not fail due to eccentric compression. The failure modes of UHPC-NC specimens connected with grooves are shown in

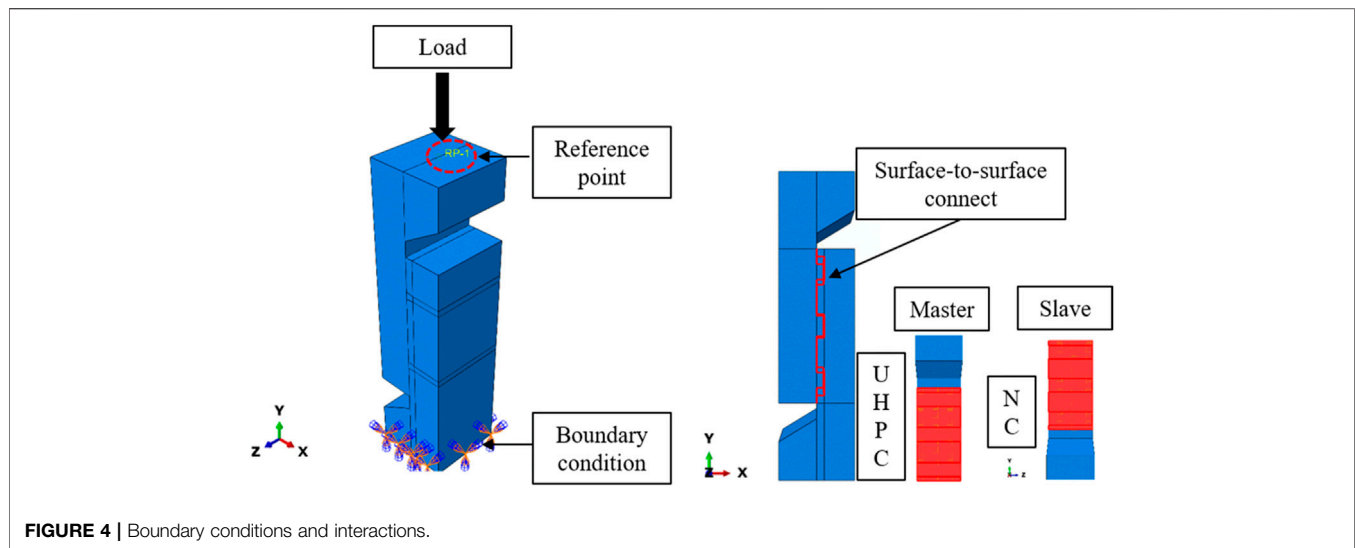


FIGURE 4 | Boundary conditions and interactions.

Figure 5. It can be seen that the NC matrix failed significantly in group S1, and the other groups mostly failed at the interface between UHPC and NC. Four types can be divided according to the failure modes.

The failure occurred at the NC matrix only (**Figure 5A**): the shear strength at the initial loading stage was mainly provided by the cohesion between UHPC and NC. Firstly, tiny shear cracks were observed on the NC matrix near the bonding surface, and then the shear bearing capacity was mainly provided by the NC matrix. With the loading process, the shear crack penetrated through the NC matrix. Then, the NC matrix was shear failed, and the failure surface was mainly on the NC matrix near the bonding area. Besides, the bonding interface of UHPC-NC remained intact, the aggregate of NC at the failure surface partly broke, and the exfoliated NC was still bonded to the UHPC.

The failure occurred at the bonding interface only (**Figure 5B**): the shear strength at the initial stage of loading was mainly provided by the cohesion between UHPC and NC. Firstly, tiny shear cracks were observed on the bonding surface, and the shear resistance was mainly provided by UHPC grooves which inhibit the propagation of cracks. However, with the loading process, the crack propagated vertically along the interface. Finally, the shear crack penetrated the interface, and the shear failure occurred at the bonding surface. The interface of the specimens was split into two parts, and there appeared no crack on the NC matrix and UHPC.

The failure occurred at the NC matrix and interface (**Figure 5C**): firstly, the crack developed obliquely to the bonding surface between UHPC and NC, and UHPC grooves mainly provided the shear strength. As the loading continued, when the load increased to 90% of the ultimate load, the bridging effect of steel fibers can be observed. Finally, the crack propagated obliquely through the NC matrix's bonding surface. Meanwhile, the bonding interface and the NC matrix failed nearly simultaneously. The failure surface was partly on the bonding interface and the NC matrix. The bonding interface of UHPC-NC was partially cracked, while the NC matrix was

damaged near the interface, and the exfoliated coarse aggregate was still bonded to UHPC.

The failure occurred at the NC matrix and interface (**Figure 5D**): it is similar to the failure mode of type C, but less UHPC is attached to the failure surface. The cohesion between UHPC and NC mainly provided the shear resistance at the initial loading stage. Firstly, a tiny shear crack appeared on the epoxy resin adhesive layer. The shear crack developed obliquely to the NC matrix with the loading process and finally penetrated. The shear failure occurred between the bonding interface and the NC matrix and was partly observed on the epoxy resin adhesive layer and the NC matrix. Most of the exfoliated NC was still bonded to the UHPC matrix.

The failure mode of S1-1 was A (**Figure 6A**), the bonding interface remained intact, and cracks only appeared at the side of the NC matrix. The failure modes of S1-2 and S1-3 specimens were type C. The failure surface was consistent with the interface. Cracks only occurred at the side of the NC matrix.

The failure modes of the S2-3 specimen were B (**Figure 6B**), the bonding surface was damaged, and there were no cracks in the matrix on both sides. The failure mode of S2-2 was C, the failure surface was consistent with the bonding surface, and cracks occurred on the side of the NC matrix. Transverse cracks developed in the middle of the NC matrix.

The failure mode of the S3-1 specimen was type B (**Figure 6C**), the failure surface was the bonding interface, and there appeared no cracks in the matrix on both sides. The failure mode of the S3-2 specimen was type C, part of the failure surface was consistent with the bonding interface, and the other cracked at the side of the NC matrix. The failure mode of the S3-3 specimen was B.

As for S4 and S5 groups, the failure mode of the S4 group was class C (**Figure 6D**, **Figure 6E**). The failure surface is within 10–20 mm from the edge of the bonding interface. Besides, there were no cracks on the UHPC side. The failure mode of group S5 was D, part of the failure surface was on the epoxy resin adhesive layer, and the other was on the NC matrix.

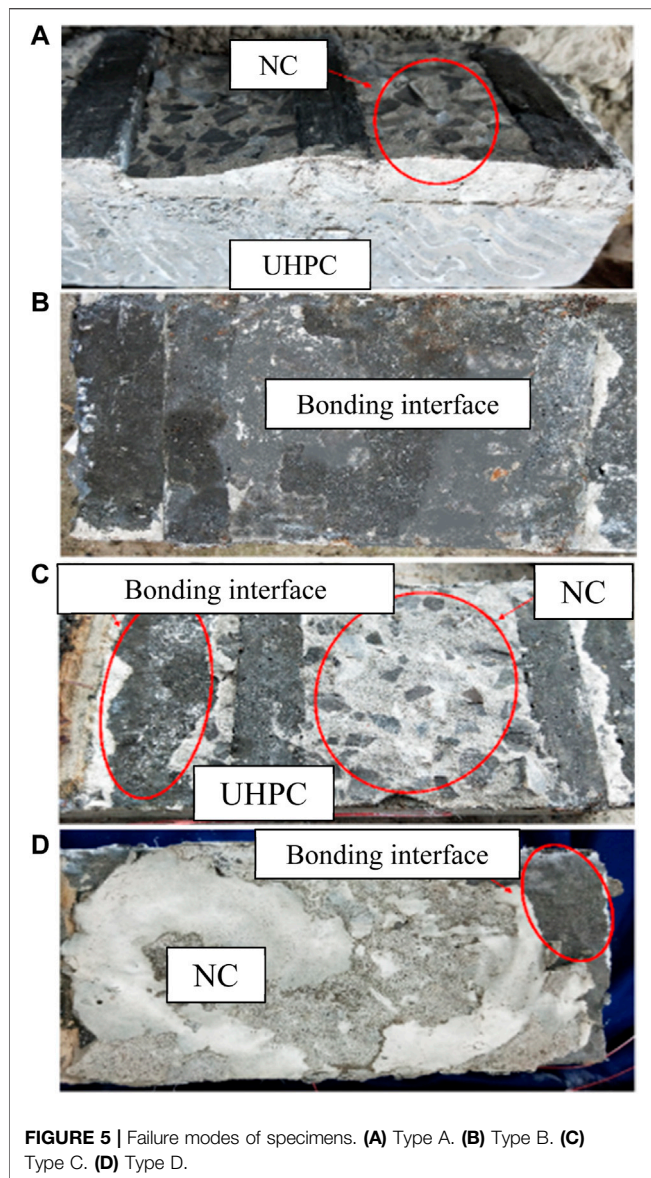


FIGURE 5 | Failure modes of specimens. (A) Type A. (B) Type B. (C) Type C. (D) Type D.

For specimens with small grooves, the convex UHPC was subjected to a larger load, especially when the shear surface cracked and slipped. During the process, a loud sound can be heard when the internal steel fibers were pulled out. The bridging effect of steel fibers was significant, and shear cracks appeared in both the UHPC and NC layers near the shear surface, as shown in **Figure 6F**. Finally, the specimens showed the failure mode of class C.

Figure 5 in the Supplementary Material shows the distribution of four failure modes, and the proportion of B (which failed at the interface only) is only 7%, indicating that the reliability of the UHPC–NC bonding interface is high. The proportion of C and D is up to 80%, indicating that the shear resistance of the UHPC–NC bonding interface with grooves is better than that of the NC matrix.

On the one hand, the water–cement ratio of UHPC is low and does not contain coarse aggregates, and the initial stress caused by temperature and shrinkage at the bonding interface is complex. When pouring UHPC, the ultra-fine silica powder in UHPC will be tightly filled on the surface of the existing concrete structure, and there will be no interlocked contact between coarse aggregates like the NC–NC interface with a dense microstructure. Due to the existence of UHPC grooves, the bonding area between UHPC and NC expands, the development of cracks is inhabited, and the ability to resist complex initial stress can be effectively improved. On the other hand, UHPC with a low water–cement ratio can reduce the porosity of the transition layer of the interface. Therefore, the bonding strength is enhanced with the increase of compactness. After the interface cracked, the specimen can still bear about 33.3% of the ultimate load and has good ductility characteristics.

Strength–Slip Curves

The results of the EXP and FEM are shown in **Figure 7** and **Table 3**, where τ_1 and τ_2 are the peak shear strength of EXP and FEM, respectively, and S_1 and S_2 are the slip corresponding to 70% of the peak shear strength of EXP and FEM, respectively, which are used to evaluate the ductility characteristics of the specimen. Moreover, K_1 and K_2 are the interface stiffness of EXP and FEM, respectively. Meanwhile, e_1 and e_2 are the relative errors of shear strength and stiffness. The specific definition is as follows:

$$K_1 = \frac{\tau_1}{S_1}, K_2 = \frac{\tau_2}{S_2} \quad (10)$$

$$e_1 = \frac{\tau_2 - \tau_1}{\tau_1} \times 100\%, e_2 = \frac{K_2 - K_1}{K_1} \times 100\% \quad (11)$$

For the S5 group, when defining the values of shear strength and stiffness in the EXP, from the perspective of safety, the maximum and minimum values of shear strength are removed, and the median value is taken as the shear strength.

It can be seen that the FEM fits well with the EXP in terms of interface strength and stiffness, and the error is within $\pm 17\%$. In addition, S3-1 shows the highest shear strength of 3.98 MPa, and S2-3 shows the highest interface shear stiffness of 22.95 MPa/mm. Compared with that of the S5 group (bonded by epoxy resin adhesive), its shear strength is 1.2 MPa. The average stiffness is 9.23 MPa/mm, and the strength and stiffness are increased by 231.7% and 148.6%, respectively. The results show that grooving is very effective in improving interface performance. By comparing the failure modes, it can be found that failing at interface bonding occurs in S1-2, S1-3, and S2-2. Although the strength greatly improved compared with that of S5, their stiffness decreased. However, the stiffness of the S4 group with failure mode C increased significantly. The results show that reasonable shapes of grooves play an important role in enhancing interface performance.

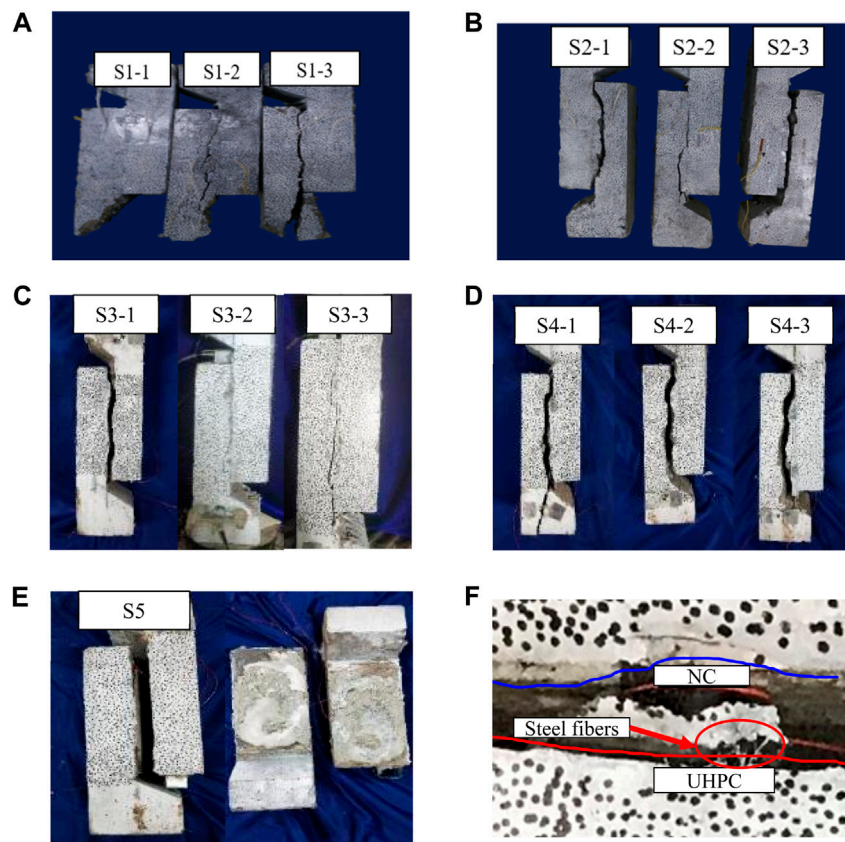


FIGURE 6 | Failure modes of interface. (A) S1. (B) S2. (C) S3. (D) S4. (E) S5. (F) Steel fibers and cracks at the interface.

Influence of the Grooves Influence on the Bonding Strength

The change in interface strength is shown in **Figure 8A**. For S1, the interfacial bonding shear strength increases with the width. When the width reaches 30mm, the maximum interfacial bonding shear strength is 3.12 MPa. Due to the existence of UHPC grooves, when there appear microcracks in the bonding interface, their propagation will be restricted and the strength ductility of UHPC is better than that of NC. The greater the width of the grooves is, the greater the shear strength provided by UHPC is. Meanwhile, the grooving treatment of the bonding interface will destroy the integrity of the concrete and produce microcracks. However, the cast-in UHPC will properly fill these microcracks, and the mechanical force between the NC matrix and UHPC gets strengthened owing to the bridge effect of steel fibers. When the width of the grooves increases from 20mm to 30mm, the shear strength of the bonding interface is provided by the NC matrix, which leads to the failure of the NC matrix, i.e., failure mode C. At this time, the increase in width will not enhance the shear strength.

For specimens of S2, the shear strength of the interface decreases with the increase of space. It is worth noting that failure modes of A occur in S2. The reason is that when the space

increases, the propagation path of microcracks between grooves along the edge of the UHPC-NC interface shrinks, which will lead to interfacial failure and reduce the bonding strength.

Comparing the specimens of the S3 group and S4 group, it is found the shear strength of grooves with angle is better than that without angle. On the one hand, the interfacial bonding shear strength of -11° is about 25% higher than that of 0° ; on the other hand, the interfacial bonding shear strength of 11° is about 13% higher than that of 0° .

Changing the angle can increase the strength by 1.25 times. The angle can improve the effect of interlock, so it brings higher bonding shear strength. As shown in **Figure 8B**, when the specimens with 11° grooves are subjected to the shear force, the shear crack will develop toward the bonding interface and aggravate the cracking of the interface. When the specimens of -11° grooves are subjected to the shear force, the shear crack will develop toward the inner part of the NC matrix, and cracking of the interface will be inhabited, therefore improving the shear resistance. In addition, the shear strength of the S3 group with 10 mm width is better than that of the S4 group with 20 mm width. It is indicated that grooves with 10 mm width perform well, and excessive width causes the failure of the NC matrix.

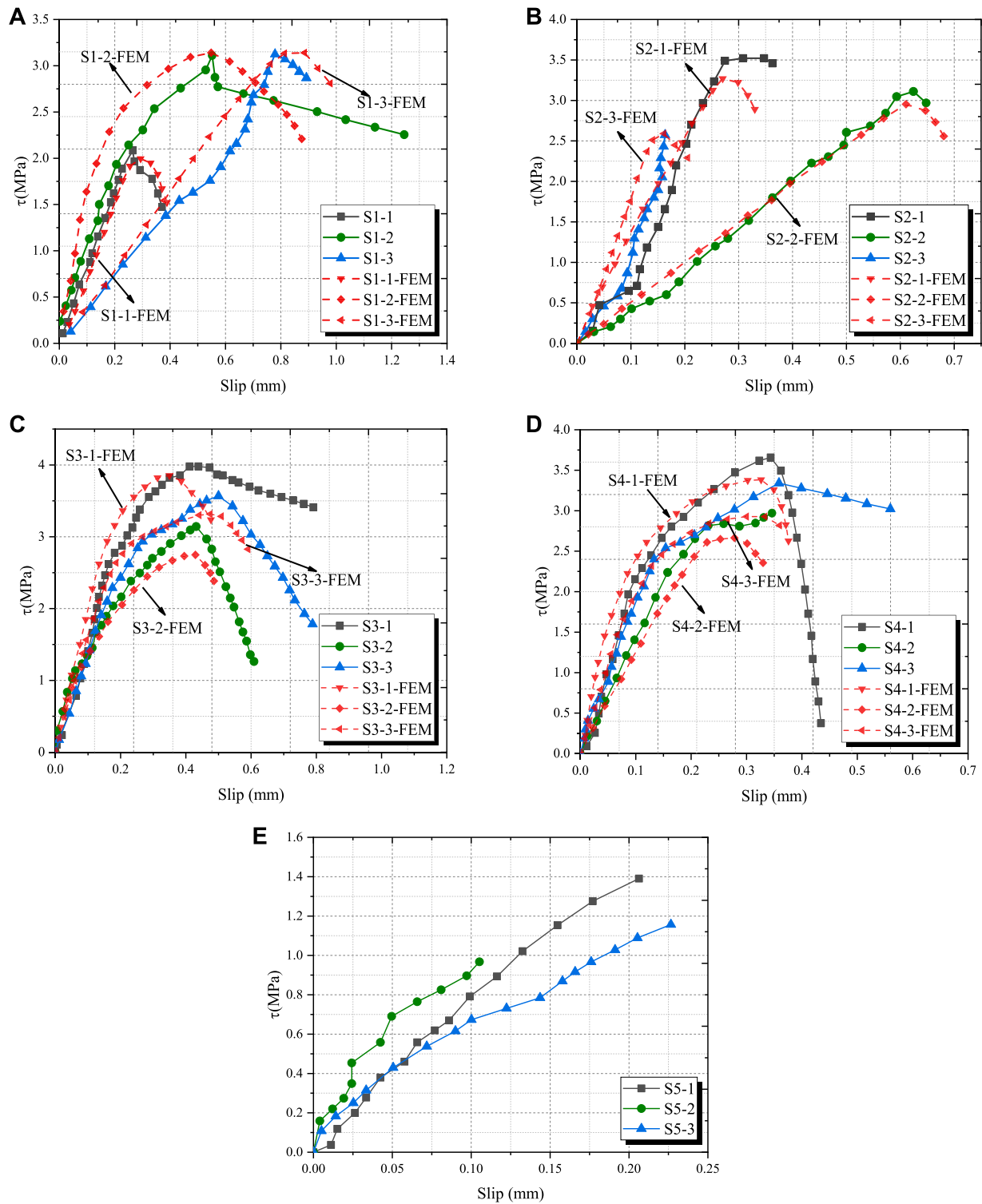
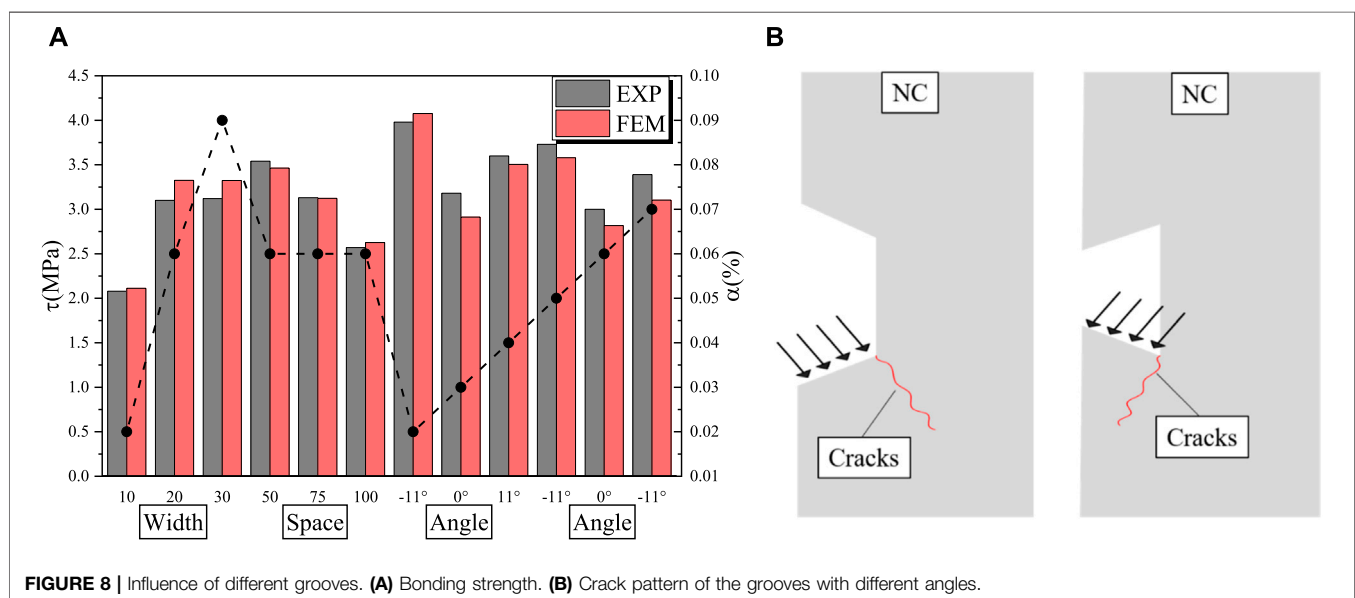


FIGURE 7 | Strength-slip curves of the specimens. (A) S1. (B) S2. (C) S3. (D) S4. (E) S5.

TABLE 3 | Results of the EXP and FEM.

Specimens	Failure modes	τ_1 (MPa)	τ_2 (MPa)	e_1 (%)	S_1 (mm)	S_2 (mm)	K_1 (MPa.mm ⁻¹)	K_2 (MPa.mm ⁻¹)	e_2 (%)
S1-1	A	2.08	2.00	-4.08	0.18	0.21	11.43	9.71	-15.05
S1-2	C	3.10	3.14	1.31	0.38	0.38	8.16	8.18	0.27
S1-3	C	3.12	3.14	0.62	0.60	0.62	5.18	5.06	-2.32
S2-1	A	3.54	3.27	-7.63	0.22	0.19	16.31	17.30	6.06
S2-2	C	3.13	2.95	-5.75	0.44	0.43	7.10	6.91	-2.66
S2-3	B	2.57	2.48	-3.50	0.11	0.12	22.95	20.84	-9.18
S3-1	B	3.98	3.85	-3.27	0.29	0.25	13.54	15.71	16.08
S3-2	C	3.18	2.75	-13.52	0.30	0.29	10.56	9.35	-11.46
S3-3	B	3.60	3.31	-8.06	0.35	0.34	10.29	9.85	-4.22
S4-1	C	3.73	3.38	-9.38	0.24	0.23	15.67	14.63	-6.64
S4-2	C	3.00	2.66	-11.33	0.22	0.20	13.39	13.57	1.33
S4-3	C	3.39	2.93	-13.57	0.25	0.23	13.45	12.68	-5.71
S5-1	D	1.2	—	—	0.13	—	9.23	—	—
S5-2	D	—	—	—	—	—	—	—	—
S5-3	D	—	—	—	—	—	—	—	—



Influence on Bonding Stiffness

The change in interface stiffness is shown in **Figure 9**. For specimens of S1, the shear stiffness decreases with the increase of the width, and the shear stiffness decreases more with the volume loss rate (α). After cracks appeared in the bonding interface, its shear stiffness was mainly provided by the UHPC grooves. However, with the increase of the width, the propagation path of cracks along the interface edge diminished, and the stress factor at the tip of the microcrack increased. Therefore, the microcrack developed in the NC matrix and finally extended to the bonding interface. The shear stiffness of the UHPC grooves was not fully utilized.

For specimens of S2, S2-2 exhibits relatively low stiffness. Therefore, without considering S2-2, when the volume loss rate and width are constant, the interfacial bonding stiffness increases with space increase. The reason is that when the

space of grooves increased to 100mm, the crack path from the edge of the interface decreased. Thus, the interfacial shear strength decreased. However, the propagation path of cracks between adjacent grooves extended, and the slip increased, resulting in enhancing the interfacial shear stiffness.

For specimens of S3 and S4, it can be seen that changing the angle of grooves can increase the stiffness by 1.17 times. When the angle is -11° , the interfacial shear stiffness exhibits best. It is notable that when the interface angle is 0° , the shear strength is slightly higher than that of 11° . Due to the change in the opening angle of the grooves, the interface microcracks with an angle of 11° accelerate the expansion due to the stress concentration. Besides, a relatively high volume of loss rate reduces the utilization of the shear stiffness of UHPC, therefore weakening the composite elastic modulus of the UHPC-NC interface.

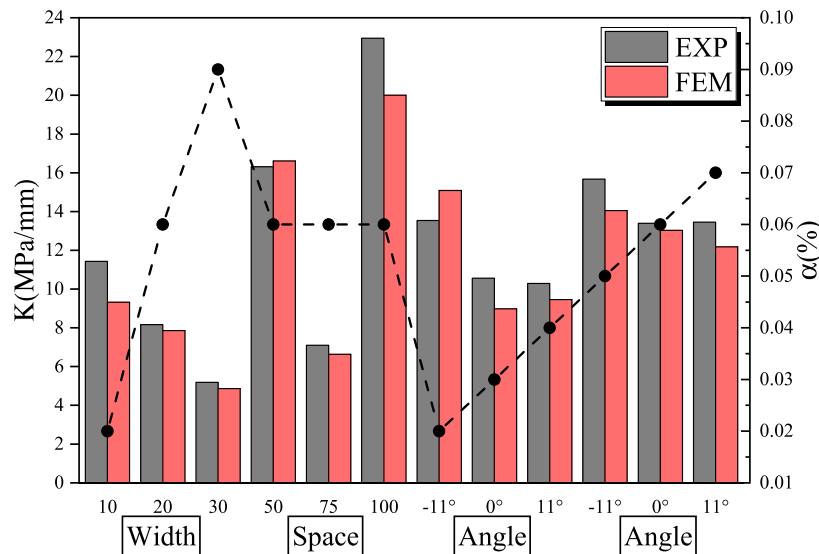


FIGURE 9 | Influence of different grooves on bonding stiffness.

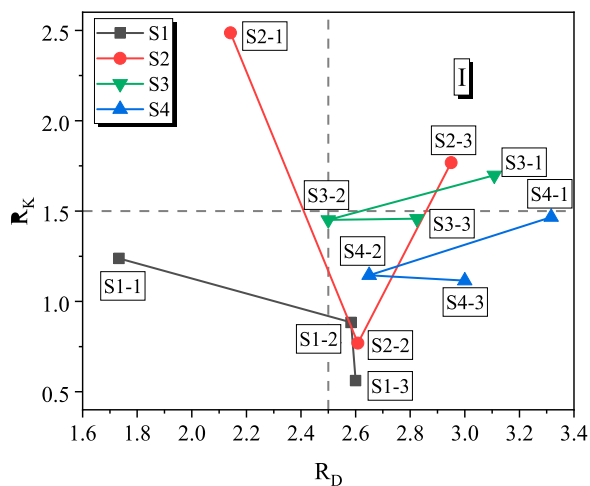


FIGURE 10 | Distribution of R_D and R_K .

Recommended Values of the Grooves

In order to compare the efficiency of different shapes of grooves at the UHPC-NC interface, the relative bonding strength R_D and bonding stiffness R_K are introduced to evaluate the influence of various factors. Their expressions are

$$R_D = \frac{\tau_{\max}}{\tau_0} \quad (12)$$

$$R_K = \frac{K_{\max}}{K_0} \quad (13)$$

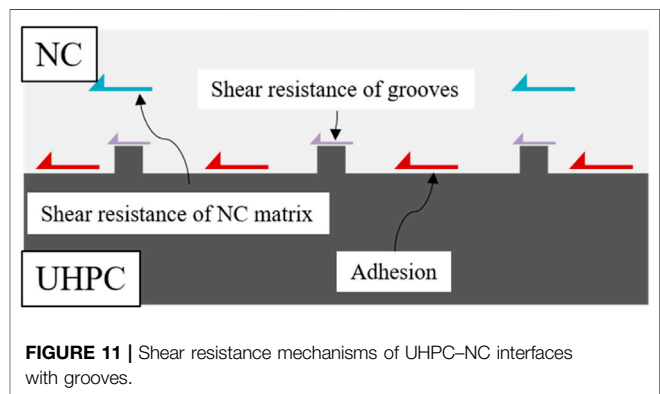


FIGURE 11 | Shear resistance mechanisms of UHPC-NC interfaces with grooves.

where τ_{\max} and K_{\max} are the bonding strength and stiffness of UHPC-NC interface with grooves, respectively, and τ_0 and K_0 are the bonding strength and stiffness of UHPC-NC interface bonded by epoxy resin adhesive, respectively. The area of R_K greater than the average value of 1.5 and R_D greater than 2.5 are taken as zone I, representing the interface bonding strength and stiffness are greatly improved through these kinds of grooves, as shown in Figure 10. For the S1 group, when the width is greater than 10 mm (S1-2 and S1-3), R_K is less than 1.5, but R_D is greater than 2.5. That is, the strength increases significantly, and the stiffness decreases slightly. Meanwhile, the width of S3 is 10 mm, and the width of S4 is 20 mm. However, the distribution of the S3 group is closer to zone I, which indicates that the grooves with 10 mm width exhibit better bonding performance. As for the S2 group, when the groove's space reaches 100 mm (S2-3), both R_K and R_D exceed the average value, which exhibits significant strength and

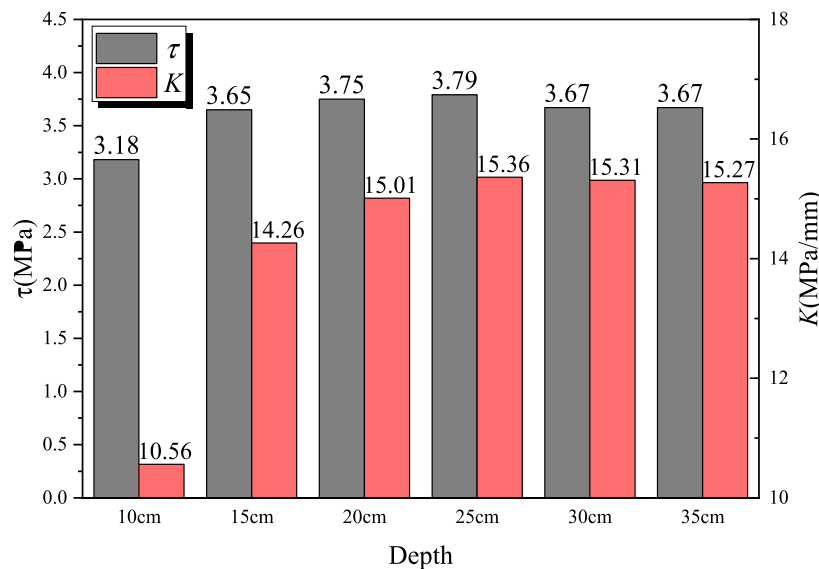


FIGURE 12 | FEM results of different grooves.

stiffness improvement effect. Therefore, 100 mm space is recommended. As for S3 and S4 groups, when the angle is -11° (S4-1 and S3-1), the best bonding performance is observed. Compared with the right angle (S4-2 and S3-2), the strength is significantly improved, but the difference in stiffness is small and R_K is greater than the average. Considering the convenience of construction and the bonding efficiency, the grooves with the right angle are recommended.

Calculation Methods of the Interface Shear Strength

There is currently no clear specification for calculating the shear strength of the UHPC-NC interface with grooves. ACI 318-14 (ACI Committee, 2008) provides the methods for the UHPC-NC interface strength with studs as follows (AASHTO, 2016):

$$V_n = \mu A_{vf} f_y \quad (14)$$

where V_n is the interface shear capacity, μ is the friction coefficient, A_{vf} is the area of interface shear reinforcement, and f_y is the yield strength of the reinforcement.

For this interface, the interface shear capacity is composed of studs' adhesion and interfacial shear resistances. And the capacity is mainly provided by the bending of the studs that is generally referred to as dowel action, as shown in Supplementary Figure 6. However, the grooved interface is connected without studs. Considering three failure modes, the shear strength of the interface is contributed by the adhesive bonding, the NC matrix, and the shear resistance of UHPC grooves embedded in NC, as shown in Figure 11. Based on the results of the EXP, the shear strength can be calculated as follows:

$$\tau_G = \frac{\tau_N A_N + \tau_U A_U + \tau_s A_s}{S_0}, \quad (15)$$

where τ_G is the shear strength of the grooved surface, τ_N is the shear resistance contributed by the NC matrix, τ_U is the shear resistance contributed by the UHPC groove, τ_s is the shear resistance contributed by adhesion, A_N is the failure area of the NC matrix, A_U is the failure area of the UHPC grooves, A_s is the failure area of the interface, and S_0 is the area of the bonding interface.

The interface without roughness, τ_s , can be taken as $0.213 \tau_N$ (Zhang, 2020b). Based on the friction shear mechanism (Santos and Júlio, 2012), τ_N and τ_U can be calculated as follows:

$$\tau_{N,U} = 0.5 \sqrt{f_c f_t} \quad (16)$$

where f_c is the cubic compressive strength and f_t is the tensile strength. In this research, $\tau_N = 4.94$ MPa and $\tau_U = 16.60$ MPa.

$A_{N,U,S}$ can be calculated by multiplying the crack length and the interface width. Finally, the interface shear strength can be obtained. The table shows the calculation results. It can be seen from Table 3 in the Supplementary Material that the calculation error of this method is within $\pm 25\%$, and the bearing capacity of the UHPC-NC grooved interface can be well calculated.

EFFECTS OF THE DEPTH OF THE GROOVES

From the sections above, a more efficient UHPC-NC interface performance can be obtained with 10 mm width, 100 mm space, and right angle. Based on the FEM, which fits well with the EXP, a parametric analysis was carried out for different depths of grooves

with the recommended dimensions in this paper. The interface strength and stiffness changes when the depth of grooves varies from 10 mm to 35 mm were compared, as shown in Supplementary Figure 7.

The FEM results are shown in Figure 12. When the depth of grooves increased from 10 mm to 15 mm, the interface bonding strength and stiffness increased to 0.47 MPa and 3.70 MPa/mm, respectively, the strength increased by 14.8%, and the stiffness increased by 35.0%. It is indicated that the interface bonding performance is sensitive to the depth of grooves. When the depth increased to 25 mm, the interface bonding strength reached the maximum of 3.79 MPa and the stiffness reached the maximum of 15.36 MPa/mm. However, when the depth increased above 25 mm, the strength decreased to 3.67 MPa and remained constant with the increase of depth and the interface bonding stiffness gradually decreased to 15.27 MPa/mm. The results show that the interfacial bonding strength and stiffness increased first and then decreased with the depth increase. Grooves with 25 mm depth were recommended to improve interfacial bonding performance.

CONCLUSION

This paper aimed at investigating the interfacial bonding performance between UHPC and NC connected with grooves, and a push-off test with 15 UHPC-NC specimens was carried out. Conclusions can be drawn as follows:

- 1) Due to the grooves' interlock effect, there is a strong mechanical performance between UHPC and NC, the development of interfacial cracks can be delayed, and the shear strength of the interface is even better than that of the NC matrix.
- 2) Grooves can significantly enhance the bonding performance. Besides, reasonable shapes of grooves were critical. Compared with specimens bonded by epoxy resin adhesive, the interface strength and stiffness are increased by 3.32 times and 2.48 times, respectively. Changing the angle can increase the strength by 1.25 times and the stiffness by 1.17 times. A method to calculate the bonding strength was provided.
- 3) The FEM was established for the push-off test. This model applied hard contact and tangential friction coefficient for the

interface. From the test results, it can be found that the model can predict the shear strength and slip well, and the error was within $\pm 17\%$. Based on the FEM, the parameter analysis of different depths was carried out. The interfacial bonding strength and stiffness increased first and then decreased with the depth increase. Grooves with 25 mm depth performed best.

- 4) Through comprehensive comparison of interfacial performance, the convenience of construction, and the volume loss rate of the matrix, grooves with 10 mm width, 100 mm space, and right angle are recommended.

DATA AVAILABILITY STATEMENT

The original contributions presented in the study are included in the article/Supplementary Material, and further inquiries can be directed to the corresponding author.

AUTHOR CONTRIBUTIONS

JY and JX wrote the manuscript. JX conceived the research idea. JW offered useful suggestions for the preparation and writing of this paper. CC collected the data. JZ and GW advised on data analysis and paper organization.

FUNDING

This research was performed under grants from the National Natural Science Foundation of China (U20A20314, 51908093), the Natural Science Foundation of Chongqing (cstc2020jcyj-msxmX0088), the Science Foundation of Hubei Provincial Department of Transportation (2020-186-1-6, 2020-2-1-1), and the Scientific and Technological Research Project of Chongqing Education Commission (KJQN201900733).

SUPPLEMENTARY MATERIAL

The Supplementary Material for this article can be found online at: <https://www.frontiersin.org/articles/10.3389/fmats.2022.859717/full#supplementary-material>

REFERENCES

- AASHTO (2016). *Standard Specification for Manufacture of Precast Reinforced concrete Three-Sided Structures for Culverts and Stormdrains: Astm C1504-2016*. Washington DC, USA: American Association of State Highway and Transportation Officials.
- ACI Committee (2008). *Building Code Requirements for Structural concrete (ACI 318-08) and Commentary*. Farmington Hills, Michigan, USA: American Concrete Institute.
- Al-Osta, M. A., Isa, M. N., Baluch, M. H., and Rahman, M. K. (2017). Flexural Behavior of Reinforced concrete Beams Strengthened with Ultra-high Performance Fiber Reinforced concrete. *Constr. Build. Mater.* 134, 279–296. doi:10.1016/j.conbuildmat.2016.12.094
- Chen, L., and Graybeal, B. A. (2012). Modeling Structural Performance of Ultrahigh Performance concrete I-Girders. *J. Bridge Eng.* 17, 754–764. doi:10.1061/(ASCE)BE.1943-5592.0000305
- Code for Design of Concrete Structures (2011). *Code for Design of concrete Structures. Gb50010-2010*. Beijing, China: Ministry of Housing and Urban-Rural Development.
- Feng, S., Xiao, H., and Li, H. (2020). Comparative Studies of the Effect of Ultrahigh-Performance concrete and normal concrete as Repair Materials on Interfacial Bond Properties and Microstructure. *Eng. Struct.* 222, 111122. doi:10.1016/j.engstruct.2020.111122
- Ganesh, P., and Murthy, A. R. (2020). Simulation of Surface Preparations to Predict the Bond Behaviour between normal Strength concrete and Ultra-high Performance concrete. *Constr. Build. Mater.* 250, 118871. doi:10.1016/j.conbuildmat.2020.118871

- Guan, D., Liu, J., Jiang, C., Chen, Z., and Guo, Z. (2021). Shear Behaviour of the UHpc-Nsc Interface with Castellated Keys: Effects of Castellated Key Dimension and Dowel Rebar. *Structures* 31, 172–181. doi:10.1016/j.istruc.2021.01.088
- Harris, D. K., Sarkar, J., and Ahlborn, T. M. (2011). Characterization of Interface Bond of Ultra-high-performance concrete Bridge Deck Overlays. *Transport. Res. Rec.* 2240, 40–49. doi:10.3141/2240-07
- Hussein, H. H., Walsh, K. K., Sargand, S. M., and Steinberg, E. P. (2016). Interfacial Properties of Ultrahigh-Performance Concrete and High-Strength Concrete Bridge Connections. *J. Mater. Civ. Eng.* 28, 04015208. doi:10.1061/(ASCE)MT.1943-5533.0001456
- Hussein, H. H., Walsh, K. K., Sargand, S. M., Al Rikabi, F. T., and Steinberg, E. P. (2017). Modeling the Shear Connection in Adjacent Box-Beam Bridges with Ultrahigh-Performance concrete Joints. I: Model Calibration and Validation. *J. Bridge Eng.* 22, 04017043. doi:10.1061/(ASCE)BE.1943-5592.0001070
- Jiang, H., Dong, X., Fang, Z., Xiao, J., and Chen, Y. (2020). Experimental Study on Shear Behavior of a UHpc Connection between Adjacent Precast Prestressed concrete Voids Beams. *J. Bridge Eng.* 25, 04020106. doi:10.1061/(ASCE)BE.1943-5592.0001644
- Jiang, H., Shao, T., Fang, Z., Xiao, J., and Hu, Z. (2021). Shear-friction Behavior of Grooved Construction Joints between a Precast UHpc Girder and a Cast-In-Place concrete Slab. *Eng. Struct.* 228, 111610. doi:10.1016/j.engstruct.2020.111610
- Lee, M.-G., Wang, Y.-C., and Chiu, C.-T. (2007). A Preliminary Study of Reactive Powder concrete as a New Repair Material. *Constr. Build. Mater.* 21, 182–189. doi:10.1016/j.conbuildmat.2005.06.024
- Li, J., and Deng, Z. (2021). Tensile Behavior of Hybrid Fiber-Reinforced Ultra-high-performance Concrete. *Front. Mater.* 8, 455. doi:10.3389/fmats.2021.769579
- Li, V. C. (2004). High Performance Fiber Reinforced Cementitious Composites as Durable Material for Concrete Structure Repair/Faser verstärkte, Zement gebundene, zusammen gesetzte Hochleistungswerkstoffe für das dauerhafte Instandsetzen von Betontragwerken. *Restor. Build. Monu.* 10, 163–180. doi:10.1515/rbm-2004-5844
- Lian, J., Hu, C., Fu, T., and Wang, Y. (2021). Review of Self-Sensing Capability of Ultra-high Performance concrete. *Front. Mater.* 8, 467. doi:10.3389/fmats.2021.746022
- Murthy, A. R., Aravindan, M., and Ganesh, P. (2018). Prediction of Flexural Behaviour of Rc Beams Strengthened with Ultra High Performance Fiber Reinforced concrete. *Struct. Eng. Mech.* 65, 315–325. doi:10.12989/sem.2018.65.3.315
- Nasrin, S., and Ibrahim, A. (2018). Finite-element Modeling of UHpc Hybrid Bridge Deck Connections. *Int. J. Adv. Struct. Eng.* 10, 199–210. doi:10.1007/s40091-018-0192-2
- Qin, F., Zhang, Z., Yin, Z., Di, J., Xu, L., and Xu, X. (2020). Use of High Strength, High Ductility Engineered Cementitious Composites (Ecc) to Enhance the Flexural Performance of Reinforced concrete Beams. *J. Build. Eng.* 32, 101746. doi:10.1016/j.jobbe.2020.101746
- Reactive Powder Concrete (2015). *Reactive Powder concrete. Gb/t 31387-2015*. Beijing, China: General Administration of Quality Supervision, Inspection and quarantine.
- Santos, P. M. D., and Júlio, E. N. B. S. (2012). A State-Of-The-Art Review on Shear-Friction. *Eng. Structures* 45, 435–448. doi:10.1016/j.engstruct.2012.06.036
- Shafieifar, M., Farzad, M., and Azizinamini, A. (2017). Experimental and Numerical Study on Mechanical Properties of Ultra High Performance concrete (UHpc). *Constr. Build. Mater.* 156, 402–411. doi:10.1016/j.conbuildmat.2017.08.170
- Standard for Test Method of Mechanical Properties on Ordinary Concrete (2002). *Standard for Test Method of Mechanical Properties on Ordinary concrete. Gb/t 50081-2002*. Beijing, China: Ministry of Housing and Urban-Rural Development.
- Tayeh, B. A., Abu Bakar, B. H., Megat Johari, M. A., and Voo, Y. L. (2012). Mechanical and Permeability Properties of the Interface between normal concrete Substrate and Ultra High Performance Fiber concrete Overlay. *Constr. Build. Mater.* 36, 538–548. doi:10.1016/j.conbuildmat.2012.06.013
- Tayeh, B. A., Abu Bakar, B. H., and Megat Johari, M. A. (2013). Characterization of the Interfacial Bond between Old concrete Substrate and Ultra High Performance Fiber concrete Repair Composite. *Mater. Struct.* 46, 743–753. doi:10.1617/s11527-012-9931-1
- Tong, T., Yuan, S., Wang, J., and Liu, Z. (2021). The Role of Bond Strength in Structural Behaviors of UHpc-Nc Composite Beams: Experimental Investigation and Finite Element Modeling. *Compos. Struct.* 255, 112914. doi:10.1016/j.compstruct.2020.112914
- Wang, Z., Nie, X., Fan, J.-S., Lu, X.-Y., and Ding, R. (2019). Experimental and Numerical Investigation of the Interfacial Properties of Non-steam-cured UHpc-Steel Composite Beams. *Constr. Build. Mater.* 195, 323–339. doi:10.1016/j.conbuildmat.2018.11.057
- Wu, X., and Zhang, X. (2018). Investigation of Short-Term Interfacial Bond Behavior between Existing concrete and Precast Ultra-high Performance concrete Layer. *J. Build. Struct.* 39, 156–163. doi:10.14006/j.zjgxb.2018.10.018
- Yang, J., Zhou, J., Wang, Z., Zhou, Y., and Zhang, H. (2019). Structural Behavior of Ultrahigh-Performance Fiber-Reinforced concrete Thin-Walled Arch Subjected to Asymmetric Load. *Adv. Civil Eng.* 2019, 1–12. doi:10.1155/2019/9276839
- Yoo, D.-Y., and Banthia, N. (2016). Mechanical Properties of Ultra-high-performance Fiber-Reinforced concrete: A Review. *Cement Concrete Composites* 73, 267–280. doi:10.1016/j.cemconcomp.2016.08.001
- Zhang, Y., Zhu, P., Liao, Z., and Wang, L. (2020a). Interfacial Bond Properties between normal Strength concrete Substrate and Ultra-high Performance concrete as a Repair Material. *Constr. Build. Mater.* 235, 117431. doi:10.1016/j.conbuildmat.2019.117431
- Zhang, Y., Zhu, P., Wang, X., and Wu, J. (2020b). Shear Properties of the Interface between Ultra-high Performance concrete and normal Strength concrete. *Constr. Build. Mater.* 248, 118455. doi:10.1016/j.conbuildmat.2020.118455
- Zhang, Z., Liu, S., Yang, F., Weng, Y., and Qian, S. (2021). Sustainable High Strength, High Ductility Engineered Cementitious Composites (Ecc) with Substitution of Cement by rice Husk Ash. *J. Clean. Prod.* 317, 128379. doi:10.1016/j.jclepro.2021.128379
- Zhu, Y., Zhang, Y., Hussein, H. H., and Chen, G. (2020). Numerical Modeling for Damaged Reinforced concrete Slab Strengthened by Ultra-high Performance concrete (UHpc) Layer. *Eng. Struct.* 209, 110031. doi:10.1016/j.engstruct.2019.110031
- Zhu, Y., Zhang, Y., Li, X., and Chen, G. (2021). Finite Element Model to Predict Structural Response of Predamaged Rc Beams Reinforced by Toughness-Improved UHpc under Unloading Status. *Eng. Struct.* 235, 112019. doi:10.1016/j.engstruct.2021.112019

Conflict of Interest: The authors JY and JW were employed by Guangxi Communications Investment Group Corporation Ltd.

The remaining authors declare that the research was conducted in the absence of any commercial or financial relationships that could be construed as a potential conflict of interest.

Publisher's Note: All claims expressed in this article are solely those of the authors and do not necessarily represent those of their affiliated organizations, or those of the publisher, the editors, and the reviewers. Any product that may be evaluated in this article, or claim that may be made by its manufacturer, is not guaranteed or endorsed by the publisher.

Copyright © 2022 Yang, Xia, Cheng, Wang, Zhang and Wang. This is an open-access article distributed under the terms of the Creative Commons Attribution License (CC BY). The use, distribution or reproduction in other forums is permitted, provided the original author(s) and the copyright owner(s) are credited and that the original publication in this journal is cited, in accordance with accepted academic practice. No use, distribution or reproduction is permitted which does not comply with these terms.



Compressive Behavior of Corroded RC Columns Strengthened With Ultra-High Performance Jacket

Jun Chen^{1,2}, Zongshan Wang^{1,3*}, Anqi Xu⁴ and Jianting Zhou¹

¹School of Civil Engineering, Chongqing Jiaotong University, Chongqing, China, ²Chongqing City Transportation Development & Investment Group Co., Ltd., Chongqing, China, ³Chongqing Railway Group Co., Ltd., Chongqing, China, ⁴Second Harbor Engineering Company Ltd., Wuhan, China

This paper performed compressive tests on corroded reinforced concrete (RC) columns with externally confined ultra-high performance concrete (UHPC) jacket. The studied parameters in this testing program was the corrosion ratio of specimens. The influences of this parameter on the compressive behavior of concrete columns confined by UHPC jacket was reported and discussed. The test results revealed that when the rust rate was less than 20%, axial cracking was the typical failure mode of unreinforced specimens, and the cracks in the rusted area gradually increased with the increase of the rust rate. When the corrosion rate reached 30%, the concrete of the protective layer fell off significantly, and the longitudinal reinforcement also yielded. The ultimate load and peak displacement of the specimens reinforced with UHPC were significantly improved, and the improvement rates of the two were more than 80% and 30%, respectively. The failure mode of the specimen with a corrosion rate of 30% also changed to longitudinal cracking of the UHPC layer. An analytical model was proposed to predict the ultimate load of RC columns with externally strengthening UHPC jacket. The validations of the predictions against the reported test results confirmed the accuracy of the analytical model.

Keywords: ultra-high performance concrete (UHPC), confinement, bridge engineering, compressive behavior, column strengthening

OPEN ACCESS

Edited by:

Xijun Shi,
Texas State University, United States

Reviewed by:

Qing-Feng Liu,
Shanghai Jiao Tong University, China
Biao Hu,
Shenzhen University, China

*Correspondence:

Zongshan Wang
wzsh@mails.cqjtu.edu.cn

Specialty section:

This article was submitted to
Structural Materials,
a section of the journal
Frontiers in Materials

Received: 21 January 2022

Accepted: 03 March 2022

Published: 31 March 2022

Citation:

Chen J, Wang Z, Xu A and Zhou J
(2022) Compressive Behavior of
Corroded RC Columns Strengthened
With Ultra-High Performance Jacket.
Front. Mater. 9:859620.
doi: 10.3389/fmats.2022.859620

INTRODUCTION

Reinforced concrete (RC) columns are widely used in engineering structures, and their performance is inevitably degraded by factors such as dry-wet cycles, freeze-thaw cycles, and steel corrosion. Among these factors, the corrosion of steel bars is recognized as the main reason for the deterioration of the mechanical properties of reinforced concrete columns (Jiang et al., 2018; Hu et al., 2019; Zhou et al., 2020), because it will cause the degradation of the mechanical properties of the corroded steel bars, the corrosion-induced cracking of concrete and the deterioration of the interface bonding properties.

The rehabilitation of deteriorated RC column is becoming increasingly important due to the maintenance purpose. Several rehabilitation systems have been applied in RC columns. Steel plate is one of the traditional retrofit methods and used widely for strengthening RC columns (Wang et al., 2017; Hwang et al., 2020). However, steel plate suffers from low corrosion resistance, which raises another durability problem. Many research efforts have been focused on investigating the behavior of RC columns strengthened with fiber-reinforced polymer (FRP) (Estevan et al., 2020; Fallah Pour

et al., 2020; Karimipour and Edalati, 2020). The strength and ductility of RC columns can be increased by FRP jackets, and the confinement efficiency increases with the lateral pressure. In order to be fully effective, the deteriorated RC column surface need to be appropriately prepared. Moreover, the confinement efficiency decreases when the column is subjected to an eccentric axial load (Hadi and Li, 2004; Hadi, 2009) and the diameter of the cylindrical concrete column increases (Lam and Teng, 2003). From a different perspective, an increasing number of FRP layers not only incurs additional cost but also causes bond failure (Wu et al., 2006).

In fact, concrete jacketing is the first method to strengthen damaged concrete columns with a new layer of reinforced concrete (Ma et al., 2017). It is reported that the bonding performance between damaged concrete and jacket is good if roughening and cleaning of concrete surface are adopted to ensure good compatibility between the jacket and column surface (Ma et al., 2017). The jacket can provide protection for the core concrete, and the bearing capacity of the reinforced columns can also be increased. However, the poor durability of reinforced concrete limits its application. In the past 10 years, many researchers have worked to develop a type of high-performance fiber-reinforced cementitious composites (also known as engineered cementitious composite, ECC), which are best known for their ultra-ductility and ultra-toughness. ECC has gained increasing popularity in the retrofitting of walls and beams for its excellent tensile properties (Qin et al., 2020; Zhang et al., 2020; Zhang et al., 2021), but it cannot exert its advantages for retrofitting RC columns mainly under compression. The applications of ultra-high performance concrete (UHPC) provides a new choice for this approach. UHPC is a fiber-reinforced material that disperses a certain volume of steel fibers in high strength mortar. It has excellent mechanical properties and durability (Song et al., 2020; Du et al., 2021) as well as good bonding ability (Feng et al., 2020; Guan et al., 2021; Hu et al., 2021), showing great prospects in the field of repair and reinforcement.

Dadvar et al. (Ali Dadvar et al., 2020) investigated the axial behavior of circular RC columns strengthened with 15-mm UHPC jackets. Surface preparation using the four techniques of longitudinal and horizontal grooving, sandblasting, and abrasion were discussed. The results showed that the novel longitudinal grooving surface treatment exhibited better than the common sand blasting technique in load-carrying capacity and energy absorption. Hadi et al. (Hadi et al., 2018) studied the behavior of 16 RC columns strengthened with UHPC under uniaxial compressive and eccentric compressive loads. Their results showed that the thin RPC jacket was able to produce significant increases in both axial and flexural load capacities of their circular columns. Moreover, confining the specimens with UHPC jackets was observed to increase both their ductility and energy absorption when compared with the reference columns.

Xie et al. (Xie et al., 2019, 2020) subjected square and circular concrete columns strengthened with UHPC jackets to uniaxial compression loading. They found that increasing the thickness of confining UHPC jacket significantly improved the compressive behaviors of concrete stub columns for cylindrical shaped

column. However, this influence on that of square shaped stub columns was less significant. Moreover, Shan et al. (Shan et al., 2020) conducted an experimental study to investigate the axial behavior of concrete-filled UHPC tubes, which is composed of a prefabricated UHPC thin-wall hollow tube with FRP hoops and concrete. Researchers also focused on the establishment of theoretical models. Models to predict the stress-strain relation of RC columns strengthened with UHPC jackets have been proposed (Algburi et al., 2019; Xie et al., 2019, 2020; Ali Dadvar et al., 2020). The validations of the predictions against the reported test results confirmed the accuracy of the analytical models.

Despite the numerous studies in recent years conducted on RC columns strengthened with UHPC jackets, the reinforced objects are mainly intact RC columns rather than corroded ones. The present studies the axial behavior of corroded RC columns strengthened with 2 mm UHPC jacket and discusses the effect of corrosion rate on the bearing capacity, failure mode and deformation. An analytical model is proposed to predict the bearing capacity of corroded RC columns with externally strengthening. The model is finally verified against results reported.

TESTING PROGRAM

Specimen Design and Fabrication

A total of eight RC columns with different corrosion rates, including four corrosion rates of 0%, 10%, 20%, and 30%, were designed to explore the effect of UHPC jacket on the compressive behavior of corroded RC columns. Specimen were divided into two groups according to whether they were reinforced. All specimens were designed with square cross section and measured 150 and 900 mm in side length and height, respectively. Four steel bars with a diameter of 12 mm were arranged longitudinally. The diameter of the stirrups was 6mm, and one stirrup was set at an interval of 150 mm. Both ends of the specimen were welded with 10 mm thick steel plates as a leveling layer to avoid end damage. 400 mm central area of the specimen was selected as the study area, and electrical corrosion test was used to achieve different corrosion rates. The design of the specimens is shown in **Figure 1**, and the details of specimens is shown in **Table 1**.

The fabrication of the specimens was divided into three stages. The first stage was the production of the RC column. After the steel cage was bound, it was placed in a wooden mold and poured into a mold. The poured specimens were placed on a flat place and left for 48 h. After 2 days, the wooden formwork was removed, and then watered and cured for 28 days. Then electrical corrosion test was used to corrode the 400 mm long section in the middle of the RC columns. The RC group specimens were waiting for the test under natural curing conditions, while the URC group was chamfered and then reinforced by UHPC jacket. After the strengthening was completed, they were cured at room temperature for 28 days, and the axial compression test was carried out. **Figure 2** shows the main process of specimen fabrication.

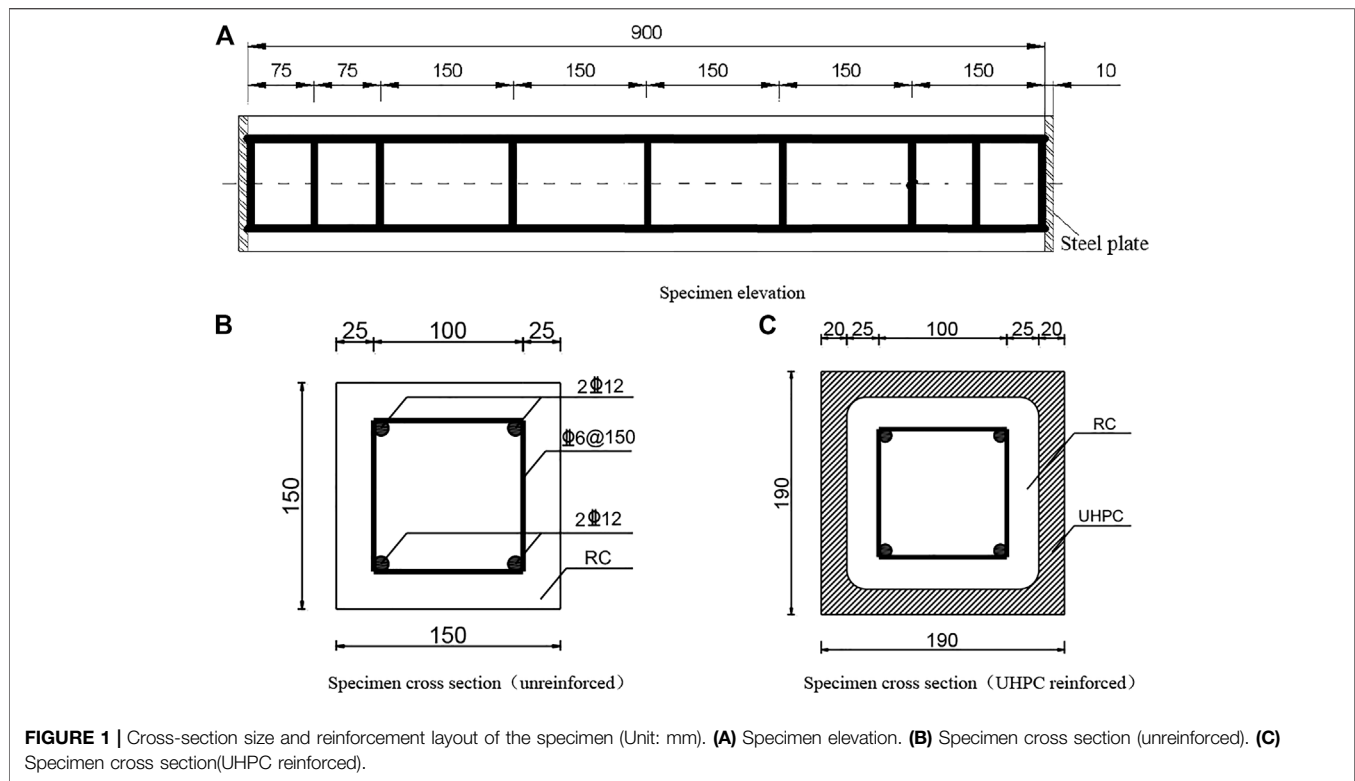


TABLE 1 | Results and details of corroded RC columns confined by UHPC jacket.

Item	<i>a</i> (mm)	<i>b</i> (mm)	<i>h</i> (mm)	<i>k</i> (%)	<i>k</i> ₁ (%)	<i>k</i> ₂ (%)	<i>t</i> (mm)	<i>p</i> _c (kN)	<i>p</i> _u (kN)	<i>Δ</i> _u (mm)
RC00	150	150	900	0	0	0	—	1,080	1,200	0.94
RC10	150	150	900	10%	10%	10%	—	900	1,101	0.87
RC20	150	150	900	20%	20%	20%	—	950	1,037	0.92
RC30	150	150	900	30%	30%	30%	—	600	876	0.82
URC00	150	150	900	0	0	0	20	1,659	2023	0.82
URC10	150	150	900	10%	10%	10%	20	1,562	1984	1.33
URC20	150	150	900	20%	20%	20%	20	1,538	1909	0.99
URC30	150	150	900	30%	30%	30%	20	1,605	1821	1.44

a and *b* denote the section size of column; *h* denotes the height of column; *k* denotes the theoretical corrosion rate; *k*₁ and *k*₂ denote the actual corrosion rate of longitudinal bars and stirrups, respectively; *t* denotes the thickness of UHPC jacket; *p*_c denotes the cracking load; *p*_u denotes the experimental ultimate compressive resistance; *Δ*_u denotes the displacement corresponding to *p*_u.

Electrical Corrosion Test

It is time consuming to achieve the corrosion and deterioration of the RC columns in the real situation, the corrosion of the steel bars in the RC columns was achieved by electrical corrosion test. While there might be a certain gap between the accelerated corrosion by electrification and the actual natural corrosion, especially the corrosion induced crack patterns and rust distributions (Meng et al., 2022), it could greatly shorten the test time and was widely used in research (Xia et al., 2021). In the electrification accelerated corrosion test, the most commonly used theory was Faraday's law, through which the current size and electrification time required to achieve the theoretical corrosion rate can be

determined, and the relationship between the corrosion quality and them is as follows:

$$\Delta m = \frac{AIt}{ZF} = \frac{55.847 \times t \times I}{2 \times 96487} \quad (1)$$

Where, *Δm* denotes corrosion quality of steel bar (g), *I* denotes corrosion current intensity (A), *t* denotes corrosion time (s). *Z* denotes the number of valence electrons lost by iron during the oxidation process. *F* is Faraday constant, taken as 96,485 C/mol.

Since the stirrups and the longitudinal bars were bound together, the stirrups would also corrode during the electrification process. Therefore, the following formula was used when calculating the total corrosion mass of the steel bars:



FIGURE 2 | Main process of specimen fabrication.

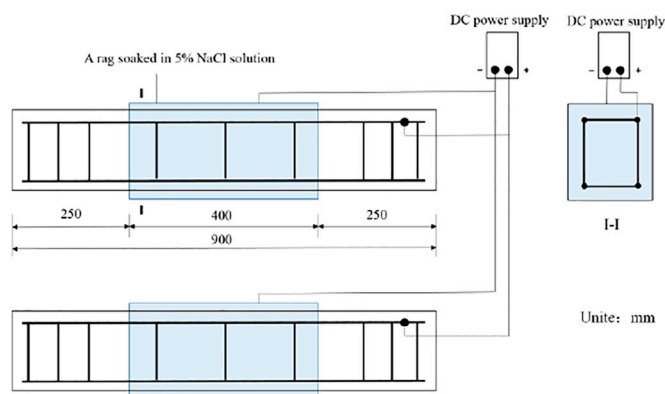


FIGURE 3 | The rust condition of the specimen when electrified.

$$m = m_1 + m_2 \quad (2)$$

From the Eqs 1, 2, the energization time required for the steel bar under a specific corrosion rate could be calculated, and it was corroded according to the theoretical corrosion rate in the table. First, configure a 5% NaCl solution, completely soak the rag to wrap the test section of the specimen that needs to be corroded. In addition, it was necessary to use a catheter to set up a liquid guiding device to ensure that the rag was always in a wet state, so that the concrete in the corroded steel bar area fully moistened. In order to prevent the end of the specimen from being damaged, the outer rag was only set in the target rust range of 400 mm in the middle of the test piece. As shown in Figure 3, connect the positive pole of the power supply to

the copper wire, and wrap the negative carbon rod in a wet rag to close to the surface of the test piece and check whether the connection is normal.

An external direct current was adopted during the accelerated corrosion test of steel bars. A power supply with adjustable current and voltage was used, the voltage adjustment range was between 0 and 30 V, and the current adjustment range was between 0 and 3 A. During the corrosion, the current was stabilized at 2.1 A, which can be chosen according to experimental conditions. After turning on the power supply, the current should be slowly adjusted to the corresponding current value after the corrosion section was fully infiltrated. During the corrosion process, the current and energization time

TABLE 2 | Mix proportion of C50 (kg/m³).

Grade	Water	Cement	Sand	Stone
C50	160	415	552	1,288

were observed in real time to ensure that the 5% NaCl solution kept the concrete in the corrosion section fully wet.

Material Test

Grade C50 normal weight concrete was selected for all of the stub concrete columns. Ordinary Portland cement PO 42.5, natural sand and crushed granite coarse aggregate with a maximum diameter of 20 mm were used. **Table 2** lists the mixture proportions. The water-cement ratio of this NWC was 0.48. Concrete cube with 150 mm length were tested for the compressive strength, and the average 28-days compressive strength was 41.3 MPa. The UHPC dry mix is produced by Hunan Guli Engineering New Materials Co., Ltd., and the material mass ratio is cement: silica fume: quartz sand: quartz powder: water reducer: water = 1:0.25:1.1:0.3:0.019:0.225. In addition, flat steel fibers with a length of 8 mm and a diameter of 0.12 mm were mixed with a volume of 2%. According to the specification (China Building Materials, 2018), the material property test of UHPC was carried out. The average cubic compressive strength of UHPC was 135 MPa, and the average flexural strength was 38.4 MPa. Its elastic modulus was 4.45×10^4 N/mm².

Measuring Point Layout and Loading Scheme

The test was carried out through the YAW-10000F electro-hydraulic servo pressure testing machine specimen to carry out the static axial compression performance test. The test was divided into two stages: preloading and formal loading. First, the tiny gap between the bearing plate and the specimen was eliminated by preloading, and the preload was 20% of the ultimate bearing capacity. In the formal loading, displacement control was used first, and the load was loaded to 50kN at a speed of 3 mm/min, and then the load was transferred to the force-controlled loading method, and the load was loaded at a speed of 50 kN/min. When the load on the component cannot continue to increase, it was considered that the component was damaged.

Figure 4 shows the layout of strain gauges and displacement gauges on the surface of the specimen. In this test, two strain gauges were arranged in the middle of the adjacent surfaces of the corroded RC column, one for measuring the horizontal strain and one for measuring the vertical strain. For the corroded column reinforced by UHPC, the same strain arrangement is adopted on the surface of UHPC. In addition, since the test section is only 400 mm in the middle of the rusted column, L-shaped steel sheets are pasted at both ends of the test section, and displacement gauges D1 and D2 with a range of 30 mm are installed at both ends of the steel sheet, and the bases of the two displacement gauges are placed on the backing plate, the vertical displacement

**FIGURE 4** | Loading set-up of the axial compression test.

of the test section can be obtained by subtracting the readings of the two displacement meters during the loading process. At the same time, two displacement gauges D3 and D4 are arranged on the other two sides to measure the lateral deformation of the corroded RC column.

ANALYSIS OF TEST RESULTS

Test Phenomenon and Destruction Characteristics

The failure morphology of the unreinforced specimen is shown in **Figure 5**. The cracks of the specimen RC00 are concentrated in the end area, and this area presents a V-shaped main crack when the specimen is damaged. The failure patterns of the specimens RC10 and RC20 are significantly different from those of the RC00 specimen, mainly because the two specimens are mainly vertical cracks when they are damaged. With the increase of the corrosion rate, the vertical cracks in the corroded area gradually increase, but the spalling of the surface concrete is not significant. The RC30 specimen is not the same. Large areas of concrete spalling occurred in the corroded area, the longitudinal bars of the column are buckled by compression, and the concrete in the uncorroded area remains intact. Obviously, with the increase of the corrosion rate, the bonding force between the steel bar and the concrete, and



FIGURE 5 | Failure mode of the unreinforced specimen.

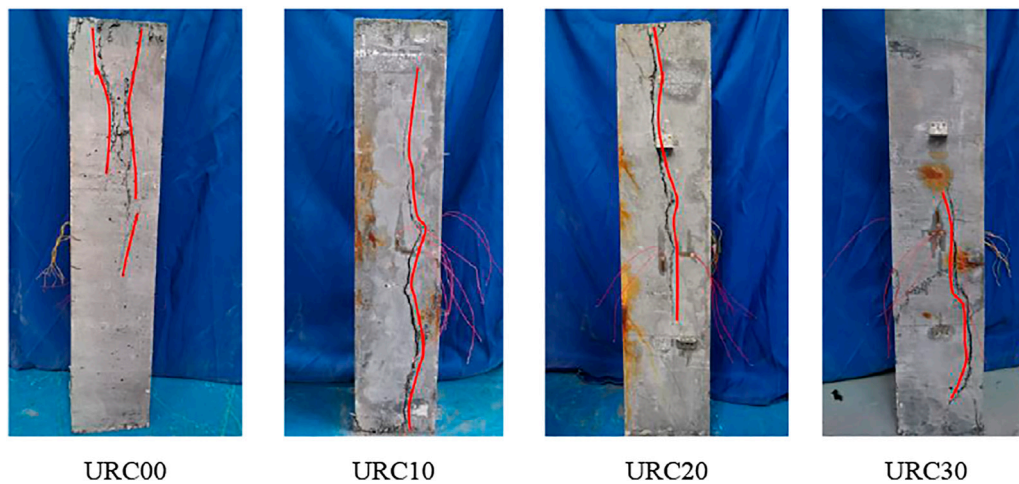


FIGURE 6 | Failure mode of the strengthened specimen.

the restraint ability of the stirrup to the longitudinal bar are greatly reduced.

The failure patterns of the specimens reinforced with UHPC are basically similar shown in **Figure 6**, and have nothing to do with the degree of corrosion. The typical failure pattern is a longitudinal crack that does not penetrate the specimen. There are some small cracks on both sides of the main crack, and UHPC debris falls during the loading process. But no UHPC peeling occurred. Obviously, UHPC greatly constrains the corrosion column and changes the failure morphology of the specimen.

Load-Displacement Curve

Figure 7 is the load-displacement curve of the test column. It can be seen from the figure that the load-displacement curve can be roughly divided into two stages, one is the elastic stage, where the load and displacement show a linear relationship, and the other is the plastic stage, where the displacement increases faster than the load. The bearing capacity of the specimen decreased with the increase of the corrosion rate.

RC00 and URC00 were not affected by corrosion, and their bearing capacity was the largest among similar specimens. RC30 and URC30 were most affected by corrosion and had the smallest bearing capacity. In the RC group, the slopes of the curves of the specimens with corrosion rates of 0%, 10%, and 20% are all close, indicating that the difference in the stiffness of the structure is small, but when the corrosion rate of the components reaches 30%, the stiffness of the structure decreases significantly. When the corrosion rate of the steel bar is high, the surface of the original specimen will have rust expansion cracks, and the adhesion between the steel bar and the original structure will become poor, which may be the main reason for this phenomenon. Compared with the RC group, the average peak load of the specimen in the URC group increased from 1000 to 1900 kN, and the average peak displacement increased from 0.85 to 1.2 mm, which indicates that the bearing capacity and ductility of corroded columns have been significantly improved after UHPC retrofitting. In addition, the slope of URC30 is close to that

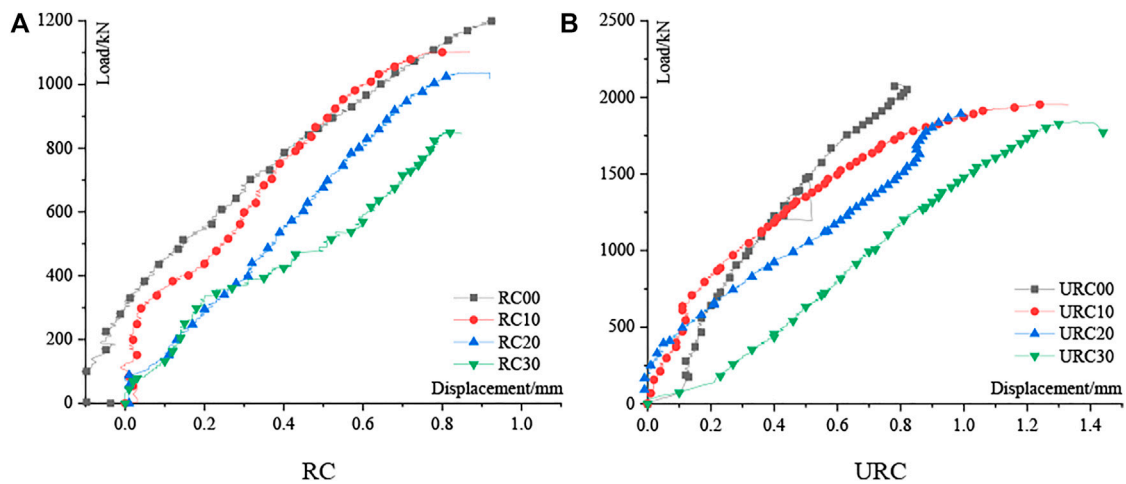


FIGURE 7 | Load-displacement of the specimen. (A) RC. (B) URC.

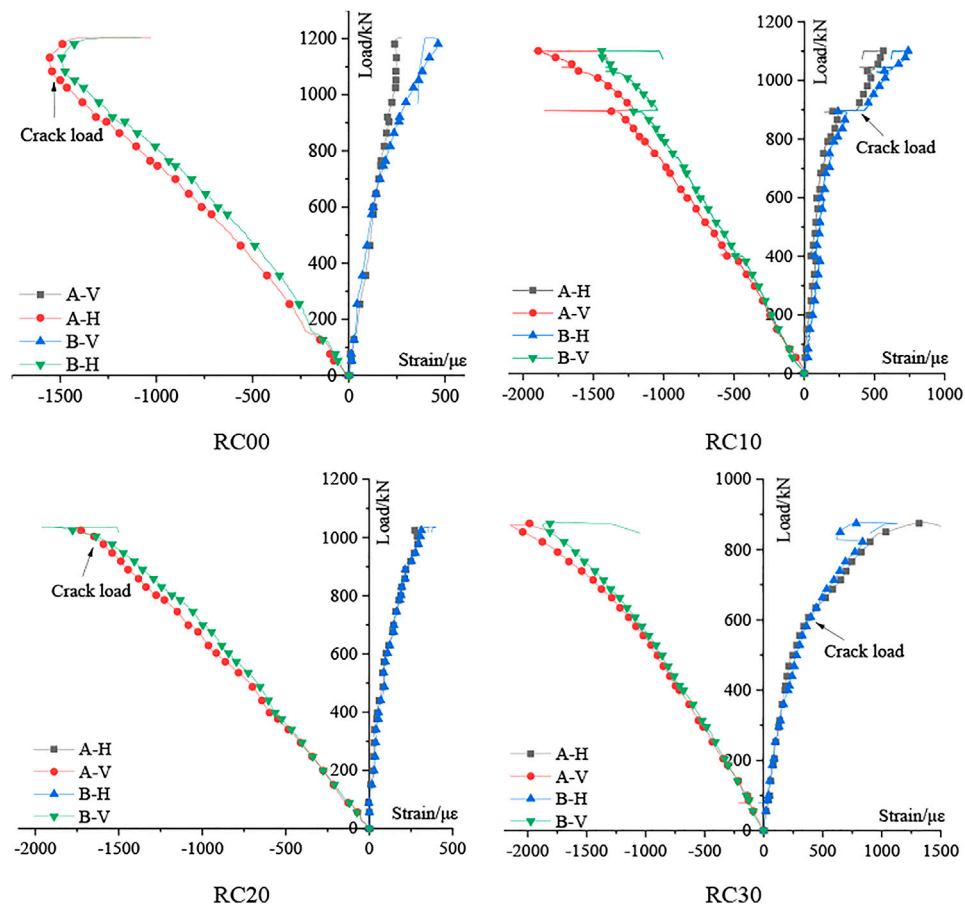


FIGURE 8 | Load-strain curve of unreinforced columns.

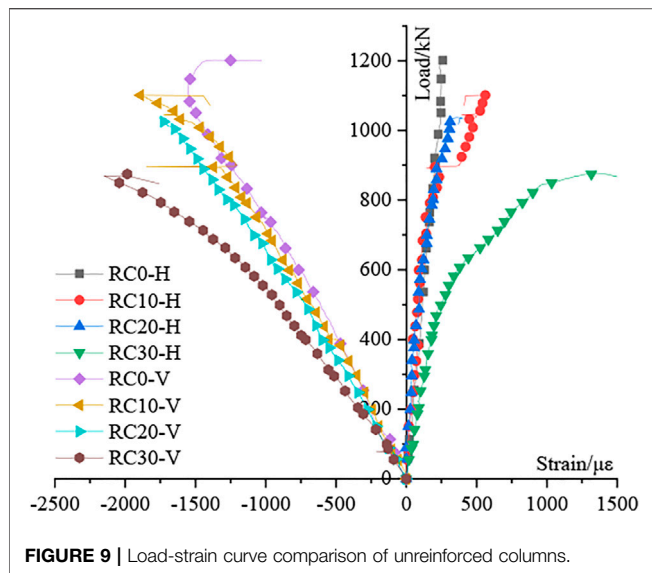


FIGURE 9 | Load-strain curve comparison of unreinforced columns.

of other specimens in this group, and there is no significant decrease in stiffness, indicating that UHPC has a good retrofitting effect on RC columns with high corrosion rates.

Load-Strain Curve Unreinforced Specimen

Figure 8 shows the load-strain curve of the unreinforced column. “A” and “B” denote adjacent two sides, and “V” and “H” represent vertical and horizontal strain, respectively. It can be seen that the difference between the same strains on the adjacent two sides is very small, indicating that the test column basically maintains a good axial compression state under the vertical load. Similar to the load-displacement curve, the load-strain curve can be roughly divided into two stages. The first stage is the linear elastic stage. The load and strain increase in equal proportions, and the integrity of the structure is good. The second stage is the plastic stage. The growth rate slows down, the strain increases more significantly. The surface begins to produce micro-cracks and begins to develop, and the overall stiffness of the structure gradually decreases. Cracks appear on the surface of the structure, indicating that the specimens entered the second stage. The cracking loads of the four specimens are 1,080, 900, 950, and 600 kN in turn. Obviously, when the corrosion rate increases significantly, the cracking load of the structure is smaller. In addition, the longitudinal strain is significantly larger than the transverse strain during the loading process, and the Poisson coefficient of the test columns with the design corrosion rate of 0%, 10%, and 20% is about 0.25, but the test column with the design corrosion rate of 30% increases to 0.65.

Figure 9 is a comparison diagram of the four specimens, from which it can be seen that the slope of the load-strain curve decreases with the increase of the corrosion rate. The transverse strain and longitudinal strain of the test columns with the corrosion rate of 0%, 10%, and 20% are relatively close, indicating that when the corrosion rate is not high, the stiffness of the structure does not decrease significantly, but

when the corrosion rate reaches 30%, the stiffness of the specimen is significantly weakened. This is because with the increase of the corrosion rate, the restraint of the stirrups on the core concrete and the supporting effect of the longitudinal bars are greatly reduced, and even the stirrups are rusted, which leads to the buckling of the longitudinal bars. Under the vertical action, the specimen has a large deformation in the horizontal direction.

Ultra-High Performance Concrete Reinforced Specimen

Figure 10 is the load-strain curve of the reinforced column. It can be seen that with the increase of the load, the mechanical performance of the reinforced column shows two stages: in the first stage, whether the reinforced column is the core concrete or the retrofitting layer, it is in the completely linear elastic stage, the longitudinal and transverse strains are small and basically synchronous, and the restraint effect of the retrofitting layer is not yet obvious; in the second stage, the specimen enters the elastic-plastic working stage, the UHPC surface strain and the core concrete strain development are no longer synchronized, the UHPC surface begins to generate micro-cracks and begins to develop, the steel fibers in the UHPC material begin to provide tensile strength, and the retrofitting layer begins to core concrete provides restraint.

In addition, it can be seen that when the corrosion rate is low, the strain of the UHPC reinforced layer is not completely consistent with the original structure, and the strain growth will be lower than that of the original structure, but it can basically work together until failure. With the increase of the corrosion rate, the retrofitting layer is more prone to relative slippage with the original structure, which leads to the phenomenon of peeling and failure of the retrofitting layer, so that the longitudinal and transverse strains of the reinforcement layer are small. However, in general, compared with the corroded column, the ultimate load, peak strain and ductility of the reinforced column have been significantly improved, indicating that the UHPC retrofitting layer can effectively share a certain axial load of the original structure. Compared with the corroded column, the strain of the core concrete increases significantly, indicating that the retrofitting layer has a certain lateral restraint effect on the original structure. Further analysis of the curve shows that the ratio of the strain when the strain of the retrofitting layer begins to lag behind the original structure and the ultimate strain of the original structure is in the range of 0.46–0.61, which is also consistent with the theoretically derived strength utilization coefficient of the retrofitting layer in the range of 0.4–0.7. It can also be seen that the strength utilization coefficient of the UHPC retrofitting layer tends to be lower in practical applications, which can also ensure a greater safety reserve.

ANALYTICAL MODEL

Corroded Reinforced Concrete Columns

When the RC column is subjected to the axial load, the longitudinal bars and stirrups have different constraints on the

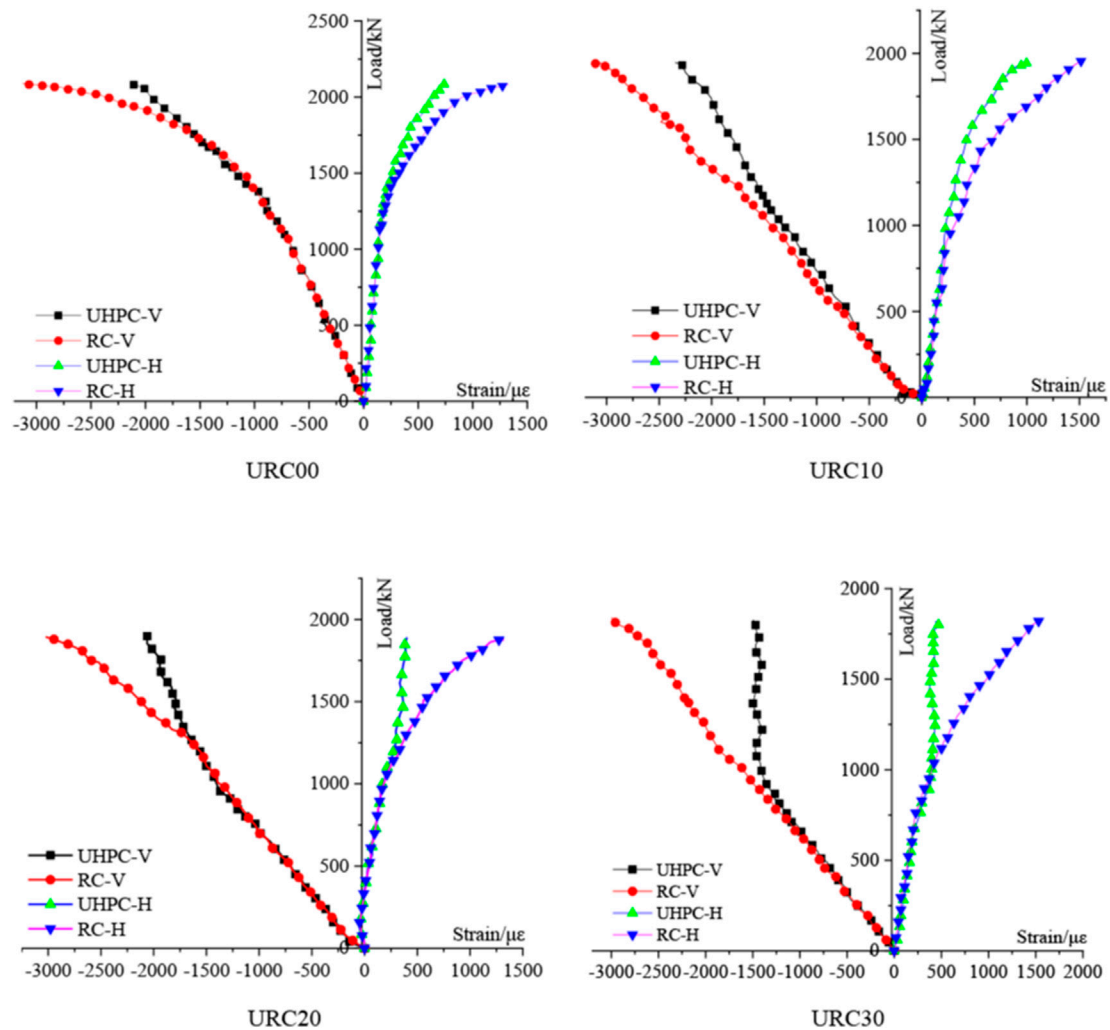


FIGURE 10 | Load-strain curve of reinforced column.

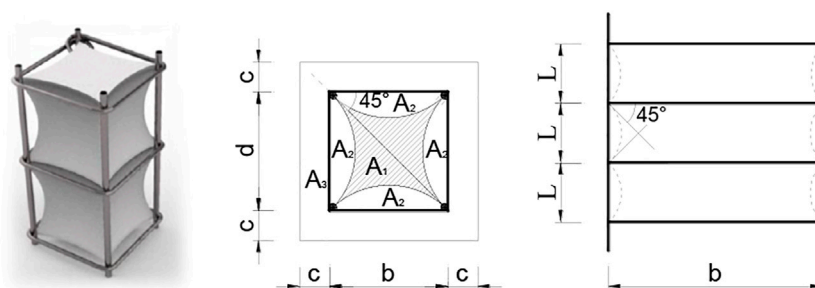


FIGURE 11 | Schematic diagram of restraint partition of RC column.

concrete at different positions, resulting in different stress states of the concrete at different positions. According to the study of Sheikh et al. (Sheikh and Uzumeri, 1982), in the direction of the axis and the cross section of the column, the concrete at the

intersection of the longitudinal bars and stirrups is the most constrained and its confinement decays outward in a parabolic fashion, as shown in Figure 11. For the convenience of calculation, it is considered that the intersection angle between

TABLE 3 | The damage coefficient of the RC column subjected to axial compression corrosion.

w/mm	$0 < w < 2$	$2 \leq w < 3$	$w \geq 3$
α	$1-0.3w$	$1-0.3w + 0.25(w-2)$	0

the parabola and the stirrup is 45° , the ultimate bearing capacity of the corroded RC column can be expressed with Eq. 3.

$$N = f_{cc}A_1 + f_{ca}A_2 + f_cA_3 + f'_sA'_s \quad (3)$$

Where N is the ultimate bearing capacity of the corroded RC columns, f_{cc} , f_{ca} are the strength of the concrete in the strong restraint area and weak restraint area respectively. f_c is the strength of the protective layer concrete, f'_s is the yield strength of the longitudinal reinforcement. A_1 , A_2 and A'_s represent the concrete area of the strong and weak restraint areas and the cross-sectional area of the longitudinal reinforcement after corrosion, respectively. A_3 is the area of the concrete protective layer. When the corrosion-induced cracking occurs, the area of the protective layer within the range of the crack length is no longer considered in the calculation of the area of the concrete protective layer.

Since the concrete in the strong restraint area is under triaxial compression, the dual effects of the section where the stirrup is located and the vertical section of the stirrup needs to be comprehensively considered. The strong restraint area of the square RC column (A_1) can be expressed with Eq. 4. A_{cor} represents the concrete area of the core area.

$$A_1 = \frac{1}{3} \left(1 - \frac{l}{2b} \right)^2 A_{cor} \quad (4)$$

$$A_{cor} = b \cdot d = A_1 + A_2$$

The damage coefficient α is introduced to evaluate the effective thickness of the concrete protective layer of the corroded RC column. Its value is related to the crack width and Table 3 lists values in different crack widths. The concrete protective layer considering the section damage for corrosion can be calculated by Eq. 5.

$$A_3 = 4\alpha(bc + \alpha c^2) \quad (5)$$

In order to calculate the constraining effect of corroded steel bars on the core concrete, the constrained concrete strength model established in reference (Qian et al., 2002) is used to obtain the concrete strength expression in the strongly constrained area.

$$f_{cc} = (1 + 1.79\lambda_v)f_{c0}$$

$$\lambda_v = \rho_v \frac{f_{yc}}{f_{c0}} \quad (6)$$

$$\rho_{vc} = (1 - \eta_s)\rho_v$$

where λ_v denotes the characteristic value of the stirrups calculated according to the measured values of the stirrup and concrete strength, ρ_v denotes volume hoop ratio without considering

stirrup corrosion; f_{yc} denotes yield strength of uncorroded stirrups, f_{c0} denotes standard value of concrete axial compressive strength.

Since the improvement of the strength of the concrete in the weakly constrained area is limited, for the convenience of calculation, the increase of the strength of the concrete in the weakly constrained area is not considered, its strength can be expressed as Eq. 7.

$$f_{ca} = f_c = f_{c0} \quad (7)$$

Electrical corrosion test was adopted to achieve different corrosion rates, the relationship between the yield strength of the steel bar and the corrosion rate can be expressed as Eq. 8 (Xia et al., 2021). The cross-sectional area of the steel bar after corrosion is calculated according to the maximum damaged cross-section, and the steel bar is considered to be uniformly corroded based on the maximum corrosion rate. The cross-sectional relationship before and after corrosion is shown in Eq. 7.

$$f_{yc} = \frac{1 - 1.196 \times \eta_s}{1 - \eta_s} f_{y0} \quad (8)$$

$$A'_s = (1 - \eta_s)A_0 \quad (9)$$

where, f_{yc} denotes the nominal yield strength of the steel bar after corrosion; η_s denotes the maximum corrosion rate of the section; f_{y0} denotes the yield strength of the corroded steel bar. A_0 and A'_s denote the cross-sectional areas before and after the steel bar is corroded.

Corroded Reinforced Concrete Columns With Ultra-High Performance Concrete Jackets

Based on the axial compressive performance of the corroded RC column, considering the retrofitting methods and theoretical researches such as normal concrete enlarged section method, steel hoop retrofitting and FRP retrofitting, the model of the corroded RC column reinforced around the plain UHPC is preliminarily drawn up.

$$N_d = 0.9\varphi(\alpha_c f_{cd1}A_{c1} + f'_{sd1}A'_{s1} + \alpha_U f_{Ucd}A_{U2}) \quad (10)$$

where N_d denotes the combined value of the axial force of the reinforced column, φ denotes the stability coefficient of the axial compression member, f_{cd1} denotes the compressive strength value of the corroded RC member concrete axial center, α_c denotes the strength improvement factor of original structure concrete, and α_U denotes the UHPC intensity utilization degree coefficient.

The restraint effect of the retrofitting layers on the original structure is actually a passive restraint caused by the original structure's deformation, and the restraint effect depends on the deformation of the original structure concrete and retrofitting layers' hoop stiffness. Due to the improvement factor of the concrete strength of the original member, combined with the stirrup constraint model and the FRP constraint model (China

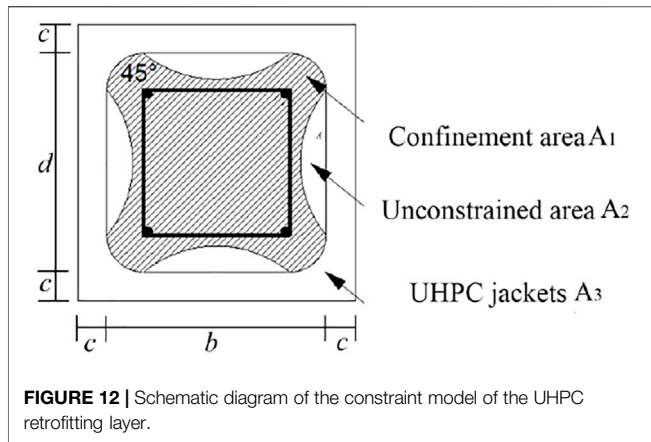


FIGURE 12 | Schematic diagram of the constraint model of the UHPC retrofitting layer.

Building Materials Association, 2010), the calculation formula of the Mander's model (Mander et al., 1988) is defined as follows:

$$f_{cc} = f_{c0} \left(-1.254 + 2.254 \sqrt{1 + 7.94 \frac{f_1}{f_{c0}}} - 2 \frac{f_1}{f_{c0}} \right) \quad (11)$$

$$f_1 = k_e f'_1$$

where f_{c0} denotes the peak stress of plain concrete, f_1 denotes the effective lateral restraint force, k_e denotes the effective restraint coefficient related to the overall shape of the section, f'_1 denotes the equivalent binding force, which refers to the overall equivalent lateral binding force in the two directions of the integrated rectangle.

The original structure was chamfered and chiseled in the retrofitting process, and the constraint model of the plain UHPC retrofitting layer to the concrete in the core area is shown in **Figure 12**. According to the literature (China Building Materials Association, 2013), the constraint coefficient is defined in **Eq. 12**.

$$k_e = \frac{A_1}{A_{cor}} \quad (12)$$

$$A_1 = b \cdot d - 0.213(b^2 + d^2)$$

The central concrete is in biaxial compression in the plane, and the transverse force diagram for a square section is shown in **Figure 13**. The relationship between the stress level f'_1 and the lateral restraint forces f'_{lx} and f'_{ly} in the direction of the long and short sides are proposed in **Eqs 13, 14**.

$$f'_1 = \frac{f'_{lx} + f'_{ly}}{2} + \sqrt{\left(\frac{f'_{lx} - f'_{ly}}{2} \right)^2} \quad (13)$$

$$\begin{aligned} f'_{lx} &= 2t\sigma_x / (b - 2c) \\ f'_{ly} &= 2t\sigma_y / (d - 2c) \end{aligned} \quad (14)$$

where σ_x is the transverse stress of the long side at the peak force, σ_y is the transverse stress of the short side at the peak force, b and d are the longitudinal and transverse widths of the reinforced column, c is the wall thickness of the UHPC retrofitting layer.

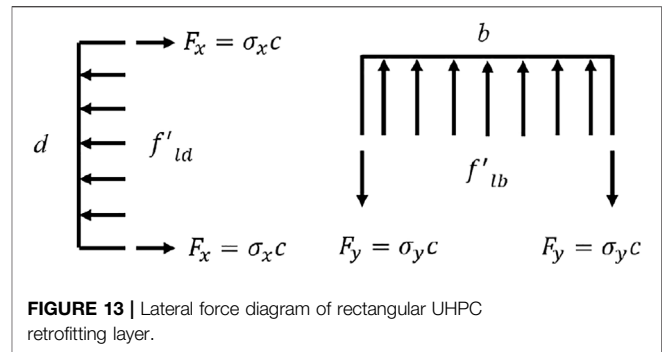


FIGURE 13 | Lateral force diagram of rectangular UHPC retrofitting layer.

The deformation of the old and new structures is considered to be consistent for the corroded RC column reinforced by UHPC, and the deformation of the reinforced structure conforms to the assumption of plane section. For normal concrete, Sargin's model (Mander et al., 1988) gives the stress-strain relationship **Eq. 15** of the structure before the bearing capacity reaches the ultimate state. The material properties of UHPC reinforced layer are between concrete and steel, so its compression state is similar to the ideal elastic-plastic. Its constitutive relation can be obtained with **Eq. 16**.

$$\sigma = f_c \frac{A(\varepsilon/\varepsilon_0) - (\varepsilon/\varepsilon_0)^2}{1 + (A - 2)(\varepsilon/\varepsilon_0)}, \quad \varepsilon \leq \varepsilon_0 \quad (15)$$

$$\begin{aligned} \sigma &= f_c, & \varepsilon_0 &\leq \varepsilon \leq \varepsilon_u \\ \sigma_{uhpc} &= E_u \varepsilon, & \varepsilon &\leq \varepsilon_{0,uhpc} \\ \sigma_{uhpc} &= f_{uc}, & \varepsilon_{0,uhpc} &\leq \varepsilon \leq \varepsilon_{u,uhpc} \end{aligned} \quad (16)$$

where ε_0 and ε_u are the peak strain and ultimate compressive strain of normal concrete, which are taken as 0.002 and 0.0033, respectively. $\varepsilon_{0,uhpc}$ and $\varepsilon_{u,uhpc}$ are the peak strain and ultimate compressive strain of UHPC. f_c and f_{uc} are the peak stress of normal concrete and UHPC. A is ratio of ratio of the elastic modulus of UHPC (E_u) to that of normal concrete (E_0), which is taken as 2.13.

There is an initial stress (σ_1) on the corroded column under constant load before retrofitting, and the corresponding strain can be defined as ε_1 . The ratio between the initial stress and the peak stress is defined as ε_1 . The relationship between the initial strain ε_1 and peak strain ε_0 are shown in **Eq. 17**.

$$\begin{aligned} B &= \eta A - 2\eta - A \\ \varepsilon_1 &= \frac{-B - \sqrt{B^2 - 4\eta}}{2} \varepsilon_0 \end{aligned} \quad (17)$$

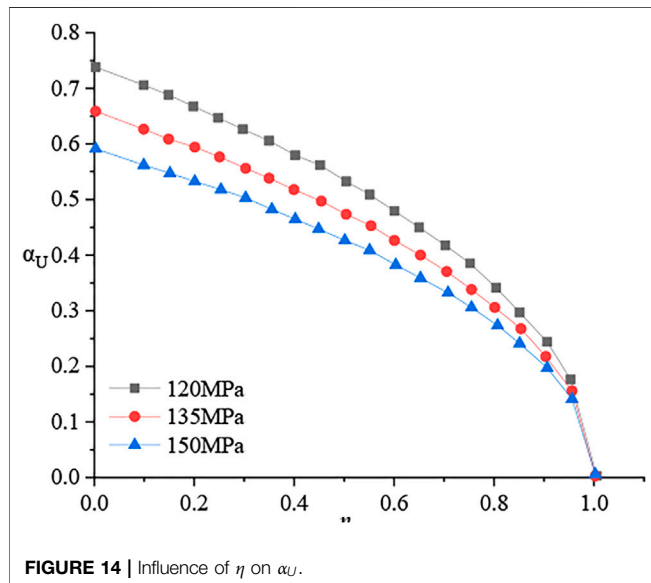
Normal concrete's peak strain (ε_0) is equal to UHPC layer's peak strain ($\varepsilon_{0,uhpc}$) according to the deformation coordination. The maximum strain difference generated after retrofitting can be expressed as follows.

$$\varepsilon = \varepsilon_0 - \varepsilon_1 = \frac{2 + B + \sqrt{B^2 - 4\eta}}{2} \varepsilon_0 \quad (18)$$

Combined **Eq. 18** with **Eq. 15**, the material utilization degree coefficient of UHPC (α_U) can be obtained.

TABLE 4 | strength utilization factor of UHPC without initial stress.

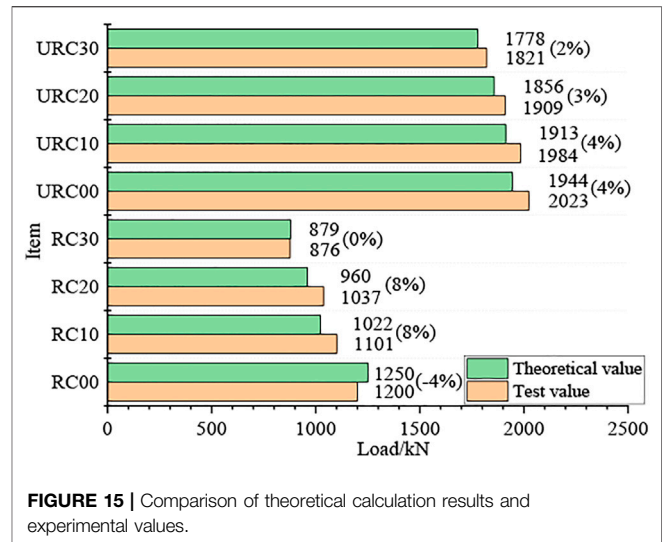
Repair materials	Normal concrete	UHPC120	UHPC135	UHPC150
α_U	0.8	0.68	0.61	0.54

**FIGURE 14** | Influence of η on α_U .

$$\alpha_U = \sigma_{0,uhpc} / f_{uc} = E\varepsilon / f_{uc} = \frac{2 + B + \sqrt{B^2 - 4\eta}}{2} E\varepsilon_0 / f_{uc} \quad (19)$$

Obviously, α_U and η are closely related, and **Figure 13** shows their relationship. It can be seen that as the strength of the UHPC increases, the utilization degree coefficient of UHPC will be lower. When the initial stress ratio is less than 0.6, α_U basically maintains a relatively slow decline in slope with the increase of η . When the initial stress ratio is more than 0.6, the utilization degree coefficient decreases rapidly.

The calculation of RC columns strengthened with UHPC jacket is similar to that with RC jacket. When normal concrete is used to strengthen, the strength utilization factor is suggested to be 0.8 (Mander et al., 1988). However, it can be seen that the strength of UHPC material is much greater than that of normal concrete, when η is less than 0.6, the strength utilization factor of UHPC can take values from 0.4 to 0.75. When calculating the axial compressive bearing capacity of corroded RC columns reinforced with UHPC, it is suggested that the value of the material strength utilization coefficient of the retrofitting layer ranges from 0.4 to 0.7 for safety, and the specific parameters should be determined according to the actual peak strength of UHPC. **Table 4** lists suggested strength utilization factor of UHPC with different strength grades, the value is relatively conservative to ensure the security of calculation. In addition, when calculating corroded RC columns reinforced with UHPC with initial stress, the utilization degree coefficient of UHPC can refer to **Figure 14**.

**FIGURE 15** | Comparison of theoretical calculation results and experimental values.

Verification of Proposed Model

When calculating the axial compressive bearing capacity of corroded RC columns, several important parameters need to be determined experimentally. The standard value of concrete cube strength ($f_{cu,k}$) is 48.6 MPa, so the standard value of axial compressive strength of normal concrete (f_{ck}) is 32.1 MPa.

It is also necessary to obtain the damage coefficient of the protective layer section by measuring the width of the rust expansion crack on the surface of the rusted column before loading, so as to characterize the reduction of the compression section of the member due to the corrosion of the steel bar. The damage coefficients of RC10, RC20 and RC30 are 0.97, 0.91, and 0.79, respectively.

In addition, the influence of corrosion on the axial compressive bearing capacity of steel bars is considered, which is mainly reflected in the two aspects of cross-sectional area and yield strength. After taking out the steel bar, the cross section at the maximum pit corrosion is used as the calculation index to obtain the control cross-sectional area of the steel bar under different corrosion rates, and then the yield strength of the longitudinal bar after corrosion is calculated.

When calculating the axial compressive bearing capacity of corroded RC columns reinforced with UHPC, calculating the ultimate bearing capacity of corroded RC columns is necessary. Then, the concrete strength improvement coefficient is needed to be determined. Combined with the theoretical model calculation and the actual test situation, the concrete strength improvement coefficient α_c is 1.065 and the material strength utilization degree coefficient α_U is taken as 0.5. **Equation 10** finally can be written as **Eq. 20**.

$$N_d = 0.9\varphi(1.065f_{cd1}A_{c1} + f_{sd1}A'_{s1} + 0.5f_{Ucd}A_{U2}) \quad (20)$$

Figure 15 compares the results of theoretical calculations and experiments. It can be seen that the error between the experimental results and the theoretical calculation values is

within 8%, indicating that the theoretical calculation values are in good agreement with the experimental values. It shows that the reliability of the theoretical calculation model of the axial compressive bearing capacity of corroded RC column reinforced with UHPC.

CONCLUSION

- 1) The ultimate compressive resistance and failure mode of the RC corroded column were affected by the corrosion rate. Compared with the uncorroded column, the ultimate compressive resistance of the specimen with the corrosion rate of 10%, 20%, and 30% decreased by 8.3%, 13.5%, and 27% respectively. Axial cracking was the typical mode when the rust rate was less than 20%, and the cracks in the rusted area gradually increased with the increase of the rust rate. However, the concrete of the protective layer fell off significantly, and the longitudinal reinforcement also yielded obviously when the corrosion rate reached 30%.
- 2) The ultimate compressive resistance and corresponding displacement of the specimens reinforced with UHPC were significantly improved, and the improvement rates of the two were more than 60 and 30%, respectively. The failure mode of the specimen with a corrosion rate of 30% also changed to longitudinal cracking of the UHPC layer. It shows that UHPC jacketing is a fair choice for retrofitting corroded RC columns.
- 3) On the basis of considering the influence of bar corrosion, the concrete strength improvement coefficient and the UHPC strength utilization coefficient were introduced, and the

calculation formula of the bearing capacity of the corroded RC column before and after retrofitting was established. The error between the experimental value and the theoretical calculation value was within 8%.

DATA AVAILABILITY STATEMENT

The original contributions presented in the study are included in the article/Supplementary Material, further inquiries can be directed to the corresponding author.

AUTHOR CONTRIBUTIONS

JC: program formulation; ZW: Thesis writing; AX: Test implementation. JZ: Technical support.

FUNDING

The authors highly appreciate the financial support from the National Natural Science Foundation of China (Grant No. U20A20314, 51908093, and 52008066), the Natural Science Foundation of Chongqing, China (Grant No. cstc2019jcyj-cxttX0004, cstc2020jcyj-bshX0007, and cstc2020jcyj-msxmX0088), China Postdoctoral Science Foundation (2021M693919), the Science and Technology Project of Huibei Provincial Transportation Department (Grant No. 2020-2-1-1), and the Chongqing Jiaotong University Graduate Research and Innovation Fund (Grant No. 2020B0004).

REFERENCES

- Algburi, A. H. M., Sheikh, M. N., and Hadi, M. N. S. (2019). Analytical Investigation on the Behavior of Circular and Square RC Columns Strengthened with RPC and Wrapped with FRP under Uniaxial Compression. *J. Building Eng.* 25, 100833. doi:10.1016/j.jobbe.2019.100833
- Ali Dadvar, S., Mostofinejad, D., and Bahmani, H. (2020). Strengthening of RC Columns by Ultra-high Performance Fiber Reinforced concrete (UHPFRC) Jacketing. *Construction Building Mater.* 235, 117485. doi:10.1016/j.conbuildmat.2019.117485
- China Building Materials Association (2018). *Fundamental Characteristics and Test Methods of Ultra-high Performance concrete*[S].
- China Building Materials Association (2010). *Code for Design of concrete structures*[S].
- China Building Materials Association (2013). *Code for Design of Strengthening concrete structure*[S].
- Du, J., Meng, W., Khayat, K. H., Bao, Y., Guo, P., Lyu, Z., et al. (2021). New Development of Ultra-highperformance concrete (UHPC). *Composites B: Eng.* 224, 109220. doi:10.1016/j.compositesb.2021.109220
- Estevan, L., Baeza, F. J., Bru, D., and Ivorra, S. (2020). Stone Masonry Confinement with FRP and FRCM Composites. *Construction Building Mater.* 237, 117612. doi:10.1016/j.conbuildmat.2019.117612
- Fallah Pour, A., Nguyen, G. D., Vincent, T., and Ozbakkaloglu, T. (2020). Investigation of the Compressive Behavior and Failure Modes of Unconfined and FRP-Confined concrete Using Digital Image Correlation. *Compos. Structures* 252, 112642. doi:10.1016/j.compstruct.2020.112642
- Feng, S., Xiao, H., and Li, H. (2020). Comparative Studies of the Effect of Ultrahigh-Performance concrete and normal concrete as Repair Materials on Interfacial Bond Properties and Microstructure. *Eng. Structures* 222, 111122. doi:10.1016/j.engstruct.2020.111122
- Guan, D., Liu, J., Jiang, C., Chen, Z., and Guo, Z. (2021). Shear Behaviour of the UHPC-NSC Interface with Castellated Keys: Effects of Castellated Key Dimension and Dowel Rebar. *Structures* 31, 172–181. doi:10.1016/j.istruc.2021.01.088
- Hadi, M. N. S., and Li, J. (2004). External Reinforcement of High Strength concrete Columns[J]. *Compos. Structures* 65 (3), 279–287. doi:10.1016/j.compstruct.2003.11.003
- Hadi, M. N. S., Algburi, A. H. M., Sheikh, M. N., and Carrigan, A. T. (2018). Axial and Flexural Behaviour of Circular Reinforced concrete Columns Strengthened with Reactive Powder concrete Jacket and Fibre Reinforced Polymer Wrapping. *Construction Building Mater.* 172, 717–727. doi:10.1016/j.conbuildmat.2018.03.196
- Hadi, M. N. S. (2009). Behaviour of Eccentric Loading of FRP Confined Fibre Steel Reinforced concrete Columns. *Construction Building Mater.* 23 (2), 1102–1108. doi:10.1016/j.conbuildmat.2008.05.024
- Hu, B., Zhou, Y., Xing, F., Sui, L., and Luo, M. (2019). Experimental and Theoretical Investigation on the Hybrid CFRP-ECC Flexural Strengthening of RC Beams with Corroded Longitudinal Reinforcement. *Eng. Structures* 200, 109717. doi:10.1016/j.engstruct.2019.109717
- Hu, M., Han, Q., Wu, S., et al. (2021). Shear Capacity of Precast Concrete Shear Keys with Ultrahigh-Performance Concrete for Connections[J]. *J. Bridge Eng.* 26 (7), 4021036. doi:10.1061/(asce)be.1943-5592.0001734
- Hwang, Y.-H., Yang, K.-H., Mun, J.-H., and Kwon, S.-J. (2020). Axial Performance of RC Columns Strengthened with Different Jacketing Methods. *Eng. Structures* 206, 110179. doi:10.1016/j.engstruct.2020.110179
- Jiang, C., Wu, Y.-F., and Dai, M.-J. (2018). Degradation of Steel-To-concrete Bond Due to Corrosion. *Construction Building Mater.* 158, 1073–1080. doi:10.1016/j.conbuildmat.2017.09.142

- Karimipour, A., and Edalati, M. (2020). Retrofitting of the Corroded Reinforced concrete Columns with CFRP and GFRP Fabrics under Different Corrosion Levels[J]. *Eng. Structures* 228, 111523.
- Lam, L., and Teng, J. G. (2003). Design-oriented Stress–Strain Model for FRP-Confined Concrete[J]. *Construction Building Mater.* 17 (6), 471–489. doi:10.1016/s0950-0618(03)00045-x
- Ma, C.-K., Apandi, N. M., Sofrie, C. S. Y., Ng, J. H., Lo, W. H., Awang, A. Z., et al. (2017). Repair and Rehabilitation of concrete Structures Using Confinement: A Review. *Construction Building Mater.* 133, 502–515. doi:10.1016/j.conbuildmat.2016.12.100
- Mander, J. B., Priestley, M. J. N., and Park, R. (1988). Theoretical Stress-Strain Model for Confined Concrete. *J. Struct. Eng.* 114 (8), 1804–1826. doi:10.1061/(asce)0733-9445(1988)114:8(1804)
- Meng, Z., Liu, Q. f., Xia, J., Cai, Y., Zhu, X., Zhou, Y., et al. (2022). Mechanical-transport-chemical Modeling of Electrochemical Repair Methods for Corrosion-induced Cracking in marine concrete. *Computer aided Civil Eng.* doi:10.1111/mice.12827
- Qian, J., Cheng, L., and Zhou, D. (2002). Behavior of Axially Loaded concrete Columns Confined with Ordinary Hoops [J]. *J. Tsinghua Univ. (Science&technology)* (10), 1369–1373.
- Qin, F., Zhang, Z., Yin, Z., Di, J., Xu, L., and Xu, X. (2020). Use of High Strength, High Ductility Engineered Cementitious Composites (ECC) to Enhance the Flexural Performance of Reinforced concrete Beams. *J. Building Eng.* 32, 101746. doi:10.1016/j.jobbe.2020.101746
- Shan, B., Xu, C., Lai, D. D., Xiao, Y., and Li, T. Y. (2020). Experimental Research on Compressive Behavior of Seawater and Sea Sand concrete-filled RPC Tubes. *Eng. Structures* 222, 111117. doi:10.1016/j.engstruct.2020.111117
- Sheikh, S. A., and Uzumeri, S. M. (1982). Analytical Model for Concrete Confinement in Tied Columns. *J. Struct. Div.* 108 (12), 2703–2722. doi:10.1061/jsdeag.0006100
- Song, Q., Yu, R., Shui, Z., Rao, S., Fan, D., and Gao, X. (2020). Macro/micro Characteristics Variation of Ultra-high Performance Fibre Reinforced concrete (UHPFRC) Subjected to Critical marine Environments. *Construction Building Mater.* 256, 119458. doi:10.1016/j.conbuildmat.2020.119458
- Wang, L., Su, R. K. L., Cheng, B., Li, L. Z., Wan, L., and Shan, Z. W. (2017). Seismic Behavior of Preloaded Rectangular RC Columns Strengthened with Precambered Steel Plates under High Axial Load Ratios. *Eng. Structures* 152, 683–697. doi:10.1016/j.engstruct.2017.09.048
- Wu, Y.-F., Liu, T., and Oehlers, D. J. (2006). Fundamental Principles that Govern Retrofitting of Reinforced Concrete Columns by Steel and FRP Jacketing. *Adv. Struct. Eng.* 9 (4), 507–533. doi:10.1260/136943306778812769
- Xia, R., Zhang, H., Zhou, J., Liao, L., Zhang, Z., and Yang, F. (2021). Probability Evaluation Method of cable Corrosion Degree Based on Self-Magnetic Flux Leakage. *J. Magnetism Magn. Mater.* 522, 167544. doi:10.1016/j.jmmm.2020.167544
- Xie, J., Fu, Q., and Yan, J.-B. (20192019). Compressive Behaviour of Stub concrete Column Strengthened with Ultra-high Performance concrete Jacket. *Construction Building Mater.* 204, 643–658. doi:10.1016/j.conbuildmat.2019.01.220
- Zhang, Z., Liu, S., Yang, F., Weng, Y., and Qian, S. (2021). Sustainable High Strength, High Ductility Engineered Cementitious Composites (ECC) with Substitution of Cement by rice Husk Ash. *J. Clean. Prod.* 317, 128379. doi:10.1016/j.jclepro.2021.128379
- Zhang, Z., Yang, F., Liu, J.-C., and Wang, S. (2020). Eco-friendly High Strength, High Ductility Engineered Cementitious Composites (ECC) with Substitution of Fly Ash by rice Husk Ash. *Cement Concrete Res.* 137, 106200. doi:10.1016/j.cemconres.2020.106200
- Zhou, Y., Chen, X., Wang, X., Sui, L., Huang, X., Guo, M., et al. (2020). Seismic Performance of Large Rupture Strain FRP Retrofitted RC Columns with Corroded Steel Reinforcement. *Eng. Structures* 216, 110744. doi:10.1016/j.engstruct.2020.110744

Conflict of Interest: Author JC was employed by the company Chongqing City Transportation Development & investment Group Co., Ltd. Author ZW was employed by the company Chongqing Railway Group Co., Ltd. Author AQ was employed by the company Second Harbor Engineering Company Ltd.

The remaining author declares that the research was conducted in the absence of any commercial or financial relationships that could be construed as a potential conflict of interest.

Publisher's Note: All claims expressed in this article are solely those of the authors and do not necessarily represent those of their affiliated organizations, or those of the publisher, the editors and the reviewers. Any product that may be evaluated in this article, or claim that may be made by its manufacturer, is not guaranteed or endorsed by the publisher.

Copyright © 2022 Chen, Wang, Xu and Zhou. This is an open-access article distributed under the terms of the Creative Commons Attribution License (CC BY). The use, distribution or reproduction in other forums is permitted, provided the original author(s) and the copyright owner(s) are credited and that the original publication in this journal is cited, in accordance with accepted academic practice. No use, distribution or reproduction is permitted which does not comply with these terms.



Analytical Model of Crack Width in Hogging Moment Regions of Steel–Concrete Composite Beams Under Fatigue Loading

Aiming Song¹, Hongtao Xu^{2*}, Shui Wan^{3*} and Qi Luo⁴

¹School of Civil Engineering, Yancheng Institute of Technology, Yancheng, China, ²School of Civil Engineering, Hebei University of Science and Technology, Shijiazhuang, China, ³School of Transportation, Southeast University, Nanjing, China, ⁴School of Civil Engineering, Chongqing Jiaotong University, Chongqing, China

OPEN ACCESS

Edited by:

Zhigang Zhang,
Chongqing University, China

Reviewed by:

Fengjiang Qin,
Chongqing University, China
Xiaoqing Xu,
Tongji University, China

*Correspondence:

Hongtao Xu
xht1978@hebust.edu.cn
Shui Wan
seufpbridge@163.com

Specialty section:

This article was submitted to
Structural Materials,
a section of the journal
Frontiers in Materials

Received: 21 January 2022

Accepted: 04 March 2022

Published: 07 April 2022

Citation:

Song A, Xu H, Wan S and Luo Q (2022)
Analytical Model of Crack Width in
Hogging Moment Regions of
Steel–Concrete Composite Beams
Under Fatigue Loading.
Front. Mater. 9:859687.
doi: 10.3389/fmats.2022.859687

A modified formula for average crack spacing and a numerical model for crack width in hogging moment regions of steel–concrete composite beams under fatigue loading are proposed in this article. First, the existing calculation formulas and test data of average crack spacing are discussed and summarized. By introducing the factor of transverse reinforcement spacing, a modified formula of crack spacing is suggested based on the method of non-linear fitting. Then, a numerical model for crack width in negative moment regions under fatigue loading is proposed. In the analytical model, the explicit formulations of slip occurring at both the beam–slab interface and the reinforcement–concrete interface are included by considering fatigue effects, as well as the stress of reinforcement in the cracked section. Finally, a fatigue test on two steel–concrete composite plate beams subjected to hogging moment is designed and conducted. Compared with the crack width evaluation methods in the existing literature, the analysis results of the numerical model show more reasonable agreement with the data of the experimental beams performed in this study.

Keywords: steel–concrete composite beam, hogging moment region, fatigue, crack width, numerical model

INTRODUCTION

A steel–concrete composite beam is a new type of structure developed on the basis of steel structures and reinforced concrete structures. It has been widely accepted by the engineering field, such as buildings and bridges (Liu et al., 2016; Wang et al., 2021). The steel beam and concrete slab are combined as a whole by welding shear connectors to achieve the purpose of synergistic work. Through reasonable section design, steel–concrete composite beams can give full play to the advantages of tensile strength of steel and the compressive strength of concrete. However, in the negative moment regions near the intermediate support of steel–concrete continuous composite beams, a complex non-linear behavior under the action of a low static load is due to the existence of adverse factors such as concrete tension and steel beam compression (Chen et al., 2009; Sun et al., 2014). In addition, under the long-term action of fatigue loads such as moving vehicles and wind strength, the service performance and durability of the structure are often further weakened (Wang et al., 2018). Among these shortcomings, cracking of the concrete slab has been one of the most crucial issues in hogging moment regions in composite girder bridges. For the design of a steel–concrete composite bridge, it is an economical and convenient solution to allow for the

formation of cracks within the limit of acceptable widths (Ryu et al., 2004; Ryu et al., 2007). Moreover, the introduction of high-performance materials such as engineered cementitious composites (ECCs) (Qin et al., 2020; Zhang et al., 2021; Zhang et al., 2022) and ultra-high performance concrete (UHPC) (Luo et al., 2020) also provides an effective method for crack control.

There have been considerable experimental and theoretical studies on the concrete cracking and crack control of composite beams subjected to negative moments in the past. Ryu et al. (2007) studied the crack development and crack control measures in negative bending moment regions through fatigue loading tests of a full-size model of a two-span continuous composite beam manufactured with a prefabricated concrete slab. The structural strength and stiffness under fatigue loading still presented a good performance for the composite section, and the crack width of the prefabricated slab can be effectively controlled within the allowable range. El-Shihy et al. (2010) and El-Zohairy et al. (2017) conducted experimental tests and finite element analysis on composite beams under negative moments bonded with CFRP laminates. The results showed that CFRP laminates can effectively improve the cracking performance and bearing capacity in negative bending moment regions. Su et al. (2012) conducted an experimental study on the inelastic behavior in negative moment regions of steel–concrete composite box girders manufactured with inclined webs. The results showed that the longitudinal reinforcement ratio has an important influence on the crack propagation of concrete slabs, and the higher the reinforcement ratio, the better the effect of crack control. Fan et al. (2020) conducted static loading tests on steel and ECC beams under negative moment by taking the reinforcement ratio as the characteristic parameter. The results showed that ECC could significantly improve the stiffness and crack resistance of composite beams in the negative moment regions. Based on the four-parameter fiber bridge model, the tensile hardening equation of reinforced ECC members was deduced, and the crack width in negative moment regions of steel–ECC beams was calculated and analyzed. Song et al. (2021) developed a numerical calculation model of the crack width of steel–concrete composite beams under static negative moment regions by taking the bond–slip relationship at the reinforcement–concrete interface and the slip effect at the beam–slab interface into consideration. In addition, it was reported that the development of cracks is decisively influenced by transverse reinforcement (Ryu et al., 2005; He et al., 2010). To determine the minimum reinforcement with reference to the service load and to calculate the crack width, the transverse reinforcement must be taken into account (Ramm and Elz, 2002).

Till now, there are still no standard and applicable analytical methods for crack spacing and crack width in the negative moment regions of steel–concrete composite beams in the present design codes. In Eurocode 4-2 (2005), a simple way is suggested that crack width under negative moment could be calculated according to Eurocode 2 (2004). In China Code GB 50917-2013 (2013), the calculation formula for crack width in China Code GB 50010-2010 (2010) is employed to check the crack width of continuous composite beams. Moreover, very limited reports have studied

the development laws of crack spacing and crack width in negative moment regions. Nie and Zhang (1997) conducted an experimental study on four simply supported composite steel–concrete beams under negative moments and two continuous two-span composite beams under point loads. Based on the experimental results and analysis, the formulas were proposed for estimating crack spacing and maximum crack width, which have been applied to the design practice of engineering. Yu and Guo (2004) conducted an experiment of eighteen partially prestressed steel–concrete composite beams subjected to negative moment. In terms of the test results, the formulas for calculating crack width in the negative bending region were presented, which coincided well with the current code for the design of concrete structures.

However, it is found that the models of present codes proposed to calculate the crack width of composite beams were employed from axial tension members, while the combination effect of steel beam on concrete slab was not fully considered. Like the analytical models presented in some existing literature, the fitted data from the tests conducted previously was limited and the slip at the beam–slab interface was not included. As a result, the existing models may attain unreasonable crack widths in the negative moment regions. For these reasons, it is very important to have a reliable analysis method for crack width that takes into account the effective behavior of steel–concrete composite beams under hogging moment. As a detailed and accurate method in the last decades, the finite element model based on suitable numerical procedures was utilized for the analysis of non-linear mechanical behavior and the calculation of crack width of reinforced concrete beams (Manfredi and Pecce, 1998; Fabbrocino et al., 2007; Oliveira et al., 2008; Castel et al., 2012), as well as the overall flexural behavior of composite beams under hogging moment (Manfredi et al., 1999). However, few researchers have conducted numerical research on crack width in the negative moment regions of continuous composite beams. In addition, most of the analytical methods were presented statically, while fatigue effects were rarely considered.

Set against the above background, this study aims to investigate the analytical methods of crack spacing and crack width in the hogging moment regions of steel–concrete composite beams under fatigue loading. A modified formula for crack spacing is suggested based on the existing equations by introducing the factor of transverse reinforcement spacing. The parameter associated with transverse reinforcement spacing is achieved by fitting the data from this study and some literature data. Owing to the fact that the current studies have not yet included an accurate method to evaluate the crack width in the negative moment regions of continuous composite beams considering fatigue effect, a numerical model is then proposed that includes explicit formulations of slip occurring at both the beam–slab interface and the reinforcement–concrete interface. Finally, a fatigue test on a steel–concrete composite plate beam subjected to hogging moment was conducted. Through comparing with the measured values of experimental work and the crack width evaluation methods in existing literature, the analysis results of the numerical model were verified.

MODIFIED FORMULA FOR AVERAGE CRACK SPACING

Crack spacing directly affects the crack width of concrete. When the fatigue upper limit of the test beam is set at the crack development stage, new cracks will occur after a certain number of repeated cycles. And with the increase in loading times, the number of cracks tends to be stable. However, fatigue loading has little influence on the final crack spacing in the negative moment regions of composite beams when compared with static loading, which is similar to the development law obtained in reinforced concrete structures (Song, 2006). Therefore, the calculation method of the average crack spacing given in this section can be applied to the composite beams with studs both under fatigue loading and static loading, which can provide a basis for the establishment of the analytical method of crack width in the negative moment regions in the following section.

Analysis of Existing Formula for Average Crack Spacing

At present, several formulas have been proposed to predict the average crack spacing in the negative moment regions of continuous composite beams. However, the views on the influence factors of the existing formulas are not yet unified. The models employed by the design codes to calculate the average crack spacing were based on reinforced concrete structures, while the factors associated with composite beams were not fully taken into account. The common models in CEB-FIP (1978), China Code GBJ 10-89 (1989) and China Code GB 50010-2010 (2010) can be expressed, respectively, as follows:

$$l_{cr} = 2 \left(c_s + \frac{l_s}{10} \right) + k_1 k_2 \frac{d_{eq}}{\rho_{te}}, \quad (1)$$

$$l_{cr} = 1.1 \left(2.7c_s + 0.11 \frac{d_{eq}}{\rho_{te}} \right) \nu, \quad (2)$$

$$l_{cr} = 1.1 \left(1.9c_s + 0.08 \frac{d_{eq}}{\rho_{te}} \right). \quad (3)$$

An improved model based on China Code GBJ 10-89 (1989) was proposed by Wu et al. (1993), while the transverse reinforcement ratio and diameter were considered. The equation obtained was then as follows:

$$l_{cr} = 2.7c_s + \frac{0.1}{\rho_{te}/d_{eq} + 1.2\rho_{Hte}/d_{Heq}}. \quad (4)$$

As the aforementioned models for average crack spacing showed no relation with the combination effect, the previous studies took the combined force ratio and spacing of stud connectors into consideration (Nie and Zhang, 1997; Yu and Guo, 2004), and two novel models were then proposed according to China Code GBJ 10-89 (1989) and China Code GB 50010-2010 (2010). The two equations are shown, respectively, as follows:

$$l_{cr} = 1.1 \left(2.7c_s + \frac{0.11}{\rho_{te}/d_{eq} + 0.25R_p^2/p} \right) \nu \quad (5)$$

$$l_{cr} = 1.9c_s + \frac{0.08}{\rho_{te}/d_{eq} + 0.04R_p^2/p}. \quad (6)$$

The development of cracking in slabs as part of composite beams is decisively influenced by the transverse reinforcement (Ramm and Elz, 2002). But this influence factor was not considered in the models mentioned earlier. A simple model which took the combined force ratio and transverse reinforcement spacing into account was established then by Zhang et al. (2011), while other important factors were not taken into account. The equation is given as follows:

$$l_{cr} = l_a (1 - R_p^3). \quad (7)$$

In the aforementioned equations, l_{cr} is the average crack spacing; k_1 is the bonding performance coefficient of longitudinal tensile bars, and $k_1 = 0.4$ is for a deformed bar; k_2 is the influence coefficient of component stress distribution, and $k_2 = 0.25$ is for a tension member; ν is the surface characteristics coefficient of longitudinal tensile bars, and $\nu = 0.7$ is for deformed bar; c_s is the concrete cover thickness of reinforcement; l_s and l_a are the spacings of longitudinal reinforcement and transverse reinforcement, respectively; d_{eq} and d_{Heq} are the equivalent diameters of longitudinal tensile bars and transverse bars, respectively; ρ_{eq} and ρ_{Heq} are the tensile reinforcement ratio and transverse reinforcement ratio, respectively; R_p is the combined force ratio; and p is the spacing of stud connectors.

In summary, the average crack spacing in the negative moment regions of continuous composite beams is mainly related to the concrete cover thickness of reinforcement, equivalent diameters of longitudinal tensile bars, the tensile reinforcement ratio, the combined force ratio, the spacing of stud connectors, and transverse reinforcement. However, the influence factors considered in the existing formulas mentioned before, proposed by researchers and codes, were not comprehensive.

Analysis of a Modified Formula for Average Crack Spacing

In this section, a total of 38 specimen tests from previous literature were summarized and analyzed to study the influence factors of average crack spacing, as can be seen in Table 1. According to Eq. 6, which was based on China Code GB 50010-2010 (2010), a modified formula of crack spacing was proposed by introducing the factor of transverse reinforcement spacing l_a and taking the consistency of dimension into consideration. The parameters were achieved by fitting the data listed in Table 1 with the procedure shown in Figure 1. In this way, the novel model obtained was then as follows:

$$l_{cr} = 1.9c_s + \frac{0.08}{0.25\rho_{te}/d_{eq} + 0.05R_p^2/p + 0.07/l_a}. \quad (8)$$

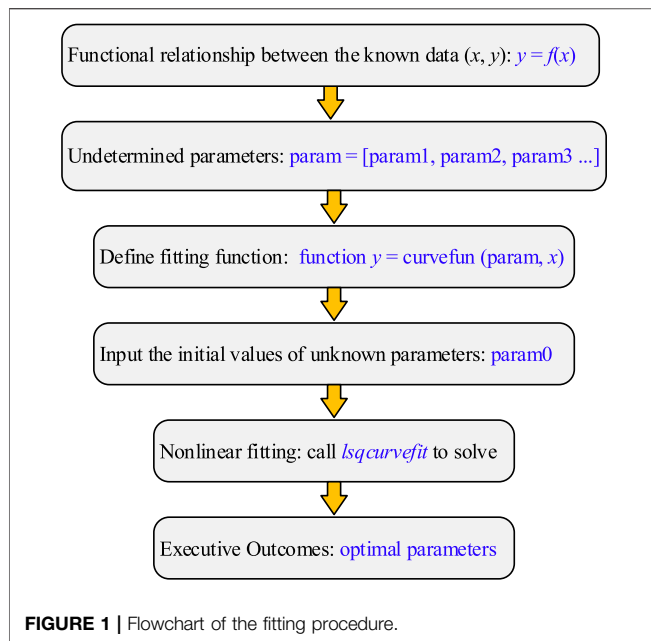
TABLE 1 | Analysis of experimental test data obtained from the existing literature.

Specimen		Test results l_{cr} (mm)	Equation 3		Equation 4		Equation 5		Equation 6		Equation 7		Equation 8	
			l_{cr3} (mm)	l_{cr}/l_{cr3}	l_{cr4} (mm)	l_{cr}/l_{cr4}	l_{cr5} (mm)	l_{cr}/l_{cr5}	l_{cr6} (mm)	l_{cr}/l_{cr6}	l_{cr7} (mm)	l_{cr}/l_{cr7}	l_{cr8} (mm)	l_{cr}/l_{cr8}
Nie and Zhang (1997)	SCB1	188	109.3	1.72	105.8	1.77	112.3	1.67	108.5	1.73	198.6	0.94	165.0	1.14
	SCB2	169	97.3	1.74	100.4	1.69	90.9	1.86	94.8	1.78	185.2	0.91	147.0	1.15
	SCB3	207	109.3	1.89	105.8	1.95	112.3	1.84	108.5	1.90	198.6	1.04	161.9	1.28
	SCB4	214	109.3	1.96	105.8	2.02	108.1	1.98	107.8	1.99	198.6	1.08	162.0	1.32
	SCB5	167	97.3	1.71	100.4	1.66	82.2	2.03	92.5	1.80	185.2	0.90	133.9	1.25
	SCB6	200	109.3	1.83	105.8	1.89	108.1	1.85	107.8	1.86	198.6	1.01	159.1	1.26
Ryu et al. (2005)	CR1	165	145.0	1.14	—	—	154.5	1.07	144.8	1.14	172.2	0.96	183.2	0.90
Yu and Guo (2004)	SCB-1	121	130.9	0.92	108.0	1.12	85.7	1.41	113.8	1.06	77.3	1.57	111.5	1.09
	SCB-2	129	130.9	0.99	108.0	1.19	91.9	1.40	117.4	1.10	77.3	1.67	115.7	1.11
	SCB-3	125	130.9	0.95	108.0	1.16	96.8	1.29	119.7	1.04	77.3	1.62	118.6	1.05
	SCB-4	146	209.2	0.70	104.4	1.40	127.6	1.14	182.0	0.80	87.5	1.67	131.8	1.11
	SCB-5	123	136.9	0.90	99.6	1.23	98.4	1.25	124.1	0.99	77.3	1.59	119.6	1.03
	SCB-6	135	183.1	0.74	103.1	1.31	86.1	1.57	137.1	0.98	34.1	3.95	112.8	1.20
	SCB-7	119	163.3	0.73	101.9	1.17	70.7	1.68	108.8	1.09	90.7	1.31	96.2	1.24
	SCB-8	95	98.9	0.96	94.0	1.01	78.5	1.21	91.5	1.04	46.9	2.03	103.9	0.91
	CCB-1	115	130.9	0.88	108.0	1.06	94.9	1.21	118.8	0.97	81.5	1.41	117.5	0.98
	CCB-2	110	134.2	0.82	108.6	1.01	99.0	1.11	122.7	0.90	85.1	1.29	119.8	0.92
	CCB-3	119	195.8	0.61	116.3	1.02	96.5	1.23	153.1	0.78	71.3	1.67	119.8	0.99
	CCB-4	140	272.7	0.51	121.2	1.16	173.7	0.81	242.8	0.58	96.4	1.45	140.9	0.99
	CCB-5	85	130.9	0.65	108.0	0.79	77.9	1.09	107.7	0.79	36.4	2.34	104.6	0.81
	CCB-6	141	209.2	0.67	104.4	1.35	142.5	0.99	189.0	0.75	92.6	1.52	135.2	1.04
	CCB-7	130	136.9	0.95	99.6	1.30	101.6	1.28	125.5	1.04	81.5	1.60	121.1	1.07
	CCB-8	89	105.4	0.84	95.3	0.93	73.2	1.22	92.0	0.97	—	—	98.6	0.90
	CCB-9	128	136.9	0.94	99.6	1.28	109.4	1.17	128.5	1.00	81.5	1.57	124.4	1.03
	CCB-10	122	136.9	0.89	99.6	1.22	96.3	1.27	123.1	0.99	81.5	1.50	118.5	1.03
Hou et al. (2001)	T1	89	96.6	0.92	115.9	0.77	103.7	0.86	96.5	0.92	139.2	0.64	136.2	0.65
	T2	89	96.6	0.92	115.9	0.77	102.9	0.87	96.4	0.92	139.2	0.64	135.5	0.66
Zhang et al. (2011)	CCB-1	112	143.5	0.78	116.5	0.96	141.3	0.79	141.4	0.79	74.1	1.51	116.2	0.96
	CCB-2	72	95.3	0.76	102.2	0.70	86.2	0.84	91.9	0.78	63.8	1.13	100.4	0.72
	SCB-5	145	143.5	1.01	116.5	1.24	146.1	0.99	142.3	1.02	74.1	1.96	116.8	1.24
	SCB-6	103	119.7	0.86	110.7	0.93	119.1	0.86	118.1	0.87	71.8	1.43	112.0	0.92
	SCB-7	81	109.4	0.74	107.5	0.75	105.7	0.77	107.3	0.75	69.8	1.16	108.4	0.75
	SCB-8	78	95.3	0.82	102.2	0.76	91.4	0.85	93.2	0.84	63.8	1.22	102.8	0.76
Wu et al. (1993)	L-1	123	160.0	0.77	116.3	1.06	158.1	0.78	157.8	0.78	148.4	0.83	170.8	0.72
	L-2	108	122.8	0.88	110.1	0.98	112.4	0.96	119.1	0.91	138.9	0.78	148.4	0.73
	L-3	116	122.8	0.94	116.4	1.00	112.6	1.03	119.1	0.97	185.2	0.63	164.7	0.70
	L-4-L	89	94.1	0.95	104.0	0.86	83.7	1.06	90.0	0.99	114.3	0.78	118.2	0.75
	L-4-R	100	94.1	1.06	107.5	0.93	83.7	1.20	90.0	1.11	152.3	0.66	125.0	0.80
Statistical results	Average value			1.001		1.174		1.223		1.072		1.350		0.978
	Standard deviation			0.377		0.349		0.359		0.361		0.608		0.193
	Coefficient of variation			0.377		0.297		0.293		0.337		0.450		0.198

The physical meaning of Eq. 8 is consistent with Eqs. 1–7 which were empirical formulas derived from data fitting. To verify the validity of the modified model described before, existing experiments conducted by Song et al. (2021) and He et al. (2010) were selected and analyzed with other proposed models expressed in Eqs 3–7. As is shown in Table 2, the maximum error was controlled within 10% for Eq. 8. Generally, it can be seen that the results of the modified formula are in better agreement with the experimental results compared with existing models. Hence, it is effective to use the modified model to study the average crack spacing in the negative moment regions of continuous composite beams.

ANALYTICAL MODEL FOR CRACK WIDTH UNDER FATIGUE LOADING

Crack opening of reinforced concrete beams under fatigue loading depends on several factors, most of which can be related to bond quality and to the effective area where reinforcement–concrete bond interaction may develop (Fabbrocino et al., 2007). As for composite beams, shear force at the beam–slab interface should also be included as an important factor in the analysis of the cracked section (Manfredi et al., 1999). In order to model these behaviors, it is



necessary to give suitable constitutive laws of materials and an analytical model for crack width prediction.

Constitutive Relations

Material Models

When the fatigue upper limit is reached under normal service conditions, cracks in the concrete slab of composite beams under hogging moment will develop into the stabilized stage after a certain number of repeated cycles, and crack spacing will be almost unchanged. Then it can be assumed that the material properties between the two cracks in the negative moment regions of continuous composite beams under fatigue loading can be considered linear elastic (Han et al., 2014). Thus, the stress-strain laws considering the fatigue effect of steel and concrete in tension can be formally expressed as follows:

$$\begin{cases} \sigma_{ct}(n) = E_c \varepsilon_{ct}(n) \\ \sigma_s(n) = E_s \varepsilon_s(n) \end{cases}, \quad (9)$$

where $\sigma_{ct}(n)$ and $\sigma_s(n)$ are stresses of concrete and steel under fatigue loading; $\varepsilon_{ct}(n)$ and $\varepsilon_s(n)$ are strains of concrete and steel under fatigue loading; and E_c and E_s are the young's modulus of concrete and steel, respectively.

Bond Behavior of Reinforcing Bars

Slip at the reinforcement–concrete interface kept increasing, due to the gradual deterioration of the bond property between these two materials. When the limit of bonding stress is kept constant during the fatigue loading process, the total slip increases with the repeated cycles characterized as an S-shaped curve (Balázs, 1991), as exhibited in **Figure 2A**. When the slip develops to stage III, as shown in **Figure 2A**, the reinforced concrete member is close to the state of pull-out failure. This stage is generally not considered in the theoretical analysis. Then the growth trend of slip at stage I and stage II can be approximated in exponential form (Zanuy et al., 2010). Therefore, the bond-slip relationship between reinforcement and concrete caused by fatigue loading can be directly determined by peak slip under static loading s_1 , and the peak slip after a certain number of loading cycles of n can be expressed as follows (Zhang et al., 2017):

$$s_1^f(n) = s_1 (1 + n)^{0.107}. \quad (10)$$

From the perspective of energy dissipation, the fatigue loading process of materials is the same as that of static loading (Liu and Zhou, 2018). In the reinforced concrete structure, it is shown as follows: when the bond failure occurs between the reinforcement and the concrete for a certain number of repeated cycles, the maximum slip under fatigue loading is basically consistent with the slip value on the descending section of the bond stress-slip curve under pure static loading corresponding to the maximum bond stress. Therefore, the descending section of the bond-slip curve under static loading can be used to represent the envelope curve of the remaining bonding strength under fatigue load, as shown in **Figure 2B**.

In this section, the four-linear bond-slip model between concrete and reinforcing bars suggested in CEB-FIP Model Code 1990 (1993) was employed. The following relations give its analytical formulation:

$$\begin{cases} \tau = \tau_{\max} \cdot \left(\frac{s}{s_1}\right)^\alpha, & 0 \leq s \leq s_1 \\ \tau = \tau_{\max}, & s_1 \leq s \leq s_2 \\ \tau = \tau_{\max} - (\tau_{\max} - \tau_f) \cdot \left(\frac{s - s_2}{s_3 - s_2}\right), & s_2 \leq s \leq s_3 \\ \tau = \tau_f, & s \geq s_3, \end{cases} \quad (11)$$

where τ_{\max} is the ultimate bonding strength, $\tau_{\max} = 2.0 \sqrt{f'_c}$; f'_c is the compressive strength of concrete cylinders; $\tau_f = 0.15 \tau_{\max}$; $\alpha = 0.4$; $s_1 = 0.6$; and $s_2 = 0.6$; $s_3 = 1$.

TABLE 2 | Comparison of experimental and modeling results.

Specimen		Test results l_{cr} (mm)	Equation 3		Equation 4		Equation 5		Equation 6		Equation 7		Equation 8	
			l_{cr3} (mm)	l_{cr}/l_{cr3}	l_{cr4} (mm)	l_{cr}/l_{cr4}	l_{cr5} (mm)	l_{cr}/l_{cr5}	l_{cr6} (mm)	l_{cr}/l_{cr6}	l_{cr7} (mm)	l_{cr}/l_{cr7}	l_{cr8} (mm)	l_{cr}/l_{cr8}
Song et al. (2021)	SCB1-1	105	92.6	1.13	112.9	0.93	93.5	1.12	91.4	1.15	87.6	1.20	115.9	0.91
He et al. (2010)	CB-1-1	95	63.3	1.50	63.6	1.49	65.6	1.45	62.9	1.51	87.0	1.09	86.8	1.09
	CB-1-2	94	63.3	1.48	63.6	1.48	65.6	1.43	62.9	1.49	87.0	1.08	86.8	1.08

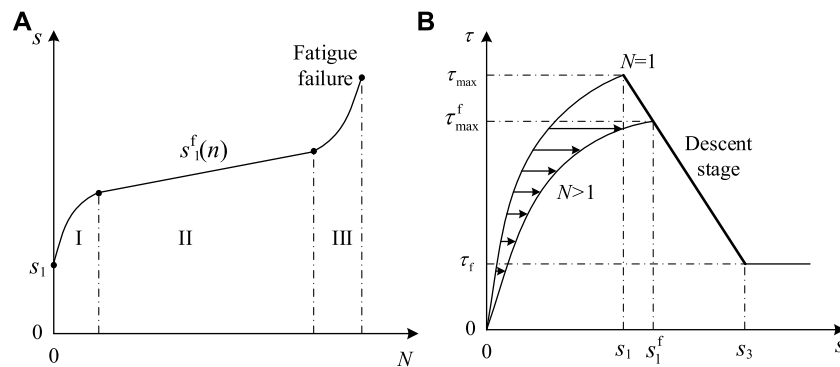


FIGURE 2 | Bond behavior of reinforcing bars: **(A)** variation curve of slip with repeated cycles and **(B)** bond-slip relationship under fatigue loading.

Then the maximum bonding stress τ_{\max}^f after repeated cycles of n can be calculated according to peak slip $s_1^f(n)$, as follows:

$$\tau_{\max}^f = \tau_{\max} - (\tau_{\max} - \tau_f) \cdot \left(\frac{s_1^f(n) - s_1}{s_3 - s_1} \right) \quad (12)$$

Shear at the Beam-Slab Interface

At present, the degradation of strength or stiffness of stud connectors in steel-concrete composite structures under fatigue loading has been studied (Hanswille et al., 2007a). According to the experimental study in the literature (Hanswille et al., 2007b), the deformation behavior of stud connectors under fatigue loading is mainly characterized by increasing residual slip and elastic shear stiffness. The load-slip (P_n - δ_n) curve after n loading cycles can be expressed by the residual shear capacity $P_{u,n}$ in the following form:

$$P_n = K_{el,n} \cdot P_{u,n} \cdot (\delta_n - \delta_{std,N}), P_n \leq 0.8P_{u,n}. \quad (13)$$

The residual slip $\delta_{std,N}$ between the stud and concrete after fatigue loading can be expressed as follows (Hanswille et al., 2007a):

$$\delta_{std,N} = C_1 - C_2 \ln \left(\frac{1}{n/N_f} - 1 \right) \geq 0, \quad 0 < n/N_f < 0.9 \quad (14)$$

$$\delta_{std,N} = 0, \quad n/N_f = 0, \quad (15)$$

where the coefficients C_1 and C_2 are given as follows:

$$C_1 = 0.104e^{3.95P_{\max}/P_{u,0}} \quad (16)$$

$$C_2 = 0.664P_{\min}/P_{u,0} + 0.029. \quad (17)$$

Then the interface shear-slip (v_n - δ_n) relationship at the beam-slab interface under fatigue loading can be given as follows:

$$v_n = \frac{K_n \cdot \delta_n}{p}. \quad (18)$$

After n loading cycles, the residual stiffness $K_{s,n}$ of the stud connectors can be expressed as follows:

$$K_{s,n} = K_{el,n} \cdot P_{u,n}. \quad (19)$$

The residual shear capacity $P_{u,n}$ can be determined by the following formula:

$$\frac{P_{u,n}}{P_{u,0}} = 0.74 \frac{P_{\max}}{P_{u,0}} \left(1 - \frac{\Delta P}{P_{\max}} \right) + 0.54 - 0.04 \ln \left(\frac{n}{10^{0.1267 - 0.1344 \frac{P_{\max}}{P_{u,0}} \left(1 - \frac{\Delta P}{P_{\max}} \right) - n}} \right). \quad (20)$$

In the formulas given earlier, n denotes the number of repeated cycles; N_f is the fatigue life of studs; $K_{el,n}$ is a constant, and it is equivalent to 1.41 (unit: mm^{-1}); $K_n = n_s K_{s,n}$; p is the longitudinal spacing of the studs; $P_{u,0}$ and ΔP are the ultimate static strength and shear amplitude of the studs, respectively; $\Delta P = P_{\max} - P_{\min}$; and P_{\max} and P_{\min} are the fatigue upper limit and fatigue lower limit of studs, respectively.

Stress of Reinforcing Bar in Cracked Section

The fatigue stress state of the reinforcing bar in the concrete slab of composite beams under negative moment is basically the same as that of a reinforced concrete structure. With the increase of repeated cycles, the effective tensile area of the reinforcing bar will decrease, especially at the cracking location (Song, 2006). When the loss of cross-sectional area of the reinforcing bar in the process of fatigue loading conforms to Miner's rule, the effective area of reinforcing bar at cracking position after n cycles can be determined by Eq. 21. Considering the degradation of the effective area of the reinforcing bar and the shear stiffness of studs under fatigue loading, an equation proposed by Fan and Nie (2005) can be modified and applied to the stress calculation of the reinforcing bar in the cracked section, which was defined as the following Eq. 22. In the equations given earlier, the parameters or coefficients can refer to the existing literature (Song et al., 2020). By solving Eq. 21 and Eq. 22, the cycle-dependent stress of the reinforcing bar can be obtained.

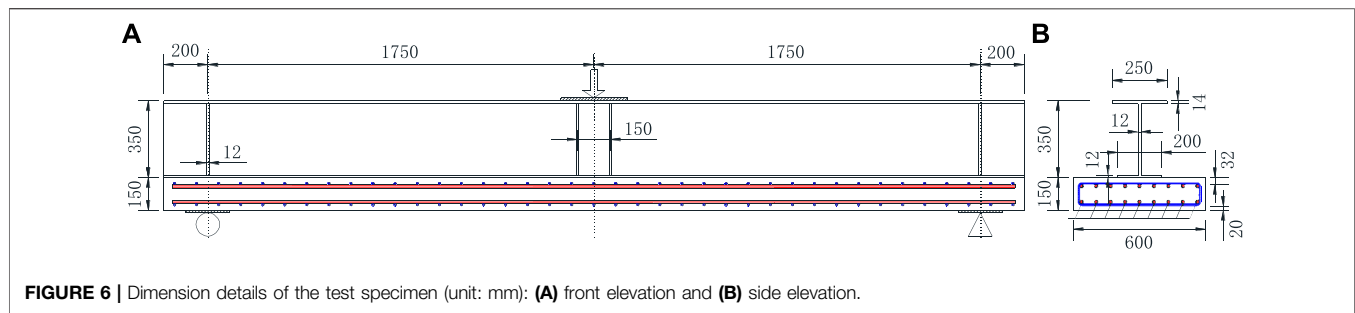


FIGURE 6 | Dimension details of the test specimen (unit: mm): **(A)** front elevation and **(B)** side elevation.

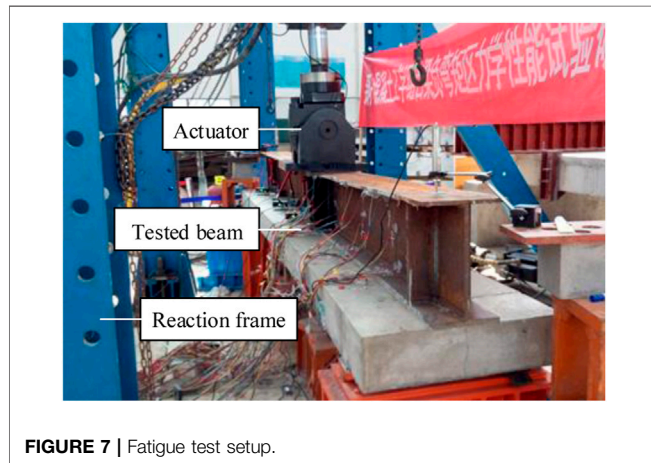


FIGURE 7 | Fatigue test setup.

According to Eqs 23, 24, the distribution coefficient of the stress increments of reinforcement bars can be defined as follows:

$$\xi = \frac{d\sigma_b(n)}{d\sigma_u(n)} = \frac{\tau_b^f d_u}{\tau_u^f d_b}. \quad (26)$$

Based on assumption 2, the following equation is obtained:

$$s_u^f = \frac{h_u}{h_b} s_b^f, \quad (27)$$

where s_u^f and s_b^f are the slips of reinforcing bars in the top layer, and bottom layer, respectively; h_u and h_b are the distances of the beam-slab interface to reinforcing bars.

Then the stress increments of the tension concrete can be expressed as follows:

$$d\sigma_c(n) = \frac{\mp n_u A_u^f d\sigma_u(n) \mp n_b \xi A_b d\sigma_u(n) - v_n dx}{A_{eff}}. \quad (28)$$

Analytical Model for Crack Width

The stress variable in a sub-element depends on the relative slip between reinforcing bars and surrounding concrete, that is, the difference in longitudinal displacements between them. Thus, this description can be given as follows:

$$\frac{ds(x)}{dx} = \frac{d[u_s(x) - u_c(x)]}{dx} + \varepsilon_{sh} = \varepsilon_s(x) - \varepsilon_c(x) + \varepsilon_{sh}, \quad (29)$$

where $u_s(x)$ and $u_c(x)$ are the longitudinal displacements of reinforcement bars and surrounding concrete, respectively; $\varepsilon_s(x)$ and $\varepsilon_c(x)$ are, respectively, the strains of reinforcement bars and surrounding concrete; ε_{sh} is the shrinkage strain of concrete, and $\varepsilon_{sh} = 310\mu$ is for this work according to China Code GB 50917-2013 (2013).

According to the division for the sub-element with small length Δx (see Figure 4), the finite difference forms of Eqs 23, 28, 29 are as follows:

$$\sigma_{su,i+1}^{(j)}(n) = \sigma_{su,i}^{(j)}(n) \mp \frac{4}{d_u} \tau_{su,i}^f \Delta x, \quad (30)$$

$$\sigma_{c,i+1}^{(j)}(n) = \sigma_{c,i}^{(j)}(n) + \frac{\pm (n_u d_u + n_b \xi d_b) \pi \tau_{su,i}^f - v_i^{(j)}}{A_{eff}} \Delta x, \quad (31)$$

$$s_{su,i+1}^f = s_{su,i}^f \mp \left(\frac{\sigma_{su,i+1}^{(j)}(n) + \sigma_{su,i}^{(j)}(n)}{2E_s} - \frac{\sigma_{c,i+1}^{(j)}(n) + \sigma_{c,i}^{(j)}(n)}{2E_c} + \varepsilon_{sh} \right) \Delta x. \quad (32)$$

The values of σ_{su} and σ_c in the $i+1$ section are determined from the values attained in the i section, by using the method of finite difference (Castel et al., 2012). Based on the bond-slip theory, the crack widths of steel-concrete composite beams under hogging moment can be expressed as follows:

$$w_i^{(j)}(n) = \begin{cases} 2s_{su,0}^{(j)} & j=1, i=0 \\ s_{su,0}^{(j-1)} + s_{su,m}^{(j)} & j>1, i=0 \\ 2s_{su,m}^{(j)} & j=k, i=m. \end{cases} \quad (33)$$

The boundary conditions in the cracked section $x=(j-1)l_{cr}$ of each sub-element numbered j applied to Eqs 31–33 can be expressed as follows:

$$\sigma_{s,0}^{(j)}(n) \neq 0; \sigma_{c,0}^{(j)}(n) = 0. \quad (34)$$

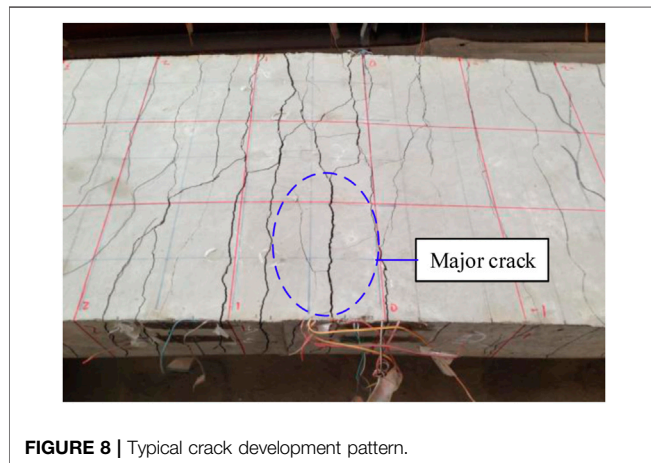
And the boundary condition at the abscissa $x = jl_{cr}$ established as the condition of convergence can be given in the following form:

$$\sigma_{c,m}^{(j)}(n) = 0. \quad (35)$$

Figure 5 shows the flowchart of the procedure for numerical solution. Through giving a tentative value $s_{su,0}$, it is possible to

TABLE 3 | Typical experimental results.

Specimen	Load mode	Fatigue load (kN)			F_{cr} (kN)	F_u or F'_u (kN)	Repeated cycles (10^4)	N_f (10^4)	Failure mode
		F_{max}	F_{min}	ΔF					
SCB1-1	Static	—	—	—	70	1,033	—	—	Compression buckling of bottom profile
SCB1-2	Fatigue	250	25	225	68	973	250	—	No fatigue failure
SCB1-3	Fatigue	400	40	360	67	477	152	152	Fatigue cracking of top profile

**FIGURE 8** | Typical crack development pattern.

predict the crack widths along the composite beam corresponding to a certain loading level. The specific steps are as follows:

- 1) Input basic information and data of composite beam. Calculate the average crack spacing l_{cr} according to Eq. 8. Divide a half-span structure into k sub-elements. Divide a sub-element into m sub-domains. Take the sub-element (i.e., numbered j) as the research object and input the repeated cycles n . Obtain the reinforcement stress $\sigma_{s,0}(n)$ at the cracked section by combining Eq. 21 and Eq. 22. Calculate the concrete stress $\sigma_{c,0}(n) = 0$ at the cracked section by Eq. 34.
- 2) Assume the slip between the reinforcing bar and the concrete at the initial cracked section (i.e., the node number is $i = 0$) as an arbitrary value. Use Eq. 10 and Eq. 12 to modify Eq. 11, and obtain the bond-slip constitutive relation between the reinforcing bar and concrete under fatigue loading. Calculate the bond stress $\tau_{su,i}^f$ on sub-domain numbered $i+1$. Calculate the shear force v_i^f of unit length at the beam-slab interface on sub-domain numbered $i+1$ by Eq. 18.
- 3) Calculate reinforcing bar stress $\sigma_{su,i+1}(n)$, concrete stress $\sigma_{cu,i+1}(n)$ and the slip $s_{su,i+1}^f$ between reinforcing bar and concrete by Eqs 30–32.
- 4) Set $i = i+1$ and repeat Step 3 until $i = m$, on the condition of the initial set of slip value $s_{su,0}$ and number of iterations of $t = 1$. Calculate the crack width according to Eq. 33 if the concrete stress $\sigma_{c,m} = 0$ or within the allowable error range, according to the control condition in Eq. 35. If $\sigma_{c,m} \neq 0$ or the allowable error is exceeded, correct the initial slip value $s_{su,0}$ and continue the iterative operation of $t = t+1$ (i.e., repeat steps 2–4), until you get a reasonable value.

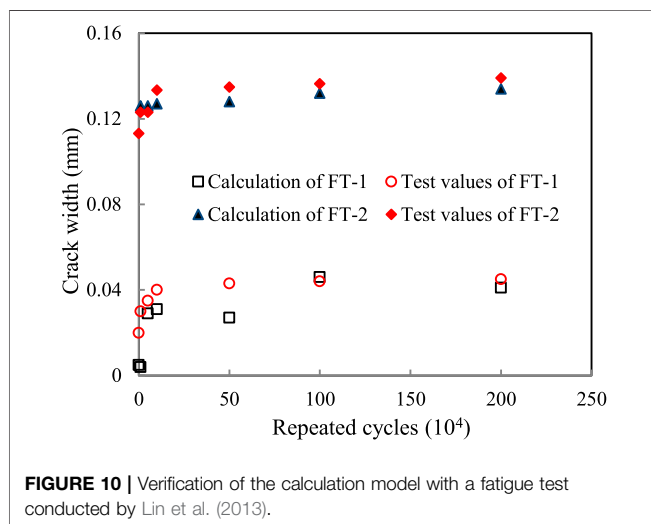
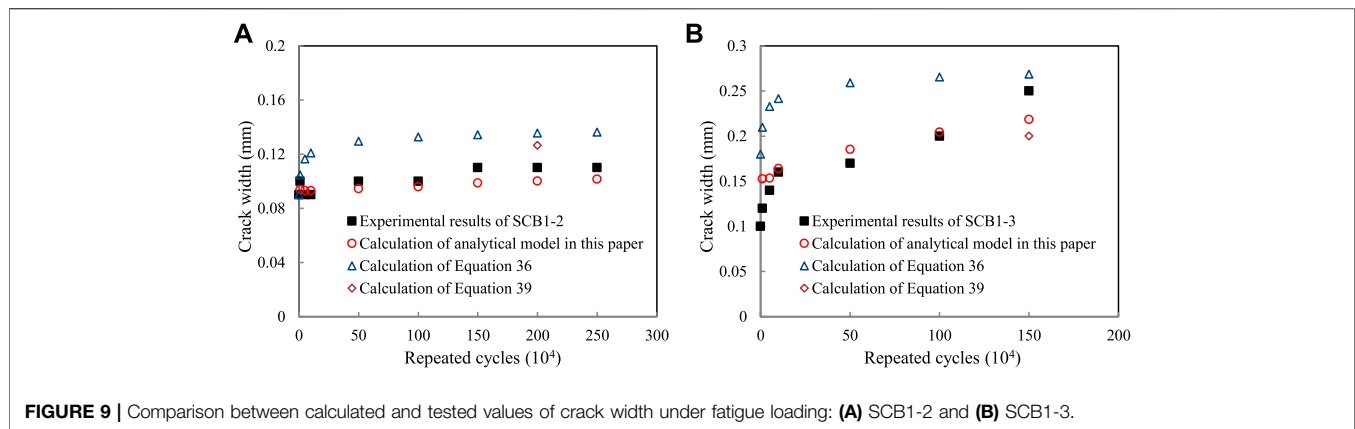
MODEL VALIDATION

Outline of the Experiment

In order to obtain the experimental values of crack width in the negative moment regions of steel–concrete composite beams under fatigue loading, a total of three test beams were designed and manufactured. The specimens were placed upside down on two steel supports to simulate the action of a negative moment. Among them, the specimen numbered SCB1-1 was used for a static loading test, while the specimens numbered SCB1-2 and SCB1-3 were used for fatigue loading tests. Figure 6 shows the dimension details of the specimens. All test beams are equipped with stud connectors with a diameter, height, and spacing of 16 mm, 90 mm, and 100 mm, respectively. The ratio of longitudinal reinforcing bars is designed as 4.0% with a diameter of 16 mm. Material tests were conducted on concrete and steel before the formal loading of the specimens. The strength grade of the concrete was designed to be C50. The tensile reinforcement bars and steel plates used HRB400 and Q345, respectively (of the same factory batch). The axial tensile strength, elastic modulus, and the average result of compressive strength of concrete are 3.44 MPa, 3.47×10^4 MPa, and 51.2 MPa, respectively. Meanwhile, the average results of the tensile yield strengths of the web (or top flange), bottom flange, and reinforcing bars are 443 MPa, 391 MPa, and 592 MPa, respectively. The setup of the fatigue test is illustrated in Figure 7. The fatigue load limits of SCB1-2 and SCB1-3 were designed as 25% F_u and 40% F_u , where F_u is the ultimate bearing capacity of SCB1-1 obtained from the static test. The loading ratio and frequency were set as 0.1 and 2 Hz, respectively. And the sine wave was used for the fatigue loading. The fatigue loading was suspended when the repeated cycles reached the specified times of 1×10^4 , 5×10^4 , 10×10^4 , 50×10^4 , 100×10^4 , 150×10^4 , 200×10^4 , and 250×10^4 . Then the static loading test was performed to measure the crack width by an electronic crack width measurement instrument. The typical experimental results are listed in Table 3, in which ΔF is the fatigue load amplitude, that is, $F_{max} - F_{min}$; F_{cr} is the cracking load in a static test; N_f is the fatigue life. The typical pattern of crack development is shown in Figure 8.

Existing Calculation Methods for Crack Width Under Fatigue Loading

The relative slip between the reinforcing bar and concrete increases gradually under the action of fatigue load, resulting in the growth of crack width with repeated cycles. At



present, there is no specific method to calculate the crack width in the negative moment regions of composite beams under fatigue loading. For reinforced concrete structures, the crack width under fatigue loading is generally expressed by the method under static loading through appropriate correction, that is, the experimental regression formula obtained by using the initial crack expansion coefficient (Song, 2006). According to the test results, a statistical empirical formula was given for the maximum crack width after n loading cycles:

$$\omega_{\max} = \omega_0 (0.382 - 0.0227 \lg n) \lg n, \quad (36)$$

where, ω_0 is the initial maximum crack width, which can be calculated according to the conventional method under static loading. In this study, it is calculated according to the recommended formula in JTG D62-2004 (2004), which is expressed as follows:

$$\omega_0 = C_1' C_2' C_3' \frac{\sigma_s}{E_s} \left(\frac{30 + d_{\text{eq}}}{0.28 + 10\rho} \right), \quad (37)$$

$$\rho = \frac{A_r + A_p}{bh_0 + (b_f - b)h_f}, \quad (38)$$

where A_p is the area of prestressed reinforcement in the tensile zone; b_f and h_f are the width and thickness of the tensile concrete slab; $C_1' = 1.0$ is for the deformed bar; $C_2' = 1.0$ is for load effect; $C_3' = 1.2$ is for the axial tension members.

In GB 50010-2010 (2010), the non-uniform coefficient φ of tensile rebar strain for reinforced concrete specimens under fatigue loading is equivalent to 1.0, that is, the bond between the rebar and the concrete fails completely, considering the fatigue effect. The calculation method is proposed based on the assumptions that the fatigue failure occurs in reinforced concrete structures or the loading cycles reaches 200×10^4 , and the maximum crack width can be expressed as follows:

$$\omega_{\max} = \alpha_{\text{cr}} \frac{\sigma_s}{E_s} \left(1.9c_s + 0.08 \frac{d_{\text{eq}}}{\rho_{\text{eq}}} \right), \quad (39)$$

where α_{cr} is the characteristic coefficient of tension members under the action of force; f_{tk} is the standard value of concrete tensile strength; for other coefficients, refer to the explanation given before.

Verification of the Calculation Model

Figure 9 shows the load–crack width response of the experimental test, the existing calculation methods, and the proposed model in this study. It can be found that the crack width measured in the test increased with the repeated cycles. It developed rapidly in the early loading process of about 10×10^4 cycles, and then grew slowly. The crack width calculated according to Eq. 36 had a large deviation from the test results at different times of cyclic loading. The results of the maximum crack width by Eq. 39 were limited to a particular condition. In addition, the calculated values were not universal for the structure checking and were not in good agreement with the test results. As for the numerical model in this study, which fully takes the characteristics of the negative moment regions of composite beams into consideration, the computed results are in good agreement with the experimental values. And the accuracy was further verified by the tested values from other literature (Lin

et al., 2013), as shown in **Figure 10**. As a result, the numerical model can well reflect the development trend of crack width in the process of fatigue loading and provide a reference for anti-fatigue design and checking calculation of composite beam in negative moment region.

CONCLUSION

In this study, a modified formula for average crack spacing and a numerical model for crack width in hogging moment regions of steel–concrete composite beams under fatigue loading are presented. Meanwhile, an experimental test is designed and conducted to obtain the crack width at certain repeated cycles. Then the accuracy of the proposed analytical models is validated through the comparison between the proposed models and test results. The main conclusions drawn are as follows:

- (1) The modified formula of average crack spacing takes the spacing of transverse reinforcement into account through the analysis and discussion of existing equations. By comparison, the modified formula shows more reasonable results.
- (2) The analytical model for crack width under repeated loading includes the explicit formulations of slip at both the beam–slab interface and the reinforcement–concrete interface, as well as reinforcement stress in the cracked section considering fatigue effect. The analytical results can be obtained by using a suitable numerical procedure.
- (3) Compared with the empirical formulas for crack width under fatigue loading based on the axial tension members in existing literature, the analysis results of the numerical

model show more reasonable agreement with the measured values of the experimental beams conducted in this study. For engineering design and application, the work in this study can provide a reference for calculation and evaluation in the negative moment regions of steel–concrete composite beams under fatigue loading.

DATA AVAILABILITY STATEMENT

The original contributions presented in the study are included in the article/Supplementary Material, further inquiries can be directed to the corresponding authors.

AUTHOR CONTRIBUTIONS

AS conceived the work and wrote the manuscript. AS, HX, and QL developed the analytical model. SW analyzed the results and revised the manuscript. All authors read and agreed to the published version of the manuscript.

FUNDING

This research was sponsored by the school-level research project of Yancheng Institute of Technology (No. xjr2021007). QL acknowledges the National Natural Science Foundation of China (No. 52108269) and the Scientific and Technology Research Program of the Chongqing Municipal Education Commission (No. KJQN202100716).

REFERENCES

- Balázs, G. (1991). Fatigue of Bond. *ACI Mater. J.* 88 (6), 620–629.
- BS EN 1992 Eurocode 2 (2004). *Design of Composite concrete Structure*. Brussels, Belgium: European Committee for Standardization.
- BS EN 1994-2 (2005). *Eurocode 4: Design of Composite Steel and concrete Structures, Part 2: General Rules and Rules for Bridges*. Brussels, Belgium: European Committee for Standardization.
- Castel, A., Vidal, T., and François, R. (2012). Finite-element Modeling to Calculate the Overall Stiffness of Cracked Reinforced concrete Beams. *J. Struct. Eng.* 138 (7), 889–898. doi:10.1061/(ASCE)ST.1943-541X.0000520
- CEB-FIP Model Code 1978 (1978). *CEB-FIP Model Code 1978*. Lausanne, Switzerland: Comité Euro-International du Béton, Thomas Telford Ltd.
- CEB-FIP Model Code 1990 (1993). *CEB-FIP Model Code 1990*. Lausanne, Switzerland: Comité Euro-International du Béton, Thomas Telford Ltd.
- Chen, S., Wang, X., and Jia, Y. (2009). A Comparative Study of Continuous Steel-concrete Composite Beams Prestressed with External Tendons: Experimental Investigation. *J. Constructional Steel Res.* 65 (7), 1480–1489. doi:10.1016/j.jcsr.2009.03.005
- El-Shihy, A. M., Fawzy, H. M., Mustafa, S. A., and El-Zohairy, A. A. (2010). Experimental and Numerical Analysis of Composite Beams Strengthened by CFRP Laminates in Hogging Moment Region. *Steel Compos. Structures* 10 (3), 281–295. doi:10.12989/scs.2010.10.3.281
- El-Zohairy, A., Salim, H., Shaaban, H., Mustafa, S., and El-Shihy, A. (2017). Experimental and FE Parametric Study on Continuous Steel-concrete Composite Beams Strengthened with CFRP Laminates. *Construction Building Mater.* 157, 885–898. doi:10.1016/j.conbuildmat.2017.09.148
- Fabbrocino, G., Verderame, G. M., and Polese, M. (2007). Probabilistic Steel Stress–Crack Width Relationship in R.C. Frames with Smooth Rebars. *Eng. Structures* 29 (1), 1–10. doi:10.1016/j.engstruct.2006.04.002
- Fan, J., Gou, S., Ding, R., Zhang, J., and Shi, Z. (2020). Experimental and Analytical Research on the Flexural Behaviour of Steel-ECC Composite Beams under Negative Bending Moments. *Eng. Structures* 210 (1), 110309.1–110309.17. doi:10.1016/j.engstruct.2020.110309
- Fan, J., and Nie, J. (2005). Effects of Slips on Load-Carrying Capacity of Composite Beams under Negative Bending. *Eng. Mech.* 22 (3), 177–182. doi:10.3969/j.issn.1000-4750.2005.03.031
- GB 50010-2010 (2010). *Code for Design of concrete Structures*. Beijing, China: Ministry of Construction of China.
- GB 50917-2013 (2013). *Code for Design of Steel and concrete Composite Bridges*. Beijing, China: Ministry of Construction of China.
- GBJ 10-89 (1989). *Code for Design of concrete Structures*. Beijing, China: Ministry of Construction of China.
- Han, J., Song, Y., and Chang, J. (2014). Analysis Model of Crack Width of Partially Prestressed concrete Beams under Fatigue Loading. *J. Cent. South Univ. (Science Technology)* 45 (11), 3977–3985. doi:10.1016/j.jcsr.2006.06.036
- Hanswille, G., Porsch, M., and Ustundag, C. (2007a). Resistance of Headed Stud Subjected to Fatigue Loading. *J. Constructional Steel Res.* 63 (4), 475–484. doi:10.1016/j.jcsr.2006.06.035
- Hanswille, G., Porsch, M., and Ustundag, C. (2007b). Resistance of Headed Stud Subjected to Fatigue Loading Part II: Analytical Study. *J. Constructional Steel Res.* 63 (4), 485–493. doi:10.1016/j.jcsr.2006.06.036
- He, J., Liu, Y., Chen, A., and Yoda, T. (2010). Experimental Study on Inelastic Mechanical Behaviour of Composite Girders under Hogging Moment. *J. Constructional Steel Res.* 66 (1), 37–52. doi:10.1016/j.jcsr.2009.07.005

- Hou, W., Luo, R., and Ye, M. (2001). On Crack Width of Steel Cast-In-Place concrete Composite Beams with High Reinforcement Ratio. *China Railway Sci.* 22 (5), 54–60. doi:10.3321/j.issn:1001-4632.2001.05.009
- JTG D62-2004 (2004). *Code for Design of Highway Reinforced concrete and Prestressed concrete Bridges and Culverts*. Beijing, China: Ministry of Communication of China.
- Lin, W., Yoda, T., and Taniguchi, N. (2013). Fatigue Tests on Straight Steel-concrete Composite Beams Subjected to Hogging Moment. *J. Constructional Steel Res.* 80 (1), 42–56. doi:10.1016/j.jcsr.2012.09.009
- Liu, F., and Zhou, J. (2018). Experimental Research on Fatigue Damage of Reinforced Concrete Rectangular Beam. *KSCE J. Civ. Eng.* 22 (9), 3512–3523. doi:10.1007/s12205-018-1767-y
- Liu, J., Ding, F.-x., Liu, X.-m., and Yu, Z.-w. (2016). Study on Flexural Capacity of Simply Supported Steel-concrete Composite Beam. *Steel Compos. Struct.* 21 (4), 829–847. doi:10.12989/scs.2016.21.4.829
- Luo, Q., Liu, D., Qiao, P., Zhou, Z., Zhao, Y., and Sun, L. (2020). Micro-CT-based Micromechanics and Numerical Homogenization for Effective Elastic Property of Ultra-high Performance concrete. *Int. J. Damage Mech.* 29 (1), 45–66. doi:10.1177/1056789519848475
- Manfredi, G., Fabbrocino, G., and Cosenza, E. (1999). Modeling of Steel-concrete Composite Beams under Negative Bending. *J. Eng. Mech.* 125 (6), 654–662. doi:10.1061/(asce)0733-9399(1999)125:6(654)
- Manfredi, G., and Pecce, M. (1998). A Refined R.C. Beam Element Including Bond-Slip Relationship for the Analysis of Continuous Beams. *Comput. Structures* 69 (1), 53–62. doi:10.1016/S0045-7949(98)00078-9
- Nie, J., and Zhang, M. (1997). Study on the Crack of concrete Flange in Tension of Composite Steel-concrete Beams. *J. Tsinghua Univ. Sci. Technol.* 37 (6), 95–99. doi:10.3321/j.issn:1000-0054.1997.06.004
- Oliveira, R. S., Ramalho, M. A., and Corrêa, M. R. S. (2008). A Layered Finite Element for Reinforced concrete Beams with Bond-Slip Effects. *Cement and Concrete Composites* 30 (3), 245–252. doi:10.1016/j.cemconcomp.2007.09.007
- Qin, F., Zhang, Z., Yin, Z., Di, J., Xu, L., and Xu, X. (2020). Use of High Strength, High Ductility Engineered Cementitious Composites (ECC) to Enhance the Flexural Performance of Reinforced concrete Beams. *J. Building Eng.* 32, 101746. doi:10.1016/j.jobbe.2020.101746
- Ramm, W., and Elz, S. (2002). “Composite Construction in Steel and Concrete IV,” in *Proceedings of Composite Construction in Steel and Concrete IV Conference* (Fairfax, America: ASCE Press). doi:10.1061/9780784406168
- Ryu, H.-K., Chang, S.-P., Kim, Y.-J., and Kim, B.-S. (2005). Crack Control of a Steel and concrete Composite Plate Girder with Prefabricated Slabs under Hogging Moments. *Eng. Structures* 27 (11), 1613–1624. doi:10.1016/j.engstruct.2005.05.015
- Ryu, H.-K., Kim, Y.-J., and Chang, S.-P. (2007). Crack Control of a Continuous Composite Two-Girder Bridge with Prefabricated Slabs under Static and Fatigue Loads. *Eng. Structures* 29 (6), 851–864. doi:10.1016/j.engstruct.2006.06.021
- Ryu, H.-K., Shim, C.-S., Chang, S.-P., and Chung, C.-H. (2004). Inelastic Behaviour of Externally Prestressed Continuous Composite Box-Girder Bridge with Prefabricated Slabs. *J. Constructional Steel Res.* 60 (7), 989–1005. doi:10.1016/j.jcsr.2003.09.004
- Song, A., Li, Z., Xu, H., Wan, S., and Zhou, P. (2021). Numerical Calculation Model of Crack Width in Negative Moment Regions of Steel-concrete Composite Beams. *J. Harbin Inst. Technol.* 53 (3), 75–81. doi:10.11918/201912134
- Song, A., Luo, Q., Wan, S., and Li, Z. (2020). Experimental and Analytical Study on Deformation Behavior in Hogging Moment Regions of Composite Beams. *Adv. Civil Eng.* 2020 (3), 1–10. doi:10.1155/2020/6630742
- Song, Y. P. (2006). *Fatigue Behavior and Design Principle of Concrete Structures*. Beijing, China: China Machine Press.
- Su, Q.-T., Yang, G.-T., and Wu, C. (2012). Experimental Investigation on Inelastic Behavior of Composite Box Girder under Negative Moment. *Int. J. Steel Struct.* 12 (1), 71–84. doi:10.1007/s13296-012-1007-0
- Sun, Q., Yang, Y., Fan, J., Zhang, Y., and Bai, Y. (2014). Effect of Longitudinal Reinforcement and Prestressing on Stiffness of Composite Beams under Hogging Moments. *J. Constructional Steel Res.* 100 (13), 1–11. doi:10.1016/j.jcsr.2014.04.017
- Wang, B., Huang, Q., Liu, X., and Li, W. (2018). Experimental Investigation of Steel-Concrete Composite Beams with Different Degrees of Shear Connection under Monotonic and Fatigue Loads. *Adv. Struct. Eng.* 21 (2), 227–240. doi:10.1177/1369433217717121
- Wang, W., Zhang, X.-d., Zhou, X.-l., Wu, L., and Zhu, H.-j. (2021). Study on Shear Behavior of Multi-Bolt Connectors for Prefabricated Steel-concrete Composite Beams. *Front. Mater.* 8, 625425. doi:10.3389/fmats.2021.625425
- Wu, Z., Chen, H., Gao, X., and Zhu, P. (1993). Experimental Study on Crack Width of concrete Slab of Composite Beams under Negative Bending. *J. Harbin Architecture Civil Eng. Inst.* 26 (1), 58–62.
- Yu, Z., and Guo, F. (2004). Experimental Study of Crack Width in Negative Bending Region of Partially Prestressed Continuous Steel concrete Composite Beams. *J. Building Structures* 25 (4), 55–59. doi:10.3321/j.issn:1000-6869.2004.04.008
- Zanuy, C., Albajar, L., and de la Fuente, P. (2010). On the Cracking Behaviour of the Reinforced concrete Tension Chord under Repeated Loading. *Mater. Struct.* 43 (5), 611–632. doi:10.1617/s11527-009-9516-9
- Zhang, W., Ye, Z., Gu, X., and Li, S. (2017). Assessment of Fatigue Life for Corroded Reinforced concrete Beams under Uniaxial Bending. *J. Struct. Eng.* 143 (7), 04017048 1–14. doi:10.1061/(asce)st.1943-541x.0001778
- Zhang, Y., Fan, J., and Li, Y. (2011). Law of Crack Development and Calculation of Crack Width of Continuous Composite Beams. *Eng. Mech.* 28 (7), 84–90. doi:10.1080/0144929X.2011.553739
- Zhang, Z., Liu, D., Ding, Y., and Wang, S. (2022). Mechanical Performance of Strain-Hardening Cementitious Composites (SHCC) with Bacterial Addition. *J. Infrastruct. Preserv. Resil.* 3 (3). doi:10.1186/s43065-022-00048-3
- Zhang, Z., Liu, S., Yang, F., Weng, Y., and Qian, S. (2021). Sustainable High Strength, High Ductility Engineered Cementitious Composites (ECC) with Substitution of Cement by rice Husk Ash. *J. Clean. Prod.* 317, 128379. doi:10.1016/j.jclepro.2021.128379

Conflict of Interest: The authors declare that the research was conducted in the absence of any commercial or financial relationships that could be construed as a potential conflict of interest.

Publisher’s Note: All claims expressed in this article are solely those of the authors and do not necessarily represent those of their affiliated organizations, or those of the publisher, the editors, and the reviewers. Any product that may be evaluated in this article, or claim that may be made by its manufacturer, is not guaranteed or endorsed by the publisher.

Copyright © 2022 Song, Xu, Wan and Luo. This is an open-access article distributed under the terms of the Creative Commons Attribution License (CC BY). The use, distribution or reproduction in other forums is permitted, provided the original author(s) and the copyright owner(s) are credited and that the original publication in this journal is cited, in accordance with accepted academic practice. No use, distribution or reproduction is permitted which does not comply with these terms.



Bending Performance of Epoxy Adhesive Joints of Prefabricated Concrete Elements

Hongbo Peng^{1,2}, Zhongya Zhang^{1,2}, Yang Zou^{1,2*}, Jincen Guo^{1,2}, Xiaoyan Zhang^{1,2} and Xingqi Zeng^{1,2}

¹State Key Laboratory of Mountain Bridge and Tunnel Engineering, Chongqing Jiaotong University, Chongqing, China, ²School of Civil Engineering, Chongqing Jiaotong University, Chongqing, China

OPEN ACCESS

Edited by:

Zhigang Zhang,
Chongqing University, China

Reviewed by:

Kangkang Wang,
CCCC Highway Consultants Co., Ltd.,
China
Yang Wei,
Nanjing Forestry University, China

*Correspondence:

Yang Zou
zouyang@cqjtu.edu.cn

Specialty section:

This article was submitted to
Structural Materials,
a section of the journal
Frontiers in Materials

Received: 21 January 2022

Accepted: 28 February 2022

Published: 07 April 2022

Citation:

Peng H, Zhang Z, Zou Y, Guo J,
Zhang X and Zeng X (2022) Bending
Performance of Epoxy Adhesive Joints
of Prefabricated Concrete Elements.
Front. Mater. 9:859532.
doi: 10.3389/fmats.2022.859532

The assembly construction of prefabricated UHPC elements can well balance quality reliability and construction convenience, thus it has excellent application prospects in bridge engineering. The joints between prefabricated elements are the key to ensuring the overall force performance of the structure, which directly determine the load-bearing capacity and the life of structure. To clarify the bending behavior of epoxy adhesive joints between prefabricated UHPC elements, four groups of 12 bending tests were carried out with different interface treatment forms as parameters. The failure modes, load-deflection curves, and ultimate bending strength of the interface were investigated. The results reveal that the interfacial failure modes mainly include the interfacial stripping failure of epoxy-UHPC surface, steel fibers and fine aggregates into UHPC surface by pulling out, and tensile damage of UHPC at the root of key teeth on the side of the keyway interface. The load-deflection curves of all specimens exhibit the two-fold lines form. The load tends to rise linearly during the loading phase, and there is no yielding phase before the failure. The load-carrying capacity of the specimen is lost immediately after the failure, and no reliable residual strength is available except for the keyway interface. In addition, the bending strength of rough interface, groove interface, and keyway interface are respectively improved by -24.02, 2.34, and 4.64%, compared with the natural interface. So it is recommended that the joint between prefabricated UHPC elements take the form of keyway interface. Finally, a simplified force model of the keytooth adhesive joint is proposed, and a calculation formula for the flexural bearing capacity is established based on the principal of Mohr's circle, based on the experimental results and theoretical analysis. The mean ratio of the proposed adhesive joint calculation equation to the experimental results was 0.925 with a standard deviation of 0.065.

Keywords: ultra-high performance concrete, epoxy resin, prefabricated assembly, bending performance, experimental study

INTRODUCTION

Normal concrete has been widely used because of its advantages of easy material extraction, good moldability and high compressive strength, but it also has the disadvantages of low tensile strength, difficult to control the crack width after cracking and obvious brittle characteristics. To improve the brittle properties of normal concrete and limit its crack development, a large majority of scholars and

researchers at home and abroad have developed high performance fiber reinforced concrete, represented by ultra-high performance concrete (UHPC) and engineered cementitious concrete (ECC). ECC has the obvious strain-hardening characteristics, high tensile and compressive toughness, excellent durability, good deformation capacity and energy dissipation capacity. The application of this material in buildings, bridges and other structures can meet the safety, applicability and durability requirements. Qin et al. (Qin et al., 2020) applied high strength, high ductility ECC to strengthen reinforced concrete beams and investigated its flexural properties. The test results show that when the beam reaches its ultimate state, no local cracking occurs in tensile zone, but more micro-cracks appear due to the high toughness of ECC. In addition, the cracking load, yield load, ultimate load, ductility and energy absorption capacity are improved. Zhang et al. (Zhang et al., 2020; Zhang et al., 2021) developed the high strength, high ductility ECC with substitution of fly ash and cement by rice husk ash to enrich the variety of ingredients in ECC and make ECC more eco-friendly. In addition, to realize self-healing and increase the strength of ECC, Zhang et al. (Zhang et al., 2022) investigated the mechanical properties of ECC with the addition of vegetative bacterial cells. The results show that the compressive, cracking and tensile strength of ECC are increased, but the tensile strain capacity is slightly decreased due to the addition of bacteria.

UHPC is a fiber-reinforced cementitious composite material with a compressive strength of 150 MPa or more and excellent mechanical properties, durability, and toughness (De Larrard and Sedran, 1994; Wille et al., 2011; Wang et al., 2015; Xue et al., 2020; Du et al., 2021). The steel fibers into UHPC inhibit the sprouting and development of cracks, thereby enhancing their tensile properties (Liew, 2015; Lee et al., 2017; Meng and Khayat, 2017). In addition, the dense matrix microstructure provides high resistance to the intrusion of harmful chemical ions (Cl^- , SO_4^{2-} , etc.) and CO_2 , resulting in strong resistance to permeation, carbonation, corrosion, and freeze-thaw cycles, and exhibiting excellent durability performance (Meng et al., 2018; Meng and Khayat, 2018; Qi et al., 2019). UHPC is considered to be one of the most promising construction materials (Zhou et al., 2018; Cheng et al., 2021; Lian et al., 2021), and a majority of scholars have conducted studies on its application in bridge engineering structures, including piers, main girders, deck slabs, arches, bridge joints, and old bridge reinforcement (Chen et al., 2016; Haber et al., 2018; Ren et al., 2019; Su et al., 2019). The results show that the application of UHPC in bridge structures is expected to solve many technical challenges of existing conventional bridge structures. For example, UHPC-based bridge structures can significantly reduce the section size, effectively reduce the self-weight of the structure, and thus improve the spanning capacity of the structure (Zhu et al., 2020). Due to its excellent crack-resistance performance (Li and Deng, 2021), UHPC can also be applied in crack-prone structures such as concrete deck slabs in hogging moment zones to meet the requirements of tensile and crack resistance. UHPC applied in orthotropic steel decks can significantly increase the stiffness of structures and mitigate the problems of fatigue

cracking and pavement vulnerability of steel bridge decks (Dieng et al., 2013; Abdelbaset et al., 2020; Wang et al., 2021; Abdelbaset et al., 2022).

However, UHPC has a risk of early cracking due to internal self-drying and chemical shrinkage during the setting and hardening process, which can cause self-shrinkage and is usually greater than $800 \mu\epsilon$ (Yoo et al., 2014; Huang and Ye, 2017). In addition, high-temperature steam curing is an important part of the preparation of UHPC, which can improve the strength of concrete and give it excellent durability while reducing the later shrinkage. However, on-site steam curing increases the construction difficulty and cost significantly in practical engineering (Garas et al., 2009). Based on the above problems, the assembled construction of prefabricated UHPC elements can effectively solve the problems of large self-shrinkage and difficult steam curing of UHPC in cast-in-place construction and has a promising application in the rapid construction technology of assembled bridges and large-span bridge structures. Shao et al. (Shao et al., 2019) proposed three types of high-performance assembled bridge structures based on UHPC, including assembled box girder structures, fully prefabricated UHPC “ π ” shaped girders, and fully prefabricated steel-UHPC lightweight composite “ π ” shaped girders. A large quantity of experimental research and theoretical analysis shows that the self-weight of assembled UHPC bridge structures can be reduced to 40–50% of that of traditional structures under equal strength-bearing conditions. Its great transportation convenience can facilitate the rapid construction of large elements. Moreover, the size of joints between each girder on-site can be significantly reduced, significantly reduces the on-site work. Wang et al. (Wang et al., 2019) proposed a steel-prefabricated UHPC composite beam with full dry connection and carried out two full-scale beam tests combined with finite element numerical analysis to investigate the flexural and crack-resistance performance of composite beam.

In the prefabricated UHPC assembly structure, the joints can make it have better force transmission performance and ensure its impermeability and integrity. At present, the joints can be divided into three types according to the connection material at the joints: the dry joints with direct contact on the surface of the joints, the wet joints with filled concrete or mortar, and the glued joints with epoxy resin. Dry joints are banned by the AASHTO due to the disadvantages of not providing effective durability protection for post-tensioned prestressing tendons, and it is suggested that only glue joints or wet joints can be used in all precast assembled concrete structures. Pan et al. (Pan et al., 2016) compared the flexural performance of five novel wet joints of steel-RPC composite deck slabs. Since steel fibers improve the performance of the RPC layer after cracking, a durability-based RPC tensile stress is recommended to replace the initial cracking stress for a more economical deck panel design. Shao et al. (Shao et al., 2013; Shao et al., 2017) demonstrated that the crack-resistance performance of steel-plate enhanced wet joints and reinforcement-enhanced wet joints was better than conventional wet joints by bending tests on steel-RPC composite deck slabs. Xiao et al. (Xiao et al., 2022) conducted

TABLE 1 | Mix ratio of UHPC.

Components	Mass ratio	Proportion (%)
Cement	1.000	34.55
Silica fume	0.250	8.64
Quartz sand	1.100	38.01
Quartz fume	0.300	10.37
Superplasticizer	0.019	0.66
Water	0.225	7.77

a study on the flexural performance of dovetail wet joints and rectangular wet joints in steel-UHPC composite deck slabs under hogging moment. Chen et al. (Chen et al., 2018) proposed novel interfacial treatments such as epoxy resin treatment and high-pressure water jet chiseling for the wet joints of steel-UHPC composite decks and carried out experiments to study the force mechanism of wet joints. It is recommended that the interfacial treatment using a high-pressure water jet to chisel away the fine aggregate can be used. When the construction conditions are suitable. Zhao et al. (Zhao et al., 2018) conducted a full-scale test and finite element simulation study on the flexural performance of dovetail wet joints in steel-RPC composite deck slabs under hogging moment. The test results showed that: reinforcement rate is a key factor affecting crack development and load-deflection curve, and a reinforcement rate of 4.5% is recommended for a 55 mm-thick RPC layer. Lee et al. (Lee et al., 2011) investigated the shear performance and ultimate strength of cast-in-place joints and epoxy adhesive joints in prefabricated UHPC segmental bridges, considering the test parameters such as joint type, load-displacement relationship, fracture behavior, and fracture mode.

However, for the long-span bridges, wet joints are difficult to ensure the quality of joints due to the complex construction process. If the UHPC wet joints are not maintained properly, its mechanical performance will be affected greatly. Epoxy joints have the advantages of good integral performance, better shear bearing capacity than wet joints and lower requirements for maintenance conditions, etc., and have a wider range of adaptation. But the flexural performance of epoxy adhesive joints has been studied quite rarely. Therefore, in this study, four groups of 12 epoxy adhesive prefabricated UHPC bending specimens with different interfacial treatments at their joints were designed to study the bending performance. In addition, a simplified mechanical model of the key-tooth adhesive joint was proposed and a calculation formula for the flexural bearing capacity was established based on the experimental results and theoretical analysis. The research results provide a reference for the study and engineering applications of epoxy adhesive joints of prefabricated UHPC elements.

EXPERIMENTAL PROGRAM

Materials Properties

The main components of UHPC used in this test include cement, silica fume, quartz sand, quartz powder, and straight

steel fibers, and the matrix compound is shown in **Table 1**. The straight steel fiber has a volume ratio of 2%, a length of 8 mm, a diameter of 0.12 mm, and a nominal tensile strength of 2,700 MPa.

The mechanical properties of the UHPC material used in this test are listed in **Table 2**. Among them, the mechanical properties of UHPC were obtained by three 100 mm × 100 mm × 100 mm cubes, three 100 mm × 100 mm × 400 mm bending specimens, three 100 mm × 100 mm × 300 mm prisms, and three dogbone-shaped tensile specimens.

The epoxy resin is CBSR-A/B, which contains the main agent CBSR-A and curing agent CBSR-B, with a ratio of 2:1. According to The methods for properties of resin casting body (GB/T 2567-2021), the mechanical properties of epoxy resin were obtained by tensile and compression tests, as shown in **Figure 1**. The tensile strength, compressive strength, and flexural strength of the epoxy resin are 30 MPa, 100 MPa, and 45 MPa, respectively, and the tensile modulus of elasticity is 3200 MPa.

Design and Production of Specimen

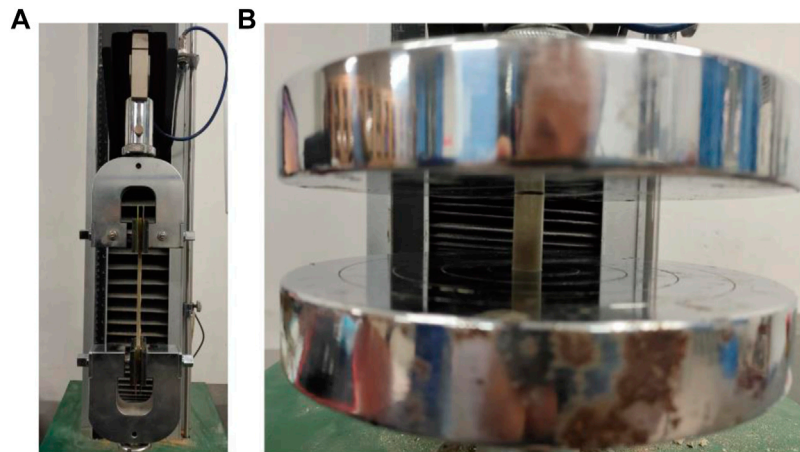
A total of 12 epoxy-adhesive UHPC-UHPC specimens in four groups were designed for this experiment. As shown in **Figure 2**, each specimen consists of two prefabricated UHPC bonded by epoxy resin. The dimension of the single UHPC are 249 mm × 100 mm × 100 mm, and the thickness of the epoxy layer is 2 mm (Zou et al., 2021). The surface at the interface of the two precast UHPC needs to be treated, which can be divided into four types of interfaces according to different treatments: 1) Natural interface, which is a smooth interface made by natural pouring; 2) Rough interface, where the UHPC surface is polished to expose the steel fibers; 3) Groove interface, where four grooves are evenly arranged on the interface, with a single groove size of 2 mm × 10 mm × 100 mm and a groove spacing of 10 mm. 4) Keyway interface. Two keyways were arranged on one side of the prefabricated UHPC interface, the width of the keyway root is 20 mm, the depth is 10 mm, and the spacing of the keyway centerline is 40 mm. The specimens were grouped as listed in **Table 3**.

As shown in **Figure 3**, the specimens were fabricated in sequential steps as follows:

- (1) Making the formwork based on the designed specimen size;
- (2) Pouring the UHPC;
- (3) The specimens were demolded after resting for 3 days in a room with the temperature of $20 \pm 5^\circ\text{C}$ and relative humidity greater than 50%, and the demolded specimens were steam cured for 48 h to ensure that the UHPC reached the design strength;
- (4) The mechanical chiseling of the interface of PD-E-R group specimens until the steel fibers are exposed;
- (5) Applying a 2-mm-thick epoxy resin layer uniformly at the interface of each group specimen and applying normal pressure to form the whole combined UHPC-UHPC specimen;
- (6) Curing all specimens naturally for 7 days to ensure that the epoxy adhesive reaches its design bond strength.

TABLE 2 | Mechanical properties of materials.

Materials	Compressive strength (MPa)	Tensile strength (MPa)	Flexural strength (MPa)	Elastic modulus (GPa)	Poisson's ratio ν_c
UHPC	150	14	20	42.1	0.2

**FIGURE 1** | Mechanical properties tests of epoxy resin. (A) Tensile test. (B) Compression test.

Test Setup and Instrumentation

The loading device is shown in **Figure 4**. The test was carried out using the MTS universal material testing machine with a capacity of 200 kN, and all specimens were loaded by the three-point bending test with a displacement-controlled loading rate of 0.1 mm/min.

The main test items are as follows: 1) Load-deflection curve; 2) Interfacial bending strength; and 3) Final failure modes of the specimen. The load-deflection curve is obtained by the data acquisition system of the MTS universal material testing machine. The interfacial bending strength is calculated by **Eq. 2.1**. The final failure modes of the specimen are observed and recorded at the end of loading.

$$\sigma_{nb} = \frac{3P_n L_m}{2bh^2} \quad (2.1)$$

where σ_{nb} is the interface bending strength, P_n is the ultimate load applied when the interface is damaged, L_m is the distance between the centerline of the two supports, b is the width of the specimen, h is the height of the specimen.

EXPERIMENTAL RESULTS AND DISCUSSION

Interfacial Failure Modes

The two parts of UHPC of each specimen were separated at the end of the test to observe the failure modes at the interface. The failure modes of the interface for a representative specimen of each group are shown in **Figure 5**.

As shown in **Figure 5A**, the interfacial failure modes of PD-E-N series specimens are mainly divided into two parts: the stripping between the epoxy layer-UHPC interface and the damage of the UHPC surface layer. The area outside the red and yellow circles in **Figure 5A** mainly shows the peeling between the epoxy layer-UHPC interface. Both the epoxy layer and UHPC surface are smooth, and no signs of damage are found, indicating that neither is broken by tension. In addition, the area inside the red and yellow circles mainly shows the damage of the UHPC surface layer with a thickness of about 1 mm. The pulled UHPC matrix can be observed on the epoxy surface, which indicates that the bonding performance of the epoxy and UHPC is better, thus leading to the damage of the UHPC surface layer under the tensile stress.

As shown in **Figure 5B**, the interfacial failure modes of PD-E-R series specimens mainly show the pull-out of the UHPC layer on one side of the interface, while the epoxy layer is intact on the other side. The steel fibers and fine aggregates pulled out of UHPC can be observed in the white circle area in **Figure 5B**, this is because some of the exposed steel fibers and fine aggregates are embedded in the epoxy layer, so its bonding performance with the epoxy layer is better. However, the mechanical chiseling treatment of the UHPC surface leads to the damage and loosening of the surface UHPC layer, which causes the interfacial normal tensile strength to be controlled by the loosened UHPC layer.

As shown in **Figure 5C**, the interfacial failure modes of PD-E-G series specimens are similar to that of PD-E-N, which mainly shows the stripping between the epoxy layer-UHPC interface inside the grooves and the damage of the UHPC surface layer

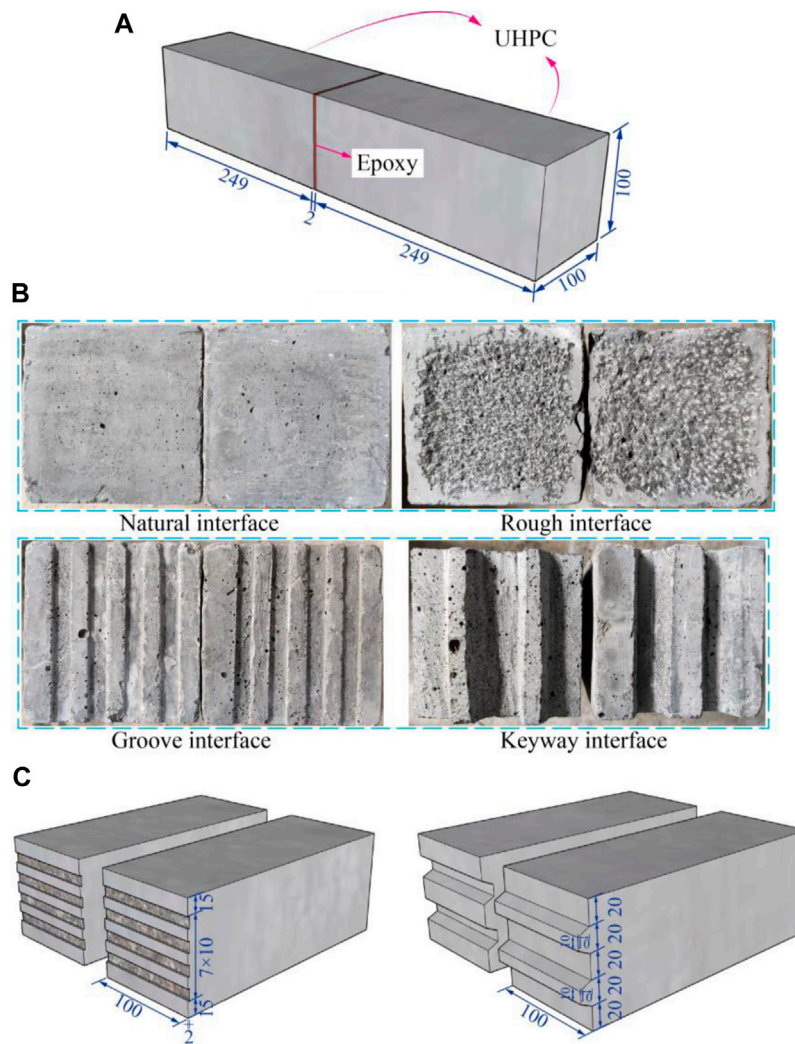


FIGURE 2 | Geometry of the specimen(Unit: mm). **(A)** 3D views. **(B)** Interface type. **(C)** Dimension details.

TABLE 3 | Details of specimens.

Specimen	Number	Surface	Epoxy thick (mm)	Loading mode
PD-E-N-1~3	3	E + N	2	TPB
PD-E-R-1~3	3	E + R	2	TPB
PD-E-G-1~3	3	E + G	2	TPB
PD-E-K-1~3	3	E + K	2	TPB

Note: PD represents prefabricated bridge deck panels, E represents epoxy resin, N, R, G and K represent different interface treatments, and TPB represents three-point Bending loading scheme.

outside the grooves. The epoxy layer and UHPC surface inside the grooves are smooth without damage signs, and they show stripping of the interface and lose the bearing capacity under the normal tension. Compared with the epoxy layer inside the grooves, the thickness of the epoxy layer in the interface area outside the grooves is thinner. Its bonding performance with the

UHPC surface is better, leading to the UHPC surface layer being damaged under normal tension.

As shown in **Figure 5D**, the interfacial failure modes of PD-E-K series specimens mainly show that the UHPC at the root of key teeth on one side is pulled and the interfacial stripping between the epoxy-UHPC surface layer in the area outside the keyway. This indicates that the bonding performance of bonded UHPC-epoxy adhesive interface is excellent after the keyway treatment, and the tensile strength of the interface is controlled by the UHPC near the root of key teeth under normal tension. In addition, after the specimen reaches the ultimate bearing capacity and is damaged, the steel fibers into UHPC limit the development of cracks. The UHPC matrix on both sides of the cracks is not completely separated. The specimen can still bear a certain load and have residual strength.

Interfacial Bond Strength

The test results of this study are summarized in **Table 4** and include the ultimate bearing capacity P_n (kN), interfacial bond

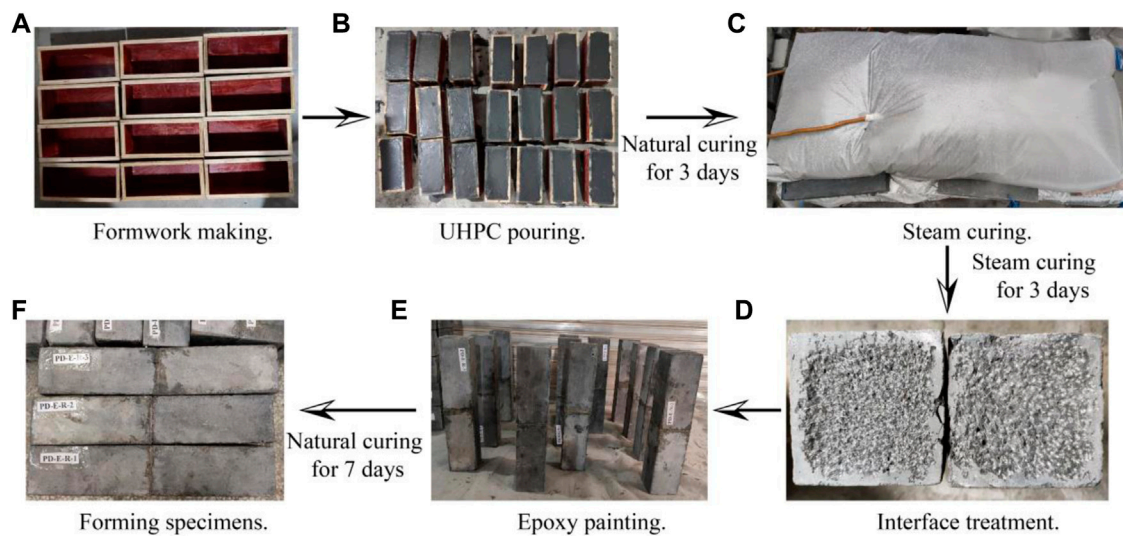


FIGURE 3 | The production process of the specimen. (A) Formwork making. (B) UHPC pouring. (C) Steam curing. (D) Interface treatment. (E) Forming specimens. (F) Epoxy painting.

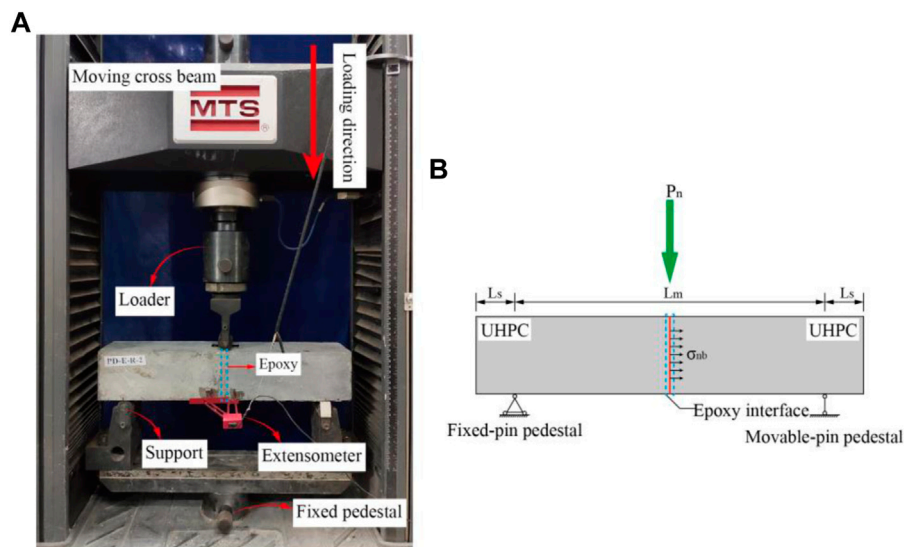


FIGURE 4 | Experimental setup. (A) Loading device diagram. (B) Force mode.

strength σ_{nb} (MPa) and its average value $\sigma_{nb,avg}$ (MPa), mid-span deflection δ_n (mm) and its average value $\delta_{n,avg}$ (mm) when the specimens reach the ultimate load, and residual strength σ_{res} (MPa) and its average value $\sigma_{res,avg}$ (MPa) after the failure of specimens. In this study, the interfacial bond strength σ_{nb} is calculated by Eq. 2.1, the residual strength σ_{res} is the nominal strength of the interface corresponding to the time when the load tends to stabilize after the specimen has reached its ultimate state and is damaged.

To compare the bending resistance of the various interfaces more intuitively way, a comparison of the bending performance of four different interfaces based on Table 4 is shown in Figure 6.

As shown in Figure 6 and Table 4, in descending order of bending strength: the keyway interface, groove interface, natural boundary surface, and rough interface. Compared with the natural interface, the bending tensile strength of rough interface, groove interface, and keyway interface were increased by -24.02, 2.34, and 4.64%, respectively. The bending tensile strength of the rough interface is the lowest among all the treatment methods, because the mechanical chiseling destroys part of the matrix on the UHPC surface. And the looser UHPC layer makes the interface fail under the normal tensile force, and its strength is reduced significantly.

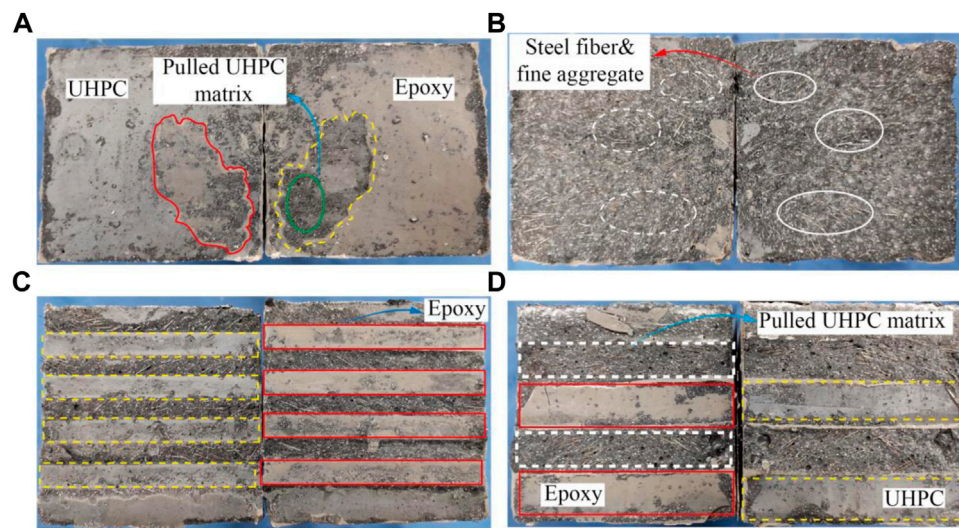


FIGURE 5 | Failure mode of specimen. (A) PD-E-N. (B) PD-E-R. (C) PD-E-G. (D) PD-E-K.

TABLE 4 | The main results of the tests.

Specimens		P_n	σ_{nb}	$\sigma_{nb,avg}$	Difference (%)	δ_n	$\delta_{n,avg}$	Difference (%)	σ_{res}	$\sigma_{res,avg}$
PD-E-N	PD-E-N-1	17.402	10.441	10.510	0	0.817	0.824	0	0.022	0.015
	PD-E-N-2	18.255	10.953			0.870			0.022	
	PD-E-N-3	16.895	10.137			0.785			0.002	
PD-E-R	PD-E-R-1	14.397	8.638	7.986	-24.02	0.528	0.523	-36.53	0.126	0.279
	PD-E-R-2	12.073	7.244			0.511			0.647	
	PD-E-R-3	13.460	8.076			0.529			0.064	
PD-E-G	PD-E-G-1	17.965	10.779	10.756	2.34	0.732	0.764	-7.28	0.031	0.230
	PD-E-G-2	19.261	11.557			0.807			0.428	
	PD-E-G-3	16.553	9.932			0.752			0.230	
PD-E-K	PD-E-K-1	19.528	11.717	10.998	4.64	0.822	0.789	-4.25	3.930	4.107
	PD-E-K-2	18.569	11.141			0.750			3.828	
	PD-E-K-3	16.895	10.137			0.796			4.563	

Note: The bolded value in the table is the minimum value of column, the underlined bolded value is the maximum value of column, the "Difference" is relative to the specimens with the natural interface (PD-E-N).

Compared with the natural interface, the keyway interface has a more significant increase in bending strength because its failure modes are mainly the tensile damage of UHPC at the root of key teeth. In addition, the deflection at ultimate bending strength is less than 0.83 mm for all four interfaces. The rough interface, groove interface, and keyway interface were reduced by 36.53, 7.28, and 4.25%, respectively, compared to the natural surface. The deflection was also significantly reduced for the rough interface due to its significantly reduced load-carrying capacity.

Furthermore, the natural interface loses its bearing capacity immediately after the failure and has almost no residual strength. Although the rough and groove interfaces have improved compared with the natural surface, their residual strengths are still relatively low, only 0.279 and 0.23 MPa, respectively. However, the keyway interface has a residual strength of 4.107 MPa. It is the only interface with reliable residual strength among the four interfaces. This is because under the action of normal tension, although the UHPC at the root of the keyway is

pulled, the presence of steel fibers limits the rapid development of crack so that the UHPC matrix on both sides of the damaged surface can still bear a certain amount of normal tension under the "connection" of steel fibers, that is, the tensile strength of UHPC after cracking constitutes the residual strength of the specimen.

Load-Deflection Curves

In this study, the load applied to the specimens and the values of mid-span deflection of the specimens were obtained by the sensor acquisition system of the MTS universal material testing machine. The load-deflection curves of four groups of specimens are shown in **Figure 7**.

As shown in **Figure 7A**, the load-deflection curves of PD-E-N series specimens exhibit two-fold line form, which is mainly divided into the loading and failure phases. The load rises steadily and almost linearly before the specimen reaches the ultimate load in the loading phase. The curves still maintain high linearity without an obvious yielding phase when the

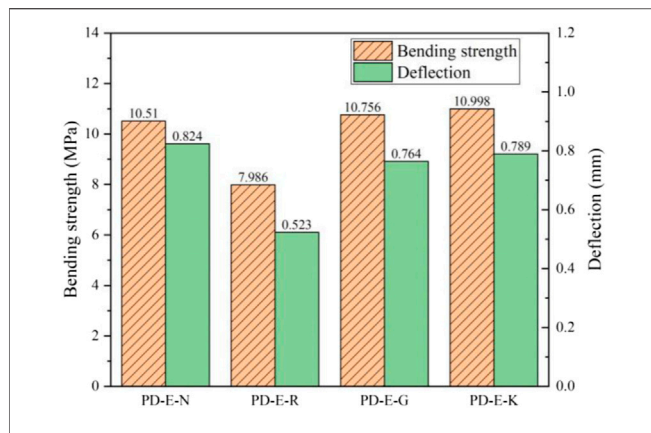


FIGURE 6 | Interfacial parameters comparison.

ultimate bearing capacity is near, which indicates that it does not have ductility. The specimens lose the load-bearing capacity immediately after reaching the ultimate load, without residual strength. This indicates that the interfacial failure belongs to brittle failure, consistent with the failure modes of epoxy layer-UHPC interfacial stripping.

As shown in Figures 7B–D, the general trend of load-deflection curves of the rough interface, groove interface, and keyway interface remains the same as that of the natural interface specimens, all of which mainly show two-fold line form. However, in contrast to the natural surface, the rough and groove interfaces have a certain residual strength after failure. The load shows a slightly increasing trend with the increment of deflection. For the keyway interface, the residual strength is significantly higher than that of the remaining three types of specimens, and the load decreases more slowly with the increment of deflection. This is due to the fact that under the action of normal tension, although the UHPC at the root of the keyway is pulled, the presence of steel fibers limits the rapid development of crack so that the UHPC matrix can still bear a certain amount of normal tension under the “connection” of steel fibers. In conclusion, the ultimate bending tensile strength and residual strength after the failure of the keyway interface are the highest among the four interface forms. The bending performance of the prefabricated UHPC-epoxy adhesive joints is the best when this interface form is adopted.

SIMPLIFIED COMPUTATIONAL METHOD

Force Model and Basic Assumption

The stress state of epoxy adhesive joint is bending-shear composite stress under three-point bending load. Since the tensile strength of epoxy resin is greater than that of UHPC, the bending-shear failure of prefabricated UHPC elements is controlled by the tensile strength of UHPC. The cracks will appear on the UHPC next to the adhesive joint. The calculation diagram is shown in Figure 8.

Since the initial damage and damage area of epoxy resin layer are difficult to define, the following basic assumptions are

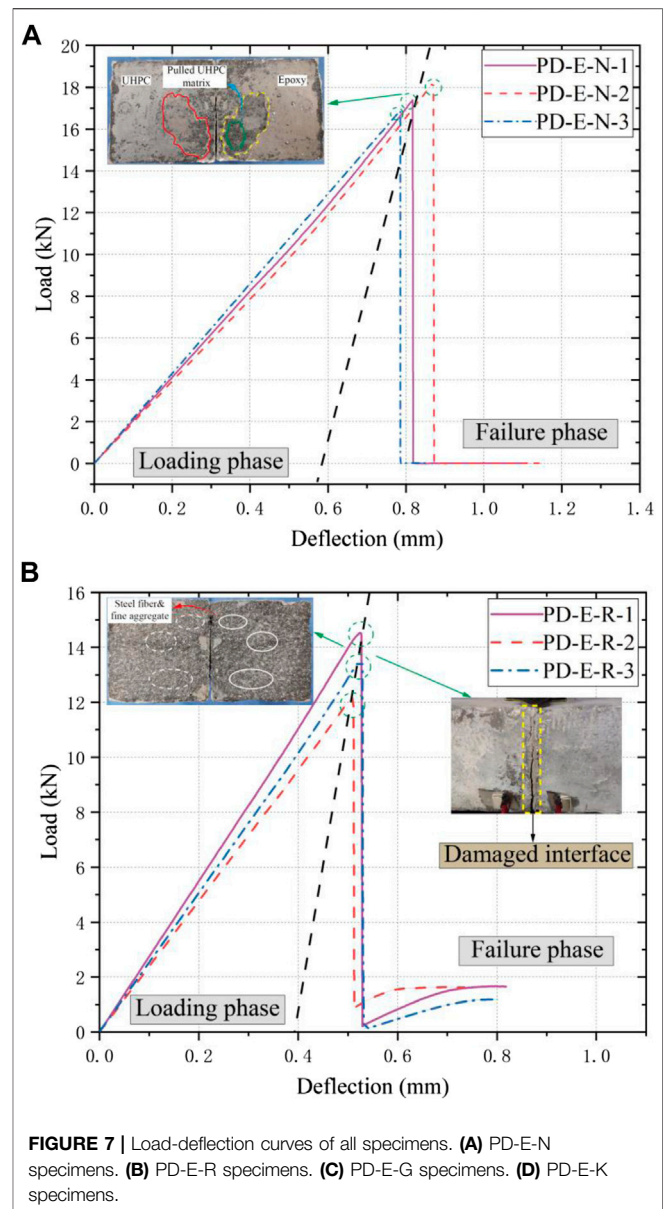


FIGURE 7 | Load-deflection curves of all specimens. (A) PD-E-N specimens. (B) PD-E-R specimens. (C) PD-E-G specimens. (D) PD-E-K specimens.

proposed according to the experimental phenomena to simplify the mechanical behavior of epoxy adhesive joints.

- (1) The joint surface does not crack before reaching the ultimate state, and only the lower half of the adhesive layer cracks after reaching the ultimate state, so the cross-section area of the lower half is only considered when calculating the bearing capacity.
- (2) The adhesive layer loses its bearing capacity after cracking immediately. The residual strength of the specimen is only provided by the bonding force of the upper adhesive layer and UHPC at the root of the key tooth.
- (3) Ignoring the contribution of adhesive layer in key tooth region of cracking zone.
- (4) The dimension of rectangular section is small, so the shear stress on the section is assumed to be uniformly distributed.

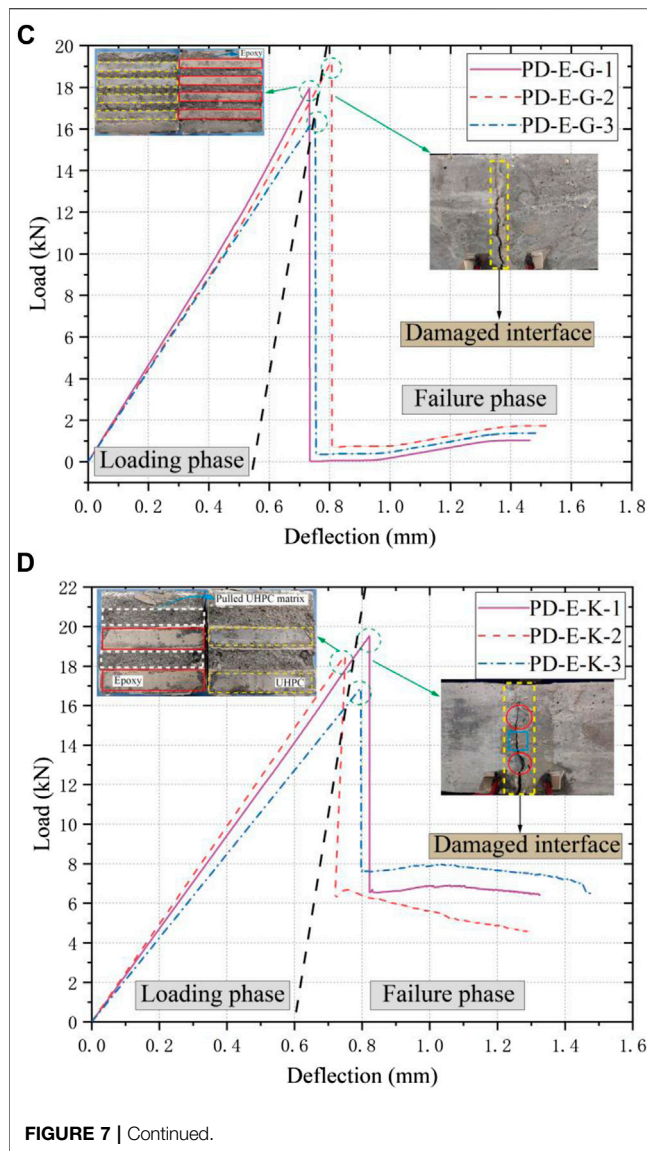


FIGURE 7 | Continued.

Calculation Method of Bearing Capacity

Based on the above basic assumptions and the experimental results of this study, the bearing capacity of the adhesive joint is provided by the bonding force of adhesive layer and UHPC at the root of the key tooth, as shown in Eq. 4.1. The contribution of the adhesive layer can be expressed as follows: Shear slip and normal separation occurred on the joint surface, and the bond strength of the adhesive layer provided resistance load. The adhesive layer begins to damage after the joint surface reaches the maximum bonding strength, and the adhesive layer quits immediately after cracking. It is worth noting that the adhesive layer cracking was observed only in the lower of the specimen, and no cracks were observed in the shear-compression zone under high stress. The failure mode of the key tooth is that the root of key tooth is pulled out under the bending-shear combined action. The adhesive layer of the key tooth region is not cracked,

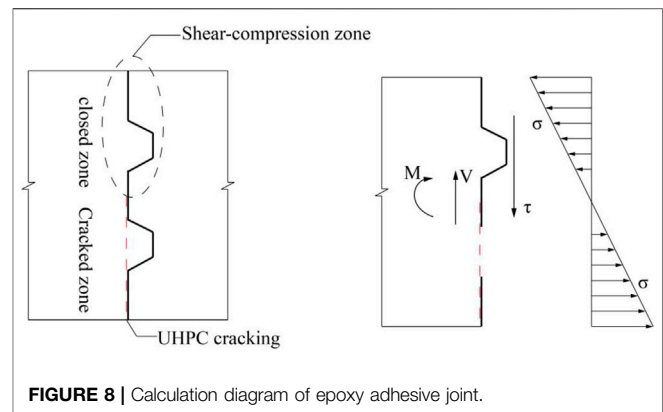


FIGURE 8 | Calculation diagram of epoxy adhesive joint.

so it can be considered that the contribution of the key tooth is only provided by the key tooth matrix itself.

$$P_n = P_a + P_k \quad (4.1)$$

where P_n represents the bearing capacity of adhesive joints, P_a represents the bonding force of adhesive layer, P_k represents the bearing capacity of UHPC at the root of key tooth. The bonding force of the adhesive layer can be obtained from the test results of the adhesive joint with smooth interface. It is worth noting that the tensile strength of UHPC on the surface of specimen and its internal UHPC matrix is quite different due to the different distribution of steel fiber. In this study, the strength reduction coefficient β was introduced to represent the tensile strength of UHPC surface. Therefore, the calculation formula of bonding force is shown in Eq. 4.2:

$$P_a = 4 \frac{\beta f_t W_z}{L_m} \quad (4.2)$$

where f_t represents the uniaxial tensile strength of UHPC, W_z represents the section modulus in bending, L_m represents the calculation span of the prefabricated UHPC elements, β is 0.729 based on the test results of adhesive joints with smooth interface.

For the key teeth, most of the existing study are based on the major principal tensile stress theory (Gopal et al., 2020). The analysis of micro-element of UHPC near the root of the key tooth is shown in Figure 9. From the principle of Mohr's circle, the major principal tensile stress can be obtained as Eq. 4.3:

$$\sigma_1 = \frac{1}{2}(\sigma_x - \sigma_y) + \frac{1}{2}\sqrt{(\sigma_x - \sigma_y)^2 + 4\tau_x^2} \quad (4.3)$$

Since the failure of key teeth is controlled by the tensile strength of UHPC, $\sigma_1 = f_t$, for the ultimate state of bearing capacity, and $\sigma_y = 0$. The calculation formulas of shear stress and normal stress on the rectangular cross-section are shown in Eq. 4.4 and Eq. 4.5, respectively:

$$\tau_x = \frac{3(P_a + P_k)}{2A_k} \quad (4.4)$$

$$\sigma_x = \frac{2(P_a + P_k)L_m}{4W_z} = \frac{(P_a + P_k)L_m}{2W_z} \quad (4.5)$$

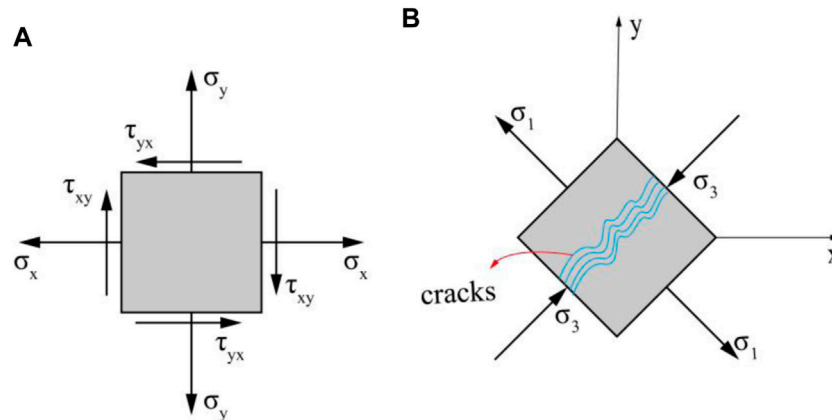


FIGURE 9 | Stress state of the key tooth. **(A)** Stresses in given coordinate. **(B)** Principal stresses (Failure criteria).

where A_k represents the root area of the key tooth. Based on the above formulas, the formula for calculating the bearing capacity of key tooth adhesive joints can be obtained, as shown in Eq. 4.6:

$$P_n = \frac{A_k f_t}{9} \left(\sqrt{\left(\frac{A_k L_m}{W_z} \right)^2 + 36} - \frac{A_k L_m}{W_z} \right) \quad (4.6)$$

In summary, for the smooth adhesive joints, the calculation formula can be expressed as Eq. 4.2 because its bearing capacity is only provided by the bonding force. For the key tooth adhesive joints, the bearing capacity can be expressed as Eq. 4.6.

Comparison of Results

As shown in Table 5, based on the calculation formulas of flexural capacity of epoxy adhesive joints proposed in this study, the smooth adhesive joints and key tooth adhesive joints are calculated, which are compared with the test results.

As can be seen from Table 5, the suggested formulas can better predict the bending capacity of smooth adhesive joints and key tooth adhesive joints. The ratio of calculated value to experimental value is 0.925, and the results are conservative. The standard deviation is 0.065, and the discreteness was small. However, the number of specimens is small in this study relatively, and for the key tooth adhesive joint, the parameters, such as the number and the geometric size of key teeth, are relatively simple. Therefore, the more applicable formula for calculating the bending capacity of key tooth adhesive joints remains to be further studied.

CONCLUSION

To clarify the bending performance of epoxy adhesive joints between prefabricated UHPC elements, the failure modes, load-deflection curves, and interfacial bond strength of prefabricated UHPC epoxy adhesive joints were studied

TABLE 5 | Comparison between calculated and experimental values.

Specimens	No.	P_c	P_n	P_c/P_n
PD-E-N	1	17.01	17.40	0.978
	2	17.01	18.26	0.932
	3	17.01	16.90	1.007
PD-E-K	1	16.02	19.53	0.820
	2	16.02	18.57	0.863
	3	16.02	16.90	0.948
The mean value				0.925
The standard deviation				0.065

Note: P_c represents the calculated values, and P_n represents the test values.

through a three-point bending test. A calculation formula for the flexural bearing capacity was established based on the experimental results and theoretical analysis. The main conclusions are as follows:

- (1) Under the action of normal bending tension, the failure modes of joints with different interface forms vary from each other. The smooth interface mainly shows interfacial stripping failure of the epoxy-UHPC surface layer. A minority of the UHPC surface layer is damaged due to the extraction of steel fibers and fine aggregate. The roughened interface shows interfacial failure due to the pull-out of steel fibers and fine aggregate embedded in epoxy. The groove interface mainly shows the stripping between the epoxy layer-UHPC interface inside the groove and the damage of the UHPC surface layer outside the groove. The keyway interface exhibits tensile damage of UHPC at the root of key teeth and the stripping of epoxy-UHPC surface layer interface in the area outside the keyway.
- (2) The load-deflection curves of all specimens exhibit a two-fold line form, which has no yielding stage before reaching ultimate strength. The mid-span deflection values corresponding to the ultimate strength are lower than

0.83 mm. The interface is instantly damaged after reaching ultimate strength, without sufficient plastic deformation, and exhibits the characteristics of brittle damage.

- (3) Compared with the natural surface, the bending tensile strength of rough interface, grooved interface, and keyway interface were improved by -24.02, 2.34, and 4.64%, respectively. Given that the mechanical chiseling method can damage the UHPC surface layer, which in turn reduces the bending strength of the interface, it is recommended to use high-pressure jet technology for the interface roughness treatment. For the keyway interface, which has the most reliable interfacial ultimate and residual strength values among the four groups of specimens, this interfacial form can be adopted for the joints of prefabricated UHPC elements.
- (4) A simplified force model of the keytooth adhesive joint is proposed based on the experimental results and theoretical analysis, and a calculation formula for the flexural bearing capacity is established based on the principal of Mohr's circle. The suggested formulas can better predict the bending capacity of smooth adhesive joints and key tooth adhesive joints. The ratio of calculated value to experimental value is 0.925, and the results are conservative. The standard deviation is 0.065, and the discreteness was small.

REFERENCES

- Abdelbaset, H., Cheng, B., Tian, L., Li, H.-T., and Zhang, Q.-H. (2020). Reduce Hot Spot Stresses in Welded Connections of Orthotropic Steel Bridge Decks by Using UHPC Layer: Experimental and Numerical Investigation. *Eng. Structures* 220 (105708), 110988. doi:10.1016/j.engstruct.2020.110988
- Abdelbaset, H., Cheng, B., Tian, L., Li, H.-T., and Zhao, J. (2022). Enhancing Fatigue Resistance of Rib-To-Floorbeam Welded Connections in Orthotropic Steel Bridge Decks by Using UHPC Layer: An Experimental Study. *Structures* 36, 153–167. doi:10.1016/j.istruc.2021.12.008
- Chen, B. C., An, M. Z., Huang, Q. W., Wu, H. C., and Zhao, Q. (2016). "Application of Ultra-High Performance Concrete in Bridge Engineering in China," in First International Interactive Symposium on UHPC, Iowa State University, Des Moines, IA, January 1, 2016 (Des Moines, Iowa, USA: Iowa State University). doi:10.21838/uhpc.2016.82
- Chen, D., Zeng, M., Su, Q., and Lou, Y. (2018). Interfacial Treatment Measures of Wet Joints in Composite Bridge Deck Composed of Steel and UHPC Layer. *China J. Highw. Transport* 31, 154–162. doi:10.19721/j.cnki.1001-7372.2018.12.015
- Cheng, Z., Zhang, Q., Bao, Y., Deng, P., Wei, C., and Li, M. (2021). Flexural Behavior of Corrugated Steel-UHPC Composite Bridge Decks. *Eng. Structures* 246, 113066. doi:10.1016/j.engstruct.2021.113066
- De Larrard, F., and Sedran, T. (1994). Optimization of Ultra-High-Performance concrete by the Use of a Packing Model. *Cement Concrete Res.* 24, 997–1009. doi:10.1016/0008-8846(94)90022-1
- Dieng, L., Marchand, P., Gomes, F., Tessier, C., and Toutlemonde, F. (2013). Use of UHPFRC Overlay to Reduce Stresses in Orthotropic Steel Decks. *J. Constructional Steel Res.* 89, 30–41. doi:10.1016/j.jcsr.2013.06.006
- Du, J., Meng, W., Khayat, K. H., Bao, Y., Guo, P., Lyu, Z., et al. (2021). New Development of Ultra-High-Performance Concrete (UHPC). *Composites B: Eng.* 224, 109220. doi:10.1016/j.compositesb.2021.109220
- Garas, V. Y., Kahn, L. F., and Kurtis, K. E. (2009). Short-Term Tensile Creep and Shrinkage of Ultra-High Performance Concrete. *Cement and Concrete Composites* 31, 147–152. doi:10.1016/j.cemconcomp.2009.01.002

DATA AVAILABILITY STATEMENT

The original contributions presented in the study are included in the article/Supplementary Material, further inquiries can be directed to the corresponding author.

AUTHOR CONTRIBUTIONS

HP conceptualized the study, formulated the methodology, performed the software and formal analysis, and wrote and prepared the original draft. ZZ, YZ, and JG reviewed and edited the manuscript, supervised the study, was in charge of the project administration, and acquired the funding. XZ and XZe conducted data curation. All authors have read and agreed to the published version of the manuscript.

FUNDING

The authors express their sincere gratitude for the financial support provided by the National Natural Science Foundation of China (52008066), the Major Science and Technology Projects in Hainan (ZDKJ2021048), the China Postdoctoral Science Foundation (Grant No. 2021M693919) and Science and technology projects in TAR (XZ202001ZY0054G).

- Gopal, B., Hejazi, F., Hafezolzhorani Esfahani, M., and Voo, Y. (2020). Shear Strength of Dry and Epoxy Joints for Ultra-High-Performance Fiber-Reinforced Concrete. *ACI Struct. J.* 117, 279–288. doi:10.14359/51718078
- Haber, Z. B., Munoz, J. F., De la Varga, I., and Graybeal, B. A. (2018). Bond Characterization of UHPC Overlays for Concrete Bridge Decks: Laboratory and Field Testing. *Construction Building Mater.* 190, 1056–1068. doi:10.1016/j.conbuildmat.2018.09.167
- Huang, H., and Ye, G. (2017). Examining the "Time-Zero" of Autogenous Shrinkage in High/Ultra-High Performance Cement Pastes. *Cement Concrete Res.* 97, 107–114. doi:10.1016/j.cemconres.2017.03.010
- Lee, C.-H., Chin, W.-J., Choi, E.-S., and Kim, Y.-J. (2011). An Experimental Study on the Joints in Ultra High Performance Precast Concrete Segmental Bridges. *J. Korea Concrete Inst.* 23, 235–244. doi:10.4334/jkci.2011.23.2.235
- Lee, N. K., Koh, K. T., Park, S. H., and Ryu, G. S. J. C. (2017). Microstructural Investigation of Calcium Aluminate Cement-Based Ultra-high Performance concrete (UHPC) Exposed to High Temperatures. *Cement Concrete Res.* 102, 109–118. doi:10.1016/j.cemconres.2017.09.004
- Li, J., and Deng, Z. (2021). Tensile Behavior of Hybrid Fiber-Reinforced Ultra-High-Performance Concrete. *Front. Mater.* 8, 455. doi:10.3389/fmats.2021.769579
- Lian, J., Hu, C., Fu, T., and Wang, Y. (2021). Review of Self-Sensing Capability of Ultra-High Performance Concrete. *Front. Mater.* 8, 746022. doi:10.3389/fmats.2021.746022
- Liew, J. Y. R. (2015). *Design Guide for Concrete Filled Tubular Members with High Strength Materials to Eurocode 4: Design Guide for Concrete Filled Tubular Members with High Strength Materials to Eurocode*. Lower Kent Ridge Rd, Singapore: Research Publishing, 4.
- Meng, W., Khayat, K. H., and Bao, Y. (2018). Flexural Behaviors of Fiber-Reinforced Polymer Fabric Reinforced Ultra-High-Performance concrete Panels. *Cement and Concrete Composites* 93, 43–53. doi:10.1016/j.cemconcomp.2018.06.012
- Meng, W., and Khayat, K. H. (2018). Effect of Graphite Nanoplatelets and Carbon Nanofibers on Rheology, Hydration, Shrinkage, Mechanical Properties, and Microstructure of UHPC. *Cement Concrete Res.* 105, 64–71. doi:10.1016/j.cemconres.2018.01.001
- Meng, W., and Khayat, K. H. (2017). Improving Flexural Performance of Ultra-High-Performance concrete by Rheology Control of Suspending

- Mortar. *Composites Part B: Eng.* 117, 26–34. doi:10.1016/j.compositesb.2017.02.019
- Pan, W., Fan, J., Nie, J., Hu, J., and Cui, J. (2016). Experimental Study on Tensile Behavior of Wet Joints in a Prefabricated Composite Deck System Composed of Orthotropic Steel Deck and Ultrathin Reactive-Powder Concrete Layer. *J. Bridge Eng.* 21, 04016064. doi:10.1061/(asce)be.1943-5592.0000935
- Qi, J., Bao, Y., Wang, J., Li, L., and Li, W. (2019). Flexural Behavior of an Innovative Dovetail UHPC Joint in Composite Bridges under Negative Bending Moment. *Eng. Structures* 200, 109716. doi:10.1016/j.engstruct.2019.109716
- Qin, F., Zhang, Z., Yin, Z., Di, J., Xu, L., and Xu, X. (2020). Use of High Strength, High Ductility Engineered Cementitious Composites (ECC) to Enhance the Flexural Performance of Reinforced concrete Beams. *J. Building Eng.* 32, 101746. doi:10.1016/j.jobbe.2020.101746
- Ren, L., Fang, Z., Zhong, R., and Wang, K. (2019). Experimental and Numerical Investigations of the Seismic Performance of UHPC Box Piers. *KSCE J. Civ Eng.* 23, 597–607. doi:10.1007/s12205-018-0567-8
- Shao, X., Chen, B., and Zhou, X. (2017). Experiment on Bending Behavior of Wet Joints in Light-Weighted Composite Deck System Composed of Steel and RPC Layer. *China J. Highw. Transport* 30, 8. doi:10.19721/j.cnki.1001-7372.2017.03.023
- Shao, X., Qiu, M., Yan, B., Hu, W., and Zhao, X. (2019). Research of High Performance Fabricated Bridge Structures Based on UHPC. *J. Xi'an Univ. Architecture Technology(Natural Sci. Edition)* 51, 8. doi:10.15986/j.1006-7930.2019.02.002
- Shao, X., Yi, D., Huang, Z., Zhao, H., Chen, B., and Liu, M. (2013). Basic Performance of the Composite Deck System Composed of Orthotropic Steel Deck and Ultrathin RPC Layer. *J. Bridge Eng.* 18, 417–428. doi:10.1061/(asce)be.1943-5592.0000348
- Su, J.-z., Ma, X.-l., Chen, B.-c., and Sennah, K. (2019). Full-Scale Bending Test and Parametric Study on a 30-m Span Prestressed Ultra-high Performance concrete Box Girder. *Adv. Struct. Eng.* 23, 1276–1289. doi:10.1177/1369433219894244
- Wang, D., Shi, C., Wu, Z., Xiao, J., Huang, Z., and Fang, Z. (2015). A Review on Ultra High Performance Concrete: Part II. Hydration, Microstructure and Properties. *Construction Building Mater.* 96, 368–377. doi:10.1016/j.conbuildmat.2015.08.095
- Wang, K., Zhao, C., Wu, B., Deng, K., and Cui, B. (2019). Fully-Scale Test and Analysis of Fully Dry-Connected Prefabricated Steel-UHPC Composite Beam under Hogging Moments. *Eng. Structures* 197, 109380. doi:10.1016/j.engstruct.2019.109380
- Wang, Y., Shao, X., Chen, J., Cao, J., and Deng, S. (2021). UHPC-Based Strengthening Technique for Orthotropic Steel Decks with Significant Fatigue Cracking Issues. *J. Constructional Steel Res.* 176, 106393. doi:10.1016/j.jcsr.2020.106393
- Wille, K., Naaman, A., and Parra-Montesinos, G. (2011). Ultra-High Performance Concrete with Compressive Strength Exceeding 150 MPa (22 ksi): A Simpler Way. *ACI Mater. J.* 108, 46–54. doi:10.14359/51664215
- Xiao, J., Guo, L., Nie, J., Li, Y., Fan, J., and Shu, B. (2022). Flexural Behavior of Wet Joints in Steel-UHPC Composite Deck Slabs under Hogging Moment. *Eng. Structures* 252, 113636. doi:10.1016/j.engstruct.2021.113636
- Xue, J., Briseghella, B., Huang, F., Nuti, C., Tabatabai, H., and Chen, B. (2020). Review of Ultra-high Performance Concrete and its Application in Bridge Engineering. *Construction Building Mater.* 260, 119844. doi:10.1016/j.conbuildmat.2020.119844
- Yoo, D.-Y., Park, J.-J., Kim, S.-W., and Yoon, Y.-S. (2014). Influence of Reinforcing Bar Type on Autogenous Shrinkage Stress and Bond Behavior of Ultra High Performance Fiber Reinforced concrete. *Cement and Concrete Composites* 48, 150–161. doi:10.1016/j.cemconcomp.2013.11.014
- Zhang, Z., Liu, D., Ding, Y., and Wang, S. (2022). Mechanical Performance of Strain-Hardening Cementitious Composites (SHCC) with Bacterial Addition. *J. Infrastructure Preservation Resilience* 3, 3. doi:10.1186/s43065-022-00048-3
- Zhang, Z., Liu, S., Yang, F., Weng, Y., and Qian, S. (2021). Sustainable High Strength, High Ductility Engineered Cementitious Composites (ECC) with Substitution of Cement by rice Husk Ash. *J. Clean. Prod.* 317, 128379. doi:10.1016/j.jclepro.2021.128379
- Zhang, Z., Yang, F., Liu, J.-C., and Wang, S. (2020). Eco-Friendly High Strength, High Ductility Engineered Cementitious Composites (ECC) with Substitution of Fly Ash by rice Husk Ash. *Cement Concrete Res.* 137, 106200. doi:10.1016/j.cemconres.2020.106200
- Zhao, C., Wang, K., Zhou, Q., Deng, K., and Cui, B. (2018). Full-Scale Test and Simulation on Flexural Behavior of Dovetail-Shaped Reactive Powder-Concrete Wet Joint in a Composite Deck System. *J. Bridge Eng.* 23, 04018051. doi:10.1061/(asce)be.1943-5592.0001265
- Zhou, M., Lu, W., Song, J., and Lee, G. C. (2018). Application of Ultra-High Performance Concrete in Bridge Engineering. *Construction Building Mater.* 186, 1256–1267. doi:10.1016/j.conbuildmat.2018.08.036
- Zhu, J.-S., Wang, Y.-G., Yan, J.-B., and Guo, X.-Y. (2020). Shear Behaviour of Steel-UHPC Composite Beams in Waffle Bridge Deck. *Compos. Structures* 234, 111678. doi:10.1016/j.compstruct.2019.111678
- Zou, Y., Jiang, J., Zhou, Z., Wang, X., Guo, J., and Zhang, Z. (2021). Study on the Static Performance of Prefabricated UHPC-Steel Epoxy Bonding Interface. *Adv. Civil Eng.* 2021, 1–15. doi:10.1155/2021/6663517

Conflict of Interest: The authors declare that the research was conducted in the absence of any commercial or financial relationships that could be construed as a potential conflict of interest.

Publisher's Note: All claims expressed in this article are solely those of the authors and do not necessarily represent those of their affiliated organizations, or those of the publisher, the editors and the reviewers. Any product that may be evaluated in this article, or claim that may be made by its manufacturer, is not guaranteed or endorsed by the publisher.

Copyright © 2022 Peng, Zhang, Zou, Guo, Zhang and Zeng. This is an open-access article distributed under the terms of the Creative Commons Attribution License (CC BY). The use, distribution or reproduction in other forums is permitted, provided the original author(s) and the copyright owner(s) are credited and that the original publication in this journal is cited, in accordance with accepted academic practice. No use, distribution or reproduction is permitted which does not comply with these terms.



Sectional Analysis of Reinforced Engineered Cementitious Composite Columns Subjected to Combined Lateral Load and Axial Compression

Chang Wu^{1*}, Yanli Su¹, Yu Sun¹, Chenhua Jin² and Zuanfeng Pan³

¹School of Civil Engineering, Southeast University, Nanjing, China, ²School of Architectural Engineering, Jinling Institute of Technology, Nanjing, China, ³College of Civil Engineering, Tongji University, Shanghai, China

OPEN ACCESS

Edited by:

Zhigang Zhang,
Chongqing University, China

Reviewed by:

Bo-Tao Huang,
Hong Kong Polytechnic University,
Hong Kong SAR, China
Hui Huang,
Southwest University of Science and
Technology, China

*Correspondence:

Chang Wu
changwu@seu.edu.cn

Specialty section:

This article was submitted to
Structural Materials,
a section of the journal
Frontiers in Materials

Received: 05 February 2022

Accepted: 15 February 2022

Published: 14 April 2022

Citation:

Wu C, Su Y, Sun Y, Jin C and Pan Z
(2022) Sectional Analysis of Reinforced
Engineered Cementitious Composite
Columns Subjected to Combined
Lateral Load and Axial Compression.
Front. Mater. 9:869835.
doi: 10.3389/fmats.2022.869835

The ultra-high tensile ductility of ECC provides an alternative way to enhance the ductility of structural members by using high-ductile matrix material instead of simply increasing reinforcements. However, the application of ECC members is still limited due to the relatively short research time and the lack of design specifications. Being equivalent to eccentric compressive members, a sectional analysis of RECC columns subjected to combined lateral load and axial compression are proposed in this paper. Based on the design theory of load capacity of eccentric compression columns and the unique constitutive model of ECC, the calculation equations for the sectional load capacity of RECC columns are derived. The analytical prediction of the load capacity of RECC column is evaluated in comparison with that of experiments that confirm the capacity of the proposed calculation method to capture the behavior of the RECC column accurately. The strength-interaction diagrams showing the axial force-moment ($N-M$) interaction curves are then constructed for analysis using the proposed calculation equations. A parametric study is also carried out by using the proposed calculation equations, demonstrating the effects of ultimate tensile strain of ECC, compressive and tensile strength of ECC, yield strength of steel bar, and reinforcement ratio on the $N-M$ interaction curves of RECC columns. The investigations exhibited in this paper are expected to provide insight into the design principles of RECC columns.

Keywords: engineered cementitious composites (ECC), column, eccentric compression, sectional load capacity, axial load-moment interaction curve

1 INTRODUCTION

Reinforced concrete (RC) columns are the lateral force resistance members in frame structures, whose seismic performance directly affects the performance of the whole structure. Modern seismic design methodology requires structural members to possess sufficient ductility and energy-absorption capacity. In some cases, RC short columns are unavoidable vertical load-bearing members in concrete structures, which are used widely in various building structures (Deng et al., 2015; Wu et al., 2017a, 2017b, 2020; Hu et al., 2021; Liu et al., 2021). However, RC short columns have poor deformation capacity and high stiffness, which are at risk of catastrophic brittle failure during earthquakes due to the intrinsic drawbacks of concrete, i.e., low tensile strength, poor toughness, and brittle failure (Doğangün, 2004; Li and Huang, 2014; Wang, 2008). To avoid the

brittle failure of concrete columns from both lateral and axial loads, the present design philosophy for RC columns is to place massive reinforcements in the expected plastic hinge zone to enhance the ductility of the concrete columns. However, in this case, dense reinforcements may create difficulties during the pouring of concrete, resulting in poor quality of concrete members. In addition, the concrete covers cannot be confined by the transverse reinforcements and, thus, may spall off during an earthquake.

In the early 1990s, a new cement-based composite material reinforced with randomly distributed short fibers called engineered cementitious composite (ECC) was proposed by Li (1993). Compared with conventional concrete, ECC possesses much higher ductility in tension attributed to its multiple cracking behavior and pseudo strain-hardening characteristics under tension (Li and Leung, 1992; Li, 1993; Yang et al., 2008; Zhang et al., 2011; Li et al., 2019; Maalej et al., 1995). The ultimate tensile strain of ECC can reach more than 3%, whereas the opening of each crack is usually controlled to be less than 60 μm when applying short fibers of less than 2% by volume (Yang et al., 2008; Zhang et al., 2011; Yuan et al., 2013; Zhang et al., 2020a; Zhang Z. et al., 2021). Moreover, in recent years, ultra-high-strength ECC has been developed with a compressive strength of more than 210 MPa and an excellent tensile strain capacity of 2%–11% (Huang et al. (2021); Xu et al., 2022). Due to its ultra-high-tensile ductility, high-strength ECC/ECC is being considered for replacing conventional concrete in structures in high-intensity earthquake regions (Maruta et al., 2005; Paulay, 2005; Montesinos and Gustavo, 2005; Qudah and Mohamed, 2014; Wu et al., 2017a; Zhang et al., 2020b), which provides an alternative way to enhance the ductility of structural members by using high-ductile matrix material instead of simply increasing reinforcements (Qin et al., 2020).

Some efforts have been made to investigate the mechanical performance of reinforced ECC (RECC) columns or RC/RECC composite columns (Cai et al., 2018; Zhang Y. et al., 2021; Li L. Z. et al., 2019; Yuan et al., 2019; Li F. et al., 2019; Li et al., 2020). Previous investigations by the first author (Wu et al., 2017a) indicate that replacing concrete with ECC material can improve the shear strength and energy dissipation capacity of the short columns. Pan et al. (2020) investigated the seismic behavior of RECC/C composite columns through experimental and numerical approaches. Results show that RECC/C composite columns had better shear capacity and higher ductility as compared with the RC column. Zhang et al. (2019) investigate the performance of RECC short columns, RC columns, and H-steel reinforced ECC short columns. Results show that the RECC columns had better crack control capacity, shear strength, and energy capacity than that of RC columns. Several studies have been done for investigating the behavior of reinforced ECC columns under eccentric compression (Yuan et al., 2018; Adnan and Mashshay, 2020; Cai et al., 2020; Li et al., 2019).

However, the application of ECC members is still limited due to the relatively short research time and the lack of design specifications. Per the code of concrete structures in China (GB50010-2010) (China's National Standard), the calculation theory of the strength of compression members has been

mature. A similar method is provided in the Technical Specification for Fiber Reinforced Concrete Structures (CECS 38: 2004) for calculating the sectional load capacity of steel fiber-reinforced concrete members under eccentric compression. However, these specifications are not perfectly suitable for ECC members. Recently, studies on the calculation of flexural strength were more mature in the case of RECC beams (Cui et al., 2021; Qiao et al., 2021; Wang et al., 2021). In the case of RECC columns, Li L. Z. et al. (2019) study the behavior of reinforced, high-strength ECC columns under eccentric compression experimentally, and an analytical model is proposed for the load-bearing capacity of RECC columns under large eccentric compression. Yuan et al. (2018) tested eight steel-reinforced columns with various longitudinal reinforcement ratios and load eccentricities under eccentric compression; in addition, a theoretical model is proposed to predict the moment-curvature response of the RECC column.

In this paper, according to mechanical characteristics, the critical section of an RECC column subjected to vertical axial compression and horizontal load is equivalent to a critical section of an eccentric compressive member. Based on the design theory of the load capacity of eccentric compression columns and the unique constitutive model of ECC, the calculation equations for the sectional load capacity of RECC columns were derived. The analytical prediction of the load capacity of RECC columns was evaluated in comparison with that of experiments that confirm the capacity of the proposed calculation method to capture the behavior of RECC columns accurately. The strength interaction diagrams showing the axial force-moment (N - M) interaction curves were then constructed for analysis using the proposed calculation equations. A numerical parametric study on the flexural performance of RECC columns was also carried out by using the proposed calculation equations, which was expected to provide insight on the design principles of RECC columns.

2 CALCULATION METHOD

2.1 Basic Assumptions

The following assumptions are used in the analysis of load capacity of the critical cross-section of RECC columns:

- 1) The normal strain distribution along the cross-section of the specimen conforms to the plane cross-section assumption.
- 2) The tensile strength of ECC is not neglected after cracking. The ultimate tensile strain of ECC usually could reach more than 3% (Li et al., 2001; Mishra and Yu, 2019; Huang et al., 2021), which is much larger than the yield strain of the tensile steel bar (about 0.2%). Columns are less likely to be damaged due to ultimate tensile strain of ECC materials. Therefore, the contribution of ECC in the tensile zone should be considered in the entire loading history.
- 3) Steel bars and ECC can work together and deform coordinately. Li (Li et al., 2019) confirms through experiments that, compared with ordinary RC beams, the deformations of steel bars and ECCs are more coordinated. It

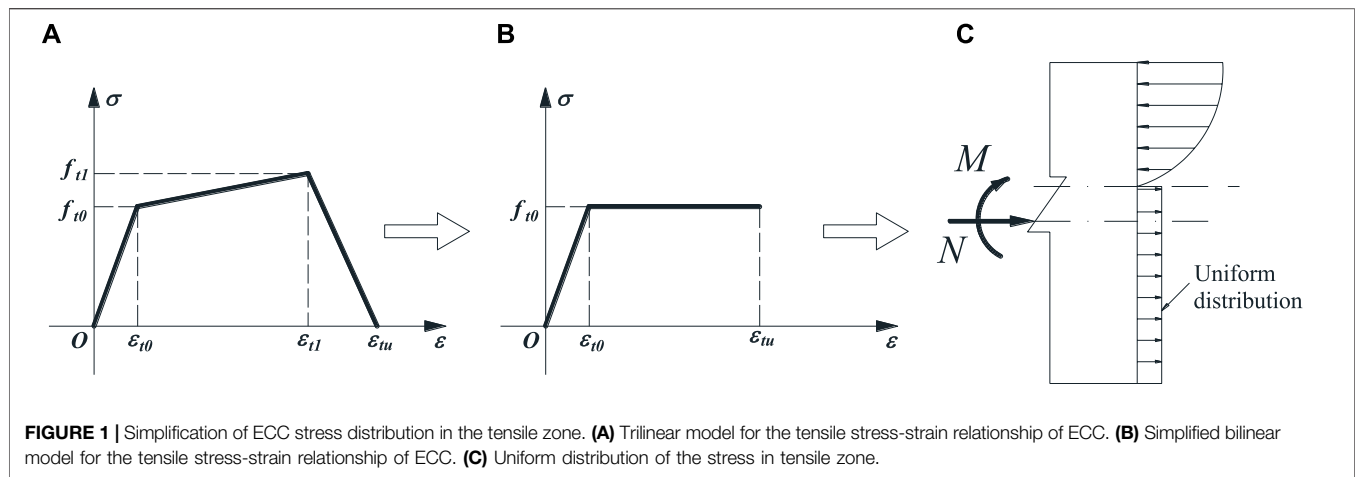


FIGURE 1 | Simplification of ECC stress distribution in the tensile zone. **(A)** Trilinear model for the tensile stress-strain relationship of ECC. **(B)** Simplified bilinear model for the tensile stress-strain relationship of ECC. **(C)** Uniform distribution of the stress in tensile zone.

is reasonable to ignore the relative slip between steel bars and ECCs in theoretical analysis.

- 4) The “second order effect” is ignored. Because RECC short columns with $l_0/h \leq 5$ are analyzed in this paper, the influence of the second order effect can be generally ignored.
- 5) The ideal elastoplastic model is adopted for the constitutive relation of steel bars. The constitutive relation expressions of steel bars are as follows.

$$\sigma_s = \begin{cases} E_s \epsilon_s & (\epsilon_s \leq \epsilon_{sy}) \\ f_y & (\epsilon_{sy} < \epsilon \leq \epsilon_{su}) \end{cases} \quad (1)$$

where f_y is the yield strength of steel bars; ϵ_{sy} and ϵ_{su} are the yield strain and ultimate strain of steel bars, respectively; and E_s is the modulus of elasticity of steel bars.

2.2 Simplified Uniaxial Tensile and Compressive Stress-Strain Relationship of Engineered Cementitious Composite

The tensile stress-strain relation of ECC can be expressed with the trilinear model and divided into three stages: linear elastic, strain hardening, and strain softening stages, as shown in **Figure 1A**. In this paper, the stress-strain relationship of ECC is simplified to a bilinear model, and the tensile stress is conservatively taken as the cracking strength, f_{t0} as shown in **Figure 1B**. The strain-hardening stage is assumed to be flat, ignoring the increasing of the stress for two reasons. First, the assumption could reduce a little accuracy, but the result is conservative, and the error is very small, which is acceptable from the design perspective. Second, the ideal elastoplastic model can significantly simplify the calculation and is easier to handle by engineers in the structural design. In addition, a similar simplified stress-strain relationship of ECC is also used by other researchers (Zheng et al., 2016; Ge et al., 2018; Wang et al., 2021), and they obtain reasonable results. The relationship of strain and stress of ECC can be written as **Eq. 2**. The simplified bilinear model used in this paper can make the calculation results conservative, which is suitable for design purposes.

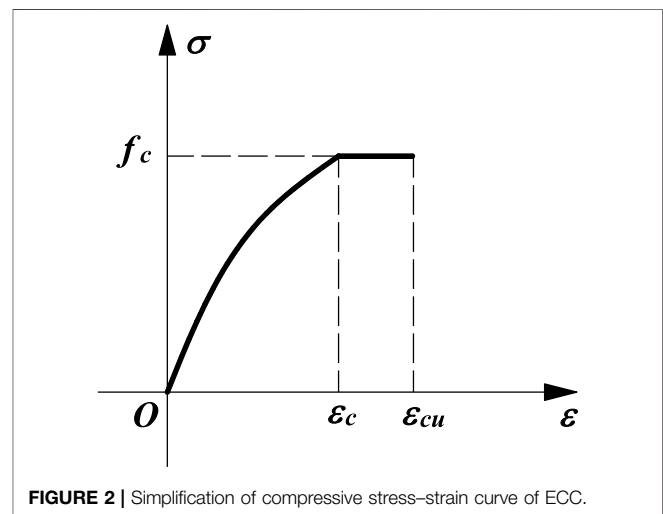


FIGURE 2 | Simplification of compressive stress-strain curve of ECC.

$$\sigma_{tens} = \begin{cases} E\epsilon & (\epsilon \leq \epsilon_{t0}) \\ f_{t0} & (\epsilon_{t0} < \epsilon \leq \epsilon_{tu}) \end{cases} \quad (2)$$

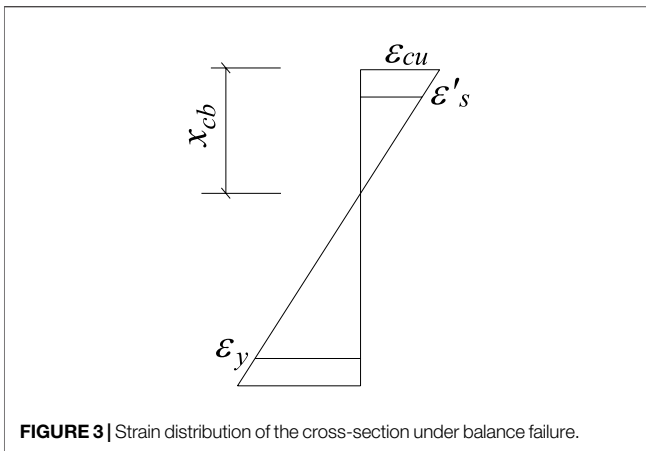
where ϵ_{t0} and ϵ_{tu} are the cracking and ultimate strain of ECC, respectively, and E is the modulus of elasticity of ECC.

The cracking strain ϵ_{t0} is basically a very small magnitude and the tensile stress distribution along the cross-section of the ECC member in the tensile zone can be further simplified to a uniform rectangular stress diagram as shown in **Figure 1C**.

In the calculation of the cross-sectional bearing capacity of RECC members, the compressive stress-strain relationship curve of ECC defined in reference Wu et al. (2016) is employed and further simplified as shown in **Figure 2**. The simplified compressive relationship of stress and strain can be expressed as

$$\sigma_{comp} = \begin{cases} f_c \left[\zeta \left(\frac{\epsilon}{\epsilon_c} \right) + (1 - \zeta) \left(\frac{\epsilon}{\epsilon_c} \right)^2 \right] & (\epsilon \leq \epsilon_c) \\ f_c & (\epsilon_c < \epsilon \leq \epsilon_{cu}) \end{cases} \quad (3)$$

where f_c and ϵ_c represent the peak stress and strain, respectively; ϵ_{cu} represents the ultimate compressive strain; and ζ is the



parameter controlling the initial stiffness. For concrete, ζ is taken as 2 and for ECC, ζ can be approximated to 1.5.

2.3 Derivation of the Bearing Capacity of Eccentric Compression Reinforced Engineered Cementitious Composite Column

According to different loading conditions, eccentric compression members can be divided into large and small eccentric compression. In large eccentric compression, with the increase of load, the steel bar away from the eccentric force side is first yielded, and then ECC at the edge of the compression zone near the eccentric force is crushed, resulting in the failure of the member. In small eccentric compression, most or even the whole cross-section of the member is under compression. The steel bar away from the eccentric force side does not yield, even in tension, whereas the ECC at the edge of the compression zone near the eccentric force side crushes. Because the small eccentric compressive failure is brittle, it is generally avoided in design. In GB50010-2010, the axial compression ratio is limited to prevent the occurrence of small eccentric compression failure.

For the compression-bending members, regardless of whether they are in the state of large or small eccentric compression, ECC in the compressive zone near the eccentric force side would be crushed at the ultimate load. This indicates that the column reached the ultimate bearing capacity. Therefore, it is assumed that, when the RECC member reaches the ultimate bearing capacity, the compressive strain of ECC at the edge of the compressive zone reaches its ultimate compressive strain, namely, $\varepsilon = \varepsilon_{cu}$.

2.3.1 Determination of Large and Small Eccentric Compression

It can be seen from the definition of large and small eccentric compression failure that the main difference between them is whether the steel bars in the tension zone away from the eccentric force are loaded to yield when the member is damaged. Therefore, the boundary between both failures can be defined as the condition when the stress of the steel bars in the tensile zone

reaches their yield strength, the strain at the edge of ECC near the eccentric force reaches the ultimate compressive strain (ε_{cu}), simultaneously, as seen in **Figure 3**. According to the plane cross-section assumption, it can be expressed as

$$\frac{\varepsilon_y}{\varepsilon_{cu}} = \frac{h_0 - x_{cb}}{x_{cb}} \quad (4)$$

where ε_y is the yield strain of the steel bar, h_0 is the effective depth of the cross-section, and x_{cb} is the critical compressive height.

The critical compressive height can be obtained by **Eq. 4** as follows:

$$x_{cb} = \frac{1}{1 + \frac{\varepsilon_y}{\varepsilon_{cu}}} h_0 = \frac{1}{1 + \frac{f_y}{E_s \varepsilon_{cu}}} h_0 \quad (5)$$

where f_y is the yield stress of the steel bar and E_s is the elastic modulus of the steel bar.

The large and small eccentric compression can be distinguished by the critical compressive height (x_{cb}). When the actual compressive height (x_c) is smaller than the critical compressive height (x_{cb}), the cross-section is in the state of large eccentric compression. Conversely, when $x_c > x_{cb}$, the cross-section is in the state of small eccentric compression.

2.3.2 Cross-Sectional Bearing Capacity Under Large Eccentric Compression

Figure 4 shows the strain and stress distribution of the cross-section. In the figure, A_s and A'_s are the area of tensile and compressive steel bars, respectively; σ_s and σ'_s are the stress of the tensile and compressive steel bars, respectively; ε_s and ε'_s are the strain of the tensile and compressive steel bars, respectively; h is the height of the cross-section and h_0 is the effective height of the cross-section; a_s and a'_s are the distance from the center to the edge of the steel bar in the tensile and compressive zones of the cross-section, respectively; C_t and C_c are the resultant force of ECC stress in the tensile and compression zones, respectively; x_c and x_t are the height of the compressive and tensile zones of ECC, respectively; and y_c is the distance from the stress resultant point of the compressive zone to the edge of the compressive zone.

For large eccentric compression members, the steel bars on one side of the tension zone far from the eccentric force reaches the yield strength (f_y) in the ultimate state, and the stress of the compression steel bar near the eccentric force is related to the height of the compression zone. Therefore, in the ultimate state, the strain of the compressive steel bar can be expressed as

$$\varepsilon'_s = \frac{x_c - a'_s}{x_c} \varepsilon_{cu} \quad (6)$$

To ensure that the compressive steel bar reaches the yield strength in the ultimate state, the height of the compression zone should satisfy the following inequality:

$$x_c \geq \frac{1}{1 - \frac{\varepsilon'_y}{\varepsilon_{cu}}} a'_s = \frac{1}{1 - \frac{f'_y}{E_s \varepsilon_{cu}}} a'_s \quad (7)$$

According to the results of the ECC compressive test, ε_{cu} can be conservatively taken as 0.006. The yield strain of the HRB400

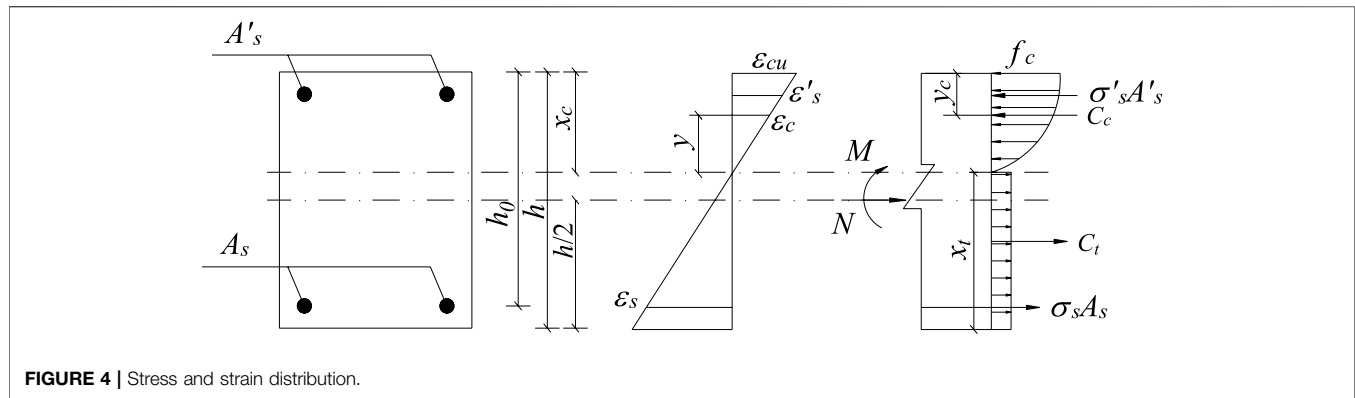


FIGURE 4 | Stress and strain distribution.

steel bar (ε_y) is taken as 0.002, and $x_c \geq 1.5a_s'$ can be obtained by inserting ε_y into the right end of Eq. 7. For eccentric compression members, this condition can generally be satisfied; therefore, in this paper, the compressive steel bar near the eccentric force side yields when it reaches the ultimate state.

According to the equilibrium condition of cross-section force shown in Figure 4, the equations of axial force (N) and flexural moment (M) under large eccentric compression can be expressed as

$$N = C_c - C_t \quad (8)$$

$$M = f_y A_s' \left(\frac{h}{2} - a_s' \right) + f_y A_s \left(\frac{h}{2} - a_s \right) + C_c \left(\frac{h}{2} - y_c \right) + C_t \frac{x_c}{2} \quad (9)$$

The resultant force of ECC compression zone can be expressed as

$$C_c = \int_0^{x_c} b \sigma_{comp}(\varepsilon) dy \quad (10)$$

According to the plane cross-section assumption, the strain at any position (y) in the height of the compression zone can be expressed as

$$\varepsilon = \frac{y}{x_c} \varepsilon_{cu} \quad (11)$$

Substituting Eqs 3, 11 into Eq. 10 for integration, the following formula can be obtained:

$$C_c = f_c b x_c \left\{ 1 + \left[\frac{1}{2} \zeta + \frac{1}{3} (1 - \zeta) - 1 \right] \frac{\varepsilon_0}{\varepsilon_{cu}} \right\} \quad (12)$$

The resultant force of ECC in the tensile zone (C_t) can be expressed as

$$C_t = \int_0^{x_t} b \sigma_{tens}(\varepsilon) dy \quad (13)$$

Because the crack strain of ECC is very small, the stress distribution of ECC in the tensile zone is simplified to uniform distribution; that is, the stress values along the height of the tensile zone is f_{t0} . Thus, C_t can be rewritten as

$$C_t = \int_0^{x_t} b \sigma_{tens}(\varepsilon) dy = f_{t0} b x_t = f_{t0} b (h - x_c) \quad (14)$$

The distance y_c from the resultant force of the compressive zone to the edge is provided as follows:

$$y_c = x_c - \frac{\int_0^{x_c} b \sigma_{comp}(\varepsilon) y dy}{C_c} \quad (15)$$

Substituting Eq. 3 and Eq. 12 into Eq. 15 for integration, it can be obtained that:

$$y_c = x_c \left\{ 1 - \frac{\frac{1}{2} + \left[\frac{1}{3} \zeta + \frac{1}{4} (1 - \zeta) - \frac{1}{2} \right] \left(\frac{\varepsilon_0}{\varepsilon_{cu}} \right)^2}{1 + \left[\frac{1}{2} \zeta + \frac{1}{3} (1 - \zeta) - 1 \right] \frac{\varepsilon_0}{\varepsilon_{cu}}} \right\} \quad (16)$$

Both N and M in the equilibrium equation of the force can be expressed as a function of the height of the compression zone. If the axial pressure (N) is known, the expression of the height of the compressive zone (x_c) can be obtained by substituting Eq. 12, and Eq. 14 into Eq. 8 as follows:

$$x_c = \frac{N + f_{t0} b h}{f_c b \left\{ 1 + \left[\frac{1}{2} \zeta + \frac{1}{3} (1 - \zeta) - 1 \right] \frac{\varepsilon_0}{\varepsilon_{cu}} \right\} + f_{t0} b} \quad (17)$$

Substituting Eq. 17 together with Eq. 16 into Eq. 9, the flexural capacity (M) of the RECC column under the axial pressure (N) can be obtained.

2.3.3 Cross-Sectional Bearing Capacity Under Small Eccentric Compression

According to the stress distribution of the failure cross-section, the bearing capacity of the section under small eccentric compression can be divided into two cases: compression in the partial cross-section (Figure 5A) and in the full cross-section (Figure 5B). The stress distribution of the former is similar to that under large eccentric compression except that the steel bar on the side away from the eccentric force does not yield in tension. The stress distribution of the latter has no tensile zone. The steel bar on the side away from the eccentric force is compressed, and its compressive stress is smaller than that on the side near the eccentric force. Whether the steel bar yields or not is determined according to the height of the compressive zone.

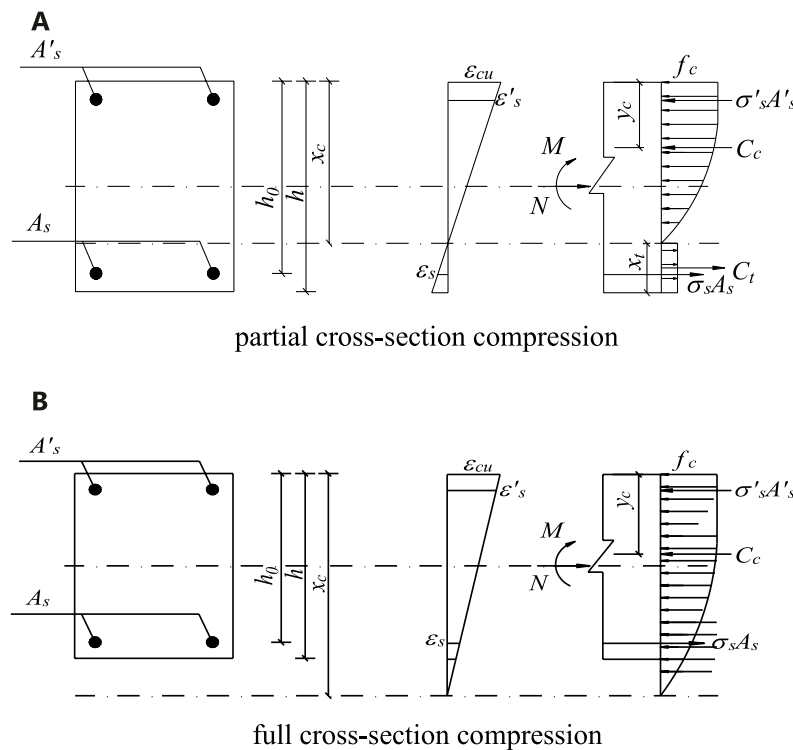


FIGURE 5 | Calculation diagram of RECC normal cross-section bearing capacity under small eccentric compression. **(A)** Partial cross-section compression. **(B)** Full cross-section compression.

1) Compression on partial cross-section

When the cross-section is partially compressed, the stress distribution is similar to that under large eccentric compression. However, the steel bar on the side away from the eccentric force does not yield in tension. Therefore, the calculation formula of axial force and bending moment can be obtained from the equilibrium condition of force. C_c , C_t , and y_c can be obtained by Eq. 12, 14 and Eq. 16, respectively.

$$N = f'_s A'_s - \sigma_s A_s + C_c - C_t \quad (18)$$

$$M = f'_s A'_s \left(\frac{h}{2} - a'_s \right) + \sigma_s A_s \left(\frac{h}{2} - a_s \right) + C_c \left(\frac{h}{2} - y_c \right) + C_t \frac{x_c}{2} \quad (19)$$

According to the plane cross-section assumption, the relationship between the stress of the steel bar away from the eccentric force side and the height of the compression zone can be obtained as follows:

$$\sigma_s = E_s \epsilon_s = \frac{h_0 - x_c}{x_c} E_s \epsilon_{cu} = \left(\frac{h_0}{x_c} - 1 \right) E_s \epsilon_{cu} \quad (20)$$

If N is known, Eqs 12–16, 20 are substituted into Eq. 18 to obtain the quadratic equation about x_c , and the height of the compression zone (x_c) can be obtained by solving the equation. Then, the value of x_c is substituted into Eq. 19 to obtain the normal cross-section bearing capacity of the RECC column.

2) Compression on full cross-section

When the cross-section is fully compressed, the steel bar away from the eccentric force side is compressed and the compressive stress can be obtained by the plane cross-section assumption.

$$\sigma_s = \left(1 - \frac{h_0}{x_c} \right) E_s \epsilon_{cu} \leq f_y \quad (21)$$

Therefore, the calculation formula of axial force (N) and bending moment (M) can be obtained from the equilibrium condition of force.

$$N = f'_s A'_s + \sigma_s A_s + C_c \quad (22)$$

$$M = f'_s A'_s \left(\frac{h}{2} - a'_s \right) - \sigma_s A_s \left(\frac{h}{2} - a_s \right) + C_c \left(\frac{h}{2} - y_c \right) \quad (23)$$

Under the fully cross-sectional compression, the theoretical height of the compressive zone may exceed the actual height of the cross-section. Therefore, the resultant force of the compressive zone can be expressed as

$$C_c = \int_0^h b \sigma_{comp}(\epsilon) dy \quad (24)$$

According to the plane cross-section assumption, the strain at any position (y) in the cross-section can be expressed as

$$\varepsilon = \left(1 - \frac{h - y}{x_c}\right) \varepsilon_{cu} \quad (25)$$

Substituting Eq. 25 into Eq. 24, C_c can be obtained as

$$C_c = f_c b x_c \left\{ 1 + \left(\frac{1}{6} \zeta - \frac{2}{3} \right) \left(\frac{\varepsilon_0}{\varepsilon_{cu}} \right) - \frac{1}{2} \zeta \left(\frac{\varepsilon_{cu}}{\varepsilon_0} \right) \left(1 - \frac{h}{x_c} \right)^2 - \frac{1}{3} (1 - \zeta) \left(\frac{\varepsilon_{cu}}{\varepsilon_0} \right)^2 \left(1 - \frac{h}{x_c} \right)^3 \right\} \quad (26)$$

The distance (y_c) from the resultant force of the compression zone to the edge is

$$y_c = h - \frac{\int_0^h b \sigma_{comp}(\varepsilon) y dy}{C_c} \quad (27)$$

Substituting Eqs 3, 26 into Eq. 27, it can be obtained that

$$y_c = x_c \frac{G}{F} \quad (28)$$

in which

$$F = 1 + \left(\frac{1}{6} \zeta - \frac{2}{3} \right) \left(\frac{\varepsilon_0}{\varepsilon_{cu}} \right) - \frac{1}{2} \zeta \left(\frac{\varepsilon_{cu}}{\varepsilon_0} \right) \left(1 - \frac{h}{x_c} \right)^2 - \frac{1}{3} (1 - \zeta) \left(\frac{\varepsilon_{cu}}{\varepsilon_0} \right)^2 \left(1 - \frac{h}{x_c} \right)^3, \\ G = \frac{1}{2} + \left(\frac{1}{6} \zeta - \frac{2}{3} \right) \left(\frac{\varepsilon_0}{\varepsilon_{cu}} \right) + \left[\frac{1}{4} - \frac{1}{12} \zeta \right] \left(\frac{\varepsilon_0}{\varepsilon_{cu}} \right)^2 - \frac{1}{6} \zeta \left(\frac{\varepsilon_{cu}}{\varepsilon_0} \right) \left(1 - \frac{h}{x_c} \right)^2 \left(1 + \frac{2h}{x_c} \right) - \frac{1}{12} (1 - \zeta) \left(\frac{\varepsilon_{cu}}{\varepsilon_0} \right)^2 \left(1 - \frac{h}{x_c} \right)^3 \left(1 + \frac{3h}{x_c} \right)$$

If N is known, Eqs 24–28 are substituted into Eq. 22 to obtain the cubic equation about x_c , and the height of the compression zone (x_c) can be obtained by solving the equation. Then, substitute x_c into Eq. 23 to obtain the normal cross-section bearing capacity of the RECC column.

2.4 Code Equations for N - M Interaction Curves for Reinforced Engineered Cementitious Composite Columns

The calculation formula of the normal cross-section bearing capacity of the RECC column under large and small eccentric compression is derived in the previous section. The formulas for calculating the normal cross-section bearing capacity of the column under different pressure zone height (x_c) are summarized as follows.

When $x_c \leq \frac{1}{1+\frac{\varepsilon_0}{\varepsilon_{cu}}} h_0$, the member failures due to the large eccentric compression and the bearing capacity can be expressed as

$$\begin{cases} N = C_c - C_t \\ M = f_y A'_s \left(\frac{h}{2} - a'_s \right) + f_y A_s \left(\frac{h}{2} - a_s \right) + C_c \left(\frac{h}{2} - y_c \right) + C_t \frac{x_c}{2} \\ C_c = f_c b x_c B \\ C_t = f_{t0} b (h - x_c) \\ y_c = x_c \left(1 - \frac{D}{B} \right) \end{cases} \quad (29)$$

When $\frac{1}{1+\frac{\varepsilon_0}{\varepsilon_{cu}}} h_0 < x_c < h$, the member failures due to the small eccentric compression under the partial cross-sectional compression and the bearing capacity can be expressed as

$$\begin{cases} N = f'_s A'_s - \sigma_s A_s + C_c - C_t \\ M = f'_s A'_s \left(\frac{h}{2} - a'_s \right) + \sigma_s A_s \left(\frac{h}{2} - a_s \right) + C_c \left(\frac{h}{2} - y_c \right) + C_t \frac{x_c}{2} \\ \sigma_s = \left(\frac{h_0}{x_c} - 1 \right) E_s \varepsilon_{cu} \\ C_c = f_c b x_c B \\ C_t = f_{t0} b (h - x_c) \\ y_c = x_c \left(1 - \frac{D}{B} \right) \end{cases} \quad (30)$$

When $x_c \geq h$, the member failures due to the small eccentric compression under the full cross-sectional compression and the bearing capacity formulas are as follows.

$$\begin{cases} N = f'_s A'_s + \sigma_s A_s + C_c \\ M = f'_s A'_s \left(\frac{h}{2} - a'_s \right) - \sigma_s A_s \left(\frac{h}{2} - a_s \right) + C_c \left(\frac{h}{2} - y_c \right) \\ \sigma_s = \left(1 - \frac{h_0}{x_c} \right) E_s \varepsilon_{cu} \leq f_y \\ C_c = f_c b x_c F \\ y_c = x_c \frac{G}{F} \end{cases} \quad (31)$$

where parameters B , D , F , and G can be calculated by the following equations, respectively.

$$B = 1 + \left[\frac{1}{2} \zeta + \frac{1}{3} (1 - \zeta) - 1 \right] \frac{\varepsilon_0}{\varepsilon_{cu}} \\ D = \frac{1}{2} + \left[\frac{1}{3} \zeta + \frac{1}{4} (1 - \zeta) - \frac{1}{2} \right] \left(\frac{\varepsilon_0}{\varepsilon_{cu}} \right)^2 \\ F = 1 + \left(\frac{1}{6} \zeta - \frac{2}{3} \right) \left(\frac{\varepsilon_0}{\varepsilon_{cu}} \right) - \frac{1}{2} \zeta \left(\frac{\varepsilon_{cu}}{\varepsilon_0} \right) \left(1 - \frac{h}{x_c} \right)^2 - \frac{1}{3} (1 - \zeta) \left(\frac{\varepsilon_{cu}}{\varepsilon_0} \right)^2 \left(1 - \frac{h}{x_c} \right)^3$$

TABLE 1 | Values of cross-section size, steel bar, and material parameters.

Material parameters			
Parameters	ECC	Concrete	Steel bar
ε_0	0.005	0.002	—
f_c	45 MPa	45 MPa	—
ε_{cu}	0.006	0.0033	—
f_{t0}	4.0 MPa	0	—
ζ	1.5	2	—
f_y, f_y'	—	—	400 MPa
E_s	—	—	2×10^5 MPa
Size of cross-section and steel bars			
b	300 mm		
h	300 mm		
a_{s1}, a_{s1}'	35 mm		
A_{s1}, A_{s1}'	628 mm ²		

$$G = \frac{1}{2} + \left(\frac{1}{6} \zeta - \frac{2}{3} \right) \left(\frac{\varepsilon_0}{\varepsilon_{cu}} \right) + \left[\frac{1}{4} - \frac{1}{12} \zeta \right] \left(\frac{\varepsilon_0}{\varepsilon_{cu}} \right)^2$$

$$- \frac{1}{6} \zeta \left(\frac{\varepsilon_{cu}}{\varepsilon_0} \right) \left(1 - \frac{h}{x_c} \right)^2 \left(1 + \frac{2h}{x_c} \right)$$

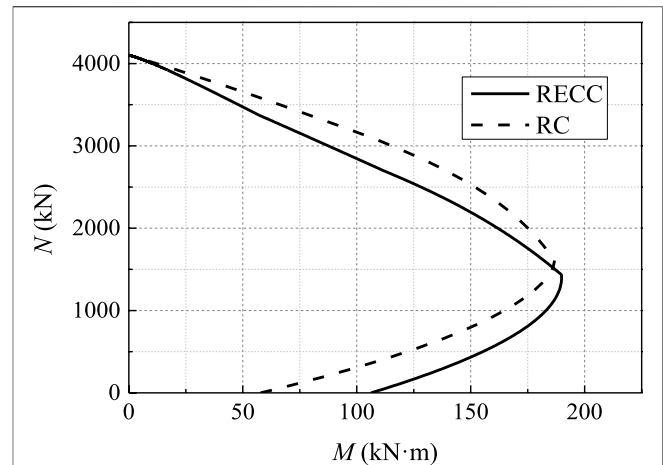
$$- \frac{1}{12} (1 - \zeta) \left(\frac{\varepsilon_{cu}}{\varepsilon_0} \right)^2 \left(1 - \frac{h}{x_c} \right)^3 \left(1 + \frac{3h}{x_c} \right)$$

For eccentric compression members and compression-bending members with given cross-section size, steel bar and material parameters, the ultimate bearing capacity can be obtained under different combinations of axial force and bending moment. Axial force and bending moment under all possible ultimate states are plotted as curves, namely, the N - M interaction curve, which is the envelope of the ultimate state of eccentric compression members.

The former calculation formulas were adopted to investigate the difference of the N - M interaction curves between RECC and RC columns. The values of cross-section size and steel bar and material parameters used are shown in **Table 1**.

Figure 6 shows the N - M interaction curves of RECC and RC columns. It can be seen that

- 1) When the balance failure occurs, the M of the RECC column is larger than that of the RC column and the N of the RECC column is smaller. The reason is that the small eccentric compression failure is similar to the over-reinforced failure in flexural members, and the ECC tensile zone still works, which is equivalent to adding reinforcement in the tensile zone. Therefore, compared with the RC column, it is easier for the RECC column to enter the small eccentric compression state. However, for RECC columns, even if a small eccentric compression failure occurs, it can generally still have good ductility.
- 2) When large eccentric compression failure occurs, the bearing capacity of the RECC column is larger than that of the RC

**FIGURE 6** | N - M interaction curves of RECC and RC columns.

column under the same axial force. It indicates that the fiber bridging effect of ECC can effectively improve the flexural bearing capacity of the specimen.

- 3) When small eccentric compression failure occurs, the bearing capacity of the RECC column is smaller than that of the RC column under the same axial force. This is because, under small eccentric compression, the height of the tensile zone is small or even no tensile zone. Therefore, the excellent tensile properties of ECC cannot be well-utilized. The elastic modulus of ECC is low, and the peak compressive strain and ultimate compressive strain are larger than those of concrete. Under the same axial force, to balance the axial force of the section, the height of the compression zone is larger than that of the RC column, resulting in the flexural bearing capacity of the RECC column being smaller than that of the RC column. Because the compressive strength of the two materials is assumed to be the same, the bearing capacity of the two materials under axial compression is the same.

3 EXPERIMENTAL VERIFICATION

3.1 Experimental Program

Experiments of seven short columns reported in reference Wu et al. (2017a) were selected to evaluate the accuracy of the above calculation method. The tested columns, including one RC reference column (C1) and six RECC columns (C2~C7), were loaded under constant axial compression and lateral cyclic loading. All the columns have a cross-section of 300 mm × 300 mm. The schematic diagram of the tested column is shown in **Figure 7**. The column heights were 500, 600, and 900 mm, and the corresponding shear span-to-depth ratios were 1.42, 1.75, and 2.75, respectively. The longitudinal reinforcement ratio of all the specimens was 1.4%. The test matrix is shown in **Table 2**, in which the shear span-to-depth ratio, axial force, and transverse reinforcement ratio are taken into account as variables. The detailed mechanical properties of ECC are listed in **Table 3**,

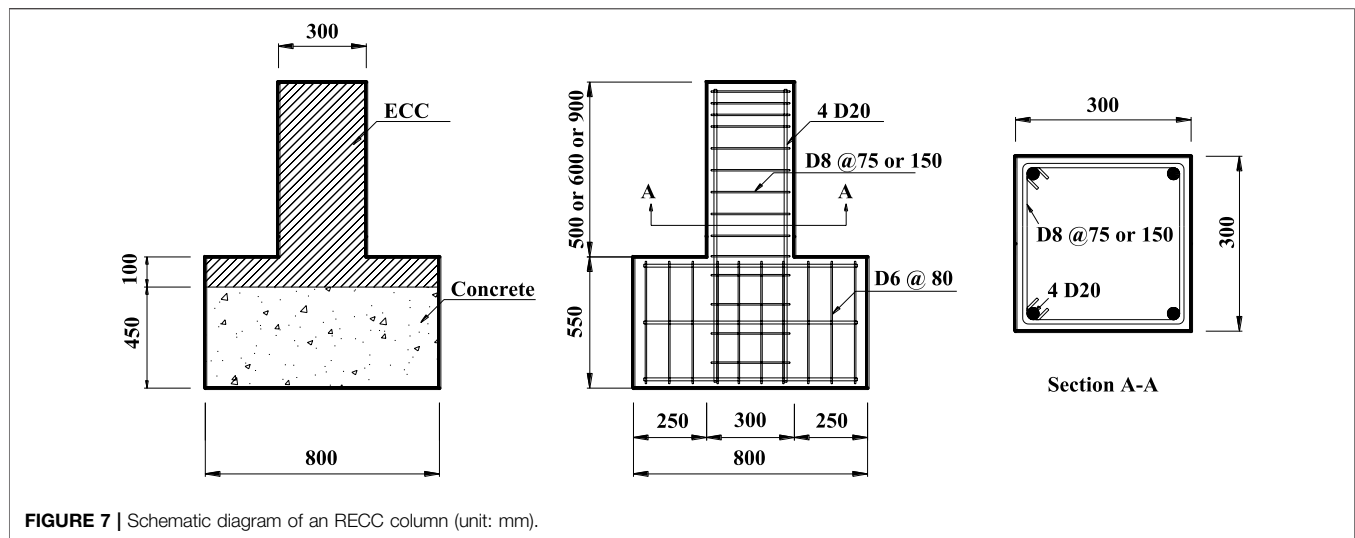


FIGURE 7 | Schematic diagram of an RECC column (unit: mm).

TABLE 2 | Test matrix of the columns.

Specimen	Material	H (mm)	λ	N (kN)	ρ_{sv} (%)
C1	Concrete	600	1.75	350	0.45
C2	ECC	500	1.42	350	0.45
C3	ECC	600	1.75	350	0.45
C4	ECC	900	2.75	350	0.45
C5	ECC	600	1.75	700	0.45
C6	ECC	600	1.75	350	0.22
C7	ECC	600	1.75	350	0

Note: H is the column height; λ is the shear span-to-depth ratio; N is the axial force; ρ_{sv} is the transverse reinforcement ratio.

the average yield stress of the longitudinal steel bars is 498 MPa, and the stirrup yield stress is 408 MPa.

The base mat of each specimen was completely fixed while the top of the specimen could be free to move horizontally. In the loading process, the vertical load was first applied on the centroid of the free-end section of the specimen, and then, the transverse load provided by the horizontal actuator (with force and displacement control system) was applied on the top of the column. The detailed test setup and loading configuration are described in reference Wu et al. (2017b).

3.2 Comparison Between the Calculated and Measured Flexural Strength

The analytical and experimental values of load capacity of the RECC columns are shown in Table 4. All the tested columns yielded in the tensile zone at the ultimate load, so the calculation method of the bearing capacity of the cross-section under large eccentric compression was adopted. It can be seen from Table 4

that analytical predictions of the load capacity are in good agreement with the experimental values in columns C3, C4, C6, and C7, whose relative errors are less than 10%. Considering the deviations in experiments, the relative errors between analytical and experimental results are acceptable in engineering applications. However, the analytical load capacity of column C2 is around 19% lower than the experimental values. The reason is that the column exhibited shear failure rather than flexural failure at the ultimate load, and consequently, the force transmission mechanism of the column C2 is different from that of the specimens failed by flexure. Moreover, the obvious principal diagonal cracks led to the inapplicability of the plane section assumption, resulting in calculation error. In addition, the flexural strength of column C5 under high axial compression ($N = 700$ kN) is seriously underestimated (the test result is 50% higher than the analytical result). This may be attributed to the constraint effect at the end of column due to the loading configuration of the axial compression because the high compression restrained the rotation of the free end of the column.

The comparison above indicates that the proposed equations are able to predict the load capacity of RECC columns whose failure modes are governed by flexure with reasonable accuracy.

4 PARAMETRIC ANALYSIS

The effects of the ultimate tensile strain of ECC, compressive and tensile strength of ECC, yield strength of steel bars, and reinforcement ratio on the N - M interaction curves of RECC columns are investigated by using the proposed calculation equations. The detailed analysis is provided below.

TABLE 3 | Mechanical properties of ECC.

Material	$f_{c,u}$ (MPa)	f_c (MPa)	E (GPa)	ε_{t0} (%)	f_{t0} (MPa)	ε_{tt} (%)	f_{tt} (MPa)
ECC	49.7	45.0	22.2	0.023	3.44	4.46	4.39

TABLE 4 | Comparison of analytical and experimental results.

Specimens	V_m /kN	V_{test} /kN	V_{test}/V_m
C2	362.4	432.3	1.19
C3	293.4	299.5	1.02
C4	186.7	187.3	1.00
C5	348.8	536.5	1.54
C6	293.4	283.0	0.96
C7	293.4	263.4	0.90

Note: V_m is the equivalent shear force, calculated as M/H , which reflects the load capacity of the column; V_{test} is the experimental load capacity of RECC column.

4.1 Effect of Ultimate Tensile Strain of Engineered Cementitious Composite

The ultimate tensile strain of ECC has little effect on the sectional bearing capacity of RECC columns. Under small eccentric compression, the steel bars in the tensile zone do not yield, so the ECC at the edge of the tensile zone cannot reach the ultimate tensile strain. The edge of the tensile zone of the RECC column under large eccentric compression generally does not reach the ultimate tensile strain either.

We assume that, when the RECC column failed, the compressive strain at the edge of the compressive zone reached the ultimate compressive strain ε_{cu} and the tensile strain at the edge of the tensile zone reached the ultimate tensile strain ε_{tu} . The height of the compressive zone can be deduced according to the plane section assumption as follows:

$$x_c = \frac{1}{1 + \frac{\varepsilon_{tu}}{\varepsilon_{cu}}} h \quad (32)$$

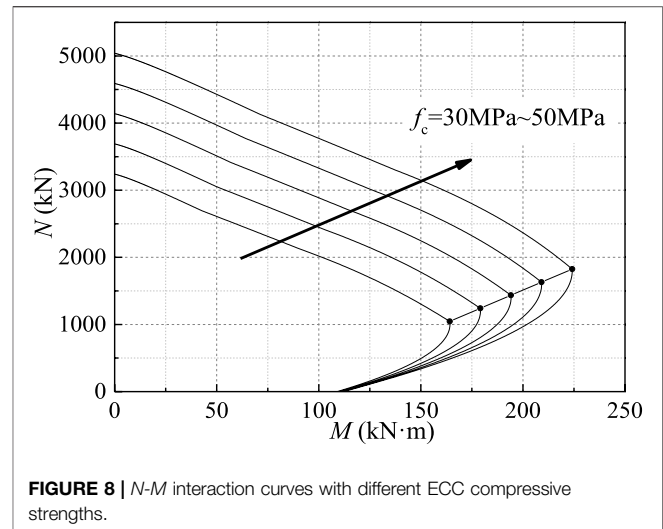
Therefore, as long as the height of the compressive zone (x_c) satisfies the inequality $x_c > \frac{1}{1 + \frac{\varepsilon_{tu}}{\varepsilon_{cu}}} h$, ECC at the edge of the tensile zone will not reach the ultimate tensile strain. In other words, the column will not fail due to tensile damage. The eccentric compressive member is designed to easily satisfy the yield of the compression steel bar yields under the ultimate state, i.e., $x_c \geq \frac{1}{1 - \frac{f'_y}{E_s \varepsilon_{cu}}} a'_s$. It is sufficient to satisfy Eq. 33 so that the tensile strain at the edge of the tensile zone does not easily reach the ultimate tensile strain ε_{tu} when the RECC column fails.

$$\frac{1}{1 + \frac{\varepsilon_{tu}}{\varepsilon_{cu}}} h \leq \frac{1}{1 - \frac{f'_y}{E_s \varepsilon_{cu}}} a'_s \quad (33)$$

It can be further deduced from Eq. 33 that

$$\varepsilon_{tu} \geq \frac{h}{a'_s} \left(\varepsilon_{cu} - \frac{f'_y}{E_s} \right) - \varepsilon_{cu} \quad (34)$$

Assume that the ultimate compressive strain of ECC (ε_{cu}) is 0.005, the strength of the steel bar (f'_y) is 450 MPa, the elastic modulus of the steel bar (E_s) is 2×10^5 MPa, the height of the RECC column section (h) is 300 mm, and the distance between the position of the steel bar to the edge (a'_s) is 35 mm. The inequality $\varepsilon_{tu} \geq 0.026$ can be obtained by substituting the parameters above into Eq. 34. The ultimate tensile strain of

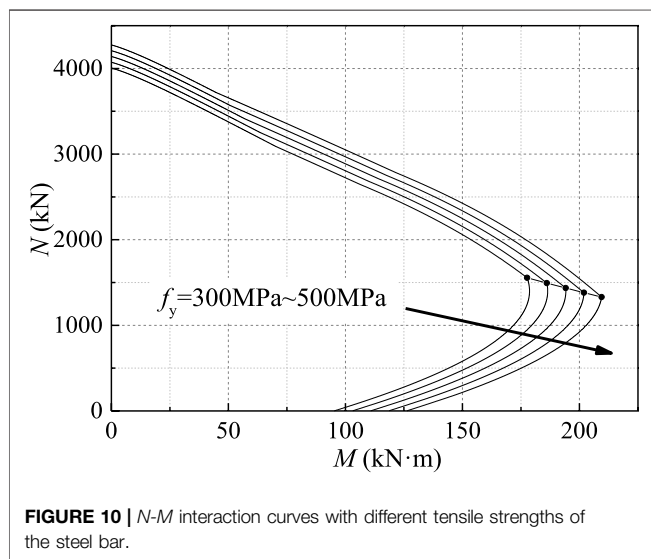
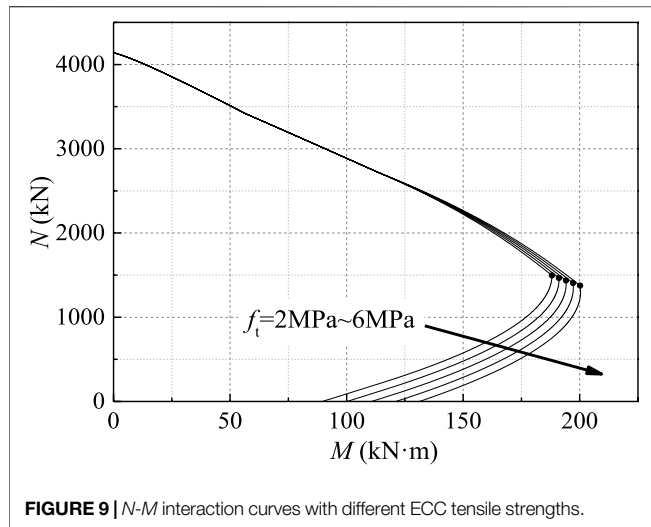
**FIGURE 8** | N - M interaction curves with different ECC compressive strengths.

ECC is generally more than 0.03; therefore, for RECC columns under eccentric compression, as long as the ultimate tensile strain of the prepared ECC is large enough, i.e., ε_{tu} satisfies Eq. 34, the edge of the tensile zone generally will not reach the ultimate tensile strain at the ultimate load. It also proves that it is feasible to ignore the effect of ultimate tensile strain of ECC in calculation.

4.2 Effect of Compressive Strength of Engineered Cementitious Composite

Figure 8 plots the N - M interaction curves of the RECC column with different ECC compressive strength ranging from 30 to 50 MPa. The tensile strength of ECC is 4 MPa. The tensile strength of the longitudinal steel bar is 400 MPa, and the reinforcement ratio is 1.5%.

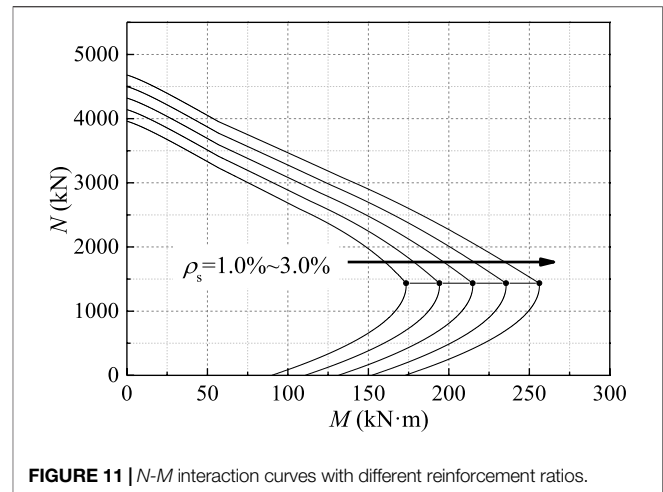
It can be seen that the area enveloped by the N - M curve increases with the increase of compressive strength, which indicates that the sectional load capacity increases with the increasing compressive strength. When the axial force N is less than 500 kN, the N - M interaction curves of the RECC columns with different compressive strength are very close. With the increase of axial force N , the difference of the N - M interaction curves gradually becomes more obvious. When the RECC column enters the small eccentric compression state, the sectional load capacity is mainly controlled by the compressive properties of the material. Therefore, the area enveloped by the N - M interaction curve increases with the increase in ECC compressive strength. The N - M interaction curves in the conditions of small eccentric compression are almost paralleled and extend outward with approximately equal intervals. Observing the N and M at the balance failure point of each curve, it can be seen that both axial force and flexural moment increase with the increasing ECC compressive strength. The connecting line of the balance failure point of each column is basically a straight line extending to the upper right corner.



4.3 Effect of Tensile Strength of Engineered Cementitious Composite

Figure 9 plots the N - M interaction curves of the RECC column with different ECC tensile strengths ranging from 2.0 to 6.0 MPa. The compressive strength of ECC is 40 MPa, and the tensile strength of the steel bar is 400 MPa. The steel bar ratio is taken as 1.5%.

In **Figure 9**, the sectional load capacity increases with the increase of tensile strength, and the spacing of N - M curves is basically equal when the columns fail under large eccentric compression. The N - M interaction curves under small eccentric compression are almost unchanged with the increasing ECC tensile strength. The reason is that the tensile area of the cross-section is large under large eccentric compression, and the tensile strength of ECC can be fully employed, resulting in the increase of flexural strength of RECC columns along with the increasing tensile strength when the axial compression stays. In the



case of small eccentric compression, the cross-section is mostly compressed, and the tensile properties of ECC cannot be fully exerted, so the ECC tensile strength has an insignificant effect on the bearing capacity of the section. The balance failure point of each column moves to the lower right, indicating that RECC columns with higher ECC tensile strength enter the state of smaller eccentric compression earlier with the increase of axial force. Owing to the higher ductility of ECC under compression compared with normal concrete and the confinement effect due to the randomly distributed fibers in ECC, the RECC columns are not prone to brittle failure even under small eccentric compression.

4.4 Effect of Yield Strength of Steel Bar

Figure 10 plots the N - M interaction curves of RECC columns with different tensile strengths of the steel bar ranging from 300 to 500 MPa. The compressive strength of ECC is 40 MPa, and the tensile strength is 4.0 MPa. The steel bar ratio is 1.5%.

The area enveloped by the N - M interaction curve of the RECC column increases under both large and small eccentric compression as seen in **Figure 10**. It indicates that the sectional load capacity increases with the increasing yield strength of steel bars. Comparing the N and M at the balance failure of each curve, it can be seen that the balance failure point of each column moves to the lower right. It indicates that as the strength of the steel bar increases, the flexural moment increases, but the axial force gradually decreases. This is because the failure under the small eccentric compression is similar to the over-reinforced failure. The increase of the strength of the steel bar makes the member more prone to the “over-reinforced” phenomenon.

4.5 Effect of Steel Bar Ratio

Figure 11 plots the N - M interaction curves of RECC columns with different reinforcement ratios of steel bars ranging from 1% to 3%. The compressive strength and tensile strength of ECC is taken as 40 and 4.0 MPa, respectively. The tensile strength of steel bar is 400 MPa.

As shown in **Figure 11**, the area enveloped by the N - M interaction curve of the RECC column increases under both large and small eccentric compression with the increase of the reinforcement ratio. It indicates that the sectional load capacity increases with the increase of the reinforcement ratio. Comparing the N and M at the balance failure of each curve, it can be seen that the connection line of the balance failure point of each member is almost a horizontal straight line. With the increasing reinforcement ratio, the moment at the balance failure point increases, but the axial force remains unchanged. It indicates that the increase of the reinforcement ratio can not only improve the flexural capacity of the column, but also delay the column into the small eccentric compression state.

5 CONCLUSION

In this paper, based on the design theory of the load capacity of eccentric compression columns and the unique constitutive model of ECC, the calculation equations for the sectional load capacity of RECC columns subjected to combined lateral load and axial compression are derived. Strength interaction diagrams showing the axial force-moment (N - M) interaction curves can be constructed by using the proposed calculation equations. A numerical parametric study was then carried out, demonstrating the effects of ultimate tensile strain of ECC, compressive and tensile strength of ECC, yield strength of the steel bar, and reinforcement ratio on the N - M interaction curves of RECC columns. The following conclusions can be drawn:

- 1) The comparison between the calculated results with the proposed equations and the test results of RECC columns under combined lateral load and vertical axial compression show that the relative errors between calculated and measured load capacities of columns C3, C4, C6, and C7, which were failed by flexure, are less than 10%. It indicates that the proposed equations are able to predict the load capacity of RECC columns whose failure modes are governed by flexure with reasonable accuracy.
- 2) Theoretical analysis demonstrates that the ultimate tensile strain of ECC has little effect on the sectional bearing capacity of the RECC column. As long as **Eq. 34** is satisfied, the edge of the

tensile zone on the section of RECC columns can hardly reach the ultimate tensile strain when the specimen fails. Generally, **Eq. 34** can be easily satisfied for ECCs whose ultimate tensile strain is more than 0.03, so it is feasible to ignore the effect of ultimate tensile strain of ECC in calculation.

- 3) The N - M interaction curves of RECC columns are significantly influenced by the compressive strength of ECC under small eccentric compression and moderately affected by the tensile strength of ECC under large eccentric compression. The effects of yield strength of steel bar and reinforcement ratio on the N - M interaction curves of RECC columns are both significant under both small and large eccentric compression. The numerical parametric studies are expected to provide insight on the design principles of RECC columns.

DATA AVAILABILITY STATEMENT

The original contributions presented in the study are included in the article/Supplementary Material, further inquiries can be directed to the corresponding author.

AUTHOR CONTRIBUTIONS

CW: Conceptualization; Writing the original draft; Methodology; Investigation YaS: Review and editing the draft; Investigation YuS: Writing part of the draft; Investigation CJ: Investigation ZP: Supervision.

FUNDING

This study was funded by financial support from the National Natural Science Foundation of China (Grants Number: 52108119), the Natural Science Foundation of Jiangsu Province (Grants No: BK20200376), the Fundamental Research Funds for the Central Universities (Grants No: 2242021R10081), and the Natural Science Foundation of the Jiangsu Higher Education Institutions of China (21KJB560005).

REFERENCES

- Adnan, A., and Mashshay, S. (2020). Development of Hybrid Ecc Columns Subjected to Concentric and Eccentric Loading. *Structures* 28, 309–320. doi:10.1016/j.istruc.2020.08.080
- Cai, J., Pan, J., and Lu, C. (2018). Mechanical Behavior of ECC-Encased CFST Columns Subjected to Eccentric Loading. *Eng. Structures* 162, 22–28. doi:10.1016/j.engstruct.2018.02.029
- Cai, J., Pan, J., Tan, J., Vandevyvere, B., and Li, X. (2020). Behavior of ECC-Encased CFST Columns under Eccentric Loading. *J. Build. Eng.*, 101188. doi:10.1016/j.job.2020.101188
- China's National Standard GB 50010-2010 Code for Design of concrete Structures (In Chinese).
- Cui, T., He, H., Zhao, X., and Zhou, D. (2021). Bending Performance Analysis of Precast Composite Beams with Precast Ecc Plate. *Structures* 33, 986–998. doi:10.1016/j.istruc.2021.04.090
- Deng, M., Zhang, H., Liang, X., and Bu, X. (2015). Experimental Study on Seismic Behavior of High Ductile Fiber Reinforced concrete Short Column. *J. Build. Struct.* 36, 62–69. doi:10.14006/j.jzjgxb.2015.12.008
- Doğangün, A. (2004). Performance of Reinforced concrete Buildings during the May 1, 2003 Bingöl Earthquake in Turkey/Bingöl Earthquake in Turkey. *Eng. Structures* 26, 841–856. doi:10.1016/j.engstruct.2004.02.005
- Ge, W.-J., Ashour, A. F., Ji, X., Cai, C., and Cao, D.-F. (2018). Flexural Behavior of ECC-concrete Composite Beams Reinforced with Steel Bars. *Construction Building Mater.* 159, 175–188. doi:10.1016/j.conbuildmat.2017.10.101
- Hu, X., Chen, Z., and Bu, X. (2021). Axial Compressive Behavior on Steel Tube-Retrofitted Circular RC Short Columns with Grout under Preload. *Structures* 33, 2500–2519. doi:10.1016/j.istruc.2021.05.079
- Huang, B.-T., Weng, K.-F., Zhu, J.-X., Xiang, Y., Dai, J.-G., and Li, V. C. (2021). Engineered/strain-hardening Cementitious Composites (ECC/SHCC) with an Ultra-high Compressive Strength over 210 MPa. *Composites Commun.* 26, 100775. doi:10.1016/j.coco.2021.100775

- Li, V. C., Stang, H., and Krenchel, H. (1993). Micromechanics of Crack Bridging in Fibre-Reinforced concrete. *Mater. Structures* 26, 486–494. doi:10.1007/bf02472808
- Li, X., Chen, K., Hu, P., He, W., Xiao, L., and Zhang, R. (2020). Effect of ECC Jackets for Enhancing the Lateral Cyclic Behavior of RC Bridge Columns. *Eng. Structures* 219, 110714. doi:10.1016/j.engstruct.2020.110714
- Li, Y.-A., Huang, Y.-T., and Hwang, S.-J. (2014). Seismic Response of Reinforced Concrete Short Columns Failed in Shear. *ACI Struct. J.* 111, 945–954. doi:10.14359/51686780
- Li, F., Feng, Z., Deng, K., Yu, Y., Hu, Z., and Jin, H. (2019). Axial Behavior of Reinforced PP-ECC Column and Hybrid NSC-ECC Column under Compression. *Eng. Structures* 195, 223–230. doi:10.1016/j.engstruct.2019.06.010
- Li, L. Z., L.-Z., Bai, Y., Yu, K.-Q., Yu, J.-T., and Lu, Z.-D. (2019). Reinforced High-Strength Engineered Cementitious Composite (ECC) Columns under Eccentric Compression: Experiment and Theoretical Model. *Eng. Structures* 198, 109541. doi:10.1016/j.engstruct.2019.109541
- Liu, Jin., Li, X., Zhang, R., and Du, X. (2021). Meso-scale Modelling the post-fire Seismic Behavior of RC Short Columns. *Eng. Fail. Anal.* 120, 105117. doi:10.1016/j.engfailanal.2020.105117
- Maruta, M., Kanda, T., Nagai, S., and Yamamoto, Y. (2005). New High-Rise RC Structure Using Pre-cast ECC Coupling Beam. *Jpn. Concrete. Inst.* 43, 18–26. doi:10.3151/coj1975.43.11_18
- Mishra, D., and Yu, J. (2019). Engineered Cementitious Composites (ECC) - Bendable Concrete for Sustainable and Resilient Infrastructure. *Indian Concrete J.* 93, 62–69.
- Maalej, M., Li, V. C., and Hashida, T. (1995). Effect of Fiber Rupture on Tensile Properties of Short Fiber Composites. *J. Eng. Mech.* 121, 903–913. doi:10.1061/(asce)0733-9399(1995)121
- Montesinos, P., and Gustavo, J. (2005). High-Performance Fiber-Reinforced Cement Composites: An Alternative for Seismic Design of Structures. *ACI Struct. J.* 102.
- Pan, Z., Zhu, Y., Qiao, Z., and Meng, S. (2020). Seismic Behavior of Composite Columns with Steel Reinforced ECC Permanent Formwork and Infilled Concrete. *Eng. Structures* 212, 110541. doi:10.1016/j.engstruct.2020.110541
- Qiao, L., Li, L., Li, B., and Yu, J. (2021). Prediction on the Flexural Deflection of Ultra-high Strength Rebar Reinforced Ecc Beams at Service Loads. *Structures* 33, 246–258. doi:10.1016/j.istruc.2021.04.050
- Qin, F., Zhang, Z., Yin, Z., Di, J., Xu, L., and Xu, X. (2020). Use of High Strength, High Ductility Engineered Cementitious Composites (ECC) to Enhance the Flexural Performance of Reinforced concrete Beams. *J. Building Eng.* 32, 101746. doi:10.1016/j.jobbe.2020.101746
- Qudah, S., and Maalej, M. (2014). Application of Engineered Cementitious Composites (ECC) in interior Beam-Column Connections for Enhanced Seismic Resistance. *Eng. Structures* 69, 235–245. doi:10.1016/j.engstruct.2014.03.026
- Technical specification for fiber reinforced concrete structure CECS38, 2004
- Paulay, T. (2005). Experimental Study on Seismic Behavior of High-Performance Fiber-Reinforced Cement Composite Coupling Beams. *Sj* 102, 909–912. doi:10.14359/13541
- Li, V. C., and Leung, C. K. Y. (1992). Steady-State and Multiple Cracking of Short Random Fiber Composites. *J. Eng. Mech.* 118, 2246–2264. doi:10.1061/(asce)0733-9399(1992)118
- Li, V. C., Leung, C. K. Y., Dhanada, K., Yu, J., and Zhang, D. (2019). *Indian Concrete Journal: Special Issue on Sustainable Engineered Cementitious Composites (ECC)*
- Li, V. C., Wang, S., and Wu, C. (2001). Tensile Strain-Hardening Behavior of Polyvinyl Alcohol Engineered Cementitious Composite (PVA-ECC). *Mj* 98, 483–492. doi:10.14359/10851
- Wang, L., Yin, S., and Hua, Y. (2021). Flexural Behavior of BFRP Reinforced Seawater Sea-Sand Concrete Beams with Textile Reinforced ECC Tension Zone Cover. *Construction Building Mater.* 278, 122372. doi:10.1016/j.conbuildmat.2021.122372
- Wang, Z. (2008). A Preliminary Report on the Great Wenchuan Earthquake. *Earthq. Eng. Eng. Vib.* 7, 225–234. doi:10.1007/s11803-008-0856-1
- Wu, C., Pan, Z., Jin, C., and Meng, S. (2020). Evaluation of Deformation-Based Seismic Performance of RECC Frames Based on IDA Method. *Eng. Structures* 211, 110499. doi:10.1016/j.engstruct.2020.110499
- Wu, C., Pan, Z., Kim, K.-S., and Meng, S. (2017b). Theoretical and Experimental Study of Effective Shear Stiffness of Reinforced ECC Columns. *Int. J. Concr Struct. Mater.* 11, 585–597. doi:10.1007/s40069-017-0219-2
- Wu, C., Pan, Z., and Meng, S. (2016). Cyclic Constitutive Model for Strain-Hardening Cementitious Composites. *Mag. Concrete Res.* 68, 1133–1142. doi:10.1680/jmacr.15.00052
- Wu, C., Pan, Z., Su, R. K. L., Leung, C. K. Y., and Meng, S. (2017a). Seismic Behavior of Steel Reinforced ECC Columns under Constant Axial Loading and Reversed Cyclic Lateral Loading. *Mater. Struct.* 50, 78. doi:10.1617/s11527-016-0947-9
- Xu, L.-Y., Huang, B.-T., Li, V. C., and Dai, J.-G. (2022). High-strength High-Ductility Engineered/Strain-Hardening Cementitious Composites (ECC/SHCC) Incorporating Geopolymer fine Aggregates. *Cement and Concrete Composites* 125, 104296. doi:10.1016/j.cemconcomp.2021.104296
- Yang, E.-H., Wang, S., Yang, Y., and Li, V. C. (2008). Fiber-Bridging Constitutive Law of Engineered Cementitious Composites. *Acta* 6, 181–193. doi:10.3151/jact.6.181
- Yuan, F., Chen, M., and Pan, J. (2019). Experimental Study on Seismic Behaviours of Hybrid FRP-Steel-Reinforced ECC-concrete Composite Columns. *Composites B: Eng.* 176, 107272. doi:10.1016/j.compositesb.2019.107272
- Yuan, F., Chen, M., Zhou, F., and Yang, C. (2018). Behaviors of Steel-Reinforced ECC Columns under Eccentric Compression. *Construction Building Mater.* 185, 402–413. doi:10.1016/j.conbuildmat.2018.07.100
- Yuan, F., Pan, J., and Leung, C. K. Y. (2013). Flexural Behaviors of ECC and concrete/ECC Composite Beams Reinforced with basalt Fiber-Reinforced Polymer. *J. Compos. Constr.* 17, 591–602. doi:10.1061/(asce)cc.1943-5614.0000381
- Zhang, J., Leung, C. K. Y., and Gao, Y. (2011). Simulation of Crack Propagation of Fiber Reinforced Cementitious Composite under Direct Tension. *Eng. Fracture Mech.* 78, 2439–2454. doi:10.1016/j.engfracmech.2011.06.003
- Zhang, Y., Deng, M., and Dong, Z. (2019). Seismic Response and Shear Mechanism of Engineered Cementitious Composite (ECC) Short Columns. *Eng. Structures* 192, 296–304. doi:10.1016/j.engstruct.2019.05.019
- Zhang, Z., Qin, F., Ma, H., and Xu, L. (2020a). Tailoring an Impact Resistant Engineered Cementitious Composite (ECC) by Incorporation of Crumb Rubber. *Construction Building Mater.* 262, 120116. doi:10.1016/j.conbuildmat.2020.120116
- Zhang, Z., Yang, F., Liu, J.-C., and Wang, S. (2020b). Eco-friendly High Strength, High Ductility Engineered Cementitious Composites (ECC) with Substitution of Fly Ash by rice Husk Ash. *Cement Concrete Res.* 137, 106200. doi:10.1016/j.cemconres.2020.106200
- Zhang, Y., Deng, M., Li, T., and Dong, Z. (2021). Strengthening of Flexure-Dominate RC Columns with ECC Jackets: Experiment and Analysis. *Eng. Structures* 231, 111809. doi:10.1016/j.engstruct.2020.111809
- Zhang, Z., Liu, S., Yang, F., Weng, Y., and Qian, S. (2021). Sustainable High Strength, High Ductility Engineered Cementitious Composites (ECC) with Substitution of Cement by rice Husk Ash. *J. Clean. Prod.* 317, 128379. doi:10.1016/j.jclepro.2021.128379
- Zheng, Y.-Z., Wang, W.-W., and Brigham, J. C. (2016). Flexural Behaviour of Reinforced concrete Beams Strengthened with a Composite Reinforcement Layer: BFRP Grid and ECC. *Construction Building Mater.* 115, 424–437. doi:10.1016/j.conbuildmat.2016.04.038

Conflict of Interest: The authors declare that the research was conducted in the absence of any commercial or financial relationships that could be construed as a potential conflict of interest.

Publisher's Note: All claims expressed in this article are solely those of the authors and do not necessarily represent those of their affiliated organizations, or those of the publisher, the editors and the reviewers. Any product that may be evaluated in this article, or claim that may be made by its manufacturer, is not guaranteed or endorsed by the publisher.

Copyright © 2022 Wu, Su, Sun, Jin and Pan. This is an open-access article distributed under the terms of the Creative Commons Attribution License (CC BY). The use, distribution or reproduction in other forums is permitted, provided the original author(s) and the copyright owner(s) are credited and that the original publication in this journal is cited, in accordance with accepted academic practice. No use, distribution or reproduction is permitted which does not comply with these terms.



Study of the Hydration Temperature Field in the Hinge Seal Layer for a Large-Volume UHPC Arch Base

Jun Yang^{1,2}, Jieyun Wang^{1*}, Chao Luo², Yaxi Ding² and Yonghui Fan²

¹Guangxi Communications Investment Group Corporation Ltd., Nanning, China, ²State Key Laboratory of Mountain Bridge and Tunnel Engineering, Chongqing Jiaotong University, Chongqing, China

OPEN ACCESS

Edited by:

Qian Zhang,
Florida Agricultural and Mechanical
University, United States

Reviewed by:

Qing-feng Liu,
Shanghai Jiao Tong University, China
Neven Ukrainczyk,
Darmstadt University of Technology,
Germany

*Correspondence:

Jieyun Wang
wangjyqx@126.com

Specialty section:

This article was submitted to
Structural Materials,
a section of the journal
Frontiers in Materials

Received: 21 January 2022

Accepted: 21 March 2022

Published: 28 April 2022

Citation:

Yang J, Wang J, Luo C, Ding Y and
Fan Y (2022) Study of the Hydration
Temperature Field in the Hinge Seal
Layer for a Large-Volume UHPC
Arch Base.
Front. Mater. 9:859701.
doi: 10.3389/fmats.2022.859701

For large arch bridges, the sealing hinge layer at the arch footing is critical to the long-term performance and durability of the structure. This study investigated the temperature distribution of the sealing hinge layer inside a large UHPC arch seat during the hydration process in a natural environment, based on a design of a 600-m-span reinforced concrete rigid skeleton arch bridge. A certain suggestion for the design of a large-volume UHPC layer was proposed through the consideration of temperature and age effects of the thermal field solid finite element analysis of early-age UHPC hydration heat. The results show that UHPC has a hydration induction period of 10 h and reaches the peak temperature of 69°C in 20 h. Then, the hydration heat is gradually released in 70 h after pouring. The maximum temperature difference between the core and surface reaches 40°C. The results also show that the early temperature field and heat release rate of UHPC are affected by initial temperature. The actual heat release of some materials of UHPC components at 75 h is equivalent to that at 300 h, and the minimum effective age was found close to 100 h, where the heat release reaches 0.25 of the total heat release. A simplified algorithm for the spatially time-varying non-linear temperature field of the UHPC sealing hinge layer under the influence of temperature and age is proposed, which provides a simple calculation method for the temperature control of the UHPC arch seat during the hydration process in real projects.

Keywords: arch seat, UHPC layer, temperature field, temperature difference, simplified algorithm

INTRODUCTION

For large-span arch bridges, the arch seats are subjected to excessive internal force and local stress concentration, which leads to concrete cracks and spalling at the junction of the main arch and seat. As a result, it can cause corrosion of reinforcement in the arch seat and other diseases, which seriously affect the structural safety of large-span arch bridges (Teng, 2016). As UHPC has excellent characteristics of ultrahigh strength, good durability, and high tensile strength, it can be used in the hinge sealing at the foot of the arch to enhance the mechanical properties and durability of the arch foot hinge sealing, thus reducing the disease and improving the overall safety and durability of large-span arch bridges. However, the use of UHPC as the arch footing base for arch bridges has not yet been fully investigated (Bourchy et al., 2019).

Currently, the possibility of using UHPC for the key part of the bridge has been investigated in beams (Fan et al., 2021; Feng et al., 2021), columns (Wang et al., 2021; Xue et al., 2021), joints (Nasrin and Ibrahim, 2021), and shear walls (Preinstorfer et al., 2021). The structural size of UHPC is small,

and many conventional tests have been carried out for small-size UHPC specimens, including UHPC-steel thin layer (Jiang et al., 2021), UHPC-NC layer (Yang et al., 2021), and thin wall arch rib (Yang et al., 2021). Meanwhile, there are few articles on the hydration heat of UHPC, and most of the existing articles are aimed at the hydration heat release of mass concrete (Hu et al., 2017; Chen et al., 2021). In terms of cement hydration heat release, there were effects of superplasticizer on the early hydration heat of cement (Jia et al., 2021; Zhu et al., 2022) and the effects of admixture (Zhang T. et al., 2021) and construction technology (Mandal et al., 2021) on the hydration heat of cement. In terms of the finite element calculation model, it included the early thermodynamic model of concrete segmental box girder (Do et al., 2021), thermodynamic coupling model of early thermal cracking of concrete (Dong et al., 2021), and thermodynamic model of steel-concrete composite beam in the hydration process (Zhang Z. et al., 2021). The UHPC material has a large proportion of cementitious materials and a violent heat of hydration reaction (Shi et al., 2015; Zheng and Wu, 2021) and, when used in a large-volume structure, may cause early cracking of the structure. At the same time, the non-uniform thermal resistance of the plain concrete-UHPC interface leads to a complex temperature conduction process (Koenders et al., 2014; Schackow et al., 2016), so it is necessary to carry out experimental studies on the heat of hydration temperature field to obtain the form of temperature field distribution of the existing thick slab of UHPC to ensure the casting effect (Humad et al., 2019; Jia et al., 2021).

Therefore, in this research, carried out an experimental study and finite element analysis of the hydration heat field of a large-volume UHPC-sealed hinge layer based on a 600-m-span reinforced concrete stiff skeleton arch. Based on the equivalent age theory of concrete (FREIESLEBEN, 1997), the cement composite index exothermic model (Zhu, 2012) and ABAQUS transient thermal analysis finite element method (Gui, 2012) improve the traditional concrete hydration heat calculation (Teixeira de Freitas et al., 2013), through HEVAL, FILM/DISP subroutines to impose the hydration heat source considering the effect of UHPC own temperature and the heat transfer boundary under the influence of ambient temperature (Kim et al., 2010; Zhou et al., 2014), to establish a solid analysis model of the spatial time-varying thermal field of UHPC arch seal hinge layer components under the action of temperature + hydration heat coupling. Comparing the results of experimental research and finite element analysis, this study introduces the concept of equivalent age maturity of the temperature field finite element calculation method to consider the influence of temperature and age on the development of the exothermic rate of the cementitious material, which can be better applied to the early exothermic intense UHPC components (Yang et al., 2022a; Yang et al., 2022b; Tang et al., 2022).

THEORETICAL MODEL

Cement Hydration Model

The heat release process of early-age UHPC materials is complex, assuming that the concrete is homogeneous and isotropic after casting, that is, cement mortar, aggregates, etc. show a uniform

distribution, and the release of its heat of hydration is irrelevant to spatial location, but is only a function of time. Therefore, the accumulated heat of hydration at each age should be calculated in order to derive the exothermic rate of hydration and substitute it as an internal heat source in the subsequent calculation of the transient temperature field. The cumulative heat of hydration of cement is age-dependent, and three common calculation models are exponential (Eq. 1), hyperbolic (Eq. 2), and compound exponential (Eq. 3) heat of hydration expressions (Zhu, 2012).

$$Q(t) = Q_0(1 - e^{-mt}), \quad (1)$$

$$Q(t) = Q_0t/(n + t), \quad (2)$$

$$Q(t) = Q_0(1 - e^{-at^b}). \quad (3)$$

In formulas (1) to (3), $Q(t)$ is the cumulative heat of hydration of cement at age t ; Q_0 is the final heat of hydration of cement when $t \rightarrow \infty$; t is the age; m is a constant; n is a constant, which is the age when the heat of hydration reaches half, unit: days d ; and a and b are constants.

In this study, the composite exponential equation is used; for P.O 525r cement, each parameter is taken as the value $Q_0 = 350 \text{ kJ/kg}$, $a = 0.36$, $b = 0.74$. The exothermic rate is given as follows:

$$q(v) = abQ_0t^{b-1}e^{-at^b}. \quad (4)$$

Equivalent Age Theory

The equivalent age function has the following form (FREIESLEBEN, 1997; Hansen and Pedersen, 1977):

$$t_e = \int_0^t \frac{E_a}{R} \left(\frac{1}{237 + T_r} - \frac{1}{237 + T} \right) dt. \quad (5)$$

Discrete as

$$t_e = \sum_0^t \exp \left(\frac{E_a}{R} \left(\frac{1}{237 + T_r} - \frac{1}{237 + T} \right) \right) \Delta t, \quad (6)$$

where E_a is the concrete activation energy, J/mol ; R is the gas constant, J/(molK) , $R = 8.3144 \text{ J/(molK)}$; T_r is the reference temperature, $^{\circ}\text{C}$, generally taken as 20; T is the average temperature of the concrete during the time period Δt , $^{\circ}\text{C}$; and t_e is the equivalent age maturity of the concrete relative to the reference temperature, d . The equivalent age t_e includes both time and temperature concepts, which can fully reflect the growth of mechanical parameters in concrete. For the finite element simulations, the corresponding equivalent age values are calculated in the form of a cumulative superposition of time steps. Considering the high active content of UHPC, a constant value of 4000 K is used for the calculation of E_a/R in this study.

UHPC Early Exothermic Theoretical Model

From this, the time in the transient analysis of the temperature field can be replaced by the equivalent time of the concrete to obtain a modified model of the cement exotherm taking into account the effect of temperature as follows (Gui, 2012):

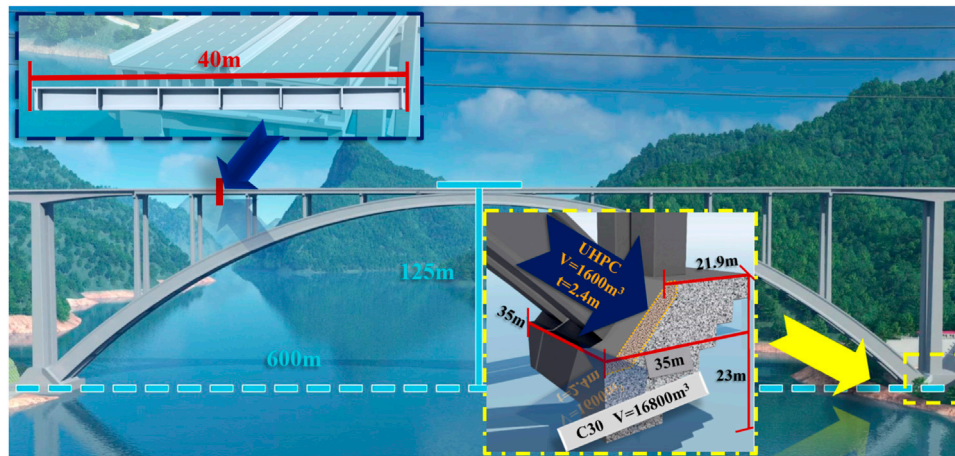


FIGURE 1 | General arrangement of a bridge (unit: m).

$$\frac{dQ(t)}{dt} = Q_0(1 - e^{-at_b^c}), \quad (7)$$

$$t_e = t_e + \Delta t, \quad (8)$$

$$\eta = 1 - e^{-at_b^c}, \quad (9)$$

where η is the ratio of the actual heat release from UHPC to the total heat release.

The theoretical model considers the influence of cement hydration temperature on its hydration heat release rate and can be better suited for UHPC materials with a less water binder ratio and intense early heat release.

EXPERIMENTAL PROGRAM

Project Overview

A bridge adopts a top-loaded rigid skeleton concrete arch bridge, the main arch axis adopts a catenary, and the calculated span is 600 m (Figure 1). The arch seat adopts an open-cut expansion foundation, and the arch seat is poured with 16,800 cubic meters of C30 concrete. The hinge layer at the arch foot is poured with 1600 square meters and a thickness of 2.4 m UHPC, which is completed in one pour. UHPC has a less water-to-binder ratio and a large amount of unilateral cement. The violent hydration process leads to rapid changes in its spatial time-varying temperature field, which in turn causes complex temperature effects.

Material and Test Parameters

In order to simulate the actual temperature boundary of the sealing-hinged concrete of the arch foot, the UHPC components were surrounded by film-coated wood framework with a thickness of 15 mm, and the framework was covered with 20 mm plastic foam to simulate the thermal insulation layer of the conventional concrete-UHPC interface; the pouring was completed at 6 p.m. on 2021/11/17, and the measured ambient temperature of the laboratory was 12.5°C, with a daily

temperature variation amplitude of 10°C, according to the sinusoidal distribution (Figure 2). The initial temperature of UHPC was 25°C; UHPC was made of P.O 525r cement, and the thermal parameters of UHPC are given in Table 1. The material matching ratio was given as follows:

Cement:fly ash:silica fume:sand:water:steel fiber:admixture = 1:0.2:0.17:1.1:0.24:0.17:0.0275.

To test the shrinkage characteristics of UHPC, experiments related to self-shrinkage and constrained shrinkage of UHPC were carried out (Figures 3, 4). The self-shrinkage test was carried out by pre-bedding a vibrating string transducer in the prismatic specimen, and the UHPC constrained shrinkage was performed using a circular specimen with circular dimensions according to ASTM C 1581-04. The strain gauges were attached to the four corners of the inner steel ring to output a strain value through the full-bridge wiring.

Among them, UHPC-1 was a universal UHPC, UHPC-2 was a low-shrinkage UHPC, and UHPC-3 was an early strength UHPC developed by the author's team. In this work, we studied the hydration heat of UHPC-3.

The early self-shrinkage of UHPC specimens develops rapidly, reaching 200 $\mu\epsilon$ in 1 d, 350 $\mu\epsilon$ in 3 days, and 400 $\mu\epsilon$ in 28 days; the development trend of constrained shrinkage was smoother, with little change after reaching 150 $\mu\epsilon$ in 20 days (Figure 5).

It should be pointed out that the content of the early shrinkage test of UHPC is not discussed in this study and is not directly related to the temperature field research involved in this study. However, the early shrinkage performance of UHPC is very important for the calculation of temperature stress, so this part is listed here in order to support further research work.

Specimen Design

The specimen size was 1000 mm long, 900 mm wide, and 300 mm thick, with a volume of 0.27 square, and was completed in one pour. Three layers of reinforcement mesh were arranged inside the structure, with a reinforcement size of 10 mm (Figure 6). In total, 29 string sensors with temperature (SZZX-A150D) were

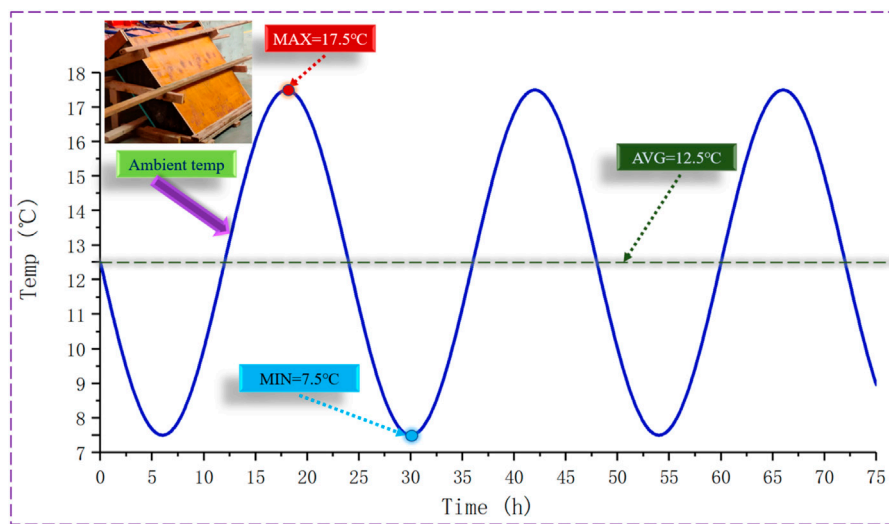


FIGURE 2 | Ambient temperature history curve after completion of pouring.

TABLE 1 | Thermal parameters of UHPC materials.

UHPC parameter	Value
Specific heat capacity	970 J/(kg·K)
Thermal conductivity	2.55 w/(m·K)
Density	2780 kN/m ³
Coefficient of linear expansion	1E-5

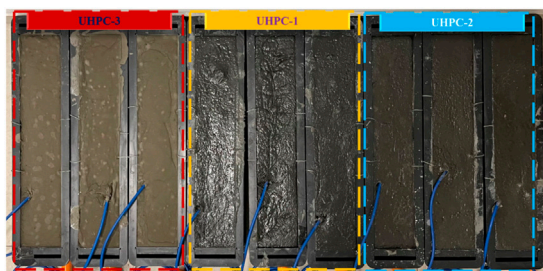


FIGURE 3 | Self-shrinking specimens.

arranged for data acquisition using the SZZDQ-ZH intelligent reading instrument (Figure 7).

RESULTS AND DISCUSSION

Evolution of the Heat of Hydration Temperature of UHPC Components

Figure 8 shows the heat of the hydration temperature curve at each measurement point, with the vertical axis showing the measured temperature values at each measurement point and the horizontal axis showing the time since the end of pouring of the UHPC component.

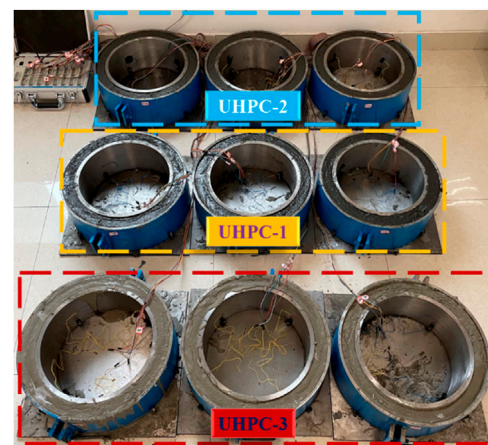


FIGURE 4 | Constrained shrinkage specimens.

From Figure 8, it can be seen that the initial hydration induction period of UHPC components is about 10 h, and the heat release of UHPC during the hydration induction period is slow, and this phenomenon is more consistent with the literature (Yang et al., 2019). The temperature change caused by convective heat dissipation of formwork-air during the hydration induction period is obvious, and the temperature change of UHPC during this period is not significant; the bottom test section surface measurement point is more obvious; the UHPC material reaches about 25°C and starts to react, and the initial temperature of UHPC greatly influences the UHPC temperature field; 10 h after the temperature rises rapidly, the peak temperature of hydration heat is 69°C and appears in 20 h. The peak temperature is located at the measuring point D-2 and at the center of the bottom of the UHPC specimen, after which the temperature of heat of hydration gradually decreases, 70 h after pouring, the heat of hydration is released, and the

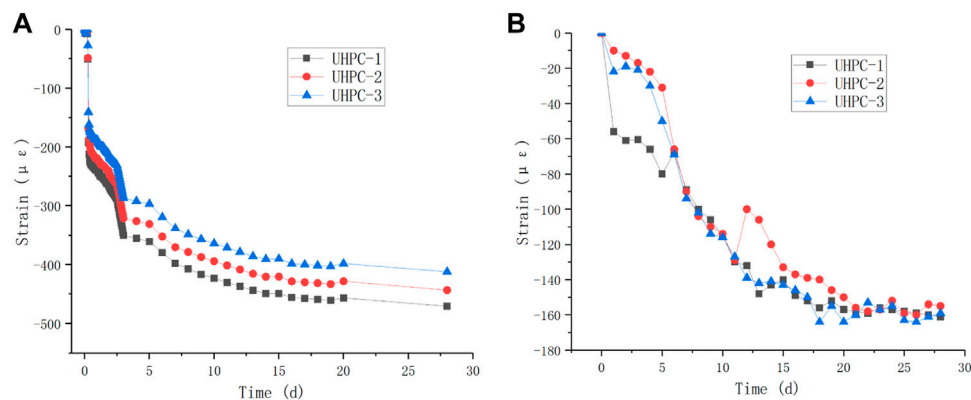


FIGURE 5 | Shrinkage characteristic test of UHPC. (A) Self-shrinkage results. (B) Constrained shrinkage results.



FIGURE 6 | Test components.

rate of temperature change in the rising section of the heat of hydration curve is greater than that in the falling section; because the temperature accelerates the process of the heat of hydration of UHPC, the greater the peak temperature of the measurement point, the shorter the time to reach the peak. This phenomenon is more obvious in the middle and bottom sections, where the temperature is higher; the temperature field of UHPC at the formwork–air interface is coupled by the external environment and the heat of hydration as the test chamber is in a relatively stable windless environment with room temperature, the environmental influence is small, and the temperature field of UHPC is mainly affected by the heat of hydration.

Temperature Difference Distribution and Temperature Transfer Paths

Figure 9 shows the difference in the heat of hydration temperature of each measurement point in the test section, which provides further insights into the temperature transfer

path in the thickness direction. As shown in Figure 7, "Z1-D1" indicates the temperature of the measurement point in the middle test section minus the temperature of the measurement point in the bottom test section.

It can be seen from Figure 9 that after 10-h hydration induction period of UHPC members, the section temperature difference develops rapidly, and the section temperature difference starts to decrease 20 h after the completion of pouring. According to the temperature difference, the temperature transfer path in the thickness direction is obtained as follows: the bottom temperature of the bottom section transfers to the center of the bottom section and the bottom of the middle section; the middle section transfers to the center of the bottom, the top, and the surface section; and the section temperature transfer is from the center to the outside (Figure 10). The maximum temperature difference of 12.5°C in the section occurs at 12 h, which is located in the middle layer–bottom of the surface layer region.

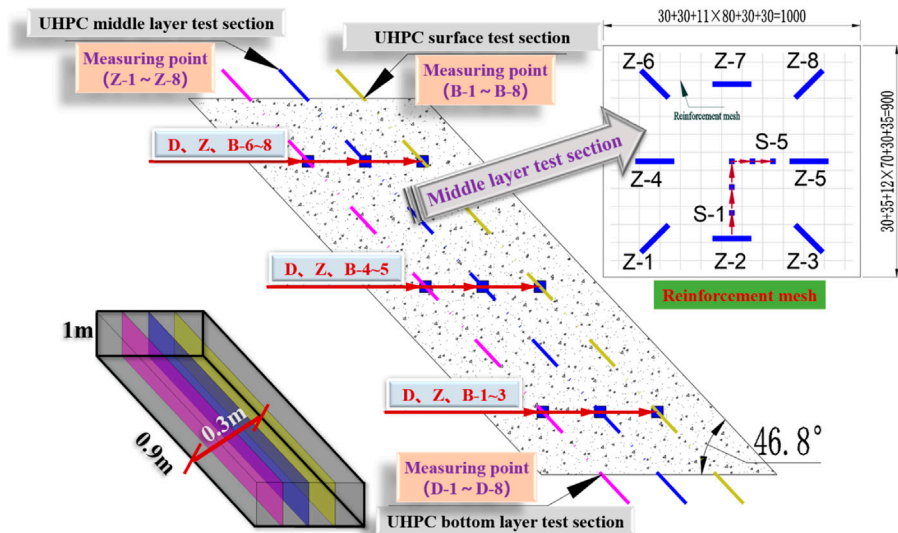


FIGURE 7 | Arrangement of the measurement points.

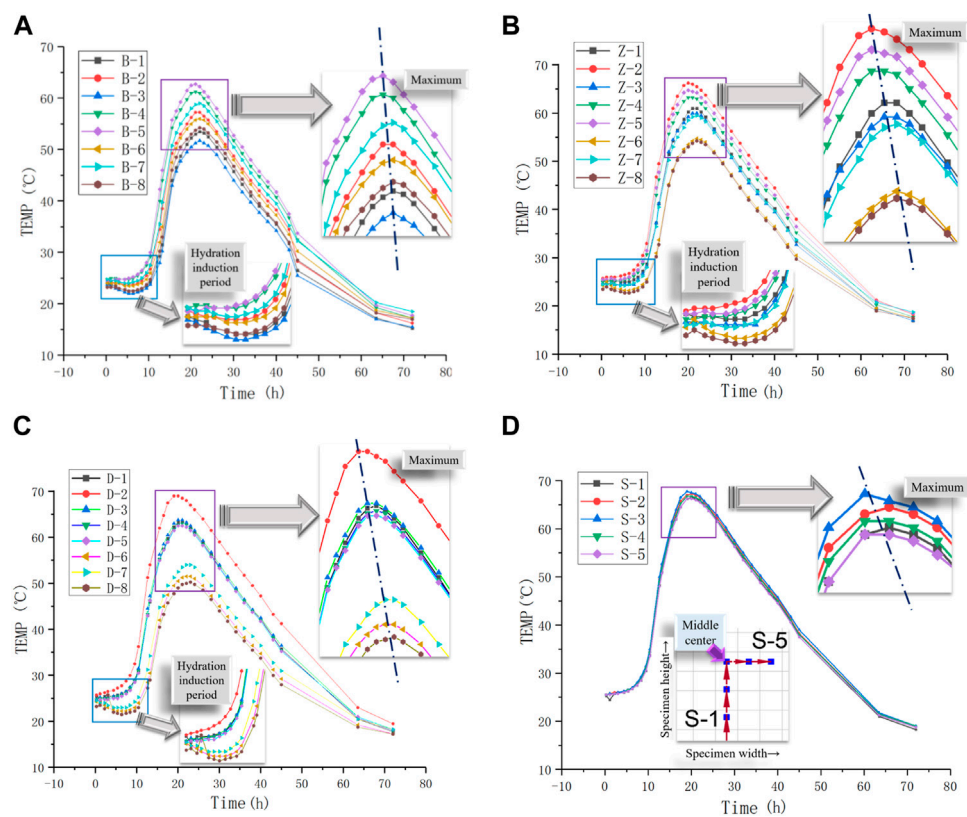


FIGURE 8 | Temperature of concrete measurement point in each test section. **(A)** Surface layer temperature evolution. **(B)** Mid-layer temperature evolution. **(C)** Bottom layer temperature evolution. **(D)** Vertical temperature measurement.

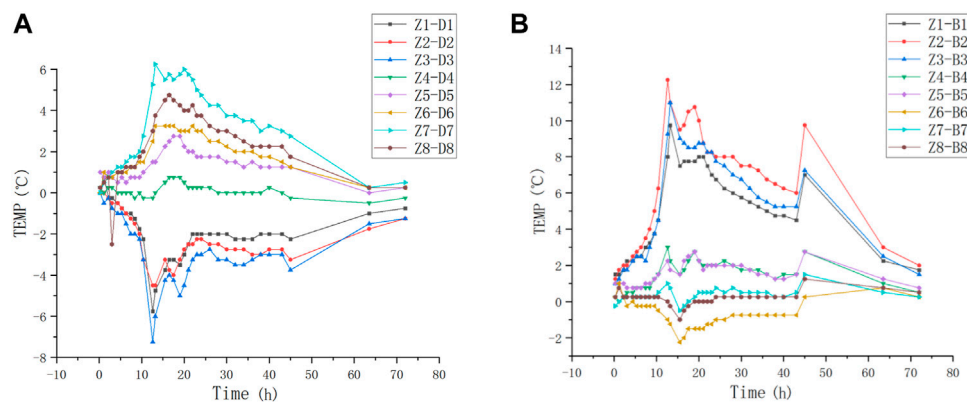


FIGURE 9 | Temperature difference distribution in the test section. **(A)** Mid-bottom test section. **(B)** Mid-surface test section.

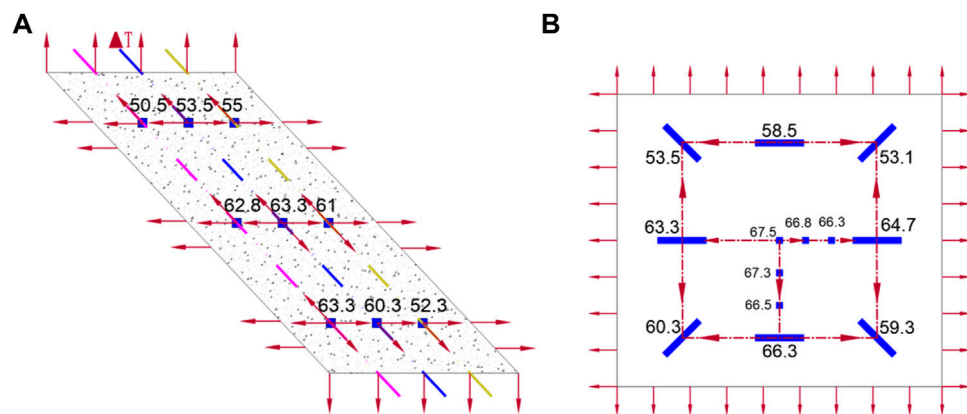


FIGURE 10 | Temperature transfer path (unit: °C). **(A)** Thickness direction transfer path. **(B)** Transfer path of the middle section at 20 h.

TABLE 2 | Heat transfer coefficients of UHPC components.

UHPC component surface	Status	Value J/(m ² ·h·K)
Top side	Natural convection	23900
Side/upper surface	15 mm template	16733
Lower surface/bottom	15 mm formwork +20 mm plastic foam	4423

Comparison of Theoretical Analysis and Experimental Results

Calculation Parameters

The model is discretized into 48000 DC3D8R heat transfer units, and the initial temperature fields of thermal convection, thermal radiation, and actual incoming temperature are imposed for transient heat transfer analysis with an analysis duration of 75 h. The specific settings are as follows: according to the relevant provisions of the Standard for the Construction of Massive Concrete (GB 50496-2018) and the production of the members, the convective heat transfer coefficient of each surface of the members is set as mentioned in **Table 2**:

The surface of the UHPC component radiates heat to the outside world, and the emissivity of the UHPC surface is taken to be 0.9; the measured entry temperature of the UHPC unit at the measurement point is input in the Python batch for steady-state temperature field analysis, and the steady-state non-uniform temperature field is obtained to simulate the actual entry temperature.

Comparison of Temperature Fields

Figure 11 shows the comparison between the hydration heat temperature curves and the simulation curves at measurement points 1, 2, 4, 6, and 7 in the surface test section, and those with ' in the figure indicate the simulation data.

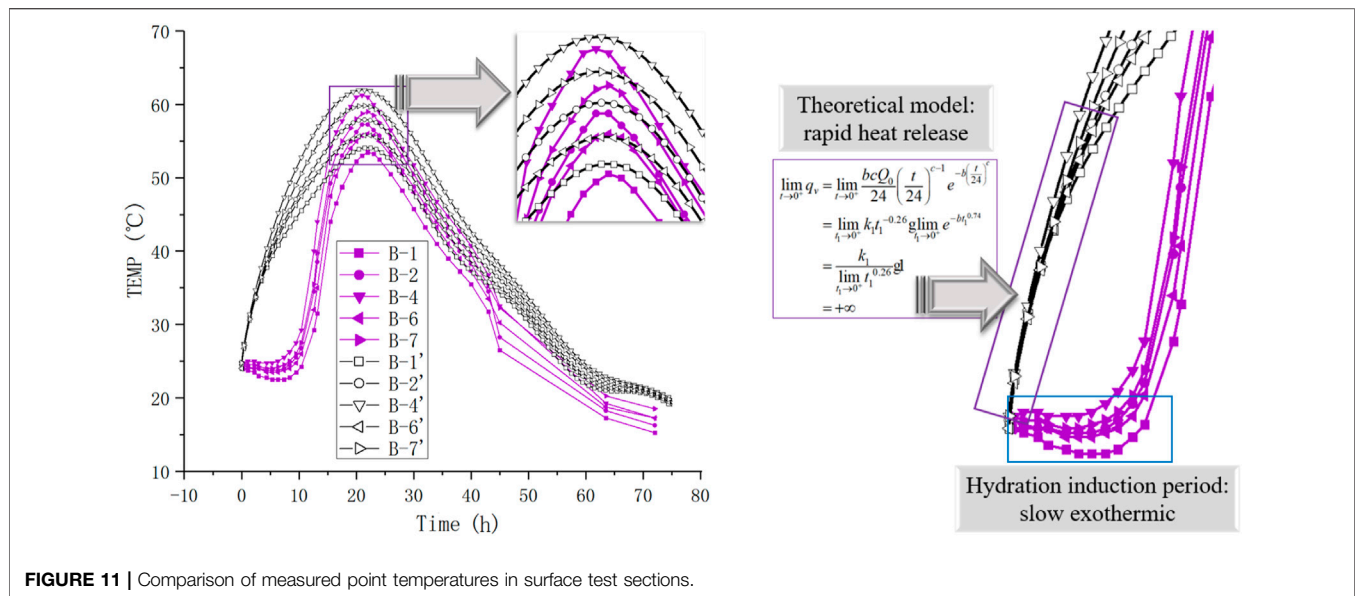


FIGURE 11 | Comparison of measured point temperatures in surface test sections.

The sensitivity analysis shows that Q_0 in formula (4) has a significant impact on the peak hydration temperature of UHPC. The greater the Q_0 , the higher the peak hydration temperature of UHPC. The accuracy of Q_0 must be ensured in the calculation, which can be determined by using the cement adiabatic heating test; Ea/R in Eq. 5 has a significant impact on the peak time of UHPC hydration. The greater the Ea/R , the shorter the peak time of UHPC hydration. In this study, $Ea/R = 4000$ K is finally determined by adjusting EA and calibrating the calculation model.

It can be seen that there is a big difference between the test curve and simulation curve in the temperature rise stage, especially in the early stage of hydration heat, and this difference is because the simulation model is based on the composite exponential theory model, the exothermic rate in $t \rightarrow 0$ for $+\infty$, which fails to take into account the slow exotherm caused by the complex process of hydration induction period; in the fall stage, the test data and simulation data fluctuate and decrease, reflecting the change in the actual convective heat transfer velocity between the specimen and the air caused by the sinusoidal variation of the external temperature. The experimental data are slightly smaller than the simulation data. Considering that the actual convection heat transfer velocity between the specimen and the outside world is larger than that in the model setting; the simulation curve is more consistent in the region near the peak and the temperature fall stage and can better calculate the peak and the time of occurrence, indicating that the total amount of heat generation and heat dissipation parameters of the model are set accurately and can simulate the test situation better.

In summary, the experimental results and the calculated results of the temperature field distribution and the evolution law are consistent due to the thermal analysis algorithm, the heat of hydration model, convective heat transfer model, and radiation heat transfer model have a certain empirical approximation, so that the calculated results and the real

results of the test in some nodes of the value show a certain deviation and this deviation can meet the engineering accuracy requirements. The transient thermal analysis model established in this study to consider the influence of temperature can be used for predicting the temperature distribution law of the hinge layer of a large-volume UHPC arch base.

SIMULATION ANALYSIS AND THEORETICAL FORMULA

Temporal Variation of the Temperature Field

Figure 12 shows the distribution of the temperature field at each time point. In order to observe the core temperature variation, the clouds are shown dissected from the center, and to save space, only the temperature clouds for 25, 40, 55, and 75 h are shown in Figure 12.

It can be seen that the core temperature of the component is the highest, and after 25 h, the heat dissipation in all parts of the component is uniform. The heat dissipation rate slows down with time, and the core temperature drops 35°C in the first 25–55 h and 10°C between 55 and 75 h. The lowest surface temperature appears in the corner position of the top surface of the UHPC and drops 13°C in the first 25–55 h, and the temperature is unchanged between 55 and 75 h, which is close to room temperature. Different moments of the component profile cloud chart section are nearly elliptical, with obvious temperature changes along the short side and a large temperature gradient.

Temperature Field Distribution Pattern

Figure 13 shows the distribution of isothermal surface and temperature field. It can be seen that the temperature decreases from the center to the surrounding area, which is in line with the general law of heat of hydration.

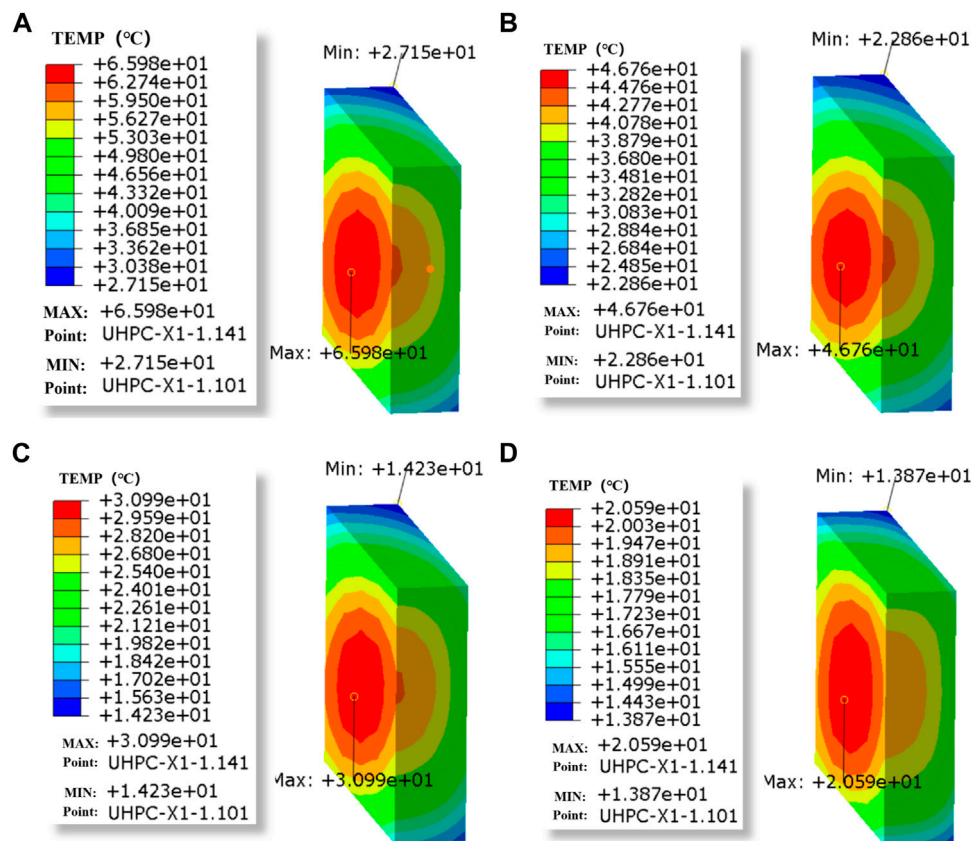


FIGURE 12 | Spatial distribution of UHPC hydration heat temperature field at different times. **(A)** Temperature field at 25 h. **(B)** Temperature field at 40 h. **(C)** Temperature field at 55 h. **(D)** Temperature field at 75 h.

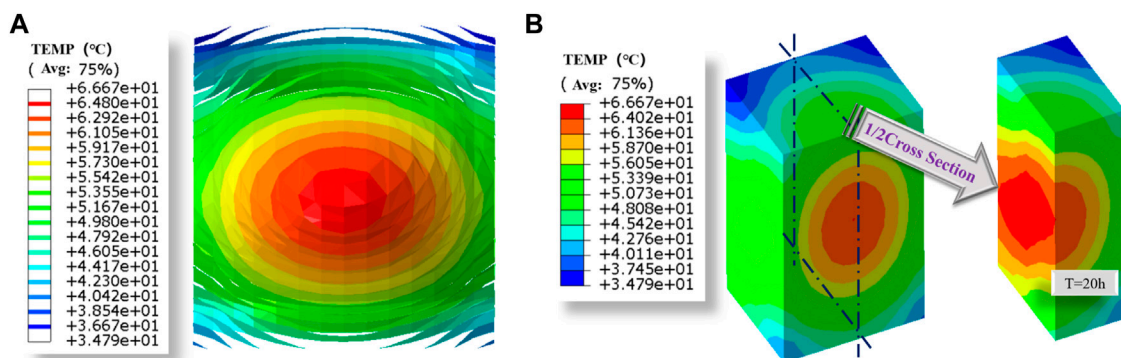


FIGURE 13 | Spatial distribution of the heat of hydration temperature field of UHPC at 20 h. **(A)** Isothermal surface at 20 h. **(B)** Temperature distribution at 20 h.

The central isothermal surface is a spherical surface, due to the width > height > thickness of the component. The isothermal surface near the boundary gradually becomes an ellipsoidal ball, with three directions in a decreasing

order, and the outer isothermal surface cannot be wrapped together due to the size limitation of the thickness direction. The temperature gradient is larger along the short side and smaller along the long side because the short side can conduct

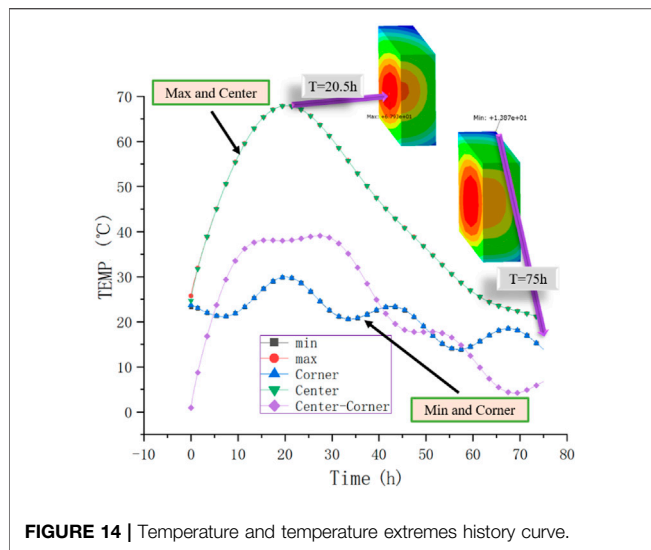


FIGURE 14 | Temperature and temperature extremes history curve.

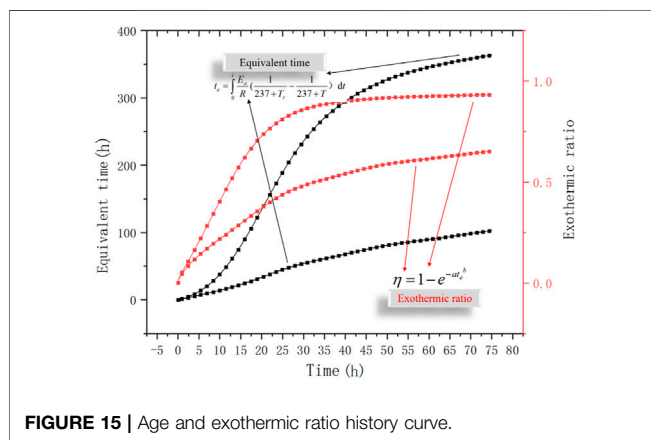


FIGURE 15 | Age and exothermic ratio history curve.

the temperature to the outside world more quickly. From the temperature distribution diagram, it can be seen that the maximum temperature is located in the center of the middle section and the bottom of the bottom section, while the temperature at the top of the UHPC member is smaller, which is consistent with the test situation.

Temperature Differences and Exothermic Time-Varying Patterns

Figure 14 shows the history curves of the maximum and minimum values of temperature at the nodes of each frame, and the temperature values of the top center node and surface corner points of the member and the maximum and minimum point temperature difference of the member read using Python. Figure 15 shows the history curves for the maximum and minimum values of the equivalent age and the ratio of the unit heat release to the total heat release at each node of each frame.

From the temperature and temperature difference curve, it can be seen that the maximum and minimum temperature

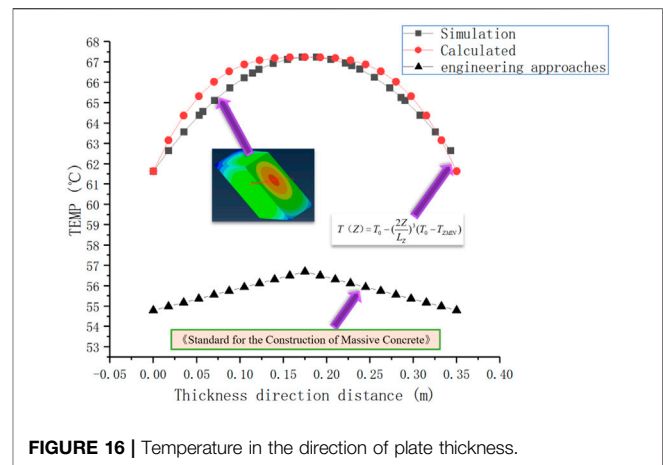


FIGURE 16 | Temperature in the direction of plate thickness.

values at the nodes and the top center nodes and surface corners of the members overlap, indicating that the maximum and minimum temperatures of the member locate at the top center nodes and surface corners of the member and do not change with time; the temperature difference curve shows that the temperature difference between the inside and outside of the members reaches 40°C, which far exceeds the temperature difference limit of 25°C specified in the Standard for the Construction of Massive Concrete (GB 50496-2018). Special attention should be paid to the temperature control of the sealing hinge layer of the large-volume UHPC arch seat.

From the age and exothermic ratio course curve, it can be seen that the maximum effective age rises to 300 h within 75 h of the actual hydration reaction, indicating that under the influence of temperature, the actual exothermic amount of UHPC component materials at 75 h reaches the exothermic amount at the age of 300 h, and the exothermic percentage is close to 1, which has fully reacted to exothermic amount; the minimum effective age is close to 100 h and the exothermic amount reaches 0.25 of the total exothermic amount.

Simplified Algorithm of Hydration Heat Temperature Field of UHPC Sealing Layer

Simplified Algorithm for the Temperature Field of a Large Volume UHPC Sealing Hinge Layer

Combining the temperature field distribution and the isothermal surface diagram shows that the isothermal surface is ellipsoidal and approximately equidistant along the space, and the ellipsoidal equation is as follows:

$$\frac{x^2}{a^2} + \frac{y^2}{b^2} + \frac{z^2}{c^2} = 1. \quad (10)$$

At this point, a set of parameters a , b , and c of an ellipsoidal surface determines a temperature value T . Assuming that the ellipsoidal surface increases in the same proportion in the

component space, we have $T = T(abc)$, for a UHPC plate of length L_X , width L_Y , and thickness L_Z .

$$\frac{L_X}{a} = \frac{L_Y}{b} = \frac{L_Z}{c}. \quad (11)$$

The temperature T_0 at the center of the plate and the temperature T_{Zmin} at the surface of the thickness, then the temperature change along the thickness direction can be expressed as follows:

$$T(Z) = T_0 - \left(\frac{2Z}{L_Z}\right)^3 (T_0 - T_{ZMIN}). \quad (12)$$

Formula Validation

Figure 16 shows the simulation temperatures, engineering approaches, and simplified formulas for calculating the temperature of the model extracted along the thickness direction at 20 h, with the node selected as the center of the thickness surface.

The comparison between the “simulation” and the “calculated” curves shows that the calculation assumes a cubic parabolic distribution of temperature along the thickness direction, which is more than reasonable and has sufficient accuracy for structural calculation. The test results are in good agreement with the calculation results, but they are quite different from the engineering calculation results.

It is found that the temperature result of the engineering approaches is small because the commonly used engineering approaches are suitable for conventional concrete, and the hydration heat release of UHPC at an early age is intense, which leads to the advancement of the hydration peak, which is different from conventional concrete. It can be seen that the commonly used engineering calculation approaches are not accurate enough for the calculation of the hydration heat of UHPC, and the simplified calculation method proposed in this study can be better applicable.

CONCLUSION AND OUTLOOK

At present, due to its excellent performance, UHPC has broad application prospects in key parts of buildings and bridge structures, especially large-volume UHPC components. The early exothermic intensity of large-volume UHPC may cause early temperature cracks, which may affect the long-term performance of the structure. At the same time, at present, there are many studies on the hydration heat temperature field of ordinary concrete, and there are relatively few studies on the hydration heat of large-volume UHPC. The hydration heat release mechanism of large-volume UHPC needs to be further clarified. This study carries out the experimental and simulation research on the early temperature field of large-volume UHPC components and puts forward a simplified algorithm of time-varying non-linear temperature field in UHPC closed hinge space under the influence of temperature

and age, which can be better applied to practical engineering. However, this study focuses on the temperature field of large-volume UHPC. Temperature stress and temperature crack are not expanded within the scope of this study, which will be reflected in the author's follow-up research works. The main conclusions of this study are as follows:

- 1) The test results show that the hydration reaction of UHPC has a hydration induction period of 10 h, and then the hydration exothermic reaction becomes intense. In the calculation process, the influence of temperature and hydration exothermic rate needs to be considered in order to carry out accurate simulation. The test and simulation results show that the maximum temperature of the component under UHPC mass pouring is 69°C, and the temperature difference between the core and surface reaches 40°C. Special attention should be paid to temperature control.
- 2) The initial temperature of UHPC has a great influence on its early hydration heat temperature field. The higher temperature of UHPC has a shorter time to leave the induction period of hydration, and the hydration reaction occurs earlier than that of UHPC at lower temperatures, resulting in drastic changes in the spatial distribution of the temperature field of UHPC at early ages. The cooling path after the temperature peak is as follows: temperature transfer from the bottom of the bottom section to the center of the bottom section and the bottom of the middle section, transfer from the middle section to the center of the bottom section, the top and the surface section, and temperature transfer from the center to the outside of the section.
- 3) Under the influence of temperature, the actual heat release of some materials of UHPC components at 75 h reaches that at 300 h, and the heat release percentage is close to 1, which fully reflects the heat release; the minimum effective age is close to 100 h, and the heat release reaches 0.25 of the total heat release. The isothermal surface of UHPC after the temperature peak is ellipsoidal from the center to the surface diffusion, this study is based on the test and simulation results of the theoretical derivation, the existing UHPC plate temperature along the thickness direction of the simplified calculation formula, for engineering structures have sufficient calculation accuracy.
- 4) It is recommended that the construction of UHPC components should be well insulated, and cold water pipes can be used to reduce the heat of hydration at an early age for large UHPC components.

DATA AVAILABILITY STATEMENT

The original contributions presented in the study are included in the article/Supplementary Material, further inquiries can be directed to the corresponding author.

AUTHOR CONTRIBUTIONS

JY organized the database and wrote the first draft of the manuscript. JW revision read, revised the first draft of the manuscript, and approved the submitted version. CL did the experiment and simulation analysis. YD and YF processed the data. All authors contributed to the choice of the review topic, to the general outline of the manuscript, and to the revision and approval the manuscript to be submitted.

REFERENCES

- Bourchy, A., Barnes, L., Besette, L., Chalencon, F., Joron, A., and Torrenti, J. M. (2019). Optimization of Concrete Mix Design to Account for Strength and Hydration Heat in Massive concrete Structures. *Cement and Concrete Composites*. 103, 233–241. doi:10.1016/j.cemconcomp.2019.05.005
- Chen, H.-L., Mardmomen, S., and Leon, G. (2021). On-site Measurement of Heat of Hydration of Delivered Mass Concrete. *Construction Building Mater.* 269, 121246. doi:10.1016/j.conbuildmat.2020.121246
- Do, T. A., Verdugo, D., Tia, M., and Hoang, T. T. (2021). Effect of Volume-To-Surface Area Ratio and Heat of Hydration on Early-Age thermal Behavior of Precast concrete Segmental Box Girders. *Case Stud. Therm. Eng.* 28, 101448. doi:10.1016/j.csite.2021.101448
- Dong, S., Wang, X., Xu, H., Wang, J., and Han, B. (2021). Incorporating Super-Fine Stainless Wires to Control thermal Cracking of concrete Structures Caused by Heat of Hydration. *Construction Building Mater.* 271, 121896. doi:10.1016/j.conbuildmat.2020.121896
- Fan, L., Teng, L., Tang, F., Khayat, K. H., Chen, G., and Meng, W. (2021). Corrosion of Steel Rebar Embedded in UHPC Beams with Cracked Matrix. *Construction Building Mater.* 313, 125589. doi:10.1016/j.conbuildmat.2021.125589
- Feng, Z., Li, C., Yoo, D.-Y., Pan, R., He, J., and Ke, L. (2021). Flexural and Cracking Behaviors of Reinforced UHPC Beams with Various Reinforcement Ratios and Fiber Contents. *Eng. Structures*. 248, 113266. doi:10.1016/j.engstruct.2021.113266
- Gui, Y. (2012). Study on Hydration Characteristics and Maturity of Sulphoaluminate Cement-Based Material. *Wuhan Univ. Sci. Technol.* doi:10.27380/d.cnki.gwkju.2020.000528
- Hansen, P. F., and Pedersen, E. J. (1977). Maturity Computer for Controlling Curing and Hardening of concrete. *Nordisk Betong*. 19, 21–25.
- Hu, X., Shi, C., Shi, Z., Tong, B., and Wang, D. (2017). Early Age Shrinkage and Heat of Hydration of Cement-Fly Ash-Slag Ternary Blends. *Construction Building Mater.* 153, 857–865. doi:10.1016/j.conbuildmat.2017.07.138
- Humad, A. M., Provis, J. L., and Wirzen, A. (2019). Effects of Curing Conditions on Shrinkage of Alkali-Activated High-MgO Swedish Slag Concrete. *Front. Mater.* 6, 287. doi:10.3389/fmats.2019.00287
- Jia, F., Yao, Y., and Wang, J. (2021). Influence and Mechanism Research of Hydration Heat Inhibitor on Low-Heat Portland Cement. *Front. Mater.* 8, 697380. doi:10.3389/fmats.2021.697380
- Jiang, J., Zou, Y., Yang, J., Zhou, J., Zhang, Z., Huang, Z., et al. (2021). Study on Bending Performance of Epoxy Adhesive Prefabricated UHPC-Steel Composite Bridge Deck. *Adv. Civil Eng.* 2021, 1–16. doi:10.1155/2021/6658451
- Kim, G., Lee, E., Kim, Y., and Khil, B. (2010). Hydration Heat and Autogenous Shrinkage of High-Strength Mass Concrete Containing Phase Change Material. *J. Asian Architecture Building Eng.* 9, 455–462. doi:10.3130/jaabe.9.455
- Koenders, E. A. B., Pepe, M., and Martinelli, E. (2014). Compressive Strength and Hydration Processes of concrete with Recycled Aggregates. *Cement Concrete Res.* 56, 203–212. doi:10.1016/j.cemconres.2013.11.012
- Mandal, R., Panda, S. K., and Chakraborty, S. (2021). Effect of Electrolyzed Water (EW) in Accelerating the Cement Setting and Hydration as Demonstrated by the Analytical Techniques. *Construction Building Mater.* 311, 125367. doi:10.1016/j.conbuildmat.2021.125367
- Nasrin, S., and Ibrahim, A. (2021). Flexural Response of Ultra-High-performance Concrete (UHPC) Hybrid Bridge Deck Connections Made with Local Materials. *Construction Building Mater.* 270, 121451. doi:10.1016/j.conbuildmat.2020.121451

FUNDING

The support by the National Natural Science Foundation of China (51908093), the Natural Science Foundation of Chongqing (cstc2020jcyj-msxmX0088), Chongqing Natural Science Foundation Innovation Group Science Foundation (cstc2019jcyj-cxttX0004), the Science Foundation of Hubei Provincial Department of Transportation (2020-186-1-6, 2020-2-1-1), and the Scientific and Technological Research Project of Chongqing Education Commission (KJQN201900733) is greatly acknowledged.

- Preinstorfer, P., Huber, P., Huber, T., Kromoser, B., and Kollegger, J. (2021). Experimental Investigation and Analytical Modelling of Shear Strength of Thin Walled Textile-Reinforced UHPC Beams. *Eng. Structures*. 231, 111735. doi:10.1016/j.engstruct.2020.111735
- Schackow, A., Effting, C., Gomes, I. R., Patruni, I. Z., Vicenzi, F., and Kramel, C. (2016). Temperature Variation in Concrete Samples Due to Cement Hydration. *Appl. Therm. Eng.* 103, 1362–1369. doi:10.1016/j.applthermaleng.2016.05.048
- Shi, C., Wang, D., Wu, L., and Wu, Z. (2015). The Hydration and Microstructure of Ultra High-Strength concrete with Cement-Silica Fume-Slag Binder. *Cement and Concrete Composites*. 61, 44–52. doi:10.1016/j.cemconcomp.2015.04.013
- Tang, Q., Xin, J., Jiang, Y., Zhou, J., Li, S., and Chen, Z. (2022). Novel Identification Technique of Moving Loads Using the Random Response Power Spectral Density and Deep Transfer Learning. *Measurement* 195, 111120. doi:10.1016/j.measurement.2022.111120
- Teixeira de Freitas, J. A., Cuong, P. T., Faria, R., and Azenha, M. (2013). Modelling of Cement Hydration in concrete Structures with Hybrid Finite Elements. *Finite Elem. Anal. Des.* 77, 16–30. doi:10.1016/j.finel.2013.07.008
- Teng, Y. (2016). *Research on Inspection and Assessment and Strengthening Technology of Steel Pipe and concrete Arch Bridge*. China; Chang'an University.
- Wang, Z.-C., Duan, D.-Y., Wang, S.-H., Mo, Y., and Yin, Y.-G. (2021). Mechanical Behavior of the Novel Gradient Concrete Tower of a Cable-Stayed Bridge. *Front. Mater.* 8, 15. doi:10.3389/fmats.2021.676440
- Xue, W., Hu, X., and Song, J. (2021). Experimental Study on Seismic Behavior of Precast concrete Beam-Column Joints Using UHPC-Based Connections. *Structures*. 34, 4867–4881. doi:10.1016/j.istruc.2021.10.067
- Yang, J., Xia, J., Cheng, C., Wang, J., Zhang, J., and Wang, G. (2022a). Research on the Bonding Performance of UHPC-NC Interfaces With Different Sizes of Grooves. *Frontiers in Materials* 9. doi:10.3389/fmats.2022.859717
- Yang, J., Xia, J., Zhang, Z., Zou, Y., Wang, Z., and Zhou, J. (2022b). Experimental and Numerical Investigations on the Mechanical Behavior of Reinforced Concrete Arches strengthened With UHPC Subjected to Asymmetric Load. *Structures* 39, 1158–1175. doi:10.1016/j.istruc.2022.03.087
- Yang, J., Zhou, J. T., Zhang, Z. Y., Wang, Z. S., and Wang, J. Y. (2021). Shear Performance of Keyway Interface between UHPC and Normal Concrete. *Chin. J. Highw.* 34 (8), 13. doi:10.19721/j.cnki.1001-7372.2021.08.011
- Yang, J., Zhou, J., Wang, Z., Zhou, Y., and Zhang, H. (2019). Structural Behavior of Ultrahigh-Performance Fiber-Reinforced Concrete Thin-Walled Arch Subjected to Asymmetric Load. *Adv. Civil Eng.* 2019, 1–12. doi:10.1155/2019/9276839
- Zhang, T., Ma, B., Jiang, D., Jiang, Q., and Jin, Z. (2021). Comparative Research on the Effect of Various mineral Admixtures on the Early Hydration Process of Cement. *Construction Building Mater.* 301, 124372. doi:10.1016/j.conbuildmat.2021.124372
- Zhang, Z., Liu, Y., Liu, J., and Zhang, N. (2021). Thermo-mechanical Behavior Simulation and Cracking Risk Evaluation on Steel-Concrete Composite Girders during Hydration Process. *Structures*. 33, 3912–3928. doi:10.1016/j.istruc.2021.06.101
- Zheng, X., and Wu, J. (2021). Early Strength Development of Soft Clay Stabilized by One-Part Ground Granulated Blast Furnace Slag and Fly Ash-Based Geopolymer. *Front. Mater.* 8, 616430. doi:10.3389/fmats.2021.616430
- Zhou, Y., Meng, D., and Wang, Y. (2014). Finite-Element Simulation of Hydration and Creep of Early-Age Concrete Materials. *J. Mater. Civ. Eng.* 26, 05014006. doi:10.1061/(ASCE)MT.1943-5533.0001105

- Zhu, B. F. (2012). *Temperature Stress and Temperature Control of Mass concrete*. Beijing, China: China water resources and Hydropower Press.
- Zhu, W., Feng, Q., Luo, Q., Bai, X., Chen, K., and Lin, X. (2022). Effect of a Specific PCE Superplasticizer on the Initial Dissolution and Early Hydration of Portland Cement. *J. Building Eng.* 46, 103786. doi:10.1016/j.jobbe.2021.103786

Conflict of Interest: JY and JW were employed by Guangxi Communications Investment Group Corporation Ltd.

The remaining authors declare that the research was conducted in the absence of any commercial or financial relationships that could be construed as a potential conflict of interest.

Publisher's Note: All claims expressed in this article are solely those of the authors and do not necessarily represent those of their affiliated organizations, or those of the publisher, the editors, and the reviewers. Any product that may be evaluated in this article, or claim that may be made by its manufacturer, is not guaranteed or endorsed by the publisher.

Copyright © 2022 Yang, Wang, Luo, Ding and Fan. This is an open-access article distributed under the terms of the Creative Commons Attribution License (CC BY). The use, distribution or reproduction in other forums is permitted, provided the original author(s) and the copyright owner(s) are credited and that the original publication in this journal is cited, in accordance with accepted academic practice. No use, distribution or reproduction is permitted which does not comply with these terms.



Interfacial Behavior of the Steel–UHPC Composite Deck With Toughened Epoxy Bonding

Jinlong Jiang^{1,2}, Jingchen Leng^{1,2}, Jiangtao Zhang^{1,2*} and Jincen Guo^{1,2}

¹State Key Laboratory of Mountain Bridge and Tunnel Engineering, Chongqing, China, ²School of Civil Engineering, Chongqing Jiaotong University, Chongqing, China

Using traditional stud connectors to connect the ultra-high-performance concrete layer and steel deck is detrimental to the construction speed and fatigue performance of the composite structure. Connecting the steel–UHPC interface with toughened epoxy bonding is a potential alternative to avoid this issue. To explore whether the toughened epoxy bonding interface can reduce the amount of bridge deck studs or even cancel the studs, a numerical simulation was conducted in this paper. The non-toughened epoxy bonding interface, the toughened epoxy bonding interface, a few studs + toughened epoxy bonding interface, and the full stud connection interface were designed to study the interfacial behavior of the steel–UHPC composite deck. Moreover, the constitutive model of the toughened epoxy bonding interface is verified through the direct shear test and compression-shear test. The results show that the maximum interface shear stress of the toughened epoxy bonding interface is 0.61 MPa under the standard wheel load, which is 20.78% lower than that of the non-toughened epoxy bonding interface. Under the overload, the interface failure of the toughened epoxy bonding interface is more concentrated and exhibits a smaller damage area compared with the non-toughened epoxy bonding interface. When the interface defect is 5%, the toughened epoxy bonding interface only has a few interface damages, exhibiting good defect tolerance. Compared to the traditional full stud connection interface, the interface shear stress in the few studs + toughened epoxy bonding interface is more uniform, which avoids the stress concentration in the root of studs, and the studs' average stress is significantly reduced by 63.21%. It is verified that using the toughened epoxy bonding interface can significantly reduce the amount of studs.

Keywords: epoxy, bonding, interfacial behavior, toughness, ultra-high- performance concrete

OPEN ACCESS

Edited by:

Zhigang Zhang,
Chongqing University, China

Reviewed by:

Fan Bai,
Beijing Jiaotong University, China
Chang Wu,
Southeast University, China

*Correspondence:

Jiangtao Zhang
zhangjiangtao@cqjtu.edu.cn

Specialty section:

This article was submitted to
Structural Materials,
a section of the journal
Frontiers in Materials

Received: 21 January 2022

Accepted: 14 March 2022

Published: 03 May 2022

Citation:

Jiang J, Leng J, Zhang J and Guo J
(2022) Interfacial Behavior of the
Steel–UHPC Composite Deck With
Toughened Epoxy Bonding.
Front. Mater. 9:859214.
doi: 10.3389/fmats.2022.859214

1 INTRODUCTION

The orthotropic steel bridge deck is the main deck form of a long-span steel bridge due to its lightweight and high-strength advantages. However, a wide range of application practices shows that there is fatigue cracking, pavement layer damage, and pavement layer interface failure of the orthotropic steel bridge deck (Wang et al., 2019a; Xu et al., 2021a). These defects are mainly caused by insufficient local stiffness, the weld density, and interface damage between the steel bridge deck and the pavement layer (Jong, 2004; Xu et al., 2021b; Li et al., 2021).

Cementitious composites have been extensively studied, including ECC, UHPC, and SHCC (Zhang et al., 2022). Ultra-high-performance concrete (UHPC), as a new type of steel fiber-reinforced concrete with high strength, high ductility, and excellent durability (Lian et al., 2021) (Zhang et al., 2021), can enhance the overall stiffness of the orthotropic steel bridge deck after forming a combined bridge deck system with the steel bridge deck. Therefore, it can solve the disease caused by the traditional asphalt pavement (Shao et al., 2013). In the steel-concrete composite bridge deck, UHPC, as a rigid pavement layer, can alleviate the fatigue cracking of the bridge deck structure and improve the crack resistance of the pavement layer (Shao et al., 2018a; Zhang et al., 2020). Murakoshi et al. (Murakoshi et al., 2008) used steel fiber concrete to conduct a rigid pavement for an orthotropic steel bridge deck and found that the stiffness of the bridge deck has been greatly improved, and the fatigue cracking of the steel bridge deck and the interface damage of the pavement layer have been well eliminated. Shao et al. proposed the steel-UHPC lightweight composite bridge deck (Shao et al., 2018a) and steel-ultrathin UHPC composite bridge deck (Shao et al., 2018b; Wang et al., 2020), respectively, for the steel-UHPC composite bridge deck system and verified the effect of UHPC on enhancing the stiffness of steel bridge deck pavement through experiments. However, the reliable connection between the UHPC layer and the steel bridge deck significantly affects the combined effect (Zou et al., 2018; Zou et al., 2021a). Affected by steel-concrete connection modes, the UHPC and the orthotropic bridge deck can be divided into the following two types of connection modes: mechanical connection parts, such as studs (Zou et al., 2020), and adhesives, such as epoxy adhesives (Duan et al., 2020). The stud connection technology has been relatively mature, which can ensure a reliable connection between the steel bridge deck and the prefabricated UHPC bridge deck. However, in practical engineering, steel bridge decks often need to be welded with a large number of studs. Welding defects and residual stresses are inevitably introduced in stud welding, which is unfavorable to the fatigue resistance of the orthotropic deck (Bouazaoui et al., 2007). Meanwhile, when UHPC is used as a structural layer of the orthotropic steel deck, the number of studs on a bridge deck may exceed millions, which brings heavy welding work (Shao et al., 2013). When epoxy bonding is used at the steel-concrete interface, both steel and concrete surfaces are fully bonded, avoiding stress concentration caused by welding studs (Si Larbi et al., 2009; Jurkiewicz et al., 2011) and uneven shear transfer (Zou et al., 2018), which is beneficial to the fatigue performance of steel structures (Qin et al., 2020).

Larbi et al. (Si Larbi et al., 2009) conducted shear and tensile tests on 11 (eleven) steel-concrete interface specimens and found that when the specimens are loaded in a single direction, the normal and tangential ultimate stresses at the epoxy-bonded interface are 3.5 and 6.4 MPa, respectively. Under the bidirectional loading condition, the shear and tensile ultimate stresses at the interface follow the quadratic relation. Berthet et al. (Berthet et al., 2011) carried out a shear test of the epoxy bond interface between steel and concrete and found that the shear strength of the epoxy bond interface is 3.4–5.4 MPa, which is greater than the shear strength of the concrete. Buitelaar et al. (Buitelaar et al., 2004) conducted an experimental study on

UHPC steel bridge decks and obtained that the stress concentration near the interface could be avoided when the steel plate surface was polished and applied with an epoxy adhesive before UHPC was poured. When the interface is subjected to normal tension, the bonding strength of the epoxy interface is 3–5 MPa. Q. Sun et al. (Sun et al., 2017) spread limestone evenly after applying epoxy on the steel plate and conducted the tensile test and push-out test on this interface form. The test results reveal that the UHPC-steel plate interface leads to high bonding performance under the single stress state of normal and tangential directions, and its tensile and shear strengths reach about 2 MPa. Luo (Luo et al., 2012) et al. simulated the mechanical properties of steel-concrete composite beams with a three-dimensional nonlinear finite element model based on push-out tests. The test results show that the epoxy adhesive between steel and concrete can provide a bond strength of 6.36 MPa, and the epoxy adhesive has a great influence on the mechanical properties of the composite beam. He et al. (He, 2020) conducted the shear test of the UHPC-steel interface and the positive bending moment loading test of the prefabricated UHPC-steel composite bridge deck. They found that the orthotropic composite bridge deck with epoxy has better ductility and higher bearing capacity and can guarantee the connection between the UHPC pavement and steel bridge deck. The above research results show that compared with the stud connectors, epoxy bonding between the interface of the steel-concrete composite structure is effective. Based on the existing research on the epoxy bonding interface, this paper introduces the quartz sand admixture while using an epoxy adhesive, aiming to realize the interface toughening between the UHPC pavement layer and orthotropic steel bridge deck.

Y. Zou et al. (Zou et al., 2021b) conducted direct shear tests, tensile tests, and tension-shear tests on the interface specimens, aiming to explore the mechanical properties of the prefabricated UHPC-steel interface with an epoxy adhesive. In this study, different admixtures were introduced in the previous epoxy bonding interface test, and the interface failure mode and interface shear tensile strength were analyzed. Based on the cohesive interface element, a numerical model of the tensile specimen was established to analyze the interface failure mechanism. The results show that the interface toughness is the best when the toughened epoxy bonding interface adopts the quartz sand bonding interface. In order to further verify the effect of an epoxy adhesive on the bending performance of the prefabricated UHPC-steel composite bridge deck, Jiang et al. (Jiang et al., 2021) carried out positive bending moment loading tests on specimens with different interface states. The results show that the bending performance is the best when the surface of the steel plate is rough and the surface of the prefabricated UHPC plate is grooved. This result is successfully verified by a finite element model based on the cohesive interface element.

In order to explore whether the toughened epoxy bonding interface can reduce the amount of bridge deck studs or even cancel the studs, this paper conducted the refined numerical simulation. The non-toughened epoxy bonding interface, the toughened epoxy bonding interface, a few studs + toughened epoxy bonding interface, and the full stud connection interface were designed to study the interfacial behavior of the steel-UHPC

composite deck. Moreover, the load cases, including local wheel load, UHPC shrinkage, and interface defects, were considered in the model.

2 CONSTITUTIVE MODEL OF COHESIVE INTERFACE ELEMENTS

The accuracy of the steel–UHPC composite deck model mainly depends on whether the constitutive of the toughened epoxy bonding interface can effectively reflect the interface's mechanical behavior. Both interfaces are simulated with zero-thickness cohesion elements (Jiang et al., 2021), but their respective constitutive behaviors are essentially different: the toughened epoxy bonding interface adopts the toughening-friction interface constitutive model, while the non-toughened epoxy bonding interface adopts a bilinear constitutive model (Zou et al., 2021b).

2.1 Bilinear Constitutive Model

The constitutive definition of the non-toughened epoxy bonding interface is divided into the elastic stage and failure stage. The failure process of the interface is mainly that the interface is not damaged in the elastic stage, the interface enters the failure stage immediately after reaching the ultimate load, and its bearing capacity is lost rapidly. This constitutive model is used for the non-toughened epoxy bonding interface in this paper, and the details are shown in **Figure 1**. The constitutive model is shown in

$$t_{n,s,t} = \begin{cases} t_{n,s,t}^0 \frac{\delta}{\delta_{n,s,t}^0} = K_{nn,ss,tt} \delta, & \delta \leq \delta_{n,s,t}^0, \\ t_{n,s,t}^0 \frac{\delta_{n,s,t}^f - \delta}{\delta_{n,s,t}^f - \delta_{n,s,t}^0}, & \delta_{n,s,t}^0 < \delta \leq \delta_{n,s,t}^f, \end{cases} \quad (1)$$

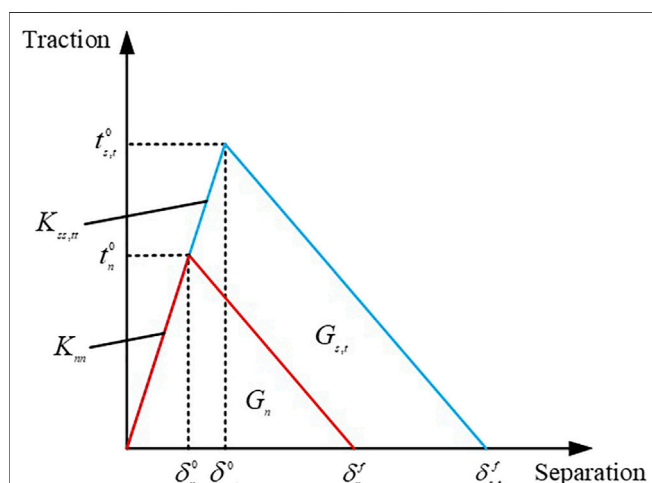


FIGURE 1 | Constitutive model of the cohesive interface element (bilinear constitutive model).

where t_n^0 , t_s^0 , and t_t^0 are the ultimate strengths of the interface; δ_n^0 , δ_s^0 , and δ_t^0 are the limit separation displacement values corresponding to the ultimate strength of the interface; and δ_n^f , δ_s^f , and δ_t^f are the limit separation displacements of the interface element. The above interface parameters are derived from the direct shear test and tensile test in the finite element model (Zou et al., 2021b). The specific calculation results are shown in **Table 1**.

2.2 Toughening-Friction Interface Constitutive Model

According to the toughening properties of the steel–UHPC epoxy toughened interface, based on the basic theory of the cohesive model, a toughening-friction interface constitutive model suitable for the zero-thickness cohesion element is proposed. Compared with the bilinear constitutive model, this interface constitutive model considers the plastic stage of the interface, and the normal compression in the failure stage will cause the interface tangential friction. In the finite element software ABAQUS, the bonding interface of quartz sand is simulated by the zero-thickness cohesion interface element, and the toughening-friction interface constitutive defined by the material is compiled by Fortran and realized by the subprogram VUMAT. The specific constitutive curve of the toughening-friction interface is shown in **Figure 2**. The constitutive model is as follows:

$$\sigma_{n,s,t} = \begin{cases} K_{nec,sec,tec} \delta_{n,s,t} & |\delta_{n,s,t}| \leq \delta_{nec,sc,tc}^0 \\ (K_{ndc,sdc,tdc} \delta_{n,s,t} + B_{ndc,sdc,tdc})(1 - D_1) & \delta_{nec,sc,tc}^0 < |\delta_{n,s,t}| \leq \delta_{nec,sc,tc}^1 \\ (K_{nfc,sfc,tf} \delta_{n,s,t} + B_{nfc,sfc,tf})(1 - D_f) & \delta_{nec,sc,tc}^1 < |\delta_{n,s,t}| \leq \delta_{nec,sc,tc}^f \end{cases} \quad (2)$$

where σ_n , σ_s , and σ_t are the traction stresses of the interface element along with the normal and tangential directions, respectively; δ_n , δ_s , and δ_t are the separation displacements of the interface element along with the normal and tangential directions, respectively; K_{iec} , K_{idc} , and K_{ifc} ($i = n, s, t$) are the slopes of the constitutive curves of the interface element in the elastic stage, plastic stage, and failure stage, respectively; B_{iec} , B_{idc} , and B_{ifc} ($i = n, s, t$) are the residual stresses of the interface element in the elastic stage, plastic stage, and failure stage, respectively; D_1 and D_f are the strength weakening coefficients, which control the interface damage and failure behavior in the plastic stage and failure stage, respectively; and the calculation expression is shown in **Eq. (3)**. In **Eq. (3)**, η_d is the strength-weakening parameter of the interface normal and tangential stress in the plastic stage, which is taken as 0.015 in the literature (Wu, 2019); δ_m is the spatial separation displacement of the interface element; δ_m^j ($j = 0, 1, f$) are the critical space separation displacements of the interface elements in each stage, and the calculation expression is shown in **Eq. (4)**.

TABLE 1 | Constitutive parameters of the non-toughened epoxy bonding interface.

Constitutive parameters	$t_{n,s,t}^0$ (MPa)	$K_{nn,ss,tt}$ (N/mm ³)	$G_{n,s,t}$ (N/mm)
Normal (n)	1.99	199	0.01194
Tangential (s)	3.63	454	0.02541
Tangential (t)	3.63	454	0.02541

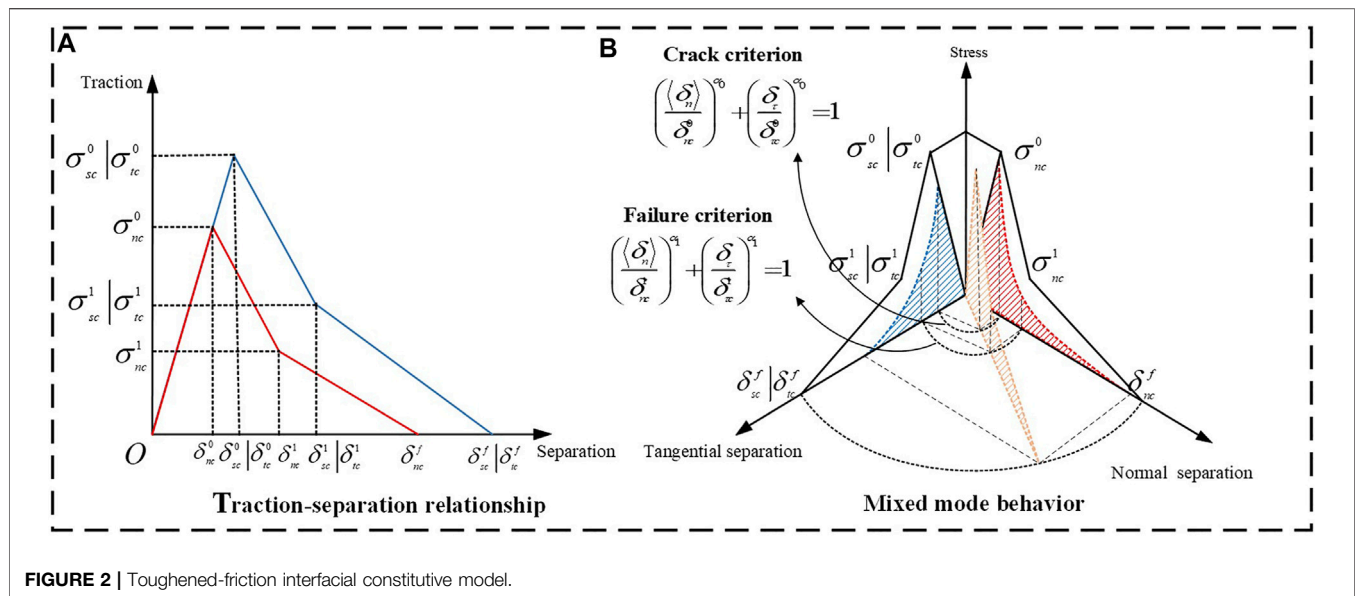


FIGURE 2 | Toughened-friction interfacial constitutive model.

TABLE 2 | Constitutive parameters of the toughened epoxy bonding interface.

Constitutive parameters	Interface stress/MPa		Interface displacement/mm		
	$\sigma_{nc}^0/\sigma_{sc}^0/\sigma_{tc}^0$	$\sigma_{nc}^1/\sigma_{sc}^1/\sigma_{tc}^1$	$\delta_{nc}^0/\delta_{sc}^0/\delta_{tc}^0$	$\delta_{nc}^1/\delta_{sc}^1/\delta_{tc}^1$	$\delta_{nc}^f/\delta_{sc}^f/\delta_{tc}^f$
Normal (n)	1.99	1.96	0.010	0.013	0.015
Tangential (s)	3.63	3.60	0.008	0.010	0.016
Tangential (t)	3.63	3.60	0.008	0.010	0.016

$$\left\{ \begin{array}{l} D_1 = \eta_d \frac{\delta_m^1 (\delta_m - \delta_m^0)}{\delta_m (\delta_m^1 - \delta_m^0)} \quad \delta_m^0 < \delta_m < \delta_m^1 \\ D_f = \frac{\delta_m^f (\delta_m - \delta_m^1)}{\delta_m (\delta_m^f - \delta_m^1)} \quad \delta_m^1 < \delta_m < \delta_m^f \end{array} \right. \quad (3)$$

$$\delta_m^j = \sqrt{(\delta_{nc}^j)^2 + (\delta_{sc}^j)^2 + (\delta_{tc}^j)^2}, j = 0, 1, f \quad (4)$$

The specific constitutive parameters of the ductile interface are shown in Table 2.

2.3 Validation

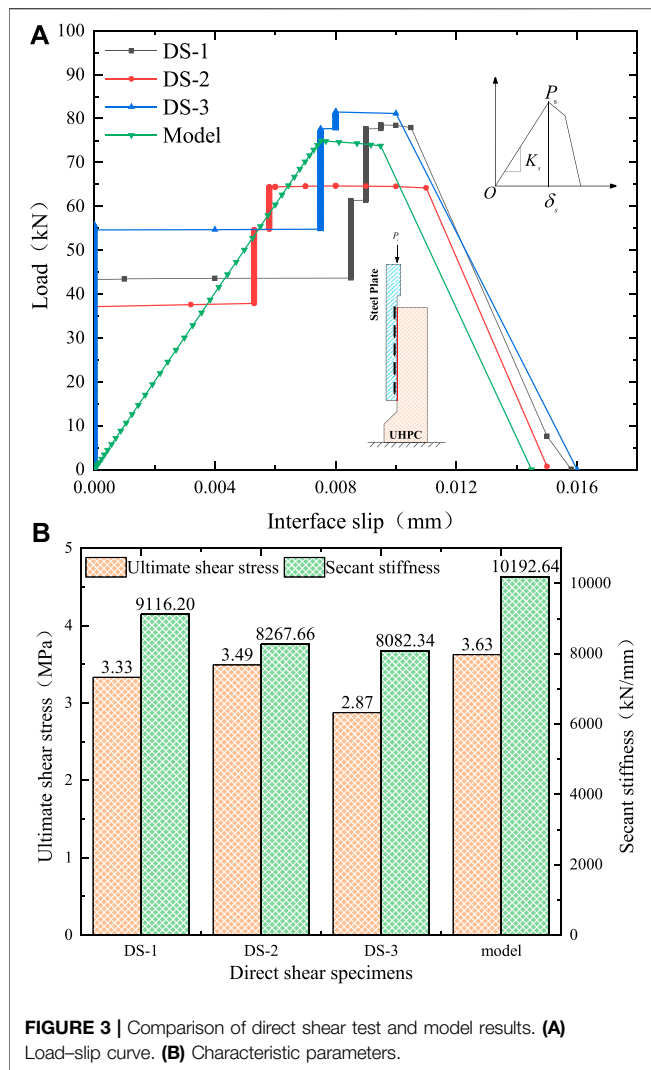
The accuracy of the steel-UHPC composite deck model mainly depends on whether the constitutive of the toughened epoxy bonding interface can effectively reflect the interface's mechanical behavior. Therefore, the toughened epoxy bonding interface constitutive will be validated in this paper. Compared with the direct shear test, the loading process of the interface in the compression shear test is still the elastic stage, plastic stage, and failure stage. However, the interface in the failure stage will be affected by tangential friction caused by normal pressure (Zou et al., 2021b). It can be seen that the toughened epoxy bonding interface has different mechanical behaviors in the direct shear state and the compression-shear state. Therefore, the interface simulation based on the toughening-friction interface constitutive model was carried out and validated by comparison

with experimental results (Zou et al., 2021b), aiming to effectively reflect the mechanical behavior of the toughened epoxy bonding interface in the state of direct shear and compression shear so as to fully verify the reliability and accuracy of the interface constitutive model.

2.3.1 Direct Shear Test

The comparison of the load-slip curves of the model and three direct shear specimens (DS-1, DS-2, and DS-3) is shown in Figure 3A. The load P_s is the ultimate vertical load applied to the specimen, the ultimate slip δ_s in the elastic stage is the tangential slip parallel to the interface, and the secant stiffness K_s of the curve is the ratio of P_s to δ_s . It can be seen from Figure 3A that the test values of the load-slip curves of the three direct shear specimens are in good agreement with the model values. In order to accurately compare the curve characteristics, the ultimate load P_s and secant stiffness K_s of each load-slip curve are extracted, respectively. The ultimate shear stress of the interface was calculated according to the formula proposed by Momayez et al. (Momayez et al., 2005), and the characteristic parameters of the curve are shown in Figure 1B.

It can be seen from Figure 3B that in the direct shear state, the ultimate shear stress of the toughened epoxy bonding interface is between 2.87 and 3.63 MPa, and the secant stiffness K_s is between 8,082.34 kN/mm and 10,192.64 kN/mm. Moreover, the

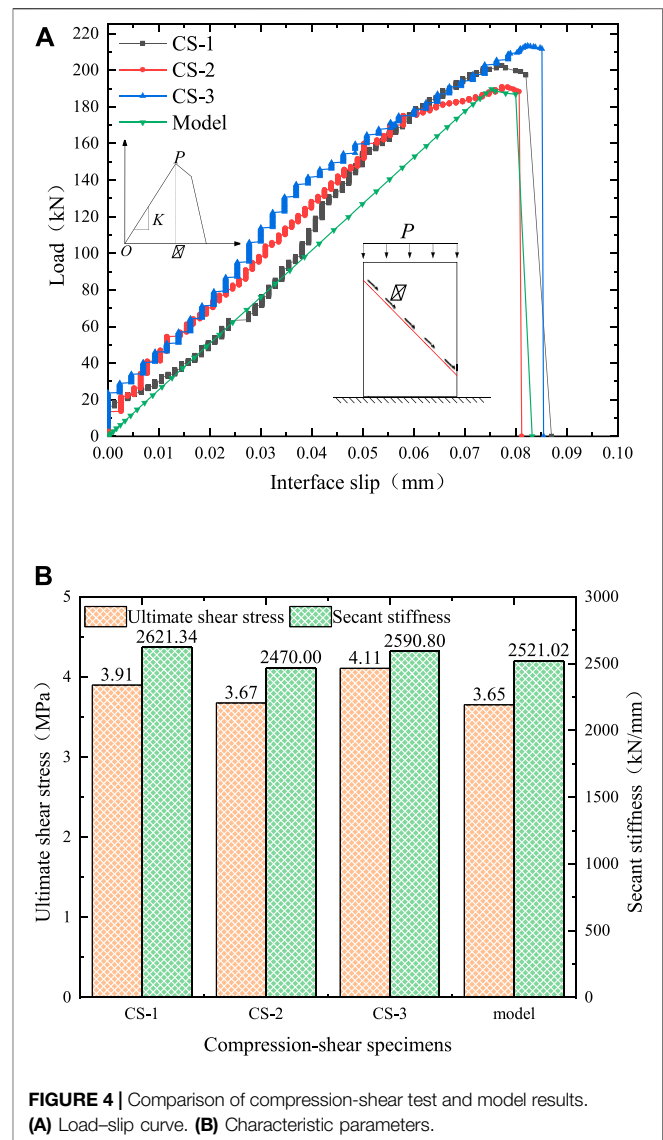


parameter comparison shows that the gap between the ultimate shear stress of the model and the specimen is -13.69% to 8.85%, and the secant stiffness K_s is -11.34% to 11.81%. The results show that the cohesive interface element defined by the toughening-friction interface constitutive model can well simulate the mechanical behavior of the toughened epoxy bonding interface in the direct shear state.

2.3.2 Compression-Shear Test

It can be seen from the curve changes of specimens CS-1, CS-2, and CS-3 in **Figure 4A** that the compression-shear action of the toughened epoxy bonding interface goes through loading processes of the elastic stage, plastic stage, and failure stage. Furthermore, the load-slip curves of the three compression-shear specimens are highly similar to the load-slip curves of the model. The ultimate load P and secant stiffness K of each load-slip curve are also extracted.

As shown in **Figure 4B**, in the compression-shear state, the ultimate shear stress of the toughened epoxy bonding interface



ranges from 3.67 to 4.11 MPa, which increases by 10.21–23.42% compared with the shear strength of the direct shear test. Since the interface friction improves the interface slip ability, the limit slip significantly increases, indicating that the overall interface performance is improved. In addition, through parameter comparison, it can be seen that the gap between the ultimate shear stress of the model and the specimen is 0.55–12.60%, and the secant stiffness K is -2.02% to 3.98%. The above analysis shows that the cohesive interface element defined by the toughening-friction interface constitutive model can well simulate the mechanical behavior of the toughened epoxy bonding interface under compression-shear stress.

In general, through the comparative analysis of the test results and the finite element interface simulation, the constitutive model of the toughened epoxy bonding interface is reliable.

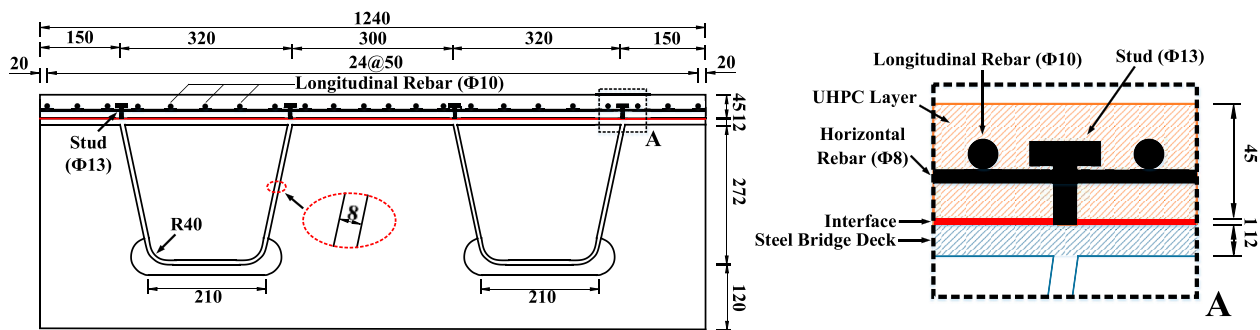


FIGURE 5 | Cross-section of the steel-UHPC composite deck (unit: mm).

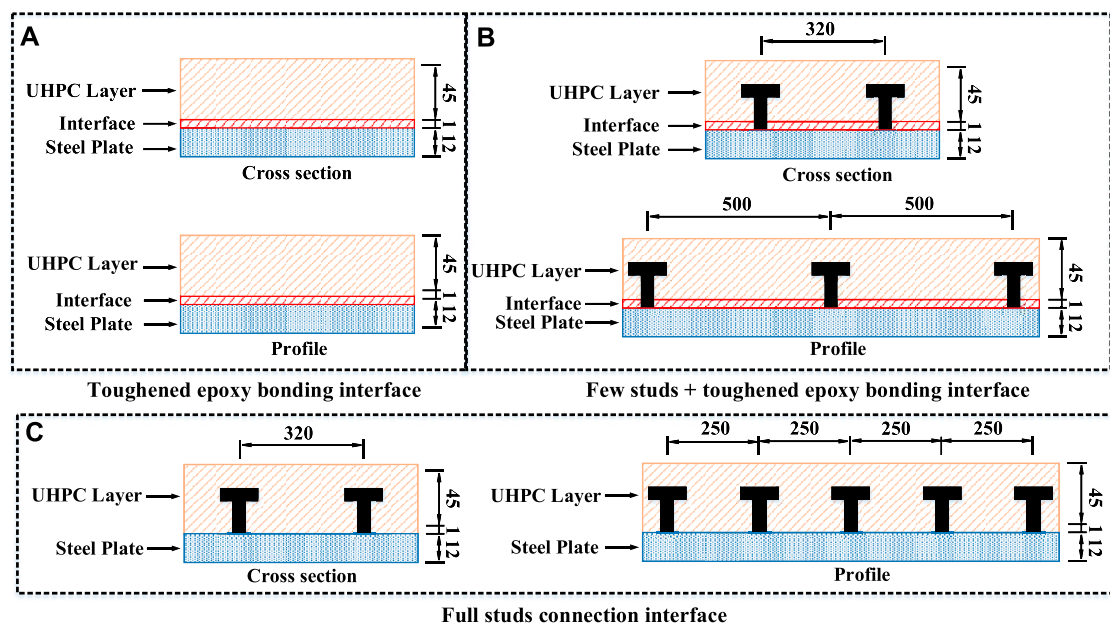


FIGURE 6 | Interface design of the steel-UHPC composite deck (unit: mm).

3 NUMERICAL MODEL

3.1 Modeling Scheme

The steel-UHPC composite deck numerically simulated in this paper is the local orthotropic steel bridge deck of Humen Bridge (Shao et al., 2013). As shown in **Figure 5**, the total width and thickness of the orthotropic steel bridge deck are 1240 and 12 mm, respectively. The thicknesses of U-shaped stiffening ribs and diaphragms are both 8 mm. On the steel bridge deck, the UHPC layer with a thickness of 45 mm is arranged with 25Φ10 rebars longitudinally and 68Φ10 rebars horizontally, and the size of the steel reinforcement mesh is 50 × 50 mm. The diameter of the bridge deck studs is 13 mm and the height after welding is 35 mm, and they are evenly arranged at the stiffening part of the steel bridge deck. In addition, different from the literature (Shao et al., 2013), a toughened epoxy bonding interface

layer with a thickness of 1 mm was added between the steel bridge deck and the UHPC layer. The longitudinal span of the entire model is 3,400 mm, the distance between the diaphragms along the longitudinal bridge direction is 3,000 mm, and the distance from the end of the composite bridge deck is 200 mm.

Two kinds of bonding interfaces are designed: the non-toughened epoxy bonding interface and toughened epoxy bonding interface. The detailed structure of each interface is shown in **Figure 6**, and the thickness of the interface layer is 1 mm. **Figure 6A** shows that the UHPC layer and the orthotropic steel bridge deck form a combined effect through the toughened epoxy bonding interface. One side of the interface and the surface of the steel plate are bonded by the epoxy layer, and the other side is paved with the UHPC layer by the embedding of quartz sand particles. In **Figure 6B**, for the few studs + toughened epoxy bonding interface, the longitudinal spacing of studs is 500 mm,

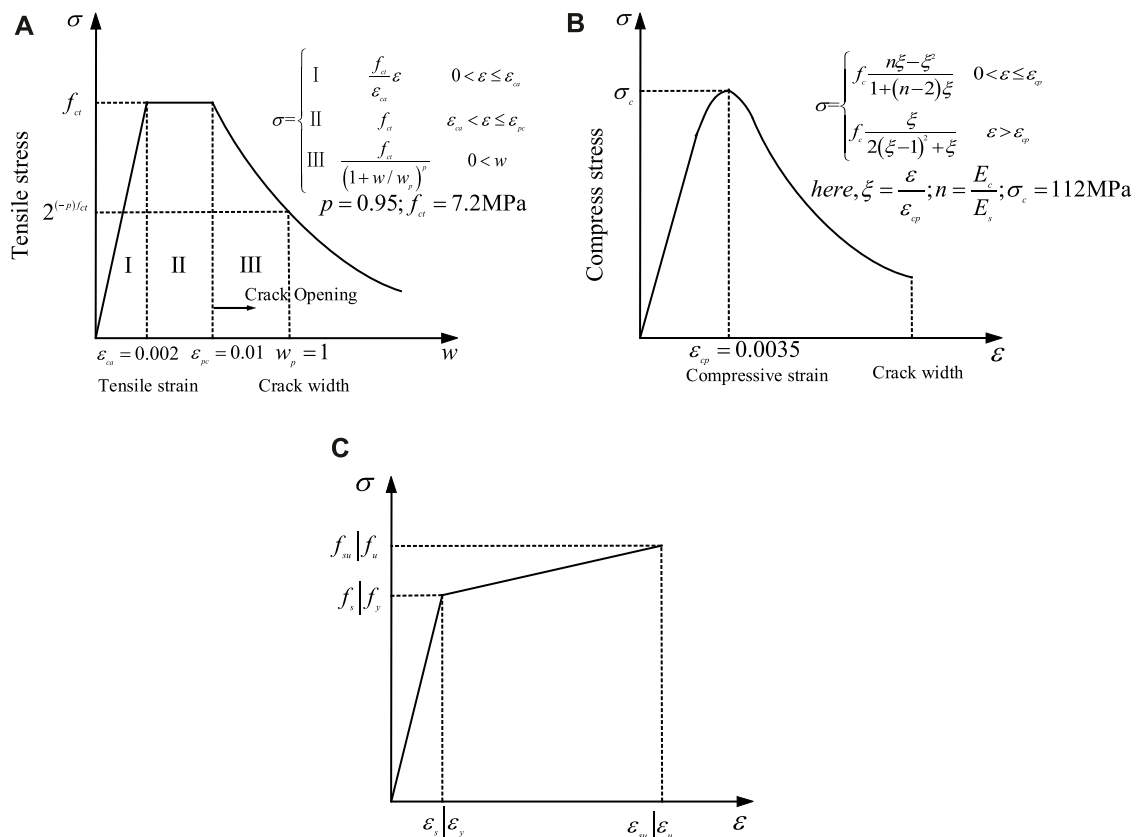


FIGURE 7 | Constitutive model of UHPC in (A) tension (Zhang et al., 2015), (B) compression (Yang, 2007), and (C) steel (Ministry of Housing and Urban-Rural Development of the People's Republic of China, 2015).

and the transverse studs are arranged at the stiffening part of the steel bridge deck with a spacing of 320 mm. Compared with the full stud connection interface, the amount of stud on the steel bridge deck is reduced by 50%; **Figure 6C** shows the full stud connection interface.

The orthotropic steel bridge deck mainly includes U-shaped stiffening ribs, diaphragms, and steel bridge decks in the numerical model. These components are all simulated using the three-dimensional 8-node linear solid element (C3D8), which can fully simulate the nonlinear behavior of the structure. The UHPC layer is simulated using three-dimensional solid elements. The steel reinforcement mesh is simulated with T3D2 trusses. Moreover, a zero-thickness cohesive interface element (COH3D8) is introduced into the finite element analysis to simulate the toughened epoxy bonding interface and the non-toughened epoxy bonding interface.

3.2 Constitutive Relation of Materials

As an elastic-plastic material, the damage and cracking behavior of UHPC can be defined by defining the CDP (concrete damaged plasticity) model in ABAQUS. In this paper, the tensile constitutive model is based on the stress-strain relationship proposed by Zhang (Zhang et al., 2015), as shown in

Figure 7A. The constitutive model of compression is based on the stress-strain relationship proposed by Yang (Yang, 2007), as shown in **Figure 7B.** In the tensile stress-strain relationship, f_{ct} is 7.2 MPa, ϵ_{ca} is 0.002, ϵ_{pc} is 0.01, w_p is 1, and p is 0.95. In the compressive stress-strain relationship, σ_c is 112 MPa, ϵ_{cp} is 0.0035, ϵ_{cu} is 0.01, E_c is 42,100 MPa, and E_s is 32,000 MPa. Poisson's ratio of UHPC is 0.2.

The stress-strain relationship of the steel and the rebar adopts the linear hardening elastoplastic constitutive model (Ministry of Housing and Urban-Rural Development of the People's Republic of China, 2015) (**Figure 7C**); that is, after the rebar stress reaches the yield stress, the stress increases to the ultimate strength with the increase of the strain. In the stress-strain relationship of the steel deck, f_s is 345 MPa, f_{su} is 400 MPa, ϵ_{su} is 0.001, and ϵ_{su} is 0.101. In the stress-strain relationship of rebar, f_s is 400 MPa, ϵ_s is 0.002, and ϵ_{su} is 0.103. In the stress-strain relationship of stud, f_s is 375 MPa, f_{su} is 450 MPa, and ϵ_{su} is 0.038.

3.3 Boundary Conditions

The existing interface test and numerical simulation results show that when using the cohesive interface element, the epoxy bonding interface layer between steel and concrete can be effectively simulated (Wang et al., 2019b; Jiang et al., 2021). Furthermore, the experimental results (Zou et al., 2021b) related

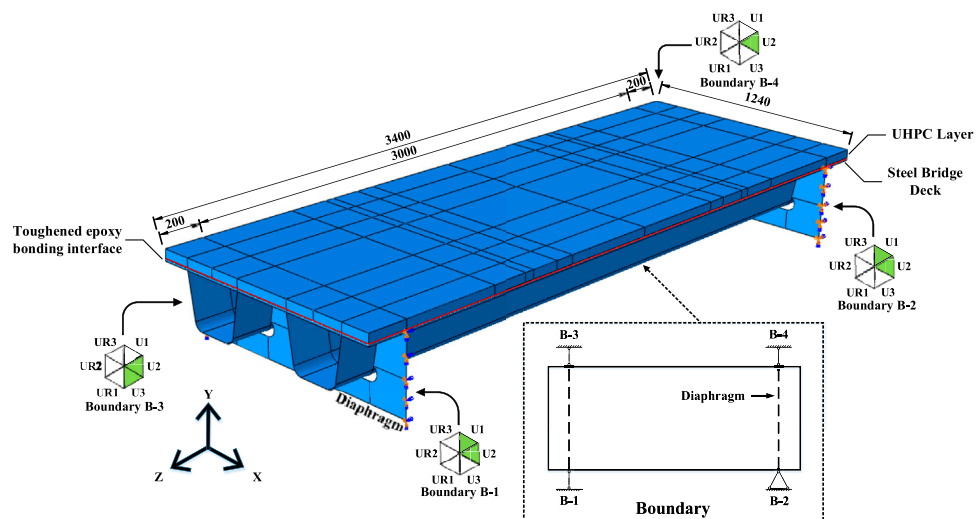


FIGURE 8 | ABAQUS finite element model.

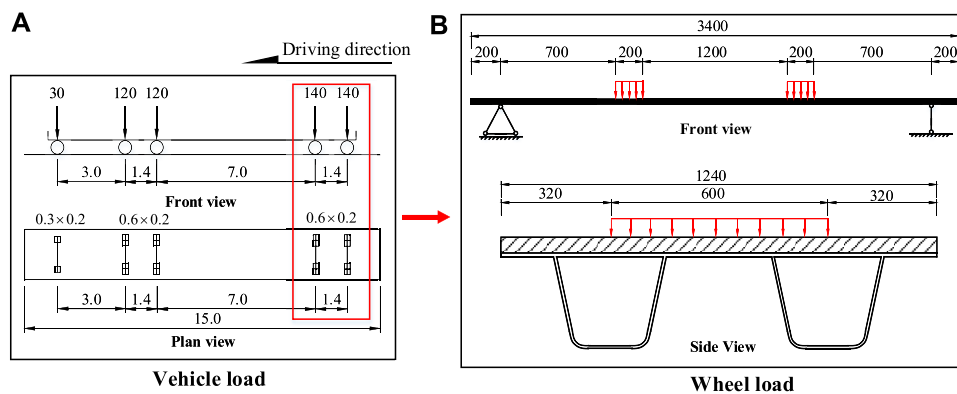


FIGURE 9 | Schematic diagram of local wheel load. (A) Vehicle load. (B) Wheel load (load unit: kN, size unit: mm).

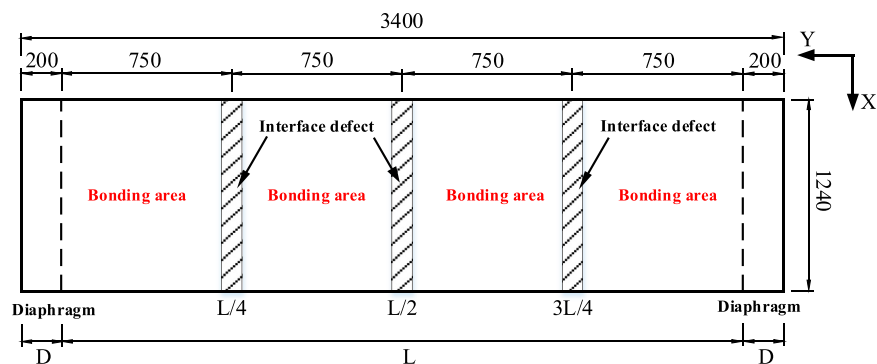
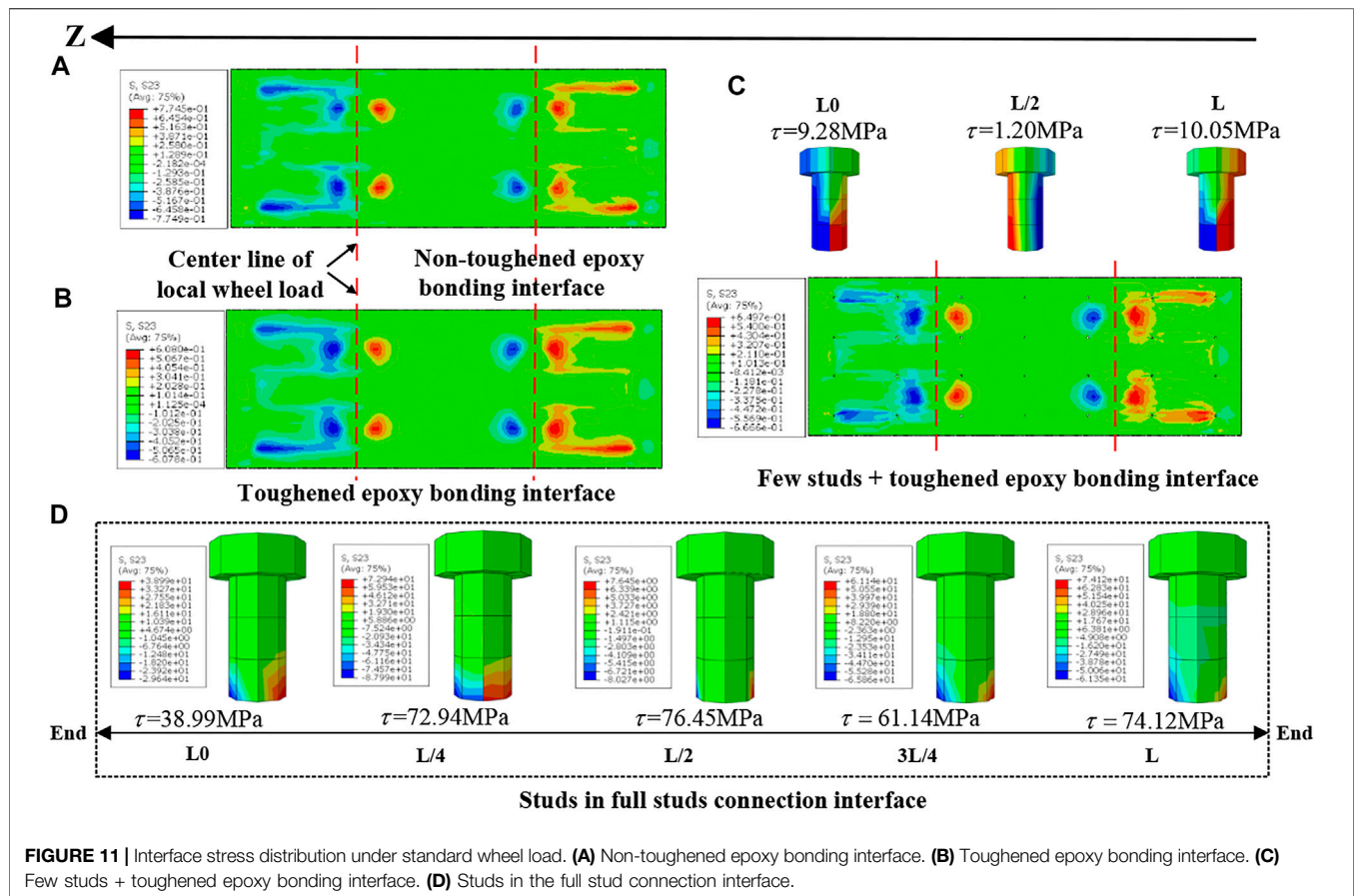


FIGURE 10 | Interface defect layout (unit: mm).



to the properties of the steel–UHPC interface show that when the steel–UHPC epoxy bonding interface is relatively thin, the epoxy layer and the steel plate interface are well bonded under pure tension or the pure shear state. Therefore, a zero-thickness cohesive interface element (COH3D8) in the model was generated by mesh offset of the steel bridge deck, and its numerical thickness was input through the material definition.

The internal constraints of the model are as follows: the U-shaped stiffening rib, diaphragms, and steel bridge decks are bound to each other achieved through “Tie” constraints; the constraint between studs and UHPC is the embedded region. The top surface of the interface layer and the bottom of the UHPC layer are bound by “Tie.” The steel reinforcement mesh is connected to the surrounding UHPC elements through embedded constraints. Given the low shear strength of the direct bond between ordinary concrete and the steel plate surface, which is only 0.4 MPa under ideal conditions, the cracked concrete will cause friction in the tangential direction of the interface (Tassios, 1979). Therefore, for the stud connection interface, the normal direction of the surface-to-surface contact properties between the UHPC layer and the steel bridge deck adopts the hard contact, and penalty function contact is adopted in the tangential direction, with a friction coefficient of 0.4 (Luo et al., 2016).

The boundary constraints of the steel–UHPC composite deck are all arranged on the side of the diaphragm. As shown in

Figure 8, both boundary B-1 and boundary B-2 only constrain the vertical and transverse translational degrees of freedom to prevent the bridge deck from flipping laterally. Boundary B-3 constrains the vertical and longitudinal translational degrees of freedom, and boundary B-4 only constrains the vertical translational degrees of freedom, ensuring the statically indeterminate system of the bridge deck structure.

3.4 Loading Scheme

The subprogram VUMAT realizes the toughening-friction interface constitutive model, and the model is calculated and solved by the ABAQUS/Explicit module. In order to ensure the calculation accuracy of the model and reduce the calculation time, the mass scaling factor set in the explicit analysis step is 100.

3.4.1 Local Wheel Load

According to Chinese codes, codes for design of highway bridges and culverts (JTG D60–2015) (Ministry of Transport of the People’s Republic of China, 2015), both Highway-I and Highway-II use a standard vehicle load with a total weight of 550 kN, and its specific layout is shown in Figure 9A. In the model, the wheel weight of the rear axle of the vehicle is 140 kN for bridge deck loading; that is, the weight of a single wheel is 70 kN, and the area acted by the wheel load is 0.6 m × 0.2 m. Referring to the relevant literature (Shao et al., 2013), the layout of the local wheel load is shown in Figure 9B. However, vehicle overloading on the

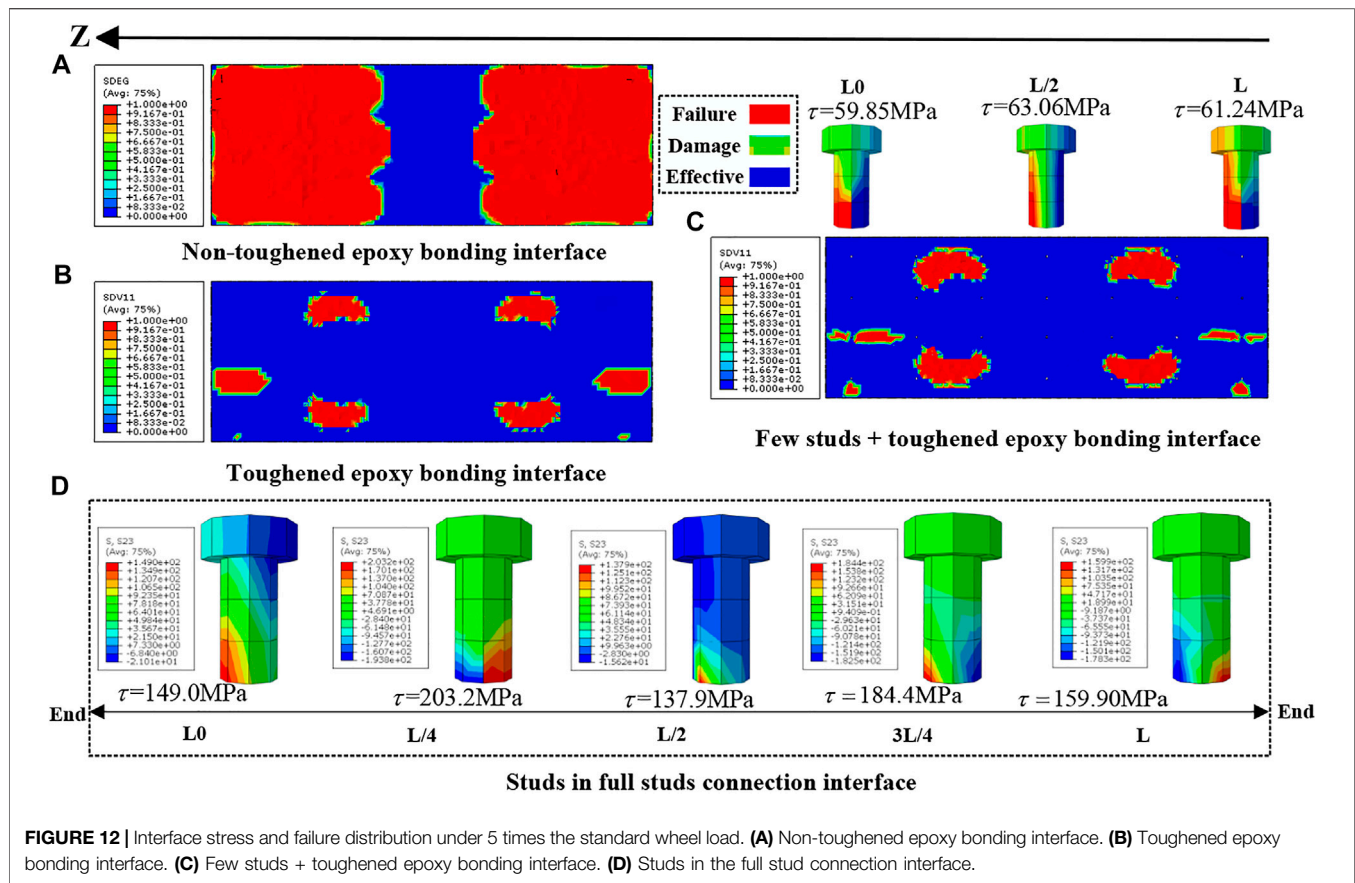


FIGURE 12 | Interface stress and failure distribution under 5 times the standard wheel load. **(A)** Non-toughened epoxy bonding interface. **(B)** Toughened epoxy bonding interface. **(C)** Few studs + toughened epoxy bonding interface. **(D)** Studs in the full stud connection interface.

bridge deck cannot be avoided in practical engineering. For this reason, the standard wheel load (70 kN) and the overload wheel load (350 kN), which is 5 times the standard wheel load, are considered in this paper.

3.4.2 Shrinkage of UHPC

Affected by the model's boundary conditions, the shrinkage of UHPC before and after curing will affect the stress state of the structure. In structural design, the shrinkage strain of UHPC is considered to be between 500 and 800 $\mu\epsilon$ (Chen et al., 2018; Kamen et al., 2008). Therefore, the UHPC shrinkage strain was set as 500 $\mu\epsilon$, and the equivalent temperature drop method was used to simulate the UHPC shrinkage in the model. After the amount of shrinkage strain ϵ_{cs} within a certain length of the structure is obtained, it can be approximated that the generation of shrinkage strain is equivalent to the decrease in temperature ΔT .

The relative temperature decrease ΔT can be calculated as follows:

$$\Delta T = \frac{\epsilon_{cs}}{\alpha} \quad (5)$$

where α is the linear expansion coefficient of UHPC, which is taken as $1 \times 10^{-5}/^\circ\text{C}$ (Luo et al., 2016). Therefore, the calculated relative temperature drop is 50°C .

3.4.3 Interface Defect Layout

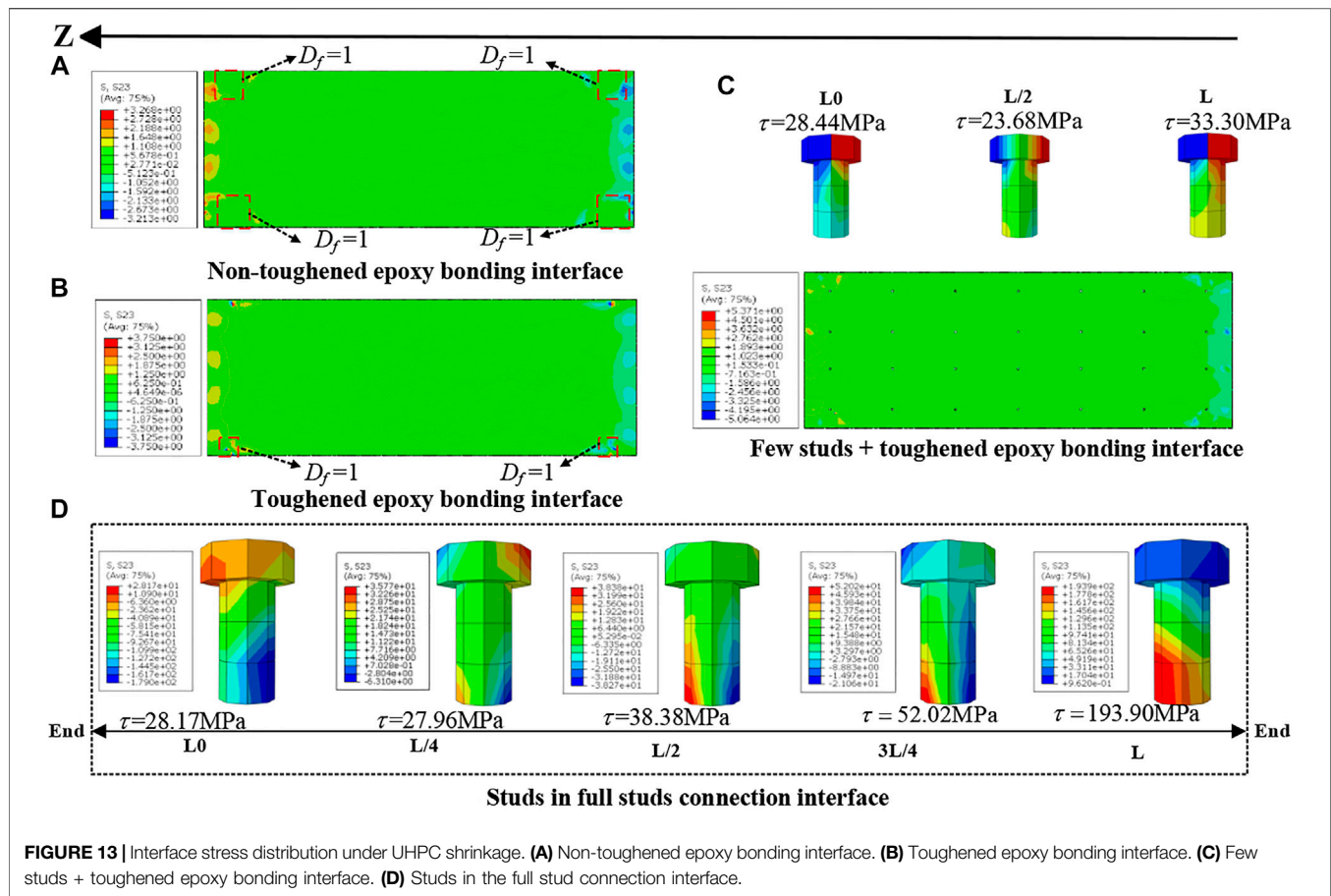
In practical engineering, the fluidity of the epoxy adhesive, inclusions or air bubbles at the interface, etc., may cause some interfaces to fail to bond effectively. Therefore, the relative bonding area becomes an important parameter for analyzing the toughened epoxy bonding interface. For prefabricated steel-concrete composite beams based on epoxy bonding, it is necessary to ensure that the relative bonding area is greater than 90% to avoid interfacial debonding damage (Luo et al., 2012). Considering the low shear strength of the toughened epoxy bonding interface, the relative bonding area is determined to be 95% in the model. The interface defects are concentrated in the L/4 span, L/2 span, and 3L/4 span along the longitudinal length of the bridge deck. The area of the void area is $1,240 \text{ mm} \times 50 \text{ mm}$. The distribution of the specific bonding area of the interface is shown in Figure 10.

4 ANALYSIS OF THE INTERFACE BEHAVIOR

4.1 Local Wheel Load

4.1.1 Standard Wheel Load

When the local wheel load is the standard wheel load (70 kN), the stress distribution of the four types of interfaces in the



steel-UHPC composite deck is shown in **Figure 11**. Here, the stress of each stud is the maximum stress of each row of studs, and the positive and negative directions of shear stress are shown in **Figure 11**. Comparing the toughened epoxy bonding interface with the non-toughened epoxy bonding interface, it can be found that the stress distribution of the two types of interfaces has the following characteristics: within the centerline of the local wheel load on both sides, the shear stress along the longitudinal interface is mainly concentrated near the wheel load area, and there is almost no shear stress at the mid-span; on the outside of the centerline, the shear stress is concentrated near the wheel load area and at the fulcrum. In this state, the interface cracking criterion QUADSCRT is less than 1 and the strength weakening coefficient is 0, indicating that both types of interfaces are in the elastic stage. As far as the shear stress value is concerned, the maximum shear stress of the toughened epoxy bonding interface inside and outside the centerline is both 0.61 MPa, which is 20.78% lower than that of the non-toughened epoxy bonding interface. It can be seen that the toughened epoxy bonding interface has a higher shear strength than the non-toughened epoxy bonding interface.

As shown in **Figure 11A,C**, under the standard load, the maximum shear stress of the studs in the full stud connection interface is mainly concentrated at the quarter-point and mid-span of the bridge deck, and the maximum shear stress is

76.45 MPa. The maximum shear stress at the fulcrum L_0 is 47.40% lower than that at the fulcrum L . Furthermore, the maximum shear stress values at both ends of the bridge deck are quite different, which is mainly caused by the constraint at the fulcrum L_0 . On the contrary, when the interface is a few studs + toughened epoxy bonding interface, the difference between the maximum shear stress values at the fulcrum L_0 and the fulcrum L is only 7.66%. The large reduction in stud shear stress may be due to the smaller model size. In this state, the toughened epoxy bonding interface's forward and reverse shear strengths are 0.65 and 0.67 MPa, respectively, and the interface is in the elastic stage.

4.1.2 Overload Wheel Load

When the local wheel load is 5 times the standard wheel load, the non-toughened epoxy bonding interface and the toughened epoxy bonding interface begin to enter the failure stage. The interface failure mode and the shear stress distribution of the stud are shown in **Figure 12**. Once the value of the indicator "SDEG" (D_1) or "SDV11" (D_f) is 1, it means that the interface has been destroyed. In **Figure 12A, B**, Under the overload, the non-toughened epoxy bonding interface immediately enters the failure stage after reaching the ultimate shear stress, resulting in a large failure area that extends from the wheel load area to the end of the composite bridge deck. In contrast, the toughened epoxy bonding interface mainly manifests as a small-scale failure

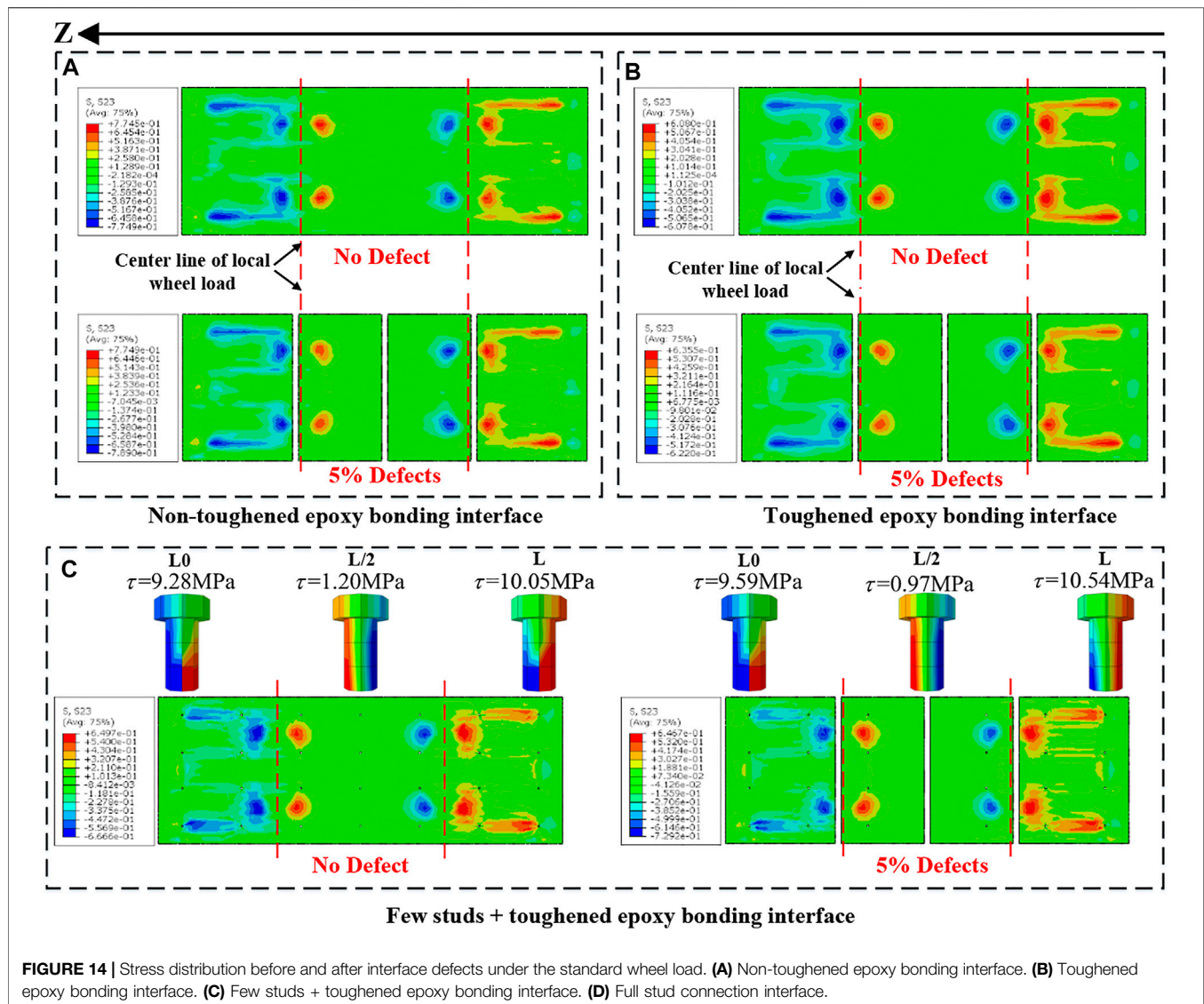


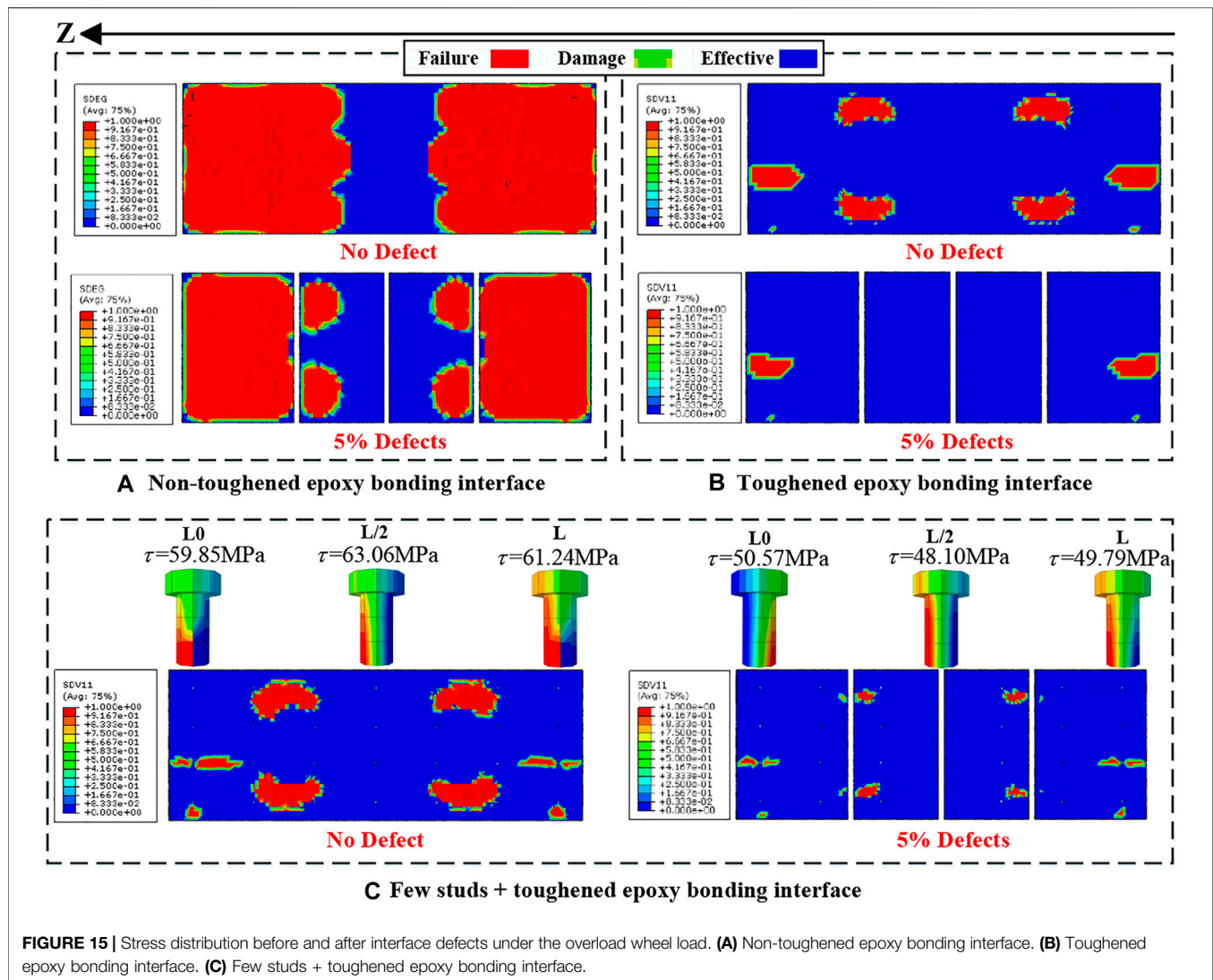
FIGURE 14 | Stress distribution before and after interface defects under the standard wheel load. **(A)** Non-toughened epoxy bonding interface. **(B)** Toughened epoxy bonding interface. **(C)** Few studs + toughened epoxy bonding interface. **(D)** Full stud connection interface.

in the wheel load region and at both ends. This is mainly because during the initial failure of the toughened epoxy bonding interface, the undamaged area around enters the plastic stage first, which greatly delays the failure process of the toughened epoxy bonding interface. Therefore, the toughened epoxy bonding interface can indeed improve the toughness of the steel-UHPC interface when the interface is damaged.

In the full stud connection interface, the shear stress distribution of the studs along the longitudinal bridge has the following characteristics (**Figure 12D**): the stud shear stress is mainly concentrated at the quarter point, and the maximum shear stress is 203.2 MPa, which is only 7.32% different from that of the stud at the fulcrum. For a few studs + toughened epoxy bonding interface, affected by the toughening of the interface, the interface failure area is concentrated in the wheel load area and near the stud's root, and the studs' average stress is significantly reduced by 63.21% compared with the full stud connection interface, which can be seen in **Figure 12C**.

4.2 Shrinkage of UHPC

After cooling by 50°C to simulate the shrinkage performance of UHPC, the stress distribution of each interface is shown in **Figure 13**, and the area surrounded by red is the concentration of shear stress at the interface. It can be seen from **Figure 13A,B** that the shear stress of the non-toughened epoxy bonding interface and the toughened epoxy bonding interface is mainly concentrated at both ends of the steel-UHPC composite bridge deck. Unlike the former, the maximum shear stress of the latter occurs at the bridge deck fulcrum. In both interfaces, as shown in **Figure 13A,B**, the stiffness degradation parameter SDEG and strength weakening coefficient D_f near the fulcrum are equal to 1, indicating that the interface has been damaged. However, compared with the small-scale failure of the toughened epoxy bonding interface at the fulcrum, the non-toughened epoxy bonding interface has a larger area of failure at the end of the bridge deck. It can be seen that the shear stress of the toughened epoxy bonding interface is relatively concentrated, and the failure area is smaller than that of the non-toughened epoxy bonding interface.



It can be seen from **Figure 13D** that the shear stress of the stud at the fulcrum L in the full stud connection interface differs by 85.47% from that of the stud at the fulcrum L_0 . The main reason is that the shrinkage effect at the fulcrum L_0 is suppressed due to the constraints of its boundary conditions. Meanwhile, **Figure 13C** shows that the shear stress of the stud is significantly reduced after combining the stud and the non-toughened epoxy bonding interface. Moreover, the shear stress of the stud at fulcrums L_0 and L is only 14.60% different. Therefore, the toughened epoxy bonding interface can significantly reduce the shear stress of the stud and make the stress distribution of the interface more uniform. Moreover, the existence of studs can further improve the shear performance of the toughened epoxy bonding interface.

4.3 Effects of Interface Defects

4.3.1 Standard Wheel Load

Five percent interface defects are arranged at the bonding interface of the bridge deck, and the interface stress

distribution under the standard wheel load (70 kN) is obtained, as shown in **Figure 14**.

It can be seen from **Figure 14** that before and after the epoxy bonding interface defect, the shear stress distribution of studs and interfaces in various interfaces basically does not change. As shown in **Figure 14A,B**, before the interface defect, the maximum shear stress in the positive and negative directions of the toughened epoxy bonding interface is 20.78% different from that of the non-toughened epoxy bonding interface. After the interface defect, the maximum shear stress in the positive and negative directions of the interface differs by 16.88 and 21.52%, respectively. This indicates that the toughened epoxy bonding interface can significantly reduce the interface shear stress after the defect. **Figure 14C** shows the shear stress distribution between the stud and the interface. It can be seen from the figures that after the interface defect, the maximum shear stress of the toughened epoxy bonding interface only increased by 8.96% in the positive direction, and the shear stress of each stud increased slightly. Therefore, it can be shown that under the

standard wheel load, the few studs + toughened epoxy bonding interface can still work normally after 5% defects, and the toughened epoxy bonding interface is still in the elastic stage.

4.3.2 Overload Wheel Load

Figure 15 shows various interfaces' damage and stress distribution under five times the standard wheel load (350 kN). In **Figure 15A**, after the non-toughened epoxy bonding interface defects, the interface failure range does not expand anymore. In addition, the interface failure in the wheel load area is no longer concentrated and slightly reduced. In **Figure 15B**, after the toughened epoxy bonding interface defects, the interface failure is mainly concentrated at the interface of both ends, and the failure area is greatly reduced. Comparing **Figure 15A,B**, it can be found that on one hand, interface defects do not significantly change the stress state of the interface; on the other hand, the toughened epoxy bonding interface still exhibits good toughening properties even after interface defects. **Figure 15C** shows that the shear stress of the toughened epoxy bonding interface in the few studs + toughened epoxy bonding interface is significantly reduced after the interface defects. The failure area is significantly more concentrated, and the shear stress of the stud is reduced. It may be due to the relief of stress concentration and interface toughness at the defect.

5 CONCLUSION

To explore whether the toughened epoxy bonding interface can reduce the amount of bridge deck studs or even cancel the studs, this paper designed four types of interfaces to study the interfacial behavior of the steel-UHPC composite deck. The load cases, including local wheel load, UHPC shrinkage, and interface defects, were considered in the numerical simulation. Moreover, the constitutive model of the toughened epoxy bonding interface is validated through the direct shear test and compression-shear test. The main conclusions are summarized as follows:

- (1) The maximum interface shear stress of the toughened epoxy bonding interface is 0.61 MPa under the standard wheel load, which is 20.78% lower than that of the non-toughened epoxy bonding interface. The toughened epoxy bonding interface mainly manifests as interface failure in the wheel load region and a smaller range at the interface of both ends. Moreover, the undamaged area around enters the plastic stage first, which greatly delays the failure process of the toughened epoxy bonding interface. However, the non-toughened epoxy bonding interface will fail rapidly once they enter the failure stage.
- (2) For a few studs + toughened epoxy bonding interface, due to the sufficient bonding between the UHPC layer and steel bridge deck, the maximum shear stress of the stud is

61.24 MPa under the overload (350 kN). The interface shear stress is more uniform than that in the full stud connection interface, which avoids the stress concentration in the root of studs, and the studs' average stress is significantly reduced by 63.21%. Therefore, the toughened epoxy bonding interface can indeed improve the toughness of the steel-UHPC interface. It is verified that using the toughening epoxy bonding interface can reduce the amount of studs.

- (3) Before the interface fails, the interface shearing effect is borne together with the bridge deck studs, the toughened epoxy bonding interface mainly bears the shear force, and the stud stress is relatively small. Even if the local interface failure begins, the shear resistance of the interface is still dominated by the toughened epoxy bonding interface, and the stud stress is significantly lower compared with the few studs + toughened epoxy bonding interface.
- (4) When the interface defect is 5%, the interface stress under the standard load in both toughened epoxy bonding interfaces is only 0.635 and 0.646 MPa, respectively. At this time, large area failure occurs at the non-toughened epoxy bonding interface under the overload. However, the toughened epoxy bonding interface only has a few interface damages, exhibiting good defect tolerance (Chen et al., 2018; Kamen et al., 2008).

DATA AVAILABILITY STATEMENT

The original contributions presented in the study are included in the article/Supplementary Material, further inquiries can be directed to the corresponding author.

AUTHOR CONTRIBUTIONS

These authors have made great contributions in the field of the steel-concrete composite structure and high-performance concrete material.

FUNDING

The authors express their sincere gratitude for the financial support provided by the National Natural Science Foundation of China (Grant Nos. 52008066), the Natural Science Foundation of Chongqing, China (Grant Nos. cstc2020jcyj-msxmX0088), the Science and Technology Project of Chongqing Municipal Education Commission (Grant Nos. KJQN201900733), and the Science and Technology Project of Hubei Provincial Transportation Department (Grant Nos. 2020-2-1-1 and 2020-186-1-8).

REFERENCES

- Berthet, J. F., Yurttdas, I., Delmas, Y., and Li, A. (2011). Evaluation of the Adhesion Resistance between Steel and concrete by Push Out Test. *Int. J. Adhes. Adhesives* 31 (2), 75–83. doi:10.1016/j.ijadhadh.2010.11.004
- Bouazouai, L., Perrenot, G., Delmas, Y., and Li, A. (2007). Experimental Study of Bonded Steel concrete Composite Structures. *J. Constructional Steel Res.* 63 (9), 1268–1278. doi:10.1016/j.jcsr.2006.11.002
- Buitelaar, P., Rene, B., and Neik, K. (2004). “Reinforced High Performance concrete Overlay System for Steel Bridges,” in Proceedings of the 5th International CROW Workshop On Fundamental Modelling of the Design and Performance of Concrete Pavements, Turkey, August 2004 (Istanbul).
- Chen, B., Li, C., Huang, W., An, M. Z., Han, S., and Ding, Q. J. (2018). Review of Ultra-high Performance concrete Shrinkage. *J. Traffic Transportation Eng.* 18 (01), 13–28. doi:10.19818/j.cnki.1671-1637.2018.01.002
- Duan, L., Brühwiler, E., and Wang, C.-s. (2020). Cold Stiffening of Orthotropic Steel Decks by a Composite UHPFRC Layer. *J. Constructional Steel Res.* 172, 106209. doi:10.1016/j.jcsr.2020.106209
- He, X. Y. (2020). Mechanical Properties of Orthotropic Steel Deck with Epoxy Adhesively Bonded Rigid Pavement. *J. Harbin Inst. Tech.* 52 (9), 25–31. doi:10.11918/201910033
- Jiang, J., Zou, Y., Yang, J., Zhou, J., Zhang, Z., and Huang, Z. (2021). Study on Bending Performance of Epoxy Adhesive Prefabricated UHPC-Steel Composite Bridge Deck. *Adv. civil Eng.* 2021, 1–16. doi:10.1155/2021/6658451
- Jong, D. (2004). “Overview Fatigue Phenomenon in Orthotropic Bridge Decks in the Netherlands,” in Proceedings of 2004 Orthotropic Bridge Conference, Sacramento, CA, USA, Aug 2004 (ASCE), 489.
- Jurkiewicz, B., Meaud, C., and Michel, L. (2011). Non Linear Behaviour of Steel-concrete Epoxy Bonded Composite Beams. *J. Constructional Steel Res.* 67 (3), 389–397. doi:10.1016/j.jcsr.2010.10.002
- Kamen, A., Denarié, E., Sadouki, H., and Brühwiler, E. (2008). Thermo-mechanical Response of UHPFRC at Early Age - Experimental Study and Numerical Simulation. *Cement Concrete Res.* 38 (6), 822–831. doi:10.1016/j.cemconres.2008.01.009
- Li, Z. X., Chan, T. H. T., and Ko, J. M. (2021). Fatigue Damage Model for Bridge under Traffic Loading: Application Made to Tsing Ma Bridge. *Theor. Appl. Fracture Mech.* 35, 81–91. doi:10.1016/S0167-8442(00)00051-3
- Lian, J., Hu, C., Fu, T., and Wang, Y. (2021). Review of Self-Sensing Capability of Ultra-high Performance Concrete. *Front. Mater.* 8, 746022. doi:10.3389/fmats.2021.746022
- Luo, Y., Hoki, K., Hayashi, K., and Nakashima, M. (2016). Behavior and Strength of Headed Stud-SFRCC Shear Connection. I: Experimental Study. *J. Struct. Eng.* 142 (2), 4015112 1–4015112 10. doi:10.1061/(asce)st.1943-541x.0001363
- Luo, Y., Li, A., and Kang, Z. (2012). Parametric Study of Bonded Steel-concrete Composite Beams by Using Finite Element Analysis. *Eng. Structures* 34, 40–51. doi:10.1016/j.engstruct.2011.08.036
- Ministry of Housing and Urban-Rural Development of the People's Republic of China (2015). *Code for Design of Concrete Structures (GB 50010-2010)*. Beijing, China: China Planning Press. [in Chinese].
- Ministry of Transport of the People's Republic of China (2015). *General Specifications for Design of Highway Bridges and Culverts: JTG D60-2015*. Beijing: People's Communication Press. [in Chinese].
- Momayez, A., Ehsani, M. R., Ramezani-pour, A. A., and Rajaie, H. (2005). Comparison of Methods for Evaluating Bond Strength between concrete Substrate and Repair Materials. *Cement Concrete Res.* 35 (4), 748–757. doi:10.1016/j.cemconres.2004.05.027
- Murakoshi, J., Yanadori, N., and Ishii, H. (2008). “Research on Steel Fiber Reinforced concrete Pavement on Orthotropic Steel Deck,” in Proceedings of the 2nd International Orthotropic Bridge Conference, Sacramento.
- Qin, F., Zhang, Z., Yin, Z., Di, J., Xu, L., and Xu, X. (2020). Use of High Strength, High Ductility Engineered Cementitious Composites (ECC) to Enhance the Flexural Performance of Reinforced concrete Beams. *J. Building Eng.* 32, 101746. doi:10.1016/j.job.2020.101746
- Shao, X., Yi, D., Huang, Z., Zhao, H., Chen, B., and Liu, M. (2013). Basic Performance of the Composite Deck System Composed of Orthotropic Steel Deck and Ultrathin RPC Layer. *J. Bridge Eng.* 18 (5), 417–428. doi:10.1061/(ASCE)BE.1943-5592.0000348
- Shao, X., Qu, W., Cao, J., and Yao, Y. (2018). Static and Fatigue Properties of the Steel-UHPC Lightweight Composite Bridge Deck with Large U Ribs. *J. Constructional Steel Res.* 148, 491–507. doi:10.1016/j.jcsr.2018.05.011
- Shao, X.-D., Gan, Q.-D., Li, J., and Qiu, M.-H. (2018). Interfacial Shear Resistance of Welded Structure of Composite Deck System Composed of Orthotropic Deck and Ultrathin UHPC Layer. *China J. Highw. Transport* 31 (11), 91–101. doi:10.3969/j.issn.1001-7372.2018.11.010
- Si Larbi, A., Ferrier, E., and Hamelin, P. (2009). Concrete to Steel Lap Joint Failure Criteria under Combined Shear and Peeling Stress. *J. Constructional Steel Res.* 65 (2), 386–394. doi:10.1016/j.jcsr.2008.03.012
- Sun, Q., Lu, X., Nie, X., Han, Z., and Fan, J. (2017). Experimental Research on Tensile and Shear Behaviour of the Interface between Non-steam-cured Uhpcc and Steel Plate Structure. *Mech. Eng.* 34 (9), 167–174. [in Chinese]. doi:10.6052/j.issn.1000-4750.2016.05.0361
- Tassios, T. P. (1979). Properties of Bond between concrete and Steel under Load Cycles Idealizing Seismic Actions. *Rome: Proceeding AICAP-CEB Symp. CEB Bull. d'Information*. 131, 67–122. doi:10.1680/rceuc1.35485.0005
- Wu, S. (2019). *Study on Interfacial Characteristics of Steel Deck Pavement with Engineered Cementitious Composites*. Doctor: southeast university, 148.
- Wang, Z., Wang, Y., and Zheng, Y. (2019). Analysis of Fatigue Crack Propagation of an Orthotropic Bridge Deck Based on the Extended Finite Element Method. *Adv. Civil Eng.* 2019, 1–14. doi:10.1155/2019/6319821
- Wang, Z., Nie, X., Fan, J.-S., Lu, X.-Y., and Ding, R. (2019). Experimental and Numerical Investigation of the Interfacial Properties of Non-steam-cured UHPC-Steel Composite Beams. *Construction Building Mater.* 195 (20), 323–339. doi:10.1016/j.conbuildmat.2018.11.057
- Wang, L. G., Shao, X.-D., Cao, J. H., Chen, Y. B., He, G., and Wang, Y. (2020). Performance of Steel-Ultrathin UHPC Composite Bridge Deck Based on Ultra-short Headed Studs. *J. Zhejiang Univ. (Engineering Science)* 54 (10), 2027–2037. doi:10.3785/j.issn.1008-973X.2020.10.021
- Xu, J.-H., Zhou, G.-D., and Zhu, T.-Y. (2021). Fatigue Reliability Assessment for Orthotropic Steel Bridge Decks Considering Load Sequence Effects. *Front. Mater.* 8, 678855. doi:10.3389/fmats.2021.678855
- Xu, Y., Lv, X., Ma, C., Liang, F., Qi, J., Chou, Z., et al. (2021). Shear Fatigue Performance of Epoxy Resin Waterproof Adhesive Layer on Steel Bridge Deck Pavement. *Front. Mater.* 7, 618073. doi:10.3389/fmats.2020.618073
- Yang, J. (2007). *Flexural Behavior of Ultra-high Performance Concrete Beams Prestressed with CFRP Tendons*. Changsha, China: Hunan University.
- Zhang, Z., Shao, X., Li, W., Zhu, P., and Chen, H. (2015). Axial Tensile Behavior Test of Ultra High Performance concrete China. *J. Traffic Transportation Eng.* 28 (8), 50–58. doi:10.19721/j.cnki.1001-7372.2015.08.007
- Zhang, X., Li, X., Liu, R., Hao, C., and Cao, Z. (2020). Dynamic Properties of a Steel-UHPC Composite Deck with Large U-Ribs: Experimental Measurement and Numerical Analysis. *Eng. Structures* 213, 1–14. doi:10.1016/j.engstruct.2020.110569
- Zhang, Z., Liu, S., Yang, F., Weng, Y., and Qian, S. (2021). Sustainable High Strength, High Ductility Engineered Cementitious Composites (ECC) with Substitution of Cement by rice Husk Ash. *J. Clean. Prod.* 317, 128379. doi:10.1016/j.jclepro.2021.128379
- Zhang, Z., Liu, D., Ding, Y., and Wang, S. (2022). Mechanical Performance of Strain-Hardening Cementitious Composites (SHCC) with Bacterial Addition. *J. Infrastruct Preserv Resil* 3 (3). doi:10.1186/s43065-022-00048-3
- Zou, Y., Zhou, X. H., Di, J., and Qin, F. J. (2018). Partial Interaction Shear Flow Forces in Simply Supported Composite Steel-concrete Beams. *Adv. Steel Construction* 14 (4), 634–650. doi:10.18057/IJASC.2018.14.7
- Zou, Y., Di, J., Zhou, J., Zhang, Z., Li, X., Zhang, H., et al. (2020). Shear Behavior of Perfobond Connectors in the Steel-concrete Joints of Hybrid

- Bridges. *J. Constructional Steel Res.* 172, 106217. doi:10.1016/j.jcsr.2020.106217
- Zou, Y., Qin, F., Zhou, J., Zheng, Z., Huang, Z., and Zhang, Z. (2021). Shear Behavior of a Novel Bearing-Shear Connector for Prefabricated concrete Decks. *Construction Building Mater.* 268, 121090. doi:10.1016/j.conbuildmat.2020.121090
- Zou, Y., Jiang, J., Zhou, Z., Wang, X., and Guo, J. (2021). Study on the Static Performance of Prefabricated UHPC-Steel Epoxy Bonding Interface. *Adv. civil Eng.* 2021 (4), 1–15. doi:10.1155/2021/6663517

Conflict of Interest: The authors declare that the research was conducted in the absence of any commercial or financial relationships that could be construed as a potential conflict of interest.

Publisher's Note: All claims expressed in this article are solely those of the authors and do not necessarily represent those of their affiliated organizations or those of the publisher, the editors, and the reviewers. Any product that may be evaluated in this article or claim that may be made by its manufacturer is not guaranteed or endorsed by the publisher.

Copyright © 2022 Jiang, Leng, Zhang and Guo. This is an open-access article distributed under the terms of the Creative Commons Attribution License (CC BY). The use, distribution or reproduction in other forums is permitted, provided the original author(s) and the copyright owner(s) are credited and that the original publication in this journal is cited, in accordance with accepted academic practice. No use, distribution or reproduction is permitted which does not comply with these terms.



Finite Element Analysis on Inelastic Mechanical Behavior of Composite Beams Strengthened With Carbon-Fiber-Reinforced Polymer Laminates Under Negative Moment

Aiming Song¹, Hongtao Xu^{2*}, Qi Luo³ and Shui Wan^{4*}

¹School of Civil Engineering, Yancheng Institute of Technology, Yancheng, China, ²School of Civil Engineering, Hebei University of Science and Technology, Shijiazhuang, China, ³School of Civil Engineering, Chongqing Jiaotong University, Chongqing, China, ⁴School of Transportation, Southeast University, Nanjing, China

OPEN ACCESS

Edited by:

Zhigang Zhang,
Chongqing University, China

Reviewed by:

Shao-Bo Kang,
Chongqing University, China
Biao Hu,
Shenzhen University, China

*Correspondence:

Hongtao Xu
xht1978@hebust.edu.cn
Shui Wan
seurpbridge@163.com

Specialty section:

This article was submitted to
Structural Materials,
a section of the journal
Frontiers in Materials

Received: 21 January 2022

Accepted: 25 April 2022

Published: 31 May 2022

Citation:

Song A, Xu H, Luo Q and Wan S (2022)
Finite Element Analysis on Inelastic
Mechanical Behavior of Composite
Beams Strengthened With Carbon-
Fiber-Reinforced Polymer Laminates
Under Negative Moment.
Front. Mater. 9:859663.
doi: 10.3389/fmats.2022.859663

This work studies the improvement in the inelastic mechanical property of steel-concrete composite beams strengthened by carbon-fiber-reinforced polymer (CFRP) laminates under a negative moment. First, the monotonic loading test was designed and performed on an inverted simply supported beam to simulate the negative moment regions of continuous composite beams. Second, the finite element analysis (FEA) on flexural capacity and cracking resistance in negative moment regions of the composite beams was carried out with ANSYS software. A series of mechanical indexes including the load-deflection curve, component strain, and crack propagation were obtained from the FEA model and verified through the test data. The results showed that the FEA model can accurately predict the general mechanical behavior of composite beams under negative moments, and the calculation results considering the interface slip effect were closer to the experimental values. Finally, based on the FEA model, the parametric study on static behavior in negative moment regions of composite beams strengthened with/without CFRP laminates was conducted. The effects of the CFRP layout width, layout position, layer number, longitudinal reinforcement ratio, and shear connection degree on the bearing capacity of the composite beams were considered. The CFRP laminates can effectively improve the bending resistance of composite beams under negative moments. At a low reinforcement ratio, the bearing capacity was greatly affected by the layout width and layer number of the CFRP laminates, but the rate of increase was not significant when the layer number was more than 3. The reinforcement ratio had a great influence on the bearing capacity of composite beams under negative moments, but the influence of the shear connection degree was not remarkable.

Keywords: steel-concrete composite beam, negative moment, CFRP laminates, finite element, parametric analysis

1 INTRODUCTION

In recent decades, new materials or structures have been widely used in civil engineering (Qin et al., 2020; Zhang et al., 2021; Zhang et al., 2022; Lin et al., 2022). As a relatively new form of construction in China, steel-concrete composite structures have been popularized in bridge engineering because of the full use of properties of the two materials (Wang et al., 2017; Wang et al., 2021). However, steel-concrete continuous composite beams have problems such as concrete cracking and compression buckling of the bottom profile under a low static load level due to the existence of a negative moment at the middle support position (Hamoda et al., 2017). In recent decades, considerable research has focused on the static behavior of composite beams under negative moments with experimental tests (Song et al., 2018; Fan et al., 2020), theoretical methods (Fan, 2003; Nguyen et al., 2009), and numerical calculations (Chen et al., 2011; Lin and Yoda, 2014). At present, the calculation and analysis methods have tended to be mature and can serve the design well. Compared with traditional building materials such as steel, reinforcing bar, and concrete, carbon-fiber-reinforced polymers (CFRPs) have excellent properties of lightweight, high strength, and corrosion and fatigue resistance, and they have been widely used in the construction and reinforcement of engineering structures. Studies showed that reinforced concrete structures (Hawileh et al., 2013; Hawileh et al., 2014), steel beam structures (Teng et al., 2015; Ghafoori et al., 2015), and steel-concrete composite structures (Tavakkolizadeh and Saadatmanesh, 2003; Karam et al., 2017) can be effectively improved in terms of flexural bearing capacity, fatigue life, and cracking performance after strengthening with CFRP laminates.

The nonlinear static behavior of defective curved steel beams strengthened by CFRP laminates was studied using the ANSYS software, and the results of the analysis showed that the utilization of CFRP laminates for strengthening the curved beams could recover the lost strength to some extent (Keykha, 2019). The model test and finite element analysis (FEA) of composite beams with CFRP laminates in negative moment regions were carried out to study the flexural mechanical behavior and cracking resistance, and the results showed that the introduction of CFRP laminates can effectively improve the cracking performance and bearing capacity (El-Zohairy et al., 2017). The flexural behavior of pre-damaged steel-concrete composite beams reinforced with CFRP laminates was studied through the experimental test of 10 beams, and the mechanical properties could be restored at a certain proportion. Meanwhile, the use of mechanical anchors in the pre-damaged steel-concrete composite beams could improve the structural strength, obviously (Karam et al., 2017). To analyze the flexural strength of steel-concrete composite beams strengthened with a pre-stressed CFRP plate, an analytical solution was proposed by applying experimental and finite element methods, and it was found that the stiffness and strength of steel-concrete composite beams could be improved effectively by using CFRP plates, and the FEA results were in good agreement with the test results (Deng et al., 2011). The flexural performance of steel beams

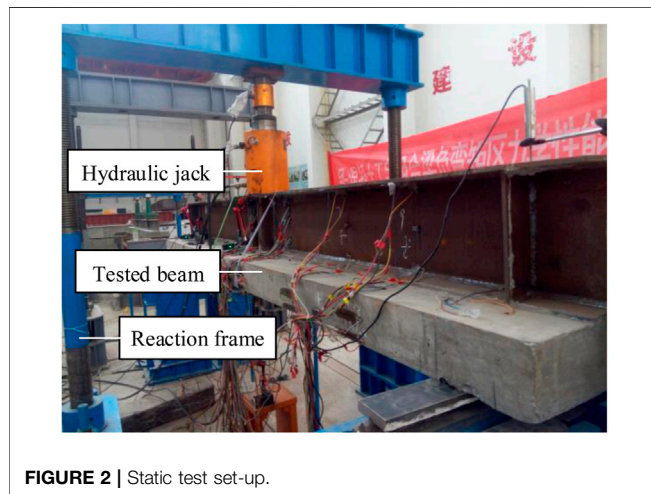
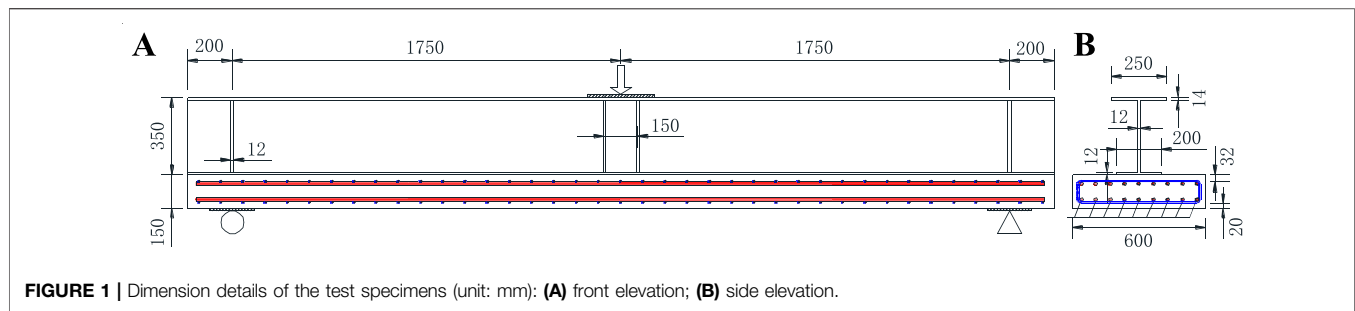
reinforced with anchored hybrid composites was analyzed and discussed, and the multiple influencing parameters involved in the length of fiber-reinforced polymers (FRPs), the thickness of the FRP, and the number of anchors were investigated in detail (Sweedan et al., 2016).

Although some studies have been done to explore the mechanical behavior of steel-concrete composite beams strengthened by CFRP laminates, most of the CFRP laminates were bonded to steel beams under positive moments. There are few reports focusing on the influence of CFRP reinforcement technology on the mechanical properties and cracking control in composite beams under negative moments. In addition, the FEA theory has become an important way to study the mechanical mechanism of structures in recent years. By establishing a fine FEA model, the reliability of the model test and theoretical analysis can be verified, and the application scope of experimental and theoretical methods can be further extended to the analysis of the mechanical behavior of complex structures under various actions (Fan, 2003). It is difficult to analyze the whole process of structural loading according to the traditional method, because of the significant nonlinear characteristics of composite beams under the action of negative moments. At this point, the FEA method can be used to analyze the inelastic mechanical properties of the structure.

This study is to understand the inelastic mechanical behavior of steel-concrete composite beams upgraded with CFRP laminates under negative moments. To simulate the negative moment regions of continuous composite beams, a monotonic loading test is performed on a plain beam in an inverted simply supported position. An FEA model is developed and validated through the test results with ANSYS software, and a series of mechanical indexes, such as load-deflection curve and component strain, are obtained. Based on the FEA model, CFRP laminates are introduced to strengthen the concrete slab, and the mechanical properties of composite beams under negative moments strengthened with/without CFRP laminates are compared and analyzed. Through the parametric analysis, the influences of the CFRP layout width, layout position, layer number, longitudinal reinforcement ratio, and shear connection degree on the bearing capability of structures are determined. It is expected to provide a reference for practical engineering design and application of such structures.

2 OUTLINE OF THE EXPERIMENT

Considering the characteristics of negative moments at the bearing position of continuous composite beam bridges in practical engineering, an inverted simply supported beam is designed and performed in this study to simulate this region. The dimension details of the test beam are shown in **Figure 1**. The total longitudinal length of the specimen is 3,900 mm and the calculated span is 3,500 mm. The height of the specimen is 500 mm, consisting of the concrete slab with a thickness of 150 mm and an I-beam with the height of 350 mm. The width of the concrete slab is 600 mm and the concrete strength grade is C50. The HRB400 hot-rolled ribbed steel bars are used in the



concrete slab, of which the longitudinal and transverse diameters are 16 and 10 mm, respectively. The ratio of the longitudinal reinforcing bars is 4.0%. The grade of the whole steel beam adopts Q345, and the thicknesses of the web, top flange, and bottom flange are 12 mm, 12, and 14 mm, respectively. The interface between the steel beam and the concrete slab is equipped with stud connectors to resist longitudinal shear force. The shear connection degree of the test beam is designed to be 0.95 with a diameter, height, and spacing of 16, 90, and 100 mm, respectively. The set-up of the static test is shown in **Figure 2**.

The compressive strength of the concrete cube is tested according to relevant regulations before the loading test. According to the test results, the averages of the cube compressive strength and axial tensile strength are 51.2 and 3.44 MPa, respectively. In addition, three tensile specimens are taken from tensile steel bars with a diameter of 16 mm and from

steel plates with a thickness of 12 and 14 mm, respectively, and then the steel properties are tested. The average values of the tensile yield strength of the rebars, web (or top flange), and bottom flange of the steel beams are 592, 443, and 391 MPa, respectively. The average values of the ultimate tensile strength are 718, 608, and 520 MPa, respectively. All the material properties are shown in **Table 1**.

3 FINITE ELEMENT MODEL

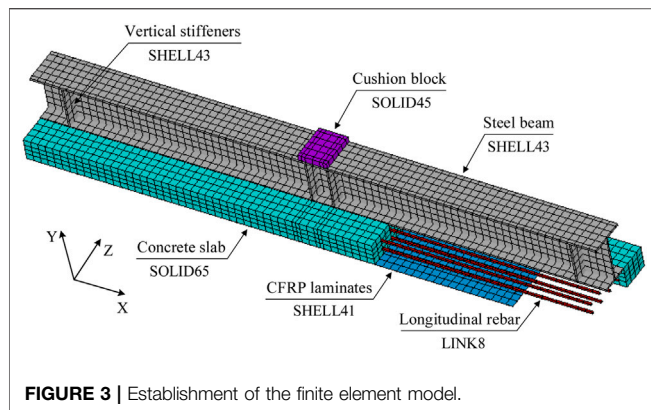
Steel-concrete composite beams are composed of different materials, and the mechanical behavior depends on the properties of each material and the interaction between each member. It is difficult to study the whole loading process of the composite structure by the traditional analytical method because of the significant nonlinear characteristics after the cracking of the concrete slab under the action of negative moments. In addition, the model test has certain limitations such as the high cost of manpower, material resources, and financial resources. Then, the FEA method can be used to analyze the mechanical properties of the steel-concrete composite beams under negative moments and the inelastic strengthened beams bonded with the CFRP.

3.1 Element Type and Meshing

The concrete slab is modeled by using a three-dimensional (3D) solid element SOLID65, which has the effects of tensile cracking and compression crushing. This type of element is defined by eight nodes and each node has 3° of freedom. The steel beam is simulated by using a SHELL43 element, each node of which has 6° of freedom of translation and rotation. This element has the characteristics of plasticity, creep, stress rigidness, large deformation, large strain, and element of life and death. The

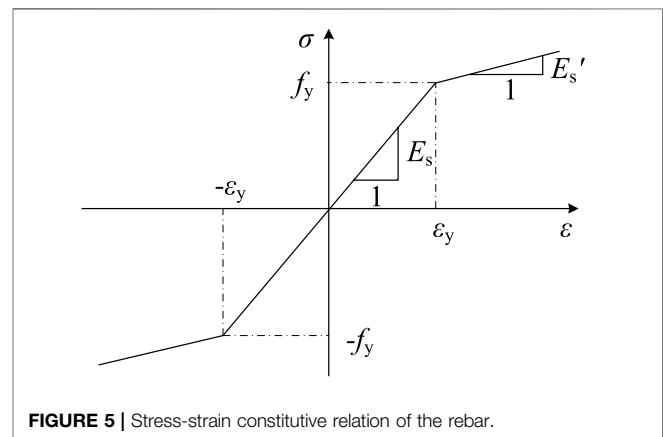
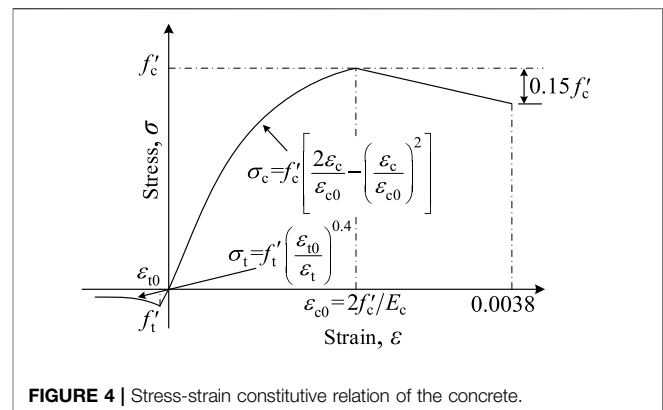
TABLE 1 | Material properties of the specimen materials.

Material type	Average value of the cube strength (Mpa)	Axial tensile strength (Mpa)	Material type	Thickness or diameter (mm)	Average yield strength (Mpa)	Average ultimate strength (Mpa)
Concrete (C50)	51.2	3.44	Top flange and web (Q345)	12	443	608
			Bottom flange (Q345)	14	391	520
			Rebar (HRB400)	16	592	718



steel block at the loading position is developed by the SOLID45 element, with the characteristics of plasticity, creep, expansion, stress hardening, large deformation, large strain, and initial stress input. The number of nodes and degrees of freedom in SOLID45 are identical to those in SOLID65. The longitudinal reinforcing bars are simulated by a 3D truss element LINK8, each node of which has 3° of freedom. This type of element can bear axial tension and compression but not bending moment, with the characteristics of plasticity, creep, stress rigidification, and large deformation. A non-linear spring element COMBINE39 is used to simulate the longitudinal shear behavior of the stud connectors. The element has unidirectional characteristics with a nonlinear generalized force-deformation curve, and each node has 3° of freedom. At present, the element types used to simulate CFRP laminates include SOLID46 with layered structure characteristics and SHELL41 with membrane characteristics. In addition to the characteristics mentioned previously, SOLID46 allows more than 250 layers of different materials, with stress hardening and large deformation properties. SHELL41 is defined by four nodes, each of which has 3° of freedom. This type of element only has the plane inner membrane stiffness but no out-of-plane bending stiffness. It has the characteristics of stress rigidness, large deformation, non-linearity, and element of life and death. According to the contrast, the mechanical properties of SHELL41 are more consistent with the loading state of CFRP laminates in structural reinforcement. Thus, this element is used to simulate CFRP laminates in the modeling process of this study.

When the load acting on the composite beam is in the normal service stage, the slip between the steel and concrete is negligible compared with the slip between the steel beam and concrete slab (Nie et al., 2004). Therefore, it can be assumed that a good bond relationship exists between reinforcement and the concrete, and the coupling of node degrees of freedom is adopted in modeling. When CFRP laminates are introduced to strengthen the concrete slab of composite beams, high strength epoxy resin is usually used as a reliable adhesion agent, which can better realize the bond between the CFRP laminates and the concrete slab. Thus, it is also assumed that CFRP laminates and the concrete slab are perfectly bonded during the establishment process of the FEA model. The existing literature shows that the phenomenon of lifting will be produced between the steel beam and the concrete slab under the



action of the load, and a certain tension will be generated in the studs. However, compared with the longitudinal slip, this phenomenon has little effect on the overall performance of composite beams. Therefore, the lateral and vertical degrees of freedom of the adjacent nodes at the interface between the top flange of the steel beam and the concrete slab are coupled to achieve the purpose of ignoring the lifting effect (Fan, 2003). The final FEA model is shown in Figure 3.

3.2 Material Constitutive Relation

3.2.1 Concrete

In this study, the classic Hognestad model (Hognestad, 1951) is adopted to represent the stress-strain constitutive relationship of concrete, as shown in Figure 4. During the developing process of the FEA model, the multi-linear isotropic strengthening model (MISO) is used to define the curve. From Figure 4, we can see that a descending section existed in the stress-strain curve of the concrete in the tension process. But different from the case of compression, it is generally considered that the concrete is damaged when it reaches the ultimate tensile strength. Thus, only the ascending section of the straight line in the tensile process is considered. During the FEA, the axial tensile strength f'_t can be obtained from the axial compressive strength of the cylinder f'_c by using the following conversion relation:

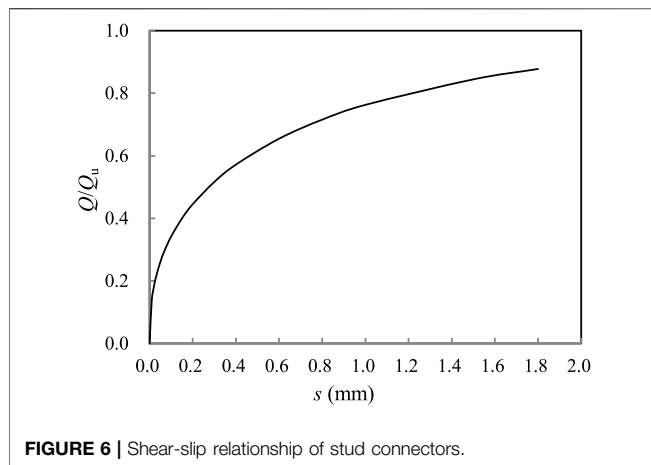


FIGURE 6 | Shear-slip relationship of stud connectors.

$$f'_t = 0.23 f'_c{}^{2/3}. \quad (1)$$

3.2.2 Steel

Considering the elasticity and strengthening characteristics of the stress-strain curves of the steel, the bilinear kinematic strengthening model (BKIN) is used to simulate the constitutive relationship of steel beams or reinforcing bars during the modeling process, as shown in **Figure 5**. From **Figure 5**, we can see that the stress-strain curve will be simplified to a gentle oblique line after the steel reaches the yield point f_y . To ensure the convergence of model calculation, the strengthening modulus E_s' is uniformly taken as $1/20,000$ of the elastic modulus E_s by referring to the selection method in the literature (Fan, 2003), and the constitutive curves under tension and compression are assumed to be the same. In addition, the ultimate tensile strain of longitudinal tensile reinforcement is equivalent to 0.01 in this study (GB 50010-2010, 2010).

3.2.3 Shear-Slip Relationship of Stud Connectors

For stud connectors, various shear-slip curves have been proposed. The calculation method in this study adopts the highly recognized exponential model proposed by Ollgaard et al. (1971) as shown in **Figure 6**, and the specific form is as follows:

$$Q = Q_u (1 - e^{-0.71s})^{0.4}, \quad (2)$$

where, Q is the shear force of the studs; s is the slip generated at the welding position of the studs; Q_u is the ultimate shear bearing capacity of studs; and $Q_u = 0.5 A_{su} \sqrt{E_c f'_c} \leq A_{su} f_{su}$ where A_{su} is the cross-sectional area of studs and f_{su} is the tensile strength of the studs.

3.2.4 Carbon-Fiber-Reinforced Polymers Laminates

When reaching the ultimate tensile stress, the CFRP laminates will fracture directly, and the stress immediately drops to 0. The ultimate tensile strain of the CFRP laminates is generally 0.015–0.02. In this study, it is assumed that CFRP laminates are an ideal linear elastic material with a designed thickness of

0.167 mm. The tensile elastic modulus, the ultimate tensile strength, and the Poisson ratio are equivalent to 2.2×10^5 MPa, 3,200 MPa, and 0.2, respectively.

4 FINITE ELEMENT ANALYSIS MODEL VALIDATION AND DISCUSSION

4.1 Load-Deflection Curve

Based on the static test performed previously, an FEA model is established and verified in this section. It is worth explaining that the load-deflection curve of a structure generally includes a rising section and a descending section, and the latter is related to the ductility of the structure. However, the maximum deformation in the FEA is difficult to realize because of the low convergence and accuracy in the simulation calculation. Therefore, this study focuses on the failure state of the component corresponding to the peak load, and does not consider the maximum deformation of the descending section. The comparison result of calculated and tested values of the load-deflection curve is shown in **Figure 7**. The two calculation curves by the FEA model take into account two working conditions with slip and without slip effects between the concrete and the steel beam. When interface slip is considered, a spring element COMBINE39 is used to simulate the shear performance of the studs. When interface slip effect is not considered, the freedom degrees of nodes in the contact interface between the concrete and the top flange plate are coupled. As can be seen from the figure, the influence of interface slip effects can be ignored before the service load (50% F_u), because the finite element calculation results of the two cases coincide well. When the structure enters the elastic-plastic stage, the slip effect has a certain influence on the mechanical properties of the structure, mainly in the smaller flexural stiffness with considering the slip effect than that without considering. But the slip has little influence on the ultimate bearing capacity of composite beams. In addition, the bending stiffness obtained by the FEA model is higher than the experimental value, especially in the nonlinear stage. The assumption of a perfect bond between reinforcement and the concrete in the modeling process and the

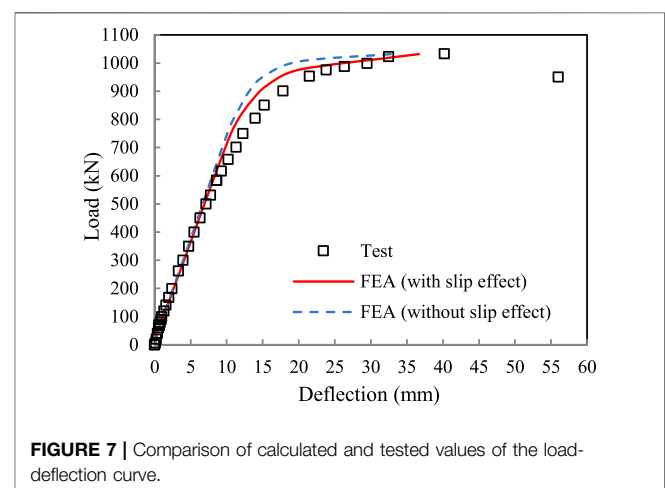
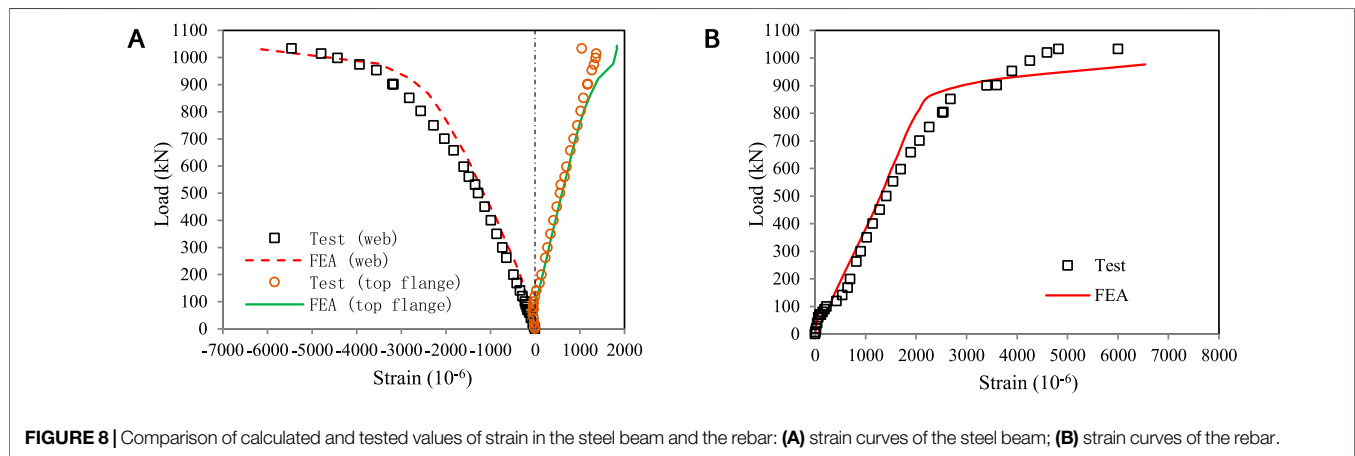


FIGURE 7 | Comparison of calculated and tested values of the load-deflection curve.

TABLE 2 | Comparison of calculated and tested values at characteristic points.

Data at characteristic points		Tested values (T_v)	Numerical result (N_v)	N_v/T_v
Concrete cracking (F_{cr})	F_{cr} (kN)	70.0	67.0	0.96
	F_{cr}/F_u	6.8%	6.5%	—
Mid-span deflection of $L/600$ ($F_{L/600}$)	$L/600$ (mm)	5.8	5.8	—
	$F_{L/600}$ (kN)	419.0	398.3	0.95
	$F_{L/600}/F_u$	40.5%	38.6%	—
Bottom flange yields (F_{sy})	F_{sy} (kN)	700.0	701.8	1.00
	f_{sy} (mm)	11.2	9.84	0.88
	F_{sy}/F_u	67.8%	63.7%	—
Tensile yield of the rebar (F_{ry})	F_{ry} (kN)	850.0	866.8	1.02
	f_{ry} (mm)	15.2	13.5	0.89
	F_{ry}/F_u	82.3%	84.0%	—
Ultimate load (F_u)	F_u (kN)	1,033.0	1,031.8	1.00
	f_u (mm)	40.2	36.7	0.91

**FIGURE 8** | Comparison of calculated and tested values of strain in the steel beam and the rebar: (A) strain curves of the steel beam; (B) strain curves of the rebar.

neglect of the weakening effect of shear connectors in concrete slabs are the main reasons for the difference in the results. But from the overall trend, the load-deflection curve calculated by the finite element is in good agreement with the experimental data, and the calculated results considering the interface slip effect are closer to the experimental values. The influence of the slip effect is considered in the FEA of the following contents.

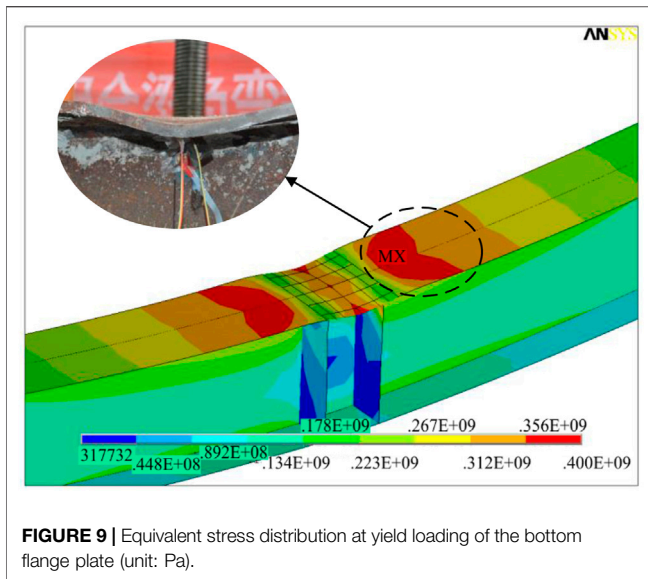
The comparison of calculated and tested values of the test beam at the characteristic points are shown in **Table 2**, including the cracking state of the concrete slab, the normal limit state of the beam when the deflection reached the ultimate value (i.e., $L/600$), and the states of the compressive yield of the bottom profile, the tensile yield of longitudinal reinforcing bars, and the limit state of structure bearing capacity. $L/600$, f_{sy} , f_{ry} , and f_u in **Table 2** represent deflections at the mid-span of each aforementioned stage, respectively. It can be seen from the table that the model calculation results of load or deflection at each characteristic point are quite consistent with the test values. Especially for the load, the error between the calculated and tested values is basically within 5%. It shows that the FEA model in this study can obtain an accurate inelastic mechanical behavior of a composite structure under negative moments.

4.2 Load-Strain Curve

In the FEA model, the strain of the bottom profile at the loading position is affected by the cushion block. Thus, the strain curves at the bottom of the web and the middle of the top steel profile are selected and compared with the experimental values. For the strain curve of the reinforcing bar, the main tension bar closest to the web of the steel beam at mid-span is selected as the research object. The comparison results of load-strain calculation curves and test values of the steel beam and the reinforcing bar are shown in **Figure 8**. It can be seen from the figure that the calculated strain of the steel beam is in good agreement with the experimental values. Because of the influence of concrete cracking, there is some deviation between the calculated and the experimental results after the structure enters the yield stage. But in general, the FEA model accurately simulates the loading process of the inverted composite beams. The results show that the reinforcing bars and steel beams in the negative moment region can work well together and give full play to their plastic deformation abilities.

4.3 Yield State of the Bottom Profile

Figure 9 shows the Mises equivalent stress cloud at the yield load of the bottom steel profile (701.8 kN). As can be seen from the



figure, the maximum compressive stress of the steel beam occurs at a position about 20 cm away from the loading point, due to the existence of vertical stiffeners. At this moment, the maximum compressive strain reaches about 2,000 $\mu\epsilon$, and then the steel plate enters the yield stage during the subsequent loading process. This phenomenon is consistent with the observation of the test.

4.4 Crack Propagation

As can be seen from **Table 2**, the finite element calculation result of the cracking load of concrete slabs is basically consistent with the test value, accounting for about 6.5% of the ultimate load. After reaching the cracking load of concrete, the ANSYS program will record the cracking situation of SOLID65 in each loading step

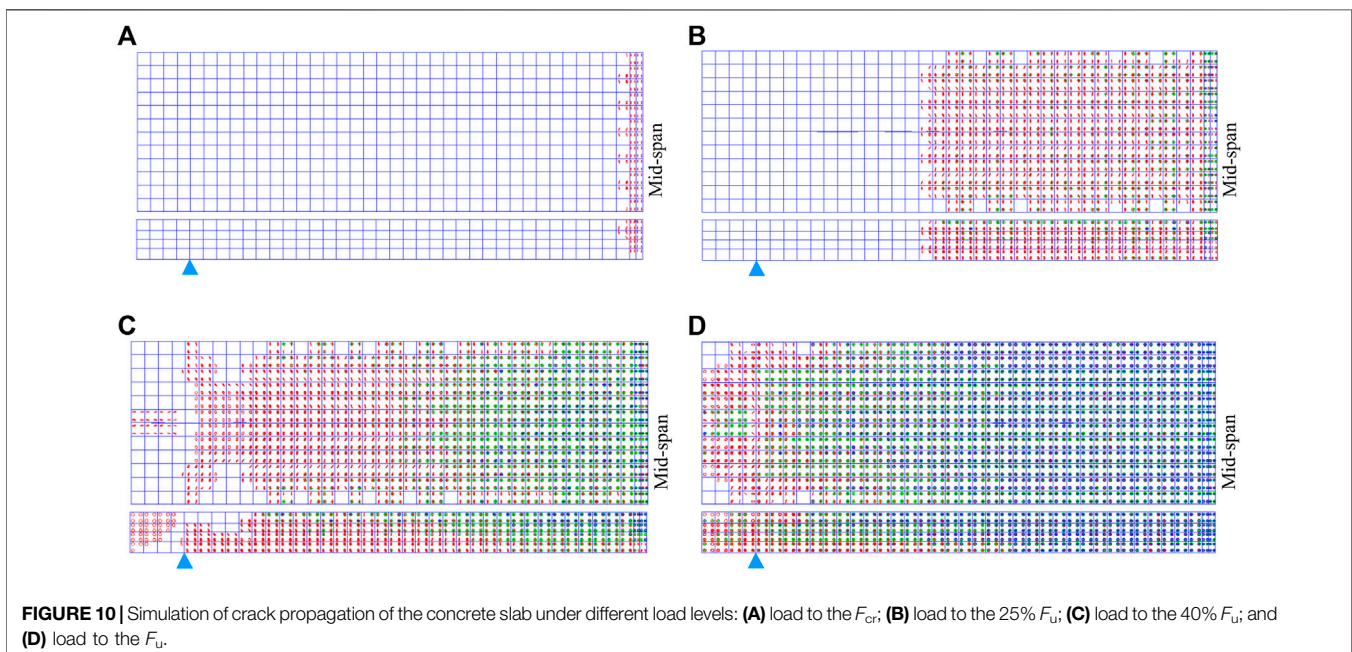
and represent the cracking and fracturing behavior with circles and octagons, respectively. **Figure 10** shows the crack propagation of a half-span concrete slab under different load grades. As can be seen from the figure, the initial cracks occur near the mid-span of the concrete slab, and then gradually propagate to the beam end with the increase of load grade. When the load reaches about 40% F_u , all transverse cracks appear basically, and several inclined cracks occurred near the support position which is consistent with the phenomenon observed in the test process.

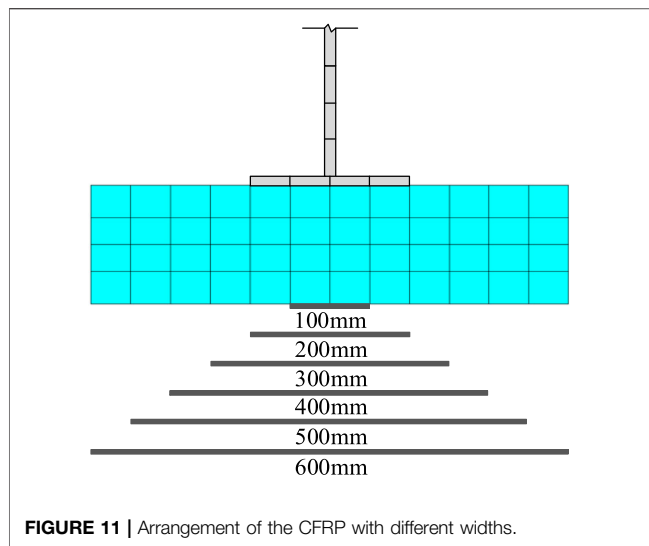
5 PARAMETRIC STUDY

The FEA model of the test beam is developed as mentioned previously, and the comparison and verification between calculation results and test data are carried out. Based on the FEA model, the parametric study on the bearing capacity in negative moment regions of composite beams strengthened with CFRP laminates is conducted in this section. The parameters considered include CFRP layout width, layout position, layer number, longitudinal reinforcement ratio, and shear connection degree.

5.1 Effect of Layout Width of Carbon-Fiber-Reinforced Polymers Laminates

To analyze the influence of the CFRP layout width on the mechanical properties of composite beams in negative moment regions, the layout width of CFRP laminates in the FEA model is equivalent to 100, 200, 300, 400, 500, and 600 mm respectively, under the premise of keeping the structural size of





composite beams unchanged, as shown in **Figure 11**. **Table 3** shows the cracking load, reinforcement yield load, and ultimate load of composite beams with different widths of CFRP laminates. The reinforcement ratio is chosen as 4.0% and 0.5%. It can be seen from the table that the mechanical properties of composite beams under negative moments with CFRP laminates are improved to a certain extent, especially when the reinforcement ratio is low. It is mainly manifested in the following aspects: the CFRP laminates can improve the crack resistance of the concrete slab in the negative moment region of composite beams, and the cracking load can be increased by about 5.0%; when the reinforcement ratio is high, the load at the yield stage of the reinforcing bar in the concrete slab with CFRP laminates is increased by less than 5% compared with the composite beam without CFRP laminates, and the growth rate reaches to 18.6% under a low reinforcement ratio; when the reinforcement ratio is high, the ultimate load of the composite beam with CFRP laminates is increased within 12% compared with the beam without CFRP, and the growth rate tends to be stable when the layout width exceeds 300 mm (**Figure 12A**); however, the growth rate at a low reinforcement ratio can reach up to 25.2%, and the ultimate load increases linearly with the increase of the layout width (**Figure 12B**).

5.2 Effect of the Layout Position of Carbon-Fiber-Reinforced Polymers Laminates

When the concrete slab in the negative moment region of the composite beam is not bonded with CFRP laminates within the full width, an FEA model considering the layout position (**Figure 13**) is carried out to analyze the impact on the bearing performance of composite beams. In the FEA model, the total width of the CFRP layout is designed as 300 mm, and the reinforcement ratio of longitudinal reinforcement in the concrete slab is designed as 0.5%. The calculation results show

TABLE 3 | Calculated values by the FEA with different widths of the CFRP.

Layout width (mm)	ρ (%)	Cracking load		Yield load of the rebar		Cracking load		Yield load of the rebar		Ultimate load	
		Result (kN)	Rate (%)	Result (kN)	Rate (%)	Results (kN)	Rate (%)	Result (kN)	Rate (%)	Result (kN)	Rate (%)
0	4.0	67.0	—	866.8	—	60.0	—	430.8	—	712.4	—
100	4.0	67.0	0.0	887.2	2.4	62.5	4.2	452.8	5.1	777.7	9.2
200	4.0	69.5	3.7	895.1	3.3	62.5	4.2	470.3	9.2	802.7	12.7
300	4.0	69.5	3.7	895.2	3.3	63.4	5.7	492.5	14.3	832.8	16.9
400	4.0	69.5	3.7	902.3	4.1	63.4	5.7	504.9	17.2	850.8	19.4
500	4.0	69.5	3.7	908.6	4.8	63.4	5.7	508.8	18.1	874.6	22.8
600	4.0	69.5	3.7	909.6	4.9	63.4	5.7	510.8	18.6	892.2	25.2
0	0.5	1,031.8	—	1,031.8	—	60.0	—	430.8	—	712.4	—
100	0.5	1,095.8	6.2	1,119.2	8.5	62.5	4.2	452.8	5.1	777.7	9.2
200	0.5	1,138.2	10.3	1,146.5	11.1	63.4	5.7	492.5	14.3	832.8	16.9
300	0.5	1,150.6	11.5	1,153.7	11.8	63.4	5.7	508.8	18.1	874.6	22.8
400	0.5	1,153.7	11.8	1,153.7	11.8	63.4	5.7	510.8	18.6	892.2	25.2

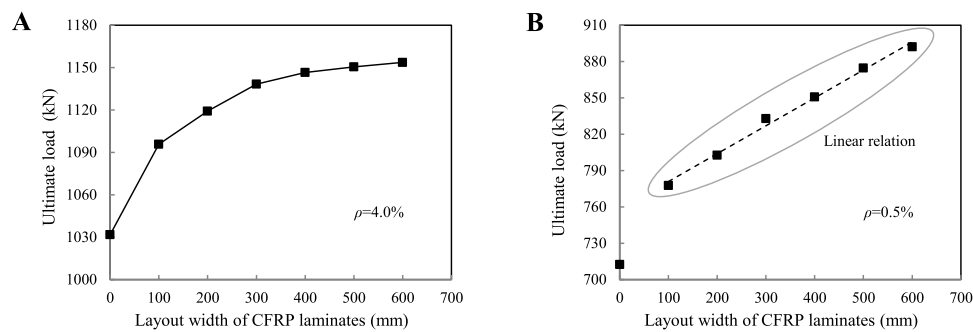


FIGURE 12 | Curve of the ultimate load varied with CFRP width: **(A)** reinforcement ratio $\rho = 4.0\%$; **(B)** reinforcement ratio $\rho = 0.5\%$.

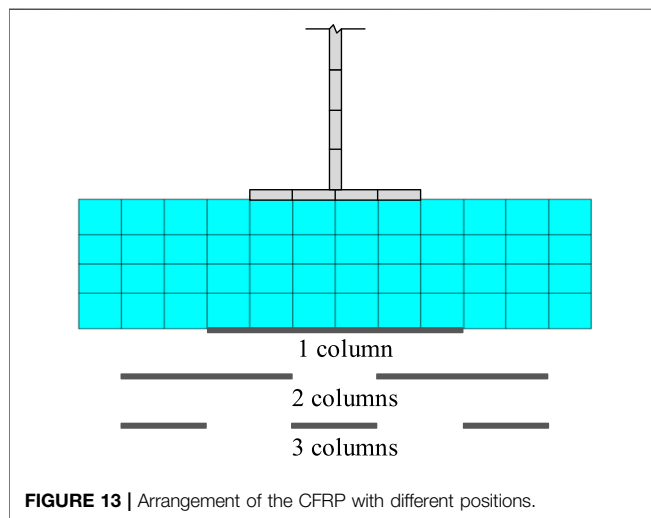


FIGURE 13 | Arrangement of the CFRP with different positions.

that the load-deflection curves of the composite beams with the different layout positions of CFRP laminates coincide well, as shown in **Figure 14A**. When the total layout width of the CFRP laminates remains unchanged, the different layout positions have little effect on the bearing performance of the composite beam, with a cracking load, reinforcement yield load, and ultimate load of about 63, 490, and 830 kN, respectively. **Figure 14B** shows the

curves of the maximum tensile stress of CFRP laminates varied with load. It can be seen that the maximum tensile stress of the CFRP laminates in the three layouts is basically the same before concrete cracking. However, the maximum tensile stress of the CFRP laminates arranged in three columns is smaller than that of the other two forms after the crack appears. Therefore, to reduce the stress of the CFRP laminates and control the crack width at the edge of the concrete slab, the CFRP laminates should be reasonably distributed along the width of the concrete slab in practical applications.

5.3 Effect of Layer Number of Carbon-Fiber-Reinforced Polymers Laminates

In practical engineering, the load-bearing performance of the structure is often guaranteed by increasing the number of CFRP adhesive layers. But this method tends to be conservative, resulting in a waste of materials. To study the influence of the layer number of CFRP laminates on the mechanical properties of composite beams under the action of negative moments, the numerical modeling and calculation analysis of composite beams with 1–5 layers of CFRP laminates on concrete slabs were carried out. The width of CFRP laminates is designed as 600 mm and it is arranged in three columns. **Table 4** shows the cracking load, reinforcement yield load and ultimate load of composite beams

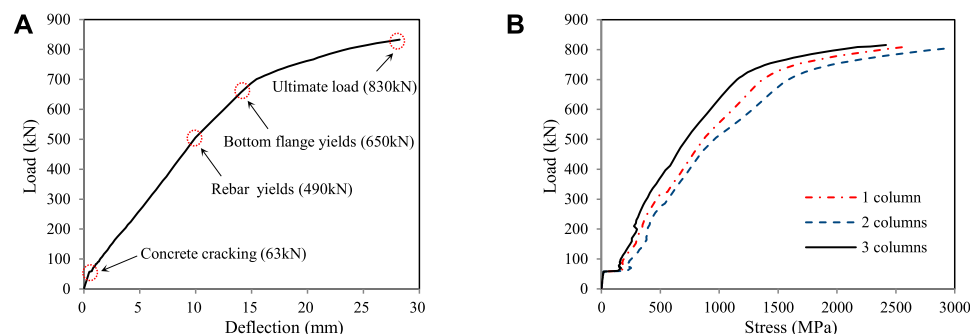


FIGURE 14 | Variation curves of deflection and CFRP stress: **(A)** load-deflection curve; **(B)** load-maximum tensile stress of the CFRP curve.

TABLE 4 | Calculated values by the FEA with different layers of CFRP.

CFRP layers	ρ (%)	Cracking load		Yield load of the rebar		Ultimate load		ρ (%)		Cracking load		Yield load of the rebar		Ultimate load	
		Result (kN)	Rate (%)	Result (kN)	Rate (%)	Result (kN)	Rate (%)			Result (kN)	Rate (%)	Result (kN)	Rate (%)	Result (kN)	Rate (%)
0															
1	4.0	67.0	3.7	866.8	—	1,031.8	—	0.5		60.0		430.8	—	712.4	—
2		69.5	3.7	913.9	5.4	1,124.3	9.0			63.4	5.7	487.8	13.2	823.0	15.5
3		69.5	3.7	928.7	7.1	1,142.2	10.7			63.4	5.7	500.6	16.2	886.9	24.5
4		69.5	3.7	929.2	7.2	1,160.8	12.5			63.4	5.7	545.2	26.5	928.5	30.3
5		69.5	3.7	944.8	9.0	1,176.6	14.0			63.4	5.7	557.4	29.4	945.0	32.6
		69.5	3.7	950.8	9.7	1,183.9	14.7			63.4	5.7	568.3	31.9	955.1	34.0

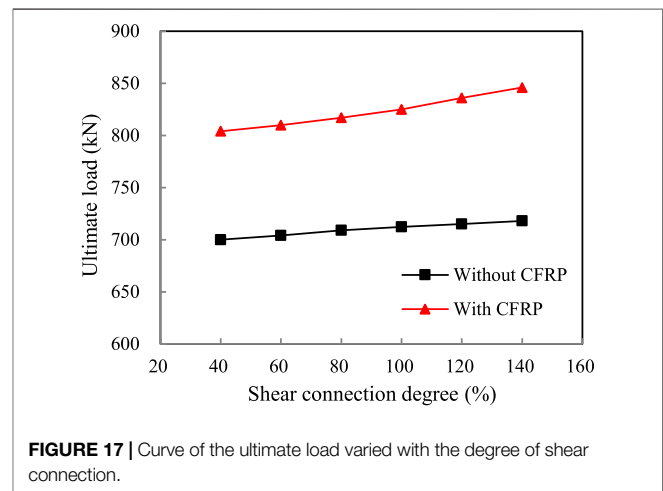
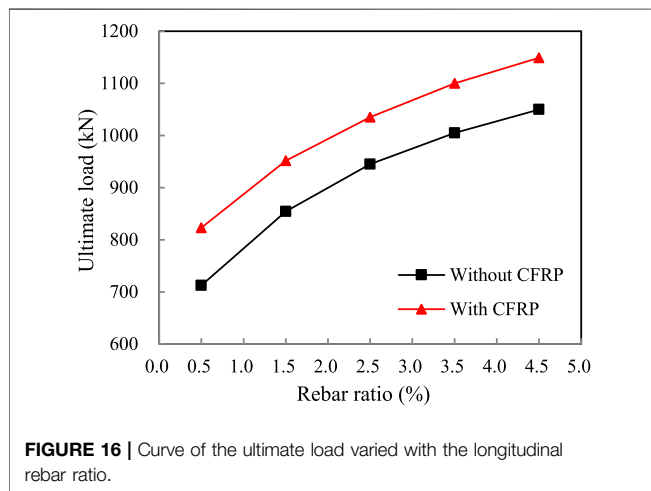
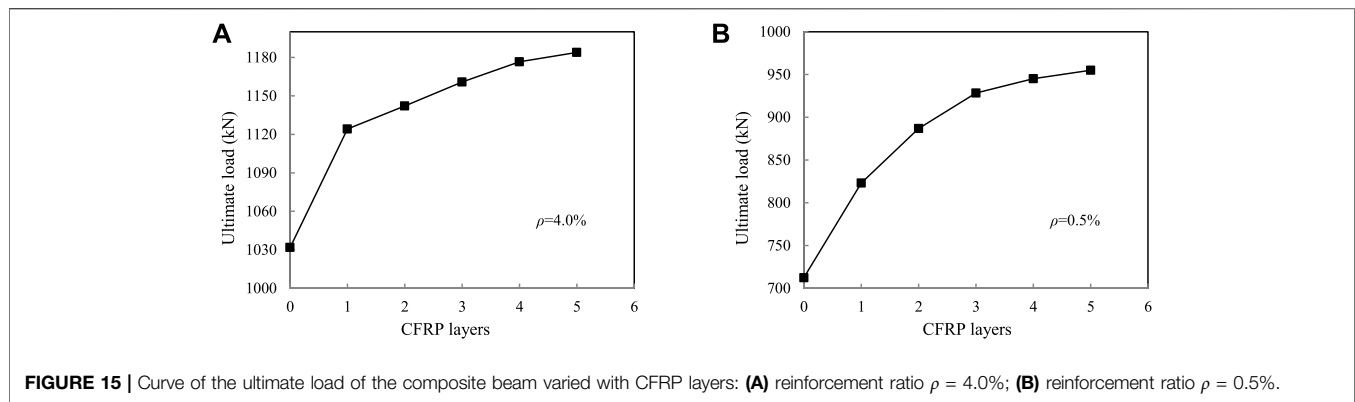
with different layer numbers of CFRP laminates. The reinforcement ratio is chosen as 4.0% and 0.5%. It can be seen from the table that the cracking load of the concrete slab bonded with CFRP laminates can be increased by about 5.0%. But with the increase in the layer number, there is no significant improvement. When the reinforcement ratio is high, the load at the yield stage of the reinforcing bar in the concrete slab bonded with CFRP laminates is increased by less than 10% compared with the composite beam without CFRP laminates. However, the load-bearing performance of composite beams with more bonded layers is not significantly improved on the whole (**Figure 15A**). When the reinforcement ratio is low, the bearing performance of the composite beam with 1 ~ 3 layers of CFRP laminates is greatly improved. The yield load of the reinforcing bar is increased by 26.5% and the ultimate load is increased by 30.3% when three layers of CFRP laminates are arranged. However, with the further increase in the number of adhesive layers, the load-bearing performance is not significantly improved (**Figure 15B**). In practical engineering, a reasonable number of layers should be arranged in combination with design requirements and theoretical calculations.

5.4 Effect of the Longitudinal Reinforcement Ratio

To study the influence of the longitudinal reinforcement ratio on the bearing capacity in negative moment regions of composite beams, the FEA model is developed with reinforcement ratios of 0.5%, 1.5%, 2.5%, 3.5%, and 4.5%, under the condition of keeping the structure and size of the composite beams unchanged. The layer number of CFRP laminates is designed as 1. The width of CFRP laminates is designed as 600 mm, and the layers are arranged in three columns. The curves of the ultimate bearing capacity of composite beams under negative moments with/without CFRP laminates varied with the reinforcement ratio are given in **Figure 16**. It can be seen from the figure that the longitudinal reinforcement ratio has a great influence on the bearing performance in the negative moment region of the composite beam. The ultimate load increases with the increase in the reinforcement ratio, and the growth rate reaches 15% ~ 45%. Compared with the composite beam without CFRP laminates, the ultimate load of the composite beam bonded with CFRP laminates is increased by 10% ~ 15%.

5.5 Effect of the Shear Connection Degree

To study the effect of the shear connection degree on the bearing performance in negative moment regions of composite beams, the FEA model is developed with shear connection degrees of 40%, 60%, 80%, 100%, and 100%, under the condition of keeping the structure and size of composite beams unchanged. The longitudinal reinforcement ratio, the width of CFRP laminates, the layer number, and the column number of CFRP laminates are designed as 0.5%, 600 mm, 1, and 3, respectively. The curves of the ultimate bearing capacity of composite beams under negative moments with/without CFRP laminates varied with shear connection degrees are



given in **Figure 17**. During the whole loading process of the FEA, it is found that when the shear connection degree is more than 40%, the maximum slip at the composite beam interface does not exceed 0.2 mm, which is less than the ultimate slip value of the stud connection (Fan, 2003). That is, no shear failure of the connectors occurs during structural loading. It can be seen from the analysis in **Figure 17** that the ultimate load of the composite beam bonded with CFRP laminates is increased by about 15% compared with the beam model without CFRP laminates under the same loading conditions. However, the shear connection degree has little effect on the bearing capacity of the composite beam under negative moments. When the shear connection degree is 100% and above, the bearing capacity of the composite beam bonded with CFRP laminates in the negative moment region increases by about 5%, while the growth rate of the ultimate load of composite beams without CFRP laminates is less than 3%. This phenomenon is consistent with the research results in the existing literature (Loh et al., 2004), that is, the ultimate bearing capacity of composite beams in the negative moment region does not significantly decrease when the shear connection degree is reduced from 100% to 33%. However, considering the factors such as the fatigue performance of the connector and the complex force in the negative moment region, it is still recommended to design the studs based on the relevant

specification (BS EN 1994-2, 2005; BS 5950, 1990), that is, the degree of shear connection should not be less than 100%.

6 CONCLUSION

In this study, the FEA model of composite beams under negative moments is developed with ANSYS software by selecting reasonable elements and material constitutive relations. The inelastic mechanical behavior of the test beam is simulated and calculated, and the accuracy of the FEA model is verified by the comparative analysis with the test results. Then the influence of CFRP laminates on the bearing performance of composite beams under negative moment is considered, and a parametric analysis is further carried out. The main conclusions are as follows:

- (1) The FEA model can accurately predict the general mechanical behavior of steel-concrete composite beams under the action of negative moments. The finite element calculation results considering the interface slip effect are closer to the experimental values. The assumption of a perfect bond between reinforcement and the concrete and the neglect of the weakening effect of shear connectors in

- concrete slabs are the main reasons for the higher nonlinear stiffness of the FEA model than the experimental results.
- (2) According to the analysis of the effect of the layout width of CFRP laminates, it is found that the bonded CFRP laminates can effectively improve the flexural performance of composite beams under negative moments. The crack resistance of the concrete slab bonding with CFRP laminates can be improved with the cracking load increasing by about 5.0%.
 - (3) From the analysis of the effect of the layout position of CFRP laminates, it can be seen that a different layout position has little influence on the load-bearing performance of composite beams, when the total width of CFRP laminates keeps unchanged. The maximum tensile stress of the CFRP laminates arranged by different layout methods remains almost unchanged before concrete cracking, while the maximum stress of CFRP laminates arranged in three columns is less than that of the other two forms after the crack appears.
 - (4) From the analysis of the influence of the layer number of CFRP laminates, it can be concluded that the load-bearing performance of the composite beams bonded with 1 ~ 3 layers of CFRP laminates is greatly improved when a low reinforcement ratio is designed. But the bearing performance is not significantly improved with the further increase in the number of layers. Compared with the low reinforcement ratio, the number of bonded layers has no significant effect on improving the bearing performance of composite beams with the high reinforcement ratio.
 - (5) From the analysis of the effect of the longitudinal reinforcement ratio and shear connection degree, it is found that the longitudinal reinforcement ratio has a great influence on the bearing performance in the negative moment region of composite beams bonded with CFRP

laminates, while the influence of shear connection degree is not significant. However, it is still suggested that the shear connection degree in the negative moment region of composite beams should not be less than 100% from the design point of view.

DATA AVAILABILITY STATEMENT

The original contributions presented in the study are included in the article/supplementary material; further inquiries can be directed to the corresponding authors.

AUTHOR CONTRIBUTIONS

AS conceived the work and wrote the manuscript. AS, HX, and QL developed the numerical model. AS and SW analyzed the results and revised the manuscript. All authors read and agreed to the published version of manuscript.

FUNDING

This research was sponsored by the school-level research project of Yancheng Institute of Technology (No. xjr2021007).

ACKNOWLEDGMENTS

QL acknowledges the National Natural Science Foundation of China (No. 52108269), and the Scientific and Technology Research Program of Chongqing Municipal Education Commission (No. KJQN202100716).

REFERENCES

- BS 5950 (1990). *Structural Use of Steel Work in Building, Part 3, Section 3.1: Code of Practice for Design of Composite Beams*. London, England: British Standard Institution.
- BS EN 1994-2 (2005). *Eurocode 4: Design of Composite Steel and Concrete Structures, Part 2: General Rules and Rules for Bridges*. Brussels, Belgium: European Committee for Standardization.
- Chen, T., Gu, X., and Li, H. (2011). Behavior of Steel-Concrete Composite Cantilever Beams with Web Openings under Negative Moment. *Int. J. Steel Struct.* 11 (1), 39–49. doi:10.1007/S13296-011-1004-8
- Deng, J., Lee, M. M. K., and Li, S. (2011). Flexural Strength of Steel-Concrete Composite Beams Reinforced with a Prestressed CFRP Plate. *Constr. and Build. Mater.* 25, 379–384. doi:10.1016/j.conbuildmat.2010.06.015
- El-Zohairy, A., Salim, H., Shaaban, H., Mustafa, S., and El-Shihy, A. (2017). Experimental and FE Parametric Study on Continuous Steel-Concrete Composite Beams Strengthened with CFRP Laminates. *Constr. and Build. Mater.* 157, 885–898. doi:10.1016/j.conbuildmat.2017.09.148
- Fan, J. (2003). Experimental and Theoretical Research on Continuous Composite Steel-Concrete Beams. PhD thesis. Beijing, China: Tsinghua University.
- Fan, J., Gou, S., Ding, R., Zhang, J., and Shi, Z. (2020). Experimental and Analytical Research on the Flexural Behaviour of Steel-ECC Composite Beams under Negative Bending Moments. *Eng. Struct.* 210, 110309. doi:10.1016/j.engstruct.2020.110309
- GB 50010-2010 (2010). *Code for Design of Concrete Structures*. Beijing, China: Ministry of Construction of China.
- Ghafoori, E., Motavalli, M., Nussbaumer, A., Herwig, A., Prinz, G. S., and Fontana, M. (2015). Determination of Minimum CFRP Pre-stress Levels for Fatigue Crack Prevention in Retrofitted Metallic Beams. *Eng. Struct.* 84 (10), 29–41. doi:10.1016/j.engstruct.2014.11.017
- Hamoda, A., Hossain, K. M. A., Sennah, K., Shoukry, M., and Mahmoud, Z. (2017). Behaviour of Composite High Performance Concrete Slab on Steel I-Beams Subjected to Static Hogging Moment. *Eng. Struct.* 140, 51–65. doi:10.1016/j.engstruct.2017.02.030
- Hawileh, R. A., Naser, M. Z., and Abdalla, J. A. (2013). Finite Element Simulation of Reinforced Concrete Beams Externally Strengthened with Short-Length CFRP Plates. *Compos. Part B Eng.* 45 (1), 1722–1730. doi:10.1016/j.compositesb.2012.09.032
- Hawileh, R. A., Rasheed, H. A., Abdalla, J. A., and Al-Tamimi, A. K. (2014). Behavior of Reinforced Concrete Beams Strengthened with Externally Bonded Hybrid Fiber Reinforced Polymer Systems. *Mater. Des.* 53, 972–982. doi:10.1016/j.matdes.2013.07.087
- Hognestad, E. (1951). A Study of Combined Bending and Axial Load in Reinforced Concrete Members. *Bull. Ser. Urbana-Champaign, Am. Univ. Ill. Eng. Exp. Stn.* 399.
- Karam, E. C., Hawileh, R. A., El Maaddawy, T., and Abdalla, J. A. (2017). Experimental Investigations of Repair of Pre-damaged Steel-Concrete Composite Beams Using CFRP Laminates and Mechanical Anchors. *Thin-Walled Struct.* 112, 107–117. doi:10.1016/j.tws.2016.12.024

- Keykha, A. H. (2019). Behavior of Defective Curved Steel Beams Strengthened by a CFRP Composite. *Mech. Compos. Mat.* 55 (6), 525–534. doi:10.1007/s11029-019-09831-y
- Lin, J., Lin, L., Peng, Z., Xu, R., and Wang, G. (2022). Cracking Performance in the Hogging-Moment Regions of Natural Curing Steel-Uhpc and Steel-Uhtcc Continuous Composite Beams. *J. Bridge. Eng.* 27 (2), 04021106. doi:10.1061/(ASCE)BE.1943-5592.0001820
- Lin, W., and Yoda, T. (2014). Numerical Study on Horizontally Curved Steel-Concrete Composite Beams Subjected to Hogging Moment. *Int. J. Steel. Struct.* 14 (3), 557–569. doi:10.1007/s13296-014-3013-x
- Loh, H. Y., Uy, B., and Bradford, M. A. (2004). The Effects of Partial Shear Connection in the Hogging Moment Regions of Composite Beams Part II-Analytical Study. *J. Constr. Steel Res.* 60 (6), 921–962. doi:10.1016/j.jcsr.2003.10.008
- Nguyen, Q. H., Hjjaj, M., Uy, B., and Guezouli, S. (2009). Analysis of Composite Beams in the Hogging Moment Regions Using a Mixed Finite Element Formulation. *J. Constr. Steel Res.* 65 (3), 737–748. doi:10.1016/j.jcsr.2008.07.026
- Nie, J., Fan, J., and Cai, C. S. (2004). Stiffness and Deflection of Steel-Concrete Composite Beams under Negative Bending. *J. Struct. Eng.* 130 (11), 1842–1851. doi:10.1061/(ASCE)0733-9445(2004)130:11(1842)
- Ollgaard, J., Slutter, R., and Fisher, J. (1971). Shear Strength of Stud Connectors in Lightweight and Normal Concrete. *AISC Eng. J.* 8 (2), 55–64.
- Qin, F., Zhang, Z., Yin, Z., Di, J., Xu, L., and Xu, X. (2020). Use of High Strength, High Ductility Engineered Cementitious Composites (ECC) to Enhance the Flexural Performance of Reinforced Concrete Beams. *J. Build. Eng.* 32, 101746. doi:10.1016/j.jobe.2020.101746
- Song, A., Wan, S., Jiang, Z., and Xu, J. (2018). Residual Deflection Analysis in Negative Moment Regions of Steel-Concrete Composite Beams under Fatigue Loading. *Constr. and Build. Mater.* 158, 50–60. doi:10.1016/j.conbuildmat.2017.09.075
- Sweedan, A. M. I., Alhadid, M. M. A., and El-Sawy, K. M. (2016). Experimental Study of the Flexural Response of Steel Beams Strengthened with Anchored Hybrid Composites. *Thin-Walled Struct.* 99, 1–11. doi:10.1016/j.tws.2015.10.026
- Tavakkolizadeh, M., and Saadatmanesh, H. (2003). Strengthening of Steel-Concrete Composite Girders Using Carbon Fiber Reinforced Polymers. *J. Struct. Eng.* 129 (1), 30–40. doi:10.1061/(ASCE)0733-9445(2003)129:1(30)
- Teng, J. G., Fernando, D., and Yu, T. (2015). Finite Element Modelling of Debonding Failures in Steel Beams Flexurally Strengthened with CFRP Laminates. *Eng. Struct.* 86, 213–224. doi:10.1016/j.engstruct.2015.01.003
- Wang, B., Huang, Q., and Liu, X. (2017). Deterioration in Strength of Stud Based on Two-Parameter Fatigue Failure Criterion. *Steel Compos. Struct.* 23 (2), 239–250. doi:10.12989/scs.2017.23.2.239
- Wang, W., Zhang, X.-d., Zhou, X.-l., Wu, L., and Zhu, H.-j. (2021). Study on Shear Behavior of Multi-Bolt Connectors for Prefabricated Steel-Concrete Composite Beams. *Front. Mat.* 8, 625425. doi:10.3389/fmats.2021.625425
- Zhang, Z., Liu, D., Ding, Y., and Wang, S. (2022). Mechanical Performance of Strain-Hardening Cementitious Composites (SHCC) with Bacterial Addition. *J. Infrastruct. Preserv. Resil.* 3 (3). doi:10.1186/s43065-022-00048-3
- Zhang, Z., Liu, S., Yang, F., Weng, Y., and Qian, S. (2021). Sustainable High Strength, High Ductility Engineered Cementitious Composites (ECC) with Substitution of Cement by Rice Husk Ash. *J. Clean. Prod.* 317, 128379. doi:10.1016/j.jclepro.2021.128379

Conflict of Interest: The authors declare that the research was conducted in the absence of any commercial or financial relationships that could be construed as a potential conflict of interest.

Publisher's Note: All claims expressed in this article are solely those of the authors and do not necessarily represent those of their affiliated organizations, or those of the publisher, the editors, and the reviewers. Any product that may be evaluated in this article, or claim that may be made by its manufacturer, is not guaranteed or endorsed by the publisher.

Copyright © 2022 Song, Xu, Luo and Wan. This is an open-access article distributed under the terms of the Creative Commons Attribution License (CC BY). The use, distribution or reproduction in other forums is permitted, provided the original author(s) and the copyright owner(s) are credited and that the original publication in this journal is cited, in accordance with accepted academic practice. No use, distribution or reproduction is permitted which does not comply with these terms.



Mechanical Performance and Failure Mode Research on the Braced Frame Joint of Tower Cranes in High-Rise Building Construction

Yang Yang, Zhen Zhang, Liangjin Xu* and Gang Yao

Key Laboratory of New Technology for Construction of Cities in Mountain Area, School of Civil Engineering, Chongqing University, Chongqing, China

OPEN ACCESS

Edited by:

Fangying Wang,
University of Nottingham,
United Kingdom

Reviewed by:

Yunchao Tang,
Guangxi University, China
Taichiro Okazaki,
Hokkaido University, Japan

*Correspondence:

Liangjin Xu
xuliangjin@yeah.net

Specialty section:

This article was submitted to
Structural Materials,
a section of the journal
Frontiers in Materials

Received: 29 November 2021

Accepted: 15 March 2022

Published: 08 June 2022

Citation:

Yang Y, Zhang Z, Xu L and Yao G
(2022) Mechanical Performance and
Failure Mode Research on the Braced
Frame Joint of Tower Cranes in High-
Rise Building Construction.
Front. Mater. 9:824693.
doi: 10.3389/fmats.2022.824693

The collapsing number of tower cranes has increased with the development of the building industry. The safety of tower cranes has the potential to improve practices of building and outcomes in construction. The mechanical performance and failure mode of braced frame joints are analyzed in this research. Firstly, a mechanical model of a braced frame joint (BFJ) is established, and the experiment is designed. The destruction process and failure mode are researched by experiment. Then finite element model is established by ABAQUS. Moreover, working conditions with different concrete strength grades (CSG) and tension direction are researched. The results prove that braced frame joint cracks seriously with ultimate bearing capacity, simultaneously, the pre-embedded steel component (PESC) is pulled out. The failure mode is tensile and bending failure of BFJ in the test. The ultimate bearing capacity of failure is controlled by concrete strength grades. The tensile strength increases with the CSG, and the ultimate capacity of BFJ improves equally. The brittle fracture characteristic is more obvious in the ultimate state. The failure mode changes from crushing failure to tensile and bending failure with increasing tension angle. The research results could provide a better understanding of the working mechanism and performance evaluation of the BFJ of the tower crane.

Keywords: braced frame joint, destruction mechanism, ultimate bearing capacity, failure mode, concrete strength grade

1 INTRODUCTION

The height of high-rise buildings increases every year. The duration of construction for most buildings typically lasts longer as building heights increase. A tower crane is an essential equipment for loading and unloading in many construction sites. Tower crane safety during construction has been widely discussed (Forcael et al., 2020; Zhou et al., 2018; Vivian and Ivan, 2011). A tower crane is a multi-degree freedom system, whose dead weight and lifting weight as well as other working loads are carried by braced frame joint (BFJ), and finally, the load is transferred from BFJ to a high-rise structure (Raviv et al., 2017; Wang et al., 2011). The BFJ of the tower crane bears dynamic magnification performance and its reliability is reduced for obvious whiplash effect with external excitation. Engineering accidents often occur during the installation and use of tower cranes, as shown in Figure 1.

Construction machinery safety and the mechanical performance of the structure in construction have been subjects of great concern among researchers (Yang et al., 2021; Yao et al., 2021a; Yao et al., 2021b;

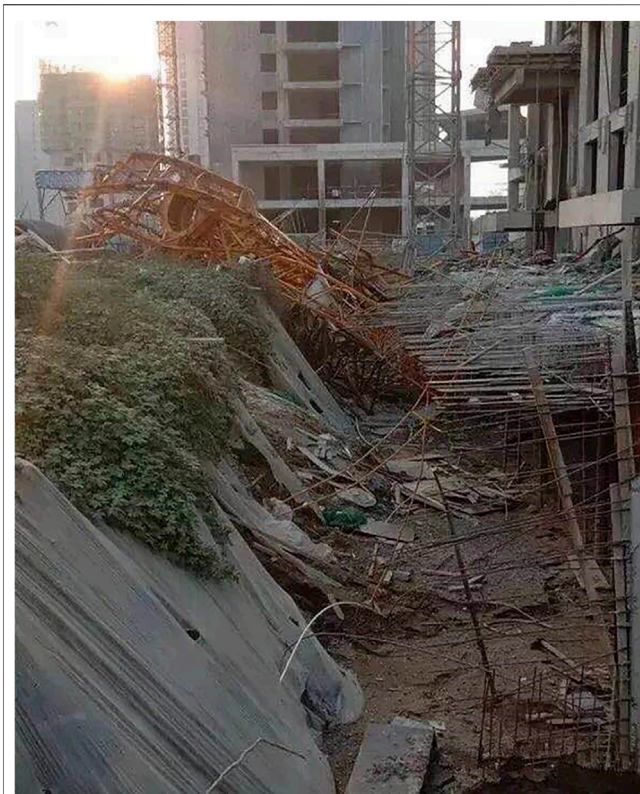
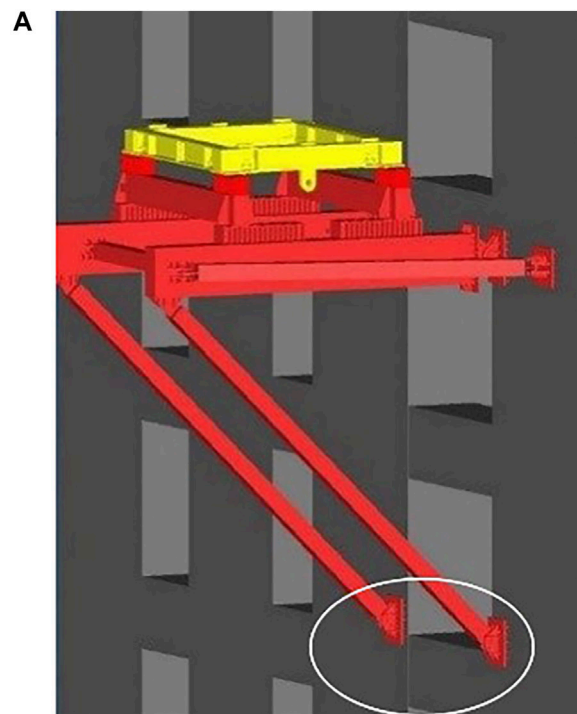


FIGURE 1 | Accident of tower crane during installation.



FIGURE 2 | BFJ of tower crane and cracks.

Zhang and Pan, 2021; Zhang et al., 2020; Chu et al., 2019; Chu et al., 2019; Duan et al., 2020). Concerning accidents include low-frequency high-severity accidents and high-frequency low-severity accidents (Jaafar et al., 2013). Tower crane safety has been analyzed according to respective issues such as the installation and dismantling stages (Shin, 2015), and other studies have considered selection (Briskorn and Dienstknecht, 2019; Sohn et al., 2014; Marzouk and Abubakr, 2016), location (Abdelmegid et al., 2015), earthquakes (Ai et al., 2013; Huang and Syu, 2014), wind



B

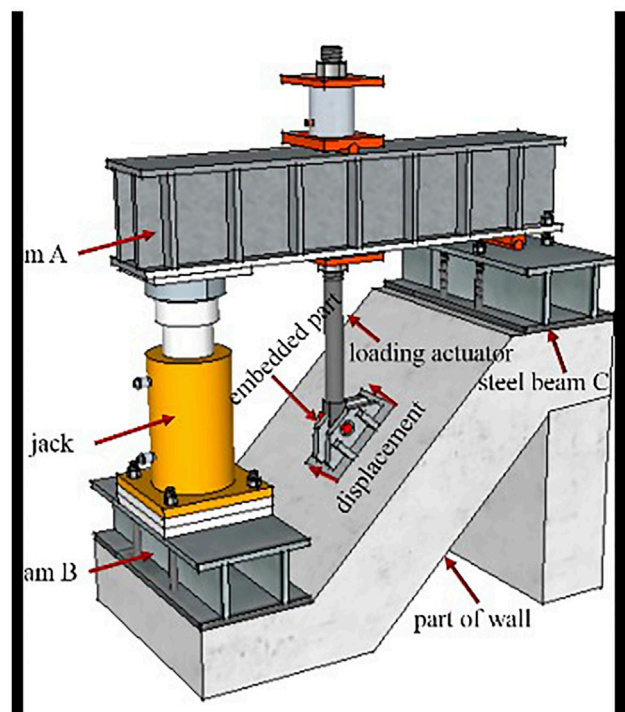


FIGURE 3 | Simplified BFJ and test device: (A) BFJ in construction, (B) test device.

(Mara, 2010; Şahin et al., 2016), and layout (Lien and Cheng, 2014; Younes and Marzouk, 2018). Intelligent monitoring systems (Zheng et al., 2013) and enhanced crane operations (Zavichi et al., 2014;

Shapira and Elbaz, 2014; Peng et al., 2018) have also been the subject of research. Numerical simulation is an efficient and feasible approach in tower crane safety research. SAP 2000, ANSYS, and ABAQUS are the main analysis platforms in establishing the tower crane finite element model (Forcael et al., 2020; Yao et al., 2021a; Ai et al., 2013; Mara, 2010). The building information model (BIM) has been applied in tower crane selection and tower crane layout planning (Ji and Leite., 2018; Wang et al., 2015). Appropriate experiments could demonstrate principles of destruction mechanism and failure mode (Heo et al., 2021; Sui et al., 2020; Wang et al., 2019). There are many kinds of research in the mechanical performance of building structures. Nevertheless, experiments exploring tower crane safety are rare. The mechanical performance of tower crane BFJ plays an important role in tower crane safety. However, few types of research are conducted to address the mechanical performance and destruction of tower crane BFJ. Traditional methods such as increasing section, increasing auxiliary measures, and embedding with both sides of the wall are often adopted to improve the reliability of BFJ. Since the BFJ is a temporary facility during construction, it is dismantled after the completion of the main structure. By increasing the reinforcement ratio or section size of the pre-embedded steel component (PESC) to improve the safety coefficient, the corresponding measures and labor cost increases, which is contrary to the limit state design method of the concept of economy.

This research aims to evaluate the mechanical performance and failure mode of BFJ in high-rise building construction. The working performance of BFJs are examined using reduced scale model tests, numerical simulations, and theoretical analysis. Firstly, a mechanical model of the joint was established, and an experiment was designed to study the destruction mechanism and failure mode of BFJ. Finite element models were established and verified, with CSG and tension direction taken as variables respectively. The failure modes and mechanisms of BFJ were then studied by numerical simulation and theoretical analysis.

2 MECHANICAL MODEL

The load applied to the tower crane transfers of the reinforced concrete core tube through the BFJ. The stability and safety of joints are the premise of the normal operation of the tower crane. Tower cranes are attached to the shear wall in high-rise buildings during construction, as shown in **Figure 2**. The concrete at the supporting point bears a composite effect by horizontal and vertical forces. It is therefore vital to establish a reasonable mechanical model of BFJ, to study the reasons and extension regularities of cracks.

The standard section of the tower crane connects with the building by PESC, the most commonly used BFJ is shown in **Figure 3A**. The vertical load of PESC and concrete in the joints include the dead weight of the tower crane, lifting weight, and the weight of concrete counterbalance. The horizontal load includes wind load, anti-overturning moment, and anti-sliding load. The seismic load, the non-uniform motion of cable and trolley, and the rotation of the crane arm in the horizontal plane will lead to dynamic actions at the joints. In engineering, the force of the tower crane joints is complex, and its direction is also uncertain. The simplified BFJ and test device are shown in **Figure 3**.

Three steel beams are used in the test device. Steel beam A (SBA) aims to provide drawing force. The loading actuator protrudes from the hole in the middle of SBA. During the loading process, the hydraulic jack transmits the thrust to SBA. Steel beam B (SBB) and steel beam C (SBC) are used to the fixed specimen. The steel beam is provided with stiffeners to improve the rigidity and reduce the deformation of SBA, SBB, and SBC. During the loading process, the end of SBA also follows the upward displacement of the hydraulic jack, meaning SBA is slightly inclined. At the same time, the bottom of the SBA separates from the top of the hydraulic jack. To ensure contact between SBA and the hydraulic jack, a movable hinge is designed to ensure contact. During installation, the laser level is used to correct the position of components, which ensures that the center of the jack, the centerline of PESC, and the midpoint of

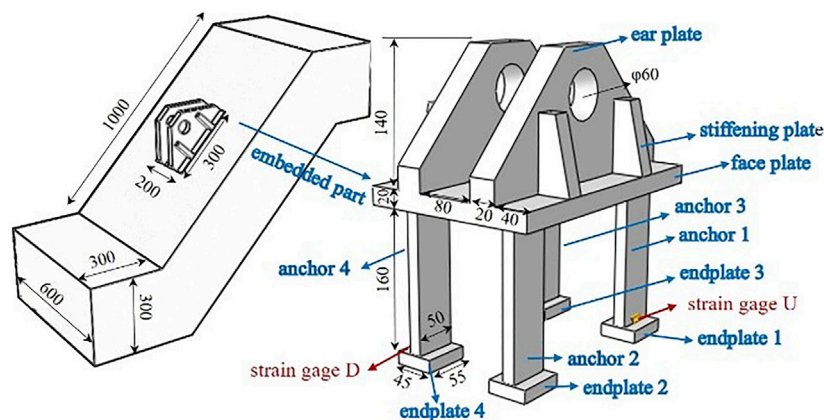


FIGURE 4 | Dimensions and composition of BFJ and PESC (mm).



FIGURE 5 | Main test instruments: (A) digital strain gauge, (B) crack width observer.

the rotating hinge are in the same vertical plane. According to the Saint-venant principle, the local load effect only influences the stress field distribution within a certain range (Bastin et al., 2021;

Bai et al., 2021; Chen and Bai, 2021). Hence, the dimension of BFJ could be increased in number threefold with PESC. The dimensions of tested BFJ specimens are shown in **Figure 4**.

The mechanical performance of BFJ is mainly controlled by the PESC parameters. PESC is composed of five parts, including ear plate, stiffening plate, faceplate, anchor, and endplate, as shown in **Figure 4**. The PESC is an axisymmetric structure, therefore displacement and extreme stress in key locations can reflect mechanical performance. Two strain gages (strain gage U and strain gage D) are placed on anchor one and anchor four respectively.

3 EXPERIMENTAL SETUP

3.1 Testing Device

The experiment was completed in the Structural Laboratory of Chongqing University. The quantitative value of load added on the BFJ is measured with Digital Strain Gauge, and the quantitative value of crack is measured with Crack Width Observer, as shown in **Figure 5**. The detailed parameters and types of main test instruments are shown in **Table 1**.

3.2 Sensor Placement

To study the mechanical properties and failure mechanism of the BFJ, the data measured include tension, displacement of PESC, and the anchor plate strain of PESC. The strain gauges are arranged on the end of the anchor, the measurement points are shown in **Figure 6**.

The pressure sensor is placed between nut and SBA, and hence the measured load value is the exact quantitative value applied on the PESC. It could directly measure the load quantitative value of the hydraulic jack, avoiding the amplified error. Considering the deformation of SBA, SBB, and SBC, measured points are directly installed on the upper side and lower side welded rebar of the PESC and named measured point I and measured point II.

3.3 Material Performance Testing

3.3.1 Concrete Performance Testing

The concrete used for the test comes from the same batch of commercial concrete. Three groups of 150 mm standard test blocks are randomly produced, and there are three specimens in each group. The test specimens are cured under the same conditions. The average actual compressive strength value of the tested concrete is taken as the representative value of the strength. The concrete performance testing is shown in **Figure 7**, and the parameters in **Table 2** are obtained.

TABLE 1 | Parameters of main test instruments.

Instrument	Specification	Resolution	Range	Measurement
Digital Strain Gauge	SDY-2202	1 $\mu\epsilon$	1 \pm 19999 $\mu\epsilon$	load
Pressure Sensor	CZLYB-481	0.1 kN	150kN	load
Rebound Strain Gauge	YCW-100AA	0.01 mm	100 mm	displacement
Static Strain Chamber	DH3816N	0.01 $\mu\epsilon$	1 \pm 19999 $\mu\epsilon$	strain
Crack Width Observer	HC-CK101	0.02 mm	40 mm	crack width

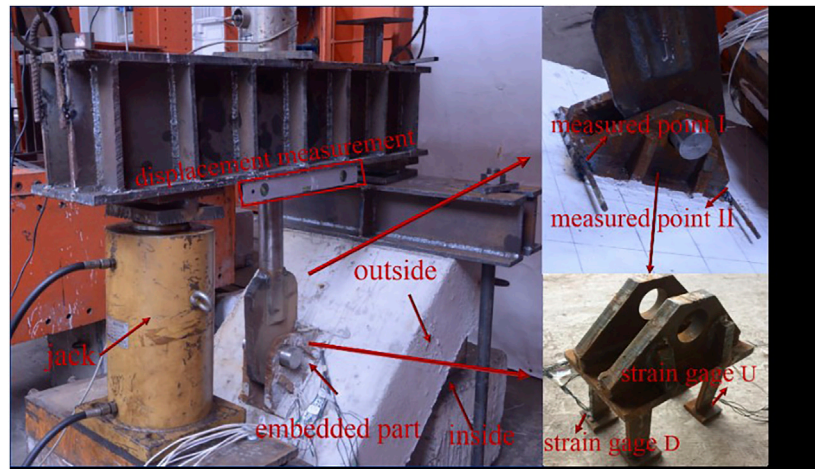


FIGURE 6 | Layout of strain stages and displacement measurement.



FIGURE 7 | Concrete performance test device.

3.3.2 Rebar Performance Testing

Ribbed rebar is used in the test, and the nominal yield strength is 400 MPa. The samples are randomly selected from the same

batch of rebar, and C8 and C10 rebar are taken from each group. Each group included three standard length test pieces, and the tensile test is carried out on the INSTRON 1342 static test-machine, as shown in **Figure 8**. The yield strength, ultimate strength, and elastic modulus are measured and shown in **Table 3**.

3.3.3 Steel Plate Performance Testing

The PESK is made of Q345C, and the nominal yield strength is 345 MPa. The standard metal plates are made of the same steel, the tensile test is carried out on the INSTRON 1342 static test-machine, and the yield strength, ultimate strength, and elastic modulus are measured and shown in **Table 4**.

3.4 Loading Scheme and Test Result

A stepwise monotonic static loading project is taken in the test. Preloading is carried out before formal loading and all the test instruments are determined to work normally and the device is reliable. The preloaded data is used to judge the relationship between load and deformation, and the test piece and the support are in contact. After preloading, unloading to 0, and then starting the formal loading, the cracking point, yield point, and limit point are captured during the loading process, the differential is adjusted downward around the point locations, and the load of each level lasts 1.0 min.

The mechanic behavior of BFJ is closely associated with crack propagation. The destruction mechanism and failure mode can be

TABLE 2 | Concrete performance parameters.

Group	Actual Compressive strength (MPa)			Average (MPa)	Characteristic Value of Axial Compressive strength (MPa)	Characteristic Value of Axial Tensile strength (MPa)	Elastic modulus ($\times 10^4$ MPa)
	Test 1	Test 2	Test 3				
Group 1	34.7	31.7	31.5	32.63	20.29	2.20	2.99
Group 2	35.1	32.7	34.9	34.23	22.15	2.31	2.98
Group 3	34.9	36.8	33.7	35.13	22.75	2.37	3.06

reflected by crack propagation. The critical points and corresponding crack states are recorded and shown in **Figure 9**. The full load–strain relationships of BFJ are shown in **Figure 10**.

The cracking load is 141.0kN, with a 2.6 mm tensile crack at the bottom of PESC. When the load is 184.0kN, two tensile cracks appeared with 2.0 and 1.6 mm in width, as shown in **Figure 9A**. When the load is 282.0kN, shear cracks appear at the bottom center of PESC. The concrete at the bottom of PESC is displacement damaged with lateral uplift, as shown in **Figure 9B**. The upper corner of the PESC produced an oblique crack with 2.4 mm in width when the load is 361.0 kN, as shown in **Figure 9C**. When the BFJ is finally destroyed, there are two main tensile cracks with 10.8 and 11.2 mm, and the largest main shear crack is 10.6 mm. **Figure 9D** indicates that there is no plastic deformation in PESC, and hence the failure of BFJ is determined by concrete. Cracks of specimens concentrate mainly on the central and bottom of PESC. Moreover, tensile shear crack concentrates mainly on a 45° angle, as shown in **Figure 9E**. The extreme values in strain gage U and D are 1,524 and 711 respectively, as shown in **Figure 10**. The PESC deformation in the anchor end has an obvious difference from the tension. Both of the strains dropped after the final destruction of BFJ, and hence PESC deformation is elastic deformation without destruction.

4 NUMERICAL ANALYSIS

4.1 Numerical Simulation

Numerical models with different working conditions are established to study the mechanical performance of BFJ. The detailed parameters of numerical models are given in **Tables 5, 6**.

The PESC element is embedded in the concrete element with the “Embedded Region” command in ABAQUS. The “surface to surface contact” of ABAQUS is set between the surfaces of PESC and the concrete component. The deformation coordination of BFJ is realized by setting the friction contact property. Mesh density and element quality should be simplified to a certain degree because of limited computer performances. The element information used in finite element models is given in **Figure 11**. In order to research the influence of tension direction and CSG, nine working conditions were set up and analyzed in the finite element model, parameters are shown in **Table 7**.

4.2 Comparison Between Model and Experiment

The cross-comparison between test and simulation was taken to verify the correctness and reliability of the numerical simulation, as shown in **Figure 12**.

TABLE 4 | Testing parameters of steel plate.

Parameter	Test 1	Test 2	Test 3	Average
Yield strength (MPa)	362.4	379.1	395.7	379.07
Ultimate strength (MPa)	525.7	576.4	550.0	550.7
Elastic modulus ($\times 10^5$ MPa)	1.99	2.00	2.24	2.08



FIGURE 8 | Steel plate performance testing.

The ultimate bearing capacity is 361.0kN in experiment and 355.0kN in numerical simulation. PESC stiffness has almost no change in the early stage of loading. The BFJ is still in the elastic stage, and only small cracks are generated. The displacements are shown in **Figure 12** and have a good consistency. The displacements gradually increase rapidly with the increasing load. The stress distribution of the PESC is also shown in **Figure 12**. The principal tensile stress on the bottom of PESC is larger. The stress of PESC is relatively lower than

TABLE 3 | Rebar performance testing parameter.

Diameter (mm)	Actual Yield strength (MPa)				Actual Ultimate strength (MPa)				Elastic Modulus ($\times 10^5$ MPa)
	Test 1	Test 2	Test 3	Average	Test 1	Test 2	Test 3	Average	
10	413.50	450.6	435.9	433.3	581.20	572.60	596.00	583.3	2.11
8	445.8	423.6	409.60	426.1	569.60	578.70	554.60	567.6	2.07

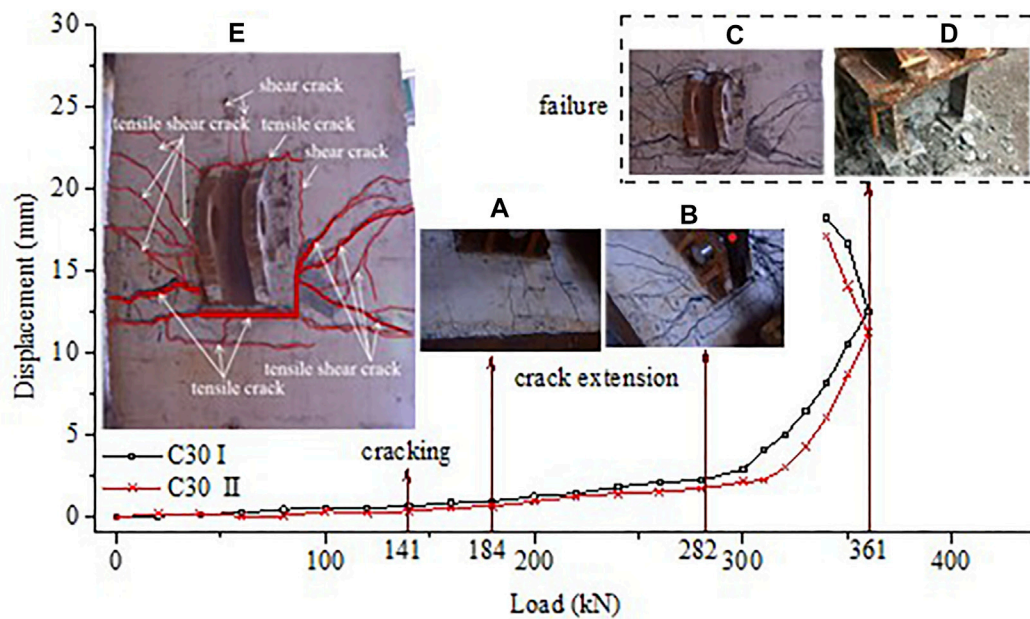


FIGURE 9 | Load-displacement relationships of BFJ.

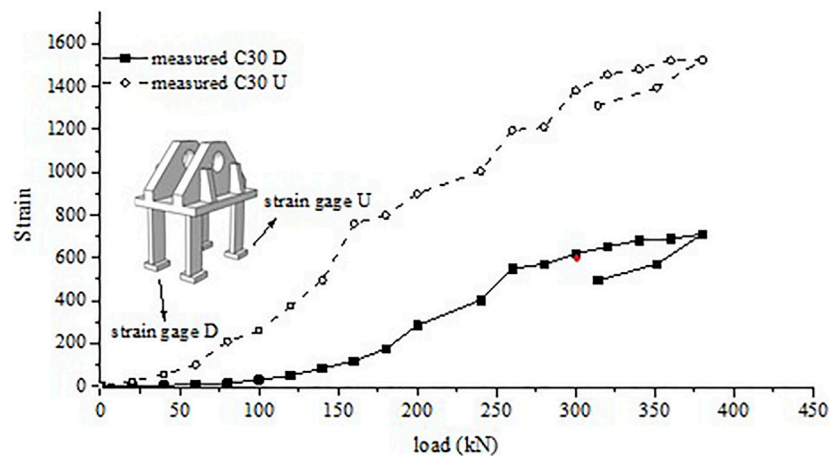


FIGURE 10 | Load-strain relationships of PESC.

TABLE 5 | Material properties in finite element model. Steel material properties.

Description	Material	Yield stress	Ultimate strength	Poisson ratio	Elastic modulus	Element selection
PESC	Q345B Steel	379.07 MPa	550. 7 MPa	0.3	2.08×10^5 MPa	C3D8R
Rebar	$\phi 8$ HRB400	426.1 MPa	567.6 MPa	0.25	2.07×10^5 MPa	T3D2
Rebar	$\phi 10$ HRB400	433.3 MPa	583.3 MPa	0.3	2.11×10^5 MPa	T3D2

the yield strength. The elastic deformation appeared in the PESC, but the PESC is not in failure mode, which is consistent with the experimental results. The PESC failure

mode in the simulation corresponds with the experiment. The numerical model has high credibility and could be used in the parametric analysis of PESC.

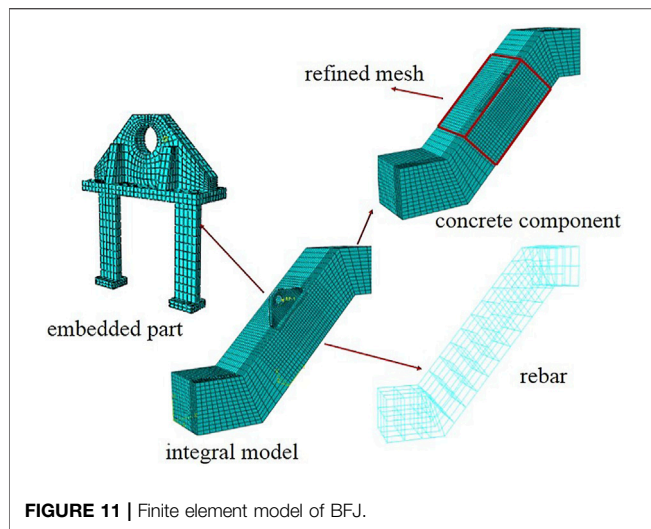


FIGURE 11 | Finite element model of BFJ.

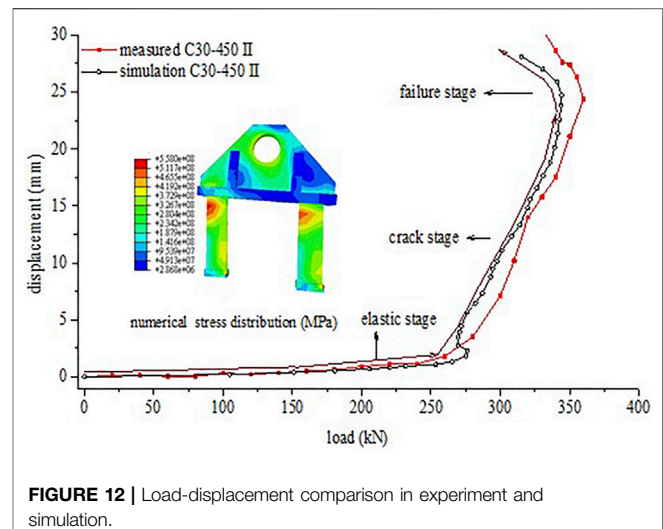


FIGURE 12 | Load-displacement comparison in experiment and simulation.

TABLE 6 | Material properties in finite element model. Steel Concrete material properties.

Description	Material	Compressive strength	Tensile strength	Elastic modulus	Element selection
Concrete component	C20 Concrete	17.6 MPa	1.76 MPa	2.55×10^4 MPa	C3D8R
Concrete component	C30 Concrete	21.09 MPa	2.09 MPa	3.03×10^4 MPa	C3D8R
Concrete component	C40 Concrete	33.6 MPa	3.36 MPa	3.25×10^4 MPa	C3D8R
Concrete component	C50 Concrete	40.0 MPa	4.00 MPa	3.45×10^4 MPa	C3D8R
Concrete component	C60 Concrete	48.0 MPa	4.80 MPa	3.60×10^4 MPa	C3D8R

TABLE 7 | Working condition parameters.

Working Condition	CSG	Tension Direction	Working Condition	CSG	Tension Direction
C20-450	C20	45.0°	C30-000	C30	0.0°
C30-450	C30	45.0°	C30-225	C30	22.5°
C40-450	C40	45.0°	C30-675	C30	67.5°
C50-450	C50	45.0°	C30-900	C30	90.0°
C60-450	C60	45.0°			

4.3 Influence of CSG

During the construction of high-rise buildings, the CSG increases with the rising of the core tube. Therefore, it is of great practical significance to study the mechanical performance of the BFJs with different CSGs. The CSGs are taken as C20, C30, C40, C50, and C60 in the study. The constitutive relationships of concrete are defined in the Property module of ABAQUS. The finite element model analysis is carried out to obtain the load-displacement relationships and ultimate bearing capacity with different CSGs, as shown in Figure 13.

Figure 13 shows that the load-displacement relationships could generally be divided into three stages, including the elastic stage, crack stage, and failure stage. During the initial loading period, the relationships show a linear relationship with a small displacement. It is speculated that concrete and the PESCs only produced elastic deformations, and hence the

initial stiffness of each specimen is relatively similar. With the increase of displacements, track transition relationships occur during the crack stage. Combining the results of the tests, it can be speculated that the concrete is cracked and the stiffness is affected. The load-displacement relationships have a significant decline phase when the specimen is pulled out. The slope of the relationships becomes steeper with increasing CSG in the failure stage, and the brittle failure phenomenon becomes more obvious. The reason for this is the constitutive relation of the concrete material and the slip on the contact surface. The ultimate bearing capacity of C20-450, C30-450, C40-450, C50-450 and C60-450 were 341.1, 350.6, 355.1, 365.8, and 388.1 MPa respectively. The ultimate bearing capacity increase with increasing CSG. In the crack stage, each finite element model has an extreme value, combining with the experiment phenomenon, which has the characteristic of major cracks appearing. The characteristic

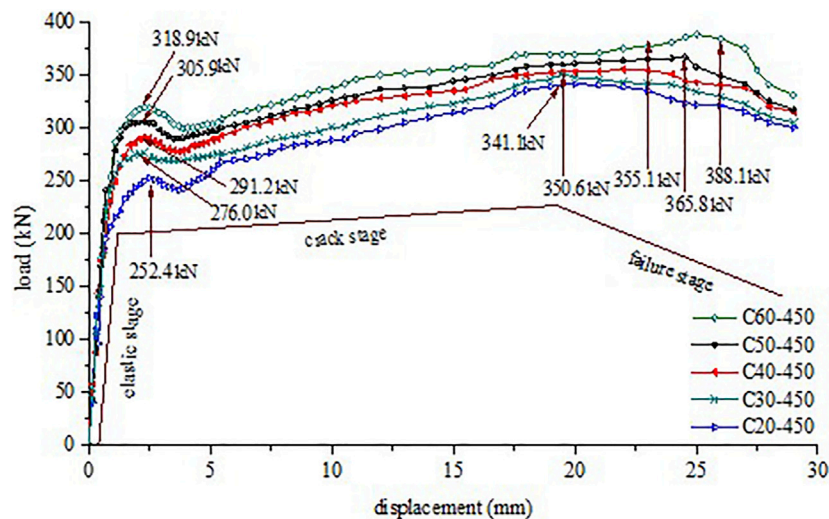


FIGURE 13 | Influence of CSG on load-displacement.

crack values of C20–450, C30–450, C40–450, C50–450, and C60–450 are 252.4, 276.0, 291.2, 305.9, and 318.9 MPa respectively, and the characteristic crack values also increase with the increase of CSG.

To explore the destruction change in PESC and concrete components with ultimate bearing capacity, the stress and damage distribution of the specimens with different CSGs are shown in Figures, 14, 15.

Based on a comparison of the PESC in Figures 14A–C, the stress distribution of different concrete grades of PESC are similar, especially in the location of stress concentration. All three locations of stress concentrations are located on the interface of anchor and faceplate. The peak value is 555.9 MPa, 562.4.9 MPa, and 594.0 MPa. The stress in ear plate and anchor are larger than the faceplate and endplate. With the action of transverse shear force, the anchor and concrete are mutually squeezed, thus stress on one side of the embed is concentrated. Other parts of the PESC are in the elastic stage, and the safety reservation is sufficient.

As shown in Figure 15, concrete crushing parts are always concentrated around the PESC. This is the result of the transverse shear action between PESC and concrete. The damage concentration area reduces with the increase of CSG. The failure modes of the specimens have similarities in Figure 15. A large number of cracks are generated on the concrete surface in a failure state, and concretes are cracked and damaged with severe tension. It is speculated that failure mode is controlled by concrete tensile strength. Ultimate bearing capacity increases with the increase of concrete.

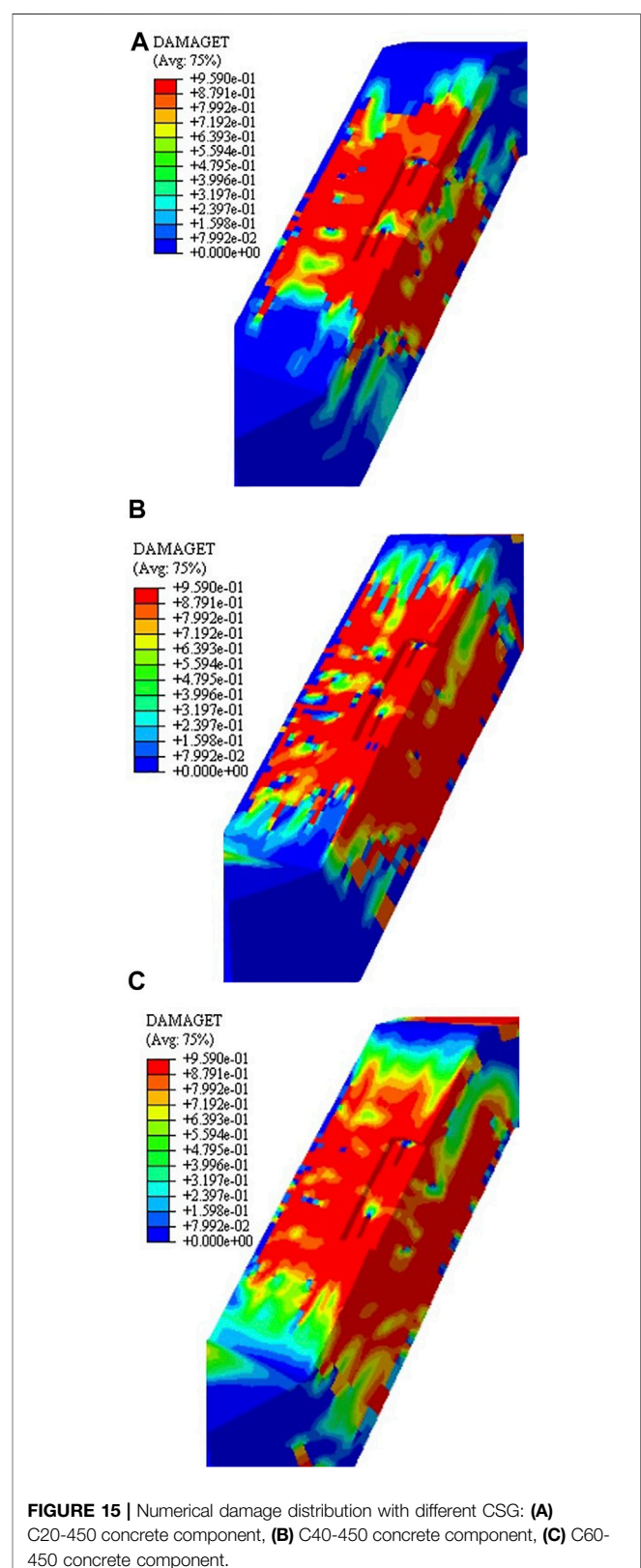
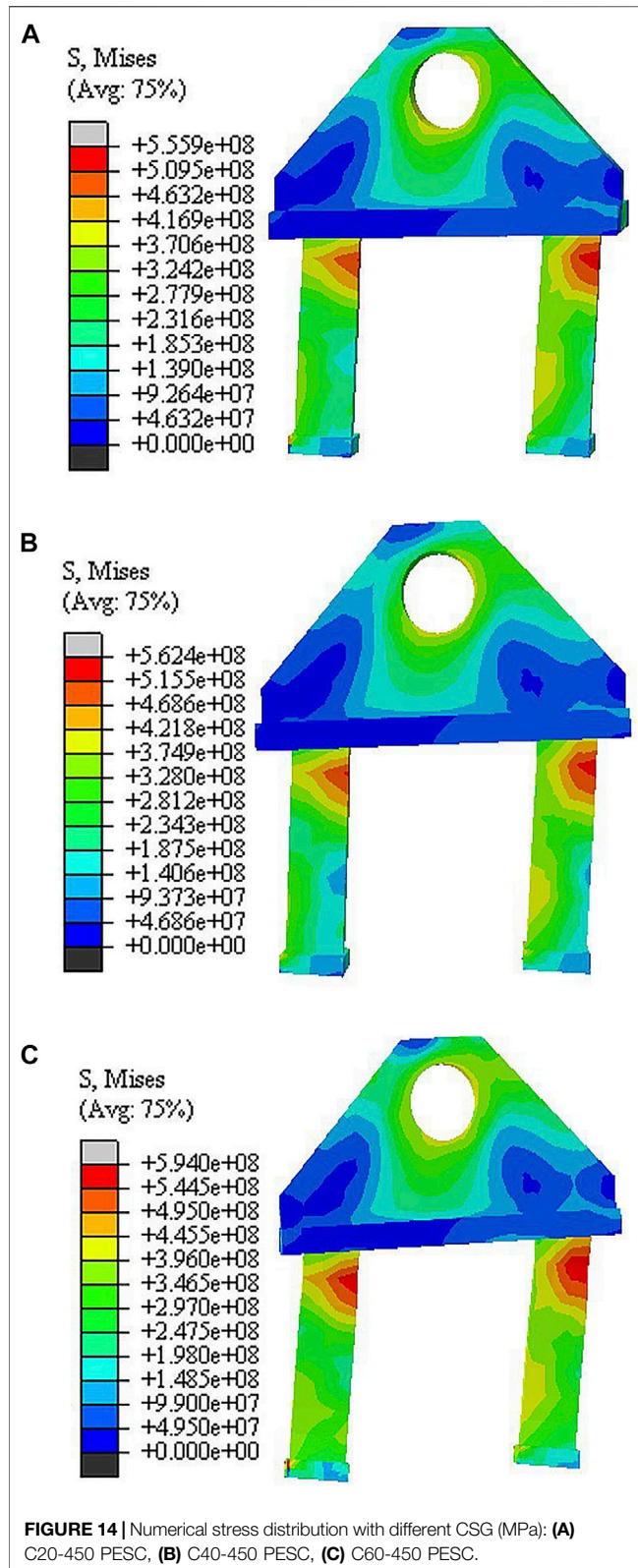
4.4 Influence of Tension Direction

To research the influence of the tension direction on BFJ, the tension directions were taken from 0.0° to 90.0°, with a 22.5° stepwise. The finite element model analysis was carried out to obtain the load-displacement relationships and ultimate bearing capacity with different tension directions, as shown in Figure 16.

Figure 16 indicates that the load-displacement relationships could generally be divided into three stages, including the elastic stage, crack stage, and failure stage. The initial stiffness of the specimens is close to different working conditions in the elastic stage. With increasing load, the specimens begin to yield. The specimens are destroyed and ultimate bearing capacity can be obtained in the failure stage. The ultimate bearing capacity of C30–900, C30–675, C30–450, C30–225 and C30–000 were 273.1, 301.6, 350.6, 363.1, and 375.7 MPa respectively. The ultimate bearing capacity has a great difference with changes of tension direction. In the crack stage, the characteristic crack values of C30–900, C30–675, C30–450, C30–225, and C30–000 are 223.7, 264.5, 276.0, 285.3, and 293.2 MPa respectively. Therefore, the tension direction has an obvious effect on the ultimate bearing capacity and characteristic crack value. When the tension direction changes to 0.0°, the concrete is subjected to tangential shear force, and compressive strength plays an important role. When the tension direction changes to 90.0°, the concrete is subjected to normal tension, and tensile strength plays an important role.

As can be seen from the numerical stress distribution of Figure 17, PESC with 0.0° tension direction has the largest deformation. There are two main locations of stress concentration in C30–000 PESC, at the top of the anchor and around the draw hole. Stress concentration is located at the top of the anchor in C30–450 PESC. Nevertheless, PESC with 90.0° tension direction is still in the elastic state when the specimen is destroyed. Stress on the anchor is larger than the ear plate and faceplate.

The numerical stress distribution outlined in Figure 18 indicates that the damaged area is largest in the C30–450 concrete component. Damage in the C30–450 concrete component is the second largest and the C30–000 concrete component is the smallest. The specimen shears mainly tangentially and the compression damage is mainly concentrated on the top of the anchor plate. The transition



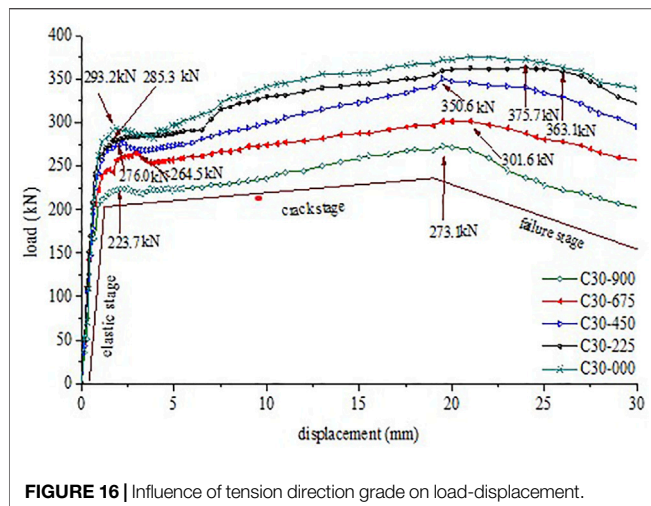


FIGURE 16 | Influence of tension direction grade on load-displacement.

region from damage to undamaged has an obvious difference. The C30-450 concrete component has the largest transition region, and C30-000 concrete component has the smallest transition region. The concrete around the upper side of PESC is crushed by the shear force, which is the reason for the failure of the specimen with 0.0° tension direction. When the tension direction changes to 90.0° , the crushed area is gradually reduced, and the tensile area gradually increases. The tension direction can affect the final failure mode. The change of tension direction has a more obvious effect than CSG.

5 CONCLUSION

This study examined the mechanical performance of BFJ by experiment and numerical simulation. The experiment used a reduced scale prototype model test and a whole process numerical simulation of the model was carried out by the finite element method. The loading process can be fitted to a straight line in the early stage with little displacement, and the structure is in the linear elastic state. The stiffness degraded as the loading and the slope of the curve decreased. In the failure stage, the crack distribution range expanded and the stiffness degradation became more serious. The cracks of BFJ can be distributed into three classes, tensile crack, tensile shear crack, and shear crack. The cracks of the specimens were concentrated mainly on the central and bottom of PESC. The development and connection of cracks may be the reason for abrupt stiffness degradation. The ultimate bearing capacity and characteristic crack value increased with the increase of CSG. The stress distribution with different concrete grades of PESC was similar, especially in the location of stress concentration. Concrete crushing parts were always concentrated around the PESC. The stress concentration area in the concrete component reduced with the increase of CSG. The failure mode was controlled by concrete tensile strength. The construction stage of BFJ should hence be taken into consideration in safety checking. The tension direction has an obvious effect on the

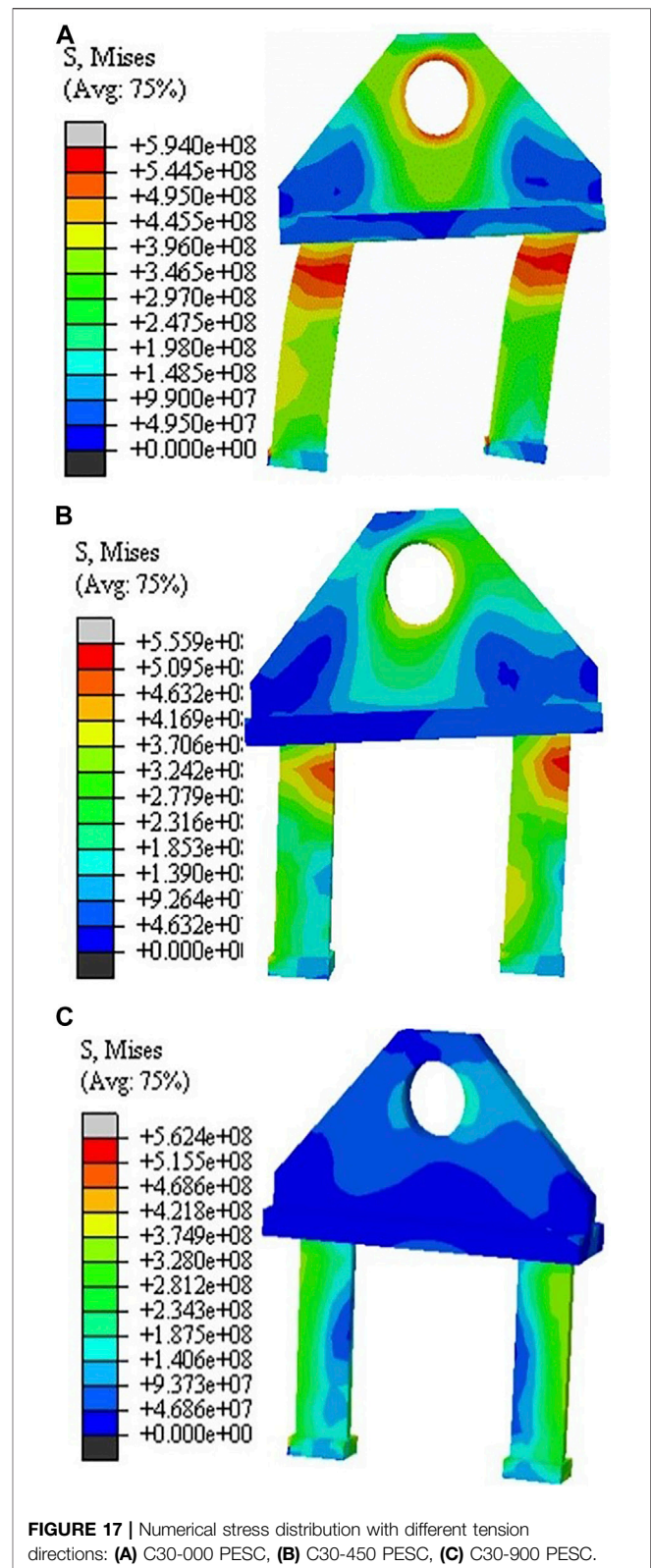
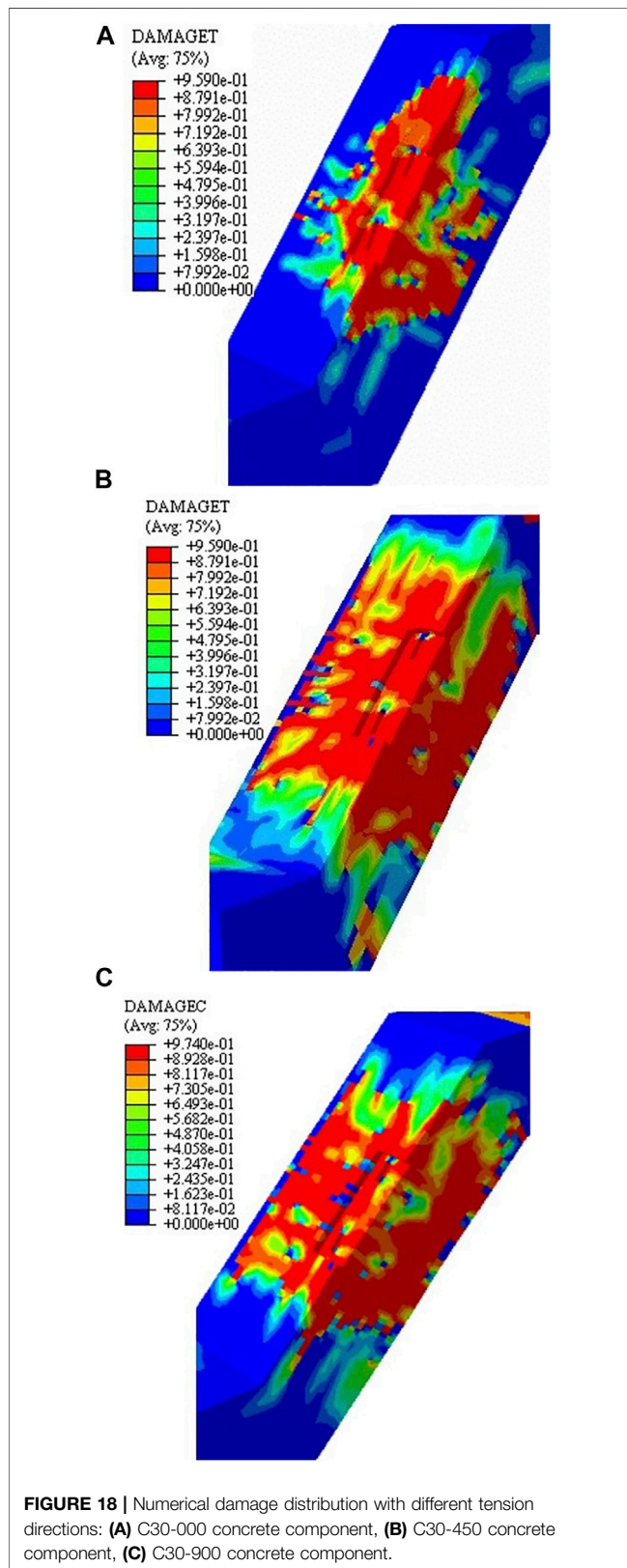


FIGURE 17 | Numerical stress distribution with different tension directions: (A) C30-000 PESC, (B) C30-450 PESC, (C) C30-900 PESC.

ultimate bearing capacity and characteristic crack value. When tension direction changes to 0.0° , concrete is subjected to tangential shear force. When the tension direction changes to



90.0°, the concrete is subjected to normal tension. The concrete around the upper side of the PESC is crushed by shear force and is the reason for the failure of specimens with 0.0° tension direction. When the tension direction changed to 90.0°, the crushed area gradually reduced, and the tensile area gradually increased. Therefore, the aggregate of all external incentives should be calculated to get the accurate direction of the force. The reasons for tower crane failures are complicated. The nodal instability and mechanical properties of the joints were studied herein by combining experiments and computer simulations, but the influence of different joint structures on the bearing capacity of the tower crane was not considered. The type of material is also critical to the crane's carrying capacity. Future research should focus on the design of the different joints of the tower crane and material properties. Seismic analysis is also necessary when monitoring the tower crane. With the pace of urbanization accelerating and the density of construction groups increasing, it is necessary to analyze the BFJ of tower cranes in high-rise building construction to improve safety and security (Tang Y. C. et al., 2021; Tang Y. et al., 2021).

DATA AVAILABILITY STATEMENT

The original contributions presented in the study are included in the article/Supplementary Material, further inquiries can be directed to the corresponding author.

AUTHOR CONTRIBUTIONS

Conceptualization, YY and GY; methodology, YY and GY; software, YY and ZZ; formal analysis, YY, ZZ and LX; writing-original draft preparation, YY and GY; writing-review and editing, YY, ZZ and LX All authors have read and agreed to the published version of the manuscript.

FUNDING

This work was funded by the 111 Project of the Ministry of Education and the National Key R and D Program of the Ministry of Science and Technology (No. 2019YFD1101005-4).

REFERENCES

- Abdelmegid, M. A., Shawki, K. M., and Abdel-Khalek, H. (2015). GA Optimization Model for Solving tower crane Location Problem in Construction Sites. *Alexandria Eng. J.* 54 (3), 519–526. doi:10.1016/j.aej.2015.05.011
- Ai, B., Yang, J. L., and Pei, Z. Z. (2013). Seismic Response Analysis of tower crane in Consideration of the Building-crane Interaction. *Appl. Mech. Mater.* 353-356, 1981–1985. doi:10.4028/www.scientific.net/amm.353-356.1981
- Bai, J., Chen, H., Zhao, J., Liu, M., and Jin, S. (2021). Seismic Design and Subassembly Tests of Buckling-Restrained Braced RC Frames with Shear Connector Gusset Connections. *Eng. Structures* 234, 112018. doi:10.1016/j.engstruct.2021.112018

- Bastin, G., Coron, J.-M., and Hayat, A. (2021). Feedforward Boundary Control of 2x2 Nonlinear Hyperbolic Systems with Application to Saint-Venant Equations. *Eur. J. Control.* 57, 41–53. doi:10.1016/j.ejcon.2020.11.002
- Briskorn, D., and Dienstknacht, M. (2019). Mixed-integer Programming Models for tower crane Selection and Positioning with Respect to Mutual Interference. *Eur. J. Oper. Res.* 273 (1), 160–174. doi:10.1016/j.ejor.2018.07.033
- Chen, H., and Bai, J. (2021). Seismic Performance Evaluation of Buckling-Restrained Braced RC Frames Considering Stiffness and Strength Requirements and Low-Cycle Fatigue Behaviors. *Eng. Structures* 239, 112359. doi:10.1016/j.engstruct.2021.112359
- Chu, Y., He, X., Yao, Y., and Hou, H. (2019). Experimental Research on the Shear Performance of the Two-Storey Composite Cold-Formed Thin-Walled Steel wall. *KSCE J. Civ. Eng.* 24 (2), 537–550. doi:10.1007/s12205-019-5519-4
- Duan, M., Zhang, S., Wang, X., and Dong, F. (2020). Mechanical Behavior in Perfbond Rib Shear Connector with UHPC-Steel Composite Structure with Coarse Aggregate. *KSCE J. Civ. Eng.* 24 (4), 1255–1267. doi:10.1007/s12205-020-0923-3
- Forcael, E., Young, G., Opazo, A., Rodríguez, C., and Bayona, A. (2020). The Effects of Temporary tower Cranes on the Construction Process and Seismic Behavior of Reinforced concrete Buildings. *KSCE J. Civ. Eng.* 24 (2), 580–595. doi:10.1007/s12205-020-1257-x
- Heo, G., Choi, H., Baek, E., and Kim, C. (2021). Development of Viscoelastic Damper System to Improve Seismic Performance of Storage Racks. *KSCE J. Civ. Eng.* 25 (9), 3390–3400. doi:10.1007/s12205-021-1024-7
- Huang, L. J., and Syu, H. J. (2014). Seismic Response Analysis of tower crane Using SAP2000. *Proced. Eng.* 79, 513–522.
- Jaafar, H. I., Mohamed, Z., Jamian, J. J., Abidin, A. F. Z., Kassim, A. M., and Ghani, Ab. (2013). Dynamic Behaviour of a Nonlinear Gantry crane System. *Proced. Tech* 11, 419–425. doi:10.1016/j.protcy.2013.12.211
- Ji, Y., and Leite, F. (2018). Automated tower crane Planning: Leveraging 4-dimensional BIM and Rule-Based Checking. *Automation in Construction* 93, 78–90. doi:10.1016/j.autcon.2018.05.003
- Lien, L.-C., and Cheng, M.-Y. (2014). Particle Bee Algorithm for tower crane Layout with Material Quantity Supply and Demand Optimization. *Automation in Construction* 45, 25–32. doi:10.1016/j.autcon.2014.05.002
- Mara, T. G. (2010). Effects of a Construction tower crane on the Wind Loading of a High-Rise Building. *J. Struct. Eng.* 136 (11), 1453–1460. doi:10.1061/(asce)st.1943-541x.0000243
- Marzouk, M., and Abubakar, A. (2016). Decision Support for tower crane Selection with Building Information Models and Genetic Algorithms. *Automation in Construction* 61, 1–15. doi:10.1016/j.autcon.2015.09.008
- Peng, B., Flager, F. L., and Wu, J. (2018). A Method to Optimize mobile crane and Crew Interactions to Minimize Construction Cost and Time. *Automation in Construction* 95, 10–19. doi:10.1016/j.autcon.2018.07.015
- Raviv, G., Fishbain, B., and Shapira, A. (2017). Analyzing Risk Factors in crane-related Near-Miss and Accident Reports. *Saf. Sci.* 91, 192–205. doi:10.1016/j.ssci.2016.08.022
- Şahin, Y., Levent, M., and Hira, K. (2016). Analysis of Active Vibration Control of Multi-Degree-Of-freedom Flexible Systems by Newmark Method. *Simul. Model. Pract. Theor.* 69, 136–148.
- Shapira, A., and Elbaz, A. (2014). Tower crane Cycle Times: Case Study of Remote-Control versus Cab-Control Operation. *J. Constr. Eng. Manage.* 40 (12), 904. doi:10.1061/(asce)co.1943-7862.0000904
- Shin, I. J. (2015). Factors that Affect Safety of tower crane Installation/dismantling in Construction Industry. *Saf. Sci.* 72, 379–390. doi:10.1016/j.ssci.2014.10.010
- Sohn, H. W., Hong, W. K., Lee, D., Lim, C. Y., Wang, X. Y., and Kim, S. (2014). Optimum tower crane Selection and Supporting Design Management. *Int. J. Adv. Robot. Syst.* 133 (11), 438. doi:10.5772/58438
- Sui, W., Li, H., Zhang, Q., and Wang, Z. (2020). Hysteretic Mechanical Behaviour of an Eccentrically Loaded partially-concrete-filled Steel Tubular Bridge Pier under Out-Of-Plane Horizontal Cyclic Loading. *KSCE J. Civ. Eng.* 24 (5), 1509–1523. doi:10.1007/s12205-020-0680-3
- Tang, Y. C., Chen, Z., Feng, W. H., Nong, Y. M., Li, C., and Chen, J. M. (2021a). Combined Effects of Nano-Silica and Silica Fume on the Mechanical Behavior of Recycled Aggregate concrete. *Nanotechnol. Rev.* 10 (1), 819–838.
- Tang, Y., Feng, W., Chen, Z., Nong, Y., Guan, S., and Sun, J. (2021b). Fracture Behavior of a Sustainable Material: Recycled concrete with Waste Crumb Rubber Subjected to Elevated Temperatures. *J. Clean. Prod.* 318, 128553. doi:10.1016/j.jclepro.2021.128553
- Vivian, W. Y. T., and Ivan, W. H. F. (2011). Tower crane Safety in the Construction Industry: a Hong Kong Study. *Saf. Sci.* 49 (2), 208–215.
- Wang, S. C., Shen, R. S., Jin, T. H., and Song, S. J. (2011). Dynamic Behavior Analysis and its Application in tower crane Structure Damage Identification. *Adv. Mater. Res.* 368–373, 2478–2482. doi:10.4028/www.scientific.net/amr.368-373.2478
- Wang, J., Zhang, X., Shou, W., Wang, X., Xu, B., Kim, M. J., et al. (2015). A BIM-Based Approach for Automated tower crane Layout Planning. *Automation in Construction* 59, 168–178. doi:10.1016/j.autcon.2015.05.006
- Wang, H., Li, P. C., and Wu, M. E. (2019). Crossarm Length Optimization and post-buckling Analysis of Prestressed Stayed Steel Columns. *Thin-walled Struct.* 144, 106371. doi:10.1016/j.tws.2019.106371
- Yang, Y., Yang, L., and Yao, G. (2021). Post-processing of High Formwork Monitoring Data Based on the Back Propagation Neural Networks Model and the Autoregressive-Moving-Average Model. *Symmetry* 13 (8), 1543. doi:10.3390/sym13081543
- Yao, G., Wu, C. Y., and Yang, Y. (2021a). Scientometric Analysis for Mechanical Performance on Broken-Line Long-Span Steel Structure in Construction Considering Geometric Nonlinearity. *Symmetry* 13 (7), 1229. doi:10.3390/sym13071229
- Yao, G., Guo, H. T., Yang, Y., Xiang, C. M., and Robert, S. (2021b). Dynamic Characteristics and Time-History Analysis of Hydraulic Climbing Formwork for Seismic Motions. *Adv. Civil Eng.* 2021, 1–17. doi:10.1155/2021/2139153
- Younes, A., and Marzouk, M. (2018). Tower Cranes Layout Planning Using Agent-Based Simulation Considering Activity Conflicts. *Automation in Construction* 93, 348–360. doi:10.1016/j.autcon.2018.05.030
- Zavichi, A., Madani, K., Xanthopoulos, P., and Oloufa, A. A. (2014). Enhanced crane Operations in Construction Using Service Request Optimization. *Automation in Construction* 47, 69–77. doi:10.1016/j.autcon.2014.07.011
- Zhang, Z., Elbashiry, M. A. E., Chen, J., Wei, P., and Fu, Y. (2020). Optimization of the Structural Parameters of the Vertical Trabeculae Beetle Elytron Plate Based on the Mechanical and thermal Insulation Properties. *KSCE J. Civ. Eng.* 24 (12), 3765–3774. doi:10.1007/s12205-020-2334-x
- Zhang, Z. Q., and Pan, W. (2021). Multi-criteria Decision Analysis for tower crane Layout Planning in High-Rise Modular Integrated Construction. *Automat. Constr.* 127, 103709. doi:10.1016/j.autcon.2021.103709
- Zheng, X. J., Zeng, J. B., and Zhang, H. (2013). Research of Intelligent Monitoring System of tower crane Based on RFID. *Adv. Mater. Res.* 706–708, 990–994. doi:10.4028/www.scientific.net/AMR.706-708.990
- Zhou, W., Zhao, T., Liu, W., and Tang, J. (2018). Tower crane Safety on Construction Sites: a Complex Sociotechnical System Perspective. *Saf. Sci.* 109, 95–108. doi:10.1016/j.ssci.2018.05.001

Conflict of Interest: The authors declare that the research was conducted in the absence of any commercial or financial relationships that could be construed as a potential conflict of interest.

Publisher's Note: All claims expressed in this article are solely those of the authors and do not necessarily represent those of their affiliated organizations, or those of the publisher, the editors and the reviewers. Any product that may be evaluated in this article, or claim that may be made by its manufacturer, is not guaranteed or endorsed by the publisher.

Copyright © 2022 Yang, Zhang, Xu and Yao. This is an open-access article distributed under the terms of the Creative Commons Attribution License (CC BY). The use, distribution or reproduction in other forums is permitted, provided the original author(s) and the copyright owner(s) are credited and that the original publication in this journal is cited, in accordance with accepted academic practice. No use, distribution or reproduction is permitted which does not comply with these terms.

Advantages of publishing in Frontiers



OPEN ACCESS

Articles are free to read
for greatest visibility
and readership



FAST PUBLICATION

Around 90 days
from submission
to decision



HIGH QUALITY PEER-REVIEW

Rigorous, collaborative,
and constructive
peer-review



TRANSPARENT PEER-REVIEW

Editors and reviewers
acknowledged by name
on published articles

Frontiers

Avenue du Tribunal-Fédéral 34
1005 Lausanne | Switzerland

Visit us: www.frontiersin.org

Contact us: frontiersin.org/about/contact



REPRODUCIBILITY OF RESEARCH

Support open data
and methods to enhance
research reproducibility



DIGITAL PUBLISHING

Articles designed
for optimal readership
across devices



FOLLOW US

@frontiersin



IMPACT METRICS

Advanced article metrics
track visibility across
digital media



EXTENSIVE PROMOTION

Marketing
and promotion
of impactful research



LOOP RESEARCH NETWORK

Our network
increases your
article's readership